SOME PROBLEMS IN NONLINEAR DIFFUSION

by G. P. Wood, B.Sc.

Thesis submitted to the University of Nottingham for the

Degree of Doctor of Philosophy, January 1996

Acknowledgments

I would like to thank my supervisor Prof. J. R. King for his help and support throughout my period of research. I would also like to thank my parents for their continued support, as well as my friends and colleagues in the Department of Theoretical Mechanics at Nottingham University. I am particularly grateful to John Ward for his assistance in the binding of this work.

Finally, special thanks to Anne Perkins for proof reading this thesis, and for her encouragement during my research.

I am grateful to the Engineering and Physical Science Research Council (formerly the Science and Engineering Research Council) for providing financial assistance for this work.

Contents

Abstract

In this thesis we investigate mathematical models for a number of topics in the field of nonlinear diffusion, using similarity, asymptotic and numerical methods and focussing on the time-asymptotic behaviour in most cases.

Firstly, we consider 'fast' diffusion in the vicinity of a mask-edge, with application to dopant diffusion into a semiconductor. A variety of approaches are used to determine concentration contours and aspect ratios.

Next we consider flow by curvature. Using group analysis, we determine a number of new symmetries for the governing equations in two and three dimensions. By tracking a moving front numerically, we also construct single and double spiral patterns (reminiscent of those observed in the Belousov-Zhabotinskii chemical reaction), and classify the types of behaviour that can occur. Finally, we analyse travelling wave solutions and the behaviour near to extinction for closed loops.

We next consider relaxation waves in a system that can be used to model target patterns, also observed in the Belousov-Zhabotinskii reaction. Numerical and asymptotic results are presented, and a number of new cases of front behaviour are obtained.

Finally, we investigate a number of systems using an approach based on the WKB method, analysing the motion of invasive fronts and also the form of the pattern left behind. For Fisher's equation, we demonstrate how modulated travelling waves can be obtained by prescribing an oscillatory initial profile. The method is then extended, firstly to Turing systems and then to oscillatory systems, for which we use an additional periodic plane wave argument to determine the unequal front and pattern speeds, as well as the periodicity. Finally, we illustrate how these methods apply to a recently-used 'chaotic' model from ecology.

Chapter 1

Introduction

In this thesis we investigate a number of related topics in the field of nonlinear diffusion. In each case, we present mathematical models of a physical situation generally involving reaction and diffusion terms, and demonstrate new solutions using a variety of methods summarised below. In obtaining solution forms, we have usually concentrated on the time-asymptotic (large time or extinction time) behaviour in each case.

The first problem, in Chapter 2, centres on so-called 'fast' diffusion of impurity atoms into a semiconductor substrate in the vicinity of the edge of a mask. Our aim is to track dopant concentration contours; in other models this is achieved by studying a moving interface, which is a case common to all of the problems studied in this thesis. We firstly show how the nonlinear model can be derived, and then consider a number of solution methods, including similarity formulations, asymptotic expansions and numerical approximations; these approaches form the basis of the whole thesis. In this particular case, we use a well-known model where the diffusivity of the dopant is given by c^m, where c is the concentration of dopant in the substrate and m is some constant. Behaviour for $m \geq 0$ is already well documented [31, 55, 45], so we look at $m < 0$ which introduces an extra problem in that there is no $c = 0$ interface (the diffusivity becomes infinite).

Chapters 3 and 4 also consider a travelling interface; here we look at an eikonal-curvature equation, which models the normal velocity of wave fronts as a linear speed with a curvature correction term and is often used as an approximation in reaction-diffusion problems. Chapter 3 investigates the case in which the wave speed is zero, in both

two and three dimensions, using similarity methods. This model also has applications in the theory of crystal growth [39]. In Chapter 4, we consider non-zero wave speeds, and demonstrate numerical solutions for spiral waves, which have been observed in a number of different contexts, in particular the Belousov-Zhabotinskii (BZ) reaction [58]. As well as the generation of single spirals, we also model numerically how symmetric 'double' spirals can form from an initially straight interface fixed at both ends, and how non-symmetric double spirals propagate from a single spiral whose 'free end' is clamped. How these spirals then interact when they collide with each other is examined in both cases to study the large-time behaviour.

Chapter 5 continues the flow-by-curvature theme, but this time we consider front motion governed by a more general function of curvature. Similarity forms and travelling wave forms are demonstrated, and behaviour near extinction is considered for a particular class of closed curves, which in particular gives rise to new shape-preserving solutions which can exist alongside the already-established collapsing circular [14] and ellipsoidal [44] solutions.

In Chapter 6 we consider a different approach to travelling fronts, this time working from the original partial differential equation system. For this chapter, we look at oscillatory solutions to the well-known two-variable system of FitzHugh [12] and Nagumo [41], which can be used when modelling target pattern formation, also observed in the BZ reaction [56] mentioned above. Other authors have previously considered these oscillatory patterns using different models [10, 49, 53, 50, 51, 52]; there has also been much general discussion of nonlinear wave propagation in one-dimensional oscillatory systems [35, 22, 42], although this has tended to consider the periodic behaviour *behind* the initial front – we will aim to consider the full problem, from the initial perturbation which creates the first front until the whole pattern is formed. As well as a one-dimensional model, we also briefly investigate the two-dimensional radial problem, and our main method of approach will be matched asymptotic expansions. We will show how the speed of the front can be calculated, and also demonstrate new behaviour where the form of the initial front can change. All of these results are confirmed by numerical calculations.

Chapter 7 introduces our final method, based on WKB theory. Using Fisher's equation [11] with a cubic reaction term (identical to the rescaled nonlinear kinetics in the FitzHugh-Nagumo model above), we show how we can predict new travelling wave behaviour for this well-known equation by prescribing a decaying oscillatory initial profile. Once again, we determine the wave speed of the front and the behaviour behind the front, and demonstrate that in a certain parameter range, modulated travelling waves are observed.

Chapter 8 extends the WKB-based method of the previous chapter to two-variable systems. In particular, we focus on Turing systems [48], showing how wave speeds and pattern type can be predicted in an analogous way to that for the Fisher equation above. These results agree with existing theory on Turing systems, although our method has a better foundation. It is can also be applied to non-Turing systems, and this is also demonstrated by discussing both non-oscillatory and oscillatory behaviour at the front and in the following 'pattern', together with an example of irregular wakes, recently obtained for two-variable systems with small perturbation initial conditions [46, 47].

We finish in Chapter 9 with some brief conclusions.

Chapter 2

Fast Diffusion Beneath a Mask-Edge

2.1 Introduction

Diffusion of an impurity into a semiconductor in the vicinity of a mask edge (see Figure 2.1) can, under appropriate simplifying assumptions, be described by the porous medium equation

$$c_t = \nabla.(c^m \nabla c), \tag{2.1}$$

subject to initial and boundary conditions dependent on the method by which the dopant is introduced; this can be (for example) by ion-implantation (where the total amount of dopant is fixed), or by diffusion from a surface source which can be modelled by imposing constant dopant concentration at the semiconductor surface (see Ghandhi [15]).

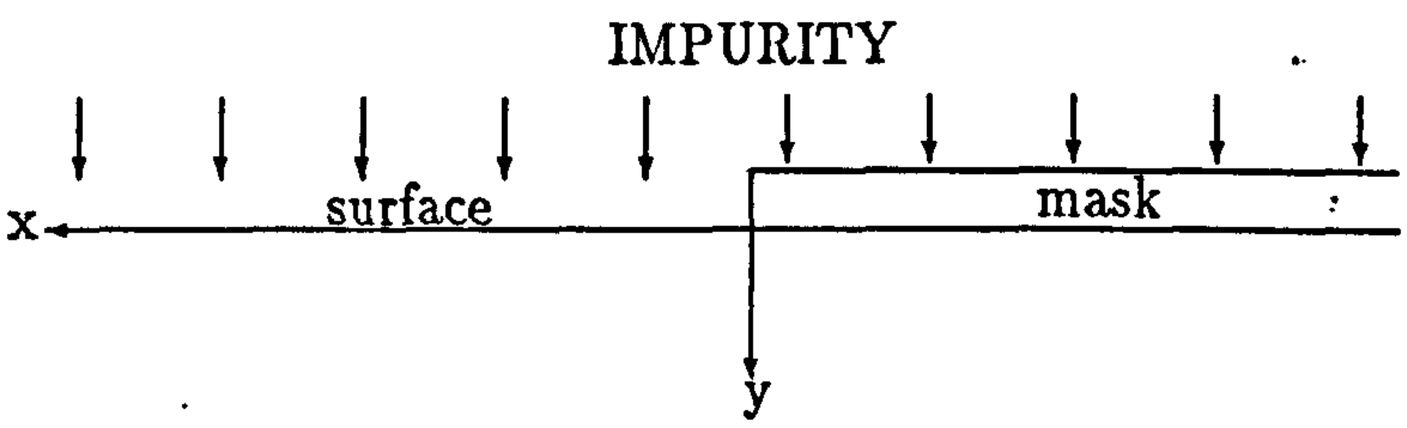

Figure 2.1: Mask-edge geometry.

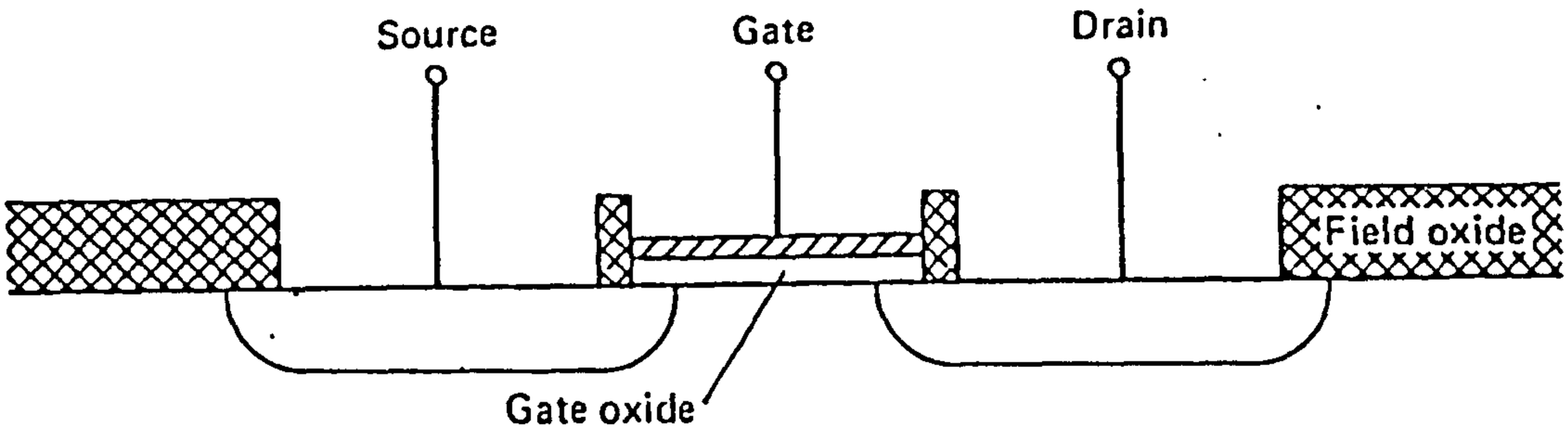

Figure 2.2: The source and drain of a MOSFET.

Solution of (2.1) can give a very reasonable model of, for example, the impurity distribution in creating both the source and the drain in a MOSFET (see Figure 2.2), a common device in VLSI circuits. It can be seen that dopant diffuses laterally under the mask in both the source and the drain; this is crucial in the design of the device, as it greatly affects the electrical behaviour, with current flowing from the source to the drain and passing under the masked region. Hence, the effective 'channel' length is of great interest to engineers.

Power-law diffusion falls into three categories, namely $m = 0$ (linear diffusion), $m > 0$ ('slow' diffusion) and $m < 0$ ('fast' diffusion). The first two cases are already fairly well documented in two dimensions; for linear diffusion, see (for example) Kennedy and O'Brien [31], and for slow diffusion, see Warner and Wilson [55] and Schwendeman [45]. We will consider the fast diffusion case, which is applicable to at least two different atomic mechanisms of semiconductor diffusion, which are detailed below.

2.1.1 Kick-out models

Substitutional-interstitial diffusion models, first proposed by Frank and Turnbull [13], suggest that a diffusing impurity atom can exist as either a *substitutional* atom s, occupying a lattice site, or as an *interstitial* atom i, occupying the 'gaps' between lattice sites. Diffusion occurs by the impurity atom becoming interstitial, and rapidly diffusing into the lattice until such a situation occurs as it can become substitutional. Several methods for this changeover have been suggested; initially a dissociative mechanism was used [13], but we will be interested in the later 'kick-out' model, proposed by Gösele

and Morehead [16], which suggests that the interstitial impurity atoms force host lattice atoms into interstitial sites to create self-interstitials I, the impurity atom thereby becoming substitutional. This can be represented by the equilibrium reaction

$$i \rightleftharpoons s + I, \tag{2.2}$$

assuming that all species are electrically neutral, and hence we have the algebraic equation

$$i = k\, s\, I, \tag{2.3}$$

which is the equilibrium condition; k is simply a rate constant. As the substitutional impurity atoms are immobile, diffusion is represented by the equations

$$\frac{\partial}{\partial t}(s + i) = D_i \nabla^2 i \tag{2.4}$$

$$\frac{\partial}{\partial t}(I - s) = D_I \nabla^2 I, \tag{2.5}$$

where D_i and D_I represent the relevant diffusivities. However, it is typically found in practice that $s \gg i, I$, so that (2.4) and (2.5) become

$$\begin{aligned} \frac{\partial s}{\partial t} &= D_i \nabla^2 i \\ -\frac{\partial s}{\partial t} &= D_I \nabla^2 I. \end{aligned}$$

By adding the above, we can thus produce the equation

$$\nabla^2 (D_i i + D_I I) = 0. \tag{2.6}$$

The boundary conditions are shown in the diagram below. The conditions for the

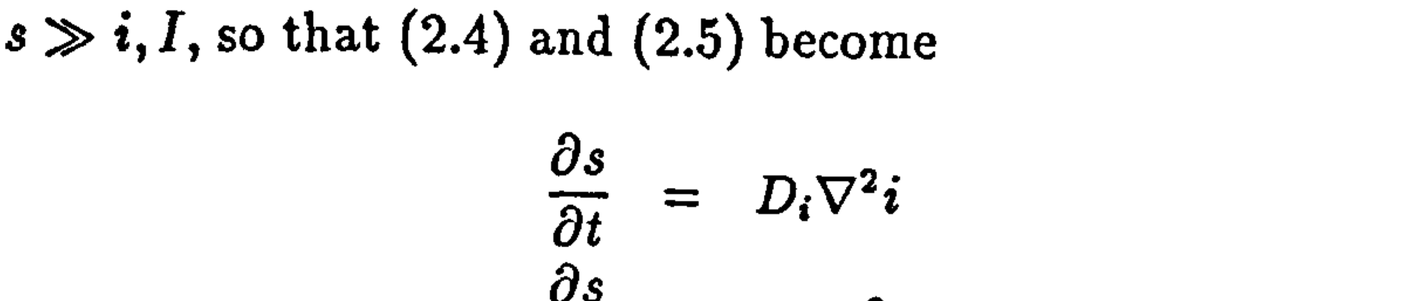

Figure 2.3: Boundary conditions for the kick-out model (surface source case).

impurity interstitials are those usually adopted, but the supposition that $I_y = 0$ is only

true if the mask is impervious to defects (this can be achieved using a nitride rather than an oxide mask); this condition is required if we are to solve (2.6) as a decoupled problem. We then obtain

$$D_i\, i + D_I\, I = D_i\, i^* + D_I\, I^*$$

and thus, substituting for (2.3) and rearranging, we have

$$I = \frac{D_i\, i^* + D_I\, I^*}{D_I + k\, D_i s}.$$

Substituting this into (2.5) (with $s \gg I$) implies that

$$\frac{\partial s}{\partial t} = -D_I\,(D_i\, i^* + D_I\, I^*)\nabla^2 \left(\frac{1}{D_I + k\, D_i s}\right)$$

and by defining

$$\begin{aligned} \varepsilon &= D_I/(k\, D_i) \\ D &= \varepsilon\,(D_i\, i^* + D_I\, I^*) \\ s &= u - \varepsilon \end{aligned}$$

we obtain

$$\frac{\partial u}{\partial t} = D\,\nabla.(u^{-2}\nabla u) \tag{2.7}$$

which is of the required form; D is a constant and ε can be interpreted as the background concentration – this is useful in later work. Equation (2.7) was derived assuming no electrical effects; by including these the power-law exponent (-2) is altered (usually being of smaller magnitude), but the equation remains of the same form.

2.1.2 Clustering models

At high concentrations of dopant in silicon, the diffusivity tends to level off as the concentration increases; this can be interpreted as being due to the formation of clusters of dopant atoms, which are immobile (see King [33]). A cluster (C) can be defined as a group of m dopant atoms (A), and thus the clustering reaction is

$$mA \rightleftharpoons C. \tag{2.8}$$

We define $u = [A]$ and $u_C = [C]$, with the square brackets denoting concentrations in the usual way; the equilibrium condition is then

$$u_C = ku^m,$$

where $m > 1$ and the diffusion is governed by

$$\frac{\partial}{\partial t}(u + ku^m) = D\nabla^2 u, \tag{2.9}$$

where D is again the diffusivity. However, we are only concerned here with high concentrations, and so

$$\frac{\partial}{\partial t}(u^m) \sim \frac{D}{k}\nabla^2 u$$

and thus by defining $u = w^{1/m}$, and rescaling, we obtain

$$\frac{\partial w}{\partial t} = \nabla.(w^{(1-m)/m}\nabla w), \tag{2.10}$$

which is again a power-law diffusion equation; this time we can see that

$$-1 < \frac{1-m}{m} < 0.$$

To determine new results for (2.1), we will consider a separable similarity formulation (instantaneous and constant source cases), a power series solution (instantaneous source), full numerical solutions on a finite domain (both cases), and asymptotic behaviour as some background concentration tends to zero (constant source).

2.2 Similarity Solutions

2.2.1 Radially Symmetric Solution (instantaneous source)

Before considering the mask-edge problem, we illustrate some relevant features of fast nonlinear diffusion by noting similarity solutions to the radially symmetric problem.

The radially symmetric form of (2.1) is

$$\frac{\partial c}{\partial t} = \frac{1}{r^{N-1}}\frac{\partial}{\partial r}\left(r^{N-1}c^m\frac{\partial c}{\partial r}\right) \tag{2.11}$$

and, for an instantaneous source, the total mass Q given by

$$Q = \int_0^\infty r^{N-1}c\,dr \tag{2.12}$$

is constant. In terms of the mask-edge problem, the solution for $N = 1$ will give the behaviour as $x \to +\infty$ in the implant case. Looking for a solution of the form (see King [34])

$$c = t^{-N/(mN+2)} f(\eta), \tag{2.13}$$

where

$$\eta = \frac{r}{t^{1/(mN+2)}}$$

then we have

$$Q = \int_0^\infty \eta^{N-1} f \, d\eta \tag{2.14}$$

and

$$(mN+2)\,\eta^{N-1} f^m f' + \eta^N f = \text{constant} \tag{2.15}$$

on substituting (2.13) into (2.11) and (2.12). Imposing the boundary conditions

$$f \to 0 \qquad \text{as } \eta \to \infty \tag{2.16}$$

$$\eta^{N-1} f^m f' = 0 \qquad \text{at } \eta = 0, \tag{2.17}$$

we arrive at either $f = 0$ or

$$f = \gamma e^{-\eta^2/4} \qquad m = 0 \tag{2.18}$$

$$f = \left(\frac{m(\gamma - \eta^2)}{2(mN+2)}\right)^{1/m} \qquad m \neq 0, \tag{2.19}$$

where γ is a constant determined from the mass integral (2.14). This tells us that we require $mN + 2 > 0$ and the solution relevant to the fast diffusion case is

$$c = t^{-N/(mN+2)} \left\{ \frac{-m}{2(mN+2)} \left[a^2 + \left(\frac{r}{t^{1/(mN+2)}} \right)^2 \right] \right\}^{1/m} \qquad -2/N < m < 0, \tag{2.20}$$

where $\gamma = -a^2$. As we shall see, the mask-edge problem also requires that m be sufficiently large in order for a solution to the zero background concentration problem to exist. The mask-edge problem has some one-dimensional and some two-dimensional features, so we may expect the critical value of m to satisfy

$$-2 < m < -1.$$

2.2.2 Far-field Behaviour

The first similarity approach we apply to the mask-edge problem describes the far-field. It is applicable to both the implant and surface source problems (not just the instantaneous source problem in (2.20)), provided that a solution exists.

If we rewrite (2.1) by introducing

$$c = v^{1/m},$$

so that

$$v_t = v\nabla^2 v + \tfrac{1}{m}|\nabla v|^2,$$

and seek a solution of the form

$$v = \frac{r^2}{t}\,G(\theta), \tag{2.21}$$

we obtain

$$G\,G'' + \tfrac{1}{m}G'^2 + 4\left(1+\tfrac{1}{m}\right)G^2 + G = 0. \tag{2.22}$$

The boundary conditions on (2.22) are determined by considering $\theta \to 0^+$, where we must match into the one-dimensional behaviour

$$c \sim \left[\frac{m}{2(m+2)}\,\frac{y^2}{t}\right]^{1/m} \qquad \text{as } y \to +\infty,\ x \to +\infty.$$

which in radial co-ordinates reads

$$c \sim \left[\frac{m}{2(m+2)}\,\frac{(r\sin\theta)^2}{t}\right]^{1/m} \qquad \text{as } r \to +\infty,\ \theta \to 0. \tag{2.23}$$

This implies boundary conditions of

$$G \sim \frac{m\,\theta^2}{2(m+2)} \qquad \text{as } \theta \to 0, \tag{2.24}$$

$$G' = 0 \qquad \text{on } \theta = \phi. \tag{2.25}$$

In the second of these conditions ϕ denotes the angle between the open semiconductor surface and the surface under the mask ($\phi = \pi$ in practice but it is instructive to consider the behaviour for arbitrary angle ϕ). We start with a special case in which (2.22) is readily solved exactly.

For $m = -1$, equation (2.22) reads

$$G\,G'' - G'^2 + G = 0. \tag{2.26}$$

Substituting $G = e^H$, (2.26) becomes

$$H'' + e^{-H} = 0,$$

which can be integrated to give

$$H'^2 = 2\,e^{-H} - K_1^2,$$

where K_1 is a constant. Reverting back to $G(\theta)$ and integrating, we obtain

$$G = \frac{1}{K_1^2}(1 - \cos K_1(K_2 - \theta)),$$

where K_2 is another constant. Applying $G(0) = 0$ and $G'(\phi) = 0$ implies

$$\begin{aligned} K_1 &= (2n_1 + n_2)\left(\frac{\pi}{\phi}\right) \\ K_2 &= \frac{2n_1}{2n_1 + n_2}\phi, \end{aligned}$$

where $n_1, n_2 = 0, 1, 2\ldots$. For the correct behaviour as $G \to 0$, we must have $K_2 = 0$, so that $n_1 = 0$. We also require $G(\theta)$ to be monotone increasing in the range $(0, \phi)$, and this fixes $n_2 = 1$. Our solution for G is thus

$$G = \left(\frac{\phi}{\pi}\right)^2 \left[1 - \cos\left(\frac{\pi}{\phi}\right)\theta\right]. \tag{2.27}$$

For $\phi = \pi$ this is simply

$$G = 1 - \cos\theta,$$

which will be useful later to compare with the numerical results.

More generally, (2.22) can be rewritten as

$$(G^{(m+1)/m})'' + 4\left(\frac{m+1}{m}\right)^2 G^{(m+1)/m} + \left(\frac{m+1}{m}\right) G^{1/m} = 0, \tag{2.28}$$

which can be integrated to give

$$\frac{\mathrm{d}G}{\mathrm{d}\theta} = \left(k\,G^{-2/m} - \frac{2\,m}{2+m}G - 4G^2\right)^{1/2}, \tag{2.29}$$

where k is an arbitrary constant of integration.

There is a further special case where we can integrate (2.29) a second time. For $m = -4/3$, the substitution $F = G^{1/2}$ transforms (2.29) to

$$\frac{\mathrm{d}F}{\mathrm{d}\theta} = \left(1 + \frac{k}{4}F - F^2\right)^{1/2},$$

which has the solution

$$F = \frac{k}{8} - \left[\left(\frac{k}{8}\right)^2 + 1\right]^{1/2} \sin(k_2 - \theta),$$

where k_2 is a second constant of integration. The boundary conditions (2.24) and (2.25) give us

$$\frac{k}{8} = \left[\left(\frac{k}{8}\right)^2 + 1\right]^{1/2} \sin k_2$$

and

$$\frac{k}{8} = -\cot\phi$$

and hence we arrive at the solution

$$G = [\sin\theta - \cot\phi(1 - \cos\theta)]^2. \tag{2.30}$$

This solution holds for all values of $\phi < \pi$; it first fails to exist at $\phi_c = \pi$, which is the critical angle for $m = -4/3$. This also suggests that for $\phi = \pi$, we can only find separable (similarity) solutions of this form for $-4/3 < m < 0$; we will expand upon this later.

2.2.2.1 The numerical solution

To produce a general numerical solution, we return to equation (2.29). By satisfying the boundary condition $G'(\phi) = 0$, we can obtain

$$k = 2\,G^{1+2/m}(\phi)\left(2G(\phi) + \frac{m}{2+m}\right)$$

and we now have a two-point boundary value problem for $G(\theta)$, which we can solve numerically using a shooting method for values of m in the range $-4/3 < m < 0$. We find that the numerical result for $m = -1$ shows good agreement with the analytical result given earlier, and that $G(\pi) \to \infty$ as $m \to -4/3$, as expected. Sample results are

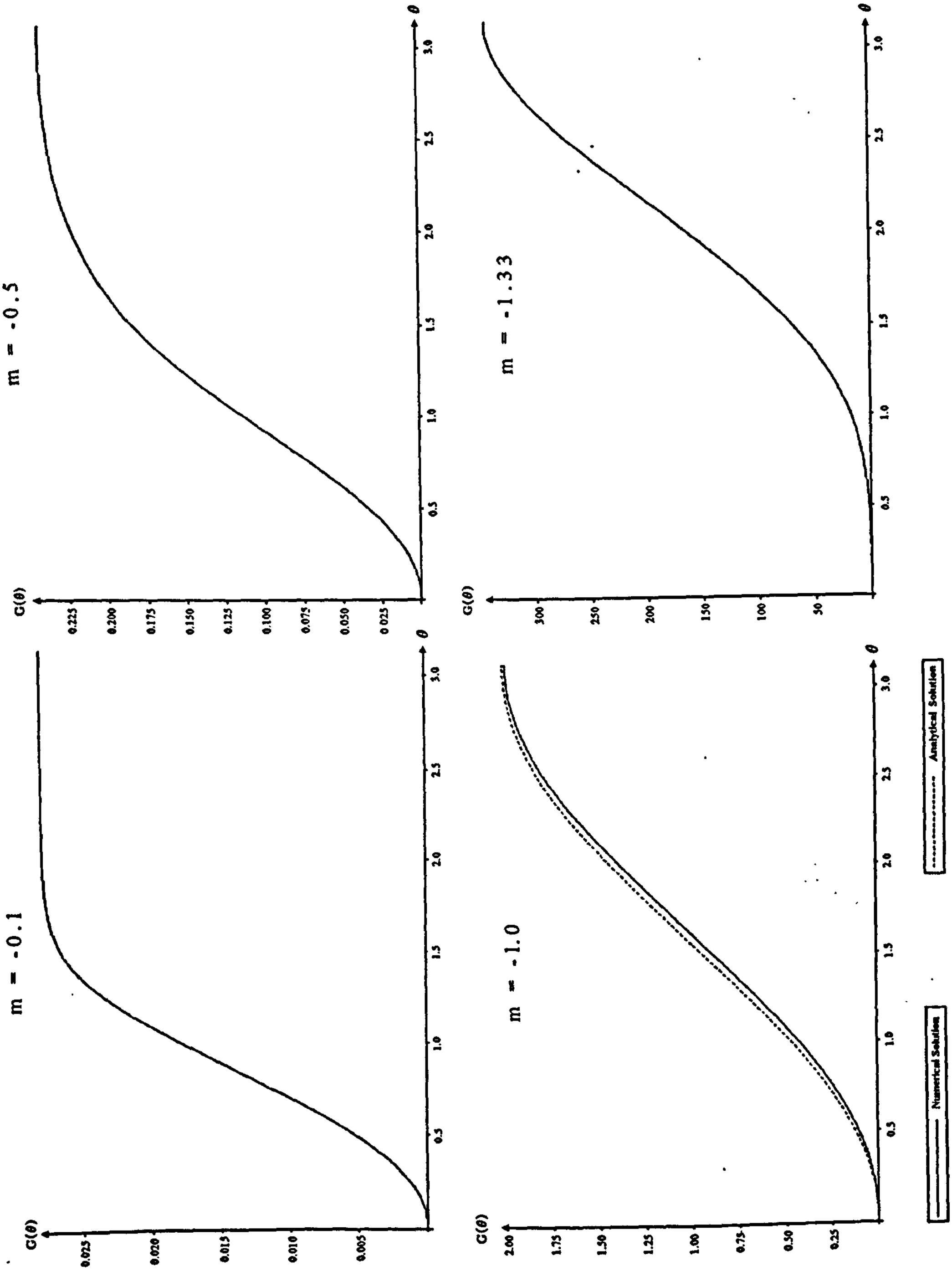

Figure 2.4: Numerical solutions for $G(\theta)$, and a comparison with the analytical result for $m = -1$.

shown below in Figure 2.4, with the analytical result obtained earlier for $m = -1$ shown to indicate their accuracy.

From these results, we can evaluate the concentration c in the far-field, and produce contour plots of the dopant diffusion at particular times for various values of m; these are illustrated in Figure 2.5.

2.2.2.2 Asymptotic Analysis

We can also proceed with an asymptotic analysis of (2.29) with $G'(\phi) = 0$ for some general angle ϕ, and try to determine the critical angle $\phi = \phi_c$ where a solution first fails to exist.

From the numerical solutions to (2.29), it is found that

$$G(\phi) \to \infty \qquad \text{as} \qquad \phi \to \phi_c \qquad \text{if and only if } m < -1.$$

Thus, to apply $G'(\phi) = 0$ near $\phi = \phi_c$, we obtain the asymptotic balance

$$kG^{-\frac{2}{m}} \sim G^2,$$

which implies that $k \to \infty$, so that

$$\frac{\mathrm{d}G}{\mathrm{d}\theta} = \left(kG^{-2/m} - 4G^2\right)^{1/2}.$$

On substituting

$$G = u^{m/(2(m+1))}$$

we obtain

$$\frac{m}{2(m+1)}\frac{\mathrm{d}u}{\mathrm{d}\theta} = u^{1/2}(k - 4u)^{1/2},$$

which can be integrated to give

$$\frac{m}{2(m+1)}\tan^{-1}\sqrt{\frac{4u}{k-4u}} = \theta - \theta_0,$$

where θ_0 is an arbitrary constant. Substituting back for G, and noting that $G = 0$ on $\theta = 0$ requires $\theta_0 = 0$, we obtain

$$G = \left(\frac{k}{4}\right)^{m/2(m+1)} \sin^{m/(m+1)}\left(\frac{2}{m}(m+1)\theta\right). \tag{2.31}$$

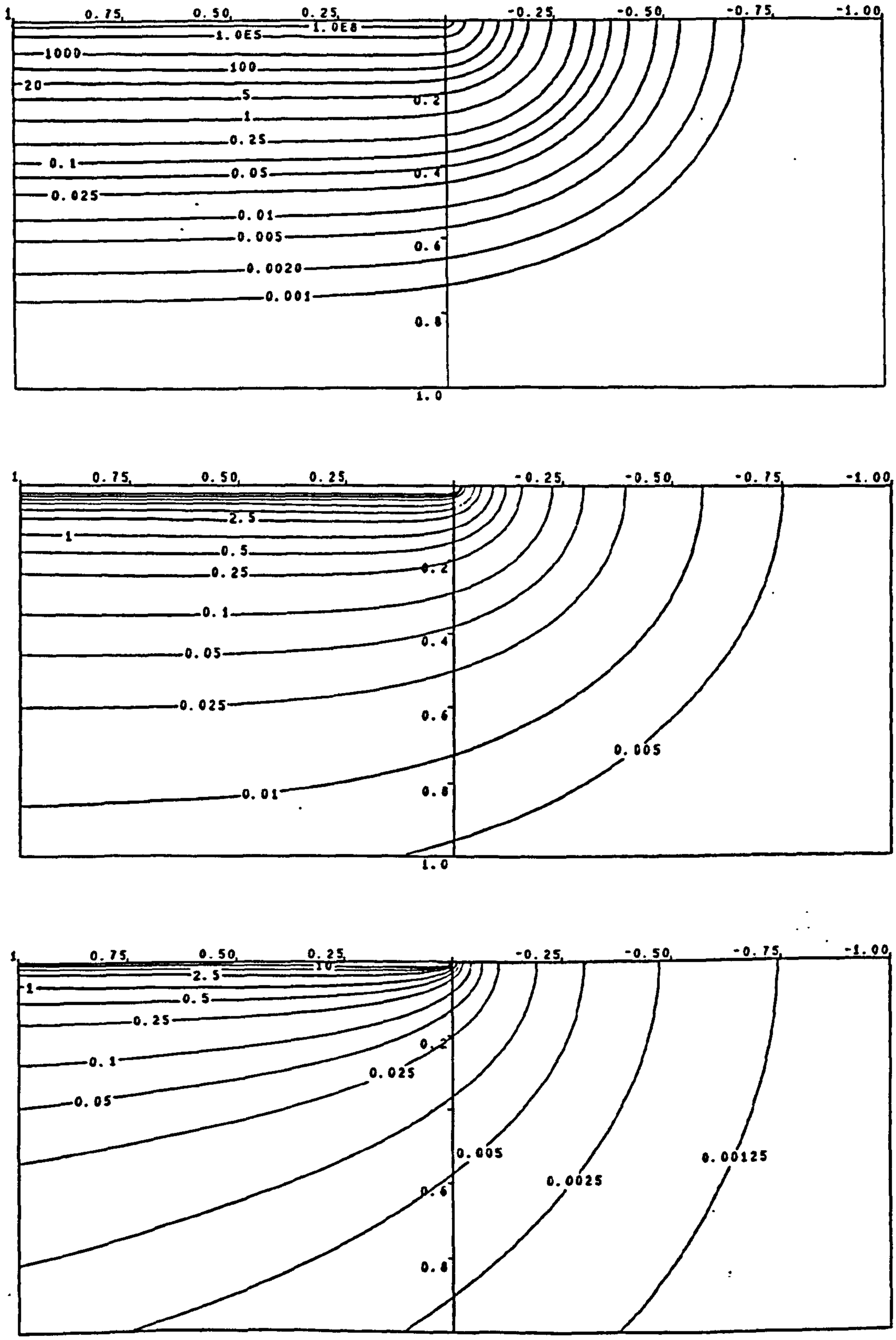

Figure 2.5: Similarity solution contour plots for $m = -0.3$ (top), $m = -0.8$ (centre) and $m = -1.3$ (bottom).

Applying the no-flux boundary condition on $\theta = \phi$, we have

$$0 = 2\left(\frac{k}{4}\right)^{m/2(m+1)} \cos\left(\frac{2}{m}(m+1)\,\phi\right) \sin^{-1/(m+1)}\left(\frac{2}{m}(m+1)\,\phi\right)$$

and hence, to avoid $G(\phi) = 0$, we must have

$$\cos\left(\tfrac{2}{m}(m+1)\phi\right) = 0$$

and thus the critical value of ϕ is given by

$$\phi_c = \frac{m\,\pi}{4\,(m+1)}. \tag{2.32}$$

This expression is valid for $m < -8/7$, since we require $0 < \phi_c < 2\,\pi$ for a meaningful solution. It is worth noting that for $m = -2$ we have $\phi_c = \pi/2$, which corresponds to 1-D diffusion. These solutions can also be obtained from the numerical integration of (2.29); once again, we find that the results obtained are in good agreement.

2.3 Power Series Solutions

2.3.1 Formulation

For this type of solution to the instantaneous source problem, we will initially follow the method of Schwendeman [45], and adapt it for the fast diffusion case.

If we look to solve (2.1) with the co-ordinate system shown in Figure 2.1 using the similarity variables

$$\xi = x/t^{1/(m+2)} \qquad \eta = y/t^{1/(m+2)},$$

where

$$c = t^{-1/(m+2)}\, f(\xi, \eta),$$

then we have, on substitution,

$$-\tfrac{1}{m+2}(f + \xi f_\xi + \eta f_\eta) = \nabla.(f^m \nabla f). \tag{2.33}$$

For $-2 < m < 0$, we let

$$u = \frac{m+2}{-m}\, f^m \tag{2.34}$$

to give

$$mu\nabla^2 u + |\nabla u|^2 = mu + \xi u_\xi + \eta u_\eta. \tag{2.35}$$

From the similarity solutions obtained earlier (see 2.20), we have (with $a = 1$)

$$c \to t^{-1/(m+2)} \left[\tfrac{-m}{2(m+2)}(1+\eta^2)\right]^{1/m} \qquad \text{as } \xi \to +\infty,$$

which gives us our first boundary condition for (2.35) :

$$u \sim \tfrac{1}{2}(1+\eta^2) \qquad \text{as } \xi \to +\infty. \tag{2.36}$$

As we can have no diffusion at the semiconductor surface ($c_y = 0$ on $y = 0$ in x-y co-ordinates), then we have

$$u_\eta = 0 \qquad \text{on } \eta = 0. \tag{2.37}$$

The concentration of dopant underneath the mask will be negligible far away from the semiconductor surface; this implies that

$$u \to \infty \qquad \text{as } \xi \to -\infty\ ,\ \eta \to +\infty. \tag{2.38}$$

2.3.2 The Power Series

We now seek a power series solution to (2.35) of the form

$$u = \sum_{k=0}^{\infty} A_k(\xi)\,\eta^{2k} \tag{2.39}$$

with the odd powers of η excluded in order to satisfy (2.37). (2.36) implies that

$$A_k \to \left\{ \begin{array}{ll} \frac{1}{2} & \text{if } k = 0,\ 1 \\ 0 & \text{otherwise} \end{array} \right\} \quad \text{as } \xi \to +\infty \tag{2.40}$$

whilst (2.38) tells us that

$$A_0(-\infty) \to +\infty. \tag{2.41}$$

To interpret this with regards to a numerical solution of (2.35), we note from the separable solution that

$$\begin{aligned} u \sim \tfrac{(m+2)}{-m} t^{\frac{-2}{m+2}} r^2 G(\theta) &= \tfrac{(m+2)}{-m}(\xi^2+\eta^2)\, G\left(\pi - \tan^{-1}\tfrac{\eta}{\xi}\right) \\ &\sim \tfrac{(m+2)}{-m}(\xi^2+\eta^2)\, G\left(\pi - \tfrac{\eta}{\xi}\right) \\ &= \tfrac{(m+2)}{-m}(\xi^2+\eta^2)\left(G(\pi) + \tfrac{1}{2}G''(\pi)\tfrac{\eta^2}{\xi^2} + \ldots\right) \quad \text{as } \xi \to -\infty \end{aligned}$$

so that

$$A_0 \sim \tfrac{(m+2)}{-m} G(\pi)\,\xi^2 \quad \text{as} \quad \xi \to -\infty \tag{2.42}$$

and thus we take

$$\left.\begin{aligned} A_0(\xi_0) &= \alpha\,\xi_0^2 \\ A_0'(\xi_0) &= 2\alpha\,\xi_0 \\ A_1'(\xi_0) &= 0 \end{aligned}\right\} \text{ as } \xi_0 \to -\infty \tag{2.43}$$

as our boundary conditions, with α being an unknown parameter.

Substituting (2.39) into (2.35), and comparing the coefficients of the powers of η^2, we have

$$A_0'' = \frac{A_0'}{m\,A_0}(\xi - A_0') - 2\,A_1 + 1, \tag{2.44}$$

$$A_1'' = \frac{1}{m\,A_0}[(2+m)\,A_1 - m\,A_0''A_1 - 2\,(2+m)\,A_1^2 + (\xi - 2\,A_0')\,A_1'] - 12\,A_2. \tag{2.45}$$

To solve for a finite number of terms, we suppose that $A_k \equiv A_k(+\infty)$ for some $k = \overline{k}$ to give $\overline{k}$ coupled second order ordinary differential equations. We will only be concerned here with one- and two-term expansions.

2.3.3 Solutions

For a one-term solution, we have $A_1 = A_1(+\infty) = \frac{1}{2}$, and thus solve

$$A_0'' = \frac{A_0'}{mA_0}(\xi - A_0') \tag{2.46}$$

in the range $[-\xi_0, +\xi_0]$ where ξ_0 is a constant taken sufficiently large. This is again achieved numerically using a shooting method, and an example plot of the solution for $A_0(\xi)$ is shown in Figure 2.6.

We can similarly solve (2.44) and (2.45) for a two-term expansion with $A_2 = 0$; this tends to be more awkward, as the boundary conditions now contain very large *and* very small numbers (see (2.43)). Nevertheless, we obtain the results shown in Figure 2.6, and find that solutions can be obtained in the range $-1.3 < m < 0$, which is roughly the same range as for the similarity solution; we would expect the lower critical value to

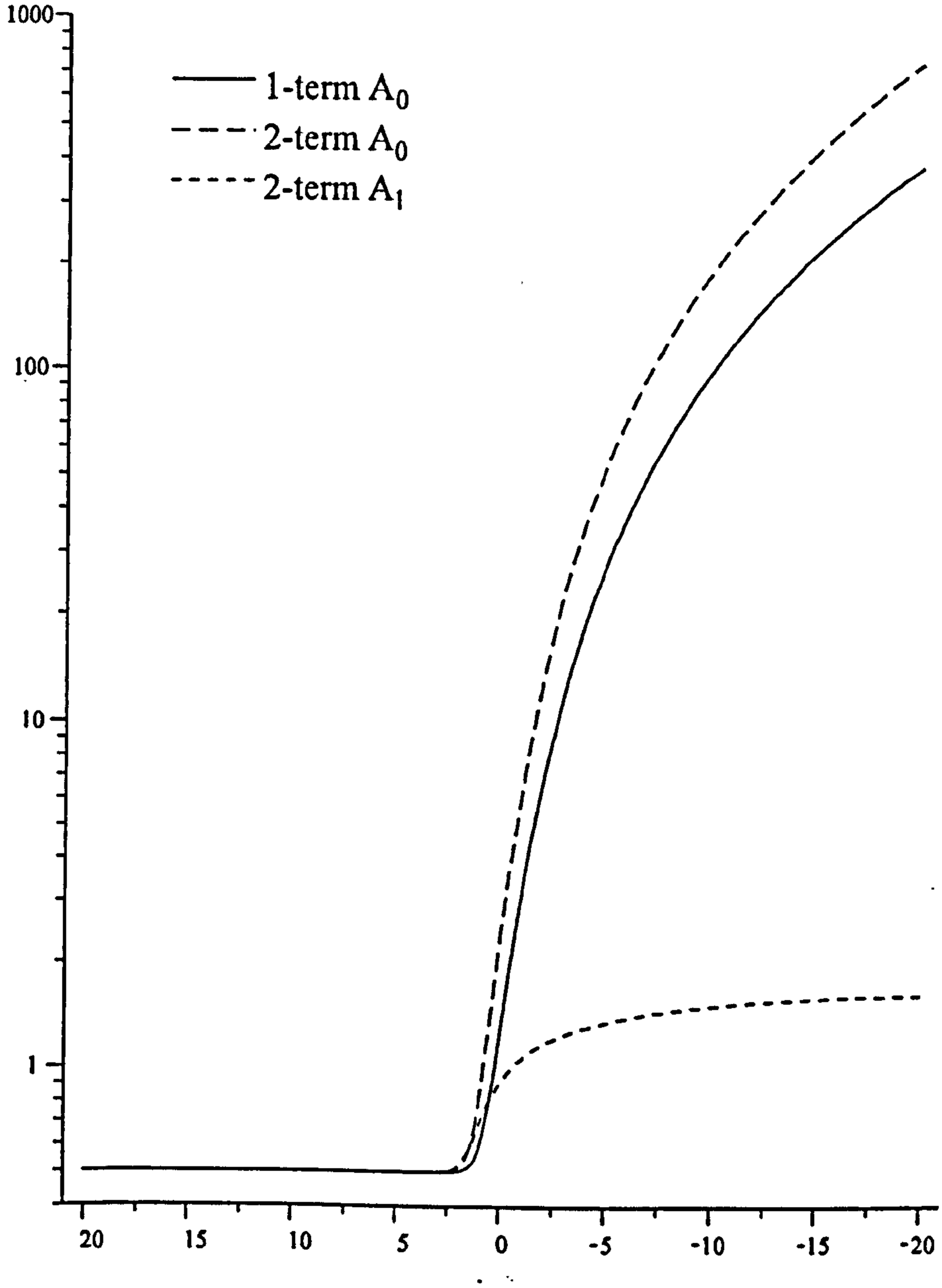

Figure 2.6: One and two-term solutions for $A_0(\xi)$ and $A_1(\xi)$ ($\dot{m} = -0.9$).

approach $-4/3$ as we included more terms in the power series expansion. It can be seen that A_1 is constant as $\xi \to -\infty$ and fairly constant as $\xi \to +\infty$ (numerical difficulties prevented solving on an increased range of ξ; this would be expected to give a more constant behaviour for $A_1(\xi)$ as $\xi \to +\infty$). There is a sharp change in value of $A_1(\xi)$ around $\xi = 0$, but this is still small in comparison with the change in A_0. We can also compare values of α obtained from the numerical solution with those of $G(\pi)$, noting that

$$\alpha \sim \frac{m+2}{-m} G(\pi)$$

from (2.42) and (2.43); this shown in Table 2.1, and it can be seen that we have fairly

m	$\frac{m+2}{-m}G(\pi)$	α	
		1-term	2-term
-0.1	0.528	0.527	0.530
-0.3	0.606	0.589	0.614
-0.5	0.735	0.668	0.755
-0.7	0.965	0.771	1.060
-0.9	1.523	0.910	1.860
-1.1	3.080	1.115	5.586
-1.3	36.56	1.432	—

Table 2.1: Comparison of values of $G(\pi)$ and α.

good agreement for small negative m; the values for more negative m can be seen to diverge from the $G(\pi)$ value, but the two-term solution *is* closer.

If we use these results to produce contour plots for the concentration c, we see that a kink develops in the contours at large η for the two-term expansion (see Figure 2.8 and especially Figure 2.10) which is more pronounced as m becomes more negative – this does not feature in the plots for the one-term solution (Figures 2.7 and 2.9). However, the two-term results should be expected to be more accurate than the one-term solutions at least close to the surface. This will be borne out when we consider aspect ratios in the following section; we thus conclude that this method is more suited to analysis of

the region just beneath the semiconductor surface, preferably with small negative m.

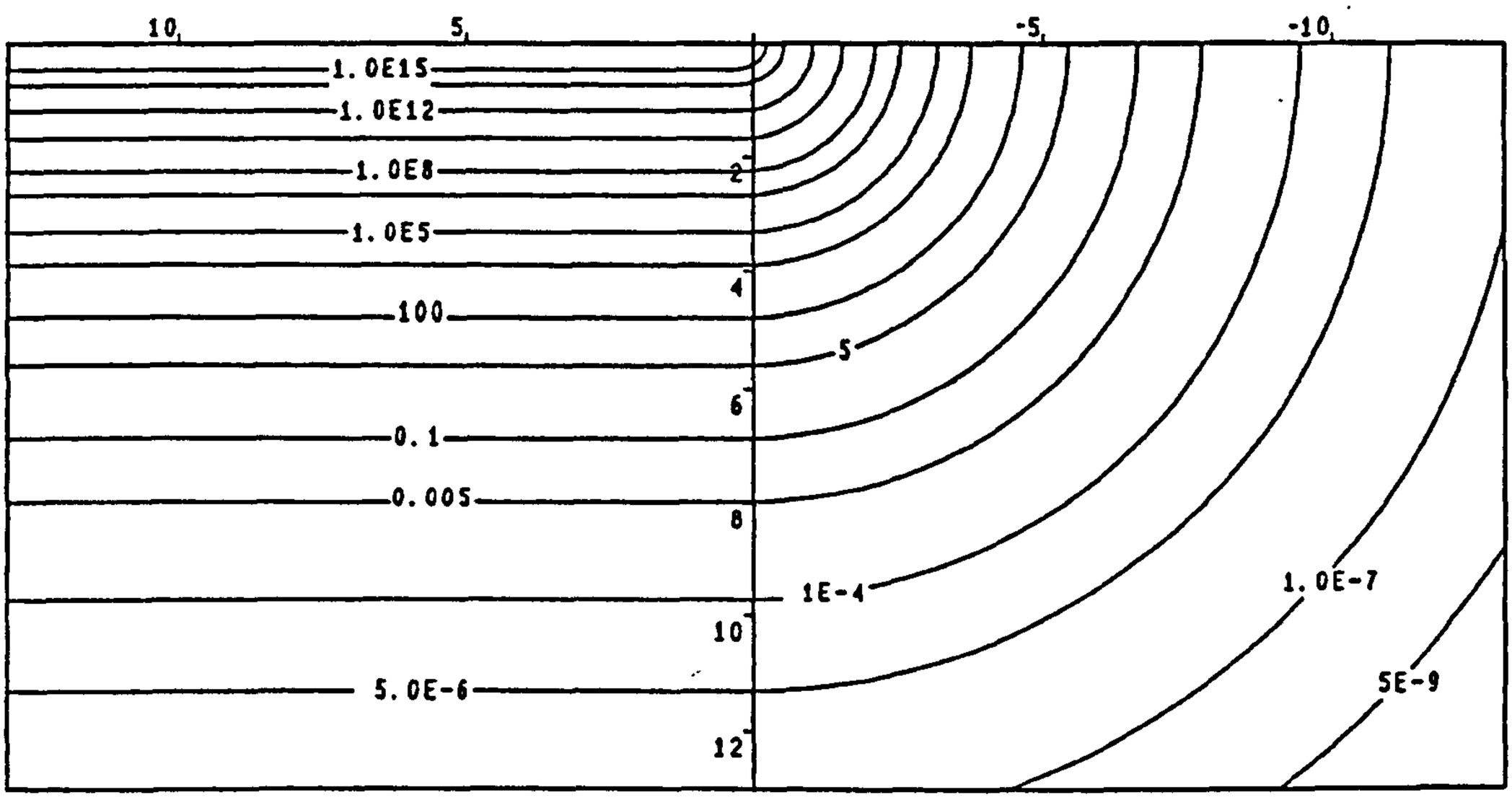

Figure 2.7: One-term solution for c; $m = -0.1$.

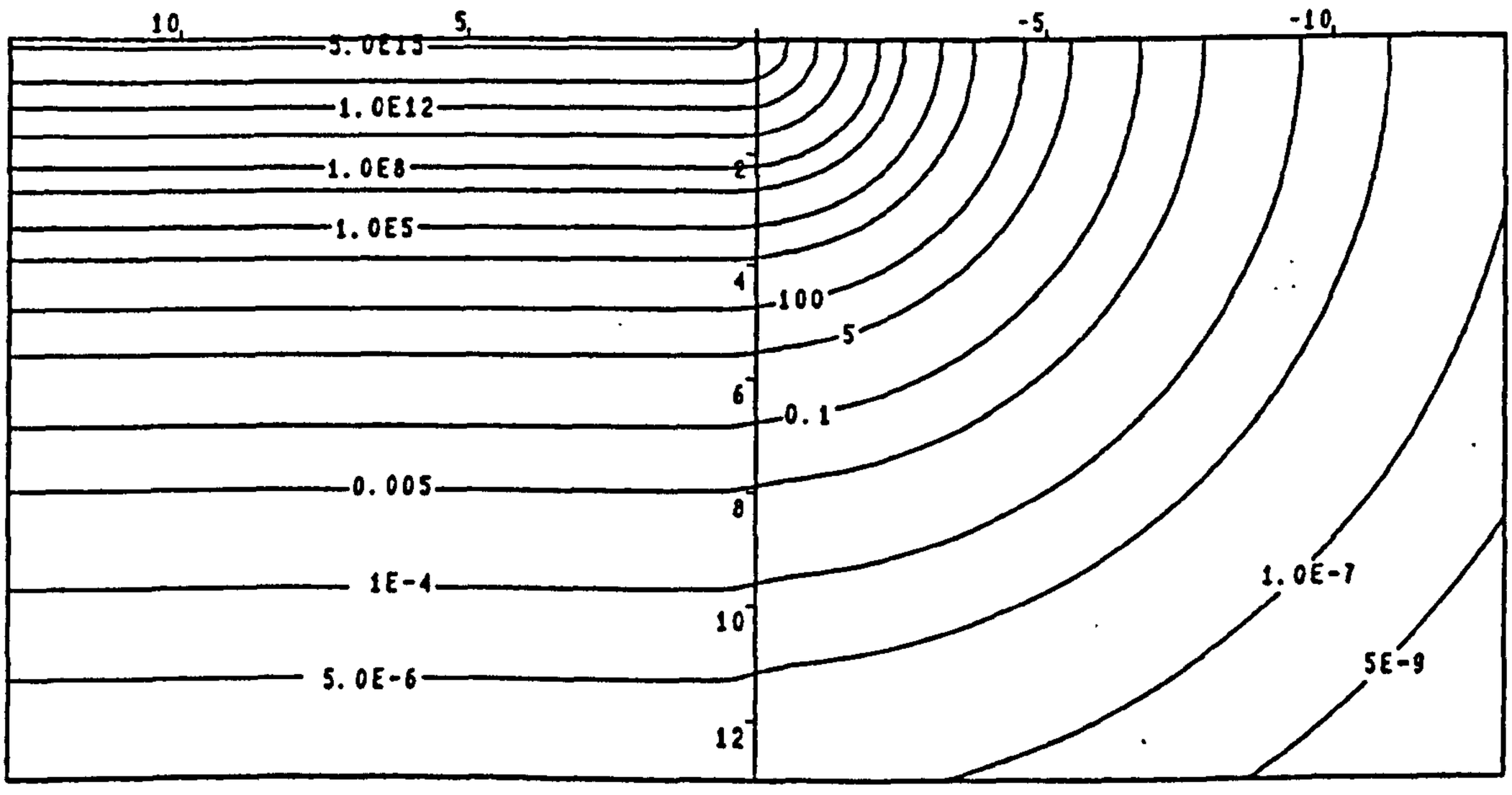

Figure 2.8: Two-term solution for c; $m = -0.1$.

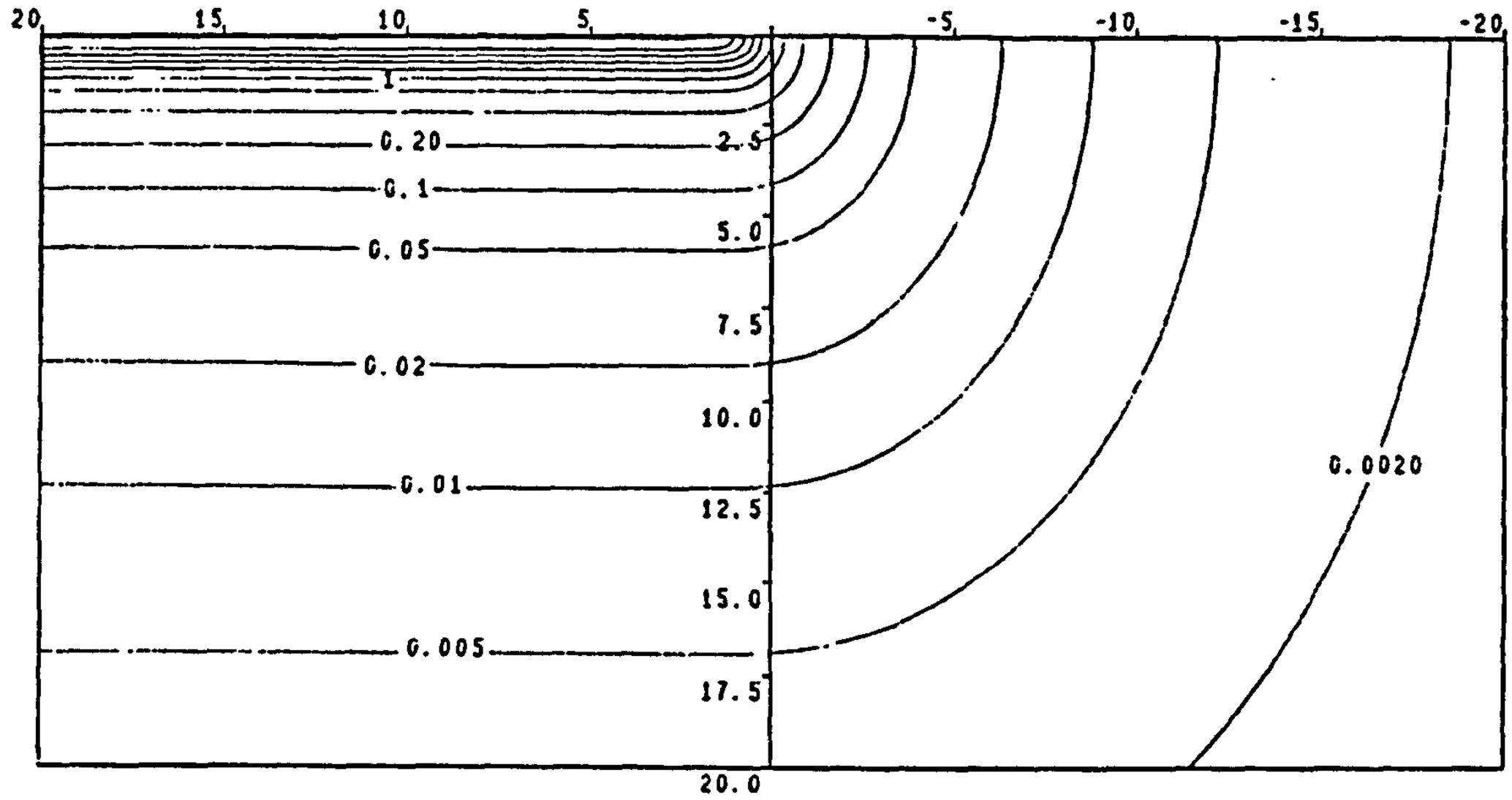

Figure 2.9: One-term solution for c; $m = -0.9$.

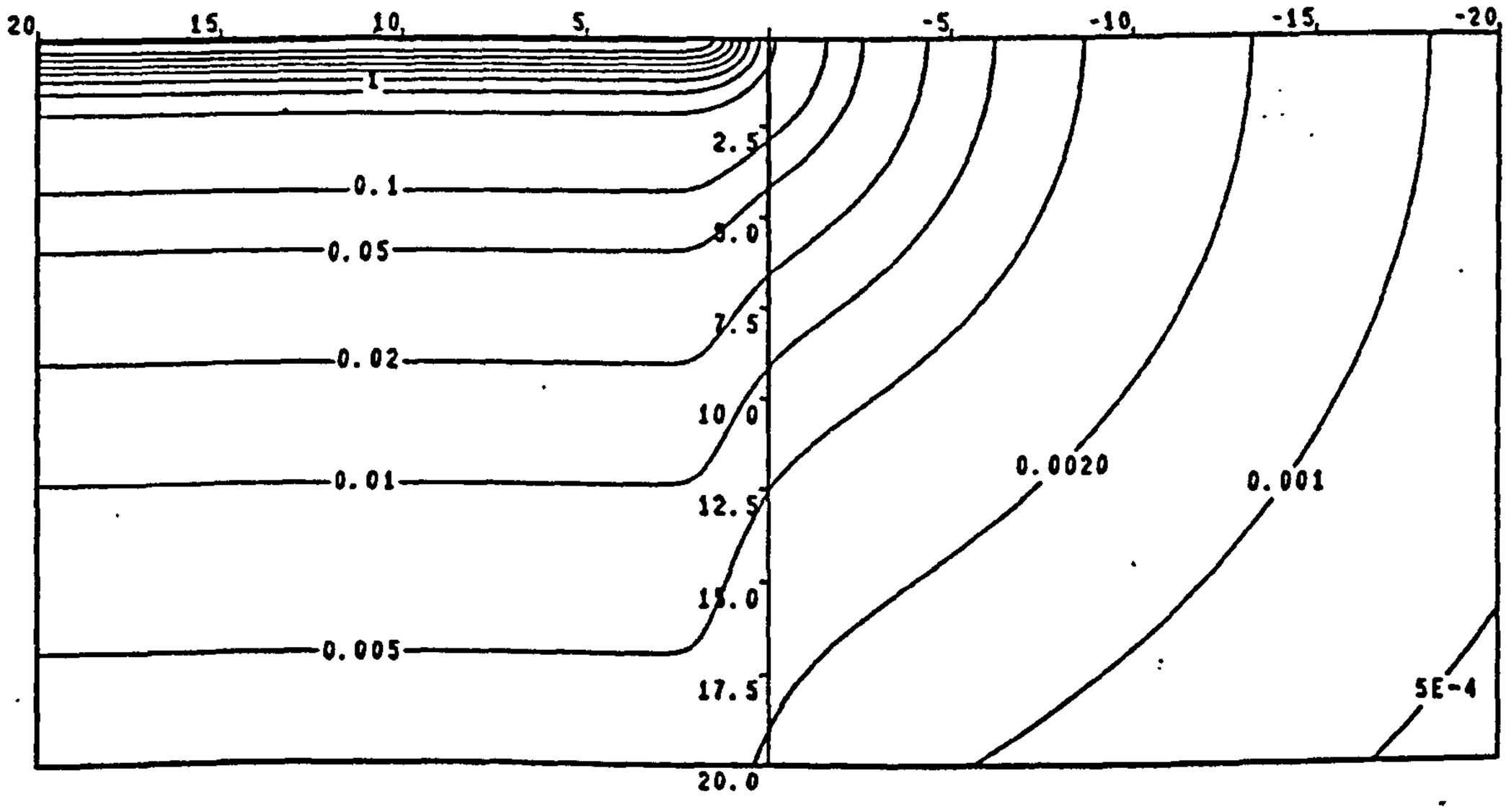

Figure 2.10: Two-term solution for c; $m = -0.9$.

2.4 A Numerical Model

We note that we can rewrite the porous medium equation as

$$c_t = \tfrac{1}{1+m}\nabla^2 c^{1+m}, \tag{2.47}$$

which is easier to discretize. We now consider the problem for the two sets of initial and boundary conditions mentioned above, according to the co-ordinate system shown in Figure 2.1.

2.4.1 Constant Source Solutions

If we consider the constant source case first, then our boundary conditions are

$$\begin{aligned} c &= 0 \quad \text{at} \quad t = 0 \\ c &= c_0 \quad \text{on} \quad y = 0 \quad x \geq 0 \\ c_y &= 0 \quad \text{on} \quad y = 0 \quad x < 0 \\ c_x &= 0 \quad \text{as} \quad x \to +\infty \\ c &\to 0 \quad \text{as} \quad y \to \infty \quad x \to -\infty \end{aligned} \tag{2.48}$$

with the mask located along $y = 0$ for the section $x < 0$, where we impose a no-flux condition.

We solve this system using a finite difference method[1] on a uniform mesh; this gives the classical scheme

$$c_{i,j}^{t+1} = c_{i,j}^{t} + \tfrac{1}{1+m}\Delta t\,(\delta_x^2 + \delta_y^2)(c_{i,j}^{t})^{1+m}. \tag{2.49}$$

Setting $\Delta x = \Delta y$, we expect (by analogy with the linear case) the method to be stable if

$$\frac{\Delta t}{(\Delta x)^2} \leq \frac{(c_{i,j}^{t})^{-m}}{4} \qquad \text{for all } i, j. \tag{2.50}$$

[1]There is no real benefit in using an implicit scheme such as an ADI method; although this can offer 'improved' stability criteria, it is not the major factor in achieving accurate results. It is easier to keep the numerical scheme as simple as possible.

We thus require $c > 0$ for all time, and hence we must introduce a background concentration of $c = \varepsilon$, where ε is small in comparison to c_0; the stability criterion is thus

$$\Delta t \leq \tfrac{1}{4}\varepsilon^{-m}(\Delta x)^2. \tag{2.51}$$

This is a fundamental difference from the similarity and power series formulations, where the background concentration was zero.

Finally, we note that we must also artificially truncate our domain for numerical purposes; no-flux conditions are imposed on its boundary. The discretized boundary conditions thus become

$$\begin{aligned}
c^t_{i,j} &= \varepsilon && \text{at} \quad t = 0 \\
c^t_{i,j} &= c_0 && \text{if} \quad j = 0 \qquad i \geq 0 \\
c^t_{i-1,j} &= c^t_{i+1,j} && \text{if} \quad i = N \\
c^t_{i,j-1} &= c^t_{i,j+1} && \text{if} \quad j = 0 \qquad i < 0 \\
c^t_{i+1,j} &= c^t_{i-1,j} && \text{if} \quad i = -N \\
c^t_{i,j+1} &= c^t_{i,j-1} && \text{if} \quad j = N
\end{aligned} \tag{2.52}$$

for the difference equations (2.49) specified on

$$\begin{aligned}
0 \leq j < N \qquad -N \leq i \leq 0 \\
1 \leq j < N \qquad 0 < i < N,
\end{aligned} \tag{2.53}$$

where N denotes the size of the mesh; we will take $N\Delta x = 1$ (so that the solution is computed for the region $-1 \leq x \leq 1$, $0 \leq y \leq 1$). It is found that with the non-zero background concentration, we are not now restricted to the range $-4/3 < m < 0$; example results are shown in Figures 2.11–2.14 for $m = -0.3$, $m = -0.9$, $m = -1.5$ and $m = -2.5$. The value of c_0 is in fact arbitrary, as we can adjust it to any value we like by simply altering the timescale; we thus choose $c_0 = 1$ throughout. We fix our background concentration at $\varepsilon = 10^{-4}$, and alter N accordingly depending on the value of m; for more negative values, it is more computationally efficient to use fewer grid points. It can be seen, especially in Figures (2.13) and (2.14), that in the far-field, where $c \approx \varepsilon$, diffusion becomes approximately linear since the concentration (and hence $D(c) = c^m$) tends to a constant (this will be shown later in the asymptotic analysis). As one of our main interests in studying mask-edge diffusion is to determine the ratio of lateral to

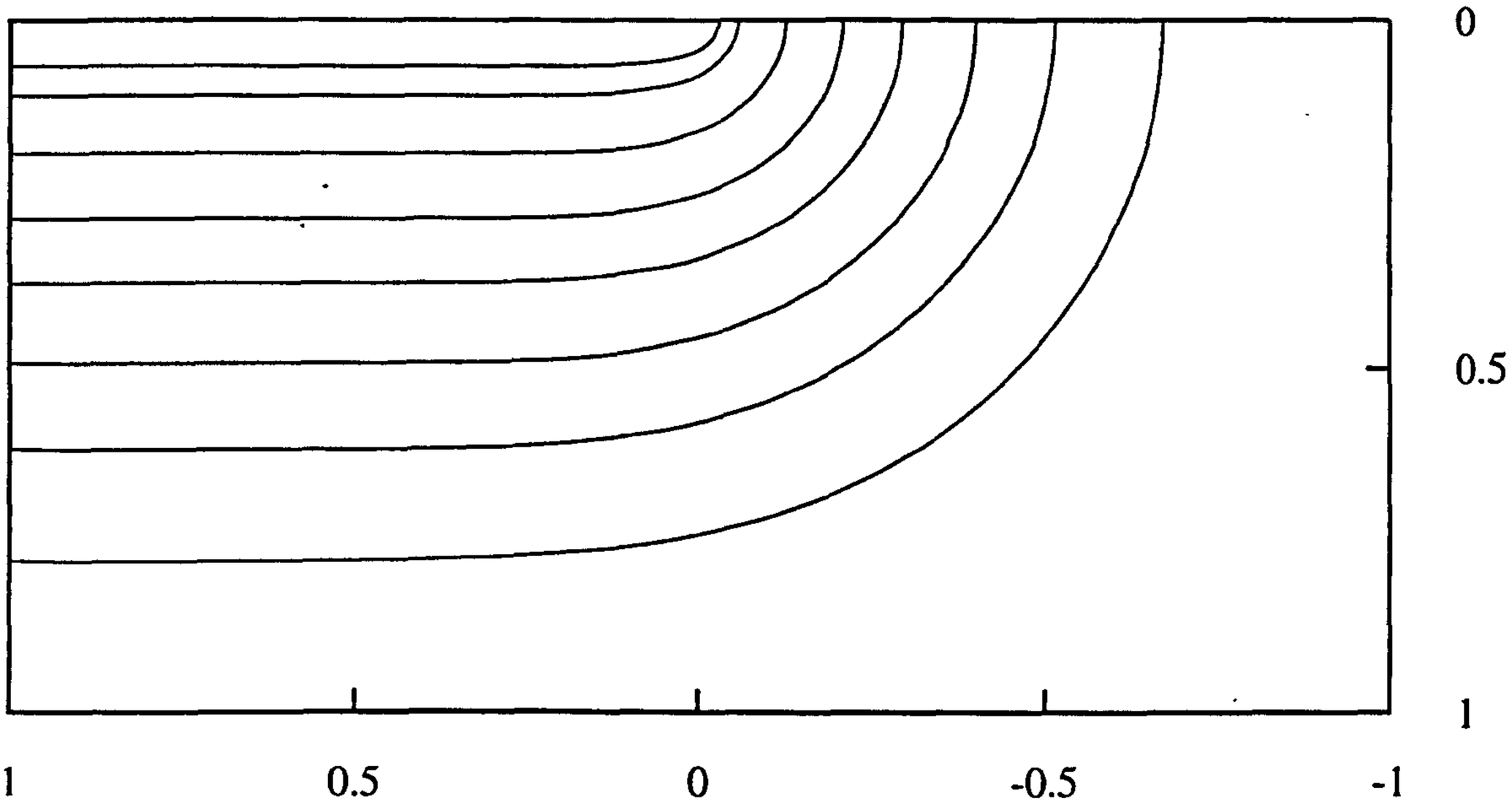

Figure 2.11: Surface source numerical solution, with $m = -0.3$, $c_0 = 1$, $\epsilon = 10^{-4}$, $N = 50$, 500 time-steps.

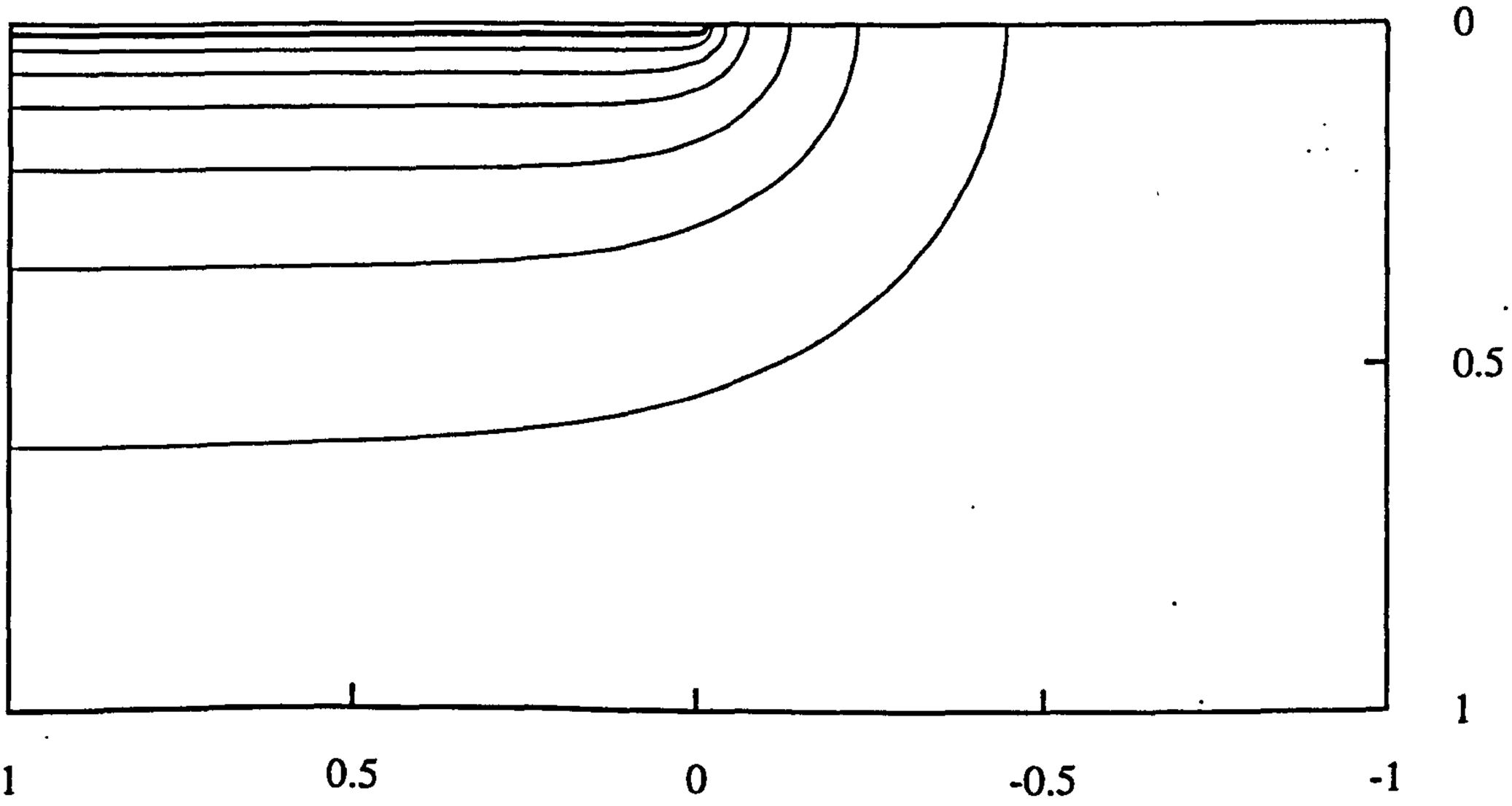

Figure 2.12: Surface source numerical solution, with $m = -0.9$, $c_0 = 1$, $\epsilon = 10^{-4}$, $N = 50$, 4000 time-steps.

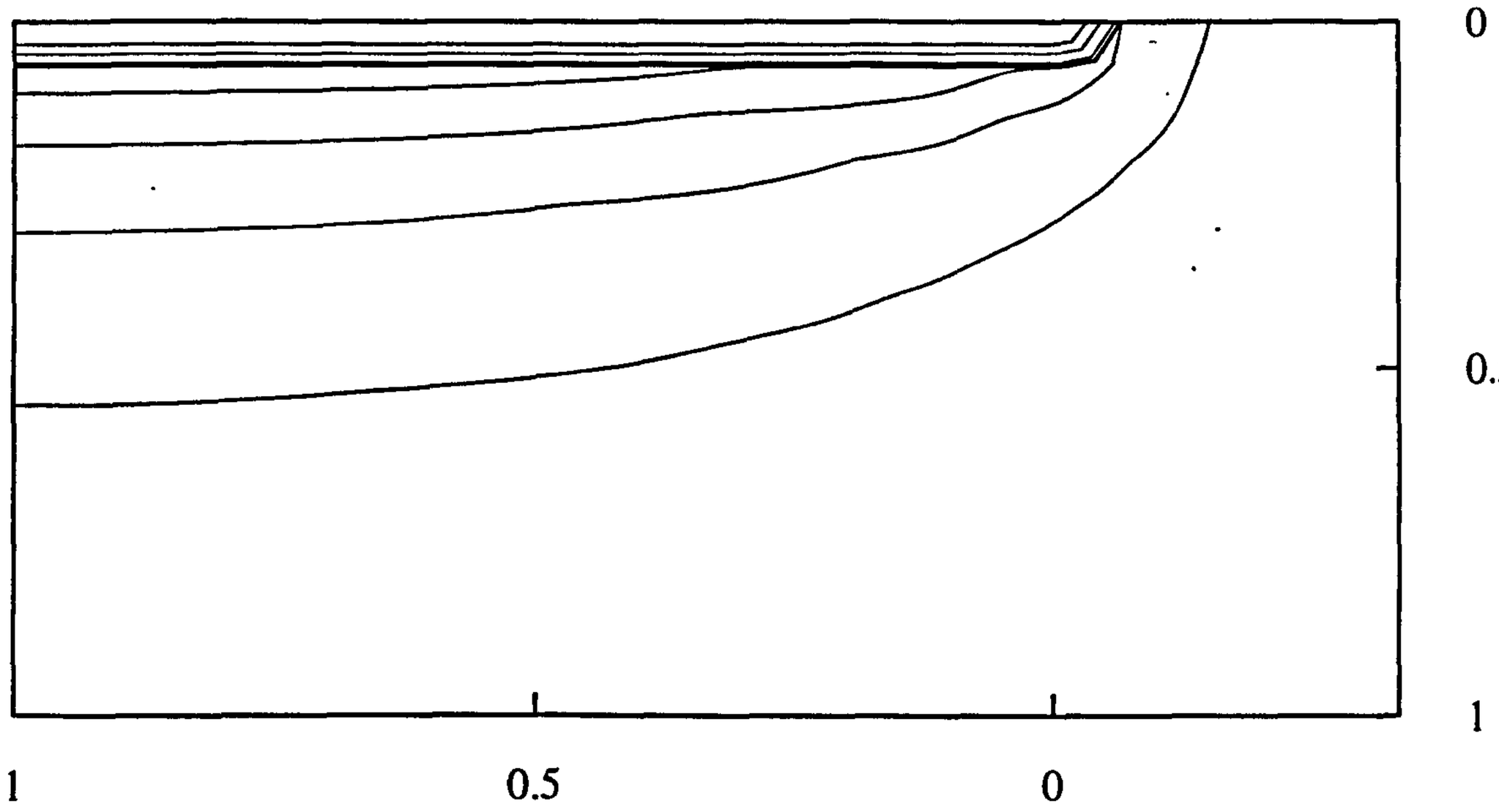

Figure 2.13: Surface source numerical solution, with $m = -1.5$, $c_0 = 1$, $\varepsilon = 10^{-4}$, $N = 20$, 10^5 time-steps.

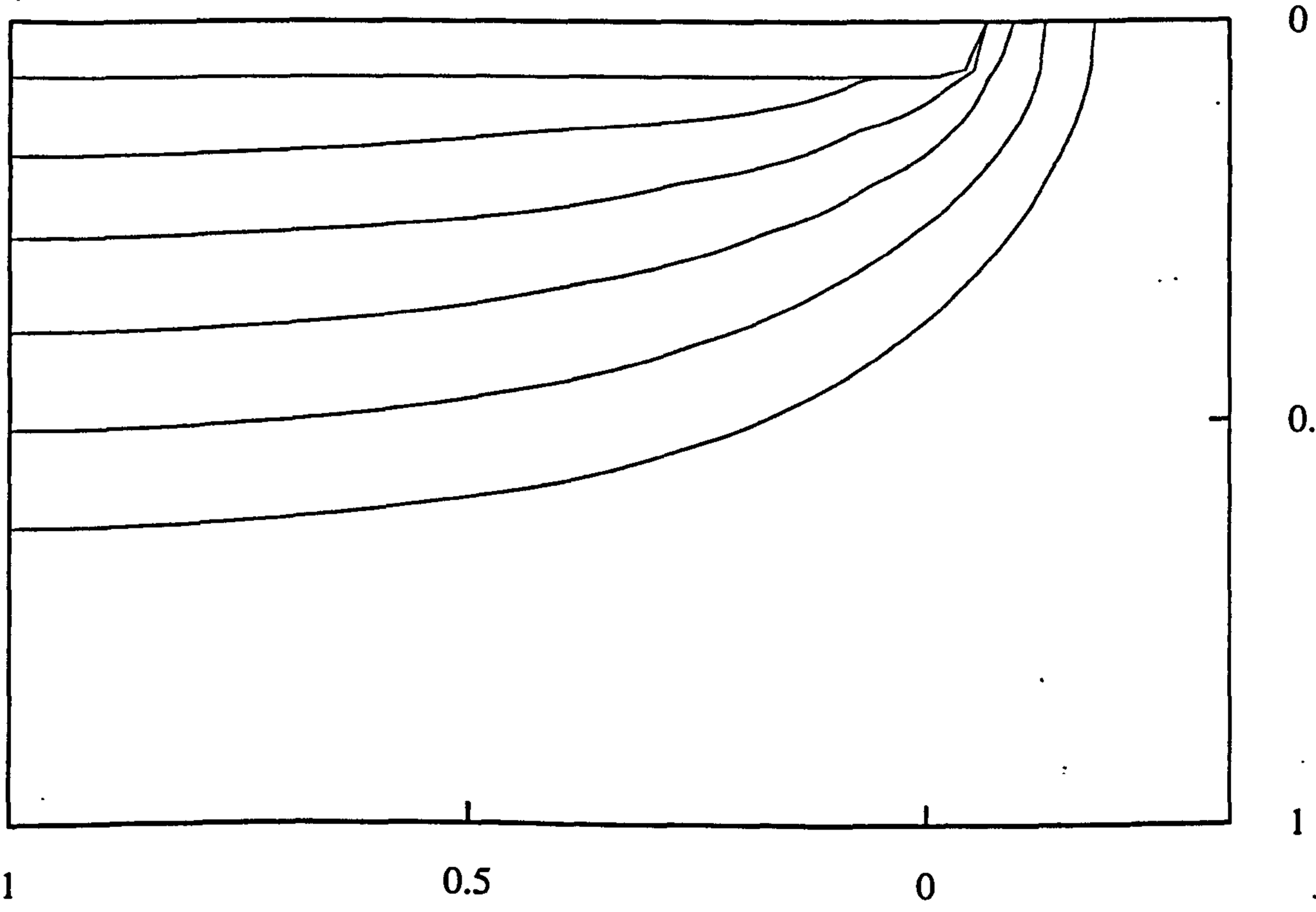

Figure 2.14: Surface source numerical solution, with $m = -2.5$, $c_0 = 1$, $\varepsilon = 10^{-4}$, $N = 15$, 5×10^6 time-steps.

vertical diffusion (the aspect ratio), this again implies that we need computations over long periods of time in order to gain information on the behaviour in the vicinity of the mask-edge for larger negative m.

As a check on our results we can compare the contours at $x = 1$, say, with the solution of the 1-D equation

$$c_t = (c^m c_y)_y. \tag{2.54}$$

Seeking a solution of the form

$$c = c(\eta) \qquad \eta = y/t^{1/2} \tag{2.55}$$

we have

$$c_{\eta\eta} = -\frac{c_\eta}{2c}(2\,m\,c_\eta + \eta\,c^{1-m}) \tag{2.56}$$

subject to the boundary conditions

$$\begin{aligned} c &= c_0 \quad \text{at} \quad \eta = 0 \\ c &\to \varepsilon \quad \text{as} \quad \eta \to \infty. \end{aligned} \tag{2.57}$$

We can solve (2.56) with (2.57) numerically; Figure 2.15 shows that there is excellent agreement between the two solutions.

2.4.2 Fixed Total Dopant

This time, the boundary conditions are

$$\begin{aligned} c &= Q\,\delta(y)\,H(x) \quad \text{at} \quad t = 0 \\ c_y &= 0 \qquad\qquad\quad \text{on} \quad y = 0 \\ c_x &\to 0 \qquad\qquad\quad \text{as} \quad x \to +\infty \\ c &\to \varepsilon \qquad\qquad\quad \text{as} \quad x \to -\infty \text{ and } y \to +\infty \end{aligned} \tag{2.58}$$

and so we are applying our source instantaneously, with a fixed amount of dopant (Q) diffusing inwards. The numerical solution is obtained in a similar way to that used

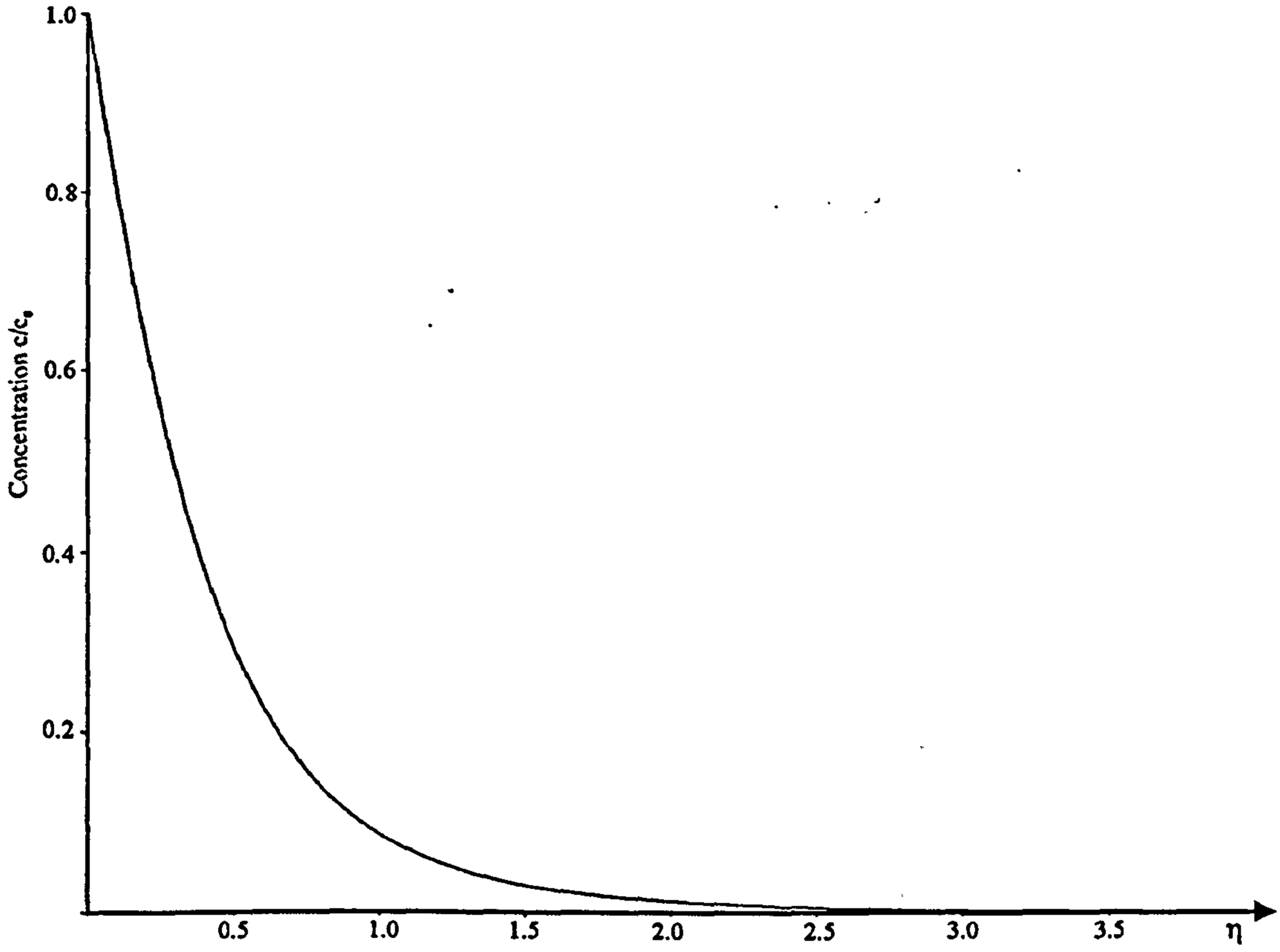

Figure 2.15: 2-D solution at $x = -1$ and 1-D solution for a constant source, $m = -0.5$. The solutions actually lie on top of each other.

previously; the discretized boundary conditions are

$$\begin{aligned} c^t_{i,j} &= \varepsilon \quad \text{if} \quad i < 0 \quad j \geq 0 \quad \text{at } t = 0 \\ c^t_{i,j} &= c_0 \quad \text{if} \quad j = 0 \quad i \geq 0 \quad \text{at } t = 0 \\ c^t_{i,j-1} &= c^t_{i,j+1} \quad \text{if} \quad j = 0 \\ c^t_{i-1,j} &= c^t_{i+1,j} \quad \text{if} \quad i = N \\ c^t_{i,j} &= \varepsilon \quad \text{if} \quad i = -N \quad \text{or} \quad j = N \end{aligned} \tag{2.59}$$

with the difference equations specified this time on the range $-N - 1 \leq i \leq N$, $0 \leq j \leq N - 1$ and

$$Q = \sum_{i=0}^{N} c^0_{i,0}.$$

Example results are shown in Figures 2.16–2.19 with the same parameter settings as used in the constant source plots (Figures 2.11–2.14). It is observed that for the lower concentration contours, there is very little difference between the plots for the two cases (surface source and instantaneous source) for *any* value of (negative) m; we deduce that the initial condition on $x > 0, y = 0$ is not seen away from the surface.

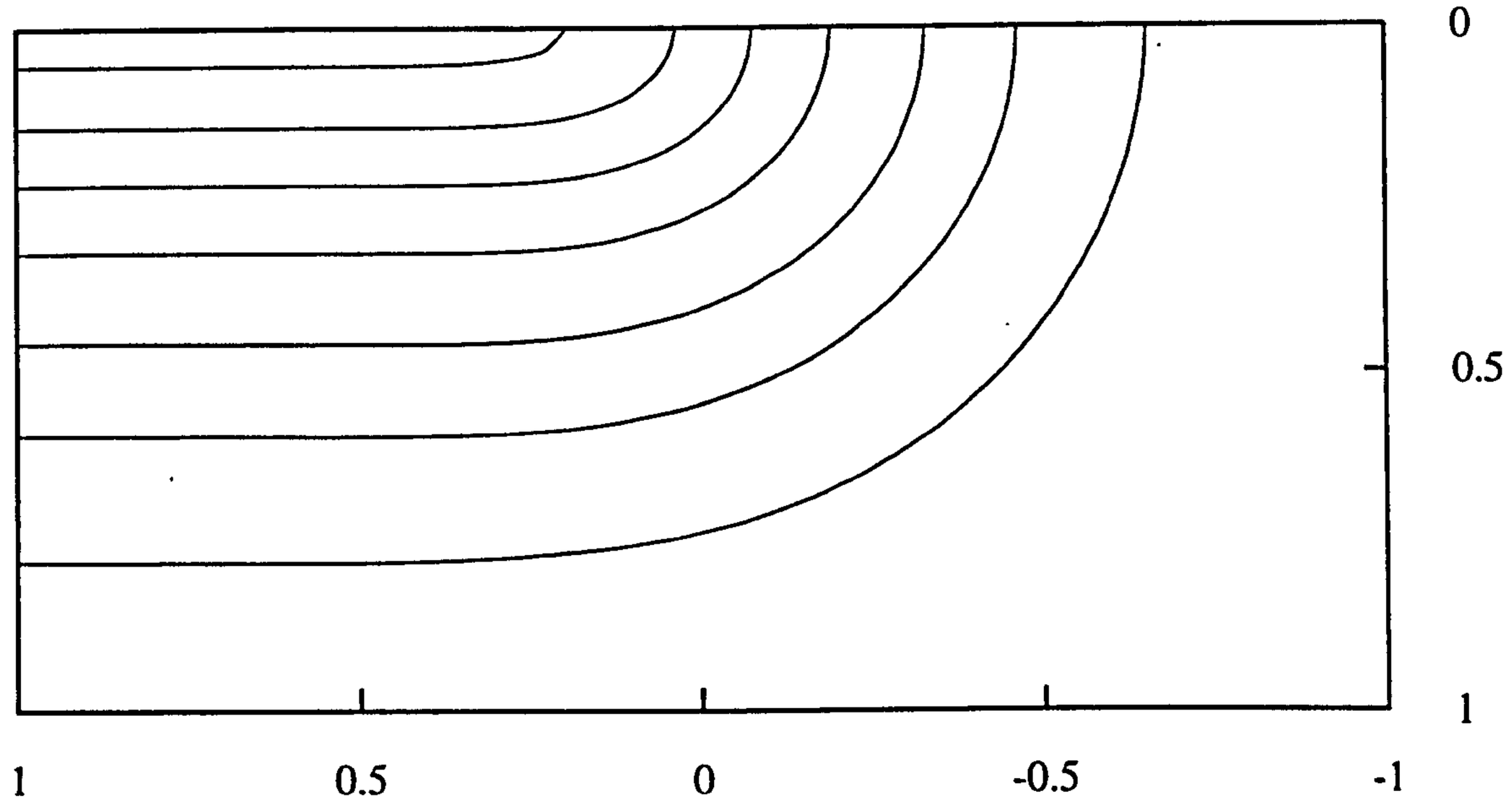

Figure 2.16: Instantaneous source numerical solution, with $m = -0.3$, $c_0 = 1$, $\varepsilon = 10^{-4}$, $N = 50$, 500 time-steps.

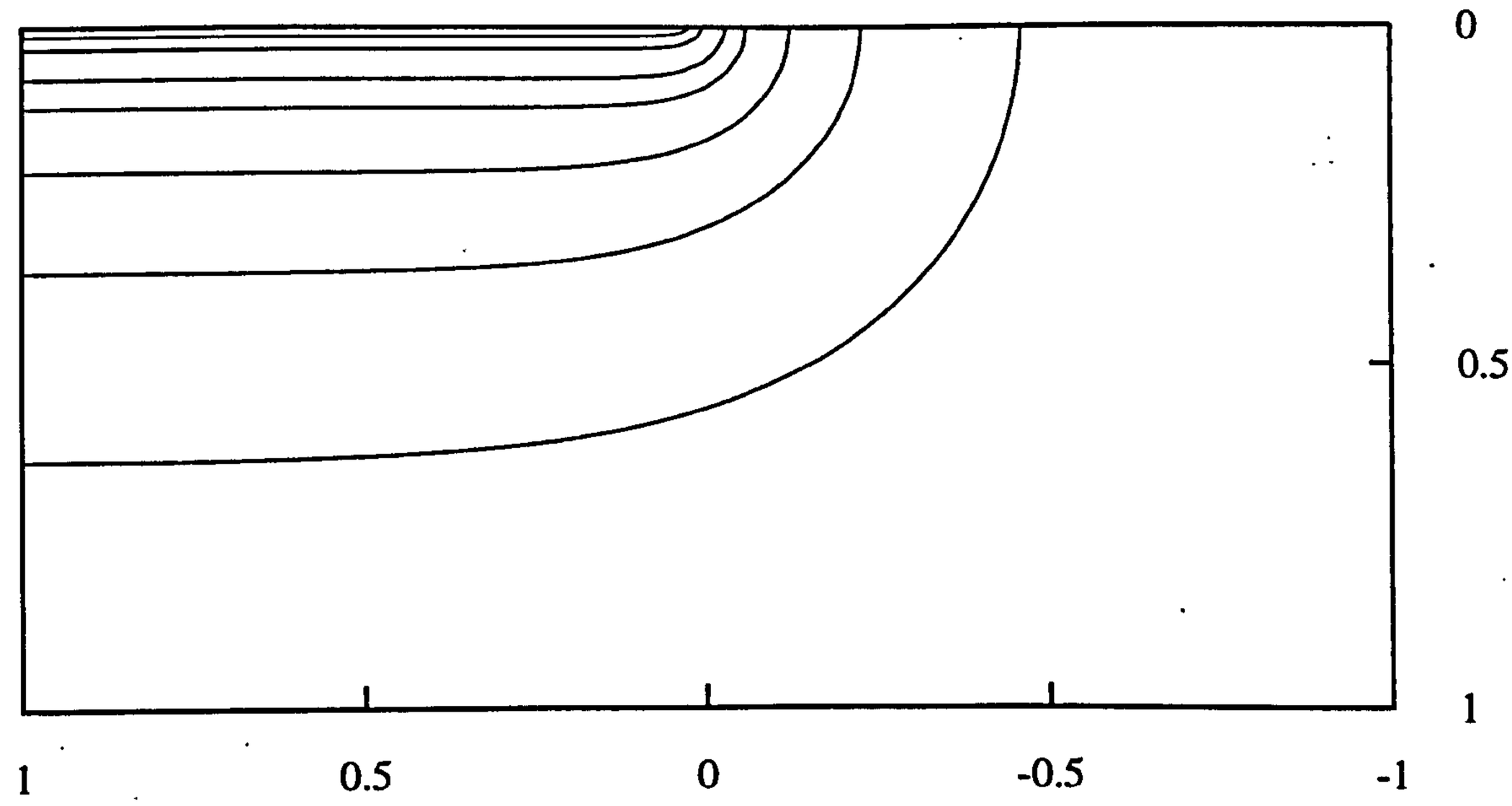

Figure 2.17: Instantaneous source numerical solution, with $m = -0.9$, $c_0 = 1$, $\varepsilon = 10^{-4}$, $N = 50$, 4000 time-steps.

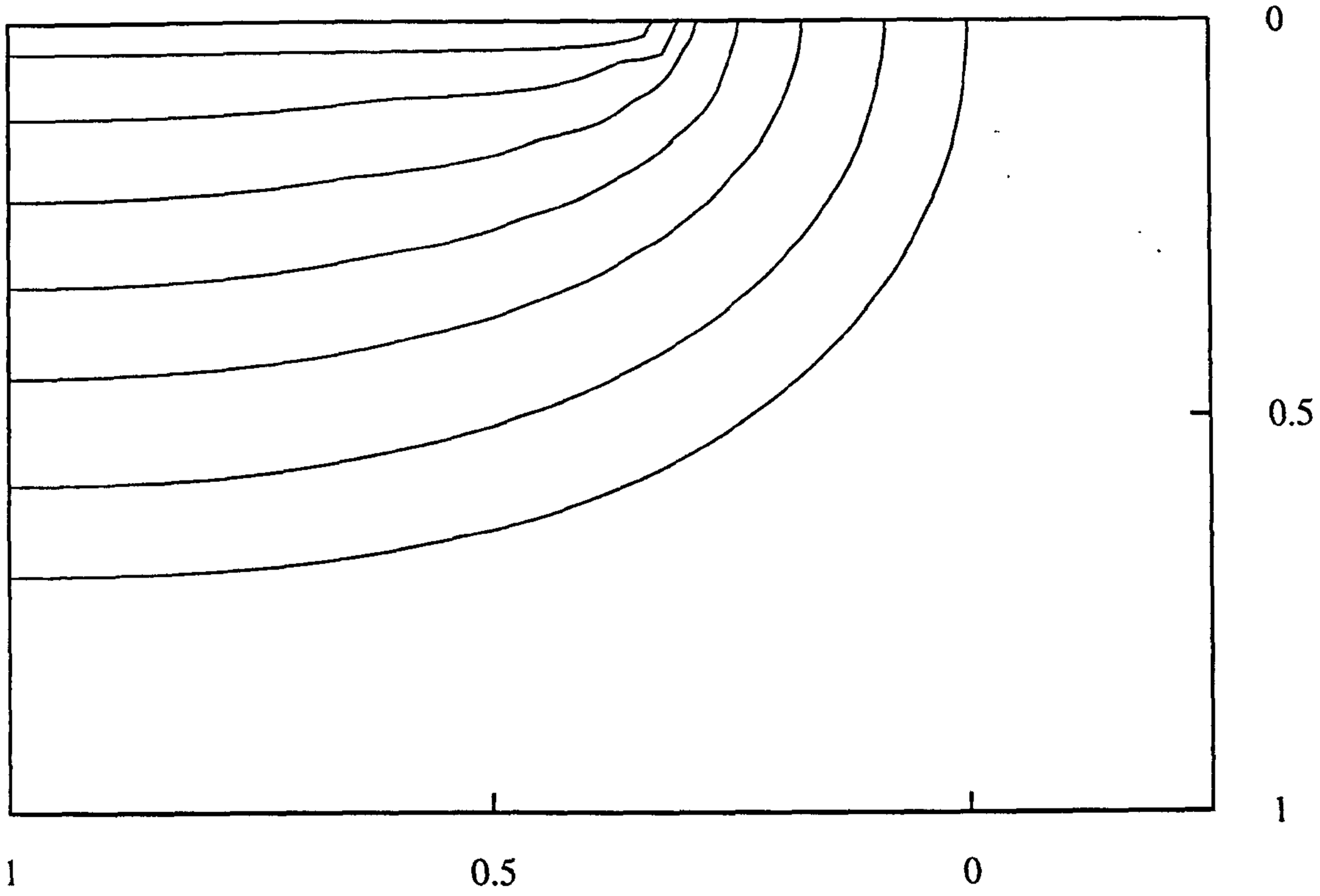

Figure 2.18: Instantaneous source numerical solution, with $m = -1.5$, $c_0 = 1$, $\varepsilon = 10^{-4}$, $N = 20$, 10^5 time-steps.

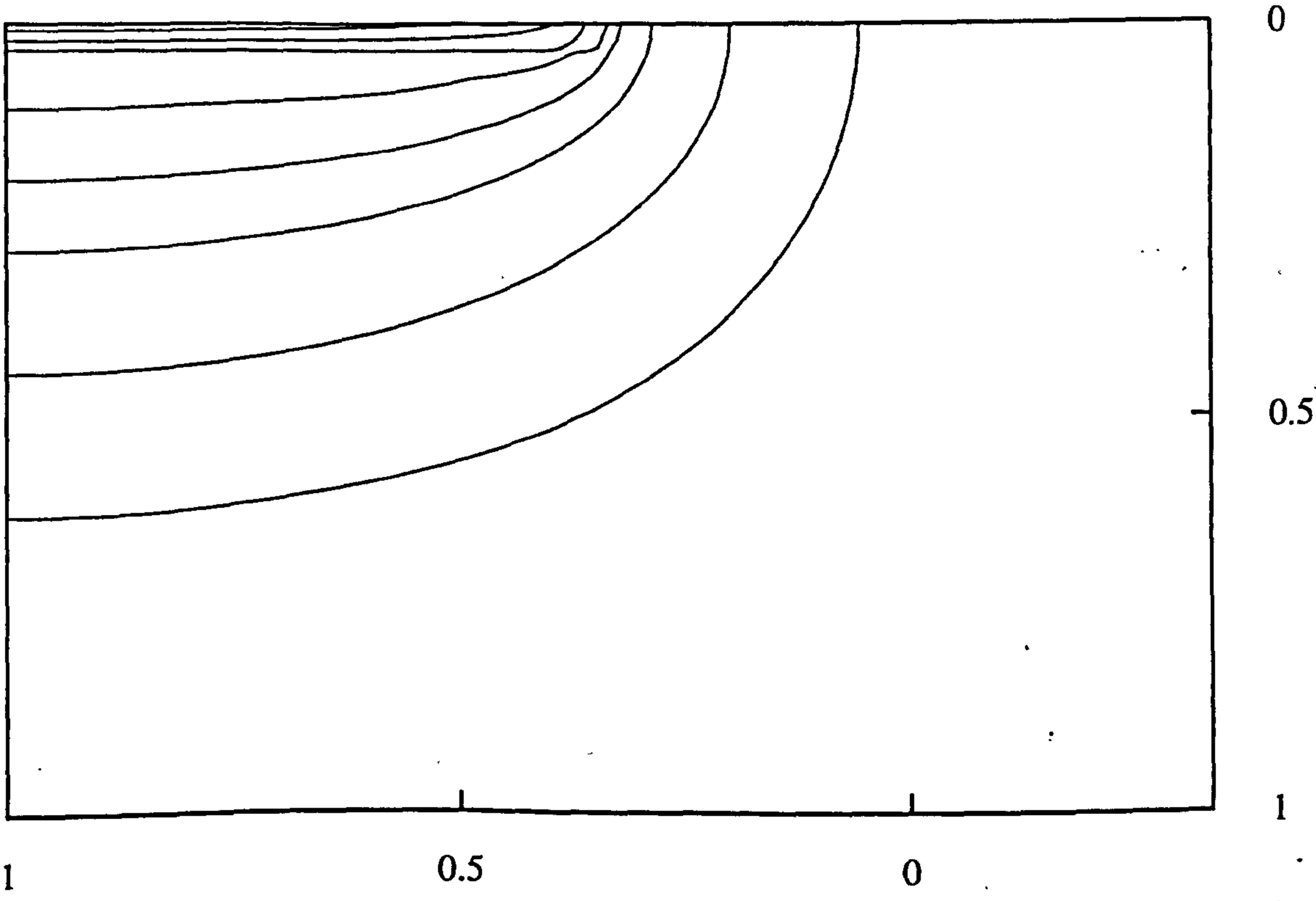

Figure 2.19: Instantaneous source numerical solution, with $m = -2.5$, $c_0 = 1$, $\varepsilon = 10^{-4}$, $N = 15$, 5×10^6 time-steps.

The 1-D solution as $x \to +\infty$ cannot be obtained from (2.56), as the necessary boundary condition on $\eta = 0$ is of the wrong form. Instead, we seek a solution to (2.54) of the form

$$c = t^{-1/(m+2)} f(\eta), \tag{2.60}$$

where

$$\eta = y t^{-1/(m+2)}$$

(i.e. this is of the form discussed in section 2.2.1). We obtain for $\varepsilon = 0$ the ordinary differential equation

$$(m+2) f^m f' + \eta f = \text{constant} = 0,$$

which for $m > -2$ has a solution relevant to our problem of

$$c = t^{-1/(m+2)} \left\{ \frac{-m}{2(m+2)} \left[a^2 + (y t^{-1/(m+2)})^2 \right] \right\}^{\frac{1}{m}}, \tag{2.61}$$

where a is a constant. Comparing (2.61) with the full solution at $x = 1$ again gives very good agreement, similar to Figure 2.15.

2.5 Aspect Ratios

A useful parameter for describing mask-edge diffusion in the far-field is the aspect ratio – the ratio of lateral diffusion under the mask to vertical diffusion for a given concentration (given by b/a in Figure 2.20). This can be used to provide an estimate of how far the impurity has diffused under the mask, and thus provides information as to the effective channel length (for a MOSFET).

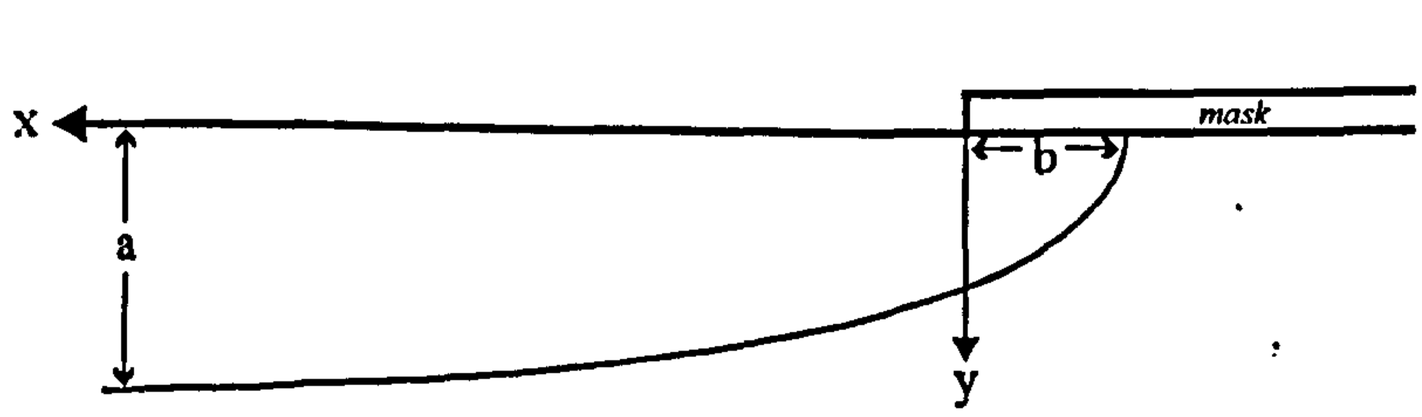

Figure 2.20: Aspect ratio definition. The curve represents a concentration contour.

For the (separable) similarity solution, which is applicable at low concentrations, this can initially be tackled analytically. In the 1-D region far away from the mask-edge, we

have

$$c \sim \left(\frac{-m}{2(2+m)}\frac{a^2}{t}\right)^{1/m},$$

whilst in the 2-D region

$$c \sim \left(G(\pi)\frac{b^2}{t}\right)^{1/m}.$$

Thus, on the same concentration contour,

$$\begin{aligned} a &\sim \left(\frac{2(2+m)}{-m}t\right)^{1/2} \\ b &\sim \left(\frac{1}{G(\pi)}t\right)^{1/2} \end{aligned}$$

and thus

$$\frac{b}{a} = \left(-\frac{2}{m}(2+m)\,G(\pi)\right)^{-1/2} \qquad (2.62)$$

is the aspect ratio. This can also be verified by comparing with measurements taken directly from the contour plots in Figure 2.5.

For the power series solutions, we calculate the aspect ratio simply by measuring the appropriate distances on the contour plots. In Figure 2.21 we compare the ratios of the one- and two-term solutions with those of the (separable) similarity solution, and it can be seen that the two-term power series and the similarity solution are fairly similar, especially at small negative values of m. The divergence as m becomes more negative may well be due to the large kink appearing in the power series contour plots (see previous section).

The aspect ratios obtained from the full numerical solutions cannot be expected to be as accurate as those for the above results. We have to bear in mind that we were required to include a background concentration ϵ in this case, which has already been shown to have an effect the solution. For more negative values of m, we also have to contend with diffusion becoming approximately linear in the far-field, as mentioned previously. This causes particular difficulty for the instantaneous source case, as the contours tend to reach $y = 0$ with $x > 0$, so that no aspect ratio can be obtained. However, the numerical solution does provide the *only* means of estimating the ratio for $m < -4/3$ so far noted.

In Figure 2.21, we show the aspect ratios calculated for all instantaneous source solutions. It can be seen that the two-term power series solution is closer than the

one-term result to the similarity solution (which is in some sense an exact solution, requiring only the integration of a single ordinary differential equation), whilst the numerical solution shows less agreement, especially when m is not small and background concentration effects are crucial; it does have the advantage however of being the only method to give us values for $m < -4/3$. It can be seen that the ratio tails off towards a constant as $m \to -\infty$. We note that the aspect ratios obtained from both numerical solutions (constant and instantaneous source) are virtually the same, for the reason mentioned earlier; the initial condition is not 'seen' in the far-field.

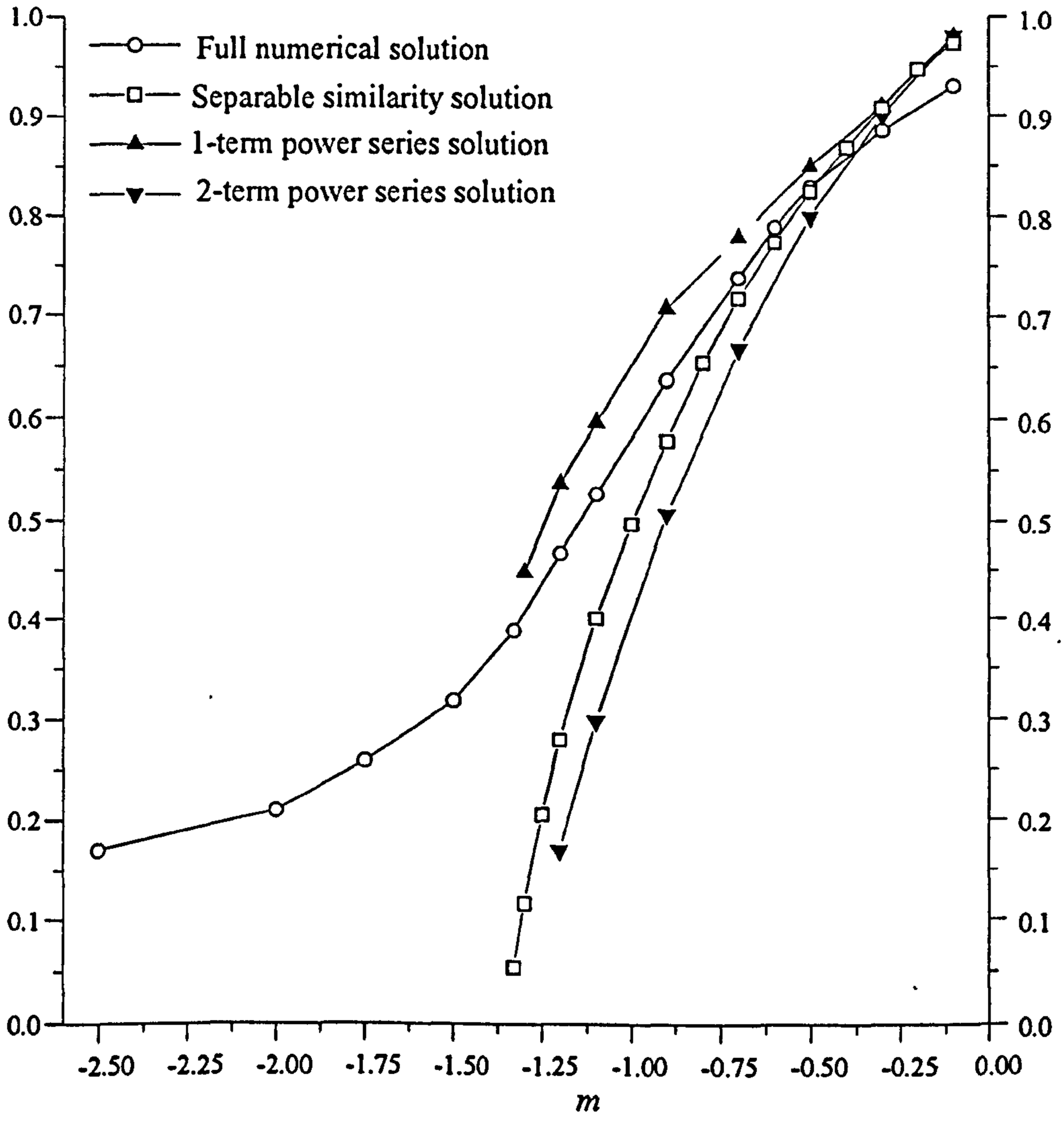

Figure 2.21: A comparison of aspect ratios for all solutions, taken at concentration contour $c = 0.005$; $\varepsilon = 10^{-4}$ where appropriate.

2.6 Comparison with Asymptotic Results

We can compare the full numerical solutions (constant source case) with asymptotic results obtained for the region in the vicinity of the mask edge. There are three cases to look at; $-4/3 < m < 0$, $-2 < m < -4/3$ and $m < -2$. We consider here the surface source case, the behaviour in the instantaneous source case being similar.

2.6.1 $-4/3 < m < 0$

Here, the analysis is fairly straightforward. We have

$$c_t = (c^m c_x)_x + (c^m c_y)_y$$

with boundary conditions

$$\begin{aligned} c &= 1 \qquad \text{on } y = 0,\ x > 0 \\ c_y &= 0 \qquad \text{on } y = 0,\ x < 0 \\ c &\to \varepsilon \qquad \text{as } x \to -\infty,\ y \to +\infty, \end{aligned}$$

where c represents the concentration and ε is again the background concentration. We introduce an outer scaling

$$\begin{aligned} C &= \varepsilon^{-1} c \\ X &= \varepsilon^{-m/2} x \\ Y &= \varepsilon^{-m/2} y \end{aligned}$$

and expand in the form

$$C = C_0 + \varepsilon C_1 + \ldots,$$

which gives us the one-term outer expansion

$$\frac{\partial C_0}{\partial t} = \frac{\partial}{\partial X}\left(C_0^m \frac{\partial C_0}{\partial X}\right) + \frac{\partial}{\partial Y}\left(C_0^m \frac{\partial C_0}{\partial Y}\right) \tag{2.63}$$

with

$$\begin{aligned} C_0 &\to \infty \qquad \text{as } Y \to 0^+,\ X > 0 \\ \frac{\partial C_0}{\partial Y} &= 0 \qquad \text{on } Y = 0,\ X < 0 \\ C_0 &\to 1 \qquad \text{as } X \to -\infty,\ Y \to +\infty. \end{aligned} \tag{2.64}$$

It can now easily be seen that diffusion will become linear at infinity.

The one-term inner expansion is

$$\frac{\partial c_0}{\partial t} = \frac{\partial}{\partial x}\left(c_0^m \frac{\partial c_0}{\partial x}\right) + \frac{\partial}{\partial y}\left(c_0^m \frac{\partial c_0}{\partial y}\right) \tag{2.65}$$

with

$$\begin{aligned} c_0 &= 1 && \text{on } y = 0,\ x > 0 \\ \frac{\partial c_0}{\partial y} &= 0 && \text{on } y = 0,\ x < 0 \\ c_0 &\to 0 && \text{as } x \to -\infty,\ y \to +\infty. \end{aligned} \tag{2.66}$$

In the one-dimensional region $X \to +\infty$ we find that

$$C_0 \sim \left(\frac{-m}{2(2+m)}\frac{Y^2}{t}\right)^{1/m} \quad \text{as } Y \to 0^+, \tag{2.67}$$

which matches with the inner solution.

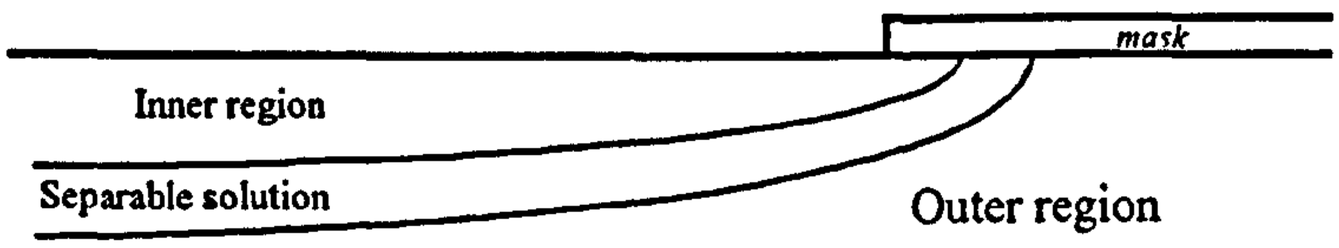

Figure 2.22: Inner and outer layers for $-4/3 < m < 0$.

Elsewhere, we can infer that the separable solution holds in the matching region, and hence

$$c_0 \sim \left(G(\theta)\frac{r^2}{t}\right)^{1/m} \qquad \text{as } r \to +\infty,\ \theta > 0 \tag{2.68}$$

$$C_0 \sim \left(G(\theta)\frac{R^2}{t}\right)^{1/m} \qquad \text{as } R \to 0^+,\ \theta > 0, \tag{2.69}$$

where $R^2 = X^2 + Y^2$.

2.6.2 $-2 < m < -4/3$

In this range, we no longer have a separable solution; however, we can obtain an asymptotic solution with three inner layers, as shown in Figure 2.23. The leading order outer solution is again given by (2.63) and (2.64).

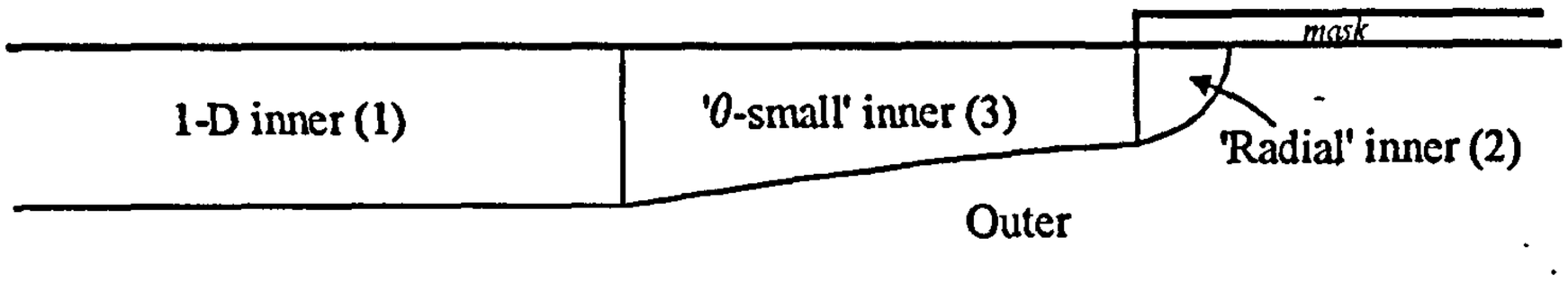

Figure 2.23: Inner and outer layers for $-2 < m < -4/3$.

Region (1)

From the previous formulation, we have

$$C_0 \sim \left(\frac{-m}{2(2+m)}\frac{Y^2}{t}\right)^{1/m},$$

which implies that $c = O(1)$ for $X = O(1)$, $Y = O(\varepsilon^{-m/2})$. Thus, for the inner region (1), we have

$$\frac{\partial c_0}{\partial t} = \frac{\partial}{\partial y}\left(c_0^m \frac{\partial c_0}{\partial y}\right) \tag{2.70}$$

and

$$c_0 = 1 \qquad \text{on } y = 0 \tag{2.71}$$

$$c_0 \sim \left(\frac{-m}{2(2+m)}\frac{y^2}{t}\right)^{1/m} \qquad \text{as } y \to +\infty. \tag{2.72}$$

Region (2)

As $R \to 0$ we find that a full balance is not possible in the outer region; assuming $C_{0t} \ll \frac{1}{1+m}\nabla^2 C_0^{1+m}$ as $R \to 0$, we obtain Laplace's equation, and a solution of the form

$$C_0 \sim (A(t)\, R^{1/2} \sin\tfrac{1}{2}\theta)^{1/(m+1)} \qquad \text{as } R \to 0 \tag{2.73}$$

is required in order to give the correct behaviour as $\theta \to 0$ and $\theta \to \pi$. $A(t)$ is in principle determined by (2.63) and (2.64). For the inner variable, we set

$$\rho = \varepsilon^{2(1+m)} R$$

so that $C_0 = O(\varepsilon^{-1})$ and $c = O(1)$. This gives us

$$c_t = \varepsilon^{4+3m}\left(\frac{1}{\rho}(\rho\, c^m c_\rho)_\rho + \frac{1}{\rho^2}(c^m c_\theta)_\theta\right)$$

and thus at leading order we have

$$\frac{1}{\rho}(\rho\, c_0^m c_{0\,\rho})_\rho + \frac{1}{\rho^2}(c_0^m c_{0\,\theta})_\theta = 0$$

with

$$c_0 = 1 \qquad \text{on } \theta = 0$$

$$\frac{\partial c_0}{\partial \theta} = 0 \qquad \text{on } \theta = \pi.$$

Looking for a solution which matches with the outer solution, we find that

$$c_0 = (1 + A(t)\,\rho^{1/2} \sin \tfrac{1}{2}\theta)^{1/(m+1)}. \tag{2.74}$$

Region (3)

From the previous result for the outer region, we can see that for $R \to 0$, $\theta \to 0$, we have

$$C_0 \sim \left(A(t)\, R^{1/2}\, (\tfrac{1}{2}\,\theta)\right)^{1/(m+1)}$$

that is

$$C_0 \sim \left(\tfrac{1}{2}A(t)\, Y/X^{1/2}\right)^{1/(m+1)}. \tag{2.75}$$

Once again, we require that $C = O(\varepsilon^{-1})$, $c = O(1)$, and so we set

$$X = \varepsilon^\alpha x^*$$

$$Y = \varepsilon^\beta y^*.$$

From (2.75), we require

$$\left(\frac{\varepsilon^\beta}{\varepsilon^{\alpha/2}}\right)^{1/(m+1)} = \varepsilon^{-1}$$

so that

$$\beta = \frac{\alpha}{2} - (1+m).$$

The inner equation now reads

$$\frac{\partial}{\partial t}\left(\frac{c}{\varepsilon}\right) = \frac{1}{\varepsilon^\alpha}\frac{\partial}{\partial x^*}\left[\left(\frac{c}{\varepsilon}\right)^m \frac{1}{\varepsilon^\alpha}\frac{\partial}{\partial x^*}\left(\frac{c}{\varepsilon}\right)\right] + \frac{1}{\varepsilon^\beta}\frac{\partial}{\partial y^*}\left[\left(\frac{c}{\varepsilon}\right)^m \frac{1}{\varepsilon^\beta}\frac{\partial}{\partial y^*}\left(\frac{c}{\varepsilon}\right)\right]$$

and thus to balance we require

$$\alpha = 2 + m,$$

$$\beta = -m/2,$$

so that to leading order we have

$$\frac{\partial c_0}{\partial t} = \frac{\partial}{\partial y^*}\left(c_0^m \frac{\partial c_0}{\partial y^*}\right) \tag{2.76}$$

with

$$c_0 = 1 \qquad \text{on } y^* = 0, \tag{2.77}$$

$$c_0 \sim \left(\frac{1}{2}A(t)\, y^*/x^{*1/2}\right)^{1/(m+1)} \qquad \text{as } y^* \to +\infty. \tag{2.78}$$

2.6.3 m < −2

Here, the asymptotic solution is simpler than for the case above; our solution now only requires two inner layers, as shown in Figure 2.24. The leading order outer solution is again given by (2.63) and (2.64).

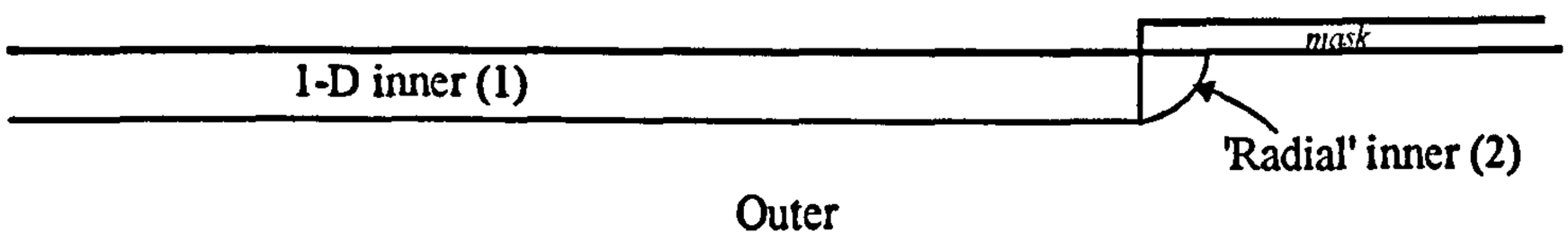

Figure 2.24: Inner and outer layers for $m < -2$.

Region (1)

Noting that the solution is quasi-steady, then we obtain the behaviour

$$C_0 \sim (B(X,t)\, Y)^{1/(m+1)} \qquad \text{as } Y \to 0^+. \tag{2.79}$$

This suggests the inner scaling

$$\hat{y} = \varepsilon^{m+1} Y,$$

which gives

$$\frac{\partial}{\partial \hat{y}}\left(c_0^m \frac{\partial c_0}{\partial \hat{y}}\right) = 0 \tag{2.80}$$

and hence

$$c_0 = (1 + B(X,t)\, \hat{y})^{1/(m+1)} \tag{2.81}$$

in order to match with the outer solution. The behaviour in Region (2) is as given for Region (2) in the previous case.

These expressions can be compared to results from the numerical solutions; plotting $\ln c_0$ against $\ln r$ for the radial region (2) should give straight lines for a particular m, whose gradient should be $2/m$ for $m > -4/3$ (corresponding to the separable solution), and $1/2(m+1)$ for $m < -4/3$. An example log-log plot is shown in Figure 2.25 to give an indication of how straight these lines are for m much less than zero; the gradients for the full range of m considered are shown in Figure 2.26 below, with the relevant portions of the curves $2/m$ and $1/2(m+1)$ shown for comparison. Agreement is fairly good, bearing in mind that the full numerical solutions are only approximate at best. The deviation as $m \to 0^-$ is due to the almost linear behaviour – diffused profiles for $m = 0$ are exponential in form and hence the log–log plots do not give straight lines, making the calculation of their (supposedly constant) gradient difficult.

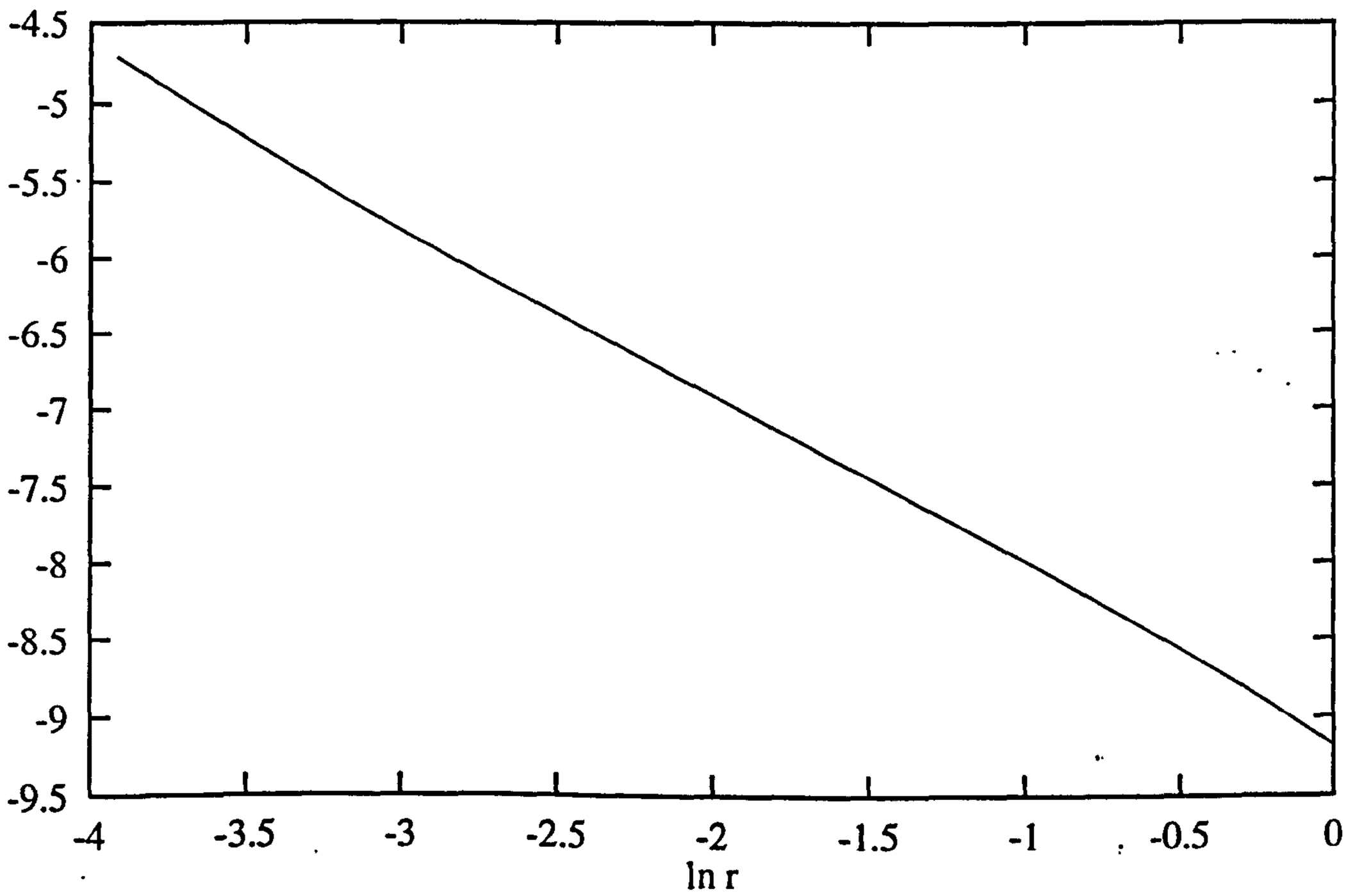

Figure 2.25: Plot of $\ln c_0$ against $\ln r$ for $m = -1.5$.

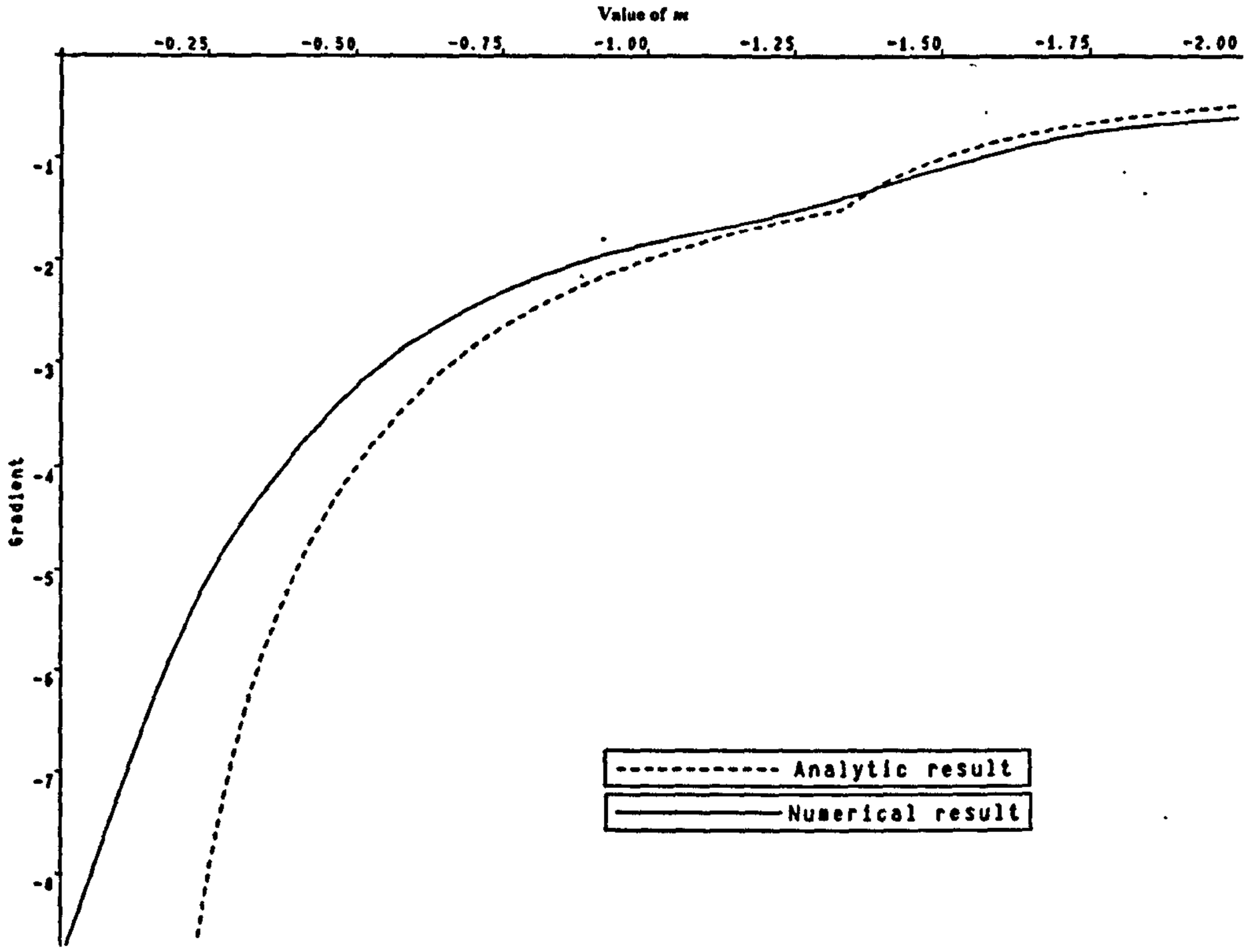

Figure 2.26: Gradient plots.

2.7 Summary

We now summarise the solutions in this chapter:

Separable similarity solution This is applicable in the far field to both the implant and surface source cases when the mask condition is replaced by (2.25), and gives a solution to the zero background concentration problem where it exists. Non-existence of a solution (where applicable) is due to the singularity in the diffusivity c^m as $c \to 0$.

Power series solution This is applicable to the instantaneous source case, and provides accurate solutions for small negative m near to the semiconductor surface.

Numerical solution This provides solutions in both implant and surface source cases where we impose a small background concentration to overcome the non-existence criterion; for $m < 4/3$, it is our only method for calculating solutions.

Asymptotic analysis We have shown the asymptotic behaviour as the background concentration $\epsilon \to 0$ for the constant source case; the analysis for the implant case is similar. For $-4/3 < m < 0$, the structure is deduced from the seperable similarity solution results. In the range $-2 < m < 4/3$, the separable solution does not exist, although the one-dimensional solution applicable as $x \to +\infty$ still does. The results suggest that the high concentration contours bunch up for $m < -4/3$, which is backed up by the numerical calculations.

Chapter 3

Flow By Curvature: $N = -\kappa$

3.1 Introduction

It has been shown previously by Keener [27, 28] that when considering the motion of wavefronts, the single bistable reaction-diffusion equation

$$\varepsilon u_t = \varepsilon^2 \nabla^2 u + f(u), \tag{3.1}$$

with $f(u)$, for example, a cubic function of u and ε small, can be asymptotically represented by the eikonal-curvature equation

$$N = c - \varepsilon\kappa, \tag{3.2}$$

where N is the normal outward velocity of the wavefront, c is the planar wave speed of (3.1) and κ is the curvature of the front.

In two dimensions, equations similar to (3.2) have previously been derived in the theory of flame propagation [38] and crystal growth [5]. The latter case considered the modelling of growth due to single and double screw dislocations, which produced rotating spiral 'pyramids' in the crystal. Mullins [39] independently considered (3.2) for $c = 0$ in a similar context, and produced three shape-preserving solutions (including a spiral solution). It is the $c = 0$ case of (3.2) that we shall consider in this chapter, i.e.

$$N = -\kappa, \tag{3.3}$$

with ε scaled out of the equation. Rubinstein et al. [43] have considered the front motion governed by (3.3) in a domain Ω with the end points of the interface (a curve in the

plane) normal to the boundary of Ω. They found that fronts can shrink to a point in a finite time, or tend to the shortest (local) diameter of Ω (which demonstrates why (3.3) is often referred to as a curve shortening equation); this ties in with Gage [14], who demonstrated that any convex curve becomes circular under curve shortening.

In three dimensions, there a number of well-documented solutions to (3.3), including shrinking cylinders, spheres and torii [23, 18]; these will be expanded upon later. Keener has also used (3.3) to model the motion of the filaments of linear and toroidal scroll waves [30] that can occur, for example, in the Belousov-Zhabotinskii reaction [29]; there has also been interest shown in the motion by mean curvature of dumbbell-shaped regions, which develop singularities in finite time [2, 8, 26].

We shall now find solutions to (3.3) using a number of similarity formulations, generally seeking to extend the work of Mullins [39]. The more general curvature equation (3.2) will be considered in the following chapter.

3.2 Formulation of One-Parameter Groups

First of all, we need to determine our similarity variables. To achieve this, we need to find the group which leaves (3.3) invariant, as described in Bluman and Cole [4]. Working in Cartesian co-ordinates, we note that (3.3) can be written as

$$f_t = \frac{f_{xx}}{1 + f_x^2}, \tag{3.4}$$

noting that f above is different from that in (3.1). Assuming that (3.4) admits a one-parameter (ε) Lie group of point transformations

$$\begin{aligned} f^* &\sim f(x,t) + \varepsilon F(x,t,f) \\ x^* &\sim x + \varepsilon X(x,t,f) \\ t^* &\sim t + \varepsilon T(x,t,f) \end{aligned} \tag{3.5}$$

with infinitesimals (F, X, T) leaving invariant (3.4), we require

$$f^*_{t^*} = \frac{f^*_{x^*x^*}}{1 + f^{*2}_{x^*}}. \tag{3.6}$$

Calculating the various derivatives of f^* in (3.6) and substituting in (3.4), we obtain (at $O(\varepsilon)$)

$$\begin{aligned}&(F_{xx} - F_t) + (2F_{xf} - X_{xx} + X_t) f_x + (T_t - T_{xx} - 2X_x) f_t + \\ &\quad (F_{ff} - F_t - 2X_{xf}) f_x^2 - 2(X_f + F_x + T_{xf}) f_x f_t + (X_t - X_{ff}) f_x^3 + \\ &\quad (T_t - T_{ff} - 2F_f) f_x^2 f_t + 2T_x f_x f_t^2 + 2T_f f_x^2 f_t^2 - 2T_x f_{xt} - 2T_f f_{xt} f_x = 0,\end{aligned} \tag{3.7}$$

where we have eliminated f_{xx} using (3.4). Equating to zero the coefficients of like derivatives of f in the usual way, we obtain a series of partial differential equations for F, X, T, which, on solution, give us

$$\begin{aligned}T &= \alpha + 2\beta t \\ X &= \gamma + \beta x - \delta f \\ F &= \lambda + \delta x + \beta f,\end{aligned} \tag{3.8}$$

where α, β, γ, δ and λ are five arbitrary parameters–(3.8) is a five-parameter Lie group of transformations leaving invariant (3.4). The global forms are obtained by solving the characteristic equations

$$\begin{aligned}\frac{dt^*}{d\varepsilon} &= \alpha + 2\beta t^* \\ \frac{dx^*}{d\varepsilon} &= \gamma + \beta x^* - \delta f^* \\ \frac{df^*}{d\varepsilon} &= \lambda + \delta x^* + \beta f^*\end{aligned} \tag{3.9}$$

together with the condition

$$t^* = t \qquad x^* = x \qquad f^* = f \qquad \text{at } \varepsilon = 0,$$

which gives us the five one-parameter groups

$$\begin{aligned}&\alpha \neq 0: && t^* = t + \varepsilon && x^* = x && f^* = f, \\ &\gamma \neq 0: && t^* = t && x^* = x + \varepsilon && f^* = f, \\ &\lambda \neq 0: && t^* = t && x^* = x && f^* = f + \varepsilon, \\ &\beta \neq 0: && t^* = t\,e^{2\varepsilon} && x^* = x\,e^{\varepsilon} && f^* = f\,e^{\varepsilon}, \\ &\delta \neq 0: && t^* = t && x^* = x\cos\varepsilon - f\sin\varepsilon && f^* = x\sin\varepsilon + f\cos\varepsilon.\end{aligned} \tag{3.10}$$

The first three groups of (3.10) represent translations, the fourth a rescaling and the fifth a rotation. As primarily we shall be interested in rotating solutions, and particularly in spiral solutions, we note that a Cartesian co-ordinate system is not suitable, as multivaluedness can occur. We thus switch to polar co-ordinates; our curvature equation (3.3) can be written as

$$\frac{\partial r}{\partial t} = -\frac{r^2 + 2r_\theta^2 - r r_{\theta\theta}}{r(r^2 + r_\theta^2)} \tag{3.11}$$

and, assuming that (3.11) admits the one-parameter Lie group of point transformations

$$\begin{aligned} r^* &\sim f(\theta,t) + \varepsilon\, R(\theta,t,r) \\ \theta^* &\sim \theta + \varepsilon\, \Theta(\theta,t,r) \\ t^* &\sim t + \varepsilon\, T(\theta,t,r), \end{aligned} \tag{3.12}$$

we can obtain the five-parameter group

$$\begin{aligned} t^* &= t + \varepsilon\,(\alpha + 2\,\beta t) \\ r^* &= r + \varepsilon\,(\beta\, r - \delta \sin\theta + \lambda \cos\theta) \\ \theta^* &= \theta + \varepsilon\,(\gamma - [\delta \cos\theta + \lambda \sin\theta]/r), \end{aligned} \tag{3.13}$$

so that α represents a translation in t, γ a translation in θ (i.e. a rotation), β a rescaling and δ, λ the translations in x, y.

We are now in a position to find our similarity variables; neglecting $O(\varepsilon^2)$ terms, we have

$$r(\theta + \varepsilon\,\Theta(\theta,t,r), t + \varepsilon\, T(\theta,t,r)) = r(\theta,t) + \varepsilon\, R(\theta,t,r) \tag{3.14}$$

due to invariance. The $O(\varepsilon)$ term of the above functional equation leads to the first-order partial differential equation

$$T\frac{\partial r}{\partial t} + \Theta\frac{\partial r}{\partial \theta} = R, \tag{3.15}$$

which is known as the invariant surface condition (see, for example, Bluman and Cole [4]). We can solve (3.15) using characteristic methods (since we have already obtained (R, Θ, T)), so that

$$\begin{aligned} \frac{dt}{ds} &= \alpha + 2\,\beta t \\ \frac{d\theta}{ds} &= \gamma \\ \frac{dr}{ds} &= \beta\, r. \end{aligned} \tag{3.16}$$

We have imposed $\delta = \lambda = 0$, as these parameters are not being used; the similarity forms obtained are thus:

$$\beta \neq 0: \qquad r = (\pm t)^{1/2} F(\theta) \tag{3.17}$$

$$\beta, \gamma \neq 0: \qquad r = (\pm t)^{1/2} F(\theta - \beta \ln(\pm t)) \tag{3.18}$$

$$\alpha, \gamma \neq 0: \qquad r = F(\theta - t/\alpha). \tag{3.19}$$

The solutions resulting from these will be detailed in the following section.

3.3 Reduction to Second-Order O.D.E.s

In this section, we will reduce (3.3) to a second-order ordinary differential equation, using the three similarity formulations (3.17)–(3.19), which we will then solve numerically; later we will show how we can further reduce (3.3) to first-order ordinary differential equations, and again produce solutions.

3.3.1 Separable Solutions

First of all, we use (3.17) and make the substitution

$$r = (\pm t)^{\frac{1}{2}} F(\theta) \tag{3.20}$$

into (3.11), which gives us the ordinary differential equation

$$F'' = F\left(1 \pm \frac{F^2}{2}\right) + \left(\frac{2}{F} \pm \frac{F}{2}\right) F'^2. \tag{3.21}$$

We can now integrate and investigate the two sets of solutions.

$r = (-t)^{1/2} F(\theta)$

Before integrating, we shall consider the phase plane. Setting

$$G = \frac{dF}{d\theta}$$

and substituting this into (3.21), we have

$$\begin{aligned} F' &= G \\ G' &= F\left(1 - \frac{1}{2}F^2\right) + \left(\frac{2}{F} - \frac{F}{2}\right) G^2. \end{aligned}$$

To remove the $2/F$ term in the second equation, we write

$$\frac{dF}{d\theta} = \frac{d\xi}{d\theta}\frac{dF}{d\xi}$$

and let

$$\frac{d\xi}{d\theta} = \frac{1}{F},$$

so that our equations read

$$\begin{aligned} F' &= FG \\ G' &= F^2\left(1 - \frac{1}{2}F^2\right) + \left(2 - \frac{1}{2}F^2\right)G^2 \end{aligned}$$

with primes now denoting derivatives with respect to ξ. We observe that there are three critical points—$(\pm\sqrt{2}, 0)$ and $(0,0)$; however, negative values of F are meaningless, as they imply a negative radial co-ordinate value, so we will not consider $(-\sqrt{2}, 0)$.

To analyse the behaviour around $(\sqrt{2}, 0)$ we set $\bar{F} = F - \sqrt{2}$. Linearising, we have

$$\begin{aligned} \bar{F}' &\sim \sqrt{2}G \\ G' &\sim -2\sqrt{2}\bar{F}. \end{aligned}$$

Looking for solutions of the form $\bar{F} \propto e^{\lambda\xi}$, $G \propto e^{\lambda\xi}$, we require

$$\lambda^2 + 4 = 0$$

and hence we have a centre at $(\sqrt{2}, 0)$. Since the system is invariant under $G \to -G$, $\xi \to -\xi$ the phase plane is symmetric about the F-axis and this centre is thus maintained under the perturbations due to the nonlinear terms. To study the critical point at $(0,0)$, we cannot use a linear approximation, as this will result in $F' = G' = 0$. We thus look at quadratic terms; this gives us

$$\begin{aligned} F' &\sim FG \\ G' &\sim F^2 + 2G^2 \end{aligned}$$

i.e.

$$\frac{dG}{dF} \sim \frac{1 + 2(G/F)^2}{(G/F)}.$$

Writing $u = G/F$, this becomes

$$F\frac{du}{dF} \sim \frac{1+u^2}{u},$$

which we can integrate to give

$$F \sim k\sqrt{1+u^2}$$

and hence

$$G \sim \pm\frac{F}{k}\sqrt{F^2-k^2}, \tag{3.22}$$

where k is the constant of integration. We can thus deduce from (3.22) that the trajectory coming into the origin has $F = 0$, whilst for $F \gg k$, we have $G \sim F^2/k$; from this we arrive at the phase plane shown in Figure 3.1. We thus expect our solution

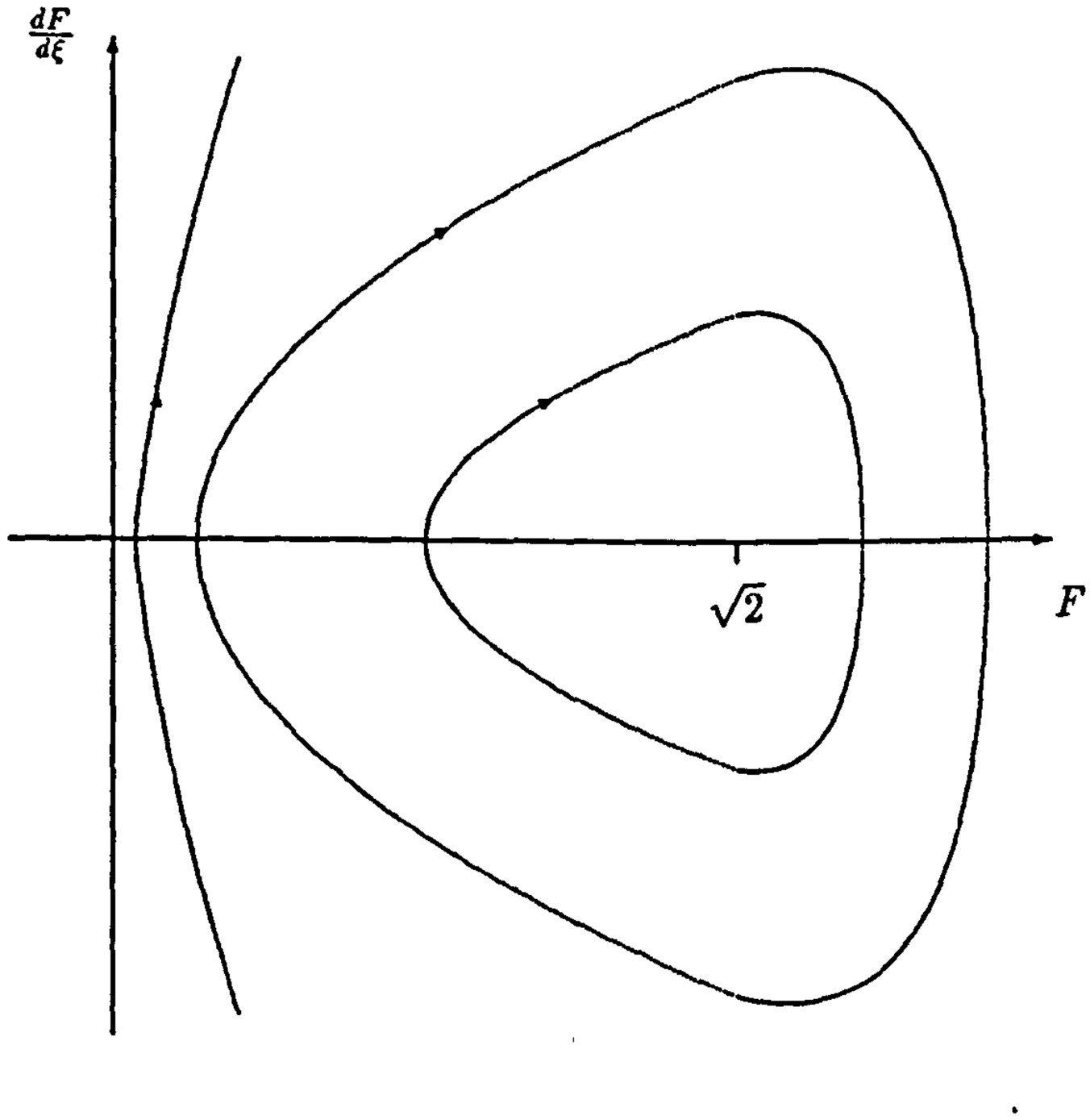

Figure 3.1: Diagram of the phase plane $dF/d\xi$ vs F for the $r = (-t)^{\frac{1}{2}}F(\theta)$ solution. Note that $dF/d\xi = F\,dF/d\theta$, so that the $dF/d\theta$ vs F phase plane would simply be a stretched version of the above; the trajectories are of the same form.

curves to be confined to an annulus with an inner radius $r_0 \leq \sqrt{2}$ and an outer radius $r_1 \geq \sqrt{2}$. In Figure 3.2, we show some numerical solutions which completely agree with

this; these solutions are analogous to those of Mullins [39] showing 'invariance under magnification'—they shrink and disappear at the origin whilst retaining shape. For special trajectories they are closed curves. It may at this point seem that these solutions will have no practical use, since they are self-intersecting, but this is not necessarily so. We are quite free to select individual 'sections' of the plots shown in Figure 3.2, by setting a finite range for values of θ. If we consider Figure 3.3, then we can observe three different types of behaviour for solution curves shrinking on a wedge, depending on whether or not they disconnect from the wedge boundary. In all cases shown, the curves eventually become circular and collapse to a point either in free space, at the vertex of the wedge (exactly as predicted by Gage [14] and Rubinstein et al. [43] for a curve which does not intersect the boundaries) or on the sides of the wedge. It can be inferred (King [32]) that there must be some dividing line between these cases, and that the similarity solutions above describe it. To assess this, we set up a simple time-stepping finite-difference scheme for (3.11), with

$$\begin{aligned} r_{t\,i,t} &\equiv (r_{i,t+1} - r_{i,t})/\Delta t \\ r_{\theta\,i,t} &\equiv (r_{i+1,t} - r_{i-1,t})/2\Delta\theta \\ r_{\theta\theta\,i,t} &\equiv (r_{i+1,t} - 2r_{i,t} + r_{i-1,t})/(\Delta\theta)^2. \end{aligned} \tag{3.23}$$

If we set the initial front to resemble one 'loop' in the lower plot in Figure 3.2, and constrain its end points to move normally, then by following its evolution, we produce a solution as shown in Figure 3.4; it can be seen that its shape *is* fairly well preserved, and that our similarity solutions *are* viable, although unstable.

$\underline{r = t^{1/2}F(\theta)}$

The analysis here follows exactly the same method as above; this time our equations read

$$\begin{aligned} F' &= FG \\ G' &= F^2\left(1+\frac{1}{2}F^2\right) + \left(2+\frac{1}{2}F\right)G^2 \end{aligned}$$

and hence we have only the single critical point at $(0,0)$. To compute the phase plane,

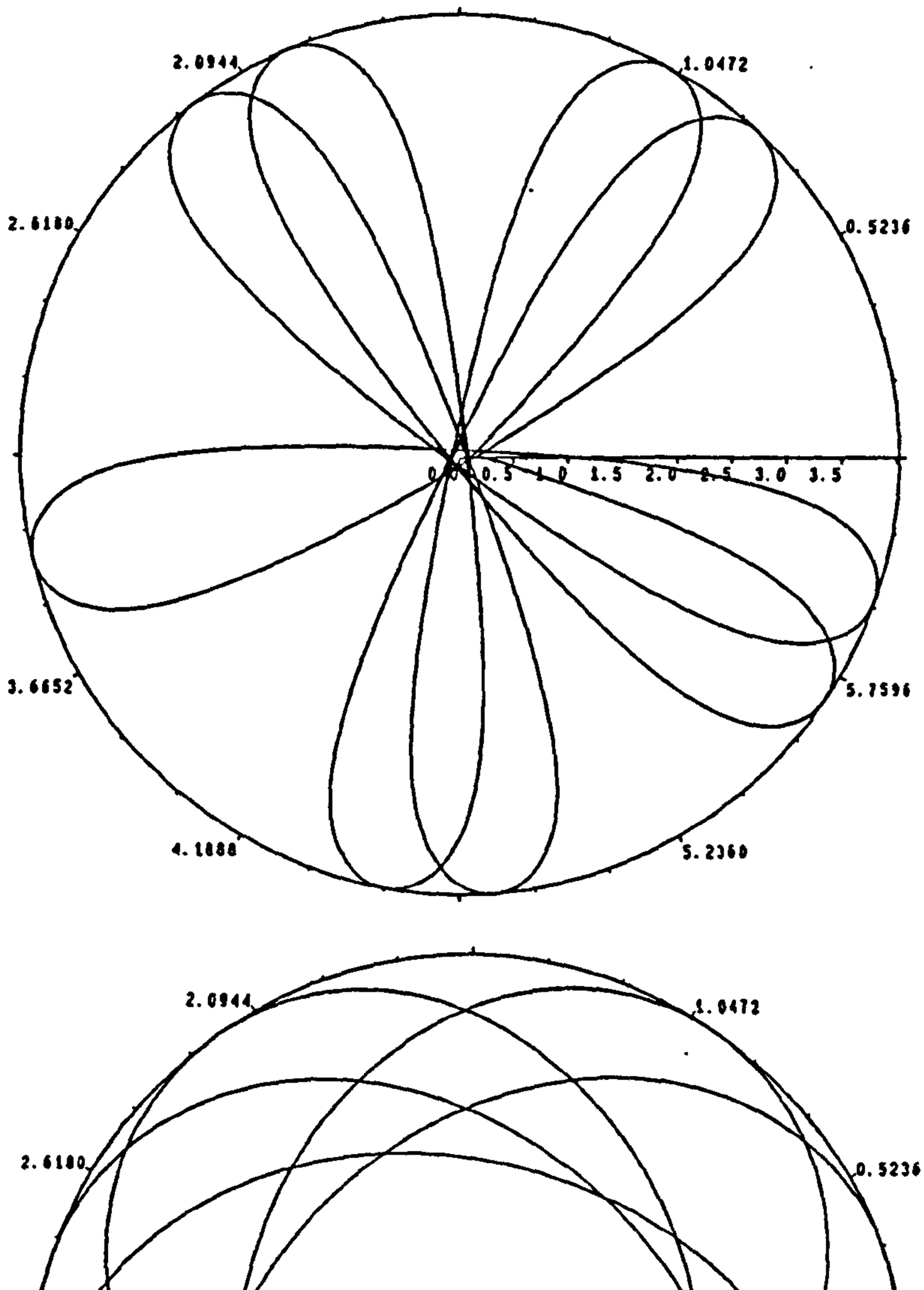

Figure 3.2: Typical solutions for $F(\theta)$ for the $r = (-t)^{\frac{1}{2}}F(\theta)$ solution; $F(0) = 0.1$, $F'(0) = 0$ (top), $F(0) = 1.0$, $F'(0) = 0$ (bottom).

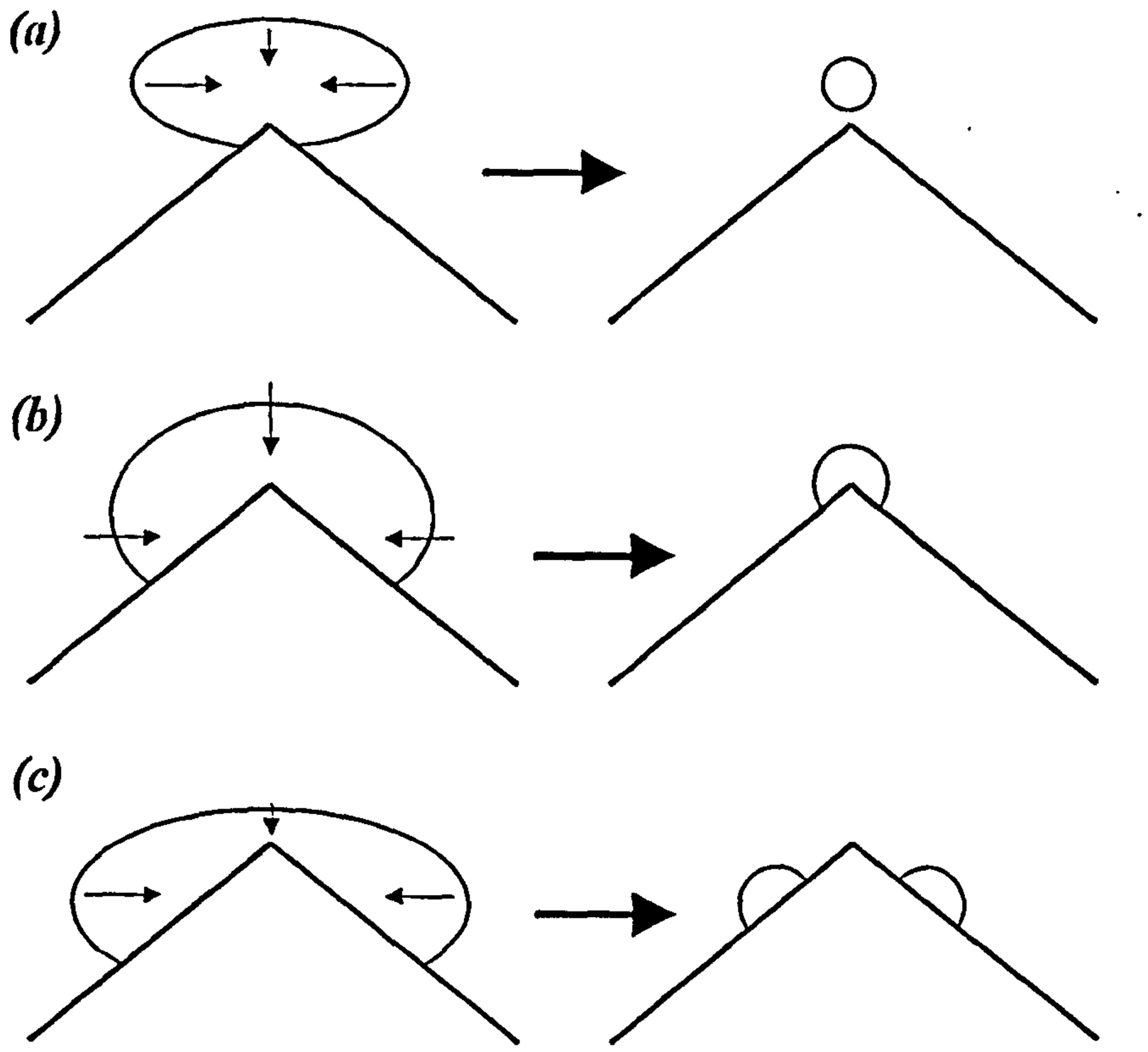

Figure 3.3: Possible evolution of curves on a wedge-shaped boundary. In (a), the curve leaves the wedge, and collapses as a circle in the usual fashion. In (b), the curve evolves to an arc of a circle as it collapses, and shrinks to a point at the vertex. In (c), the curve hits the vertex of the wedge before it has collapsed, resulting in two separate curves which collapse to a point on either side of the vertex.

we use the analysis from the previous solution together with the isoclines

$$\frac{dG}{dF} = \frac{F}{G}\left(1 + \frac{1}{2}F^2\right) + \left(\frac{2}{F} + \frac{F}{2}\right)G$$

to obtain the plot shown in Figure 3.5. We thus expect our solutions to move quickly in towards the origin, and then quickly turn away again. This is confirmed by the numerical solution shown in Figure 3.6; it can be seen that the plot is symmetric about the (chosen) axis $\theta = 0$. These solutions, which correspond to initial data containing a corner, also appear in Mullins [39].

In this subsection, we have essentially demonstrated results that have been obtained by earlier workers (albeit using a different method). However, they will prove useful

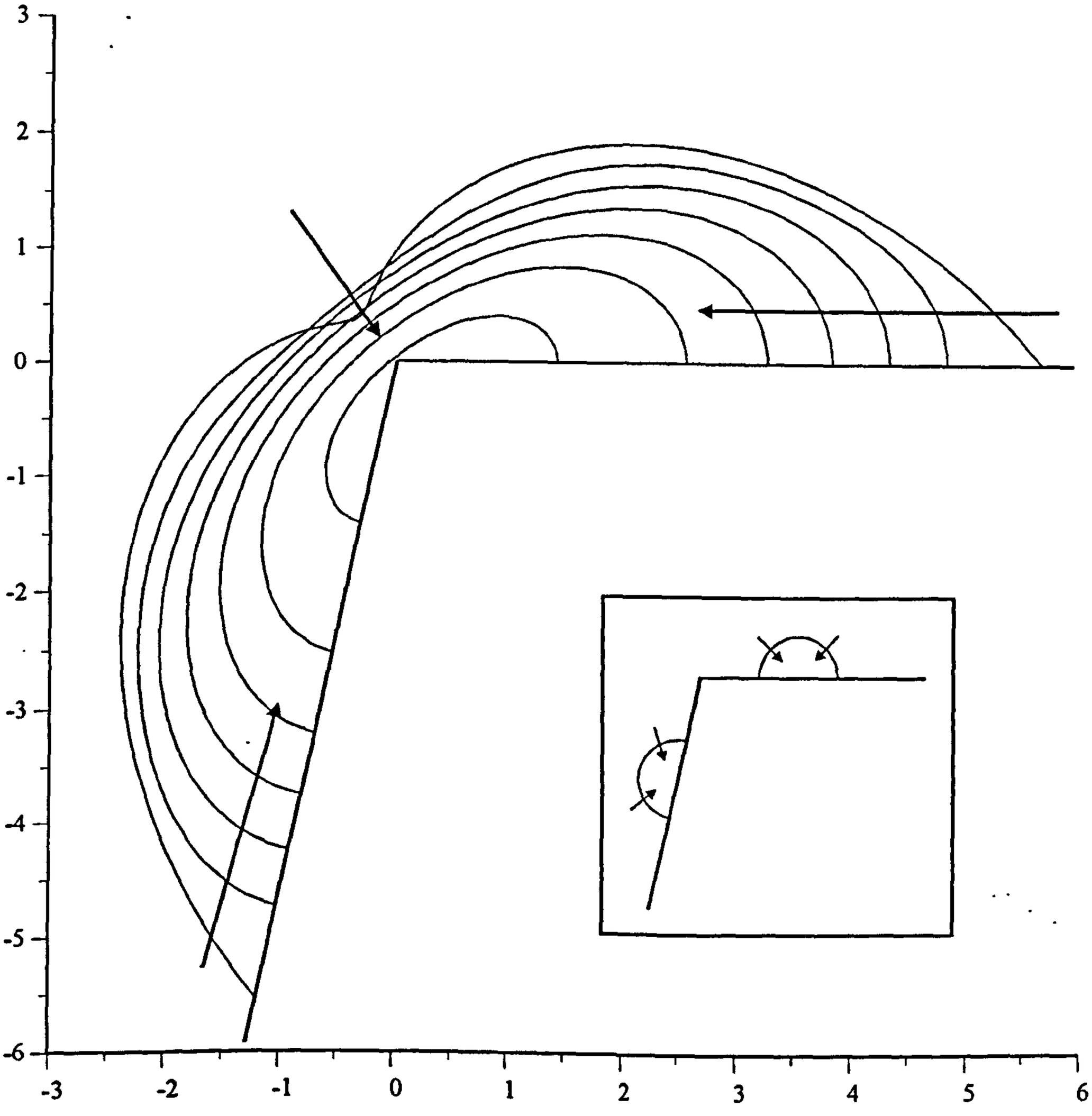

Figure 3.4: Example of front evolution in a wedge-shaped region. We would expect the curve to separate into two regions as the evolution continues (as shown in the inset, and in Figure 3.3); our radial formulation is not suitable for dealing with this, and we do not consider it further.

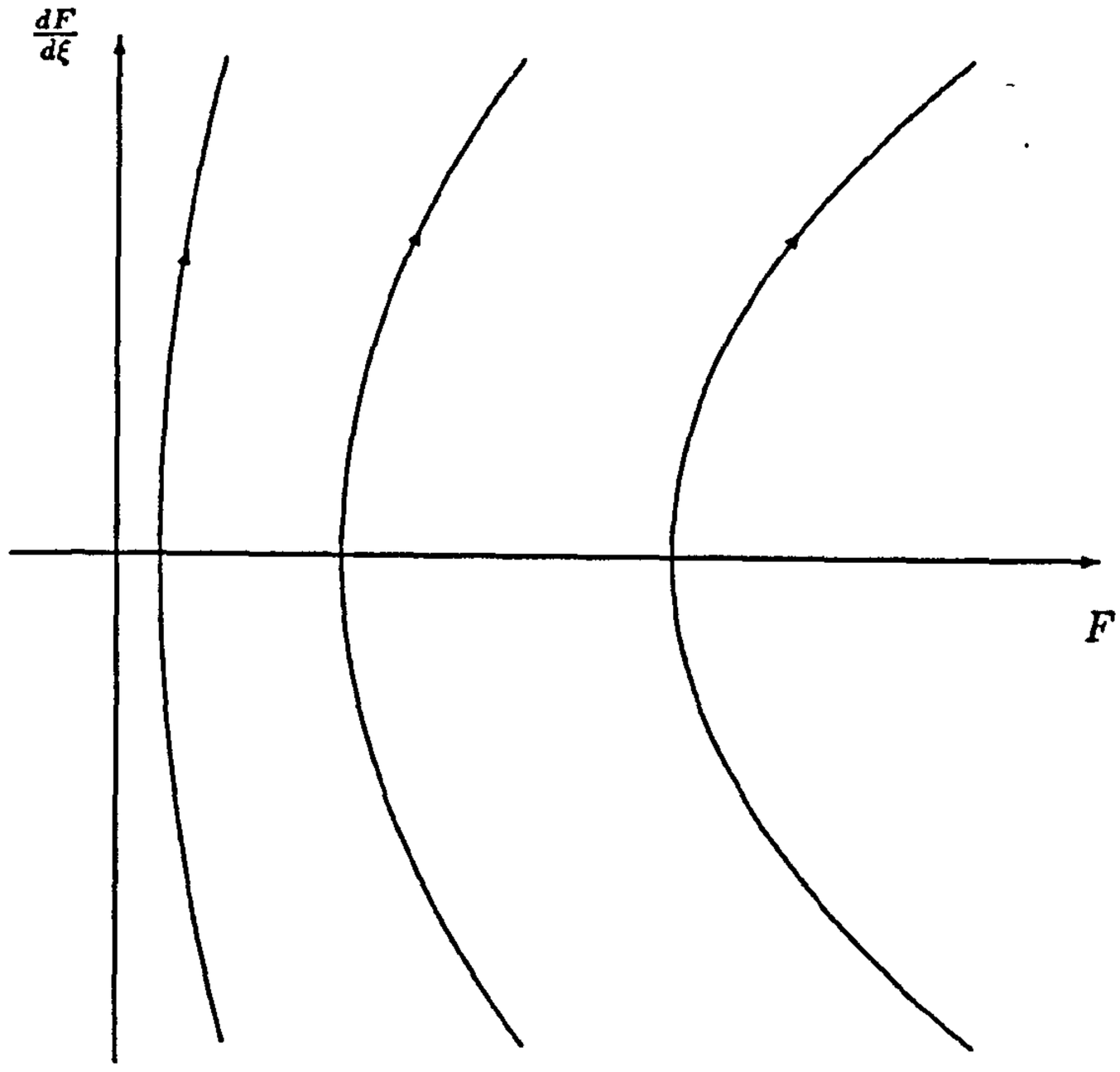

Figure 3.5: Diagram of the phase plane $dF/d\xi$ vs F for the $r = t^{\frac{1}{2}}F(\theta)$ solution.

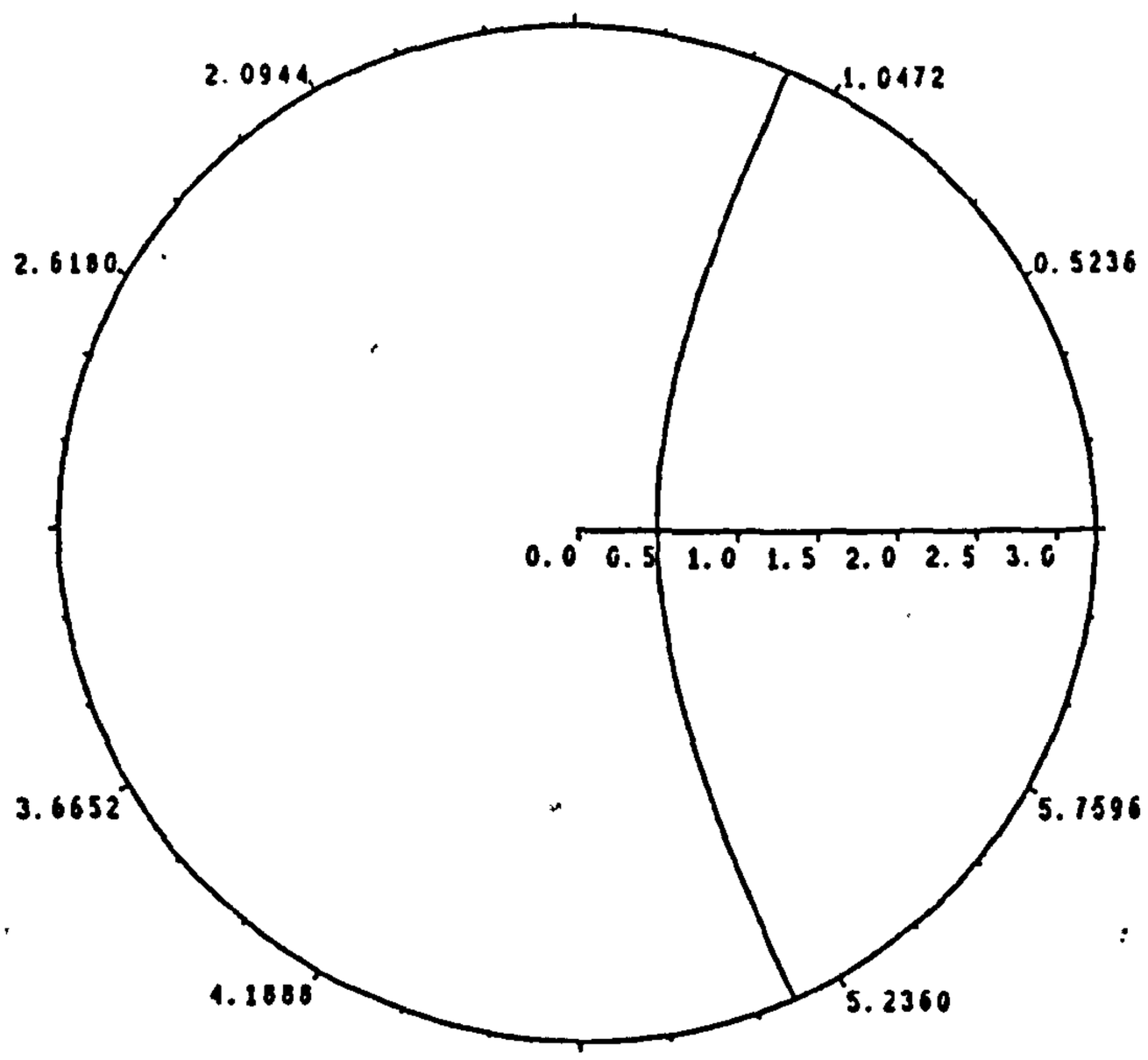

Figure 3.6: Typical solution for $F(\theta)$ for the $r = t^{\frac{1}{2}}F(\theta)$ formulation; $F(0) = 0.5$, $F'(0) = 0$.

for comparisons in the next section, when we will show how (3.21) can be integrated analytically, which does not appear to have been achieved previously. Before this, though, we will extend our 'second-order' similarity solutions (i.e. numerical solutions of second-order ordinary differential equations) by introducing a new class of symmetries.

3.3.2 A second family of similarity solutions

The method of analysis in this subsection is similar to that above. Returning to (3.11), we now use (3.18) and substitute

$$r = (\pm t)^{\frac{1}{2}} F(\eta), \tag{3.24}$$

where

$$\eta = \theta - \mu \ln(\pm t)$$

(we have exchanged β in (3.18) for μ) to obtain

$$F'' = F\left(1 \pm \frac{F^2}{2}\right) + \left(\frac{2}{F} \pm \frac{F}{2}\right) F'^2 \mp \mu(F^2 + F'^2)F'. \tag{3.25}$$

It can be seen that $\mu = 0$ corresponds to the previous formulation. Again, we need to consider the two cases separately.

$\underline{r = (-t)^{1/2} F(\eta)}$

If we investigate the phase plane, then the required equations are

$$\begin{aligned} F' &= FG \\ G' &= F^2\left(1 - \frac{1}{2}F^2\right) + \left(2 - \frac{1}{2}F^2\right)G^2 + \mu(F^2 + G^2)FG \end{aligned}$$

and we have the same critical points as previously (i.e. $(0,0)$ and $(\sqrt{2},0)$). At $(0,0)$ we have the same behaviour as we had for the previous formulation; however, linearising about $F = \sqrt{2}$, $G = 0$, we obtain

$$\begin{aligned} \bar{F}' &\sim \sqrt{2}G \\ G' &\sim -2\sqrt{2}(\bar{F} - \mu G) \end{aligned}$$

and thus, looking for exponential solutions as before, we find

$$\lambda = -\sqrt{2}(\mu \mp \sqrt{\mu^2 - 2}), \tag{3.26}$$

which gives us the following cases for the critical point :

$$\begin{aligned}
\mu < -\sqrt{2} &\Rightarrow \text{stable node} \\
\mu = -\sqrt{2} &\Rightarrow \text{stable degenerate node} \\
-\sqrt{2} < \mu < 0 &\Rightarrow \text{stable spiral} \\
\mu = 0 &\Rightarrow \text{centre} \\
0 < \mu < \sqrt{2} &\Rightarrow \text{unstable spiral} \\
\mu = \sqrt{2} &\Rightarrow \text{unstable degenerate node} \\
\mu > \sqrt{2} &\Rightarrow \text{unstable node.}
\end{aligned} \tag{3.27}$$

Thus, for $\mu < 0$, we expect solutions to move *towards* a critical point at $F(\eta) = \sqrt{2}$, whilst for $\mu > 0$, the trajectories move *away*. This is the only difference between the solutions for positive and negative values of a particular μ, and hence we shall only consider $\mu > 0$. Example phase planes in Figures 3.7 and 3.8 show the behaviour

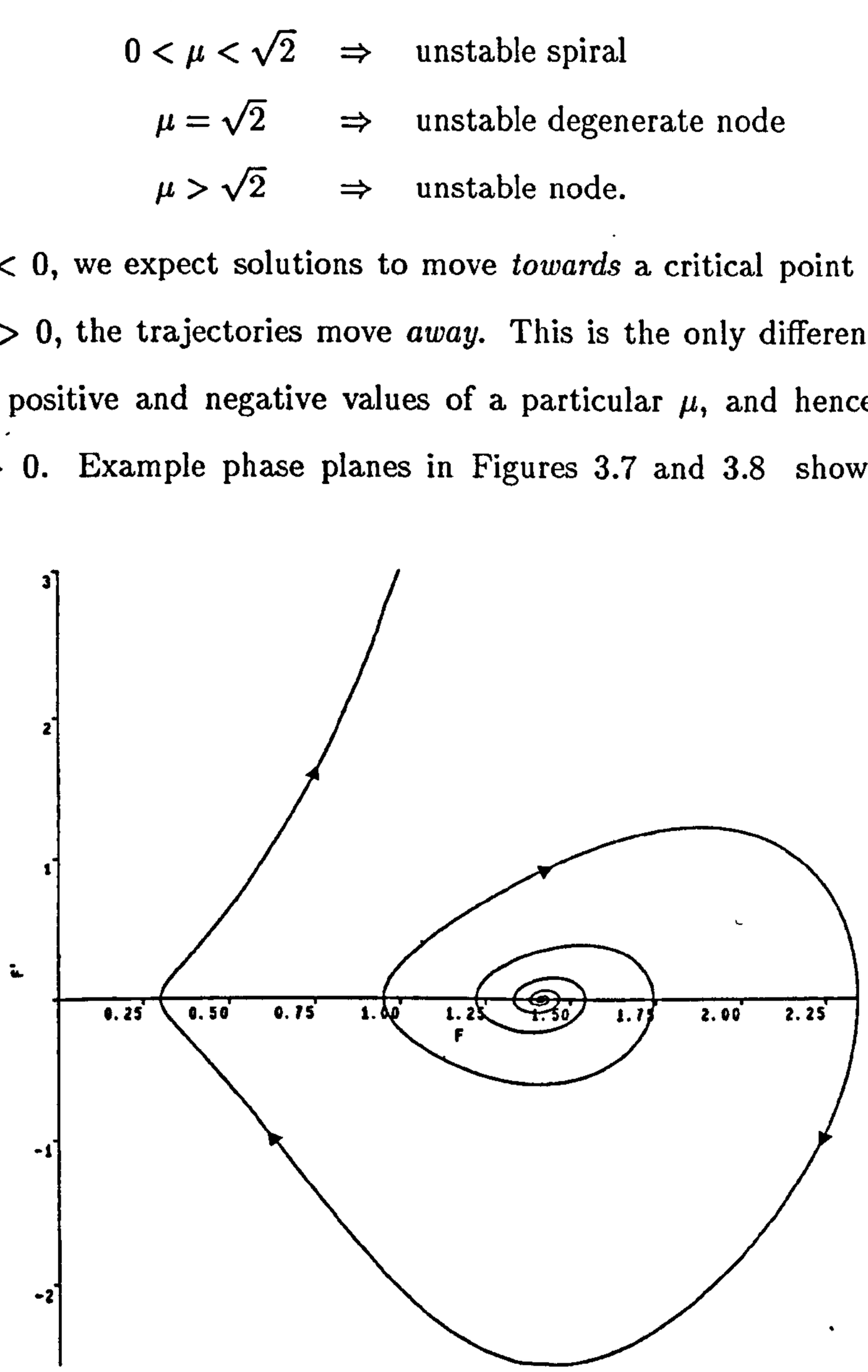

Figure 3.7: Numerical solution for the phase plane for $\mu = 0.2$.

$\mu = 0.2$ and $\mu = 2.5$. For $\mu > \sqrt{2}$, the solution curve spirals away from the critical point as shown in Figure 3.9; for small μ, our critical point becomes an unstable spiral, and the self-intersection solutions of the type seen previously become apparent as we move away

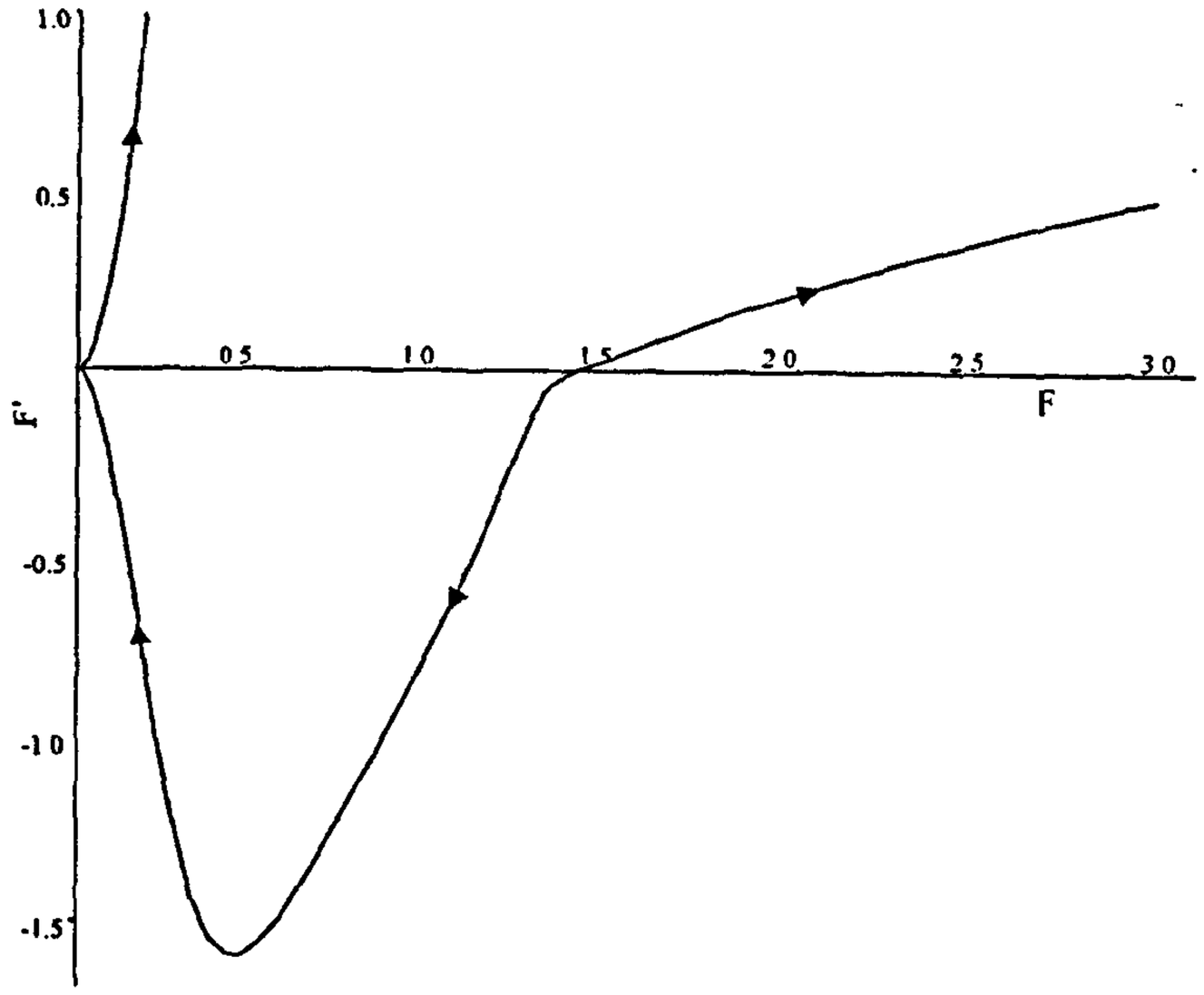

Figure 3.8: Numerical solution for the phase plane for $\mu = 2.5$.

from the critical point, until $F' \to +\infty$ (see Figure 3.7) shortly after the trajectory's nearest approach to the origin (as can be observed in the solution curve in Figure 3.10).

$\underline{r = t^{1/2}F(\eta)}$

This time, analysis of the phase plane proves more difficult, as the techniques applied above glean no more information than was available for $\mu = 0$; hence, our method of progress is to solve the equation

$$\frac{dG}{dF} = \frac{F}{G}\left(1 + \frac{1}{2}F^2\right) + \left(\frac{2}{F} + \frac{F}{2}\right)G - \mu\left(F^2 + G^2\right) \tag{3.28}$$

numerically for G in terms of F. As $|\mu|$ increases above zero, the phase plane changes from that shown in Figure 3.5 to that of Figure 3.11. Once again, we find that the solutions for positive and negative μ differ only in the direction of their trajectories and so we again restrict our investigation to $\mu > 0$; for $\mu = 0$, the solution will represent half of a 'corner' solution, mentioned earlier.

We choose to look at trajectories with initial point $F = 0.5$, $F' = 0$ to see the effect of increasing μ. This point is chosen as representative because the effect of the 'hump'

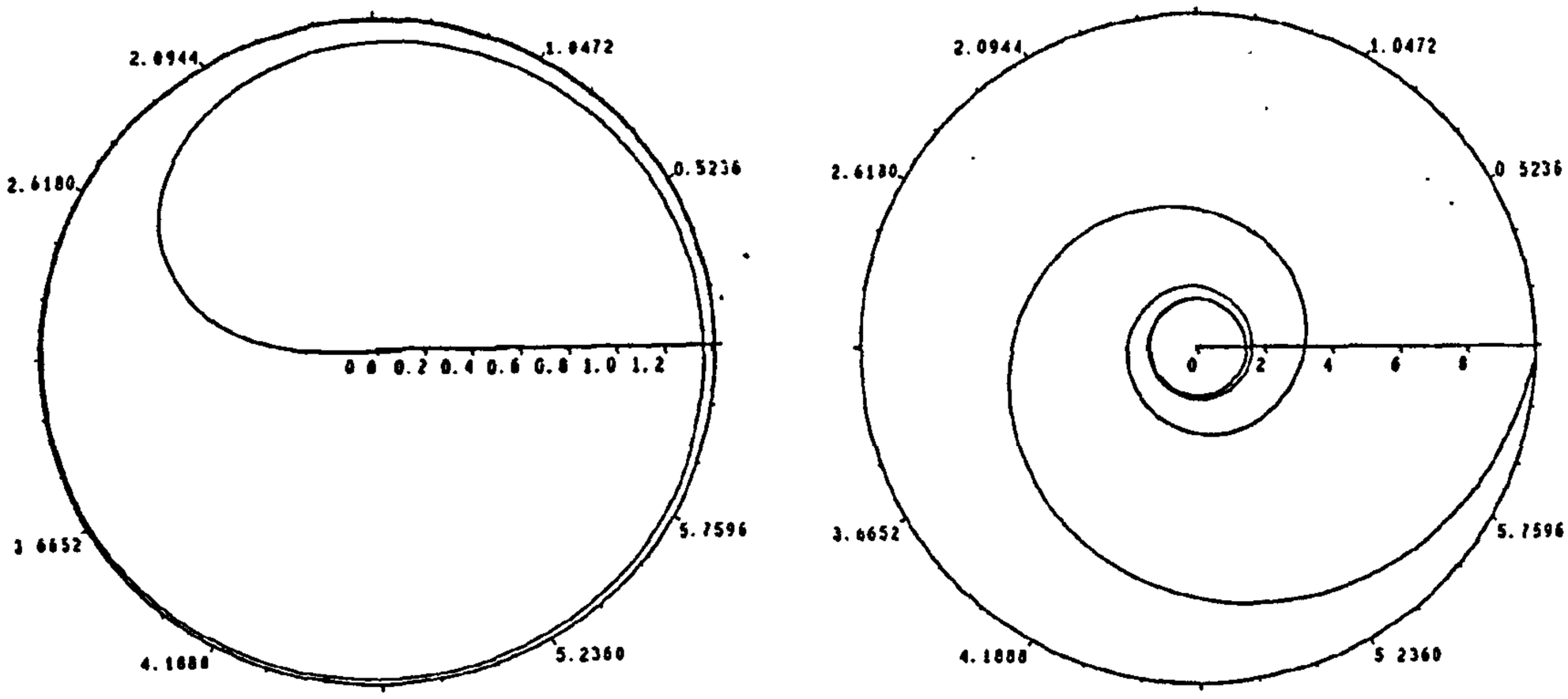

Figure 3.9: Plot of $F(\eta)$ for $\mu = 2.5$; (a) corresponds to the trajectory in Figure 3.8 leaving the critical point going to the left, and (b) corresponds to the trajectory going to the right. The initial approximately circular solution is due to $F' \approx 0$ near to the critical point. Note in (a) that the trajectory does *not* go into the origin; however $F'(\eta) \to \infty$ here and the trajectory terminates.

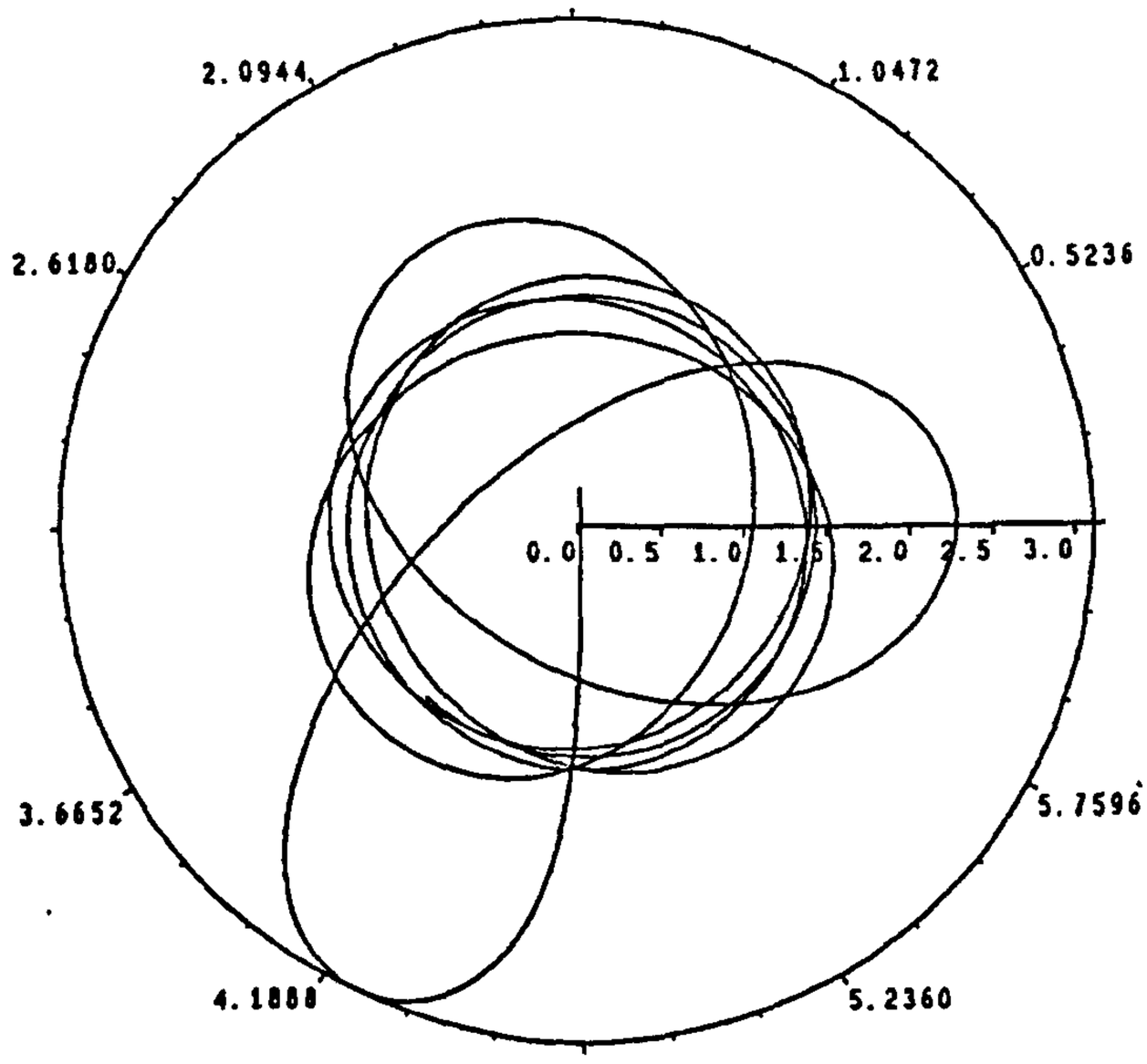

Figure 3.10: Plot of $F(\eta)$ for $\mu = 0.05$. The solution curve is terminated near $F = 0$ due to the slope becoming infinite.

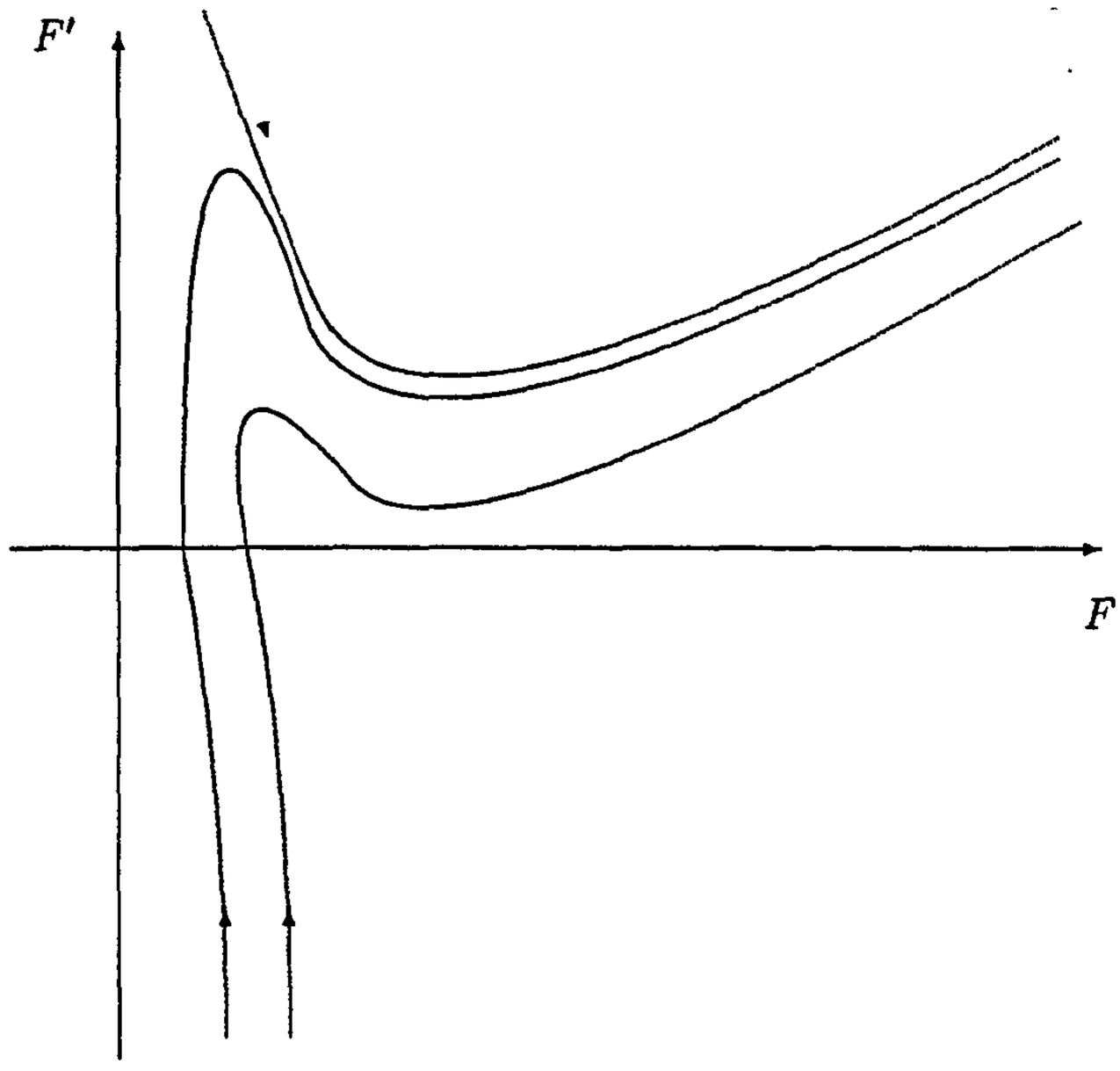

Figure 3.11: Diagram of the phase plane for $r = t^{\frac{1}{2}}F(\eta)$; $\mu > 0$. The top curve represents a trajectory where $F \to 0$ as $F' \to +\infty$.

in the phase plane (Figure 3.11) will be shown; we shall not need to investigate the behaviour for $F' < 0$, as the phase plane is not significantly different from the $\mu = 0$ case discussed earlier. The results of this investigation are shown in Figure 3.12.

It can be seen that increasing μ causes the solution curve to 'bend' back on itself, eventually resulting in a spiral which becomes more compact as μ is further increased.

If we solve along two trajectories, initiating from $F \to 0$, $F' \to \pm\infty$, and plot them together, we obtain a 'closed' spiral, as shown in Figures 3.13 and 3.14, with both a wave 'front' and a wave 'back' being produced, as described in Keener [28] in a different context. The two series of plots show how the spirals compact as μ increases, and the snapshots taken as time increases for each case show how they expand as well as rotate as they evolve. The 'curve-shortening' feature of (3.3) is evident in the way such solutions evolve.

Finally, we note an initial-value problem satisfied by this solution. F does not appear

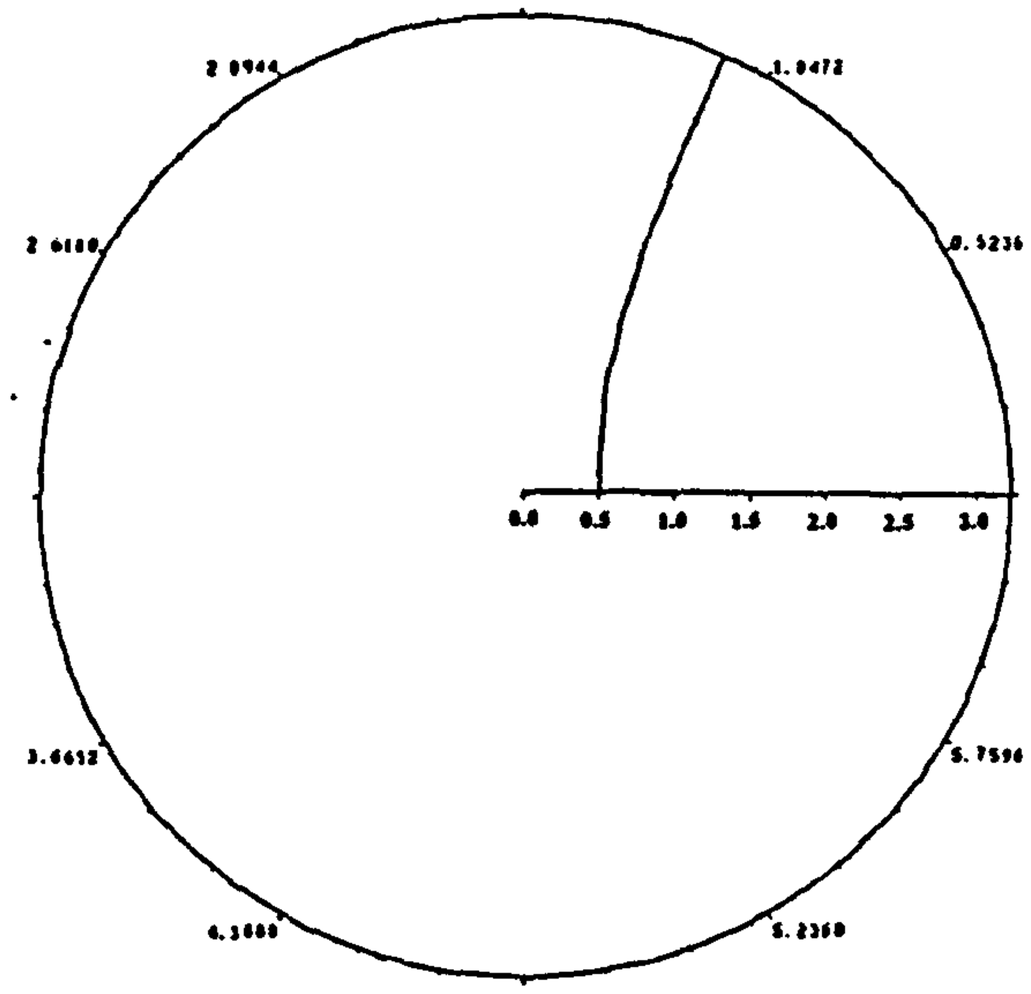

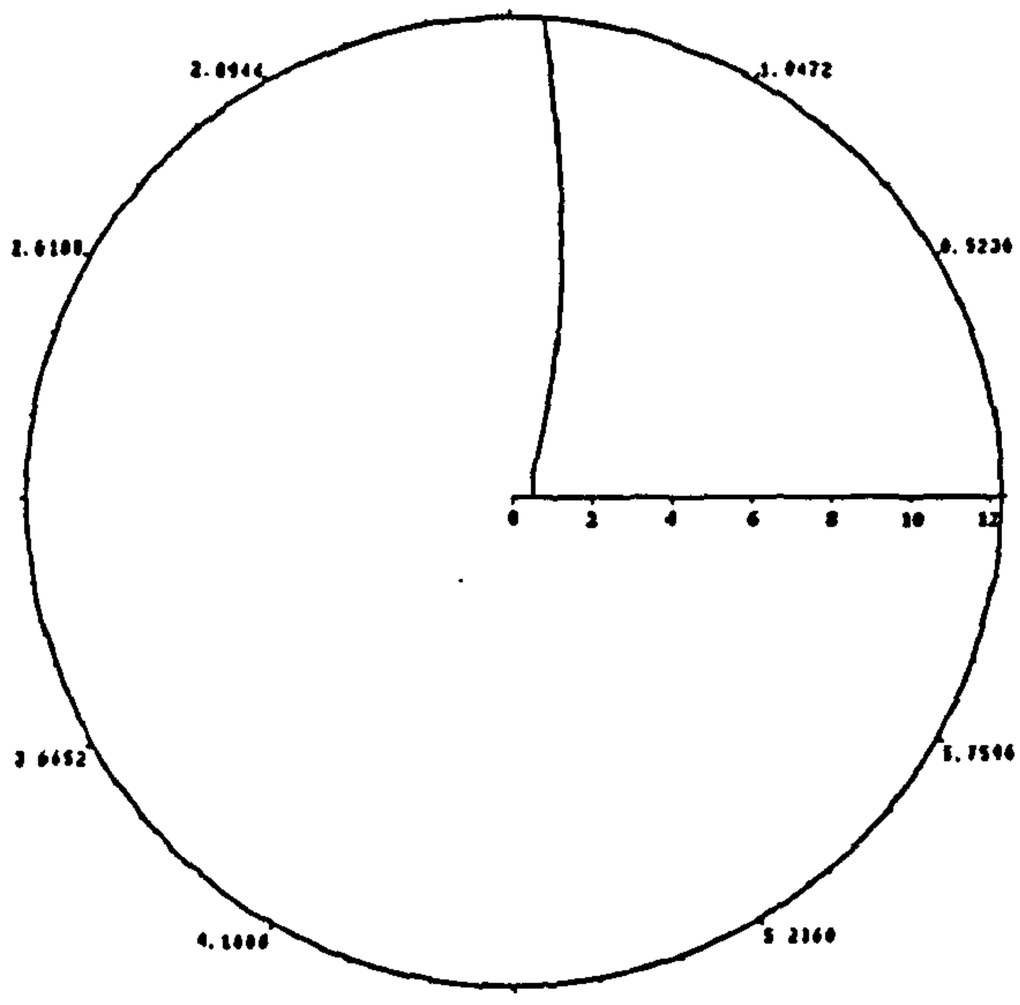

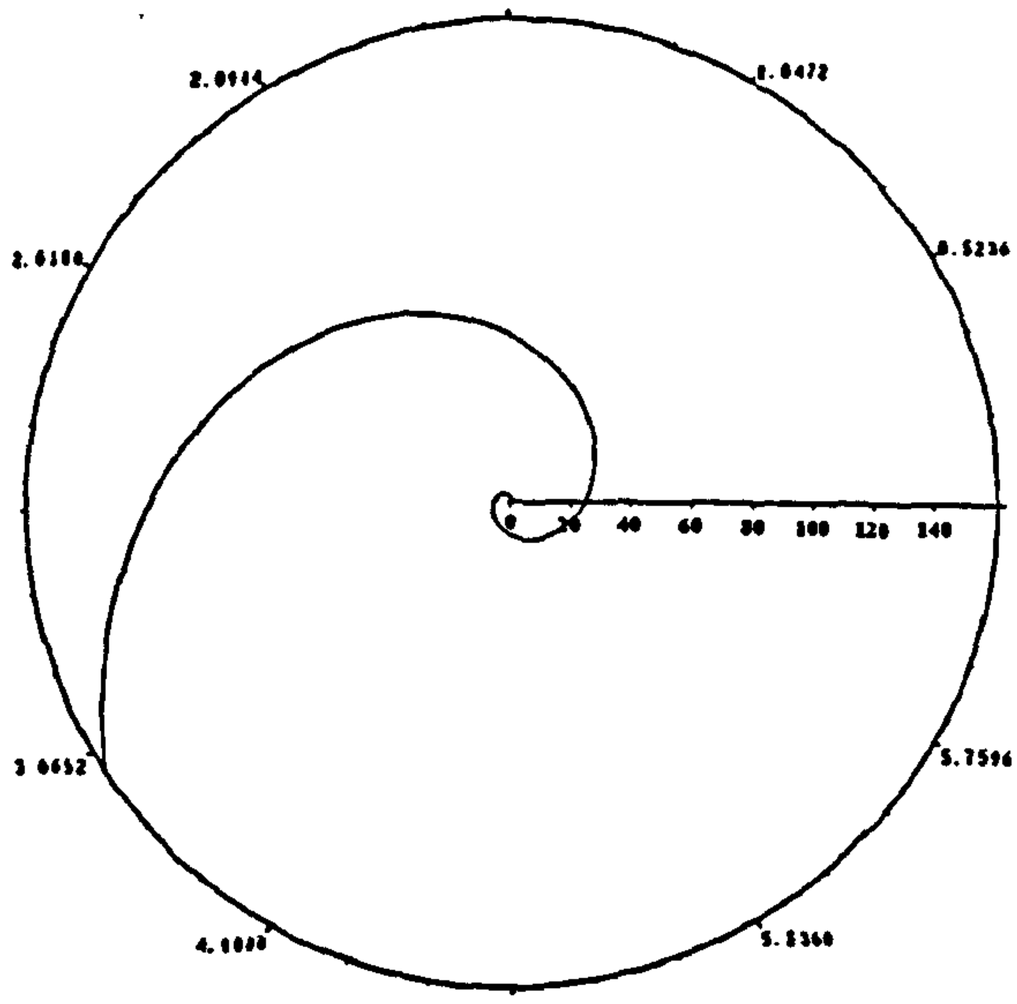

Figure 3.12: Plot of $F(\eta)$ for $F' \geq 0$ only (chosen for display purposes); (a) $\mu = 0$, (b) $\mu = 0.1$ and (c) $\mu = 1.0$. (a) represents the top half of the corner solution as shown in Figure 3.6. In (b) and (c), it can be observed how this corner solution bends back into a spiral as μ is increased.

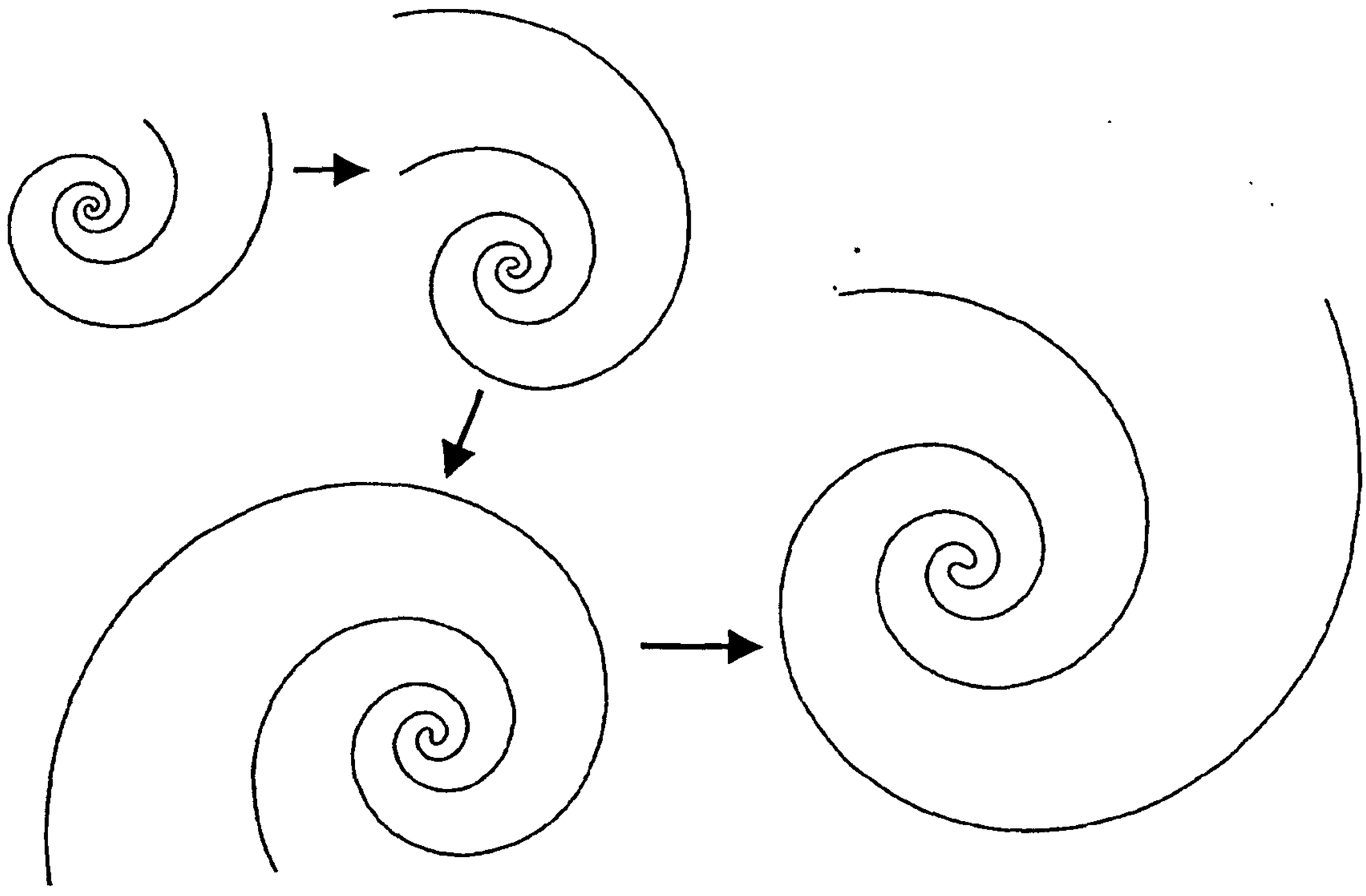

Figure 3.13: Evolving spirals for $\mu = 2$.

to be defined at $t = 0$; however, if we suppose that

$$F(\eta) \sim Ce^{\frac{\eta}{2\mu}} \qquad \text{as } \eta \to \infty,$$

then we have for fixed θ

$$r \sim Ct^{\frac{1}{2}}e^{\frac{\theta}{2\mu}-\frac{1}{2}\ln t} \qquad \text{as } t \to 0$$

i.e.

$$r = Ce^{\theta/2\mu} \qquad \text{at } t = 0. \tag{3.29}$$

This also implies that we should see Archimedian spirals in the far-field (i.e. $\ln F \propto \eta$); Figure 3.15 shows that this is indeed the case. We note that the initial condition (3.29) determines the required value of μ.

3.3.3 Rotating waves

Finally, we use (3.19) to make the substitution

$$r = F(\eta) \tag{3.30}$$

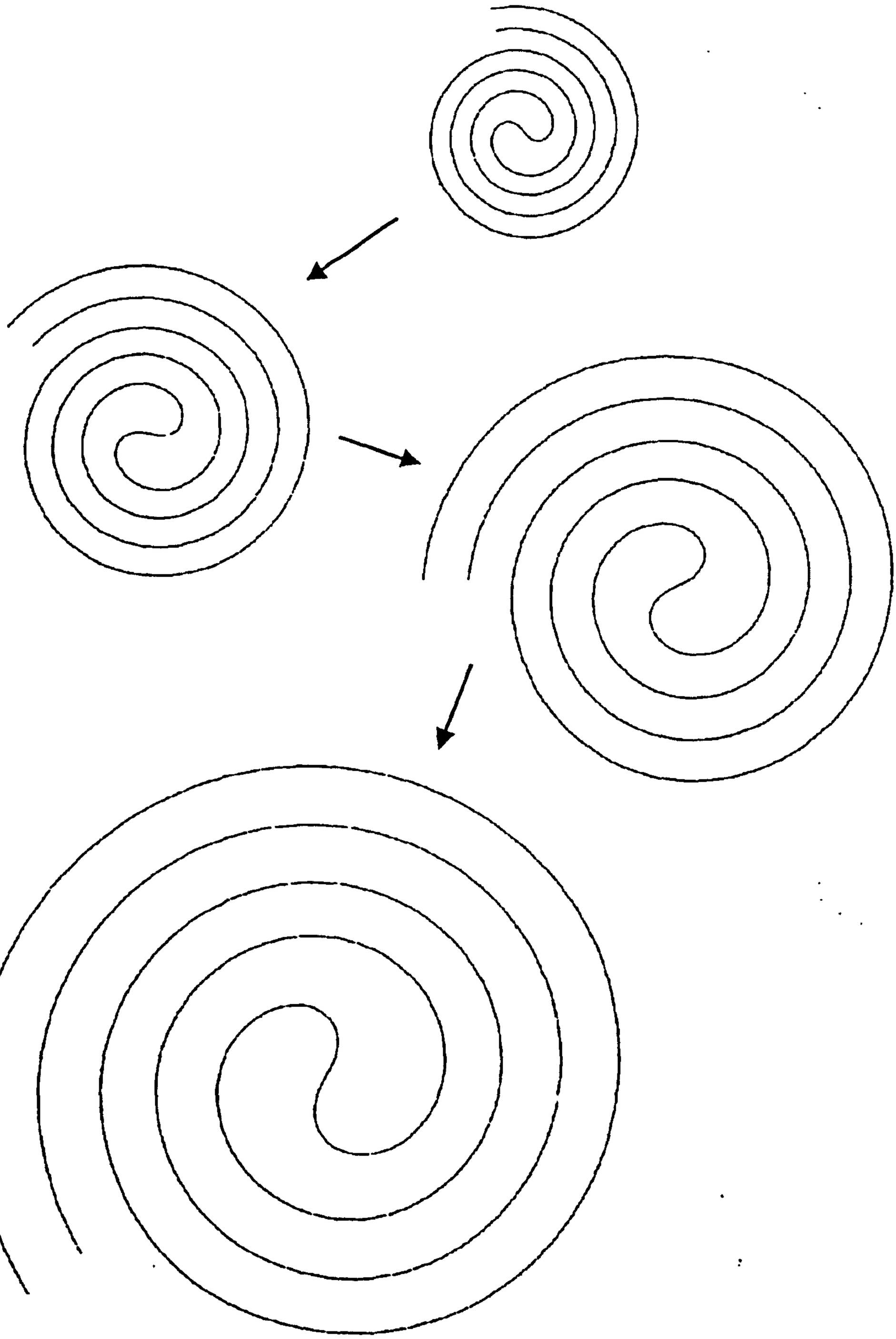

Figure 3.14: Evolving spirals for $\mu = 10$.

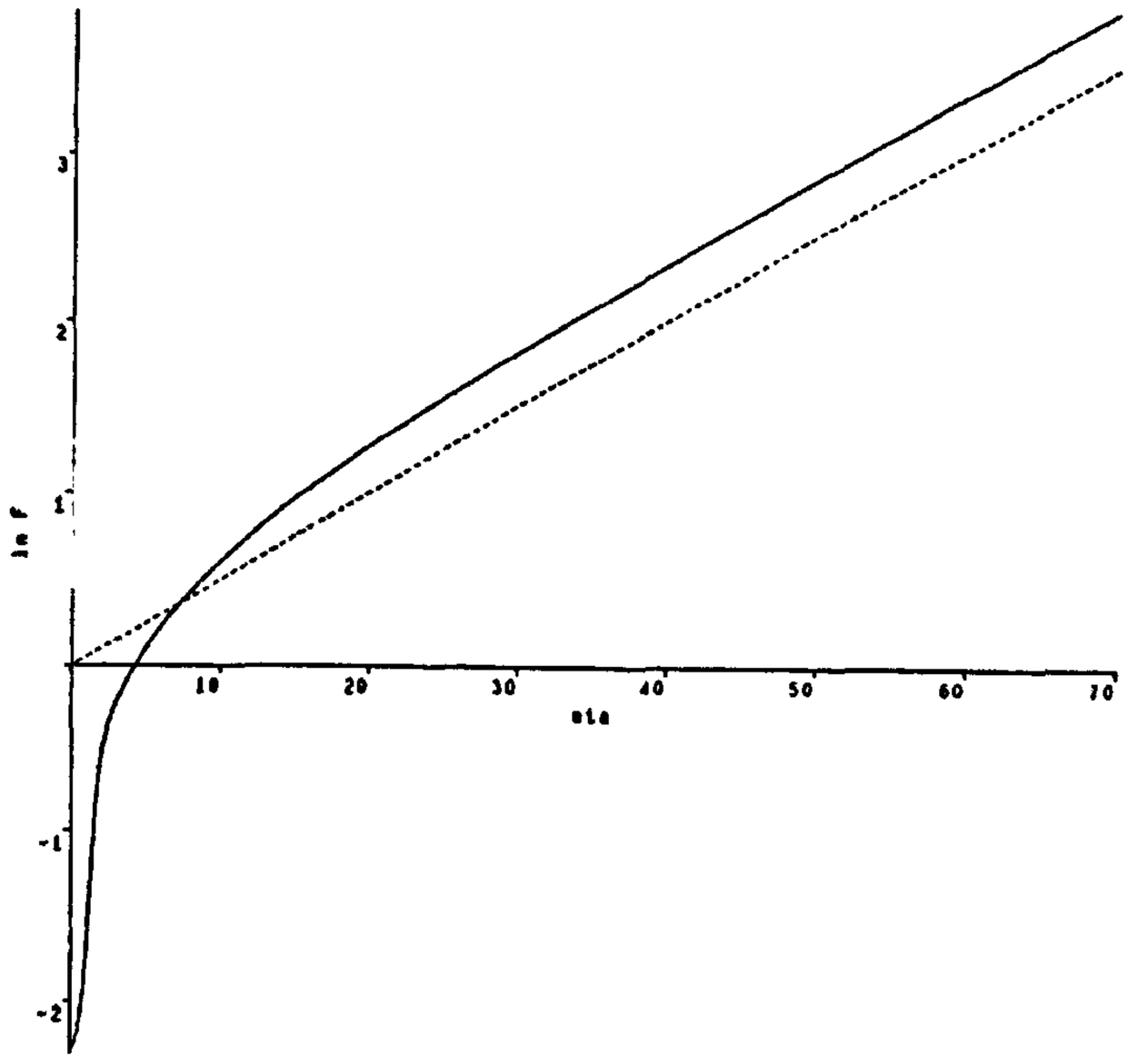

Figure 3.15: Behaviour as $\eta \to +\infty$; $\mu = 10$.

with

$$\eta = \theta - q\,t$$

(which corresponds to a rigidly rotating solution) to give us

$$F\,F'' + q\,F\,F'(F'^2 + F^2) - 2\,F'^2 - F^2 = 0. \tag{3.31}$$

The phase plane equations are

$$\begin{aligned} F' &= F\,G \\ G' &= F^2 + 2\,G^2 - q\,F\,G\,(F^2 + G^2), \end{aligned}$$

and once again we have a single critical point at $(0,0)$, with the local behaviour again being given by (3.22). The resulting phase plane is shown in Figure 3.16; it can be seen to be very similar to the $r = t^{1/2}F(\theta - \mu \ln t)$ plot (Figure 3.11), with the main difference being the behaviour in the far-field—here, $F' \to 0$ as $F \to \infty$, whereas $F' \to \infty$ as $F \to \infty$ in the previous case. Thus, we can expect our spiral solutions here to move closer and closer together in the far-field; this is backed up by the example solution shown in Figure 3.17 for $q = 1$ (the parameter q represents a simple rescaling, with no effect on the

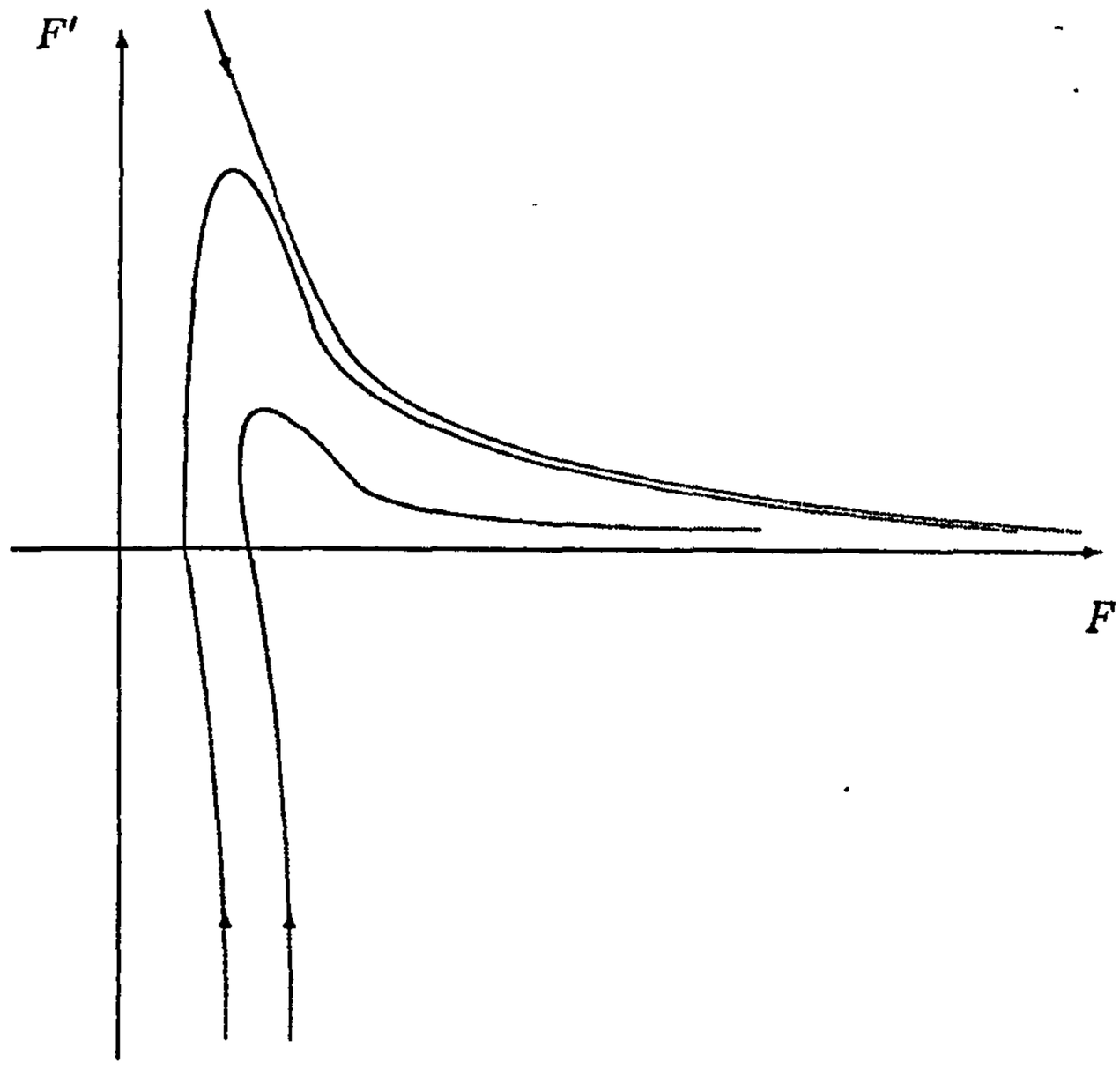

Figure 3.16: Diagram of the phase plane for $r = F(\theta - qt)$.

shape of the solution—this is apparent from the group definition (3.19), since $q = 1/\alpha$). The spiral in Figure 3.17 is the same as that produced by Mullins [39], corresponding to initial conditions $F(0) = 0$, $F'(0) = 0$; the full 'enclosed' spiral (Figure 3.18) can be obtained in the same way as for the previous similarity solution—solving along two trajectories emanating from $F(0) = 0$, $F'(0) \to +\infty$ and $F(0) = 0$, $F'(0) \to -\infty$; for numerical purposes we in fact start from some small value of $F(0)$.

3.4 Reduction to First Order Equations

In this section, we shall demonstrate methods of integrating the second order equations of the previous section analytically, and investigate the solutions.

Writing our curvature equation as

$$y_t = \frac{y_{xx}}{1 + y_x^2} \tag{3.32}$$

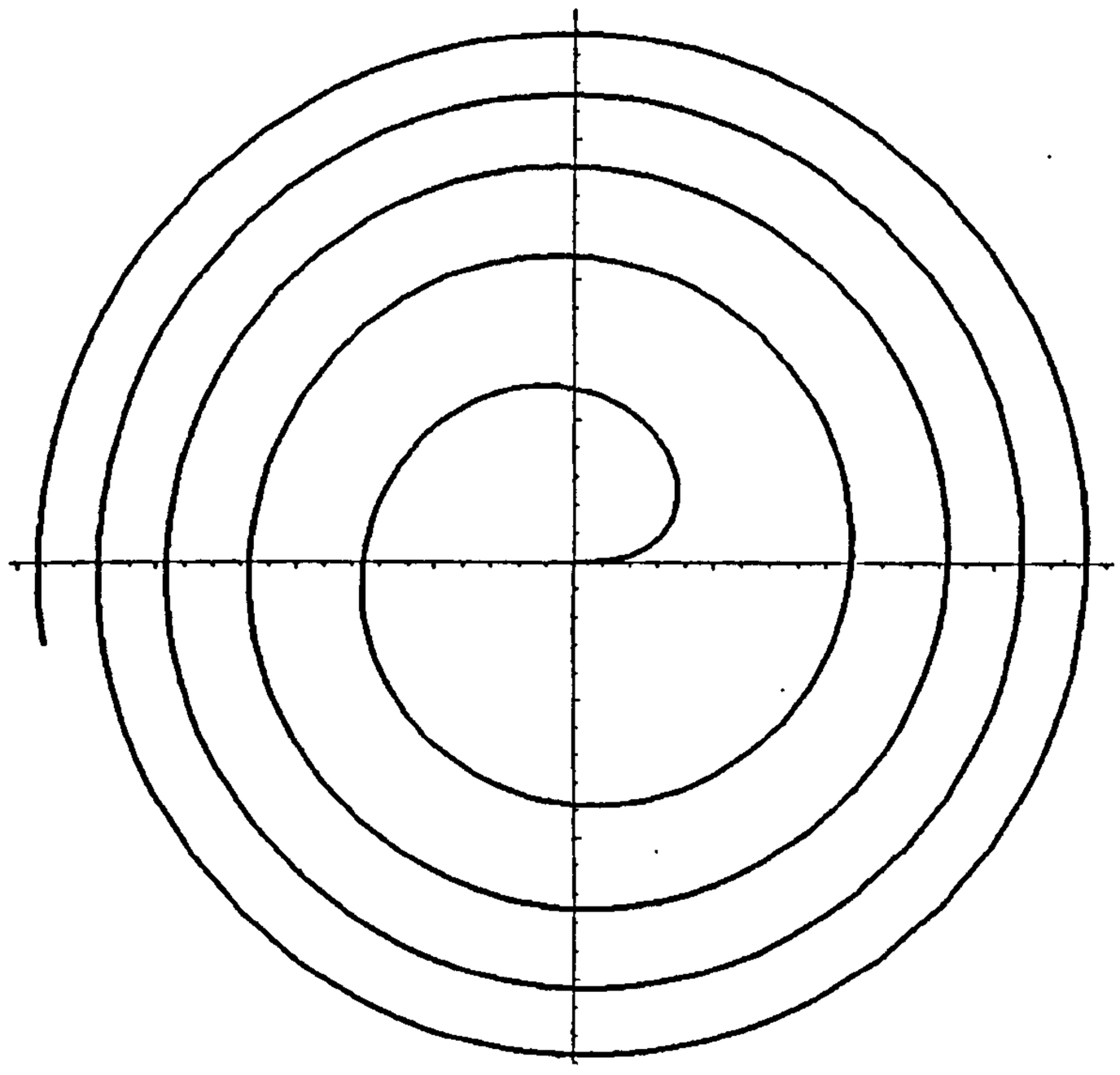

Figure 3.17: Spiral plot for $q = 1$, $F(0) = 0.001$, $F'(0) = 0$.

and making the transformation

$$\begin{aligned} u &= x - iy \quad (= re^{-i\theta}) \\ z &= x + iy \quad (= re^{i\theta}) \end{aligned} \tag{3.33}$$

then we obtain

$$u_t = \frac{u_{zz}}{u_z}. \tag{3.34}$$

3.4.1 Spiral waves

We start by giving a different approach to the solutions of section 3.3.3. We will now seek a rigidly-rotating spiral wave solution (using (3.19)) by setting

$$\theta = qt + F(r)$$

so that, from (3.33), we obtain

$$\begin{aligned} u &= r\,e^{-i(qt+F(r))} \\ z &= r\,e^{i(qt+F(r))}. \end{aligned}$$

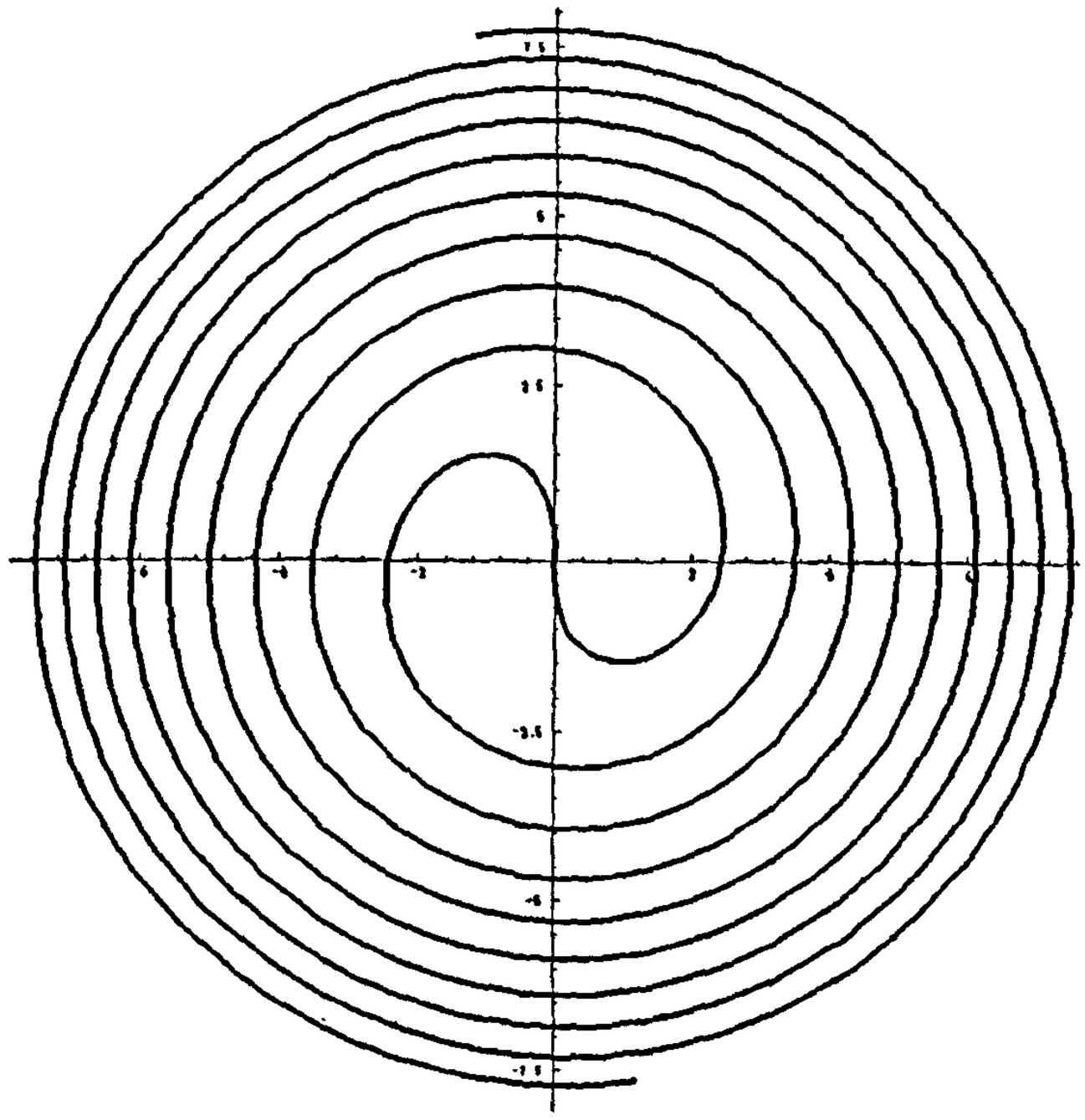

Figure 3.18: Spiral plot for $q = 1$, $F(0) = 0.001$, $F'(0) = \pm 100$ (this is essentially two rotated versions of Figure 3.17).

Thus, we have

$$\begin{aligned} u &= e^{-iqt}\,\hat{g}(r) \\ r &= G(z\,\mathrm{e}^{-iqt}) \end{aligned} \tag{3.35}$$

giving

$$u = \mathrm{e}^{-iqt}\,g(z\,\mathrm{e}^{-iqt}). \tag{3.36}$$

Letting

$$\eta = z\,\mathrm{e}^{-iqt}$$

and substituting (3.36) into (3.34), we obtain

$$g_{\eta\eta} + iqg_\eta(g + \eta g_\eta) = 0. \tag{3.37}$$

We can easily confirm that (3.37) is equivalent to (3.31); defining

$$\psi = \theta - q\,t \tag{3.38}$$

and recalling (3.33) and (3.35), it can be seen that

$$\begin{aligned} g &= re^{-i\psi} \\ \eta &= re^{i\psi}. \end{aligned} \tag{3.39}$$

The derivatives transform to

$$g_\eta = \frac{r_\psi - ir}{r_\psi + ir} e^{-2i\psi}, \tag{3.40}$$

$$g_{\eta\eta} = 2i \left[\frac{r r_{\psi\psi} - 2r_\psi^2 - r^2}{(r_\psi + ir)^3} \right] e^{-3i\psi} \tag{3.41}$$

and (3.37) becomes

$$r_{\psi\psi} = \frac{2}{r} r_\psi^2 + r - q(r^2 + r_\psi^2) r_\psi, \tag{3.42}$$

which is exactly the same as (3.31), as expected.

We can now return to (3.37). Noting that it can be written in the form

$$(\ln g_\eta)_\eta + (i\, q\, \eta\, g)_\eta = 0,$$

we can thus integrate to give

$$g_\eta = A e^{-i\, q\, \eta\, g}, \tag{3.43}$$

where A is the constant of integration. This is a complex first-order ordinary differential equation, and again needs to be converted back into the real plane. We can use (3.38)—(3.41) together with (3.43) to eliminate g_η to give

$$r_\psi = ir \left[\frac{1 + A\, \mathrm{e}^{i(2\psi - qr^2)}}{1 - A\, \mathrm{e}^{i(2\psi - qr^2)}} \right], \tag{3.44}$$

which can be written in the form

$$r_\psi = -r \cot(\psi - \frac{1}{2} q r^2 - \psi_1), \tag{3.45}$$

where the constant

$$\psi_1 = \frac{i \ln A}{4}$$

must be real to generate a real solution; by choice of the origin of ψ we take, without loss of generality, $\psi_1 = 0$.

We are now in a position to construct the phase plane. Rewriting (3.45) in the form

$$\begin{aligned} \dot{r} &= -r\cos(\psi - \tfrac{1}{2}qr^2) \\ \dot{\psi} &= \sin(\psi - \tfrac{1}{2}qr^2) \end{aligned} \tag{3.46}$$

we can see that the critical points occur at

$$\begin{aligned} r_c &= 0 \\ \psi_c &= n\pi \text{ for } n \text{ integer.} \end{aligned}$$

We find that these are all saddle points, with incoming trajectories in $r > 0$ for even values of n, and outgoing trajectories for odd n. The phase plane is periodic, with period 2π. If we now consider isoclines of (3.45), we obtain

$$\begin{aligned} r_\psi = 0 \quad &\text{on} \quad \psi = \tfrac{1}{2}qr^2 + (n + \tfrac{1}{2})\pi \\ r_\psi = \infty \quad &\text{on} \quad \psi = \tfrac{1}{2}qr^2 + n\pi \\ r_\psi = 1 \quad &\text{on} \quad \psi = \tfrac{1}{2}qr^2 - \tan^{-1} r + n\pi \\ r_\psi = -1 \quad &\text{on} \quad \psi = \tfrac{1}{2}qr^2 + \tan^{-1} r + n\pi, \end{aligned}$$

from which we can construct the phase plane shown in Figure 3.19.

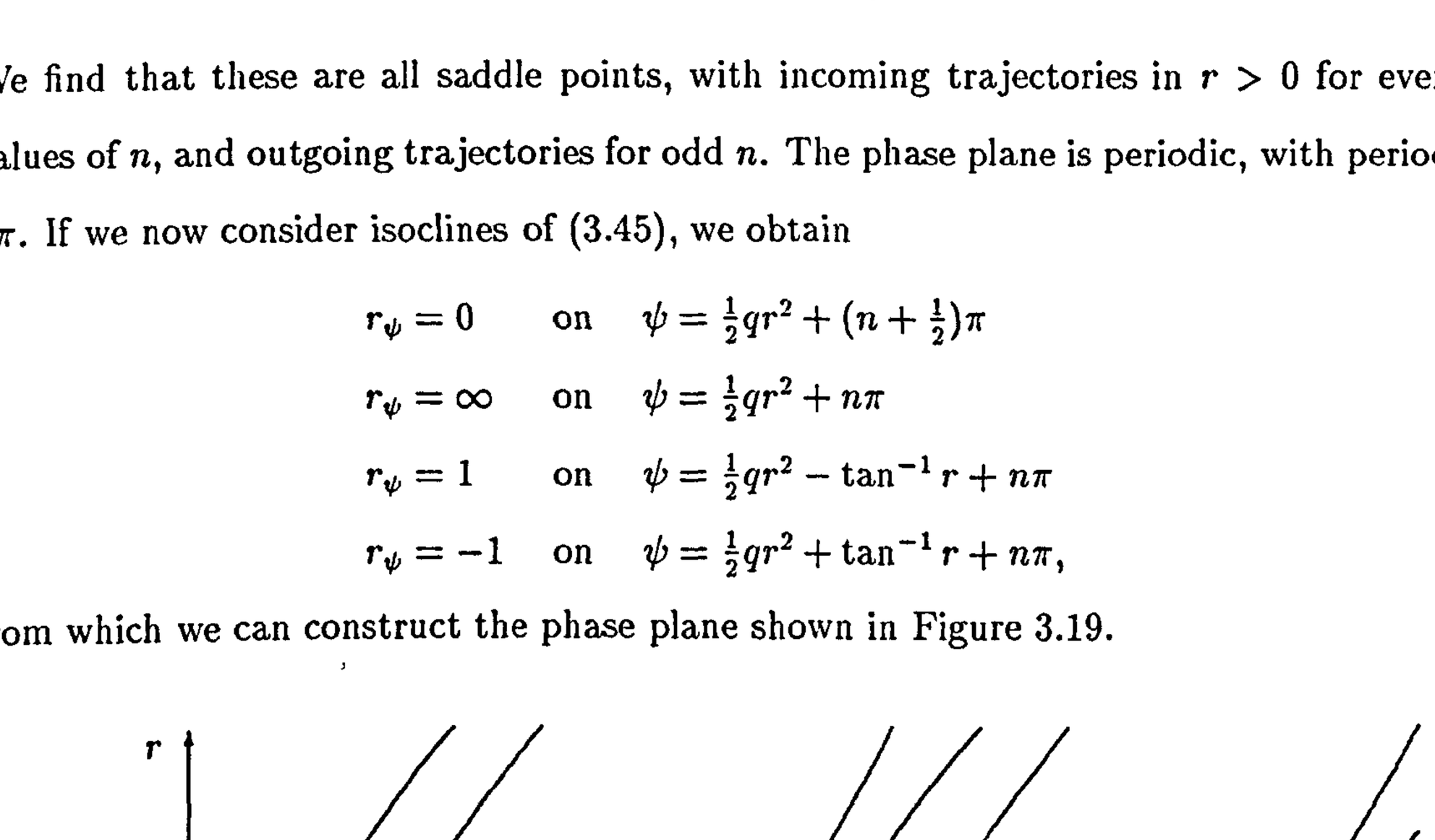

Figure 3.19: Phase plot for r against ψ.

To construct solutions, we integrate the parametric equations (3.46) numerically. Choosing any point in (r, ψ) space as our initial point, we can generate the full curve

by integrating along its trajectory in both directions (see phase plot). Some resulting spirals are shown below in Figures 3.20 and 3.21, and can be seen to be the same as those obtained previously from numerically solving the second-order system (see Figure 3.17).

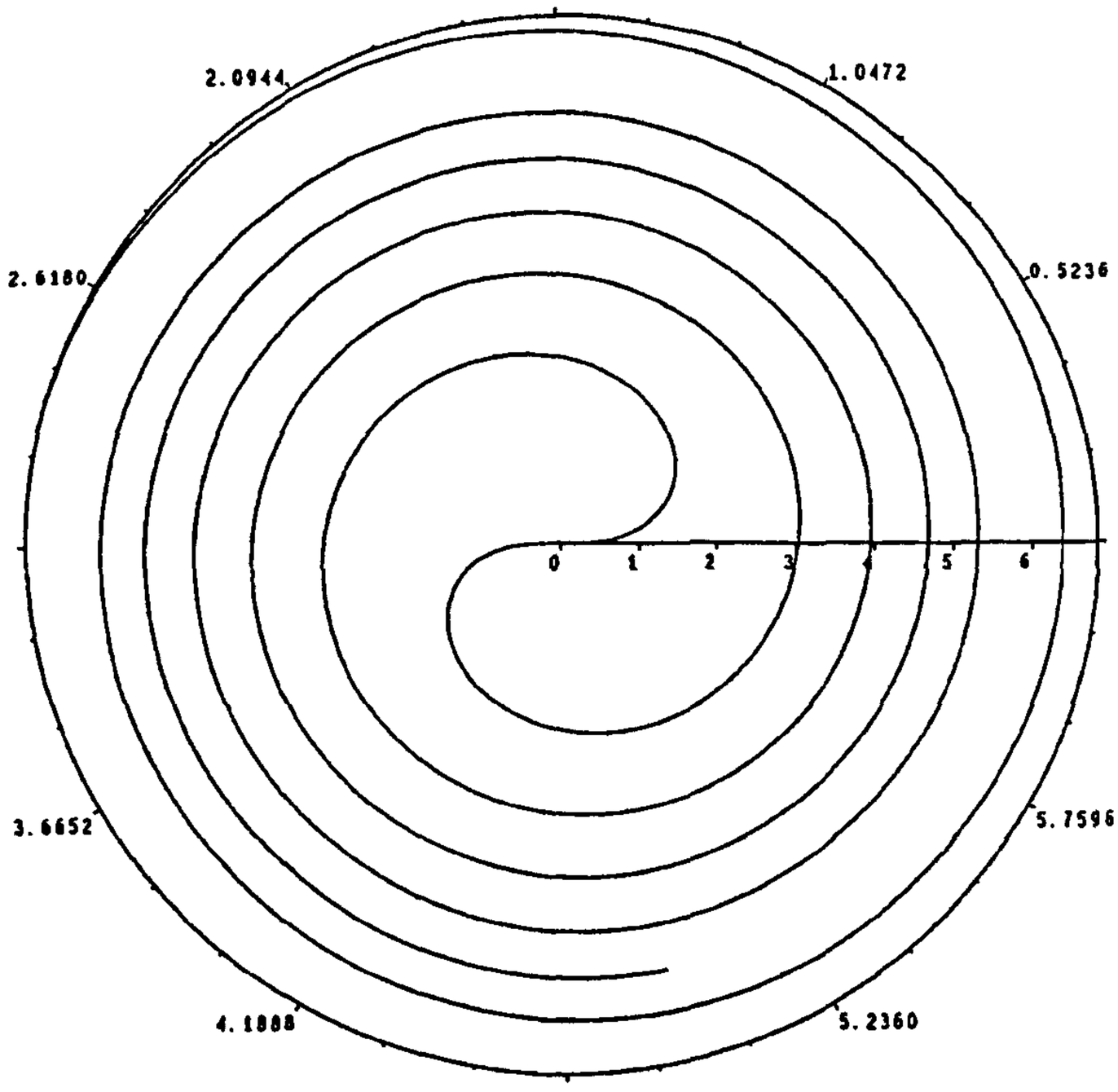

Figure 3.20: Spiral plot for $q = 1$, $r_0 = \psi_0 = 0.05$.

3.4.2 Separable solutions

This time, we substitute

$$c = u_z$$

into (3.34) and differentiate with respect to z to obtain

$$c_t = (c^{-1}c_z)_z. \tag{3.47}$$

By setting $c = g(\eta)$, we can now look for two different similarity solutions with

$$\eta = z/(\pm t)^{1/2}. \tag{3.48}$$

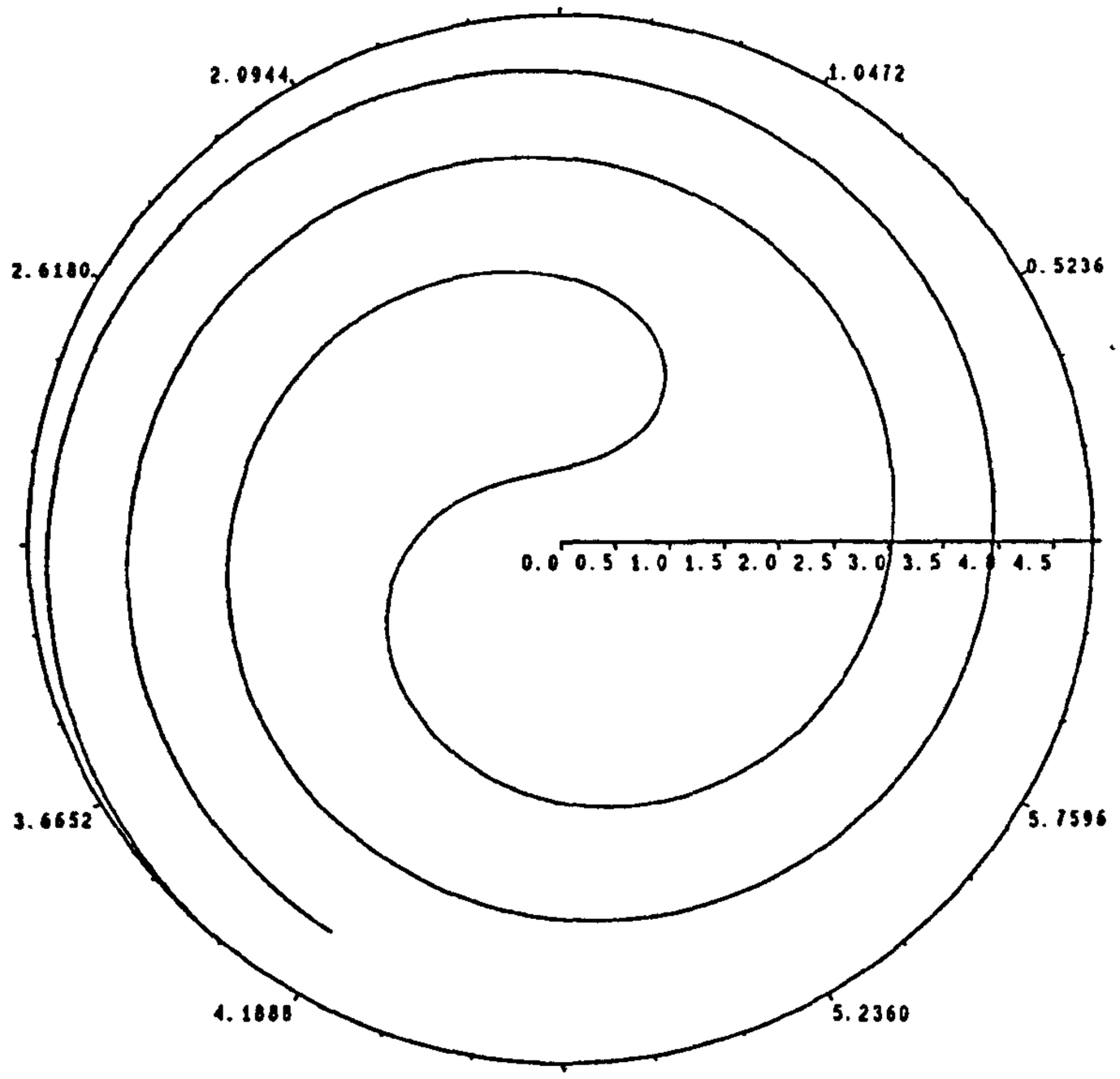

Figure 3.21: Spiral plot for $q = 1$, $r_0 = \psi_0 = 1.0$.

These are equivalent to the two solutions $r = (\pm t)^{1/2} F(\theta)$ from the previous section, and once again we shall consider the two cases separately.

$\underline{\eta = z/t^{1/2}}$

Substituting (3.48) into (3.47), we obtain

$$-\frac{1}{2}\eta g_\eta = (g^{-1} g_\eta)_\eta.$$

Letting $g = \mathrm{e}^h$, we subsequently see that

$$-\frac{1}{2}\eta \mathrm{e}^h h_\eta = h_{\eta\eta}. \tag{3.49}$$

We now set about finding an invariant group for this equation. The balance is

$$h\,\mathrm{e}^h \sim \frac{h}{\eta^2}$$

and hence

$$u = 2\ln\eta + h \tag{3.50}$$

is our first invariant. Choosing

$$\eta_1 = \alpha\,\eta, \tag{3.51}$$

we require

$$h_1 = h + 2\ln\alpha \tag{3.52}$$

for (3.50) to read the same in these new co-ordinates. Differentiating (3.51) and (3.52) with respect to η_1, we obtain

$$1 = \alpha\frac{d\eta}{d\eta_1}$$

$$\frac{dh_1}{d\eta_1} = h_\eta\frac{d\eta}{d\eta_1}$$

and thus

$$v = \eta\,h_\eta \tag{3.53}$$

is our second invariant (alternatively it is apparent that the invariants can be derived by explicitly using the rescaling invariant of (3.49)). We can now recast (3.49) in terms of u and v; after some manipulation, we obtain

$$\frac{dv}{du} = \frac{v\,(1-\frac{1}{2}e^u)}{2+v} \tag{3.54}$$

which is a separable first-order ordinary differential equation; integrating, we find that

$$2\ln v + v = u - \frac{1}{2}e^u + \text{constant}.$$

Expressing this in the (η, g) co-ordinate system (remembering that $h = \ln g$), this reads

$$\eta\,g^{-1}g_\eta + 2\ln(g^{-1}g_\eta) = \ln g - \frac{1}{2}\eta^2 g + \text{constant}. \tag{3.55}$$

We now need to return to our $u(z,t)$ formulation. Since $c = g(zt^{-\frac{1}{2}})$, if we choose

$$u = t^{\frac{1}{2}}f(zt^{-\frac{1}{2}}) = t^{\frac{1}{2}}f(\eta)$$

then $c = u_z$ holds as long as $f_\eta = g$. Using (3.34), we can see that

$$\frac{1}{2}(f - \eta f_\eta) = \frac{f_{\eta\eta}}{f_\eta} = \frac{g_\eta}{g}$$

and hence (3.55) becomes

$$\frac{1}{2}\eta(f-\eta f_\eta)+2\ln\left(\frac{f-\eta f_\eta}{2}\right)=\ln(f_\eta)-\frac{1}{2}\eta^2 f_\eta+\text{constant},$$

which, in terms of u, reads

$$\frac{z}{2t}u+2\ln(u-zu_z)-\ln u_z-\ln t=\text{constant}. \tag{3.56}$$

Finally, we are required to express this in (r,θ) co-ordinates; using (3.33) and noting that

$$u_z=\frac{r_\theta-ir}{r_\theta+ir}e^{-2i\theta},$$

we obtain

$$r_\theta=\pm r\sqrt{A\frac{r^2}{2t}e^{\frac{r^2}{2t}}-1}, \tag{3.57}$$

where A is a constant. We can at this stage check this result with the second-order equation from the previous section; setting

$$r=t^{\frac{1}{2}}F(\theta),$$

substituting this into (3.57) and differentiating, we obtain

$$F''=F\left(1+\frac{F^2}{2}\right)+\left(\frac{2}{F}+\frac{F}{2}\right)F'^2,$$

which is the same as (3.21).

To solve (3.57) we substitute

$$\rho=\frac{r^2}{2t},$$

where we are assuming $t>0$ so that $\rho>0$, into (3.57) to give

$$\rho_\theta=\pm 2\rho\sqrt{A\rho e^\rho-1}. \tag{3.58}$$

It can be seen that we require $A\geq 1/\rho e^\rho$ for real solutions; thus $A>0$ is required and each value of A defines a unique minimum 'radius' ρ_0. Integrating (3.58) numerically, we obtain the results as shown in Figure 3.23. These solutions can be thought of as the flow from a corner, as mentioned in the previous section, and demonstrated by the Figure 3.22. This is also shown more precisely in Figure 3.24, where we show the full solution evolving from an initial wedge shape.

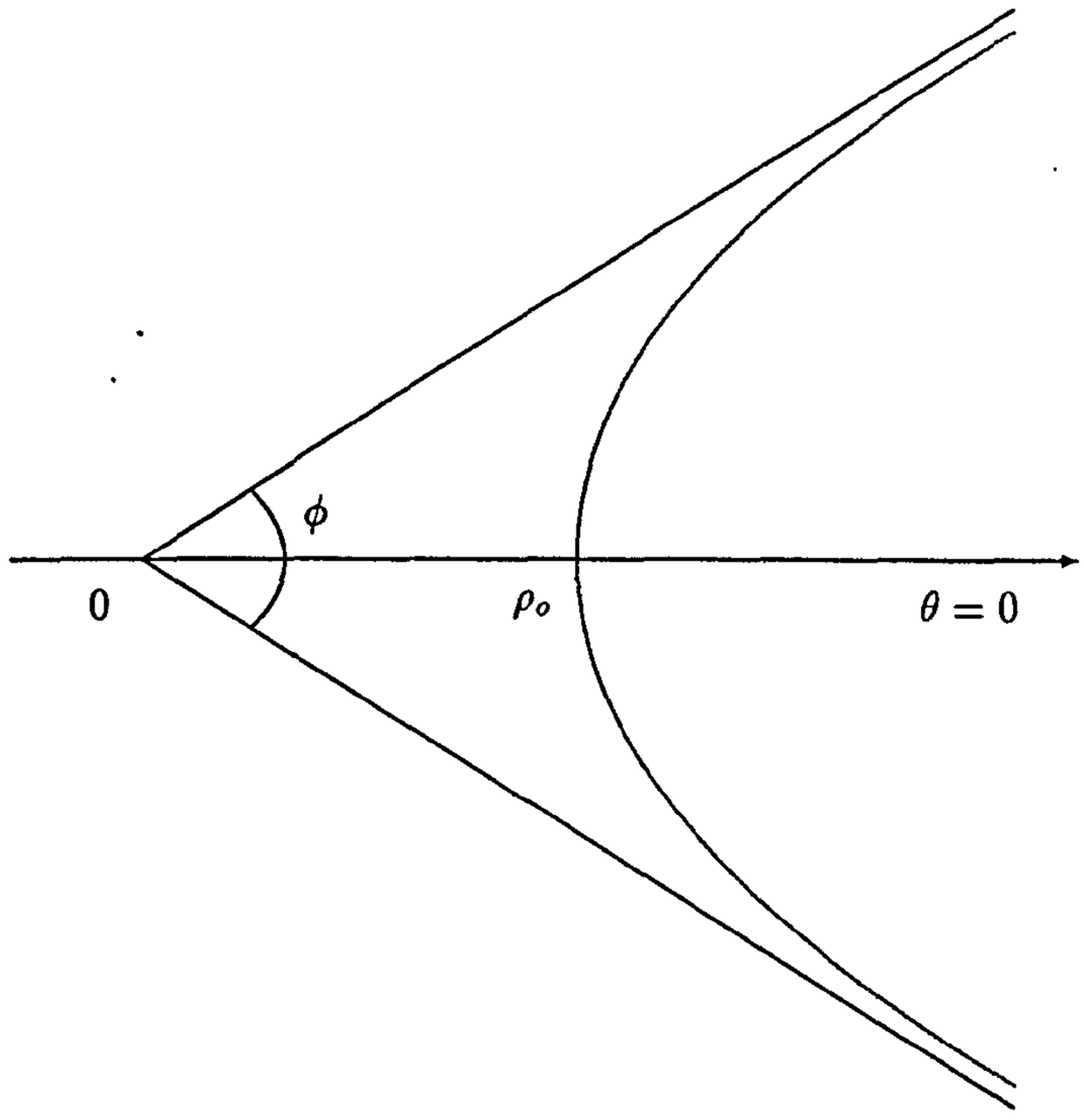

Figure 3.22: Definition of a corner solution.

We can also determine ϕ, the angle of the corner from (3.58); we find that in particular

$$\phi \to 0 \quad \text{as} \quad A \to 0 \quad (\text{large } \rho_0)$$
$$\phi \to 2\pi \quad \text{as} \quad A \to \infty \quad (\text{small } \rho_0)$$

and hence the full range of positive A is covered.

$\underline{\eta = z/(-t)^{1/2}}$

This follows exactly the same method as above, and the only difference in the various equations obtained is the occasional change of sign. Eventually, we obtain

$$r_\theta = \pm r\sqrt{\bar{A}\frac{r^2}{-2t}e^{r^2/2t} - 1}, \tag{3.59}$$

where $\bar{A}$ is a constant; not surprisingly, it can be seen on comparing (3.59) with (3.57) that the two equations are the same, with $\bar{A} = -A$. Substituting $r = (-t)^{1/2}F(\theta)$ again gives us (3.21) as a check; by setting

$$\rho = \frac{r^2}{-2t},$$

where we now take $t < 0$, (3.59) becomes

$$\rho_\theta = \pm 2\rho\sqrt{\bar{A}\,\rho\, e^{-\rho} - 1}. \tag{3.60}$$

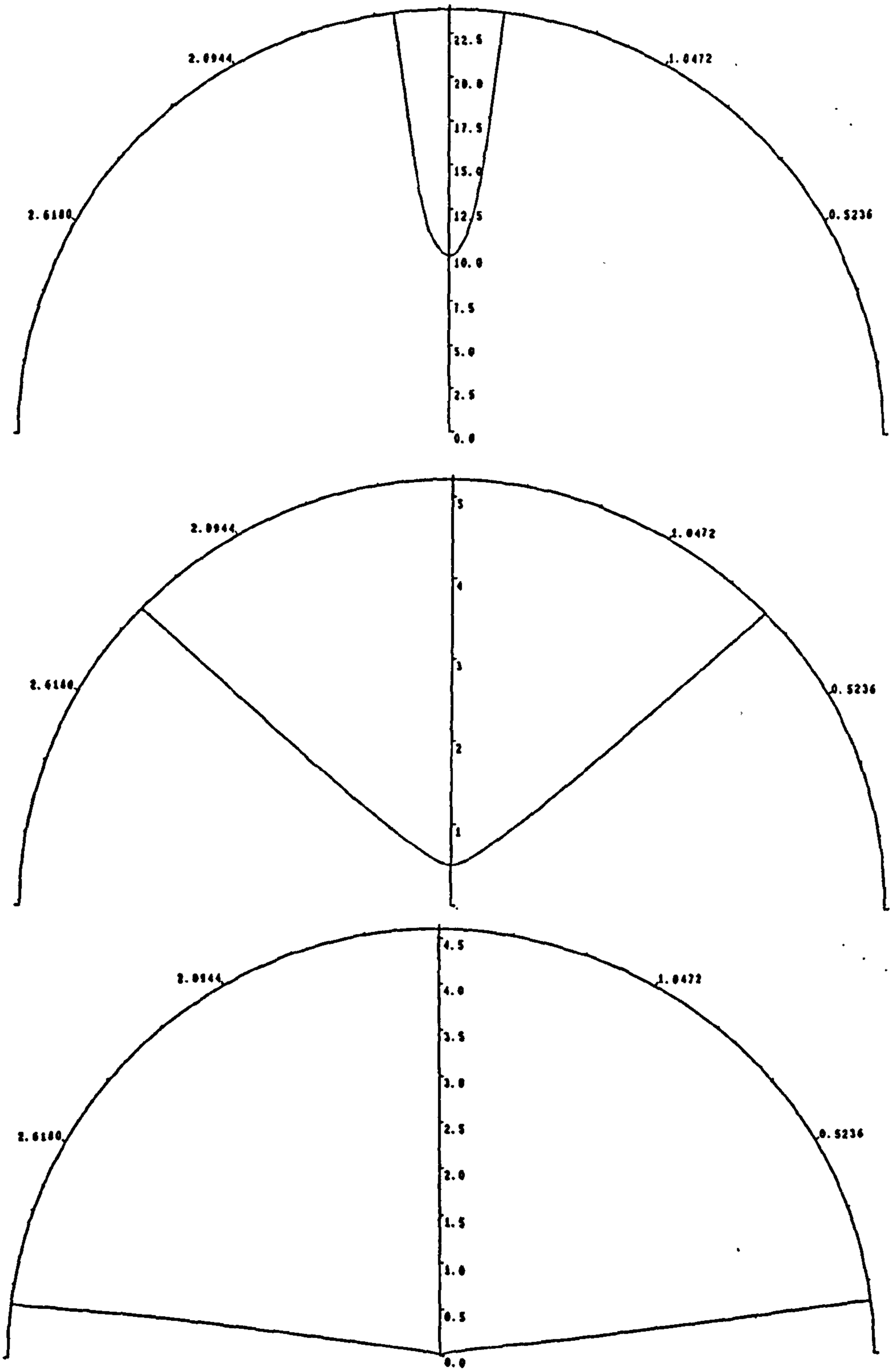

Figure 3.23: 'Corner' solutions for $\rho(\theta)$ (rotated through $\pi/2$ for display purposes) of the form shown in Figure 3.22; $A = 4.5 \times 10^{-6}$ (top), $A = 1.21$ (centre), $A = 99.0$ (bottom).

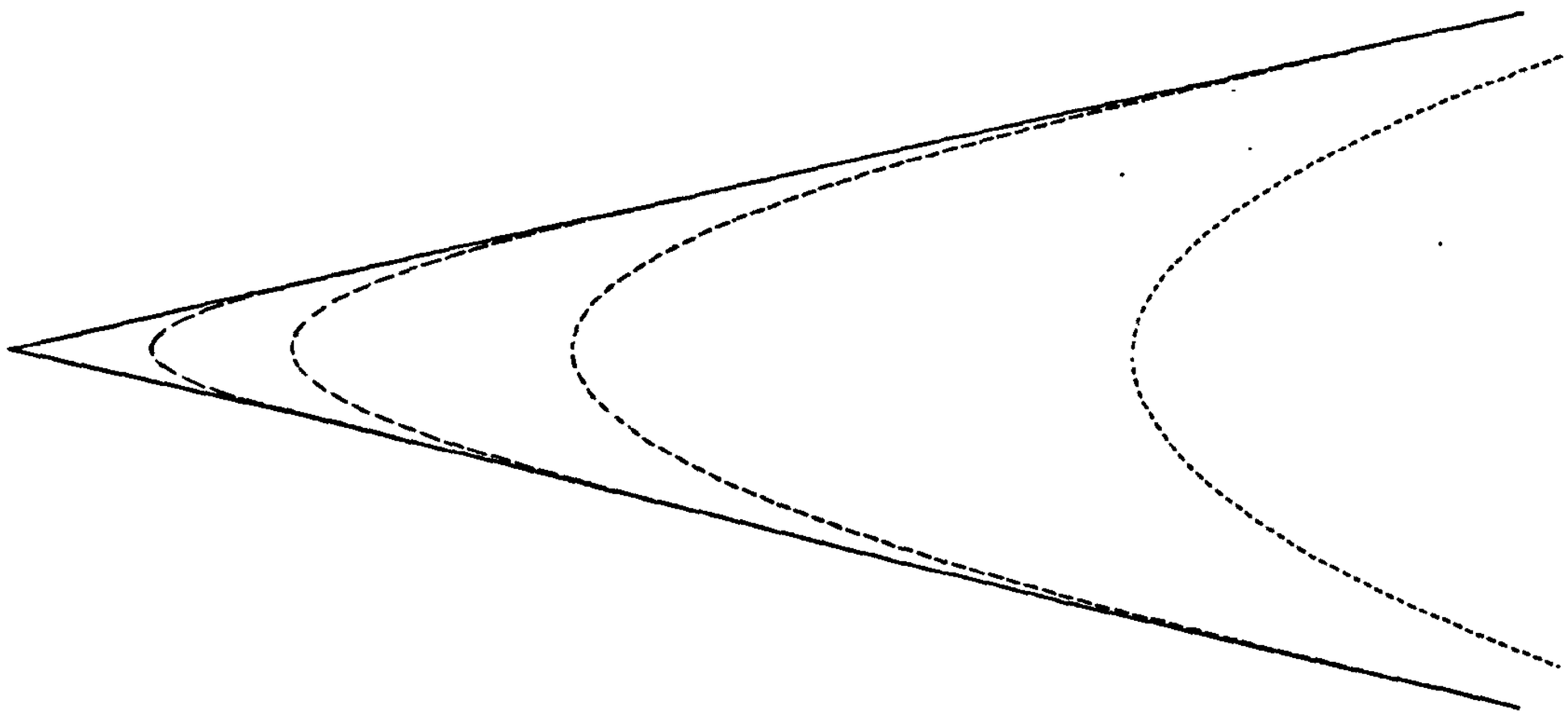

Figure 3.24: A demonstration of how the full solution for $r(\theta, t)$ evolves from a corner ($A = 1.3 \times 10^{-3}$).

We thus require $\bar{A} \geq e^{\rho}/\rho$ to maintain real solutions, which means that we must have $\bar{A} \geq e$ for a solution to exist at all; $\bar{A} = e$ will give us the solution $\rho = 1$ (i.e. a circle) and $\bar{A} > e$ implies a solution confined to an annulus, with inner radius $\rho_0 < 1$ and outer radius $\rho_1 > 1$. This is equivalent to the result obtained for the second-order equation, and the solutions to (3.60) are, not surprisingly, of the same type, as shown in Figure 3.25.

We can also investigate the behaviour of these solutions using an asymptotic analysis. Noting that as we approach the circular solution we have $\bar{A} \to e$ and $\rho \to 1$, then by setting

$$\begin{aligned} \bar{A} &= e(1 + \varepsilon^2 + \ldots) \\ \rho &= 1 + \varepsilon\phi + \ldots \end{aligned} \tag{3.61}$$

and substituting (3.61) into (3.59), we obtain

$$\frac{d\phi}{d\theta} \sim \pm 2\sqrt{1 - \frac{\phi^2}{2}}.$$

This can be integrated to give

$$\phi \sim \pm\sqrt{2}\sin(\sqrt{2}\theta) \tag{3.62}$$

and hence the period $\sim \sqrt{2}\pi$ in the limit $\bar{A} \to e$; this agrees well with numerical results;

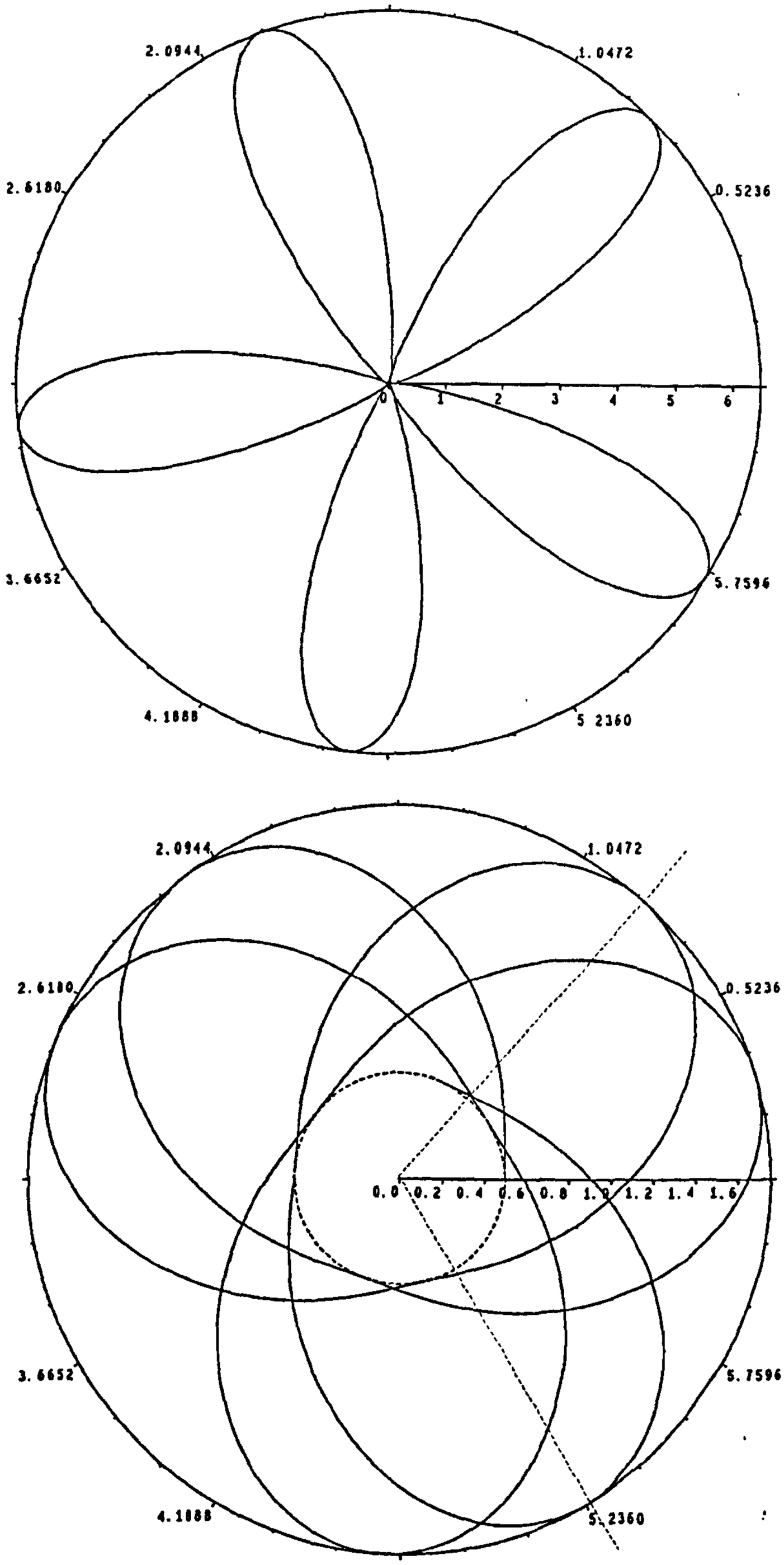

Figure 3.25: Self-intersecting solutions; (a) $\rho_0 = 0.01$ ($\bar{A} = 101.005$), (b) $\rho_0 = 0.5$ ($\bar{A} = 3.2974$). The straight dashed lines show the period of the solution, here $\approx 1.4\pi$; note that curves will only join up for discrete values.

even in Figure 3.25b, where $\bar{A}$ is not particularly close to the critical value, the period is still approximately $\sqrt{2}\pi$.

3.5 Similarity Forms for the 3-D Equation

We will now consider (3.3) in three dimensions. If we have a general surface

$$\varphi(x, y, z, t) = 0,$$

then (3.3) can be expressed as

$$\frac{\varphi_t}{|\nabla\varphi|} = \nabla.\left(\frac{\nabla\varphi}{|\nabla\varphi|}\right). \tag{3.63}$$

Setting $z = f(x, y, t)$, so that $\varphi = z - f$, then

$$\frac{\partial f}{\partial t} = \frac{(1+f_y^2)f_{xx} + (1+f_x^2)f_{yy} - 2f_x f_y f_{xy}}{1+f_x^2+f_y^2}, \tag{3.64}$$

which is our required Cartesian form. We now suppose that (3.64) admits a one-parameter (ε) Lie group of point transformations

$$\begin{aligned} f^* &\sim f(x,y,t) + \varepsilon F(x,y,t,f) \\ x^* &\sim x + \varepsilon X(x,y,t,f) \\ y^* &\sim y + \varepsilon Y(x,y,t,f) \\ t^* &\sim t + \varepsilon T(x,y,t,f) \end{aligned} \tag{3.65}$$

with the infinitesimals (F, X, Y, T) leaving (3.64) invariant; omitting details, it is found that this requires

$$\begin{aligned} T &= \alpha + 2\zeta t \\ X &= \beta + \zeta x - \lambda y - \mu f \\ Y &= \gamma + \lambda x + \zeta y - \nu f \\ F &= \delta + \mu x + \nu y + \zeta f \end{aligned} \tag{3.66}$$

and we thus have an eight-parameter group made up of four translations, three rotations and a stretching. We will now classify the similarity reductions that can be made using (3.66).

3.6 $\zeta \neq 0$

If we set all of the parameters in (3.66) to zero except ζ, then from the invariant surface condition we obtain

$$\begin{aligned} f &= (\pm t)^{1/2} G(x/(\pm t)^{1/2}, y/(\pm t)^{1/2}) \\ &= (\pm t)^{1/2} G(\xi, \eta). \end{aligned} \tag{3.67}$$

Substituting this into (3.64) gives us

$$\begin{aligned} &\pm \tfrac{1}{2}(G - \xi G_\xi - \eta G_\eta)(1 + G_\xi^2 + G_\eta^2) \\ &\quad = (1 + G_\eta^2) G_{\xi\xi} + (1 + G_\xi^2) G_{\eta\eta} - 2 G_\xi G_\eta G_{\xi\eta}. \end{aligned} \tag{3.68}$$

In order to determine a further similarity reduction, we now set

$$\begin{aligned} G^* &\sim G(\xi, \eta) + \varepsilon H(\xi, \eta, G) \\ \xi^* &\sim \xi + \varepsilon \Xi(\xi, \eta, G) \\ \eta^* &\sim \eta + \varepsilon N(\xi, \eta, G). \end{aligned} \tag{3.69}$$

For (3.68) to remain invariant, it is found that we require

$$\begin{aligned} \Xi &= -\alpha_1 \eta - \beta_1 G \\ N &= \alpha_1 \xi - \gamma_1 G \\ H &= \beta_1 \xi + \gamma_1 \eta \end{aligned} \tag{3.70}$$

and we recover the three rotations from (3.66). To reduce (3.68) to an ordinary differential equation, we take $\alpha_1 \neq 0$, $\beta_1 = \gamma_1 = 0$ in (3.70) so that the invariant surface condition gives

$$G = g(\sqrt{\xi^2 + \eta^2}) = g(\rho), \tag{3.71}$$

which, on substitution into (3.68), gives us

$$\frac{d^2 g}{d\rho^2} = \pm \frac{1}{2} \left(1 + \left(\frac{dg}{d\rho}\right)^2\right) \left[g - \frac{dg}{d\rho}\left(\rho \pm \frac{2}{\rho}\right)\right]. \tag{3.72}$$

We can now consider solutions to (3.72) for the two different cases.

3.6.1 $f = (-t)^{1/2} g([(x^2 + y^2)/(-t)]^{1/2})$

This case has two well established analytical solutions for (3.64), which can be seen in (for example) [2] namely, the sphere

$$x^2 + y^2 + f^2 = 4(-t), \tag{3.73}$$

and the cylinder

$$x^2 + y^2 = 2(-t), \qquad f \text{ arbitrary}, \tag{3.74}$$

which both shrink to the origin at time $t = 0$. The latter is a limiting case of this class of similarity solutions. If we solve for $g(\rho)$ from (3.72) numerically (using the lower signs) with the boundary conditions

$$\begin{aligned} g(\rho_0) &= 0 \\ g'(\rho_0) &\to \infty \end{aligned} \tag{3.75}$$

in order to have symmetry about $g = 0$ and hence maintain a smooth surface (ρ_0 is a constant which we vary to obtain different solutions), then we obtain the solutions as shown in Figure 3.26 (we only show solutions for $g(\rho) \geq 0$ due to the symmetry about $g = 0$). It can be seen that as well as the sphere and cylinder solutions, there is also a shrinking torus solution (as detailed in Angenent [2]), which has inner radius $r_0 = 0.4329\ldots$ and outer radius $r_1 = 3.3148\ldots$; it is unique, since this describes the only curve which has $dg/d\rho \to \infty$ at both ends. This torus is shown more clearly in Figure 3.27.

The other curves shown in Figure 3.26 do not in fact terminate in 'mid-air'; they loop back on themselves to produce meandering solutions as shown in Figure 3.28; this type of solution completes the set of solutions available for $g(\rho)$; some of these patterns can be quite ordered (see Angenent [2]), but it is unclear whether they have any application.

3.6.2 $f = t^{1/2} g([(x^2 + y^2)/t]^{1/2})$

We have three interesting solutions for this case. If we impose the boundary conditions (3.75) as we did above, then we can obtain the solutions as shown in Figure 3.29. These correspond to the so-called 'necking cylinder', as shown in Figure 3.30.

If instead of (3.75) we impose

$$\begin{aligned} g(0) &= g_0 \\ g'(0) &= 0 \end{aligned} \tag{3.76}$$

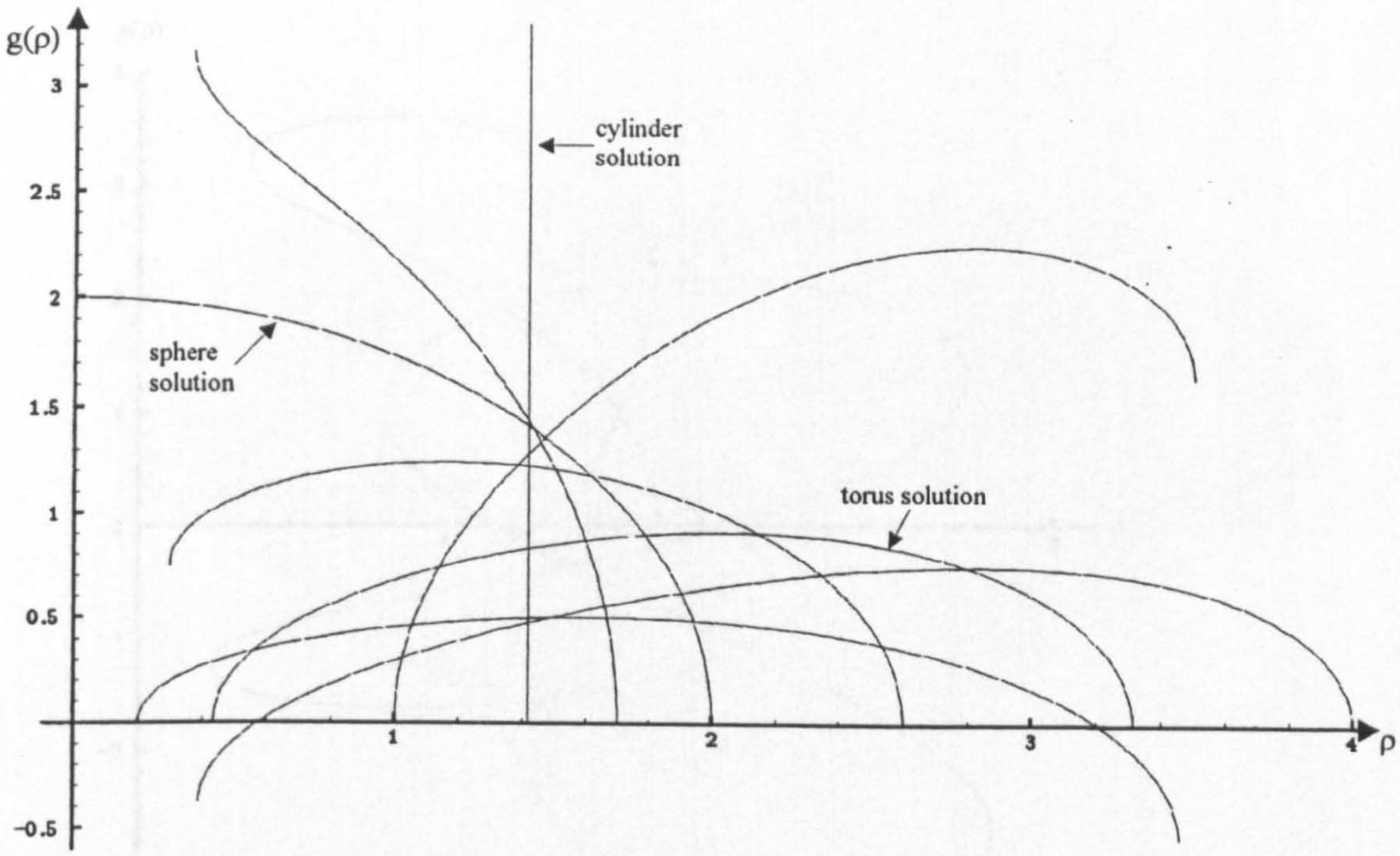

Figure 3.26: Solutions for $g(\rho)$; $(-t)^{1/2}$ case.

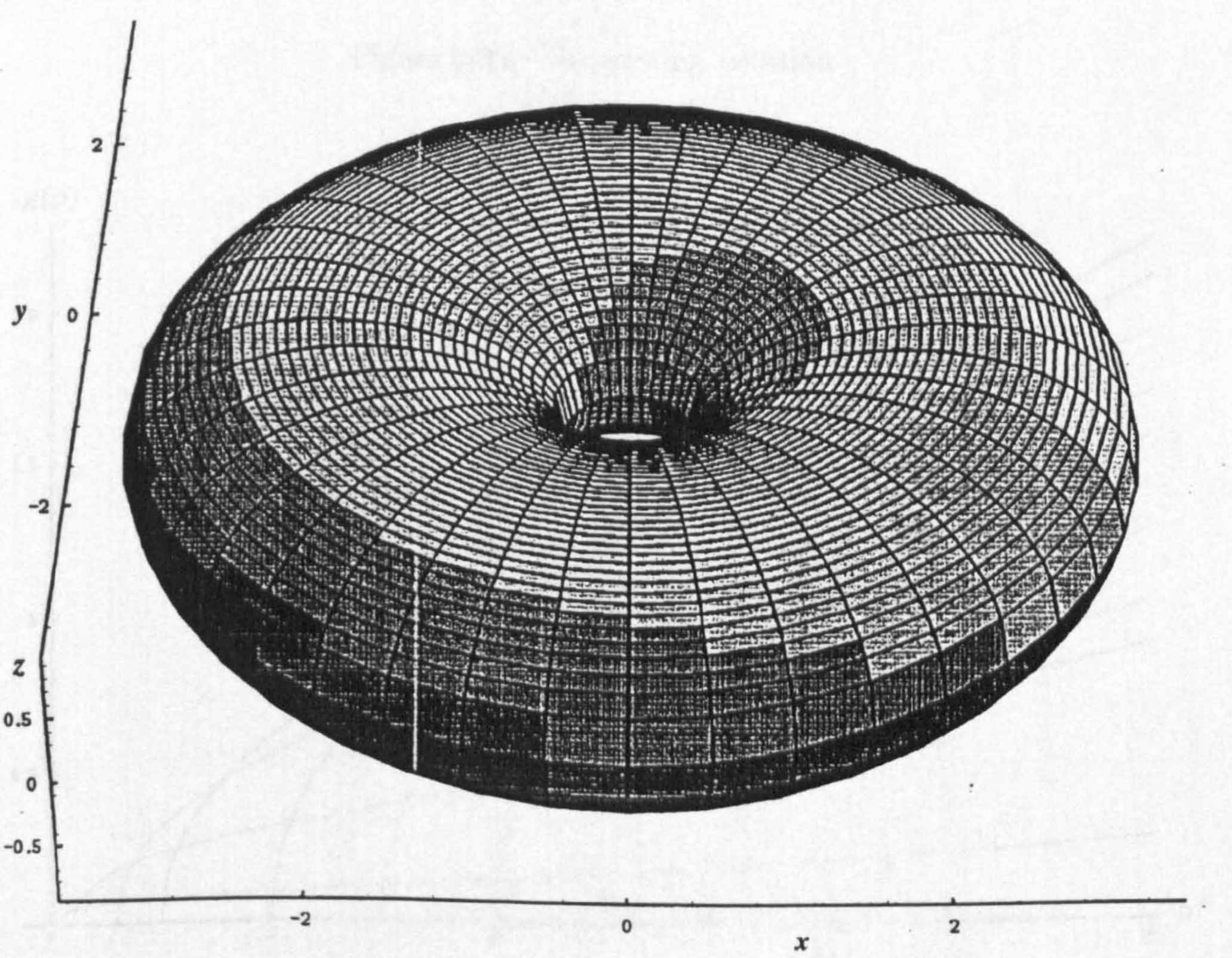

Figure 3.27: Shrinking torus solution; $\rho_0 = 0.4392$, $\rho_1 = 3.31478$. The axes shown are $z = g(\rho)$, $\rho^2 = x^2 + y^2$.

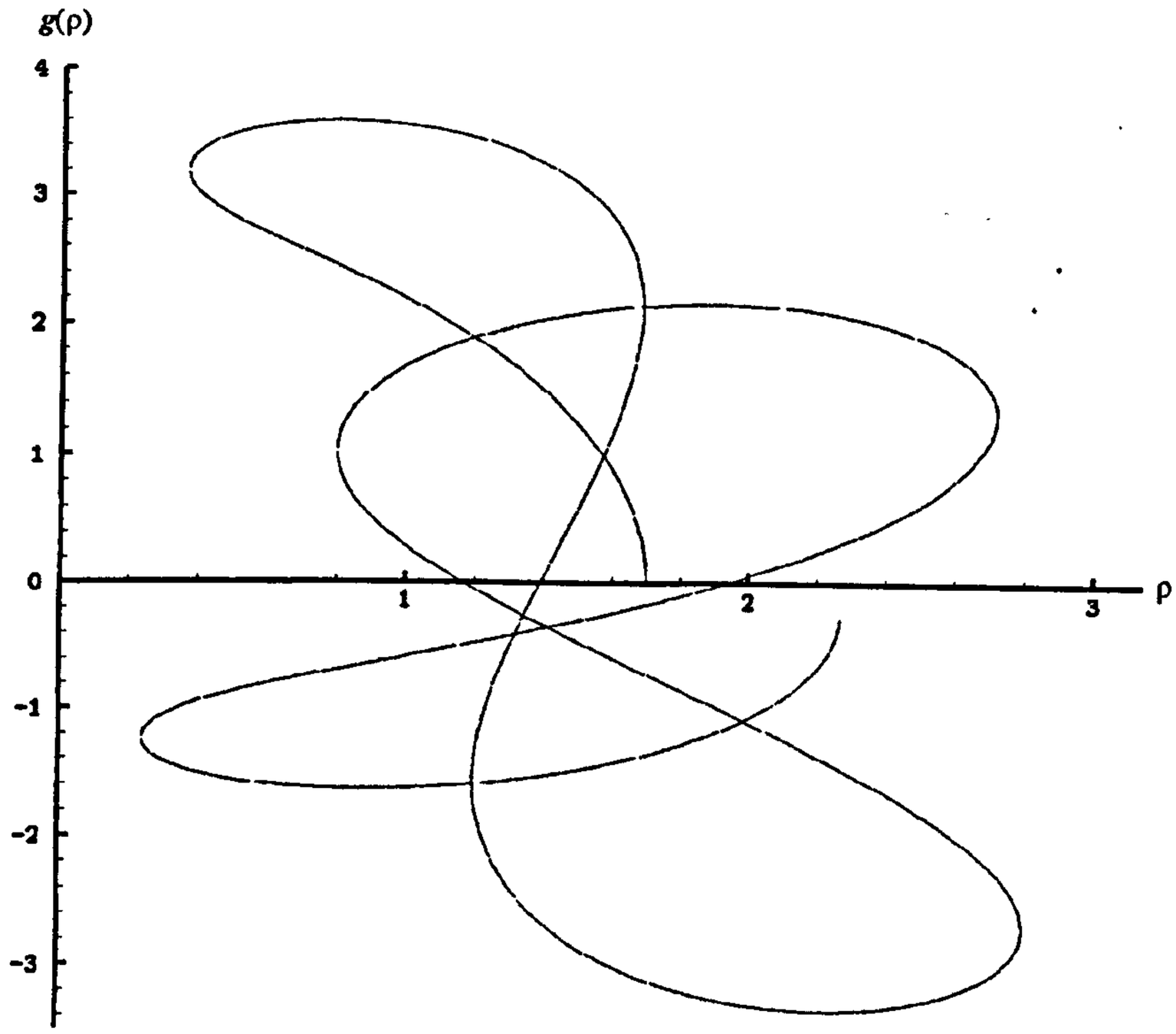

Figure 3.28: 'Meandering' solution

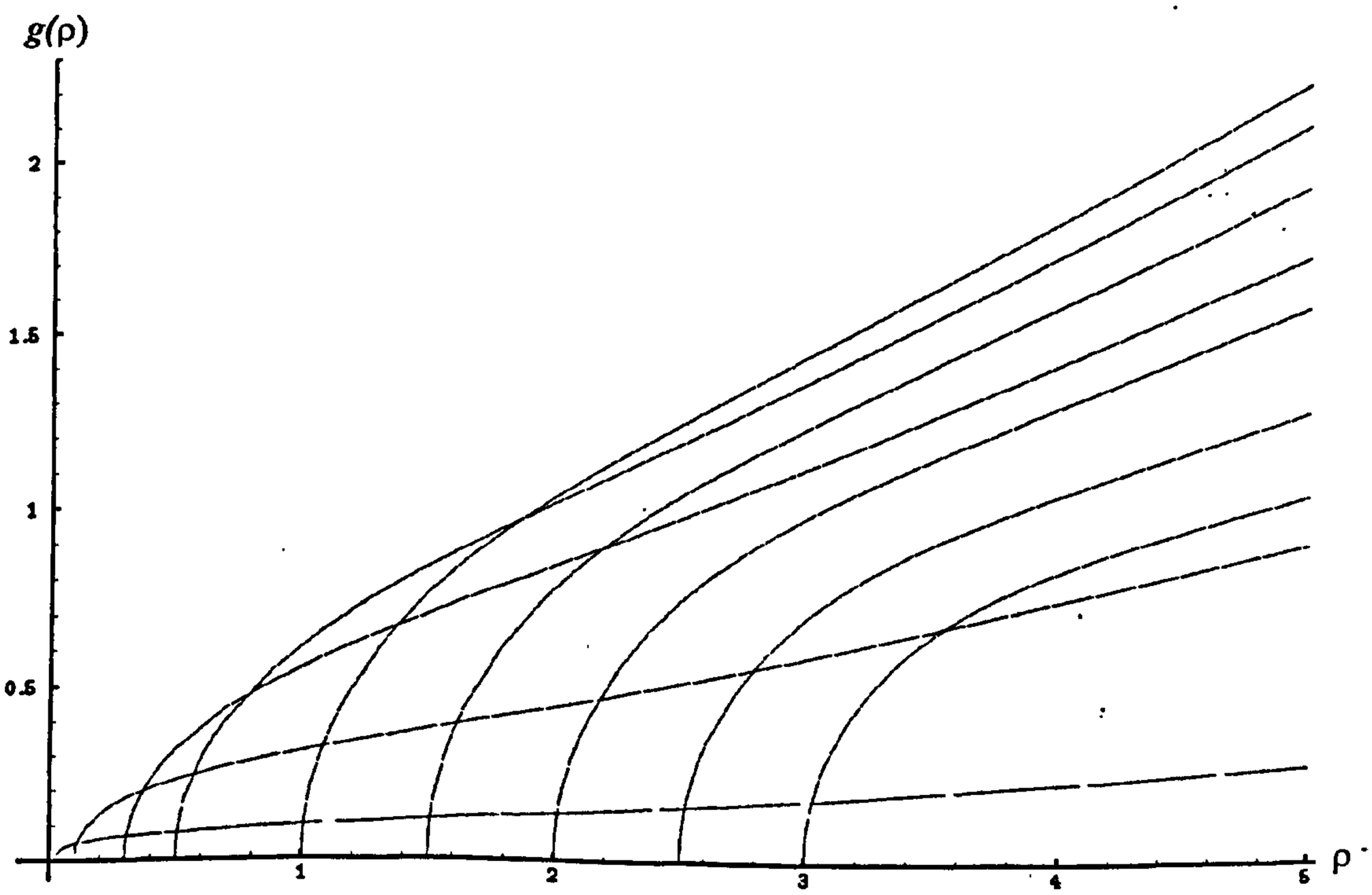

Figure 3.29: Solutions for different $g(\rho)$; $t^{1/2}$ case.

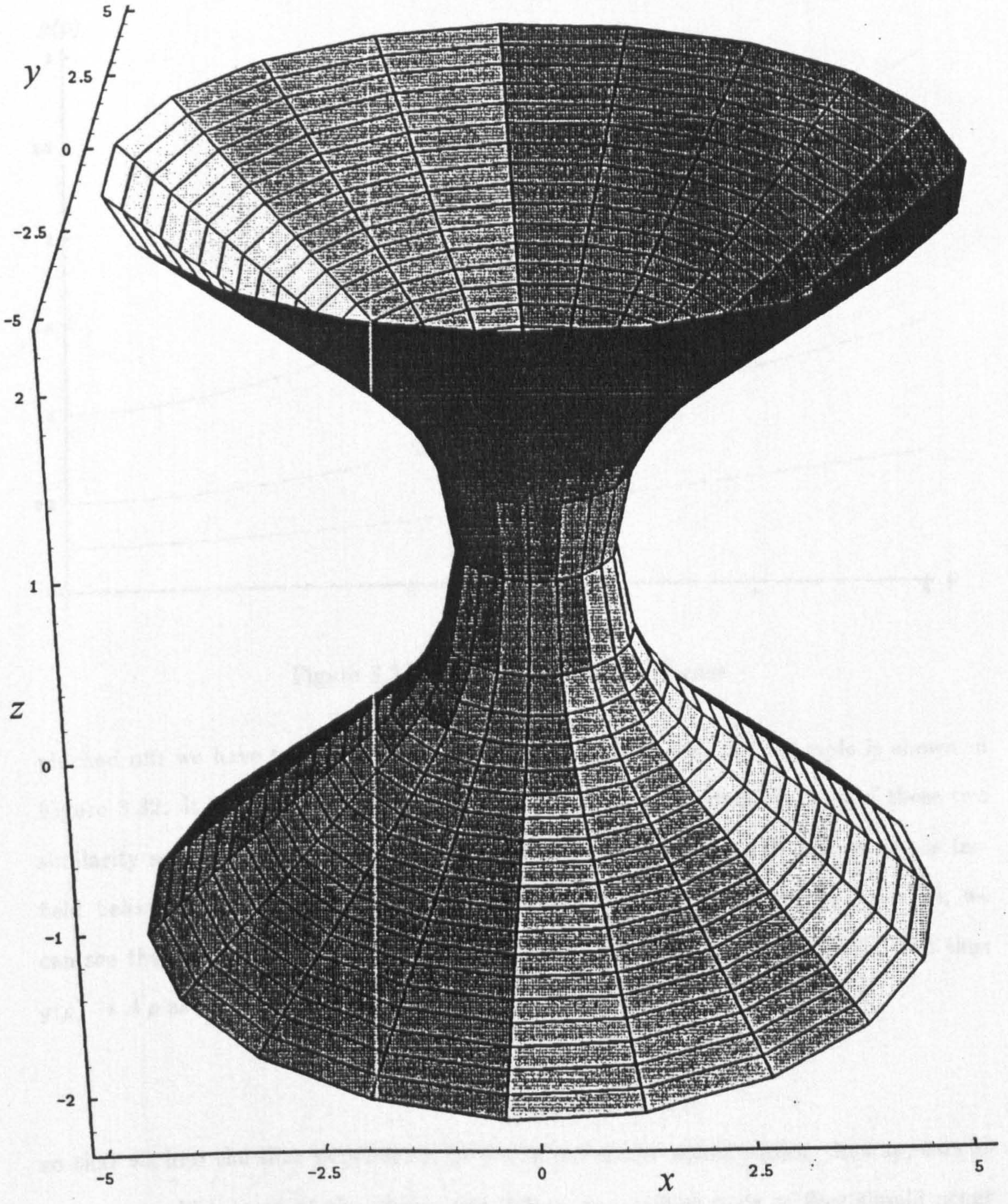

Figure 3.30: Necking cylinder solution. The axes shown are $z = g(\rho)$, $\rho^2 = x^2 + y^2$.

where g_0 is a constant, then numerical solution of (3.72) gives us profiles as shown in Figure 3.31; these correspond to the behaviour of the cylinder after the neck has been

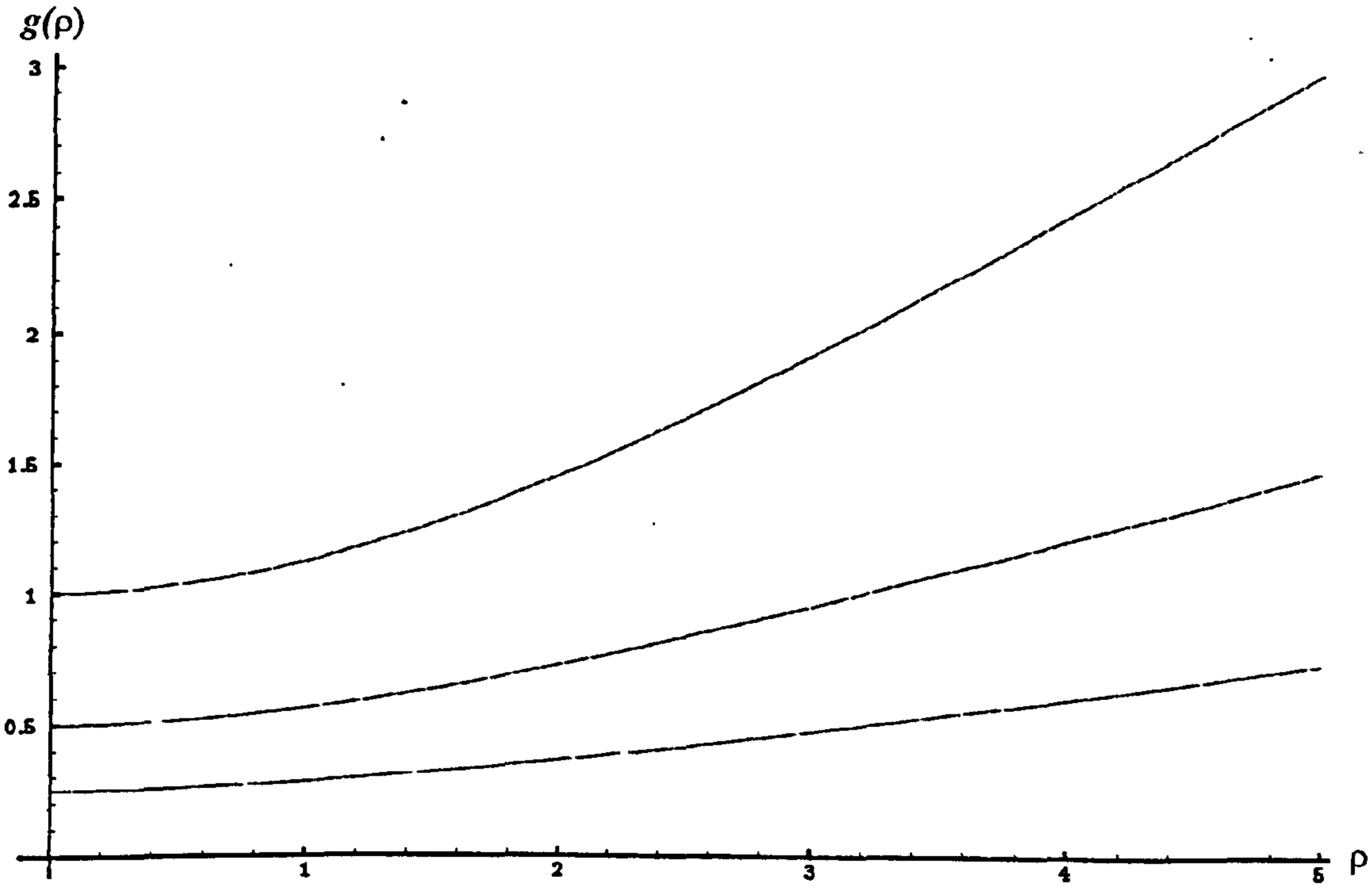

Figure 3.31: Solutions for $g(\rho)$; $t^{1/2}$ case.

pinched off; we have two separate 'cones' with rounded ends. An example is shown in Figure 3.32. It is useful at this point to consider the initial configurations of these two similarity solutions, as it is not immediately clear what they are. If we look at the far-field behaviour in our ordinary differential equation formulation (i.e. as $\rho \to \infty$), we can see that in both cases $g'(\rho)$ is constant (see Figure 3.29 and Figure 3.31), and thus $g(\rho) \to A\rho$ as $\rho \to \infty$, where A is a constant. This implies that

$$f \to Ar \qquad \text{as } t \to 0$$

so that we lose the time dependence at $t = 0$; our initial configuration thus appears as two cones which meet at the origin, and it is unclear which type of flow should occur (see Figure 3.33).

Finally, we can consider solutions which do not intersect perpendicularly with either

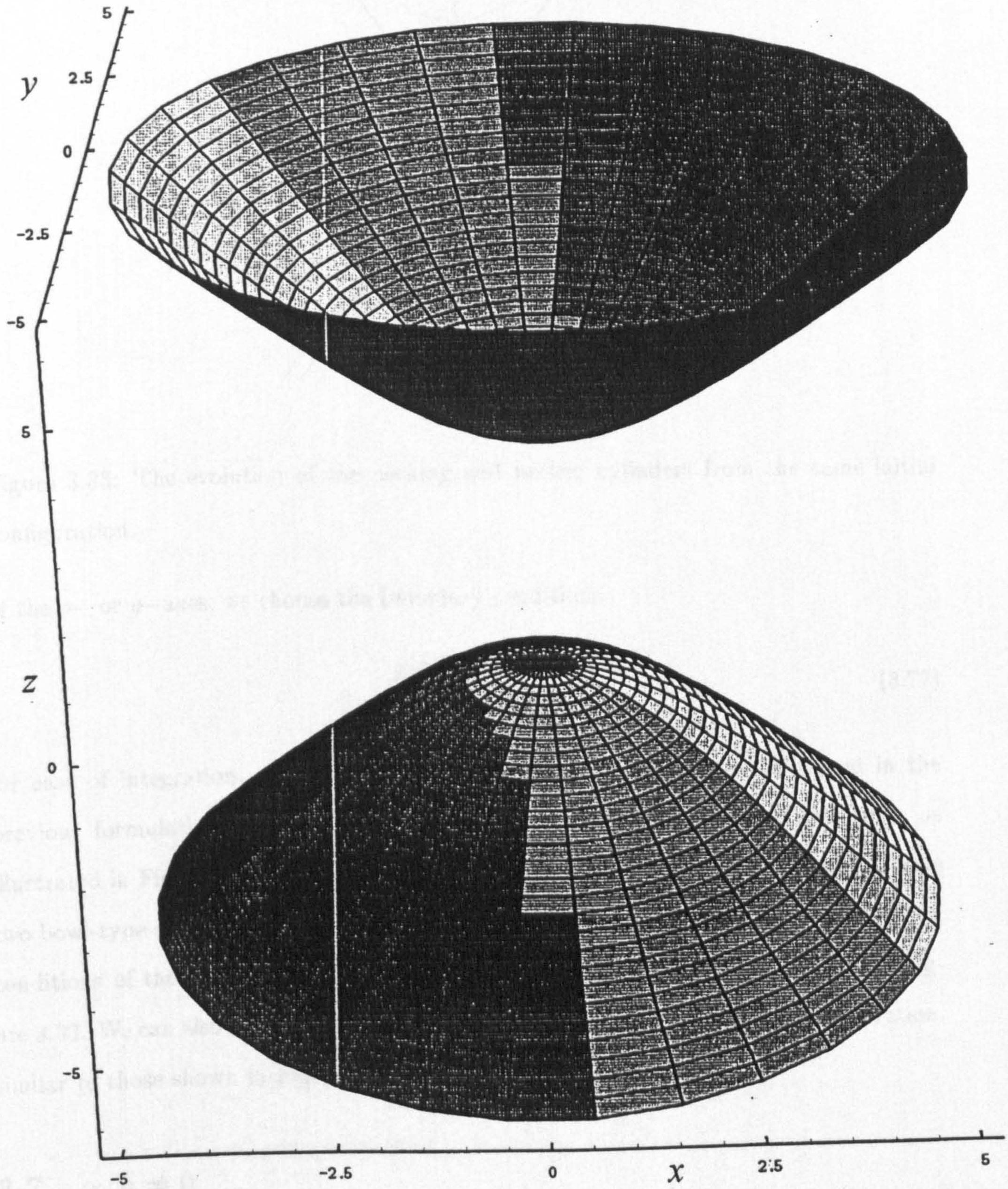

Figure 3.32: Cone solution. The axes shown are $z = g(\rho)$, $\rho^2 = x^2 + y^2$.

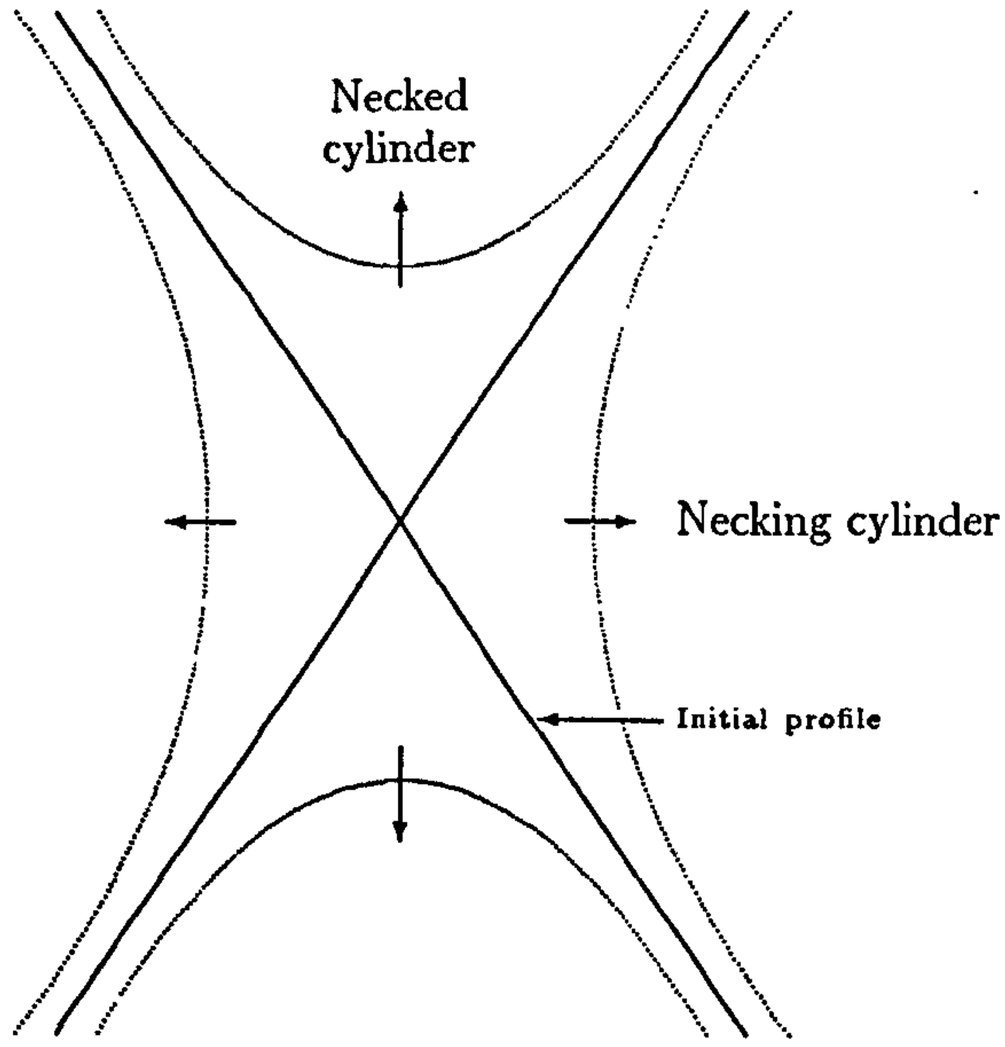

Figure 3.33: The evolution of the necking and necked cylinders from the same initial configuration.

of the $\rho-$ or $g-$axes; we choose the boundary conditions

$$\begin{aligned} g(\rho_0) &= g_0 \\ g'(\rho_0) &\to \infty \end{aligned} \tag{3.77}$$

for ease of integration. Instead of the selection of patterns that we obtained in the previous formulation (Figure 3.26), we have only one type of solution this time, as illustrated in Figure 3.34. If we consider the 3-D plot (Figure 3.35), we can see we have two bowl-type shapes, with a central hole at $r = 0$. Such solutions correspond to initial conditions of the type illustrated in Figure 3.36, i.e. to non-symmetric versions of Figure 3.33. We can also obtain the cone (necked cylinder) solutions from this configuration, similar to those shown in Figure 3.32.

3.7 $\alpha, \delta \neq 0$

Returning to (3.66), if we choose $\alpha, \delta \neq 0$ (without loss of generality by rescaling we can take $\alpha = \delta$), but take the other parameters to be zero, then writing

$$f = t + G(x, y)$$

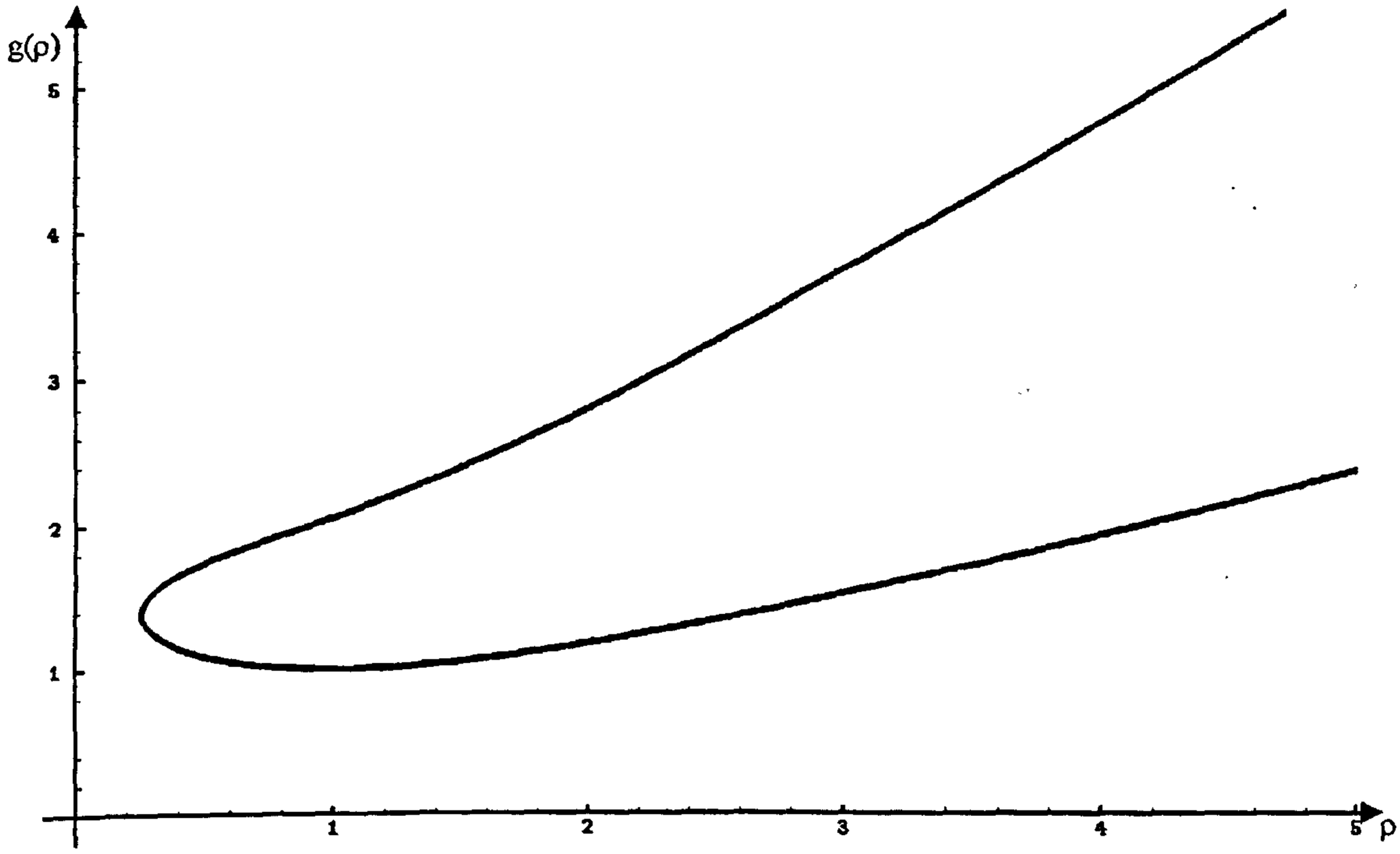

Figure 3.34: Solution for 'arbitrary' boundary conditions.

we obtain

$$1+G_x^2+G_y^2=(1+G_y^2)G_{xx}+(1+G_x^2)G_{yy}-2G_xG_yG_{xy} \tag{3.78}$$

from (3.64). This in turn admits the group

$$\begin{aligned} x^* &= x + \varepsilon(\alpha_1+\delta_1 y) \\ y^* &= y + \varepsilon(\beta_1-\delta_1 x) \\ G^* &= G + \varepsilon\gamma_1 \end{aligned} \tag{3.79}$$

which gives us a rotation and three translation groups (although γ_1 does not give similarity reductions). The rotation group will be covered below in a polar co-ordinate formulation (the algebra is easier); taking α_1 and β_1 in (3.79) to be non-zero but setting γ_1, $\delta_1 = 0$, we obtain the second similarity reduction

$$G=G(\phi), \quad \phi=y-qx,$$

where q is a constant, which, on substitution into (3.78), gives

$$\frac{d^2G}{d\phi^2}=\left(\frac{dG}{d\phi}\right)^2+\frac{1}{1+q^2}.$$

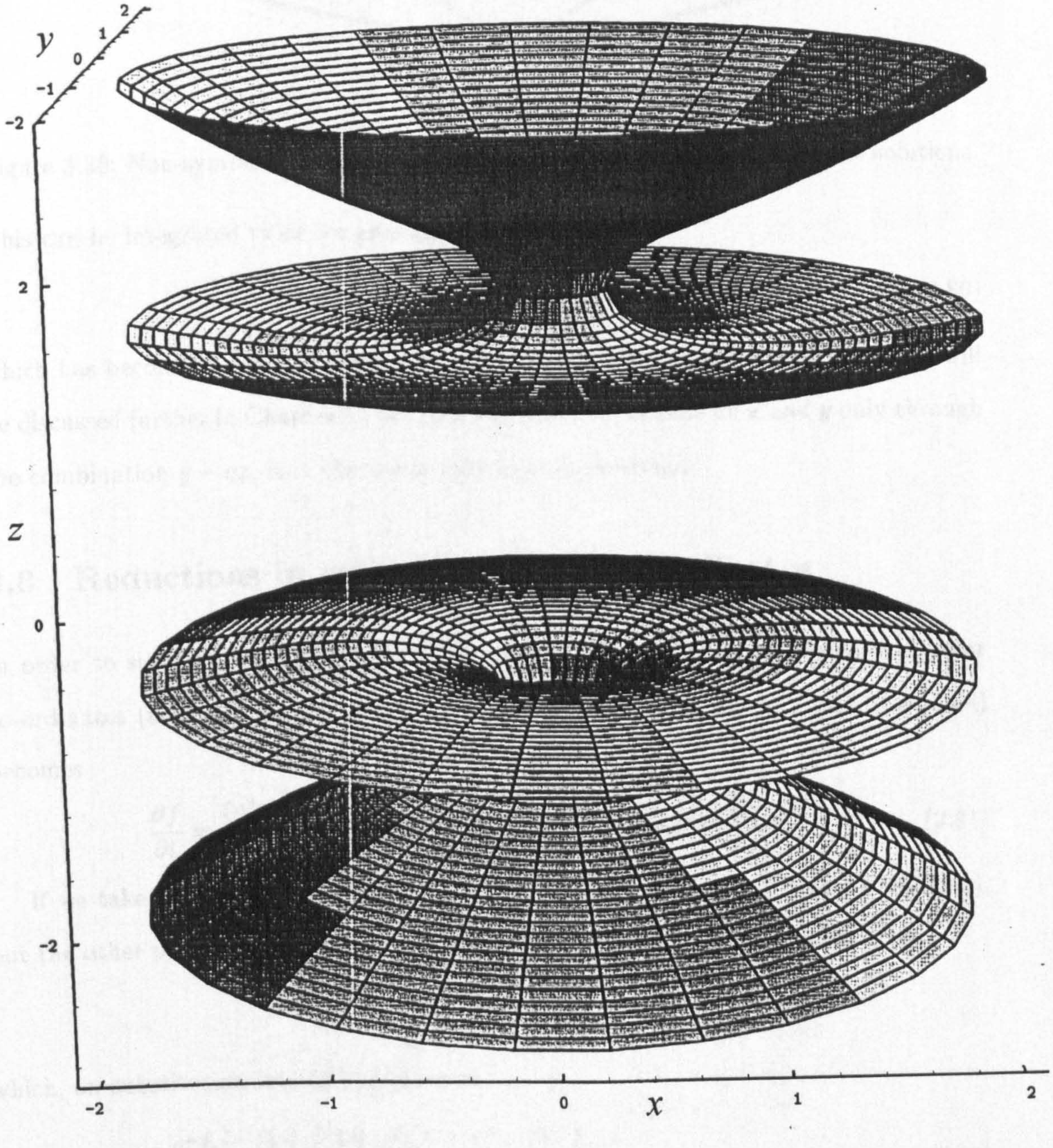

Figure 3.35: The 'bowl with a hole' solution. The axes shown are $z = g(\rho), \rho^2 = x^2 + y^2$.

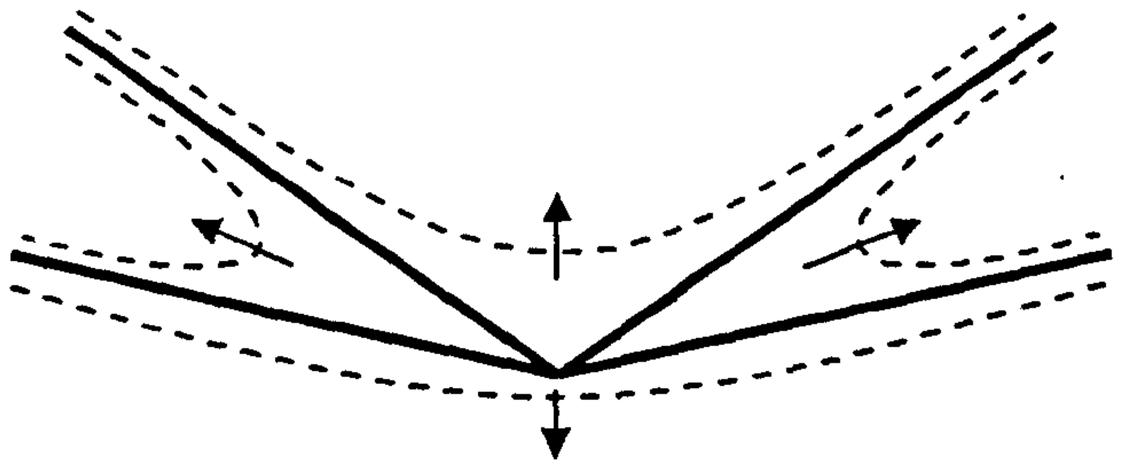

Figure 3.36: Non-symmetric initial configuration for 'bowl with hole' and cone solutions.

This can be integrated twice, to give a final solution of

$$f(x,y,t) = t - \ln\cos\left(\frac{y-qx}{\sqrt{1+q^2}}\right), \tag{3.80}$$

which has become known as the 'Grim Reaper' solution (see, for example, [2]); this will be discussed further in Chapter 5. We note that since it depends on x and y only through the combination $y - qx$, it is effectively only two-dimensional.

3.8 Reductions in cylindrical polar co-ordinates

In order to simplify the algebra, we will now express formulations in cylindrical polar co-ordinates (although we will still use (3.66) in to obtain them). We note that (3.64) becomes

$$\frac{\partial f}{\partial t} = \frac{(r^2+f_\theta^2)f_{rr} + (1+f_r^2)(f_{\theta\theta}+rf_r) + \frac{2}{r}f_r f_\theta^2 - 2f_r f_\theta f_{r\theta}}{r^2(1+f_r^2)+f_\theta^2}. \tag{3.81}$$

If we take α and λ to be non-zero in (3.66) (i.e. a translation in t and a rotation), but the other parameters to be zero, then we can look for a reduction of the form

$$f = f(r, \theta - qt) = f(r, \psi),$$

which, on substitution into (3.81), gives us

$$\begin{aligned} qr\,f_\psi[r^2(1+f_r^2)+f_\psi^2] + r\,(r^2+f_\psi^2)\,f_{rr} + \\ r\,(1+f_r^2)(f_{\psi\psi}+r\,f_r) + 2\,f_r\,f_\psi^2 - 2\,r\,f_r\,f_\psi\,f_{r\psi} = 0. \end{aligned} \tag{3.82}$$

This admits the group

$$\begin{aligned} r^* &= r \\ \psi^* &= \psi + \alpha_1 \\ f^* &= f + \beta_1, \end{aligned} \tag{3.83}$$

which, on taking α_1 and β_1 to be non-zero, allows us the second reduction

$$f = p\psi + R(r)$$

for some constant p and hence

$$R'' = -\frac{p^2 R' + (pqr + R')(p^2 + r^2(1 + R'^2))}{r(p^2 + r^2)}. \tag{3.84}$$

We can solve (3.84) numerically; we obtain the rigidly-rotating helical surface as shown in Figure 3.37 for $p = 1$.

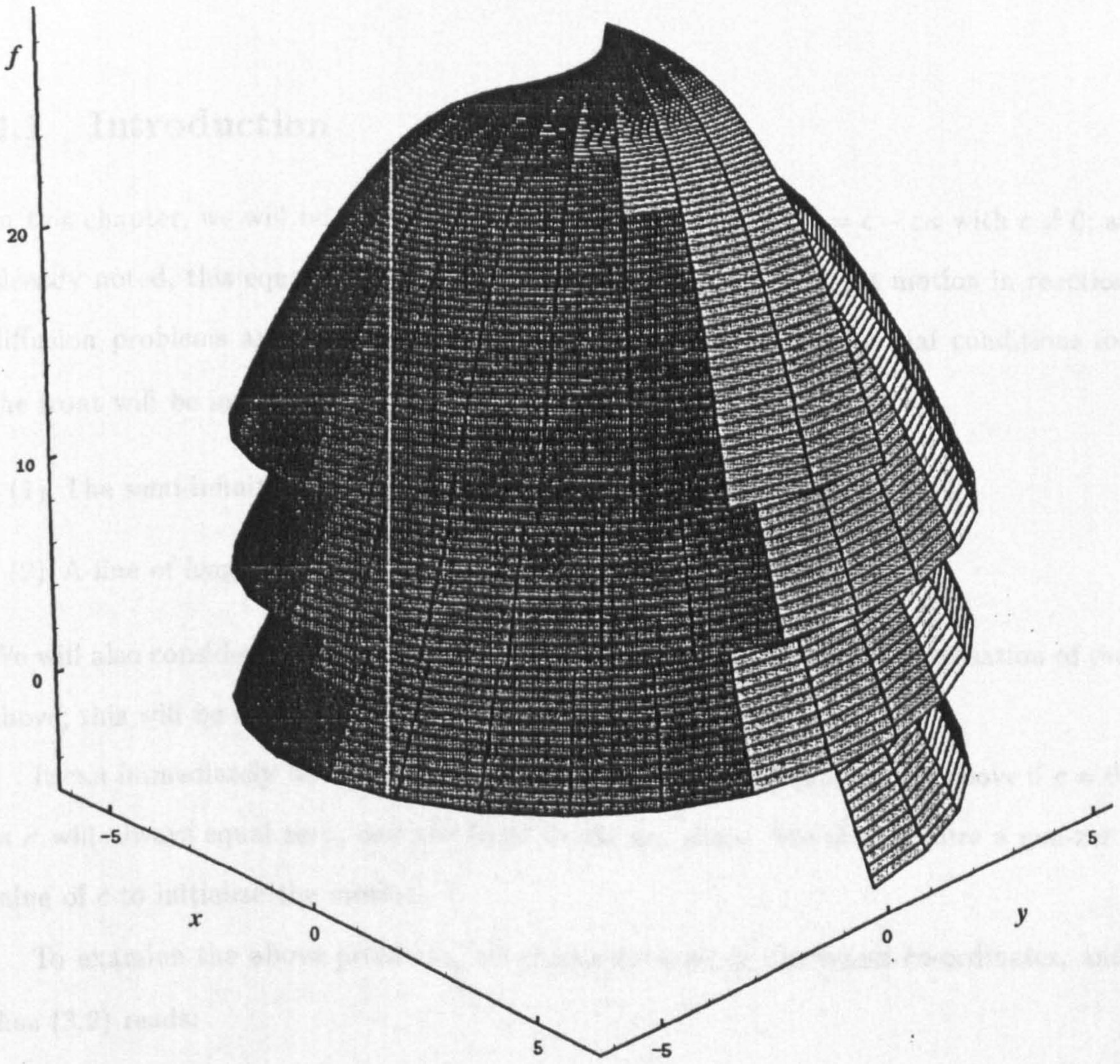

Figure 3.37: Helical solution for $p = 1$; $f = f(r, \psi)$. The axes shown have $r^2 = x^2 + y^2$.

While other similarity reductions are possible, we shall conclude our discussion of (3.3) here.

Chapter 4

Flow By Curvature: $N = c - \varepsilon\kappa$

4.1 Introduction

In this chapter, we will be considering numerical solutions to $N = c - \varepsilon\kappa$ with $c \neq 0$; as already noted, this equation has been proposed as a model for front motion in reaction diffusion problems and also arises in other contexts. Two sets of initial conditions for the front will be investigated :

(1) The semi-infinite line $0 \leq x \leq \infty$, $y = 0$ fixed at $x = 0$, $y = 0$ and

(2) A line of length $2L$, with both end points fixed.

We will also consider another configuration which in some sense is a generalisation of the above; this will be explained later.

It can immediately be seen that a trivial solution would result for the above if $c = 0$, as κ will always equal zero, and the front would not move. We thus require a non-zero value of c to initialize the motion.

To examine the above problems, we choose to work in Cartesian co-ordinates, and thus (3.2) reads:

$$y_t = \varepsilon \frac{y_{xx}}{1 + y_x^2} + c\,(1 + y_x^2)^{1/2}. \tag{4.1}$$

We non-dimensionalize (4.1) by rescaling with

$$\begin{aligned} x &\rightarrow \varepsilon x/c \\ y &\rightarrow \varepsilon y/c \\ t &\rightarrow \varepsilon t/c^2 \end{aligned} \tag{4.2}$$

to obtain

$$y_t = \frac{y_{xx}}{1+y_x^2} + (1+y_x^2)^{1/2}. \tag{4.3}$$

Thus, we need not be concerned with the values of c and ε and solution of the equation

$$N = 1 - \kappa \tag{4.4}$$

will be sufficient.

4.2 Case 1: The 'Single' Spiral

We will start by looking at the first problem mentioned above. Before embarking on the numerical methods, we briefly investigate some analytical attempts at solution.

4.2.1 Similarity Forms and Asymptotic Analysis

Here, we hope to provide some motivation for the numerical analysis, by showing the difficulties encountered when searching for exact or asymptotic solutions.

If we look for a similarity solution to (4.3) of the form

$$y = t^\alpha F(\eta), \text{ where } \eta = x/t^\beta,$$

then we find that

$$t^{\alpha-1}(\alpha F - \beta\eta F') = \frac{t^{\alpha-2\beta}F''}{1+t^{2(\alpha-\beta)}F'^2} + (1+t^{2(\alpha-\beta)}F'^2)^{1/2}. \tag{4.5}$$

It can be seen that we cannot eliminate t from (4.5) for any non-trivial values of α and β; we can, however, produce some asymptotic simplifications:

- $\alpha = 1, \beta = 1/2$

  In this case, (4.5) reduces to

$$F - \frac{1}{2}\eta F' = \frac{F''}{1 + t F'^2} + (1 + t F'^2)^{1/2}$$

  and thus for t small,

$$F - \frac{1}{2}\eta F' \sim F'' + 1,$$

  i.e.

$$y_t \sim y_{xx} + 1 \qquad \text{as } t \to 0. \tag{4.6}$$

  If we solve (4.6) (numerically, using a simple time-stepping finite differences scheme) with boundary conditions

$$\begin{aligned} y(x,0) &= 0 \\ y(0,t) &= 0, \end{aligned}$$

  we obtain a profile as shown in Figure 4.1, which is as might be expected. Alternatively, the similarity solution can be constructed analytically. However, this

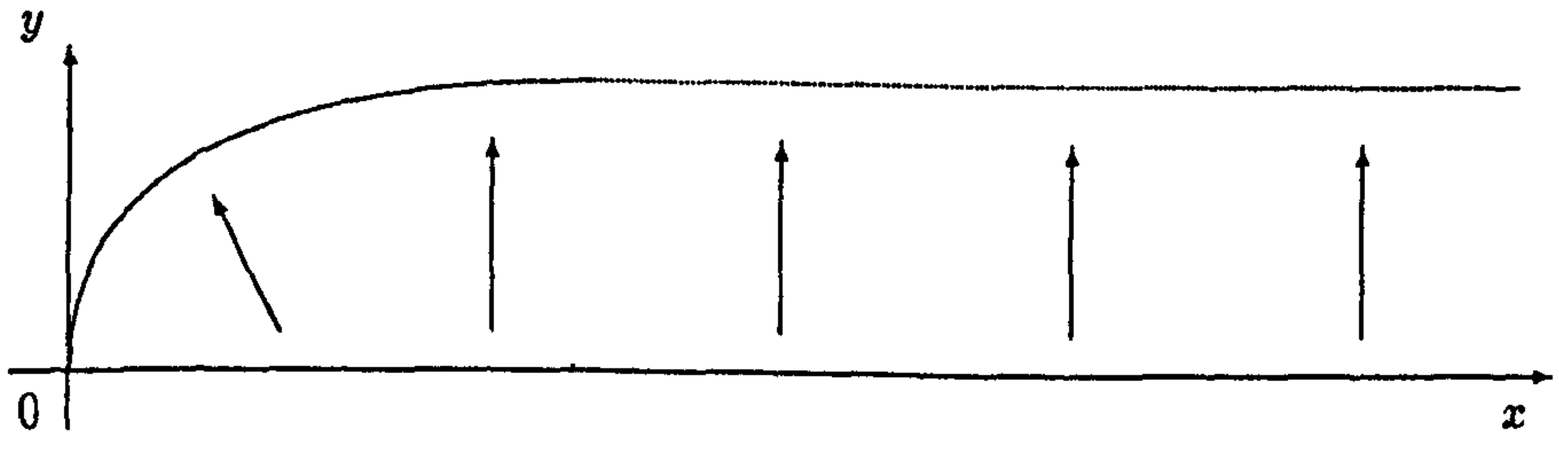

Figure 4.1: Diagram of the small time behaviour.

  small time behaviour is not particularly useful in determining the spatial structure for general t.

- $\alpha = 1, \beta = 1$

  This time, (4.5) becomes

$$F - \eta F' = \frac{t^{-1} F''}{1 + F'^2} + (1 + F'^2)^{1/2}$$

and thus for t large, we have

$$F - \eta F' \sim (1 + F'^2)^{1/2}$$

i.e.

$$y_t \sim (1 + y_x^2)^{1/2} \qquad \text{as } t \to \infty. \tag{4.7}$$

We note that the order of the equation has been reduced by one; there are two solutions of this self-similar form, the general (plane wave) solution

$$y = \alpha x + (1 + \alpha^2)^{1/2} t, \tag{4.8}$$

where α is an arbitrary constant, and the envelope (circular wave) solution

$$x^2 + y^2 = t^2. \tag{4.9}$$

We can immediately see that neither (4.8) nor (4.9) satisfy the boundary condition that $y(0,t) = 0$. However they can be used (King [32]) as the basis for an asymptotic approach to determine the large time behaviour.

In what follows we shall restrict ourselves primarily to numerical approaches.

4.2.2 A Full Time-Dependent Model–The Equations

To compute the full time-dependent behaviour, we note that a simple time-stepping discretization of (4.3) will not suffice; intuitively, we expect the initially horizontal 'front' to wrap itself around the fixed point at the origin in a spiral, giving a multi-valued solution. To overcome this difficulty, we express the position of the front in terms of an arc-length co-ordinate s (as demonstrated in Hyman's surface tracking methods [24]); (4.4) now becomes the system

$$\begin{aligned} X_t &= \left(1 - \frac{X_s Y_{ss} - Y_s X_{ss}}{(X_s^2 + Y_s^2)^{3/2}}\right) \frac{-Y_s}{(X_s^2 + Y_s^2)^{1/2}}, \\ Y_t &= \left(1 - \frac{X_s Y_{ss} - Y_s X_{ss}}{(X_s^2 + Y_s^2)^{3/2}}\right) \frac{X_s}{(X_s^2 + Y_s^2)^{1/2}}, \end{aligned} \tag{4.10}$$

where $x = X(s,t)$ and $y = Y(s,t)$. The speed of propagation of the wavefront tangential to itself is given by

$$\alpha = \frac{X_s X_t + Y_s Y_t}{(X_s^2 + Y_s^2)^{1/2}},$$

and $\alpha = 0$ since the t-tangent vector and s-tangent vector are orthogonal. We could now attempt to discretize (4.10) using a standard finite-differences scheme. However, with a little thought it is soon realised that this will fail; no matter how we initially space the points on our mesh, they will move apart as the front evolves and 'stretches'. This is illustrated in Figure 4.2. We thus deduce that the distance between any two points is

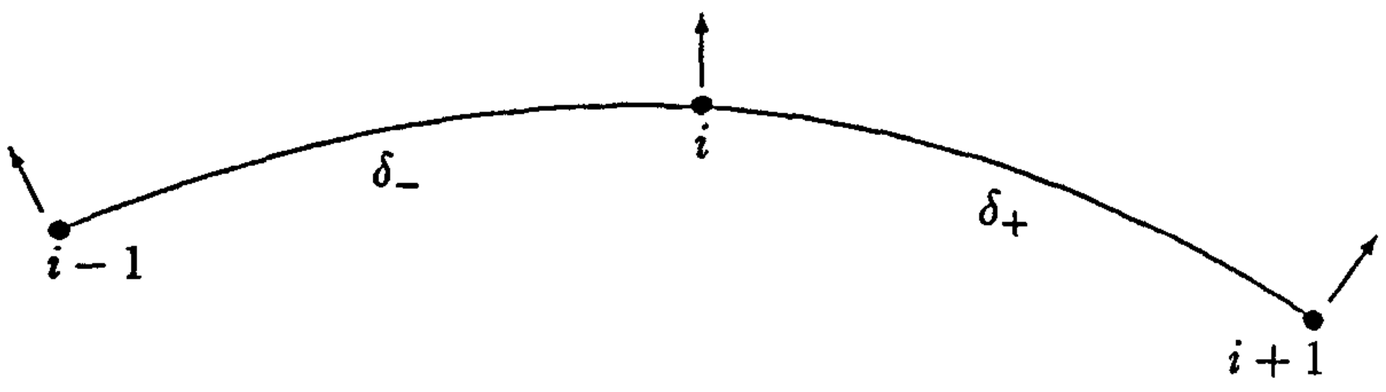

Figure 4.2: The motion of points on the front.

not constant, but a function of the shape of the front. To show how we deal with this, we consider three successive grid points $i-1$, i and $i+1$ on the front (see Figure 4.2). By Taylor expansion, we have

$$\begin{aligned} X_i &= X(s) &&= X_i \\ X_{i-1} &= X(s-\delta_-) &&\sim X_i - \delta_- X_{,i} + \tfrac{1}{2}\delta_-^2 X_{,,i} - \dots \\ X_{i+1} &= X(s+\delta_+) &&\sim X_i + \delta_+ X_{,i} + \tfrac{1}{2}\delta_+^2 X_{,,i} + \dots \end{aligned} \tag{4.11}$$

and similarly for $Y(s)$. Taking up to second order terms in δ_- and δ_+, and with a little manipulation, (4.11) implies

$$X_{,i} = \frac{\delta_-^2 X_{i+1} + (\delta_+^2 - \delta_-^2)X_i - \delta_+^2 X_{i-1}}{\delta_+\delta_-(\delta_+ + \delta_-)} + O(\delta^3), \tag{4.12}$$

$$X_{,,i} = \frac{2\left[\delta_- X_{i+1} - (\delta_+ + \delta_-)X_i + \delta_+ X_{i-1}\right]}{\delta_+\delta_-(\delta_+ + \delta_-)} + O(\delta^3), \tag{4.13}$$

where $\delta \in (\delta_+, \delta_-)$. We approximate δ_- and δ_+ by the straight line distance between the relevent grid-points; we obtain

$$\begin{aligned} \delta_- &= \sqrt{(X_i - X_{i-1})^2 + (Y_i - Y_{i-1})^2}, \\ \delta_+ &= \sqrt{(X_{i+1} - X_i)^2 + (Y_{i+1} - Y_i)^2}, \end{aligned}$$

and thus, using the equivalent versions of (4.12) and (4.13) for $Y_{,i}$ and $Y_{,,i}$, we can produce the explicit numerical scheme

$$X_{i,t+1} = X_{i,t} - Z_{i,t}\, Y_{,i,t} \tag{4.14}$$

$$Y_{i,t+1} = X_{i,t} + Z_{i,t}\, X_{,i,t} \tag{4.15}$$

where

$$Z_{i,t} = \frac{\Delta t}{(X_{,i,t}^2 + Y_{,i,t}^2)^{1/2}} \left(1 - \frac{X_{,i,t} Y_{,,i,t} - Y_{,i,t} X_{,,i,t}}{(X_{,i,t}^2 + Y_{,i,t}^2)^{3/2}} \right) \tag{4.16}$$

and the derivatives are given as above. The boundary conditions are

$$X(s,0) = s \qquad Y(s,0) = 0,$$

$$X(0,t) = 0 \qquad Y(0,t) = 0,$$

which read

$$X_{i,0} = i\Delta R \qquad Y_{i,0} = 0$$

$$X_{0,t} = 0 \qquad Y_{0,t} = 0$$

in numerical form, where ΔR is the initial mesh spacing.

4.2.3 Difficulties with the mesh spacing

If we now set an initial mesh of 30 equally spaced points, ranging from (say) $0 \leq X_i \leq 1$, we soon encounter a new problem. As the front evolves, the mesh points near the origin become very sparse (see Figure 4.3) due to the high curvature, and thus the core of the 'spiral' is incorrectly modelled. Unfortunately, simply adding extra points at the spiral core (i.e. between the first two grid points) is not sufficient, as we then observe similar problems in the region just away from the core; also we have to ensure that any method of adding grid points does *not* have any significant effect on the final solution.

In considering our grid-point addition method, we look first of all at the form of the original mesh, and the 'boundary' condition imposed at the final point. So far, we have used a uniform mesh in the range $0 \leq X_i \leq 1$, which obviously will not calculate a semi-infinite front particularly well; we need the majority of grid points to be in the vicinity

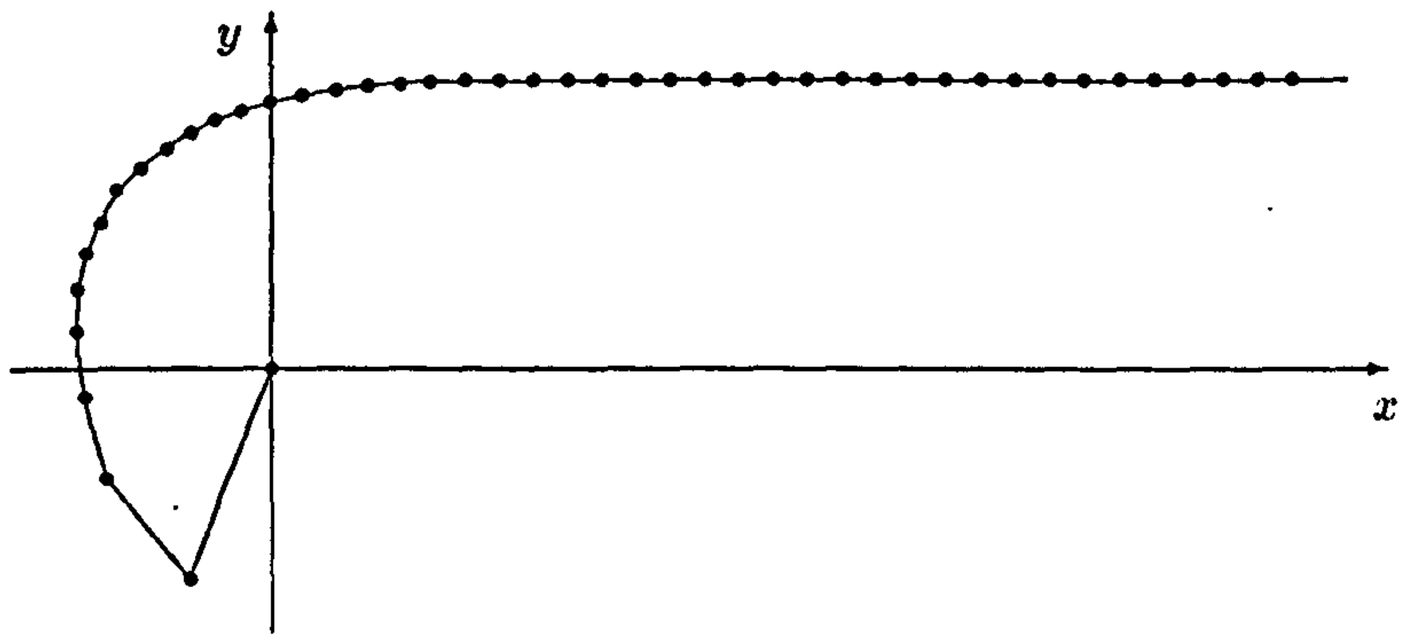

Figure 4.3: Difficulty at the origin.

of the spiral core. As $x \to \infty$, the front remains approximately horizontal, effectively moving with speed $N = 1$; thus we propose an initial mesh consisting of two parts:

- A uniformly spaced mesh of n_0 points in the range $0 \leq x \leq l$, where l is some $O(1)$ constant.

- A non-uniform mesh of n_1 points in the range $l \leq x \leq \beta l$, where β is again a constant which is chosen large enough that the far end of the front remains away from the spiralling region. We require the points to be biased towards the left-hand end of the region, so that there is a smooth transition between the two meshes.

To initialize the x-values of the second part of the mesh, we use the scaling

$$X_i = 10^{f(i)} l \qquad \text{at } t = 0, \tag{4.17}$$

where i represents the number of the grid point (as in the formulation of the equations earlier). This means that we require

$$\begin{aligned} f(n_0) &= 0 \\ f(n_0 + n_1) &= \log_{10}\beta. \end{aligned} \tag{4.18}$$

We now choose $f(i)$ to be a polynomial of degree m (it is found that a linear f will not bias the point spacing sufficiently); to satisfy (4.18), we take

$$f(i) = \left(\frac{i - n_0}{n_1}\right)^m \log_{10}\beta$$

and hence the X_i by (4.17). We still need to choose a value for m; to do so, we insist that $X_{n_0+1} - X_{n_0}$ should be equal to the space-step in the uniform mesh, which we have

denoted ΔR. Thus we require

$$X_{n_0+1} - X_{n_0} = \Delta R = \frac{l}{n_0 - 1}$$

and hence, using (4.17), we require

$$\beta^{(1/n_1)^m} - 1 = \frac{1}{n_0 - 1},$$

i.e.

$$m = \frac{1}{\ln n_1} \ln \left(\frac{\ln \beta}{\ln(n_0/(n_0 - 1))} \right). \tag{4.19}$$

We can consider now the grid-point addition method. First of all we note that the scheme must remain stable; linear analysis implies that we require

$$\Delta t < \frac{1}{2}\Delta R^2.$$

We must ensure therefore that when adding points they are greater than $\sqrt{2\Delta t}$ apart. To demonstrate our addition method, we consider three consecutive points on the mesh, as shown before in Figure 4.2. Looking to add points between $i-1$ and i (for example), we compare the distance δ_{-_i} with some reference minimum spacing δ_{ref_i}. We do *not* choose ΔR as our minimum spacing, as this will result in many extra grid points being inserted away from the spiral core, where they are not required; instead, we choose a weighted reference spacing

$$\delta_{\text{ref}_i} = \left(1 + \frac{\alpha i}{n}\right) \Delta R,$$

where α is a constant and n is the total number of points in the mesh at time t. A value of $\alpha = 5$ was found to be suitable. The number of points to add is then chosen to be

$$n_{p_i} = \max \left[\text{int} \left(\frac{\delta_{-_i}}{\delta_{\text{ref}_i}} \right) - 1, 0 \right].$$

In order to determine where these new points should be inserted, we approximate the curve through points $i-1$, i and $i+1$ by an arc of a circle and space these additional points equally along that part of the arc between points $i-1$ and i; this requires simple but lengthy geometrical calculations, which have been omitted for brevity. We eventually find that the X-values of the new points are given by

$$X_{h_i} = a_i \pm \left(r_i^2 / \left[1 + \left(\frac{(n_{p_i}+1)(Y_{i-1} - b_i) + h_i(Y_i - Y_{i-1})}{(n_{p_i}+1)(X_{i-1} - a_i) + h_i(X_i - X_{i-1})} \right)^2 \right] \right) \tag{4.20}$$

where (a_i, b_i) are the coordinates of the centre of the fitted circle, r is its radius and $h_i = 1, 2 \ldots n_{p_i}$ denotes the number of the additional point. The sign of the root is dependent on the position in the (spiral) mesh; we choose the sign which maintains a smooth curve. The Y-values are then given by the equation of our fitted circle

$$Y_{h_i} = b_i + \sqrt{r_i^2 - (X_{h_i} - a)^2}. \tag{4.21}$$

This completes the grid-point addition method, which we employ for all values of i from $i = 1$ through to $i = n - n_1$ (the 'tail' region can be excluded) at regular intervals so as to maintain the correct spiral shape (this can be checked by solving for different frequencies of addition over the same length of time, and ensuring that there is little difference between results).

4.2.4 Results

In Figure 4.4, we have an example of the type of spiral that is produced. For our calculations, we have taken $n_0 = 30$, $n_1 = 10$, $l = 2 \Rightarrow \Delta x = 0.069$, $\Delta t = 0.002$ and extra grid points have been added every 5000 iterations. It can be seen that away from the core, the distance between the coils of the spiral is virtually constant, indicating that the front motion is approximately planar. This is due to the curvature term being very small.

We have now completed our numerical work for the first problem; however, by considering a similarity formulation, we can obtain the speed of rotation of the spiral wave without solving the time-dependent problem.

4.2.5 A Similarity Method

Keener [28] and Grindrod [19] have previously shown that (4.1) can be reduced to a second order system of first-order ordinary differential equations if the spiral region only (and not the 'tail') is considered. We will now demonstrate a different formulation which clearly shows how a unique rotation speed can be determined.

Writing (4.4) in polar co-ordinates, we have

$$\frac{\partial r}{\partial t} = \frac{r r_{\theta\theta} - 2r_\theta^2 - r^2}{r(r_\theta^2 + r^2)} + \frac{(r_\theta^2 + r^2)^{1/2}}{r}. \tag{4.22}$$

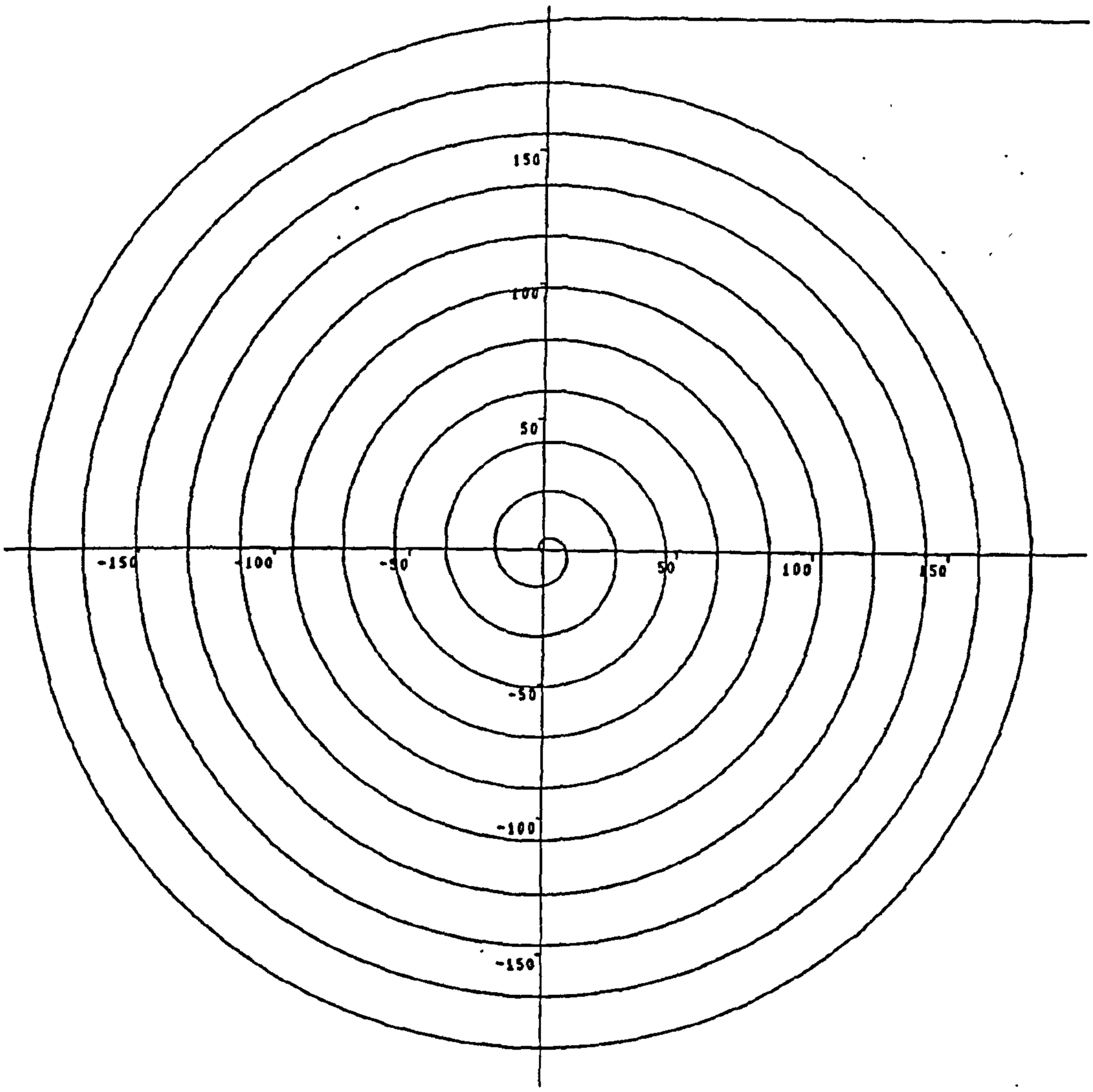

Figure 4.4: Shape of front at time $t = 200$.

To seek a rigidly rotating spiral solution, we set

$$r = F(\theta - qt) = F(\eta)$$

so that, on substitution into (4.22), we obtain the second-order ordinary differential equation

$$F\,F_{\eta\eta} + (F_\eta^2 + F^2)^{3/2} + q\,F\,F_\eta(F_\eta^2 + F^2) - 2\,F_\eta^2 - F^2 = 0. \tag{4.23}$$

We can now study the phase plane; we write

$$\begin{aligned} F' &= F\,G, \\ G' &= F^2 + 2\,G^2 - (F^2 + G^2)^{3/2} - q\,F\,G\,(F^2 + G^2), \end{aligned} \tag{4.24}$$

where $G = F_\eta$. It can be seen immediately that we have four critical points (remembering that $r = F(\eta)$ must not be negative)–$(0,0)$, $(1,0)$, $(0,2)$ and $(0,-2)$. At the origin, the behaviour is the same as in (3.22), that is

$$G \sim \pm F\sqrt{(F/k)^2 - 1},$$

where k is a constant. Around $(1,0)$, linear analysis shows that we have a spiral for $|q| < 2$, and a node for $|q| > 2$; at $(0,\pm 2)$, we have saddle points. We can thus obtain the phase planes as shown in Figure 4.5 and Figure 4.6.

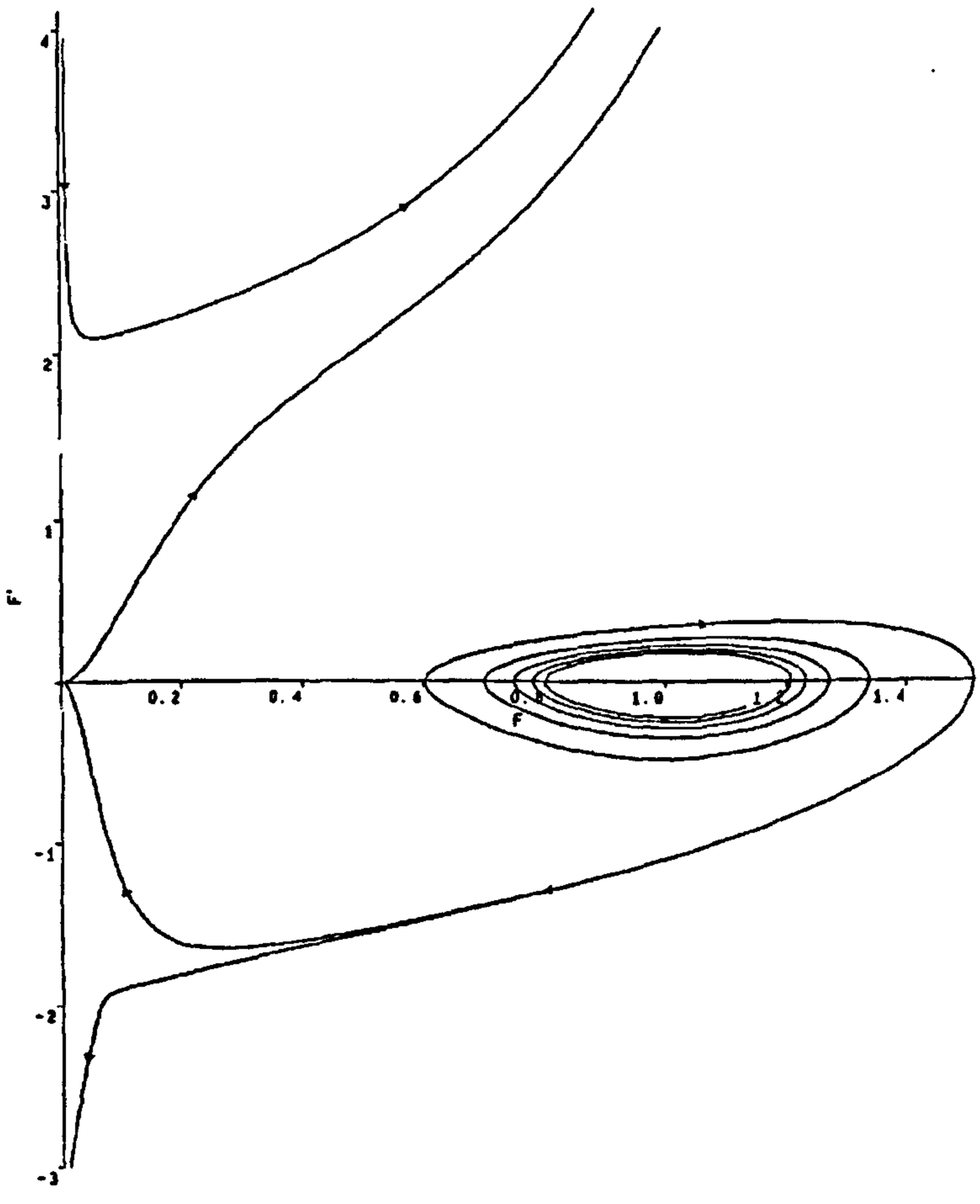

Figure 4.5: Numerical solution for the phase plane for the second-order system; $q = 1$.

We must now consider which trajectory we require. It is apparent that in view of the boundary conditions it must reach $F = 0$; this immediately limits us to the two trajectories emanating from $(0,2)$ and $(0,-2)$. If we look at the local behaviour around $F = 0$, (4.23) gives

$$(F_\eta^2)^{3/2} \sim 2F_\eta^2$$

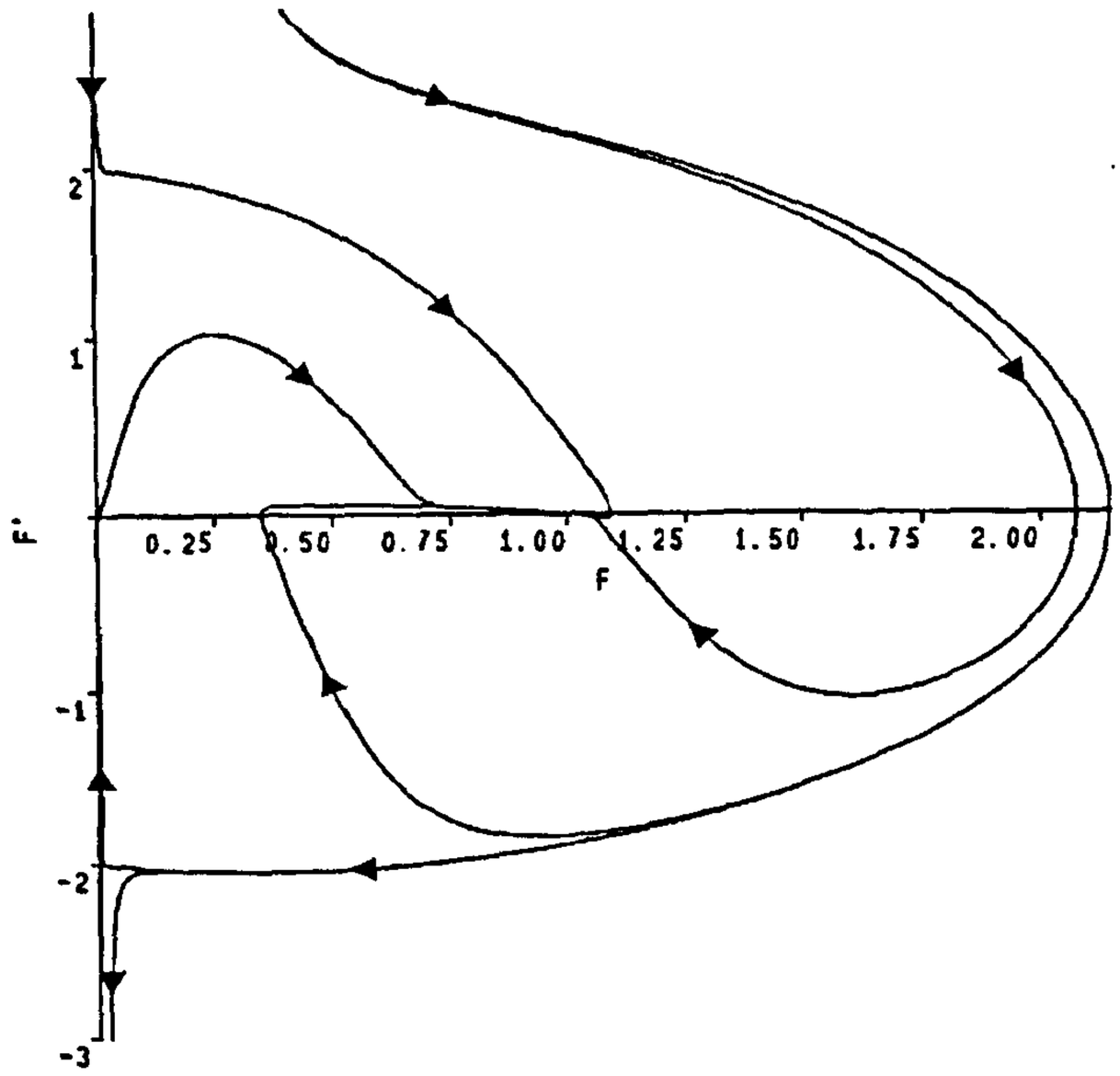

Figure 4.6: Numerical solution for the phase plane for the second-order system; $q = 3$.

and thus

$$F(\eta) \sim -2\eta \qquad \text{as } \eta \to 0^+$$

for $q > 0$. Thus we require the trajectory entering $(0, -2)$ in the phase plane.

In the far-field, the curvature term in (4.4) is negligible, and the equation is $N \sim 1$; the velocity of the front is therefore constant and hence

$$\lim_{\eta\to\infty} F_\eta = F_\infty, \tag{4.25}$$

where F_∞ is a (negative) constant. This in turn implies that in the far-field we have outgoing spherical 'waves' with a separation of

$$\lambda = -2\pi F_\infty.$$

Since the whole spiral has a period of $2\pi/q$, and it moves a distance λ in this time, we have plane periodic waves with

$$F_\infty = -1/q; \tag{4.26}$$

the result follows because the dominant balance in (4.23) is

$$F^3 \sim -qF^3 F_\eta.$$

The required trajectory is defined completely; it must come in from $F \to \infty$ with $F_\eta \sim -1/q$ and enter $F = 0$, $F_\eta(0) = -2$. It can be seen that no such trajectory exists in Figures 4.5 and 4.6; indeed, it is only possible for a unique value of q, given by $q = q^* = 0.33096\ldots$, and in Figure 4.7 we show a phase plane with two trajectories just below and just above q^*. We note that this rotation speed is the same as that found by

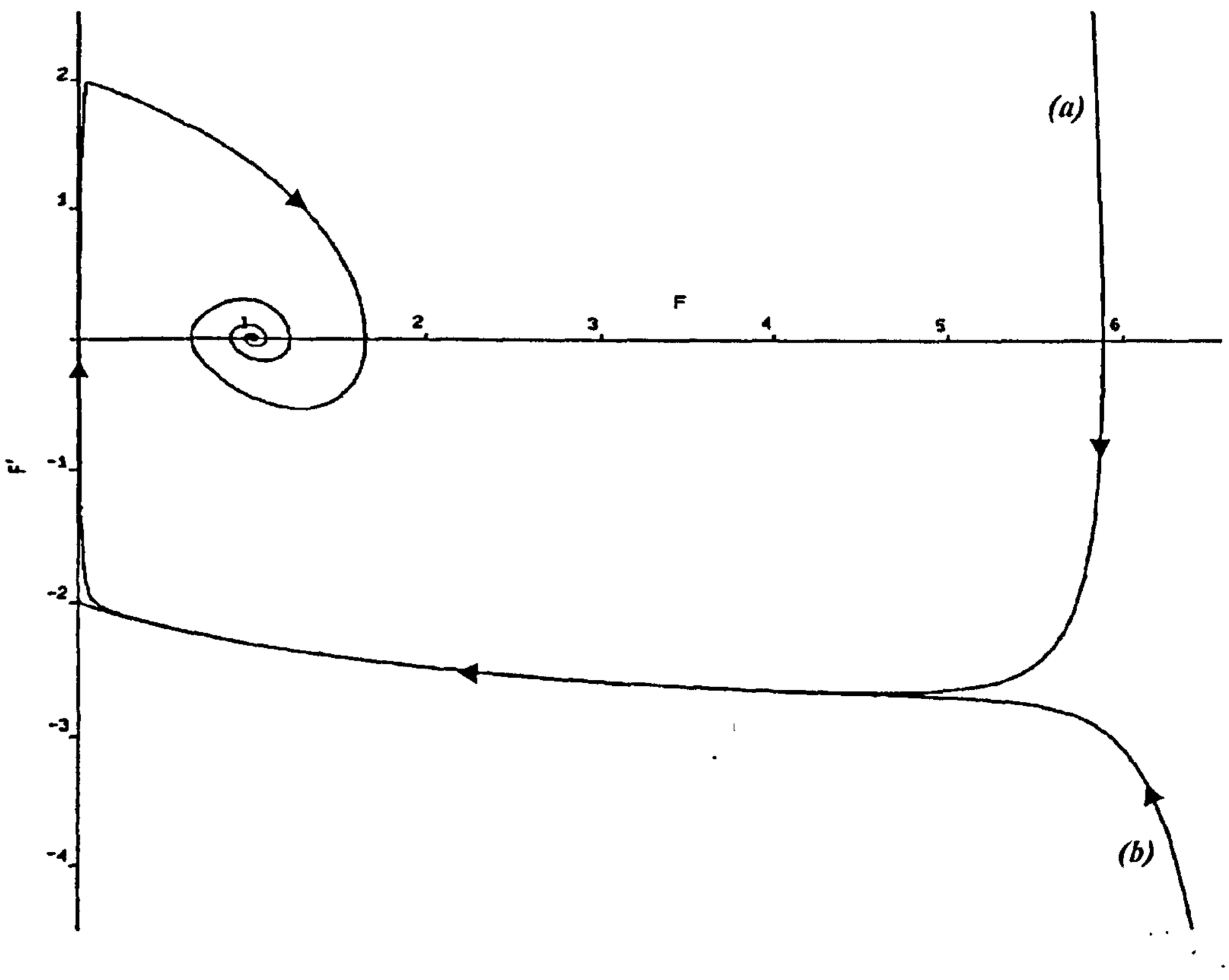

Figure 4.7: Phase plane for the second-order system; $q \approx q^*$; (a) $q > q^*$, (b) $q < q^*$.

Keener [28] using a slightly different formulation. Instead of (4.4), Keener solved

$$N = c(T) - \varepsilon\kappa$$

on an annulus (r_0, r_1), where T is the periodicity of the solution; a dispersion relation is then required to fix the speed and frequency of the solution spiral. As we can scale c and ε out of our formulation, a dispersion relation is not necessary in our problem.

If we plot out a spiral solution to our ordinary differential equation (4.23) with $q = q^*$, the agreement with our previous numerical solution in Figure 4.4 is excellent (see Figure 4.8). As a further check, we can estimate the rotation speed q for Figure 4.4

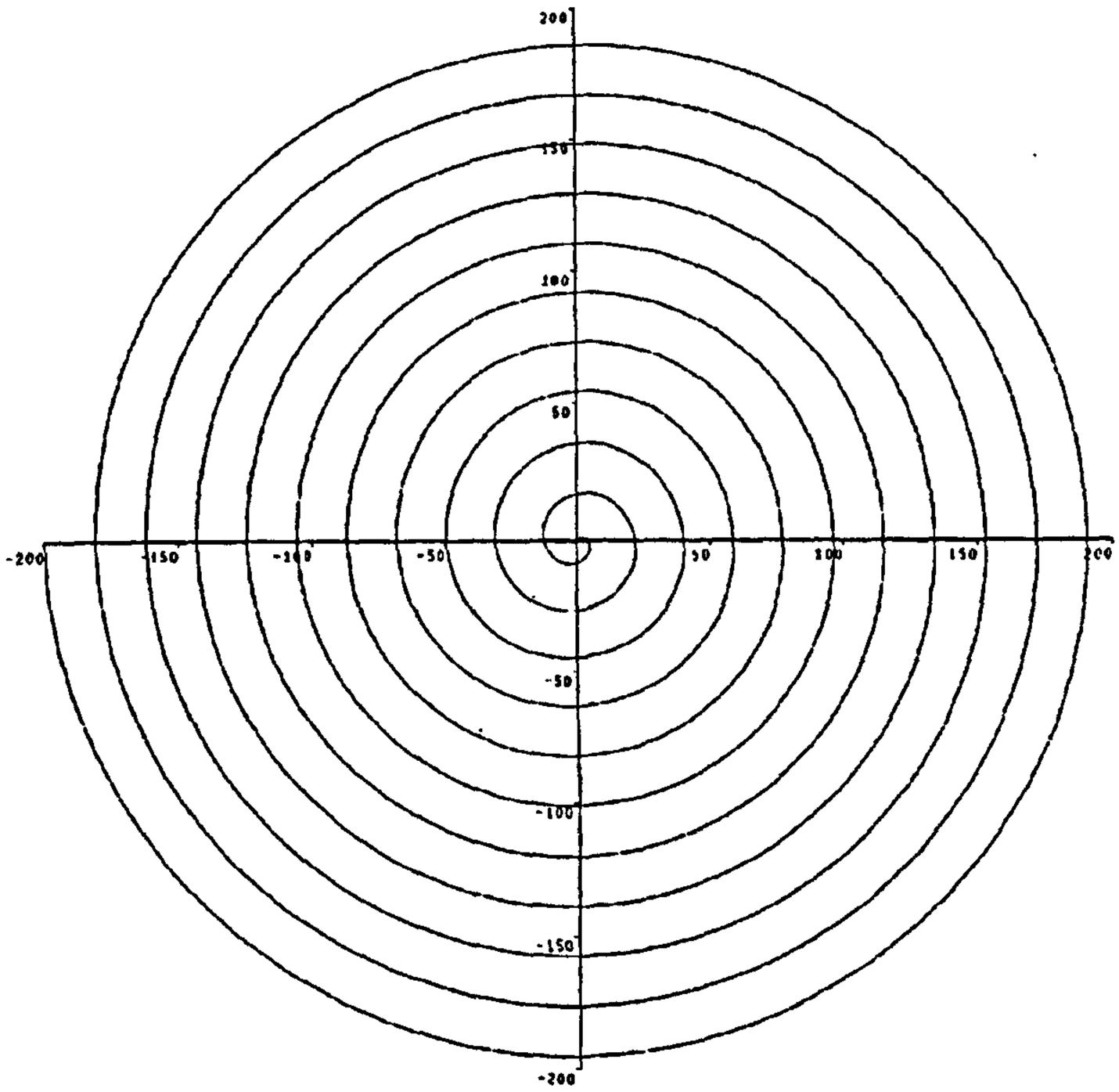

Figure 4.8: Spiral solution for the ordinarry differential equation formulation; $q = q^*$.

by measuring the distance between the outer loops of the spiral; since $N \sim 1$ away from the core, this will also be the period of rotation and hence we have $q \sim 2\pi/\text{gap}$. It is found that $q = 0.33$ to two decimal places. However, we note that this rotating wave solution gives the large-time behaviour only in the spiral core; a full description of the large-time behaviour requires a fairly complicated asymptotic structure (King [32]).

4.3 Case 2: The 'Double' Spiral

We now look at our second problem, with the initially horizontal front now fixed at both ends. From above, it is expected that spirals will form around both fixed points; it is the manner in which this is achieved by the front which is of interest.

The first point to consider is the equation to be solved. For the previous problem, we scaled out both c and ε by non-dimensionalising; this time, however, we have a third constant (the initial length of the front from the boundary conditions), which means that we will have to compute a range of solutions for different values of a single parameter

(since we can only scale a maximum of two constants out of the problem). We choose the scalings

$$x \rightarrow x/L$$

$$y \rightarrow y/L$$

$$t \rightarrow \varepsilon t/L^2$$

so that the problem becomes

$$N = \alpha - \kappa \tag{4.27}$$

with boundary conditions

$$y = 0 \qquad \text{at } x = \pm 1, \tag{4.28}$$

where

$$\alpha = \frac{cL}{\varepsilon}. \tag{4.29}$$

Before embarking on the full problem, we first consider the steady-state problem.

4.3.1 The Steady-State Problem

Our steady-state equation (from 4.27) reads

$$y_{xx} = -\frac{\alpha}{\varepsilon}(1 + y_x^2)^{3/2} \tag{4.30}$$

with boundary conditions (4.28) above. Setting $z = y_x$ and integrating, we have

$$\frac{z}{(1+z^2)^{1/2}} = \frac{c}{\varepsilon}(x - x_0),$$

where x_0 is a constant; integrating a second time, and imposing (4.28), we obtain

$$y = \frac{1}{\alpha}\left(\sqrt{1-(\alpha x)^2} - \sqrt{1-\alpha^2}\right) \tag{4.31}$$

and thus, for a real solution, we require

$$0 < \alpha \leq 1. \tag{4.32}$$

As expected, the solution in this range is a minor arc of a circle, tending to a semi-circle as $\alpha \rightarrow 1$ (a major arc solution is also possible, but it is unstable). From this, we deduce that we require $\alpha > 1$ for spiral solutions to be generated.

4.3.2 The Full Problem

To solve (4.4) numerically, we (initially) use the same scheme as for the first problem. By noting that the solution will be symmetrical (about $x = 0$), we need solve only for one side of the spiral; we choose the left hand side. As no tail region is involved this time, we initialize the front with a simple uniformly-spaced mesh in the range $-1 \leq x \leq 0$, with an extra 'mirror' point at $x > 0$ to ensure that the full double spiral joins up correctly (i.e. that $dy/dx = 0$ at $x = 0$). Our discretized boundary conditions are thus

$$\begin{aligned} X_{0,t} &= -1 \\ Y_{0,t} &= 0 \\ X_{n,t} &= 0 \\ Y_{n,t} &= Y_{n-2,t}, \end{aligned} \tag{4.33}$$

where once again we have n mesh points at time t (we are applying the grid-point addition technique used previously). We can now solve (4.27), and observe how the front evolves; for $\alpha = 1 + \delta$ with $\delta \ll 1$ (i.e. just above the critical value), we obtain the results shown in Figure 4.9. It can be seen that the front holds the steady-state shape (the semi-circle) for a reasonable length of time before spiralling round and enlarging much more quickly until there is a collision between two portions of the front at time $t = 45.9$ (which will be discussed below). In Figure 4.10, we show results for three larger values of α; we observe that increasing α increases the number of spiral turns before this front collision, but *decreases* the time required for it to occur (which is to be expected, since we are increasing the wave speed). It is also worth remembering in Figure 4.10 that the end points of each front are the same distance apart (two units); the top spiral is thus occupying a considerably larger area than the one at the bottom.

The most interesting occurrence, however, is the collision of the two spiral loops. At this point, we would expect the two colliding portions of the front to annihilate each other, resulting in two new, separate fronts; an outer closed loop, and an inner line segment (the 'seagull' shape in Figure 4.9). Modelling the behaviour past this collision time thus presents a further numerical problem, which we consider next.

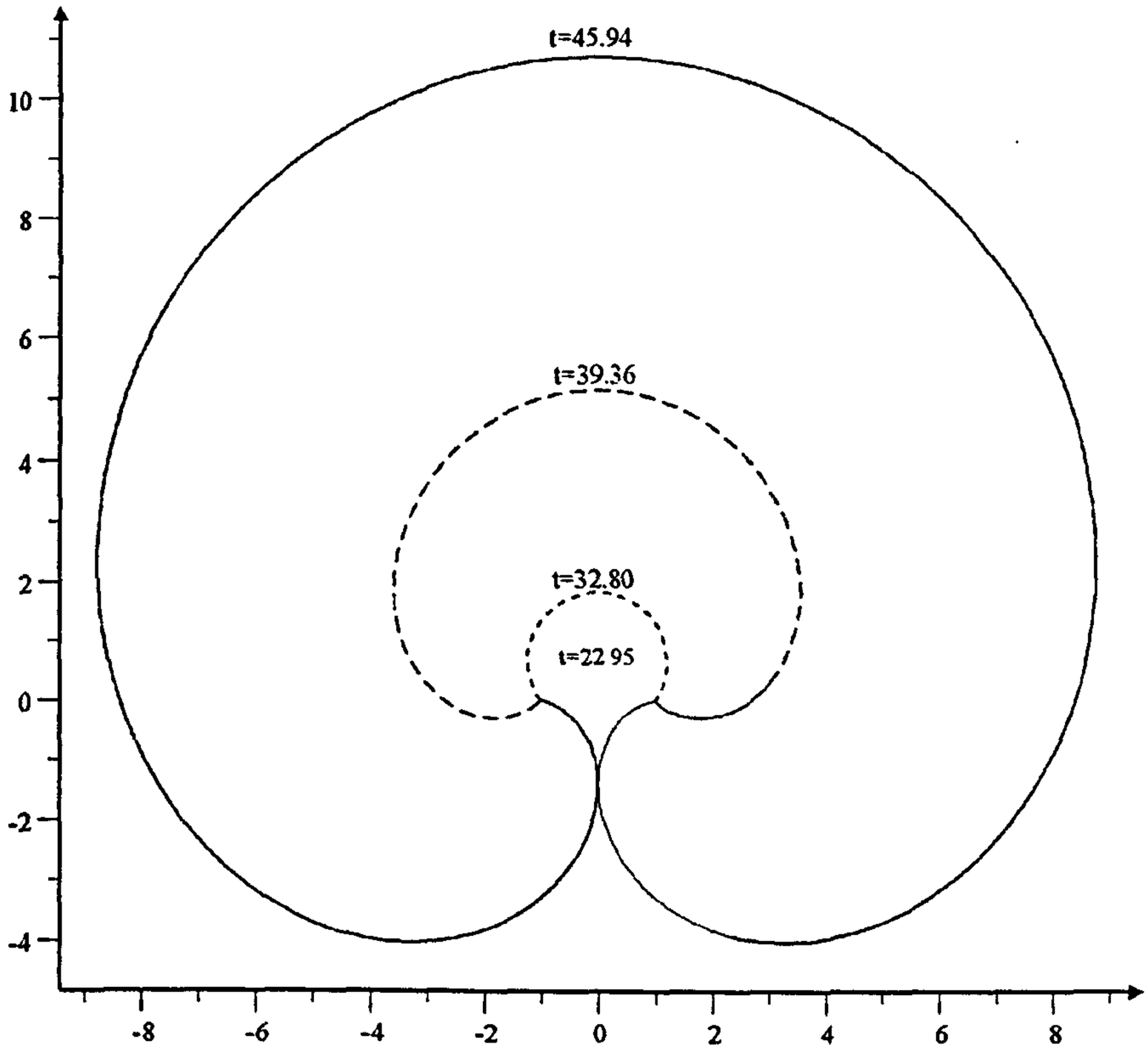

Figure 4.9: Progression of front for $\alpha = 1.01$.

4.3.3 Modelling the Post-Collision Behaviour

In our numerical model for symmetric spirals, we state that the collision of the two spiral arms occurs on the first occasion when $X_{j,t} \geq 0$ for some $j < n$, as shown in the right-hand diagram in Figure 4.11. At this time, we split the mesh into the inner and outer regions by firstly adding two new mesh points at the intersections of the spiral with the line $x = 0$; to achieve this, we approximate the spiral in this region by an arc of a circle (as we did with the grid-point addition method–this is a very accurate representation on this small scale) so that the two y-values are given by

$$y_{\pm} = b \mp \sqrt{r^2 - a^2},$$

where (a, b) are the co-ordinates of the centre of the approximating circle and r is its radius, as before. We set up two extra 'mirror' points, as shown in Figure 4.11, and thus by renumbering the grid points, we can treat the two regions (inner double spiral core and outer loop) separately (noting that we now have three extra points to consider).

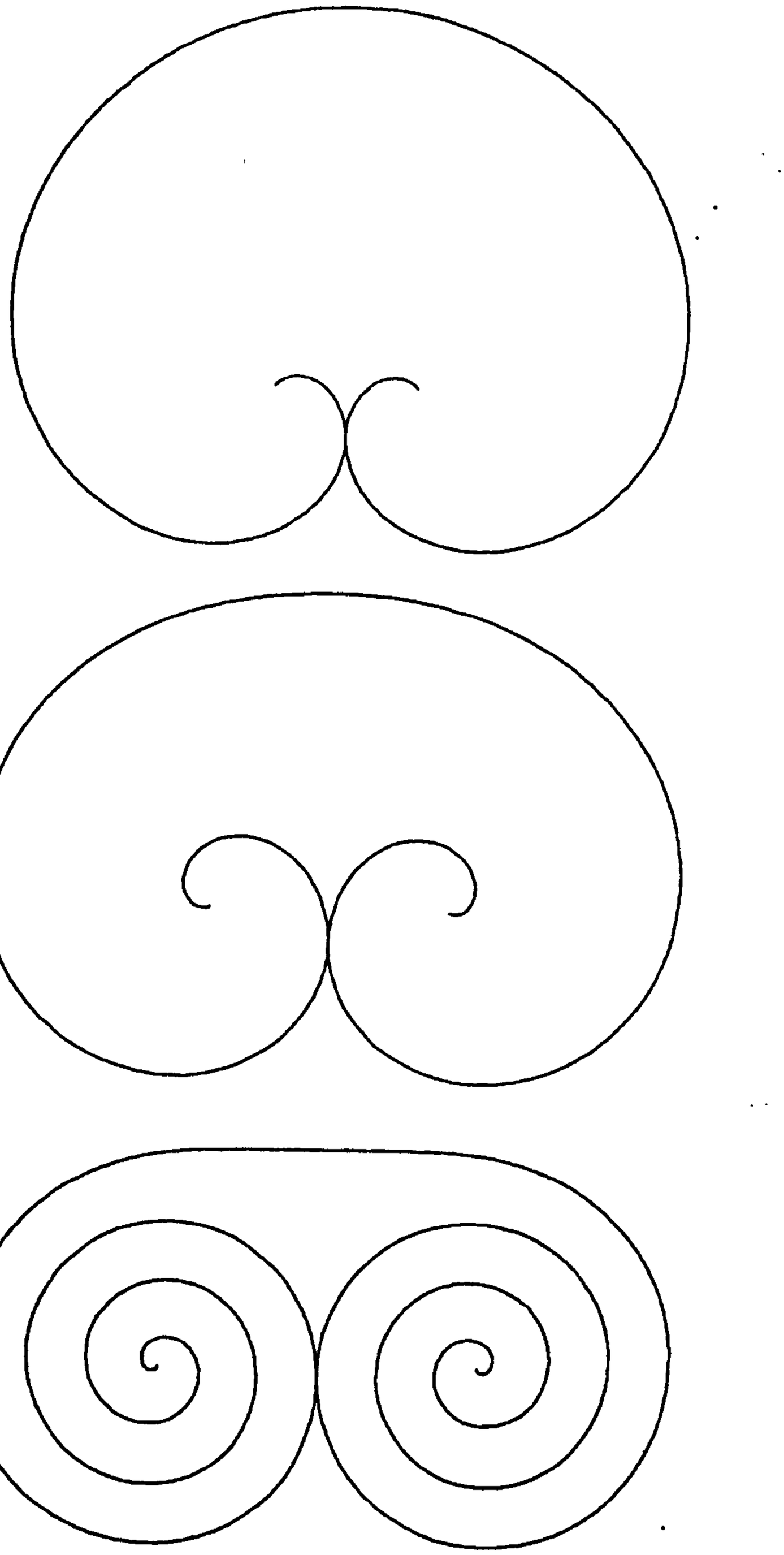

Figure 4.10: Shapes of front for $\alpha = 3$ at $t = 2.01$ (top), $\alpha = 10$ at $t = 0.264$ (centre) and $\alpha = 50$ at $t = 0.0273$ (bottom).

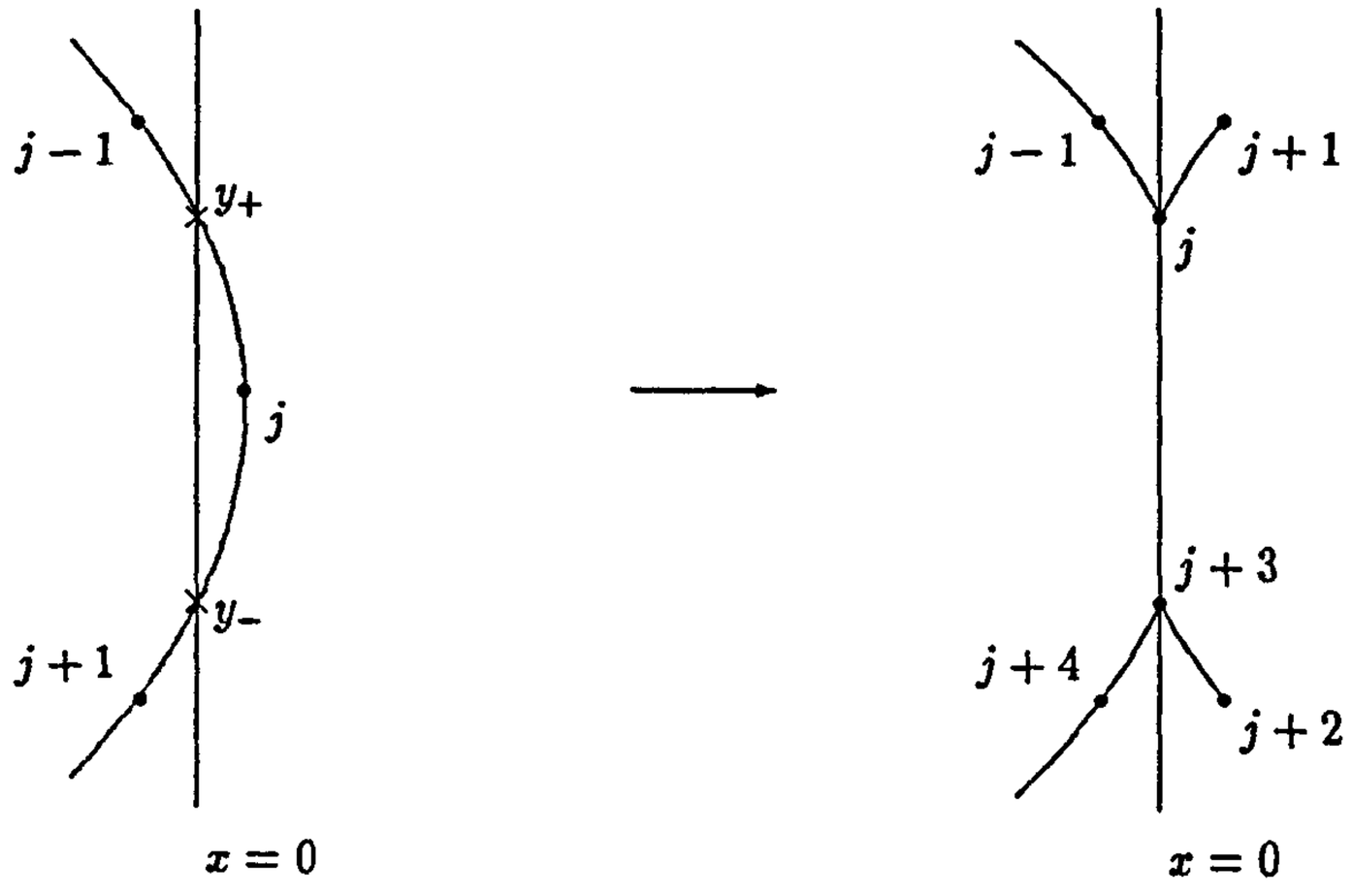

Figure 4.11: Collision of the spiral arms (not to scale).

If we now try to continue with our solutions, we soon find that the cusps which are formed (see the right-hand diagram in Figure 4.11) create a new numerical problem (since the curvature is very large). Simply reducing the time-step on its own will not remedy the situation; grid-points around $x = 0$ will still move closer together, thus forcing the distance between adjacent points to become too small (so that $\Delta t < \Delta x^2/2$ no longer holds in this region). The difficulty on this occasion is having *too many* grid-points in the cusp regions, and so we propose that the best solution is simply to remove points that are less than $\sqrt{2\Delta t}$ away from $x = 0$. This is shown in Figure 4.12; it can be seen that the omission of the original point $j-1$ has virtually no effect on the front itself. We then renumber the grid accordingly, and continue our time-stepping routine. This process is repeated again and again to generate further outer loops for subsequent collisions of the spiral arms; for an example of the results obtained, see Figure 4.13. We note the similarity of these results with the experimental spiral plots in Winfree [57].

We are now in a position to examine the patterns which occur in the behaviour of these double spirals for different values of α. Before doing so, however, we note that the outer closed loop(s) generated are *not* of great interest–they simply propagate outwards, and tend to a circle as $t \to \infty$. We will therefore retain only the inner region in further computations.

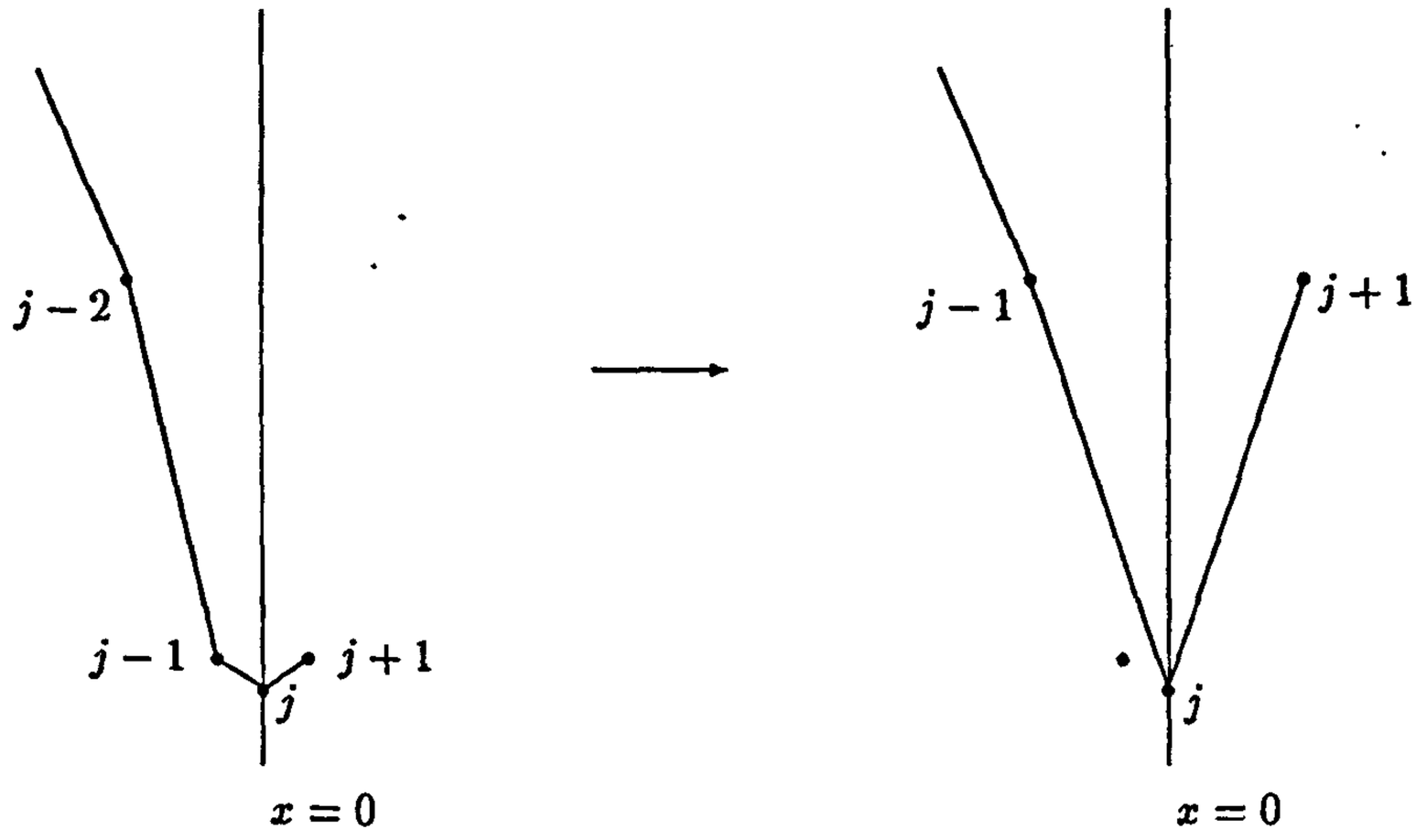

Figure 4.12: Convergence of grid points around $x = 0$, and the remedy.

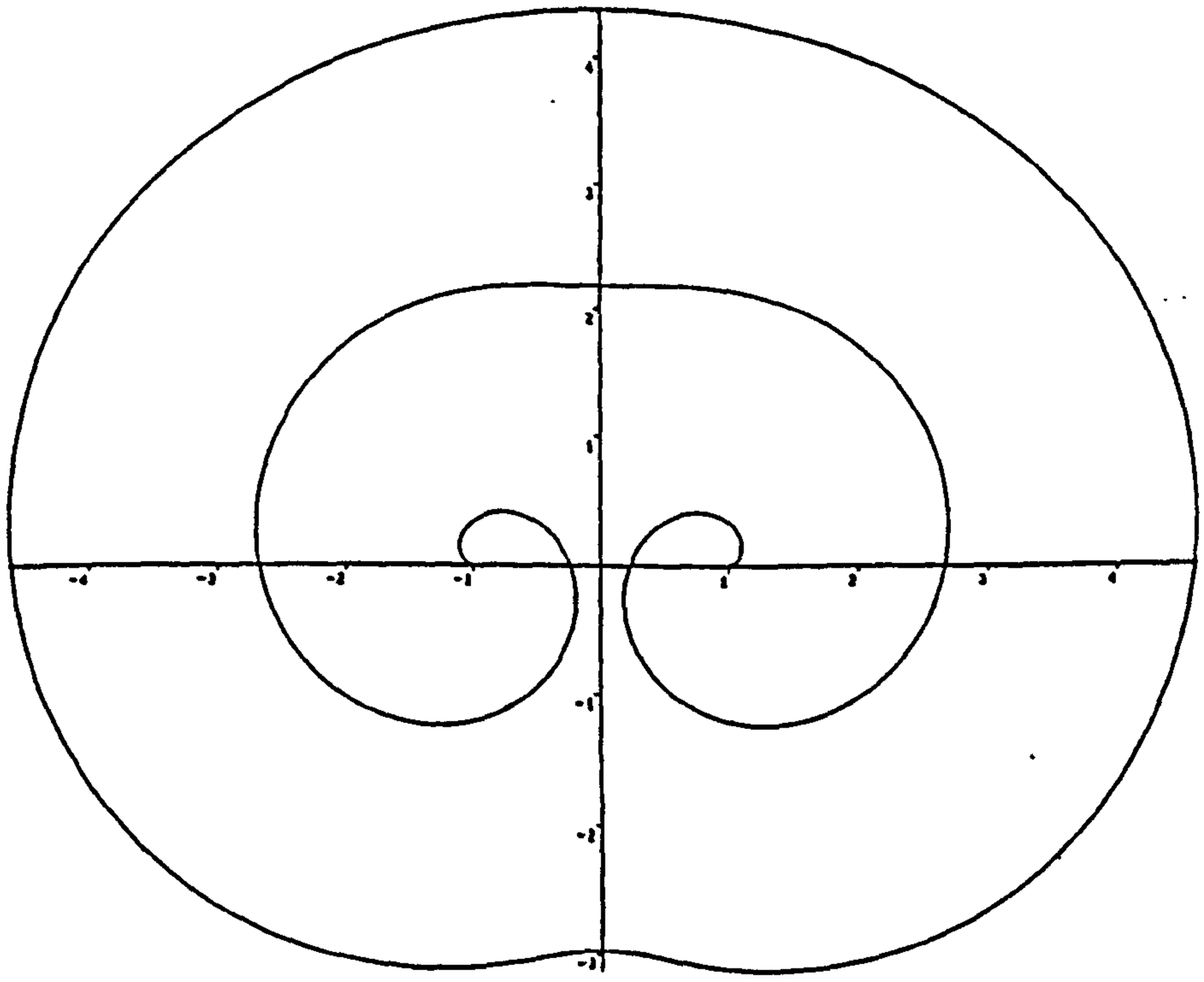

Figure 4.13: Front position at $t = 0.445$ for $\alpha = 10$.

4.3.4 Results and Observations

In order to quantify the behaviour of the front for different values of α, we choose to measure the time taken between the collisions of the spiral loops. If we refer back to the plot for $\alpha = 50$ in Figure 4.10, we can see that the time taken for the first collision to occur will be very different (in this case larger) from that of the second collision, as the front will not have so far to move for the latter. However, we can also see that we may expect the time gap between the second and third collisions to be almost equal to the gap between first and second, as the wave motion is approximately planar (consider the distances between the spiral loops; they are roughly equal). Indeed such proves to be the case (and was checked by observing the collision period up to the eighth collision–it remains almost constant after the second collision) for all values of α; in Figure 4.14 we plot the frequency of collision (i.e. 1/period) against α for both the first collision and the subsequent collisions. It can be seen that away from $\alpha = 1$, the plot for the later collisions

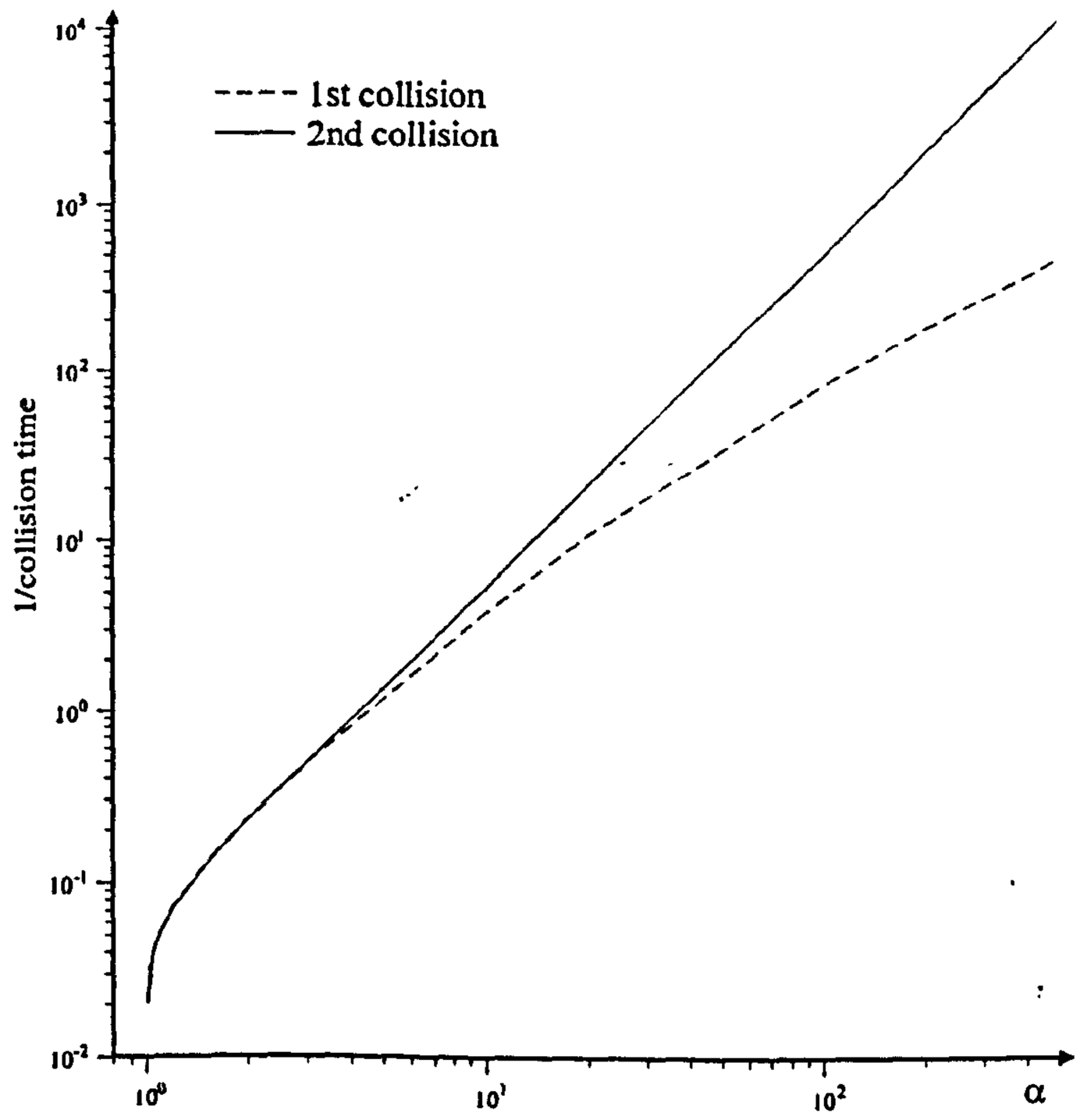

Figure 4.14: Plot of 1/period vs. α for the first and subsequent collisions.

gives an almost straight line (on logarithmic scales); its equation is approximated by

$$\log_{10}(\text{period}^{-1}) \simeq 2\log_{10}\alpha - 1.3$$

and thus

$$\frac{1}{\text{period}} \simeq \frac{\alpha^2}{20}. \tag{4.34}$$

In addition we can look at trends with regard to the time taken to the first collision. If

α	Collision period	
	1st	2nd+
1.5	7.696	7.854
3	2.004	2.007
10	0.2637	0.1905
20	0.0929	0.0478
50	0.0273	0.0077
100	0.0119	0.0020
200	0.00551	0.00050
500	0.00209	0.00008

Table 4.1: First and subsequent collision periods.

we look at the data used in Figure 4.14, we can obtain Table 4.1, from which, we can postulate that for large values of α (i.e. $\alpha \geq 50$),

$$\text{time taken for first collision, } T \approx \frac{1}{\alpha} + \text{second collision period,}$$

which, using (4.34), implies that

$$T^{-1} \simeq \frac{\alpha^2}{\alpha + 20} \qquad \text{for } \alpha \gg 1. \tag{4.35}$$

This is demonstrated in Figure 4.15.

As a final point of interest, we can count the number of spiral loops just before a collision for a range of values of α; this will not be completely accurate (especially for small values of α), as it can be awkward when considering the core since there

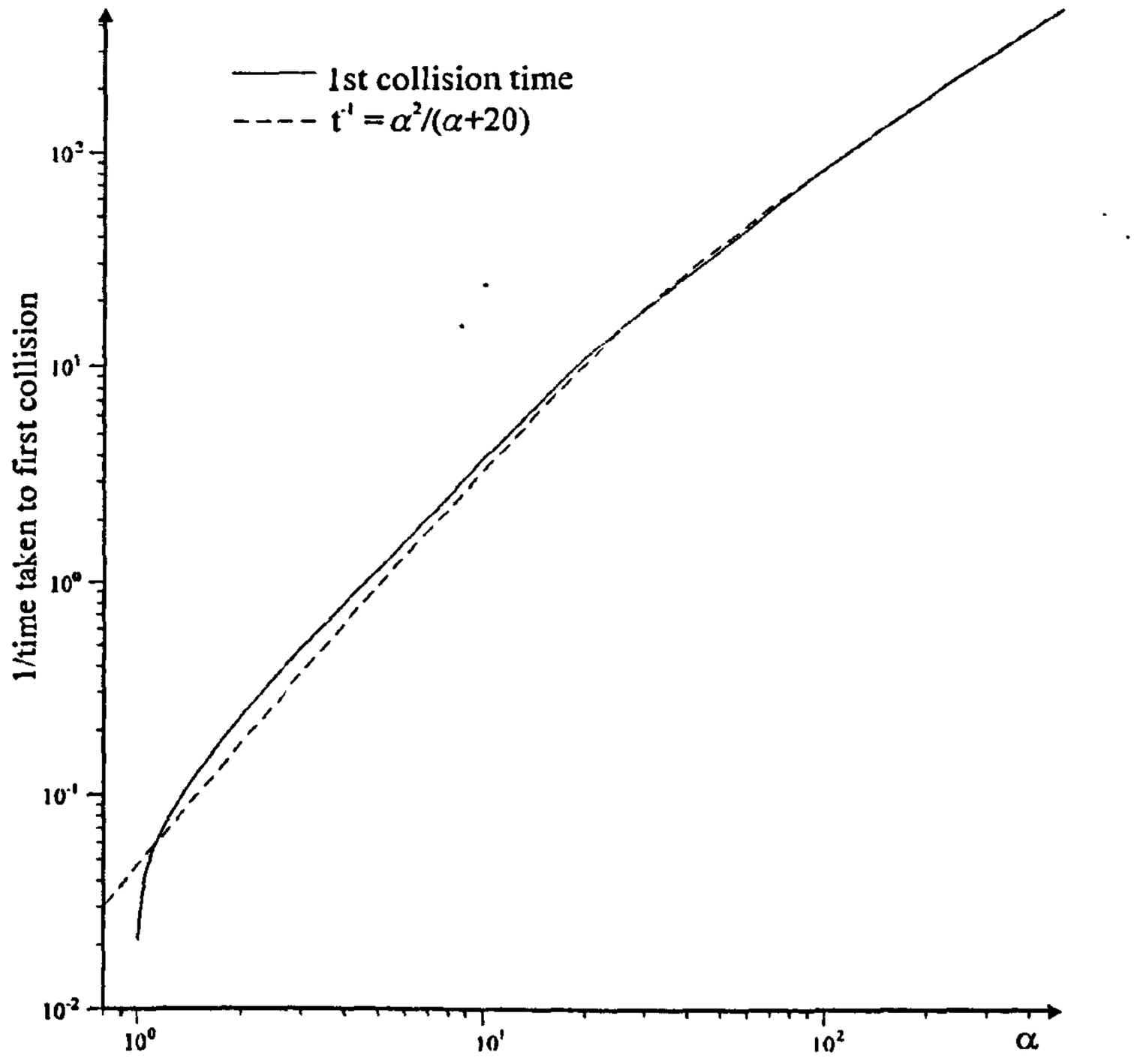

Figure 4.15: An approximation to the first collision time for $\alpha \to \infty$; for $\alpha \approx 1$, we do not obtain complete spiral loops at the time of collision, and thus the approximation is not valid.

will typically be an incomplete loop. Nevertheless, we can produce a plot as shown in Figure 4.16, and it can be seen that it approximates to a straight line for values of $\alpha \gg 1$ with the equation

$$n_{sp} \sim 1 + \frac{\alpha}{20}.$$

obtained by linear regression. The behaviour as $\alpha \to \infty$ and as $\alpha \to 1^+$ can also be analysed by asymptotic methods (King [32]), but we shall not pursue this here.

4.4 'Uneven' Double Spirals

It can be observed in experimental plots (e.g. Winfree [57]) that double spirals sometimes appear to be biased towards one side of the spiral, i.e. one of the spirals is larger than the other. We can produce a model of this situation by combining both of the above two

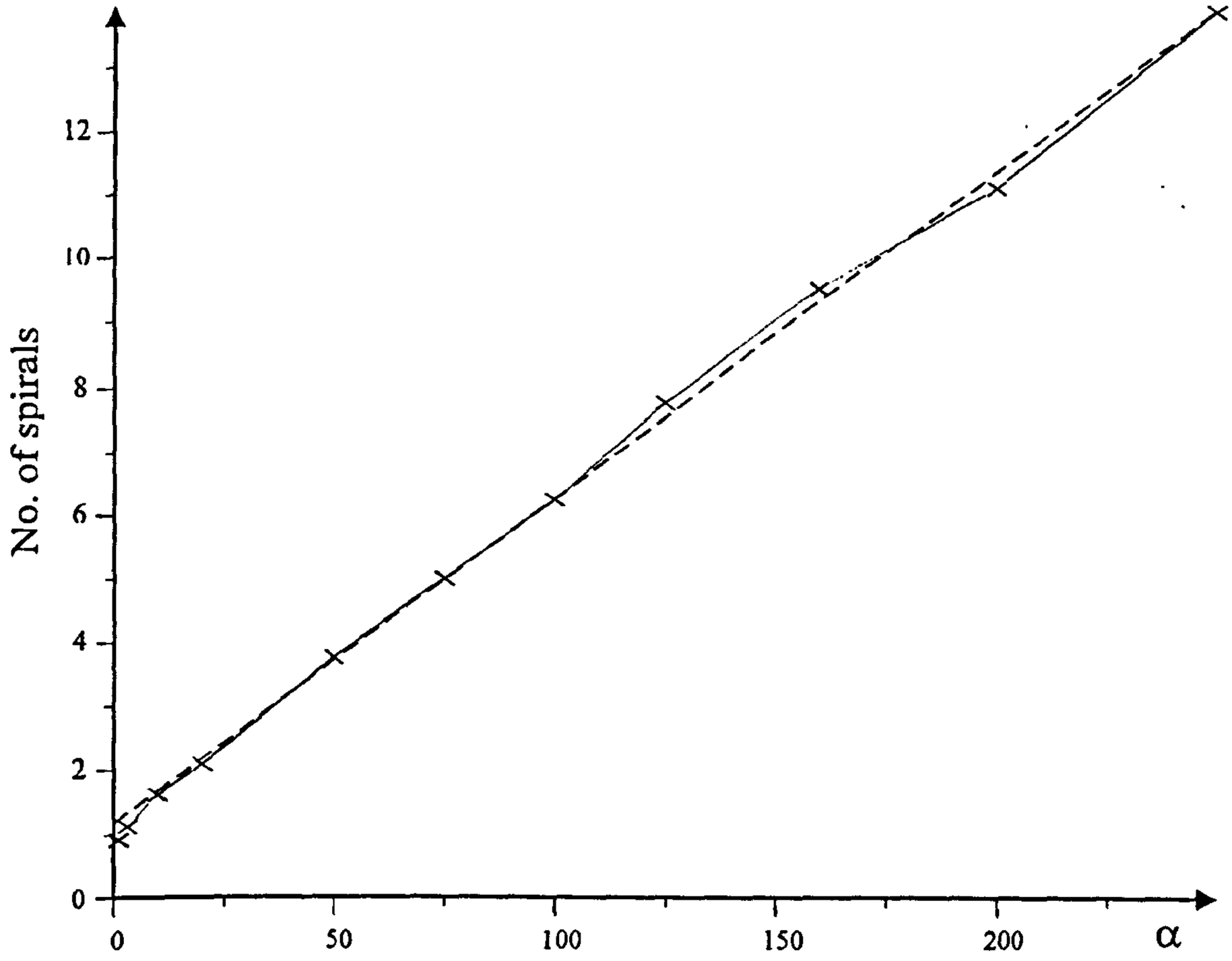

Figure 4.16: Number of spiral turns vs. α.

cases: first of all, we generate a single spiral, which we truncate at a point away from the spiral core where the wave motion is planar. We note that this time we must use the formulation including the parameter α to allow a particular double spiral to be specified. We then fix *both* end points, and generate a double spiral using a modification of the method above; this time, however, we cannot impose any symmetry conditions, and thus we have to compute the *whole* spiral instead of just half of it. We note that the value of α can be changed for this second part of the numerical scheme–the values of c and ε are fixed in (4.29), but the distance between the two end points of the front (L) depends on when we choose to stop generating a single spiral; α cannot therefore be determined until we initiate the double spiral. The point of collision between the two spiral loops also has to be tracked more carefully, since the x-position where this occurs is no longer necessarily fixed. With these issues in mind, we can generate fronts as before, with the outer loops (formed after front collision) again being discarded; an example of the type of behaviour observed is shown in Figure 4.17 with a value of $\alpha = 55.9$ during spiral

development.

It can be seen from Figure 4.17 that once the double spiral has been generated, the inner region does not appear to change. This is not quite the case, however; although the *shape* of the inner front remains virtually the same after the second spiral collision, the *point* of collision *does* change slightly. This is more clearly shown if we consider smaller initial values of α; Figure 4.18 shows profiles for the inner region for $\alpha = 9.971$ at the times of the first and thirty-eighth collisions; it can clearly be seen how the front tries to 'even itself out', i.e. the point of collision moves towards the mid-point of the two fixed ends. We demonstrate this using our numerical results obtained for the spirals generated in Figure 4.18 for $\alpha = 9.971$; Figure 4.19 shows how the x-position of the point of collision moves. It can be shown (King [32]) that the evolution towards symmetry for $\alpha \gg 1$ in fact happens on an exponentially long timescale. This is consistent with experimental results (and the numerical results given here) which suggest the persistence of non-symmetric spirals after very long timescales.

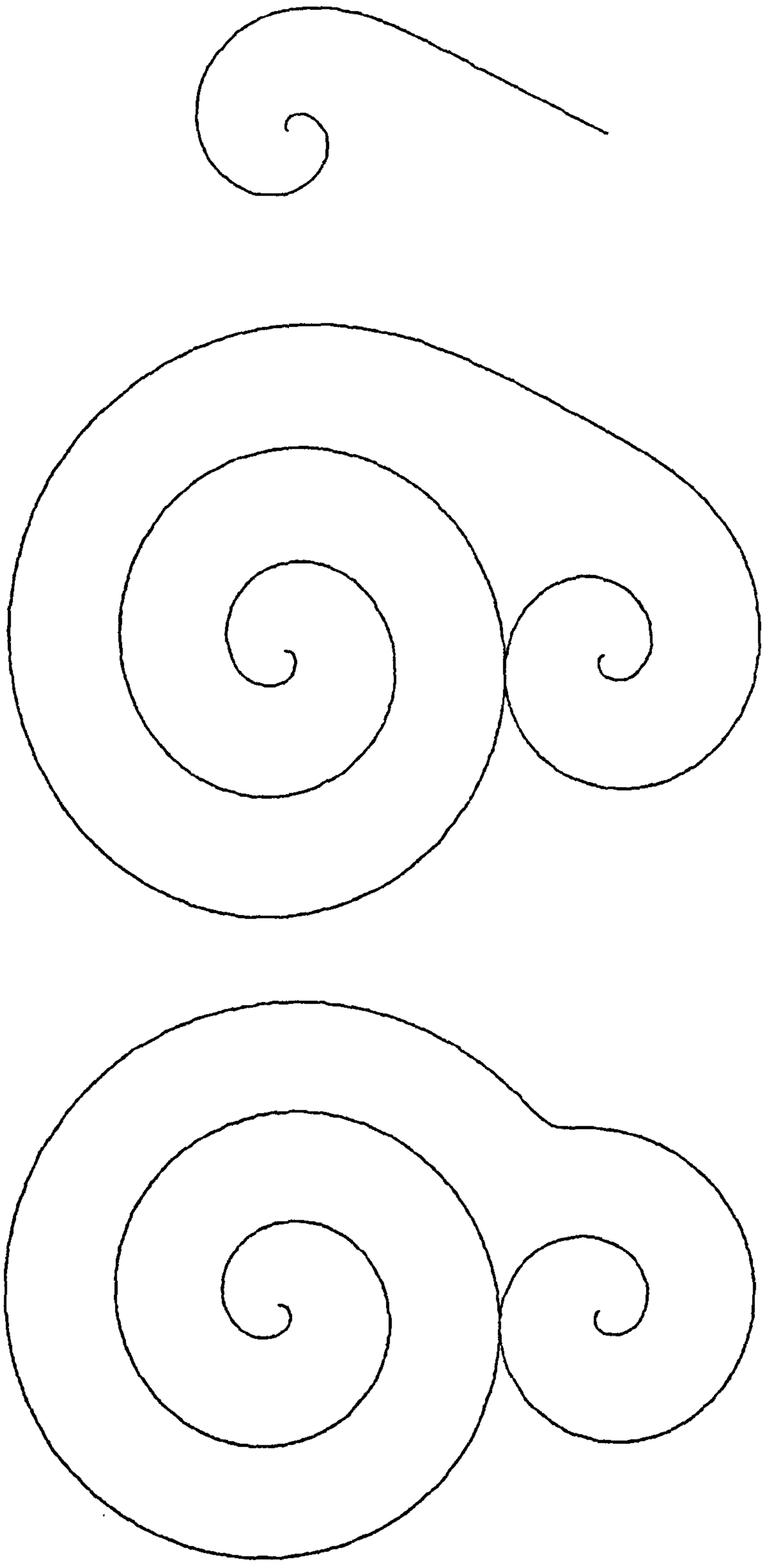

Figure 4.17: Generation of an uneven double spiral for $\alpha = 55.90$: **(a)** The initial profile for the double spiral. **(b)** The first collision of the spiral regions. **(c)** The tenth collision (inner front only).

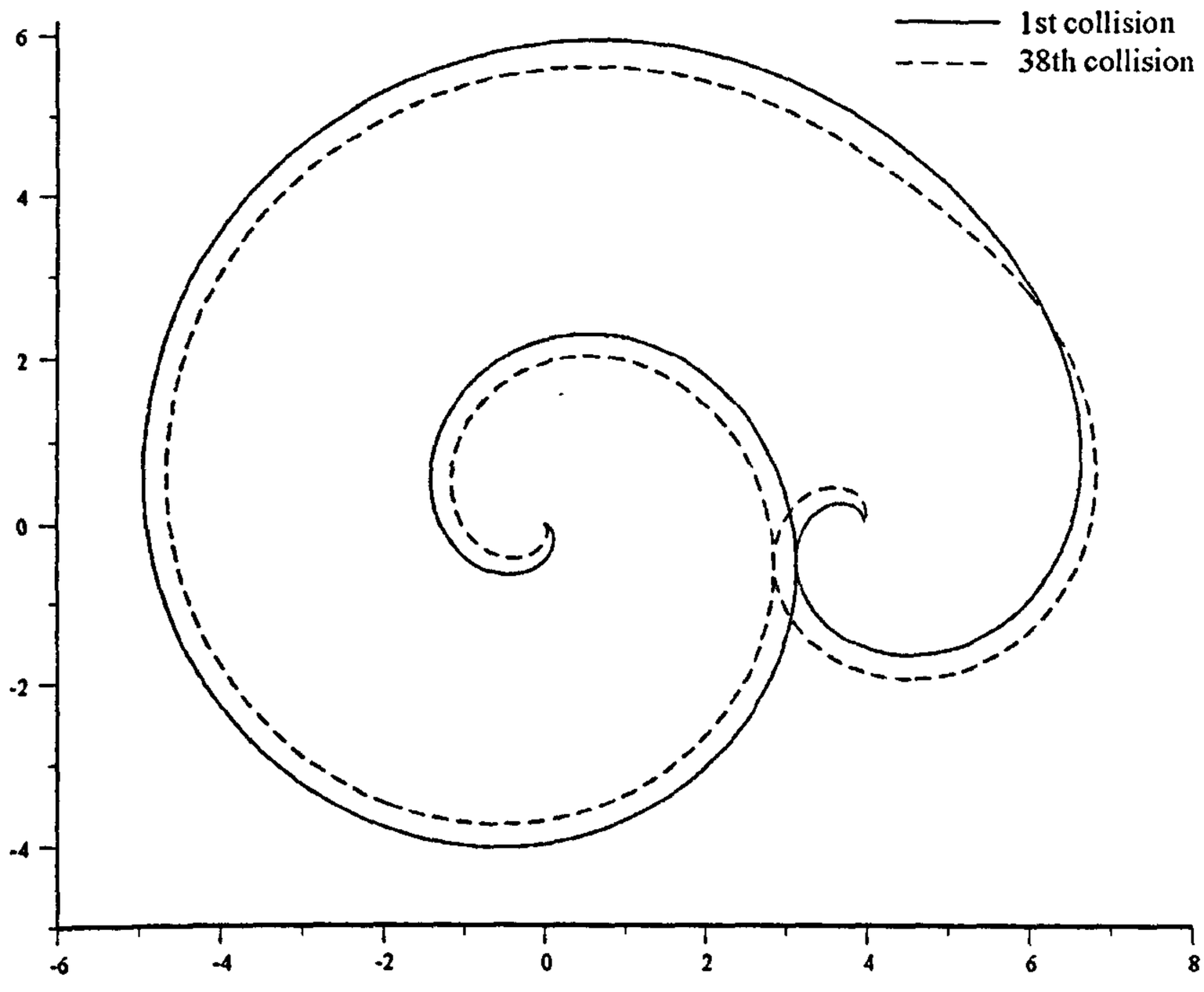

Figure 4.18: Uneven double spirals for $\alpha = 9.971$ at the times of the first and thirty-eighth collisions.

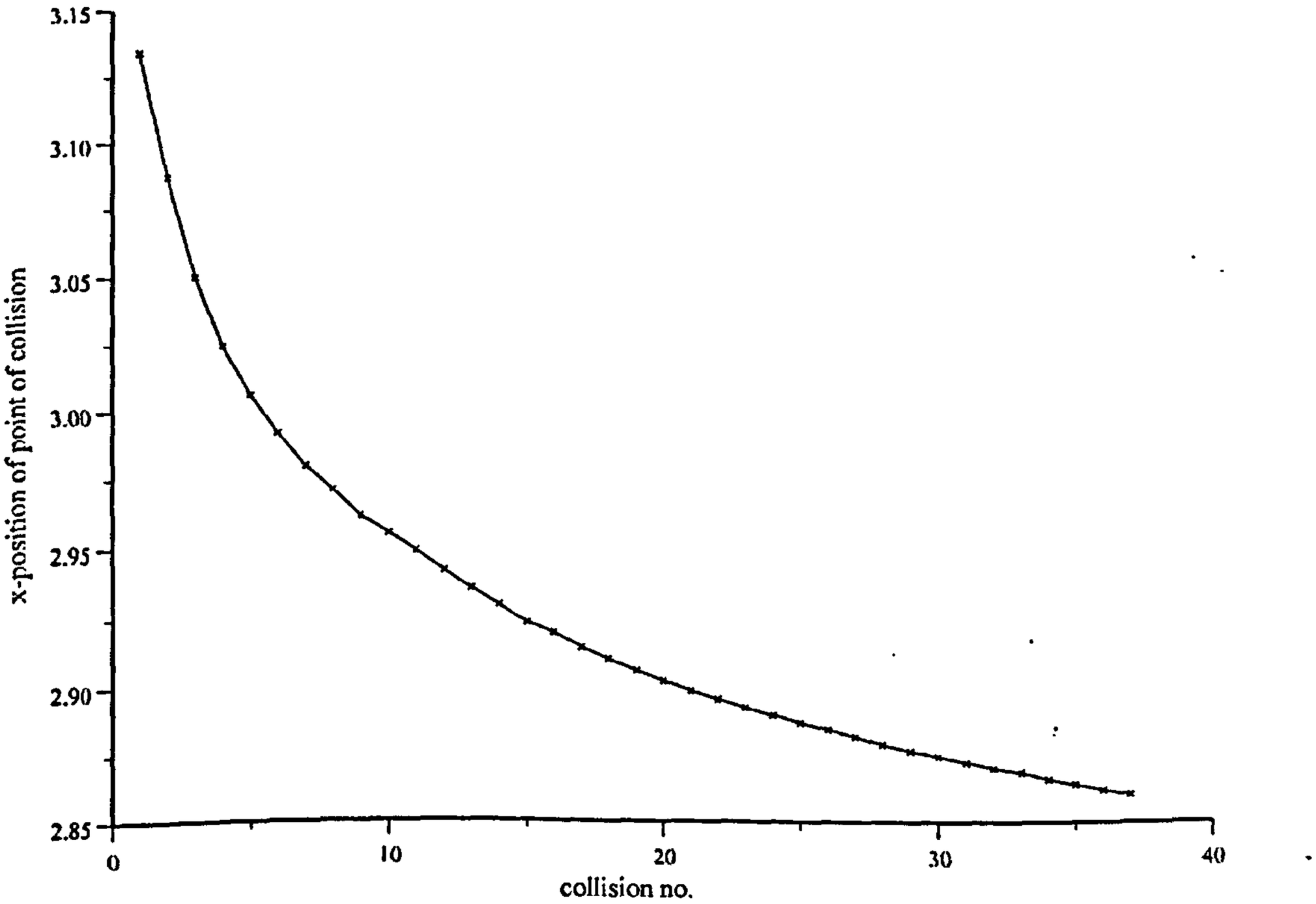

Figure 4.19: The x co-ordinate of the point of collision between the two spiral regions for $\alpha = 9.971$. The mid-point between the two fixed ends is at $x = 1.994$.

Chapter 5

Time-Asymptotic Behaviour for Generalized Flow-by-Curvature

5.1 Introduction

We now investigate the behaviour in $\mathbb{R}^2$ of a closed curve evolving according to the equation

$$N = -|\kappa|^{n-1}\kappa, \tag{5.1}$$

where n is a positive constant. The form (5.1) is one of the special forms of the general curvature equation $N = G(-\kappa)$ which is discussed in Section 5.6. For closed curves, there are already some well-established results:

(1) If $n = 1$, then we have the classic curve-shortening equation, which has been considered by many authors [39, 43]; it has been shown that all convex curves become circular in this case [14].

(2) For $n = 1/3$, curves can shrink to an ellipse in finite time. In particular, elliptic initial profiles will presere their shape until extinction [44].

Here, we focus on the behaviour for $0 < n < 1$, and demonstrate both a travelling wave solution to (5.1), and a similarity formulation which can be applied to curves shortening with 'slender' initial profiles. We will also consider the behaviour near extinction.

5.2 Travelling Wave Solutions

In $\mathbb{R}^2$, (5.1) can be written for $f_{xx} < 0$ as

$$f_t = -(1 + f_x^2)^{1/2} \left(\frac{-f_{xx}}{(1 + f_x^2)^{3/2}} \right)^n . \tag{5.2}$$

To seek a travelling wave solution, we write

$$f = f(x - qt) = f(\xi),$$

which, on substitution into (5.2), gives us

$$q f_\xi = (1 + f_\xi^2)^{1/2} \left(\frac{-f_{\xi\xi}}{(1 + f_\xi^2)^{3/2}} \right)^n . \tag{5.3}$$

Integrating, we obtain

$$f_\xi = \left(q^{\frac{2}{1-n}} \left(\frac{1-n}{n} (\xi - \xi_0) \right)^{\frac{2n}{1-n}} - 1 \right)^{-1/2} . \tag{5.4}$$

Thus we can see that

$$f \sim q^{\frac{1}{n-1}} \left(\frac{1-n}{n} \right)^{\frac{n}{n-1}} \left(\frac{n-1}{2n-1} \right) \xi^{\frac{1-2n}{1-n}}, \qquad n < 1/2, \qquad \text{as } \xi \to \infty \tag{5.5}$$

and

$$f \sim \text{constant}, \qquad n > 1/2, \qquad \text{as } \xi \to \infty. \tag{5.6}$$

This implies that for $n > 1/2$, we should expect the travelling wave profile to be horizontal as ξ becomes large, i.e. to be of the same type as the 'Grim Reaper' solution for $n = 1$ (see equation (3.80)). This is confirmed by numerical integrations of (5.4), as shown in Figure 5.1. We can determine the maximum value of the 'Grim Reaper' solution by considering the infinite integral

$$f_{max} = \int_0^\infty \frac{d\xi}{\left([q^{1/n}(1-n)(\xi - \xi_0)/n]^{2n/(1-n)} - 1 \right)^{1/2}}, \tag{5.7}$$

which is obtained from (5.4); without loss of generality, we choose ξ_0 so that $f'(0) = 0$ as $\xi \to 0$, which requires

$$\xi_0 = \frac{n}{n-1} q^{-1/n}, \qquad 1/2 < n < 1.$$

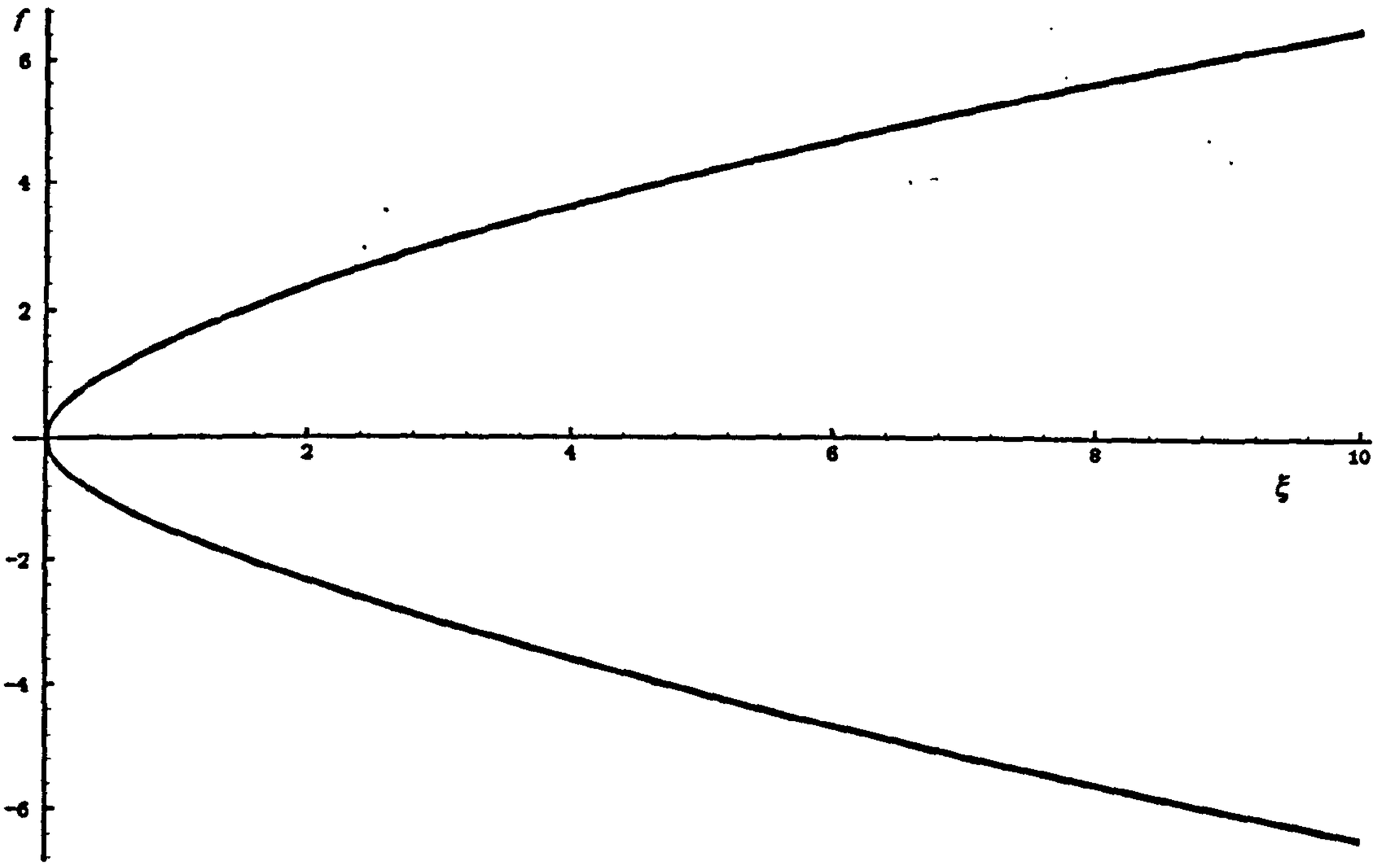

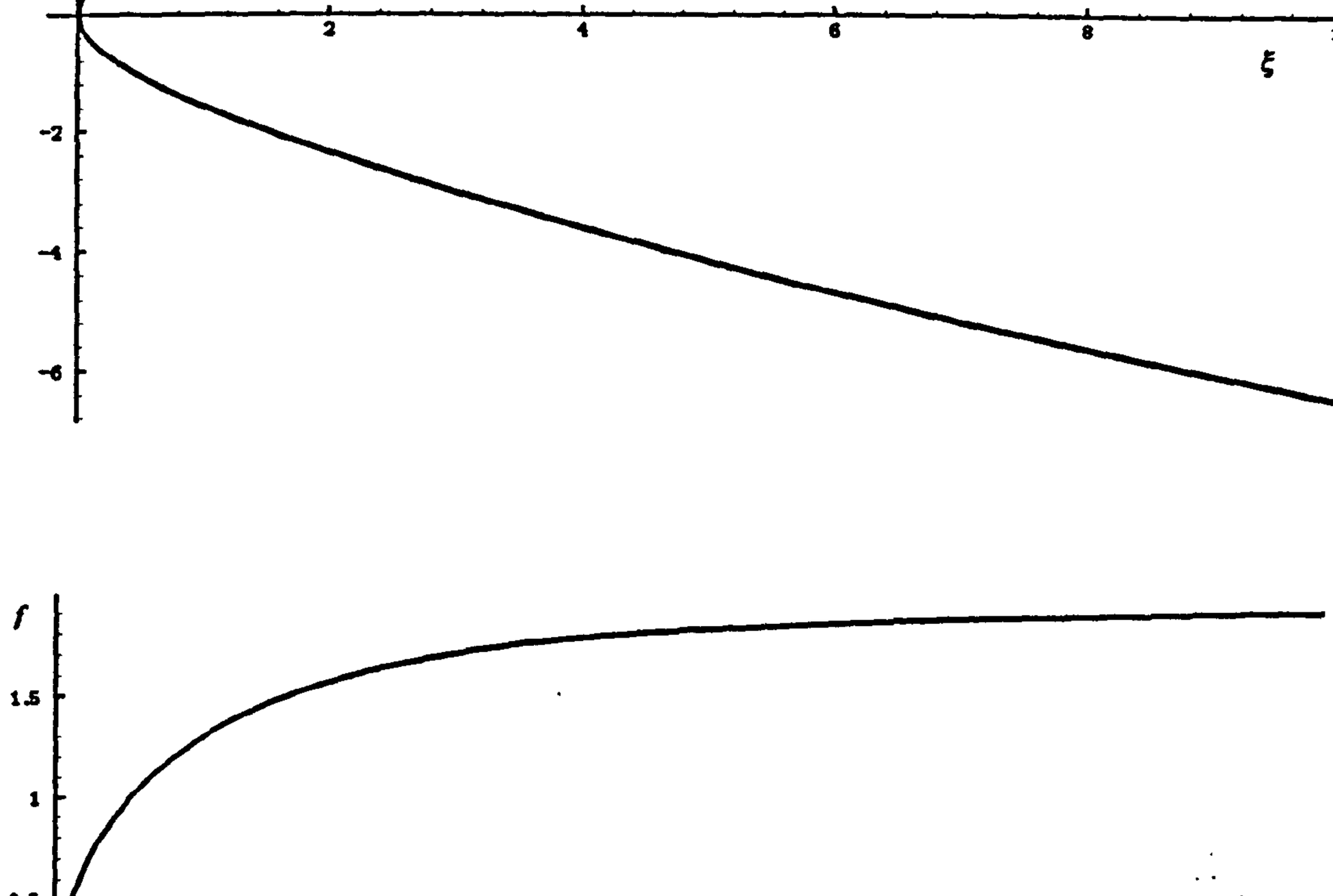

Figure 5.1: Travelling wave solutions for $n = 1/5$ (top) and $n = 4/5$ (bottom).

We then find

$$f_{\max} = \frac{\sqrt{\pi}}{2\,q^{1/n}} \frac{\Gamma\left(1-\frac{1}{2n}\right)}{\Gamma\left(\frac{3}{2}-\frac{1}{2n}\right)} \qquad n > 1/2,$$

which agrees with the numerical results; this result also holds for $n = 1$ (where $f_{\max} = \pi/(2q)$).

5.3 Slender Initial Conditions

To demonstrate what is meant by slender initial conditions, we solve (5.2) numerically using an explicit time-stepping routine, with the initial profile being an ellipse of aspect ratio 4; Figure 5.2 shows the evolving profiles for $n = 1/5$ and $n = 2/5$ (only the top right quadrant of the ellipse is shown for clarity). We can see that for $n = 1/5$, the profile

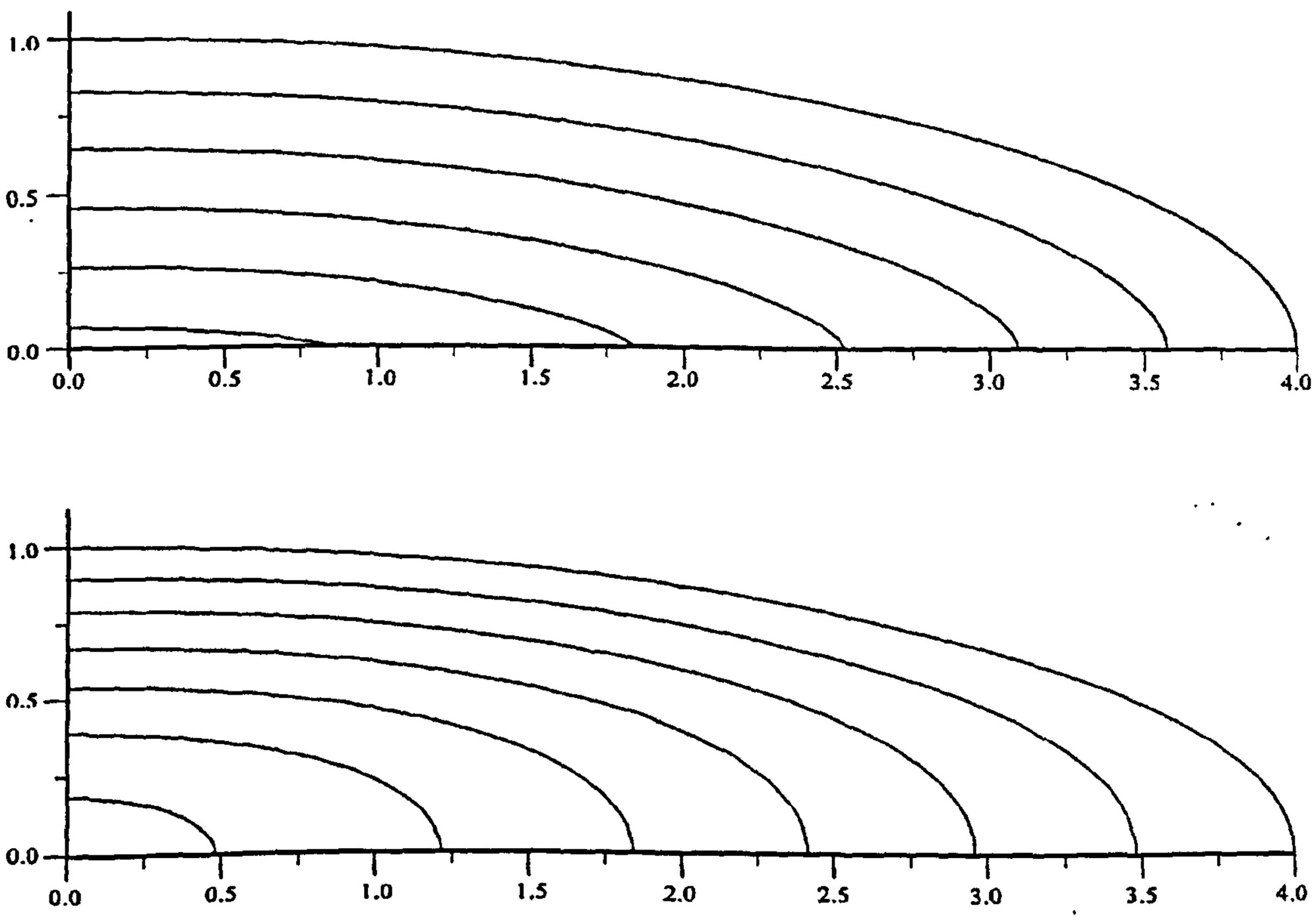

Figure 5.2: Progression of a slender initial profile for $n = 1/5$ (top) and $n = 2/5$ (bottom).

becomes more and more slender, whereas for $n = 2/5$, the reverse is the case. It can be shown numerically that $n \approx 1/3$ gives the critical value where the change between the two cases occurs; below we shall demonstrate analytically why this is true.

With the above numerical result in mind, we will now set about our asymptotic investigations; we must consider the cases $n < 1/2$ and $n > 1/2$ separately.

5.3.1 $n < 1/2$

Since our initial conditions imply that $f_x \ll 1$ in (5.2) away from x_{max}, we first of all make the rescaling

$$\begin{aligned} f &= h(X,\tau) \\ X &= \varepsilon x \\ \tau &= \varepsilon^{2n} t, \end{aligned}$$

where $\varepsilon \ll 1$ determines the aspect ratio of the initial data, so that (5.2) becomes

$$h_\tau = -(1+\varepsilon^2 h_X^2)^{1/2} \left(\frac{-h_{XX}}{(1+\varepsilon^2 h_X^2)^{3/2}} \right)^n \tag{5.8}$$

and thus to leading order we have

$$h_\tau = -(-h_{XX})^n. \tag{5.9}$$

We now seek a similarity solution by posing

$$h \sim (\tau_c - \tau)^\alpha g(X/(\tau_c - \tau)^\beta) = (\tau_c - \tau)^\alpha g(\eta), \tag{5.10}$$

where τ_c is the time at extinction and the exponent α remains to be determined (i.e. we have a similarity solution of the second kind). Substituting (5.10) into (5.9), we find that

$$\alpha = \frac{1-2n\beta}{1-n} \tag{5.11}$$

and

$$(-g_{\eta\eta})^n = \frac{1-2n\beta}{1-n} g - \beta \eta g_\eta. \tag{5.12}$$

Our initial conditions for (5.12) are

$$\left.\begin{aligned} g &= 1 \\ g_\eta &= 0 \end{aligned}\right\} \quad \text{at } \eta = 0;$$

the first condition may be made without loss of generality in view of the rescaling invariance of (5.12), and will fix η_0, the end-point of the curve. The second condition is

due to symmetry. We solve (5.12) numerically, varying β until $g_\eta \to \infty$ at $\eta \to \eta_0$ where $g = 0$, then we can obtain values for α and β for $0 \leq n < 1/2$ by using (5.11) also, as shown in Figure 5.3. We can see that $\alpha > \beta$ for $n < 1/3$ and $\alpha < \beta$ for $n > 1/3$.

For $n \geq 1/2$, there are no solutions of this form which fit the boundary conditions (as $n \to 1/2$, then $\beta \to 1/2$ and we obtain a 'corner'-type solution curve, until at $n = 1/2$ the solution to (5.12) is $g = 1$; see Figure 5.4).

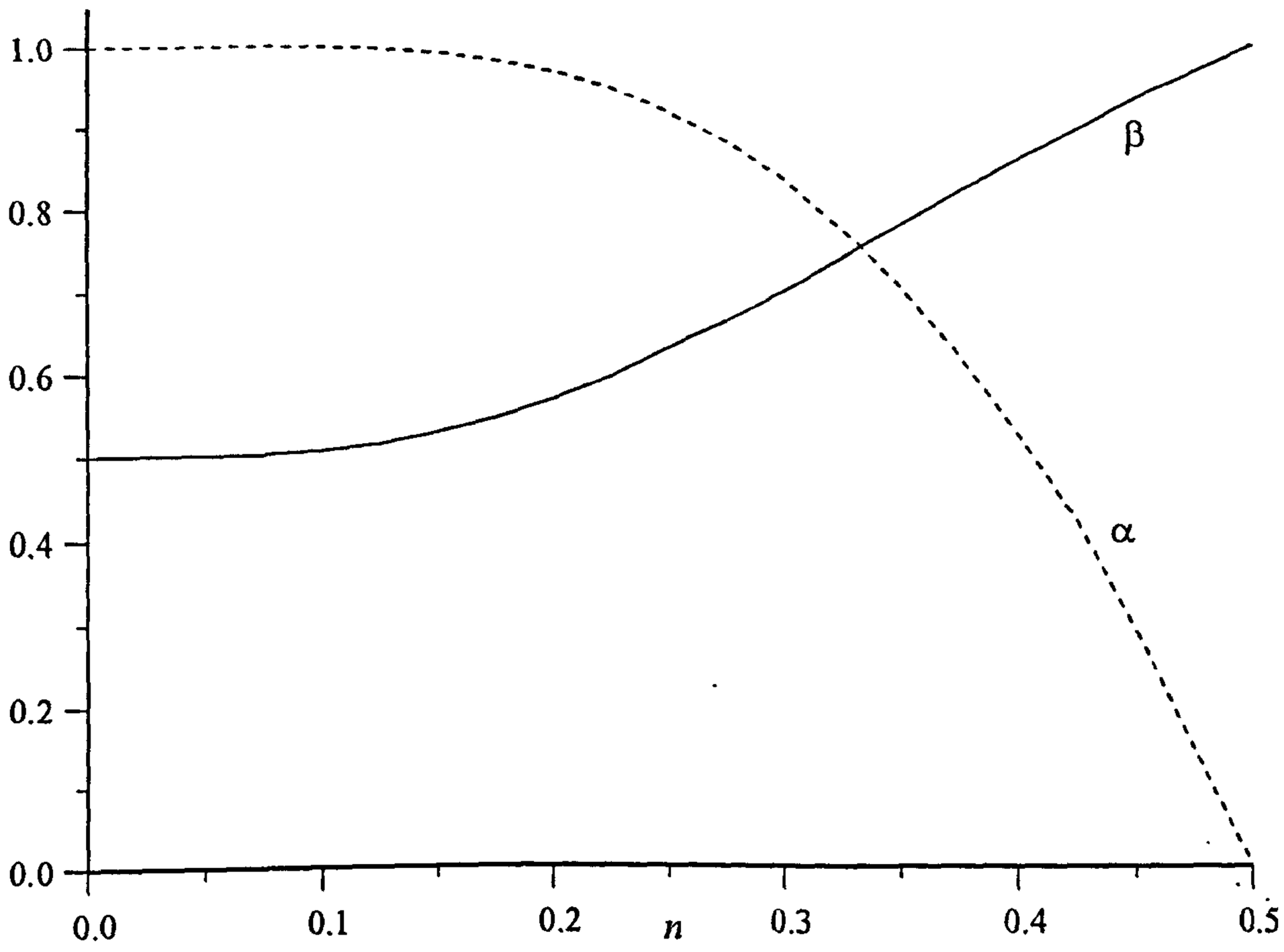

Figure 5.3: Values of α and β for $0 \leq n < 1/2$.

To complete the analysis, we need to consider what happens at the end points of our curve (i.e. where $f_x \ll 1$ does not hold). By analogy with the travelling wave solution (5.5), we can see that

$$g \sim A \left(1 - \frac{\eta}{\eta_0}\right)^m \qquad \text{as } \eta \to \eta_0, \tag{5.13}$$

where η_0 is the end-point of our curve as mentioned before, and A and m are constants (to be determined). This is essentially our matching condition between the two regions.

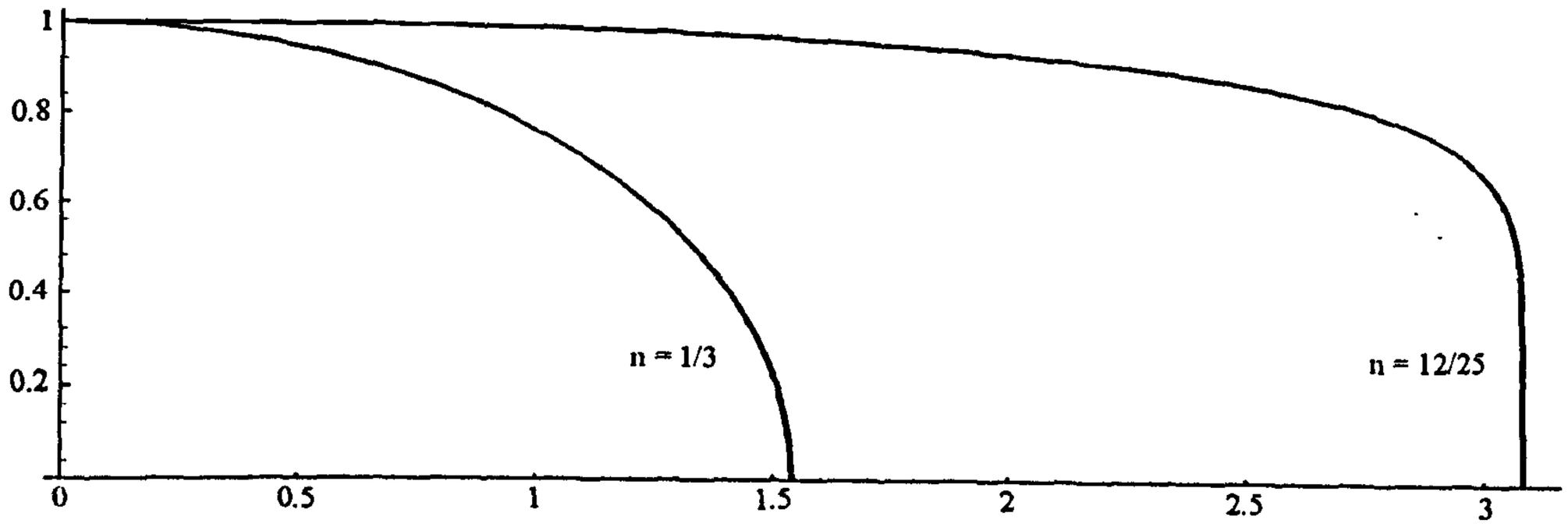

Figure 5.4: Behaviour as $n \to 1/2$.

Substituting (5.13) into (5.12), the leading order balance gives us

$$m = \frac{2n-1}{n-1} \tag{5.14}$$

and

$$A = \left(\frac{1-n}{n}\right)^{\frac{n}{n-1}} \left(\frac{n-1}{2n-1}\right) \beta^{\frac{1}{n-1}} \eta_0^{\frac{2n}{1-n}}, \tag{5.15}$$

which is consistent with (5.5).

To determine the inner region near to the front $s(\tau) = \eta_0(\tau_c - \tau)^\beta$ (an expression deduced from (5.10)), we set

$$\begin{aligned} X &= s(\tau) - \delta(\varepsilon)\, z \\ h &= \delta^m(\varepsilon) H \end{aligned} \tag{5.16}$$

and substitute these into (5.8); by taking

$$\delta = \varepsilon^{1/(1-m)}$$

we obtain at leading order

$$\dot{s}\, H_z = (1 + H_z^2)^{1/2} \left(\frac{-H_{zz}}{(1+H_z^2)^{3/2}}\right)^n, \tag{5.17}$$

which is equivalent to (5.3); we can therefore integrate (5.17) with respect to z and obtain a similar expression to (5.5), with

$$\dot{s} = q. \tag{5.18}$$

To complete the matching of the inner and outer regions, we write (5.13) as

$$h \sim B(s(\tau) - X)^m \tag{5.19}$$

and substitute this into (5.9); we obtain

$$h \sim \left(\frac{1-n}{n}\right)^{\frac{n}{n-1}} \left(\frac{n-1}{2n-1}\right) (-\dot{s})^{\frac{1}{n-1}} \, (s(\tau) - X)^{\frac{2n-1}{n-1}} \tag{5.20}$$

on applying (5.18), and hence

$$h \sim \left(\frac{1-n}{n}\right)^{\frac{n}{n-1}} \left(\frac{n-1}{2n-1}\right) (-\dot{s})^{\frac{1}{n-1}} \, s^{\frac{2n-1}{n-1}} \left(1 - \frac{\eta}{\eta_0}\right)^{\frac{2n-1}{n-1}}. \tag{5.21}$$

It can be seen that the value for m is consistent with that obtained in (5.14). Near to the front, we have

$$s = \eta_0 (\tau_c - \tau)^\beta \quad \Rightarrow \quad \dot{s} = -\beta \, \eta_0 (\tau_c - \tau)^{\beta - 1}$$

so that (5.21) becomes

$$h \sim \left(\frac{1-n}{n}\right)^{\frac{n}{n-1}} \left(\frac{n-1}{2n-1}\right) \beta^{\frac{1}{n-1}} \, \eta_0^{\frac{2n}{n-1}} \, (\tau_c - \tau)^{\frac{1-2n\beta}{1-n}} \left(1 - \frac{\eta}{\eta_0}\right)^{\frac{2n-1}{n-1}}. \tag{5.22}$$

The prefactor in (5.22) (which is B in (5.19)) can be seen to be equal to A in (5.15) as expected; the exponent of $(\tau_c - \tau)$ in (5.22) also matches with that of the outer solution (5.10). The inner limit of the outer solution is given by (5.13), and thus matches with the outer limit of the inner solution, as given by (5.22).

5.3.2 $n > 1/2$

In this case, we first need to determine the timescale of the problem. We set

$$\begin{aligned} f &= h(X, T) \\ X &= \varepsilon \, x \\ T &= \varepsilon^\mu \, t \end{aligned} \tag{5.23}$$

with μ at this stage undetermined. Substituting (5.23) into (5.2), we obtain

$$h_T = -\frac{\varepsilon^{2n-\mu} (-h_{XX})^n}{(1 + \varepsilon^2 h_X^2)^{\frac{3n}{2} - \frac{1}{2}}}. \tag{5.24}$$

From (5.4) and (5.6), we anticipate that at leading order

$$\frac{\partial h_0}{\partial T} = 0$$

and hence the outer solution is

$$h_0 = H(X), \tag{5.25}$$

the initial condition. The inner solution is a travelling wave; we set

$$X = s(T) + \varepsilon z$$

and our leading order equation for $h(z)$ reads

$$-\varepsilon^{\mu-1}\dot{s}\,h_z = (1+h_z^2)^{1/2}\left(\frac{-h_{zz}}{(1+h_z^2)^{3/2}}\right)^n. \tag{5.26}$$

Since we require a full balance for the travelling wave, then $\mu = 1$; from (5.24), we can see that this gives $h_T = 0$ at leading order for $n > 1/2$, as required. The speed of the travelling wave can be obtained from matching; equation (5.6) implies the inner balance

$$h \sim \frac{\sqrt{\pi}}{2\,\dot{s}_0^{1/n}} \frac{\Gamma\left(1-\frac{1}{2n}\right)}{\Gamma\left(\frac{3}{2}-\frac{1}{2n}\right)}$$

and thus the outer expansion of the inner solution gives

$$\frac{\sqrt{\pi}}{2\,\dot{s}_0^{1/n}} \frac{\Gamma\left(1-\frac{1}{2n}\right)}{\Gamma\left(\frac{3}{2}-\frac{1}{2n}\right)} = H(s_0), \tag{5.27}$$

which determines the wave speed of the inner solution.

The two forms of solution are shown in Figure 5.5. For $n < 1/2$, the evolution is driven by the outer solution; for $n < 1/3$, the profile becomes even more slender, whereas in the range $1/3 < n < 1/2$, the curve 'fattens'. For $n > 1/2$, the behaviour is determined by the inner solution (the 'Grim Reaper'-type travelling wave); the outer solution is essentially fixed by the initial profile.

5.4 n < 1/3: Behaviour Near Extinction

So far, we have only considered similarity formulations for a particular (i.e. slender) form of initial conditions; however, for $n < 1/3$, they apply for much more general

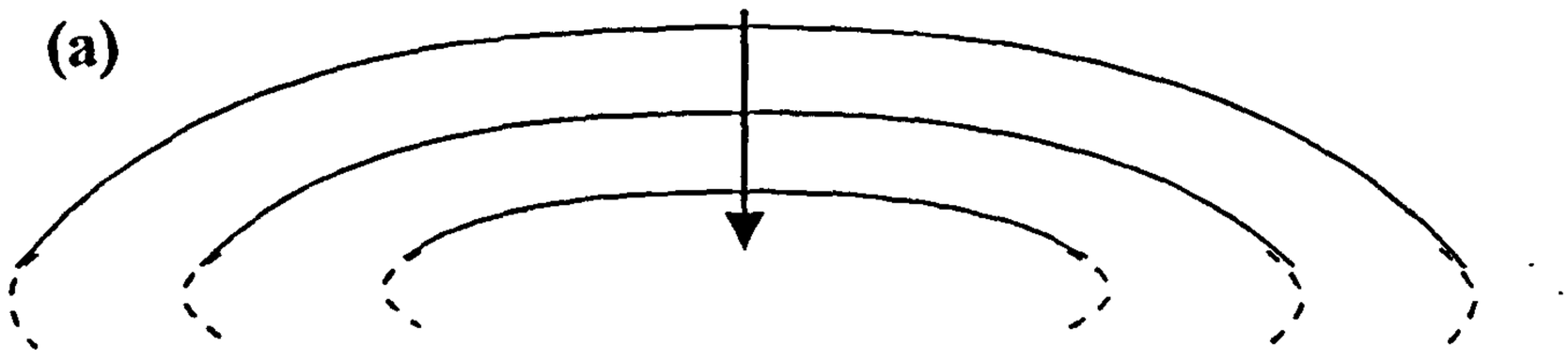

Figure 5.5: (a) $n < 1/2$: Evolution is driven by the outer solution. (b) $n > 1/2$: Evolution is driven by the inner solution.

initial conditions, i.e. close to extinction the behaviour is usually given by the similarity solutions of the second kind derived earlier.

However, other possible behaviours close to extinction can also be found. If we switch to a polar co-ordinate system, then by setting

$$\begin{aligned} x &= r\cos\theta \\ y &= r\sin\theta \end{aligned}$$

equation (5.2) becomes

$$r_t = -\frac{1}{r}(r_\theta^2 + r^2)^{1/2}\left(\frac{r^2 + 2r_\theta^2 - rr_{\theta\theta}}{(r_\theta^2 + r^2)^{3/2}}\right)^n. \tag{5.28}$$

We now look for a solution to (5.28) of the form

$$r = F(t) + G(\theta, t) \tag{5.29}$$

and linearize about $F(t)$; this leads to the radially symmetric solution

$$F(t) = ((n+1)(t_c - t))^{1/(n+1)} \tag{5.30}$$

together with

$$G_t = \left(\frac{n}{n+1}\right)\left(\frac{1}{t_c - t}\right)(G + G_{\theta\theta}), \tag{5.31}$$

where t_c is the time at extinction. Looking for a solution to (5.31) of the form

$$G = A\,(t_c - t)^{\lambda} \begin{Bmatrix} \sin p\,\theta \\ \cos p\,\theta \end{Bmatrix}$$

with A and λ constants then from (5.31) we require

$$\lambda = \frac{n}{n+1}(p^2 - 1). \tag{5.32}$$

Since we are considering closed curves, then we necessarily require p to be an integer; our solution is thus

$$r = ((n+1)(t_c - t))^{1/(n+1)} + \sum_{p=0}^{\infty} A_p (t_c - t)^{\frac{n}{n+1}(p^2-1)} \begin{Bmatrix} \sin p\theta \\ \cos p\theta \end{Bmatrix}. \tag{5.33}$$

If we now consider the effect of the additional 'modes' close to t_c, we can immediately see (by comparing powers of the $(t_c - t)$ terms) that the collapsing circle solution ($r \sim F(t)$) will be stable provided that $1/(n+1) < \lambda$, that is

$$n > \frac{1}{p^2 - 1} \tag{5.34}$$

for all p such that $p^2 - 1 > 0$, which requires $n > 1/3$. The cases $p = 0$ and $p = 1$ can be ignored, since they correspond to translations in time and space respectively; however, for larger values of p, it would appear that we can find p_c shape-preserving solutions, where p_c represents the highest value of p for which (5.34) does not hold, with different degrees of symmetry. As an example, Figures 5.6–5.9 show a series of plots for $n = 1/16$ (so that $p_c = 4$) with different initial profiles; the two-, three- and four-fold symmetry solutions can be seen to arise from initial conditions with the corresponding symmetry, but the attempt to produce a profile with five-fold symmetry results in a circle. However, the two-fold symmetry solution shown in Figure 5.6 can be seen to become 'slender' as it shrinks, and thus is *not* shape-preserving; we thus obtain new solutions with up to p_c degrees of symmetry with $p > 2$.

To show the actual form of these shape-preserving solutions (and confirm that there is no new solution for $p = 2$), we substitute

$$r = (t_c - t)^{1/(n+1)} R(\theta)$$

into (5.28); this gives us

$$R\,R'' = R^2 + 2\,R'^2 - (R^2 + 2\,R'^2)^{3/2} \left(\frac{R^2}{(n+1)(R^2 + 2\,R'^2)^{1/2}} \right)^{1/n}, \tag{5.35}$$

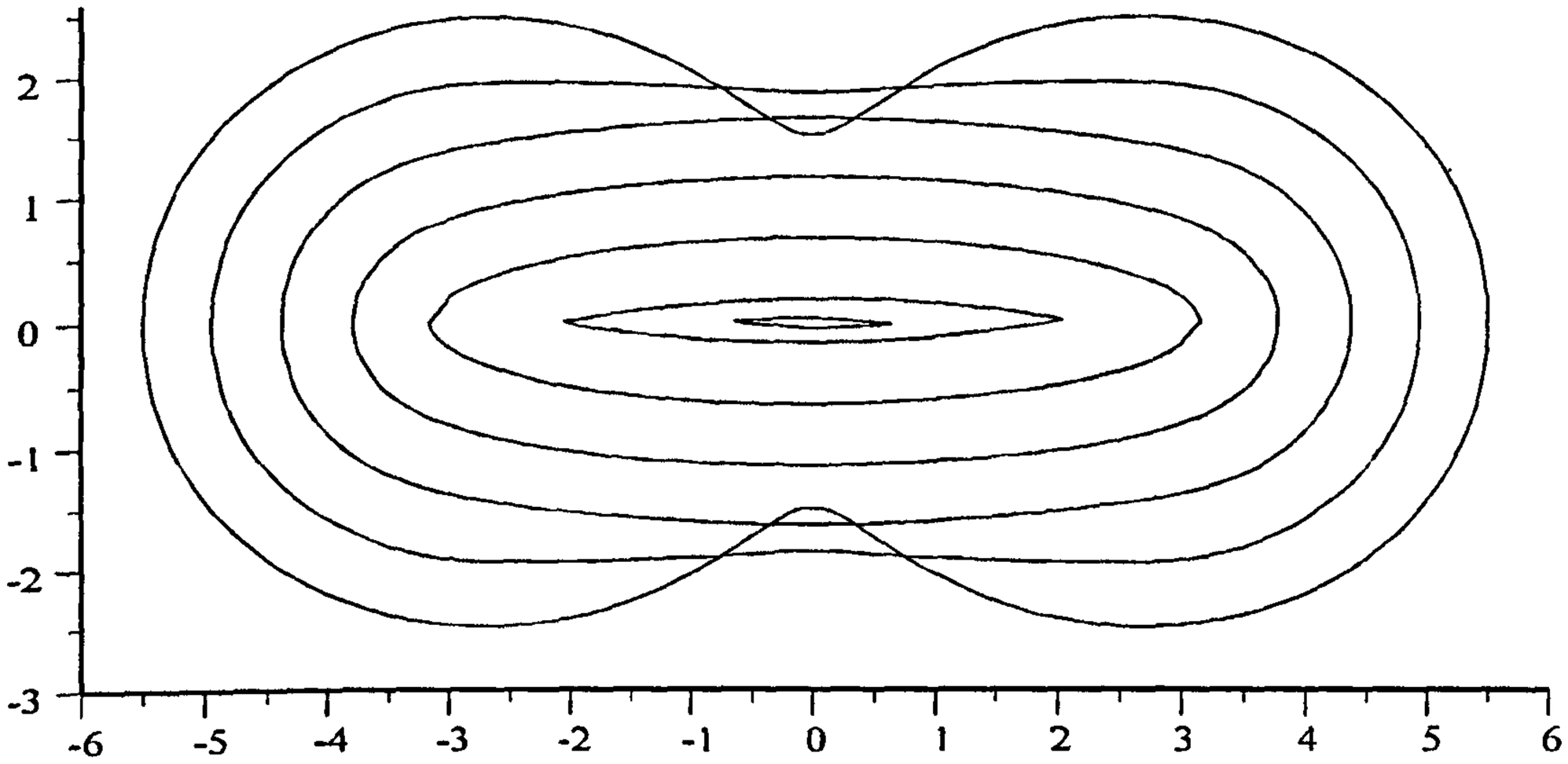

Figure 5.6: P.D.E. solution for $n = 1/16$; two-fold symmetry. It can be observed that the solution is *not* shape-preserving; it becomes 'slender'.

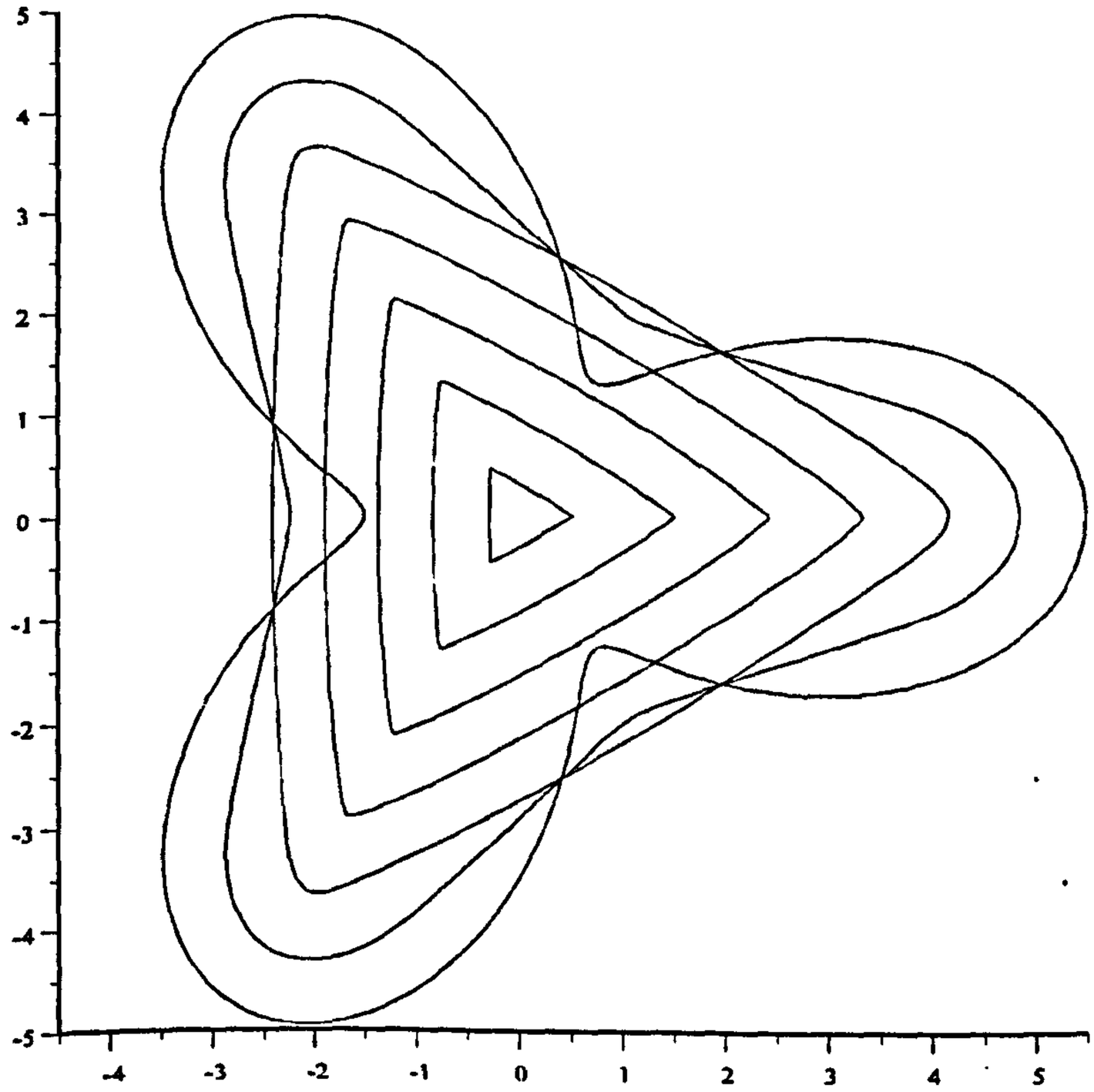

Figure 5.7: P.D.E. solution for $n = 1/16$; three-fold symmetry.

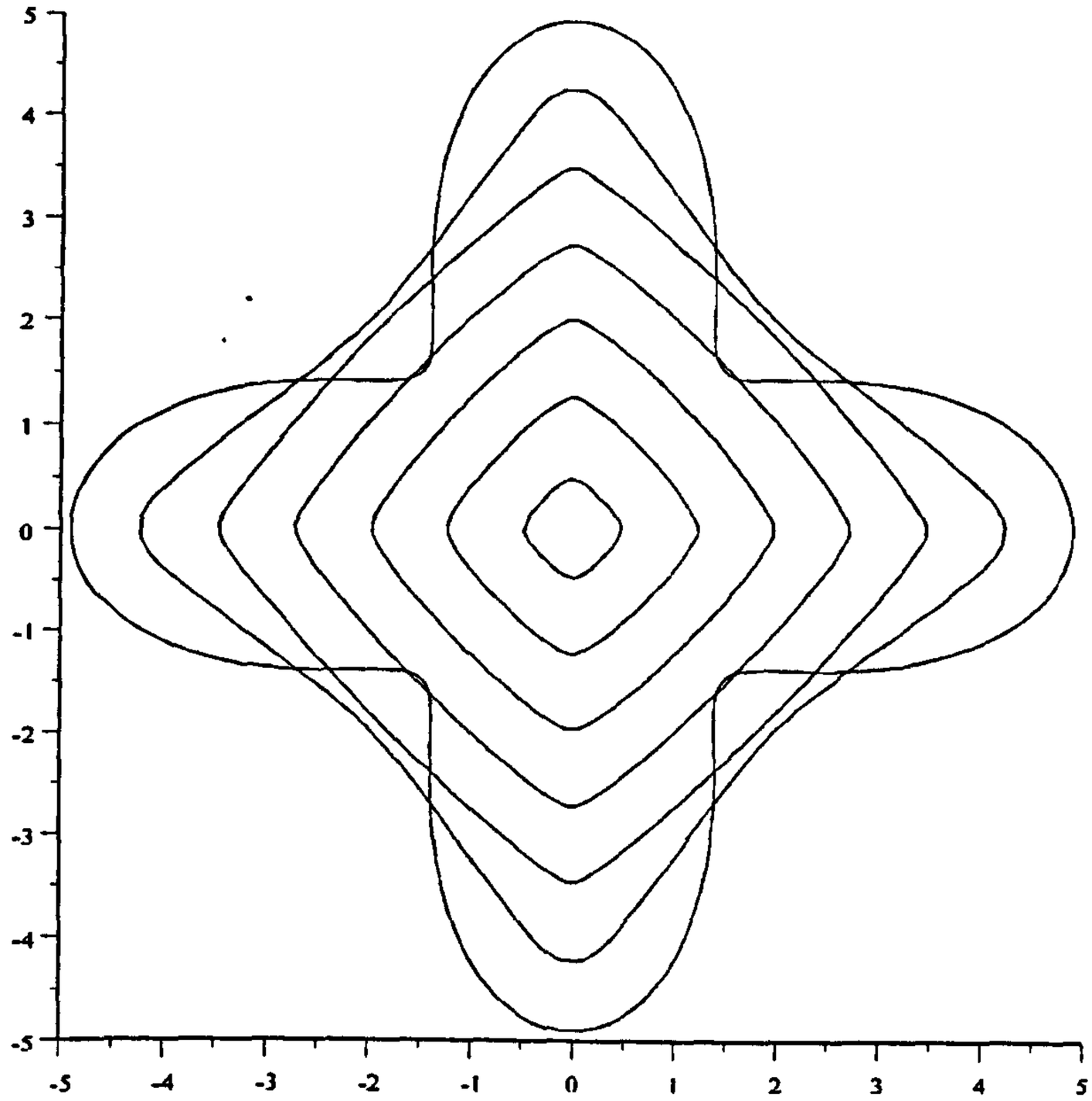

Figure 5.8: P.D.E. solution for $n = 1/16$; four-fold symmetry.

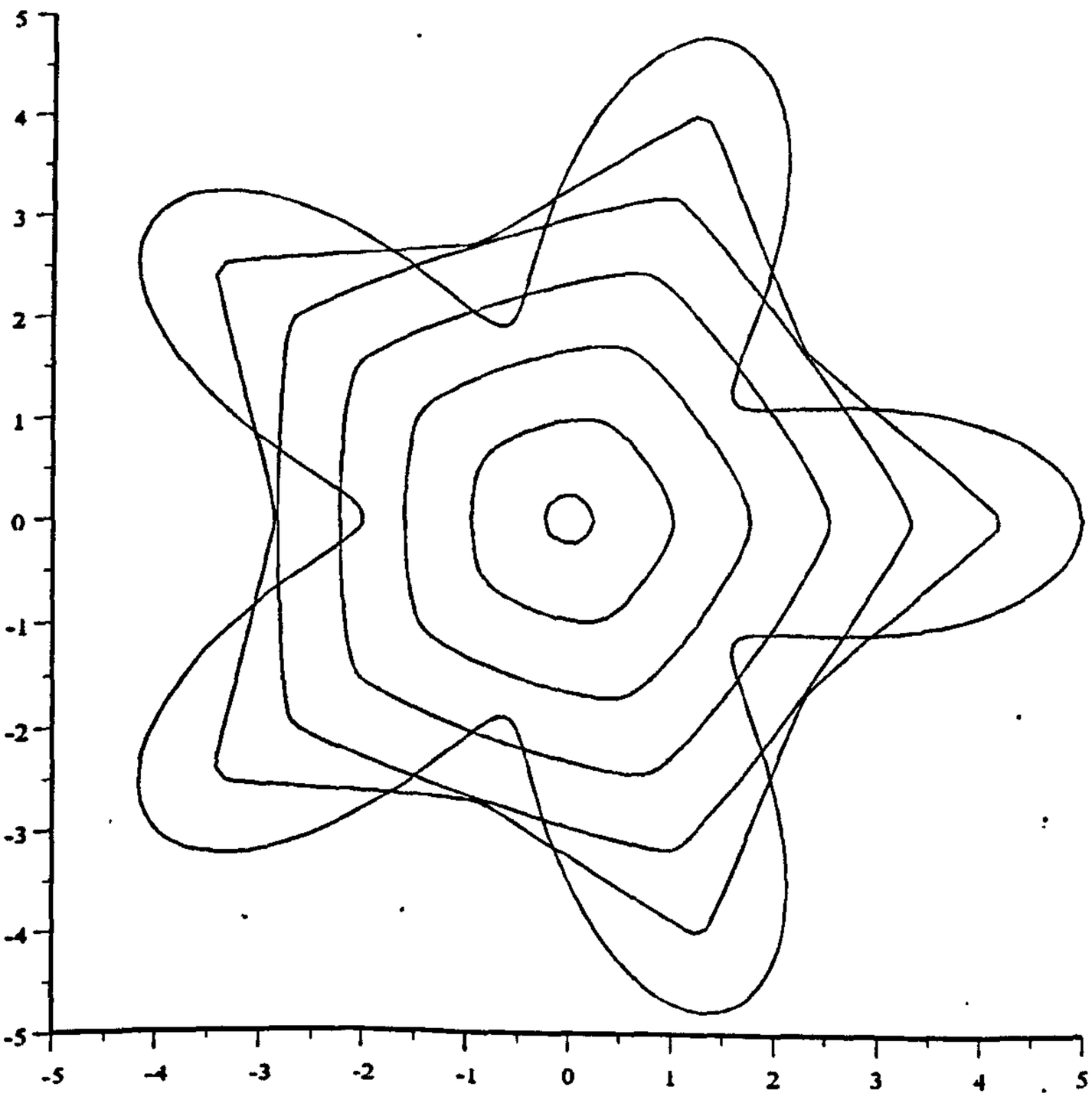

Figure 5.9: P.D.E. solution for $n = 1/16$; *no* five-fold symmetry.

which we solve numerically subject to the boundary conditions $R'(0) = 0$, $R(0) = R_0$. By varying R_0, we can again produce a series of closed curves; Figures 5.10-5.11 show the 'triangle' and 'square' solutions for $n = 1/16$, which are as expected; no 'pentagonal' solution can be found. This can be confirmed analytically by an analysis of (5.35) (King [32]). There is also no 'ellipse' solution to (5.35), which confirms that the solution shown in Figure 5.6 is of the 'slender' type.

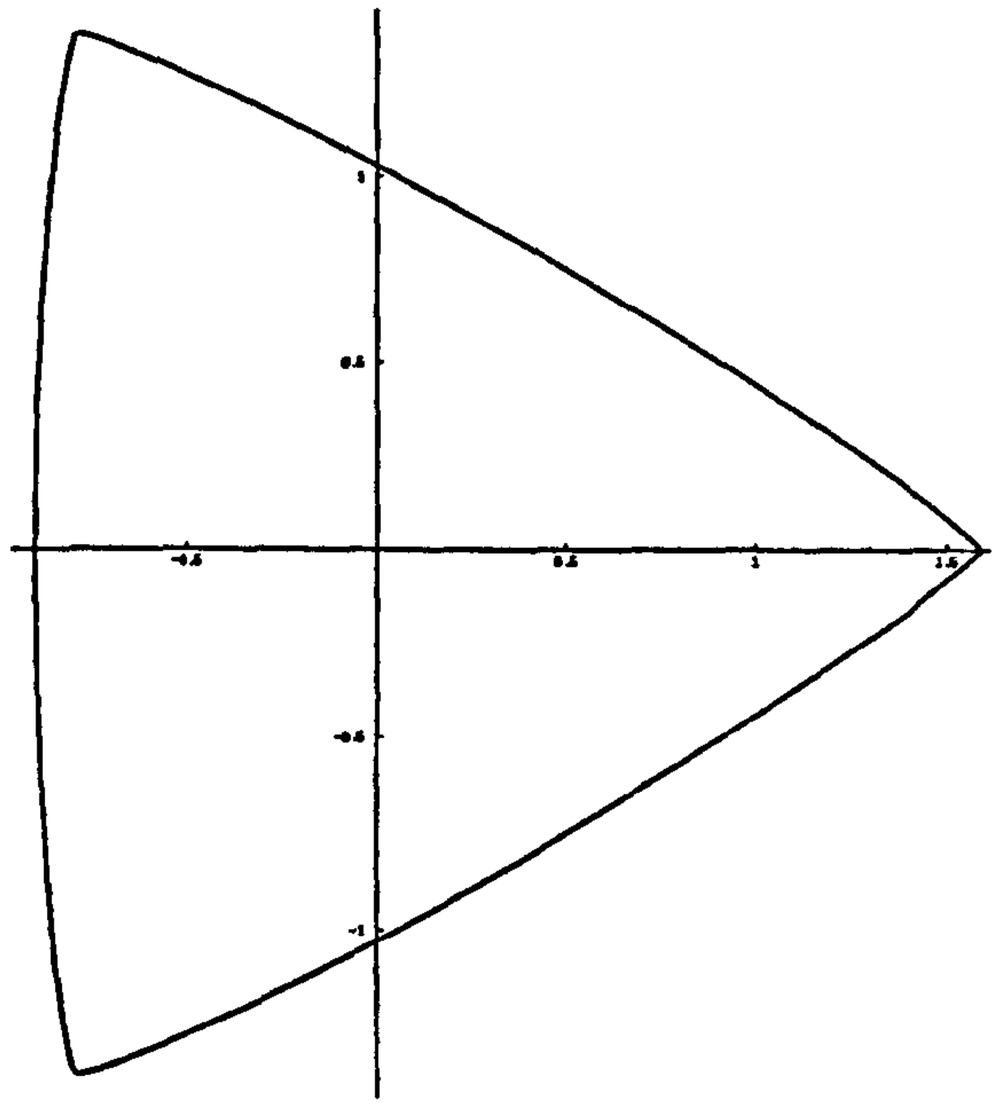

Figure 5.10: O.D.E. solution for $n = 1/16$ with $R_0 = 1.582$; three-fold symmetry.

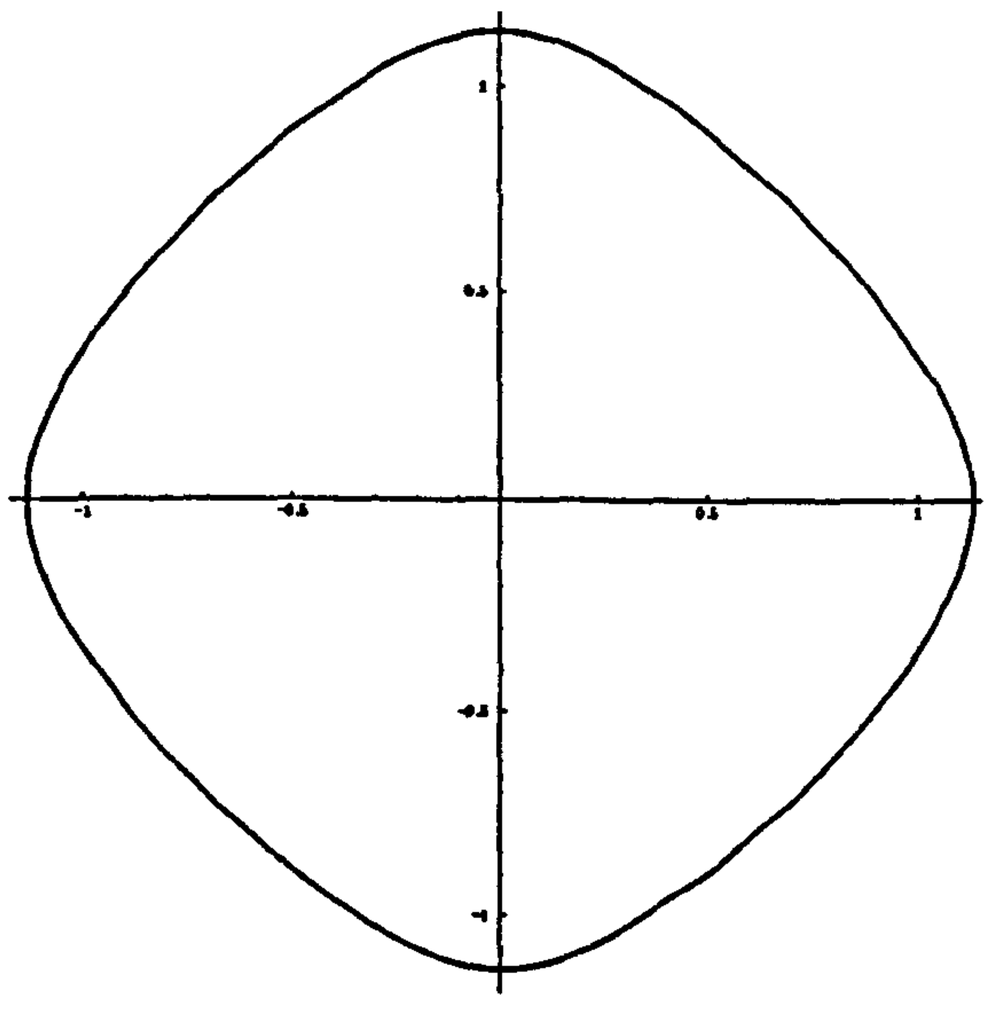

Figure 5.11: O.D.E. solution for $n = 1/16$ with $R_0 = 1.134$; four-fold symmetry.

5.5 Summary

We can now summarise the results of this chapter.

(1) As $t \to t_c$:

$$\begin{aligned} n &> 1/3 \longrightarrow \text{circle}, \\ n &= 1/3 \longrightarrow \text{ellipse}, \\ n &< 1/3 \longrightarrow \text{'slender' similarity solution of the} \\ &\qquad\qquad\qquad\quad \text{second kind for general initial conditions.} \end{aligned}$$

This significantly extends previous results, which were only known for $n = 1$ and $n = 1/3$. The first two cases always occur; in the third case there are other possibilities (see (2) below).

(2) For $0 < n < 1/3$ there are other types of extinction behaviour corresponding to various symmetries of the initial data, but they are unstable to non-symmetric perturbations. The detailed work of Chapter 3 showed no such solutions were possible for $n = 1$ where the corresponding similarity solutions were self-intersecting; for $n < 1/3$ the separable solutions are much more interesting.

(3) For slender initial conditions, the critical case is $n = 1/2$ with respect to the *existence* of a similarity solution of the second kind, but $n = 1/3$ is again identified as a critical case with respect to whether $\alpha \lesseqgtr \beta$.

5.6 Special forms of a generalized curvature equation

In this section we demonstrate how the special forms can be determined for the generalized curvature equation

$$N = G(-\kappa), \tag{5.36}$$

where N is the normal velocity of the front and κ its mean curvature (as described earlier); we find one-parameter groups which are admissible by (5.36) for *all* forms of $G(-\kappa)$, firstly in two dimensions. In $\mathbb{R}^2$, (5.36) reads

$$\frac{f_t}{(1+f_x^2)^{1/2}} = G\left(\frac{f_{xx}}{(1+f_x^2)^{3/2}}\right) = G(-\kappa). \tag{5.37}$$

If we now suppose that (5.37) admits

$$\begin{aligned} f^* &\sim f(x,t) + \varepsilon F(x,t,f) \\ x^* &\sim x + \varepsilon X(x,t,f) \\ t^* &\sim t + \varepsilon T(t), \end{aligned} \tag{5.38}$$

then we have, after Taylor expansion,

$$\begin{aligned} &[F_t - X_t f_x + 2F_t f_x^2 - 2X_t f_x^3 + F_t f_x^4 - X_t f_x^5](1+fx^2)^{-3/2} \\ &\quad +[F_f - T_t - (F_x + X_f) f_x + (X_x - T_t) f_x^2] G(-\kappa) \\ &\quad +\{[-F_{xx} + (X_{xx} - 2F_{xf}) f_x - (F_{ff} + F_{xx} - 2X_{xf}) f_x^2 \\ &\quad +(X_{ff} + X_{xx} - 2F_{xf}) f_x^3 - (F_{ff} - 2X_{xf}) f_x^4 + X_{ff} f_x^5](1+f_x^2)^{-3/2} \\ &\quad -[2X_x - F_f + 3(F_x + X_f) f_x + (2F_f - X_x) f_x^2]\kappa\} G'(-\kappa) = 0, \end{aligned} \tag{5.39}$$

which is of the form

$$A(x,t,f,f_x) + B(x,t,f,f_x)\, G(-\kappa) + [C(x,t,f,f_x) - D(x,t,f,f_x)\,\kappa]\, G'(-\kappa) = 0, \tag{5.40}$$

a first-order ordinary differential equation in $G(-\kappa)$; the ratios of A, B, C and D must therefore be constants. For arbitrary $G(-\kappa)$, we obtain the group

$$\begin{aligned} T &= \alpha \\ X &= \beta + \lambda f \\ F &= \gamma - \lambda x. \end{aligned} \tag{5.41}$$

By integrating (5.40), we can obtain a special form for $G(-\kappa)$ when (A, B, C, D) are all non-zero, namely

$$G(-\kappa) = -a|\kappa|^{n-1}\kappa, \tag{5.42}$$

where a and n are constants. We then obtain the groups

$$n \neq 1/3: \qquad \begin{aligned} T &= \alpha + (1+n)\,\delta t \\ X &= \beta + \delta x + \lambda f \\ F &= \gamma - \lambda x + \delta f, \end{aligned} \tag{5.43}$$

$$n = 1/3: \qquad \begin{aligned} T &= \alpha + \tfrac{2}{3}(\delta + \mu)\, t \\ X &= \beta + \delta x + \lambda f \\ F &= \gamma + \zeta x + \mu f. \end{aligned} \tag{5.44}$$

It can be seen from (5.43) that the classic similarity forms for the standard flow-by-curvature equation $N = -\kappa$ are in fact admissible for *all* values of n; in addition, for $n = 1/3$ we have an additional form where ellipses can preserve their shape as they collapse; these standard solutions will not be discussed here. We note that the integration of (5.40) would appear to suggest more special forms for $G(-\kappa)$, but this is not the case; they all result in the group (5.41) above.

In $\mathbb{R}^3$, the analysis is very similar. Equation (5.36) now reads

$$\frac{\varphi_t}{|\nabla\varphi|} = G\left(\nabla.\left(\frac{\nabla\varphi}{|\nabla\varphi|}\right)\right) \tag{5.45}$$

for a general surface $\varphi(x,y,z,t) = 0$; setting $z = f(x,y,t)$, so that $\varphi = z - f$, then

$$\frac{f_t}{(1+f_x^2+f_y^2)^{1/2}} = G\left(\frac{(1+f_y^2)f_{xx} + (1+f_x^2)f_{yy} - 2f_x f_y f_{xy}}{(1+f_x^2+f_y^2)^{3/2}}\right). \tag{5.46}$$

Setting

$$\begin{aligned} f^* &\sim f(x,y,t) + \varepsilon F(x,y,t,f) \\ x^* &\sim x + \varepsilon X(x,y,t,f) \\ y^* &\sim y + \varepsilon Y(x,y,t,f) \\ t^* &\sim t + \varepsilon T(x,y,t,f) \end{aligned} \tag{5.47}$$

with the infinitesimals (F,X,Y,T) leaving (5.46) invariant, then we obtain the $\mathbb{R}^3$ analogue of equation (5.40), i.e.

$$\begin{aligned} &A(x,y,t,f,f_x,f_y) + B(x,y,t,f,f_x,f_y)\,G(-\kappa) \\ &\quad + [C(x,y,t,f,f_x,f_y) - D(x,y,t,f,f_x,f_y)\,\kappa]\,G'(-\kappa) = 0. \end{aligned} \tag{5.48}$$

For arbitrary $G(-\kappa)$, we obtain

$$\begin{aligned} T &= \alpha \\ X &= \beta + \qquad - \lambda y - \mu f \\ Y &= \gamma + \lambda x + \qquad - \nu f \\ F &= \delta + \mu x + \nu y, \end{aligned} \tag{5.49}$$

and by integrating (5.48) for (A,B,C,D) non-zero, we can obtain the special case (5.42)

once again, which gives

$$\begin{aligned} T &= \alpha + (1+n)\zeta t \\ X &= \beta + \zeta x - \lambda y - \mu f \\ Y &= \gamma + \lambda x + \zeta y - \nu f \\ F &= \delta + \mu x + \nu y + \zeta f \end{aligned} \tag{5.50}$$

with an extra stretching group parametrised by ζ; this time there is no special case for $n = 1/3$ (or any other value).

As an aside, we can consider the effect of using the Gaussian curvature instead of the mean curvature in $\mathbb{R}^3$; in this case, equation (5.36) reads

$$\frac{f_t}{(1+f_x^2+f_y^2)^{1/2}} = G\left(\frac{f_{xx}f_{yy}-f_{xy}^2}{(1+f_x^2+f_y^2)^2}\right). \tag{5.51}$$

With the usual analysis, we again obtain the equation (5.48), leading to (5.49) for arbitrary $G(-\kappa)$. Once more we obtain a special case when (5.42) holds, and obtain the groups

$$n \neq 1/4: \quad \begin{aligned} T &= \alpha + (1+2n)\zeta t \\ X &= \beta + \zeta x - \lambda y - \mu f \\ Y &= \gamma + \lambda x + \zeta y - \nu f \\ F &= \delta + \mu x + \nu y + \zeta f, \end{aligned} \tag{5.52}$$

$$n = 1/4: \quad \begin{aligned} T &= \alpha + (\zeta+\psi)t \\ X &= \beta + \zeta x + \lambda y + \mu f \\ Y &= \gamma + \xi x + \zeta y - \nu f \\ F &= \delta + \phi x + \rho y + 2\psi f. \end{aligned} \tag{5.53}$$

This special case, where we obtain a 12-parameter group, was first noted by Alvarez et al. [1] using a different method; evolutions governed by $N = -\kappa^{1/4}$ have been applied in the field of image processing.

Chapter 6

Relaxation Waves in a FitzHugh-Nagumo Reaction-Diffusion Model

6.1 Introduction

The field of neural communication has produced a number of mathematical models, of which the most important are probably those derived from the now seminal work by Hodgkin and Huxley [21], concerning the electric signalling by individual nerve cells or neurons which propagates along axonal membranes. The four-variable model they obtained was solved numerically, but due to its complexity, a number of simpler mathematical models have been derived which still capture the essence of the full model; the most widely used of these is the FitzHugh-Nagumo model [12, 41], which can be written in the form

$$\begin{aligned} \varepsilon \frac{\partial u}{\partial t} &= \varepsilon^2 D \frac{\partial^2 u}{\partial x^2} + F(u) - v + I_a \\ \frac{\partial v}{\partial t} &= b\, u - v, \end{aligned} \tag{6.1}$$

where

$$F(u) = u\,(1-u)\,(u-a) \tag{6.2}$$

with $0 < a < 1$ and b is a positive constant. Here u behaves like the nerve membrane potential, v represents several variables relating to the membrane current due to ion concentrations, and D is associated with the axial current in the axon (see Murray [40] p.329). I_a is the applied current and $\varepsilon \ll 1$ is a small parameter.

The system (6.1) has been studied in various contexts by a number of authors. We note that it is not merely restricted to biological systems; it is well known that the Belousov-Zhabotinskii chemical reaction produces a number of dramatic pattern formations, including rotating spirals and expanding target patterns (see Winfree [56, 57]). We have considered spiral waves already from a flow-by-curvature point of view; we will now focus on the target patterns, which we think of as an oscillatory phenomenon (although they can also arise from periodic stimulation of an excitable medium (see Keener [28]) – this involves a particular form of boundary condition). This suggests seeking solutions to (6.1) which evolve from prescribed initial conditions for the case of limit cycle kinetics, which requires the phase plane for (6.1) with $D = 0$ to have an (unstable) critical point. This is illustrated in Figure 6.1; the conditions on the parameters to obtain a limit cycle are discussed below (see Murray [40] for a fuller phase plane analysis of (6.1) in the absence of any spatial dependence).

The existence of sustained oscillations in biological systems has been known for some time; initial work by Lotka [36] and Volterra [54] focussed purely on temporal oscillations. Turing [48] considered spatial dependence and in particular investigated how reaction and diffusion terms interact when considering a chemical basis for morphogenesis; Turing systems will be discussed in the following chapter. Since these seminal works, there has been interest in oscillatory systems in both biology and chemistry fields, especially in the modelling of the Belousov-Zhabotinskii (BZ) reaction; it was first reported by Zaikin and Zhabotinskii [58] that when a thin (covered) layer of malonic acid is oxidized by bromate in the presence of cerium ions in sulphuric acid solution, a number of bright spots appear, which then expand outwards. After a short period of time, their centres turn dark, whilst still propagating outwards; repetition of this 'switching' results in a series of concentric rings being formed (the target pattern). Observations show that concentrations continue to oscillate everywhere in the layer, but different target patterns

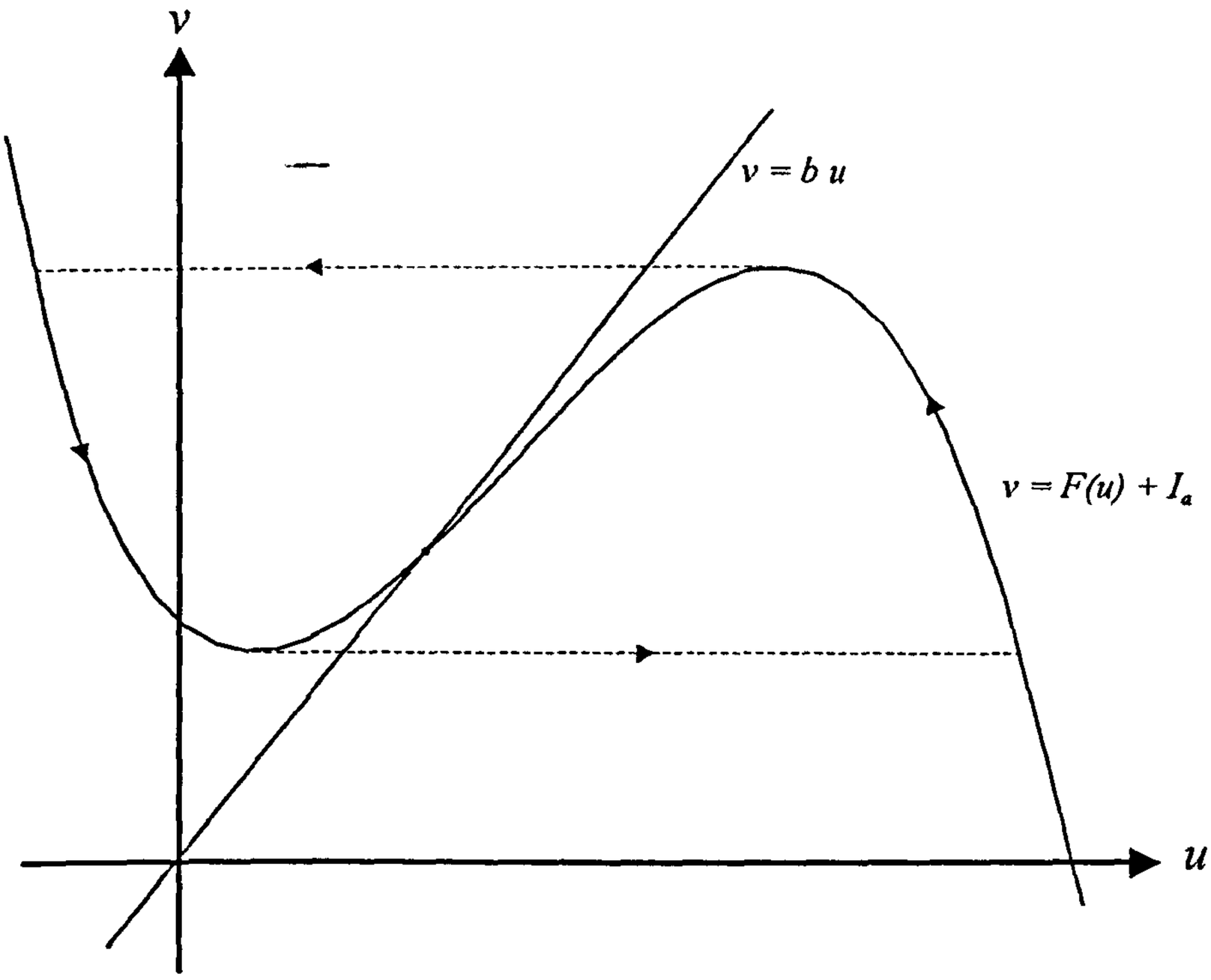

Figure 6.1: Phase plane for (6.1) with $D = 0$ showing the nullclines of the reaction terms.

within the layer can propagate at slightly differing speeds, in spite of there being no externally imposed gradient. Work on the BZ reaction has so far tended to centre on the chemical model for the spatial generation of pattern of Field, Körös and Noyes [9] (see Field and Noyes [10], Tyson [49] and Tyson and Fife [53]); we will now consider target pattern formation using the FitzHugh-Nagumo (FN) model (6.1), as this is a fairly simple model to analyse. Previous modelling using FN kinetics has generally been restricted to excitable media, where 'wave train' behaviour is achieved by repeated stimulation of the media. This is the problem studied by Keener [27, 28]; the behaviour behind the initial front is investigated by seeking periodic travelling wave solutions. Kalachev [25] *does* produce a relaxation wave solution for the FN model with excitable kinetics, but it is achieved by fixing $v \geq 0$ and ensuring that the intersection of the nullclines of the reaction terms occurs at $v < 0$, so that any trajectory in the phase plane cannot enter the stable critical point; this prevents pulse solutions (see Figure 6.2). As noted above, our work will focus on solutions with limit cycle kinetics.

We note that whilst target patterns are spatially a two-dimensional phenomenon,

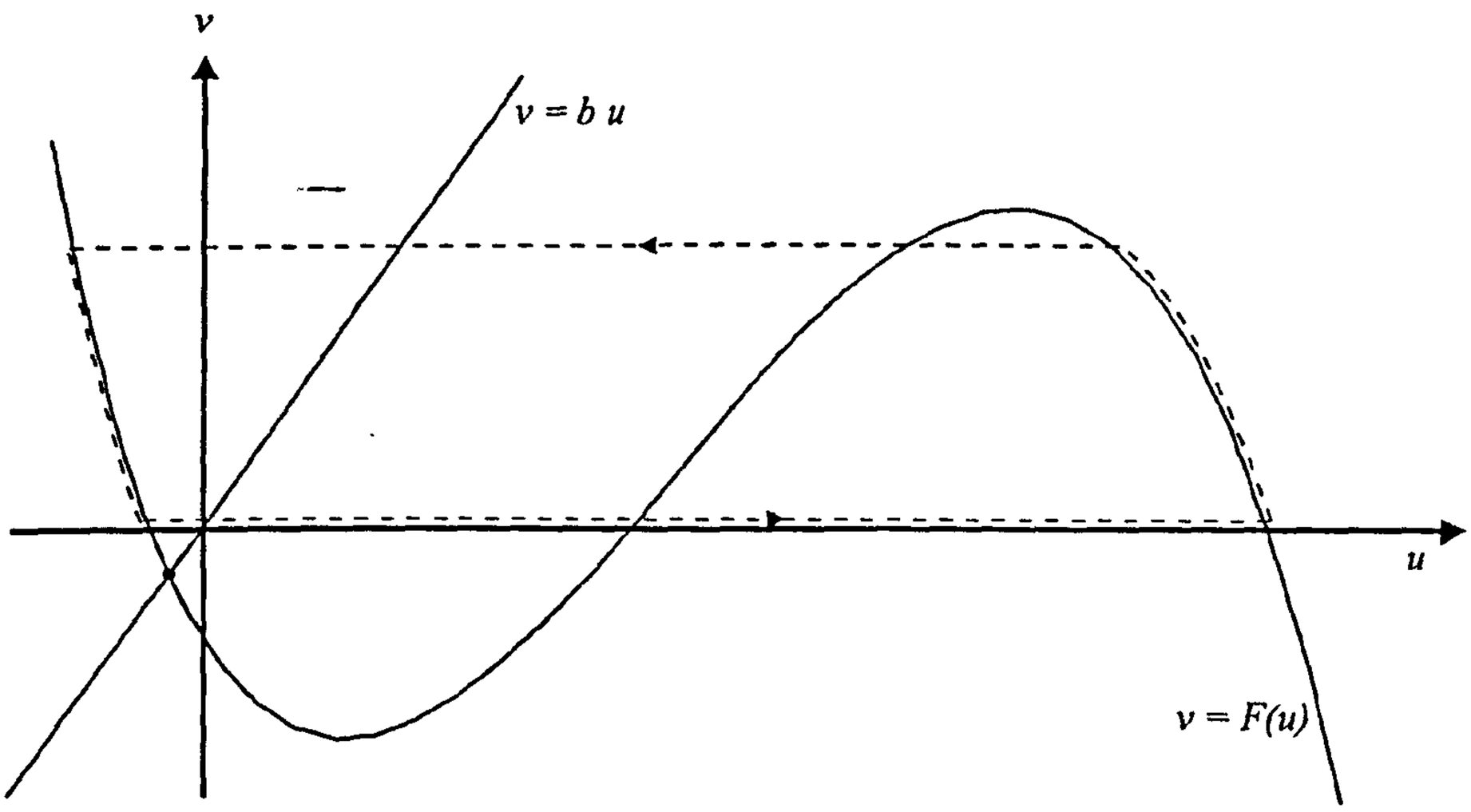

Figure 6.2: Phase plane for Kalachev's formulation showing the nullclines of the reaction terms. For $v \geq 0$, no trajectory can enter the critical point, thus forcing a periodic wave to form.

the waves are slowly-varying; if we consider a small segment of a single pattern about a radial line, then the behaviour is essentially one-dimensional (the wave is almost exactly a plane wave); it is this case on which we will generally focus, although a two-dimensional radial formulation will also be considered more briefly.

More general mathematical discussions of nonlinear wave propagation in one-dimensional oscillatory systems can be found in Kopell and Howard [35] and Howard and Kopell [22] as well as the book by Murray [40]; elements of this theory will be discussed when relevant below. We note, however, that these focus on the behaviour of fully periodic waves and use a simplified form of kinetics ('$\lambda - \omega$ type') to demonstrate the results; in our case we will consider solutions to a initial value problem with localised initial conditions.

6.1.1 Introductory Rescalings

As we will be considering (6.1) with limit cycle kinetics, we will rescale our system so that the critical point is at the origin. By simple geometry, we find that we require

$$b > \frac{1}{3}(1+a)^2 - a$$

to ensure that the slope of $v = b\,u$ is greater than that at the point of inflexion of $v = F(u)$. With no loss of generality, we take $b = 1$. Similarly, we can obtain bounds on I_a and u to ensure an unstable critical point at the origin; we find

$$I_a^{\min}{}^{\max} = \frac{1}{27}\left(7 + 12a + 3a^2 - 2a^3 \pm 2(a-2)^{3/2}(1+a)^{3/2}\right)$$

and

$$u_c^{\min}{}^{\max} = \frac{1}{3}\left(1 + a \pm (a^2 - a - 1)^{1/2}\right),$$

where u_c, the value of u at the critical point, is the only real solution to

$$u_c^3 - (1+a)(u_c - 1)\,u_c - I_a = 0.$$

We take (6.1) to be a dimensionless form of the model and now change the variables according to

$$u \to u + u_c \qquad v \to v + u_c \qquad x \to x\sqrt{D}$$

and, setting

$$a_1 = \sqrt{\alpha^2 - \beta} - \alpha \qquad a_2 = \sqrt{\alpha^2 - \beta} + \alpha,$$

where

$$\begin{aligned} 2\,\alpha &= 1 + a - 3\,u_c \\ \beta &= 3\,u_c^2 - 2(1+a)\,u_c + a, \end{aligned}$$

we obtain

$$\begin{aligned} \varepsilon\,u_t &= \varepsilon^2 u_{xx} + f(u) - v \\ v_t &= u - v \end{aligned} \tag{6.3}$$

with

$$f(u) = u\,(u + a_1)\,(a_2 - u), \tag{6.4}$$

which will be our model system. Note that the scalings of the various terms in the first of (6.3) are equivalent to those adopted earlier in (3.1). If we consider the critical point in more detail, and examine (6.3) in the absence of the diffusion term, then linear analysis gives us

$$\varepsilon < a_1\,a_2 \tag{6.5}$$

as the upper bound on ε for limit cycle kinetics (i.e. for an unstable critical point). We also obtain

$$\begin{aligned} (\varepsilon + a_1\, a_2)^2 - 4\,\varepsilon > 0 \quad &\Rightarrow \quad \text{unstable node} \\ (\varepsilon + a_1\, a_2)^2 - 4\,\varepsilon < 0 \quad &\Rightarrow \quad \text{unstable spiral} \end{aligned} \tag{6.6}$$

so that, generally for $\varepsilon \ll 1$, we will have an unstable node as our critical point; the 'special' case where we have a spiral at the origin of the (u, v) phase plane will also be discussed.

As mentioned above, our solutions will all be related to some initial condition. In all cases, we will consider a medium initially at rest (i.e. $u = v = 0$), subjected to a small disturbance around $x = 0$ at $t = 0$. The form of this disturbance will be detailed as and when required; generally, we will consider both a sharp perturbation in u at the origin (i.e. $u(x, 0) = \mu\,\delta(x)$ where μ is small) and exponentially decaying initial profiles, which we discuss later.

6.2 A Numerical Solution

As an initial exercise, we compute a numerical solution to (6.3) in the parameter range which gives us an unstable node at the origin (see (6.6)). We use a simple, finite-difference explicit time-stepping scheme; at $t = 0$ we set in the finite difference form $u(x, 0) = v(x, 0) = 0$ except for $u(0, 0) = \delta$, a small *positive* perturbation (we could equally well choose a negative perturbation; this would correspond to the same problem with a_1, a_2 interchanged. We observe a periodic form of solution (see Figure 6.3); away from the point of initial stimulation, the waveform appears fixed and to be travelling at a constant $O(1)$ speed. It would appear at first glance that we could use a similar asymptotic formulation to that used by Keener [27] for wavetrains in excitable media, which determines the wave speed by analysing the periodic behaviour behind the initial front in terms of slowly-varying 'outer' solutions and fast transition inner layers. The wave speed is determined by finding the single trajectory which connects the two stable branches of the cubic $f(u)$ in the phase plane at a particular fixed v (which is determined by frequency of the repeated stimulation of the excitable media); we will refer to this later as the 'stable-stable' wave-speed. The initial front would then require knowledge

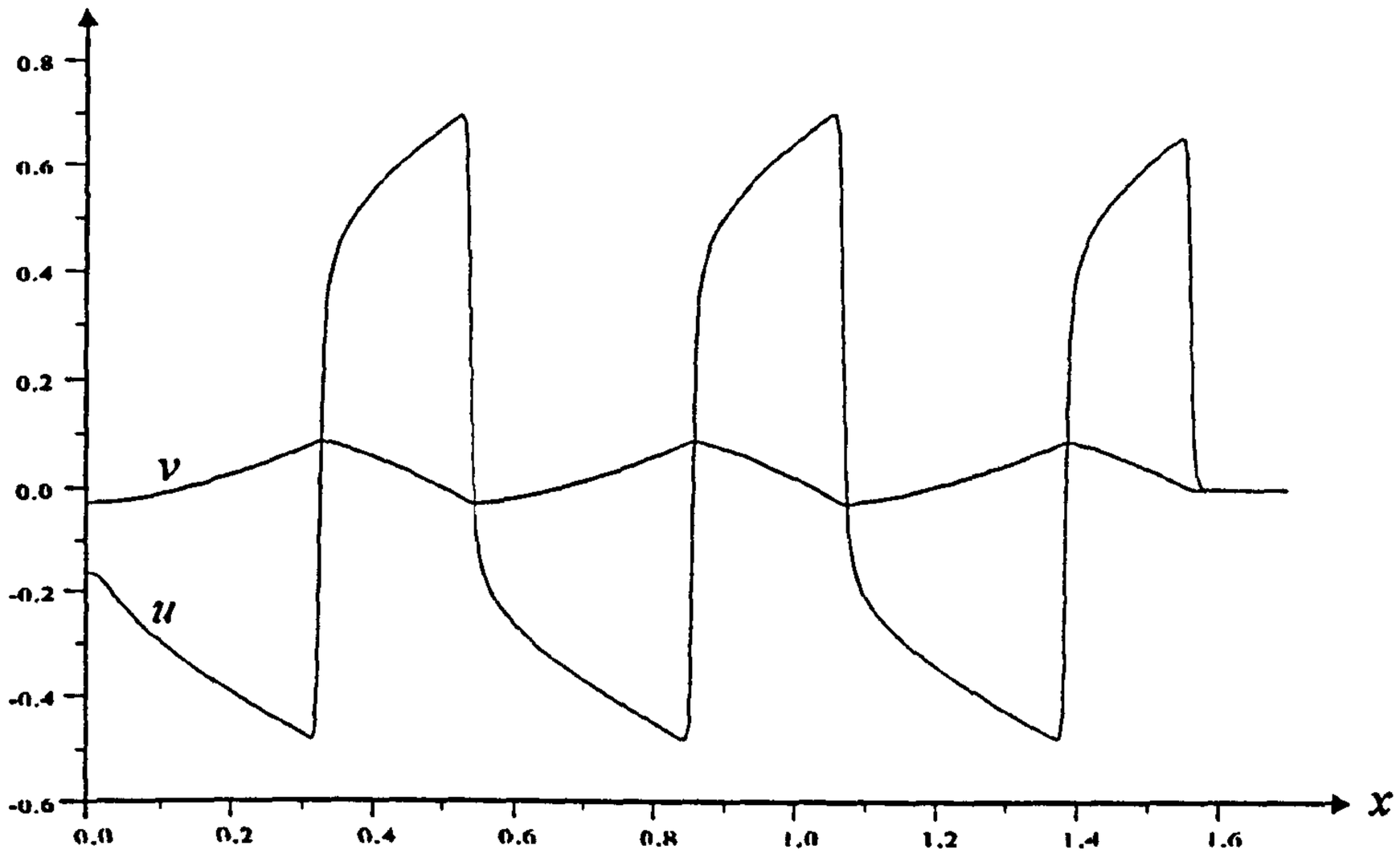

Figure 6.3: Numerical solution to (6.3) at time $t = 2$; $\varepsilon = 0.001$, $a_1 = 1/3$, $a_2 = 2/3$.

of this speed *before* the periodic portion of the front is formed; this seems unlikely to be the case (the numerical analysis also indicates that the 'stable-stable' speed is nearly always too small for all v in the range (v_{max}, v_{min}), the range of v within the limit cycle). Intuitively, we would expect the initial front to play a major part in the determination of the wave speed, and we consider this below in an asymptotic analysis investigating the whole of the wave profile. Thus we focus on the formation of travelling waves from localised initial perturbations rather than analysing travelling waves which are periodic in all space; we note, however, that much of Keener's formulation (i.e. the introduction of the inner and outer layers) is still applicable.

6.3 Asymptotic Formulation and Solutions

In order to proceed, we number the wave fronts and backs as in Figure 6.4. The 'Airy' and 'origin' regions will be discussed later. As $\varepsilon \to 0$, the phase diagram for (6.3) is as shown in Figure 6.5. The three portions of the curve $v = f(u)$ are shown as the pseudo-inverses $u = h(v)$; note that v_{min} and v_{max} correspond exactly to the maximum and minimum of $f(u)$. We now consider the various layers for u (and v) in turn, starting with the initial front.

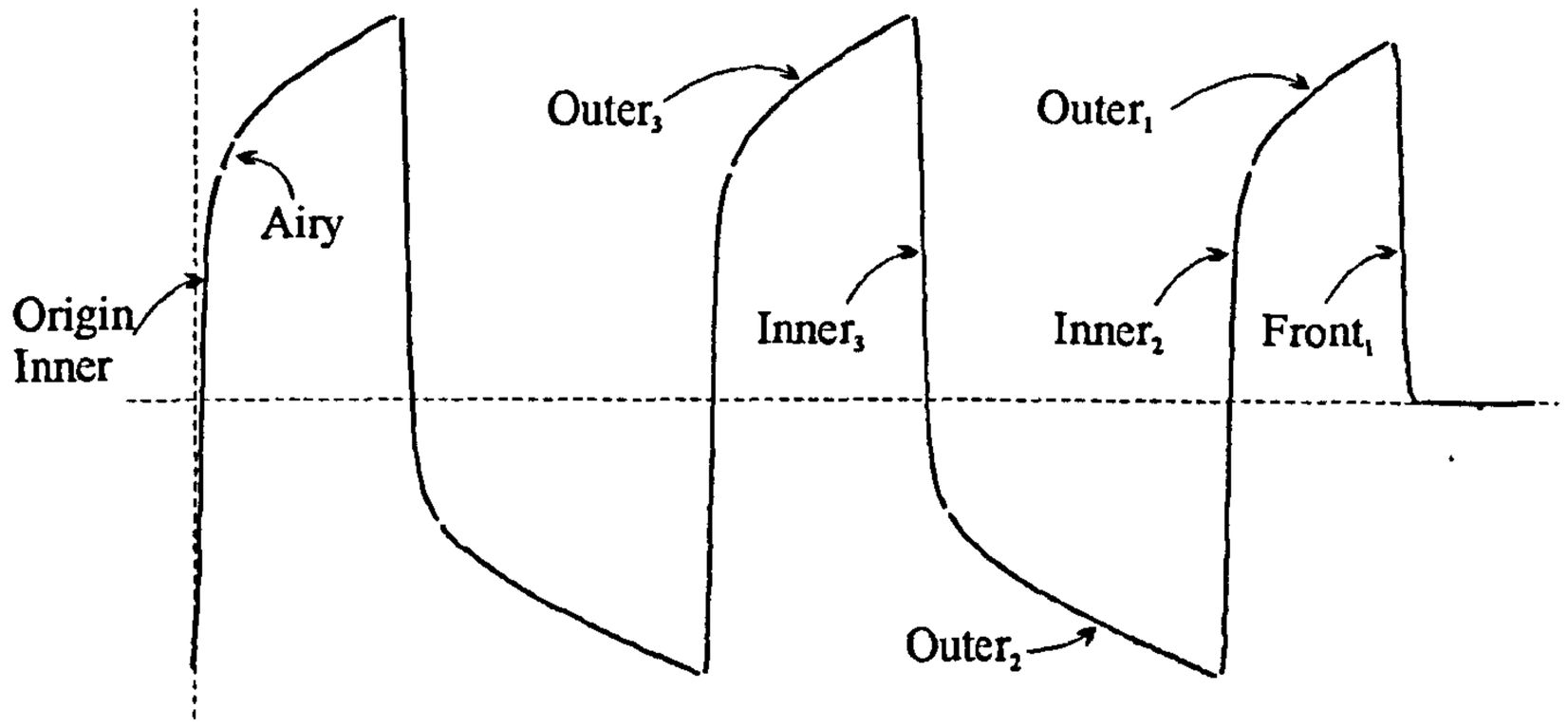

Figure 6.4: Asymptotic structure for u.

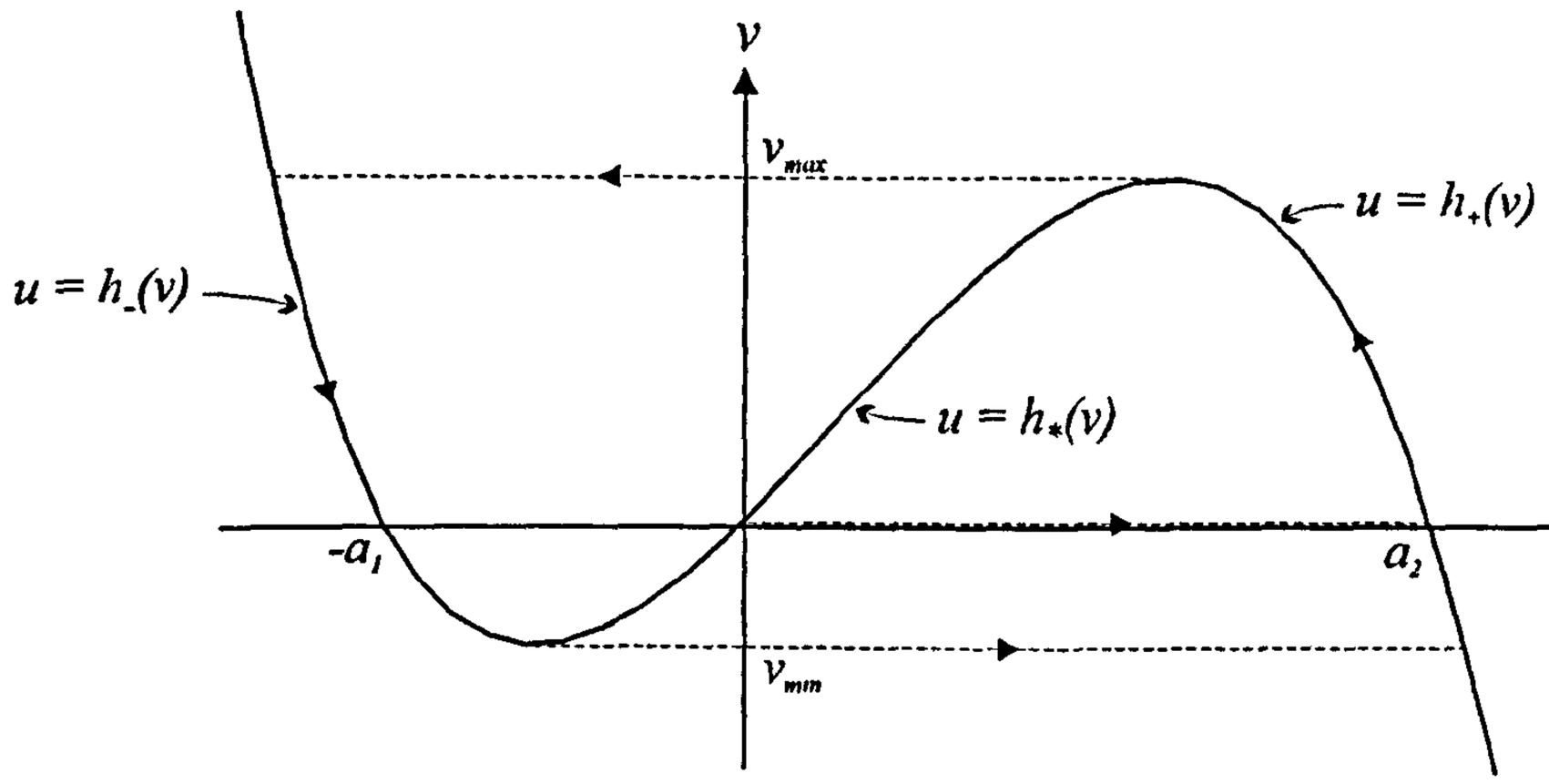

Figure 6.5: Phase diagram for (6.3).

6.3.1 Initial front

The approach for all the inner layers is basically the same; in this case we set

$$x = s^{(1)}(t;\varepsilon) + \varepsilon\, z \tag{6.7}$$

(where the superscript (1) denotes the number of the front according to Figure 6.4) and look for a solution to (6.3) of the form

$$\begin{aligned} u &= u_0 + \varepsilon^{2/3}\, u_1 + \ldots \\ v &= v_0 + \varepsilon^{2/3}\, v_1 + \ldots \\ s^{(1)} &= s_0^{(1)} + \varepsilon\, s_1^{(1)} + \ldots \quad . \end{aligned} \tag{6.8}$$

The $\varepsilon^{2/3}$ correction term for u and v is chosen with a view to matching with the 'Airy' region later. At leading order, we obtain

$$\begin{aligned} u_{0zz} + \dot{s}_0^{(1)} u_{0z} + u_0 (u_0 + a_1)(a_2 - u_0) &= v_0 \qquad (6.9) \\ \dot{s}_0^{(1)} v_{0z} &= 0 \qquad (6.10) \end{aligned}$$

with boundary conditions

$$\begin{aligned} u_0 \to h_*(v^*), \qquad v_0 \to v^* \qquad & \text{as } z \to +\infty \\ u_0 \to h_+(v^*), \qquad & \text{as } z \to -\infty, \end{aligned} \qquad (6.11)$$

where v^* is some constant. It is apparent that $v^* = 0$ for the initial front (this is shown on Figure 6.5 by the middle dashed line); however, it will be useful to leave v^* as an unknown constant for the time being. We thus have to solve the single ordinary differential equation (6.9) and determine $\dot{s}_0^{(1)}$, the wave speed (to leading order), which can be achieved by rewriting the problem in a standard form. Setting

$$u_0 = \phi_+ w_0 + \lambda, \qquad (6.12)$$

with

$$\begin{aligned} \phi_\pm &= \sqrt{\bar{\alpha}^2 - \bar{\beta}} \pm \bar{\alpha} \\ 2\bar{\alpha} &= a_2 - a_1 - 3\lambda \qquad (6.13) \\ \bar{\beta} &= 3\lambda^2 - 2(a_2 - a_1)\lambda - a_1 a_2, \end{aligned}$$

and

$$\lambda^3 - (a_2 - a_1)\lambda^2 - a_1 a_2 \lambda + v^* = 0, \qquad (6.14)$$

and choosing $\lambda = \lambda_2$, where $\lambda_1 \le \lambda_2 \le \lambda_3$ are the three roots of (6.14), (we assume v^* to be such that all roots are real) we can obtain

$$w_{0\xi\xi} + \bar{c} w_{0\xi} + w_0 (1 - w_0)(\bar{a} + w_0) = 0 \qquad (6.15)$$

with boundary conditions

$$\begin{aligned} w_0 \to 0 \qquad & \text{as } \xi \to +\infty \\ w_0 \to 1 \qquad & \text{as } \xi \to -\infty, \end{aligned} \qquad (6.16)$$

where

$$\xi = \phi_+ z \qquad \bar{c} = \frac{\dot{s}_0^{(1)}}{\phi_+} \qquad \bar{a} = \bar{a}(v^*) = \frac{\phi_-}{\phi_+} > 0. \tag{6.17}$$

Thus in our rescaled equation (6.15), we are seeking a trajectory that connects the critical point $w_0 = 0, w_0' = 0$ (unstable) to $w_0 = 1, w_0' = 0$ (stable). From the phase diagrams in Figure 6.6, we can see that there will *not* be a unique wave speed, but in fact a semi-infinite range of speeds. For a trajectory to represent a valid wave speed, it must

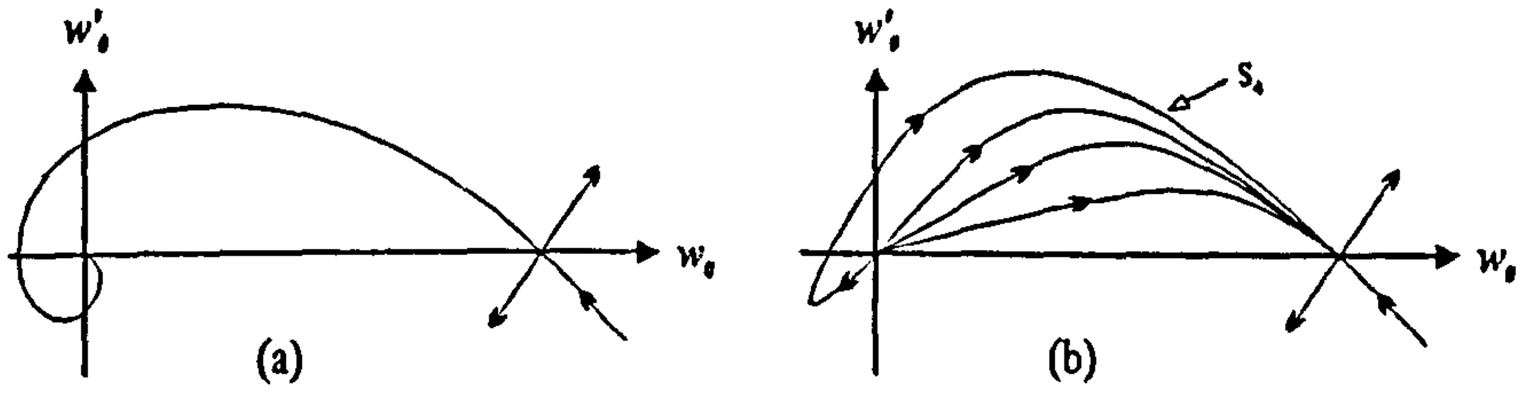

Figure 6.6: Phase portraits for $w_0(\xi)$ from (6.15). (a) $\bar{c}^2 < 4\,\bar{a}$, giving an unstable spiral at the origin. (b) $\bar{c}^2 > 4\,\bar{a}$, giving an unstable node. The different trajectories represent different speeds.

be monotone increasing from the origin to the saddle point (note that the arrows point in the direction of increasing t); we are not seeking non-generic solutions (at this stage). In Figure 6.6(a), where $\bar{c}^2 < 4\,\bar{a}$, linear analysis gives an unstable spiral at the origin, which is not monotonic increasing. Figure 6.6(b) represents $\bar{c}^2 > 4\,\bar{a}$, where we have an unstable node; it can be seen that the trajectory may not satisfy the monotone increasing condition. Thus, the trajectory in the phase plane which is monotonic increasing with the smallest value of $\bar{c}$ defines the minimum wave speed; there is no upper limit.

To determine this minimum wave speed for the initial front, it is instructive to note the two extreme cases $\bar{a} \to 0$ and $\bar{a} \to \infty$. As $\bar{a} \to 0$, then at leading order (6.15) becomes

$$w_{0\xi\xi} + \bar{c}\, w_{0\xi} + w_0^2(1 - w_0) = 0, \tag{6.18}$$

which is in fact a model of a travelling wave of chemical reaction supported by purely cubic isothermal autocatalysis (see Gray et al. [17]); it is well known that (6.18) has the solution

$$w_0 = \frac{1}{2}\left(1 - \tanh\frac{\xi}{2\sqrt{2}}\right) \tag{6.19}$$

for the minimum wave speed

$$\bar{c} = 1/\sqrt{2} \tag{6.20}$$

(see [17, 19, 20]). This may be generalised to give a solution to (6.15) of the form

$$w(\xi) = A + B \tanh \alpha \xi, \tag{6.21}$$

where

$$\begin{aligned} A &= \frac{1}{6}\left(\sqrt{2}\,\bar{c} + 2(1-\bar{a})\right) \\ B &= -\sqrt{2}\,\alpha \\ \alpha &= \frac{1}{2\sqrt{3}}\left(2(\bar{a}^2+\bar{a}+1) - \bar{c}^2\right)^{1/2} \end{aligned} \tag{6.22}$$

and $\bar{c}$ is a solution of

$$2\sqrt{2}\,\bar{c}^3 - 3\sqrt{2}(\bar{a}^2+\bar{a}+1)\,\bar{c} + 2(1-\bar{a}^3) + 3\,\bar{a}(1-\bar{a}) = 0, \tag{6.23}$$

a cubic equation due to the form of the kinetics in (6.18). Signs have been chosen in (6.22) to give a positive wave speed; in view of the boundary conditions (6.11) we find that

$$\bar{c} = \frac{1+2\,\bar{a}}{\sqrt{2}} \tag{6.24}$$

is the required root of (6.23) and hence

$$A = 1/2, \qquad B = -1/2, \qquad \alpha = 1/2\sqrt{2}$$

from (6.22). We will call (6.24) the 'tanh' wave speed.

To consider the limit $\bar{a} \to \infty$ we write $\bar{a} = 1/\varepsilon$ and (6.15) becomes

$$\varepsilon\, w_{0\xi\xi} + \varepsilon\,\bar{c}\, w_{0\xi} + w_0(1-w_0)(1+\varepsilon\, w_0) = 0. \tag{6.25}$$

On setting

$$\xi = \varepsilon^{1/2}\zeta, \qquad \bar{c} = \bar{\bar{c}}/\varepsilon^{1/2} \tag{6.26}$$

we have, to leading order,

$$w_{0\zeta\zeta} + \bar{\bar{c}}\, w_{0\zeta} + w_0(1-w_0) = 0, \tag{6.27}$$

which is Fisher's equation; as is well-known, the minimum wave speed can be found by linearizing about the unstable critical point. It is well established that wave-front solutions exist for $\bar{\bar{c}} \geq 2$, i.e. $\bar{c} \geq 2\sqrt{\bar{a}}$ (see [11, 20, 19]). If we linearize (6.15) in a similar way, we obtain

$$w_{0\xi\xi} + \bar{c}\, w_{0\xi} + \bar{a}\, w_0 = 0 \tag{6.28}$$

which can easily be solved by looking for a solution of the form

$$w_0 \sim \mathrm{e}^{-m\xi} \tag{6.29}$$

to give us the quadratic equation

$$m^2 - \bar{c}\, m + \bar{a} = 0 \tag{6.30}$$

and hence

$$m = \frac{\bar{c}}{2} \pm \frac{1}{2}\sqrt{\bar{c}^2 - 4\,\bar{a}}. \tag{6.31}$$

This implies that the (positive) minimum velocity is given by

$$\bar{c}_{\min} = 2\sqrt{\bar{a}} \tag{6.32}$$

to ensure that we do not encounter a negative square root. We will call this the 'linear' wave speed.

We thus have two possibilities for the minimum wave speed; we expect (6.24) to hold for small $\bar{a}$ and (6.32) to apply for large $\bar{a}$. It is found that the switch between the two occurs at $\bar{a} = 1/2$, as this is the only point where a smooth transition is possible; see Figure 6.7. This can also be argued by considering the nature of the eigenvectors associated with the stable node in the phase plane and their connection to the saddle point (see Gray et al. [17] for a detailed analysis).

The above formulation is applicable to any v^*; we have already noted that for the initial front $v^* = 0$ and the problem then simplifies. From (6.14), we obtain $\lambda_2 = 0$ and thus

$$\phi_+ = a_2, \qquad \phi_- = a_1 \quad \Rightarrow \quad \bar{c} = \frac{\dot{s}_0^{(1)}}{a_2}, \qquad \bar{a} = \frac{a_1}{a_2}. \tag{6.33}$$

from (6.17); the minimum front speeds for $v^* = 0$ (from (6.24) and (6.32)) are

$$\dot{s}^{(1)}_{0\,\min} = \frac{a_2 + 2\,a_1}{\sqrt{2}} \qquad a_1/a_2 \leq 1/2, \tag{6.34}$$

$$\dot{s}^{(1)}_{0\,\min} = 2\sqrt{a_1\,a_2} \qquad a_1/a_2 \geq 1/2. \tag{6.35}$$

We note that these represent the minimum velocity when considering the *initial front only*; it may well be affected by other regions, as will be shown later.

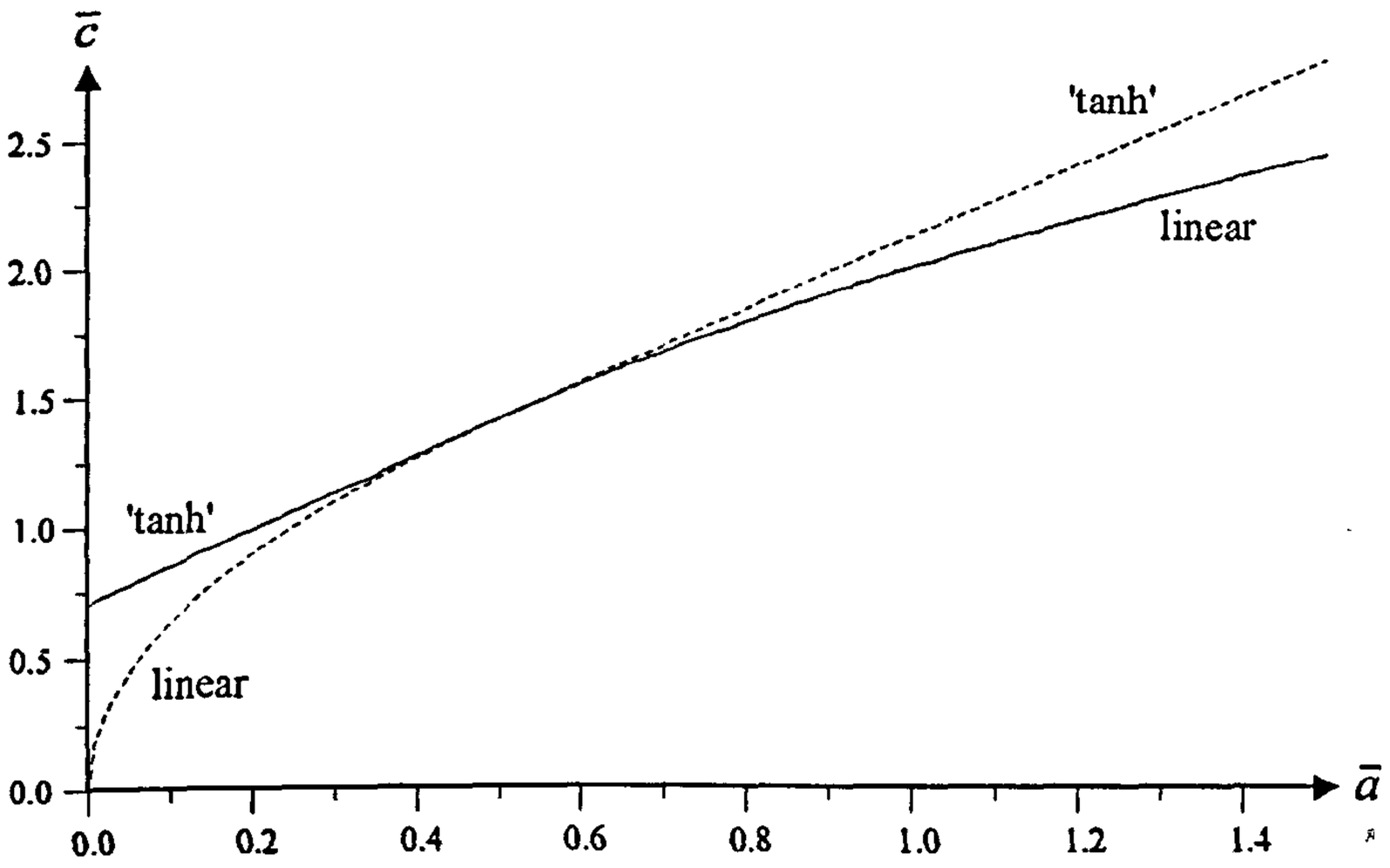

Figure 6.7: The minimum velocity $\bar{c}$, for the initial front only, shown as a solid line.

We now consider the correction term for the initial front. From (6.3), we obtain

$$u_{1\,zz} + \dot{s}^{(1)}_0\,u_{1\,z} + u_1\,f'(u_0) = v_1 \tag{6.36}$$

$$\dot{s}^{(1)}_0\,v_{1\,z} = 0. \tag{6.37}$$

We thus have $v_1 = v_1(t)$ from (6.37), but since we are matching into zero initial conditions, we must have $v_1(t) = 0$. Differentiating (6.9), we have

$$u_{0\,zzz} + \dot{s}^{(1)}_0\,u_{0\,zz} + f'(u_0)\,u_{0\,z} = 0, \tag{6.38}$$

which, on comparing with (6.36), implies that

$$u_1 = \bar{u}_1(t)\,u_{0\,z}$$

is the solution satisfying

$$u_1 \to 0 \qquad \text{as } z \to +\infty.$$

Therefore from (6.8), we have

$$\begin{aligned} u &\sim u_0\left(x - s_0^{(1)}(t)\right) + \varepsilon^{2/3}\,\bar{u}_1(t)\,u_0'\left(x - s_0^{(1)}(t)\right) \\ &\sim u_0\left(x - s_0^{(1)}(t) + \varepsilon^{2/3}\,\bar{u}_1(t)\right) \\ &\sim u_0\left(x - \left[s_0^{(1)}(t) - \varepsilon^{2/3}\,\bar{u}_1(t)\right]\right), \end{aligned} \tag{6.39}$$

which implies that a correction term would alter the wave speed; since this is not the case (the wave speed to these orders is $c = \dot{s}_0^{(1)}$ exactly) we conclude that $\bar{u}_1 = 0$.

As a final point for this region, we note that if our initial condition is not in the form of a small perturbation at $x = 0$, but instead an exponentially decaying distribution, then the value of m may already be prescribed in (6.30) by the initial data, and $\bar{c}$ is obtained from this equation if m is sufficiently small. For $\bar{a} > 1/2$ this gives a faster minimum wave speed when $m < \sqrt{\bar{a}}$; for $m \geq \sqrt{\bar{a}}$ we retain $\bar{c}_{\min}$ as our wave speed. This behaviour also applies to the case $\bar{a} < 1/2$ when $\bar{c}$ obtained from (6.30) is larger than $\bar{c}_{\min}$ in (6.24), although the critical value of m changes.

6.3.2 Outer$_1$

For the first outer solution, denoted Outer$_1$ in Figure 6.4, we set

$$\begin{aligned} u &= u_0 + \varepsilon^{2/3}\,u_1 + \ldots \\ v &= v_0 + \varepsilon^{2/3}\,v_1 + \ldots \end{aligned} \tag{6.40}$$

so that to leading order, (6.3) gives

$$\begin{aligned} v_0 &= f(u_0) \\ v_{0t} &= u_0 - v_0 \end{aligned} \tag{6.41}$$

and hence we obtain the single equation

$$v_{0t} = h_+(v_0) - v_0 \tag{6.42}$$

(where $u = h_+(v)$ is the pseudo-inverse for the positive stable branch of $v = f(u)$ as shown in Figure 6.5) with boundary conditions

$$\begin{aligned} v_0 &= 0 \qquad && \text{at } t = s_0^{(1)^{-1}}(x) \\ v_0 &= v_+^* \qquad && \text{at } t = s_0^{(1)^{-1}}(x) + t_1, \end{aligned} \tag{6.43}$$

where v_+^* is a positive constant, the value of v_0 when the second inner layer is initiated, and thus the maximum value attained by v_0 in the outer region. Generally it is found that $v_+^* = v_{max}$, as this is the limiting case of the stable-unstable connection in the phase plane for the second inner region (which we consider in the next section); if $v_+^* < v_{max}$, the connection is stable-stable, and the associated *unique* wave speed is always too small except in a special case detailed later. The stable-unstable connection allows a range of speeds, generally including the 'correct' speed which we determine below; we thus take $v_+^* = v_{max}$ in this section. We define t_1 as the time from when the front leaves a point x until the next transition layer arrives (which, as we have a travelling wave away from the origin, is a constant). It can be seen that (6.42) does not contain spatial derivatives; this confirms that the algebraic form for the wave speed is determined entirely by the inner layers, and that the solution for v_0 is of the form

$$t - s_0^{(1)^{-1}}(x) = \int_0^{v_0} \frac{dv}{h_+(v) - v}. \tag{6.44}$$

Writing (6.44) as

$$v_0 = G(t - s_0^{(1)^{-1}}(x)), \tag{6.45}$$

and using $v_+^* = v_{max}$, (6.43) gives

$$t_1 = \int_0^{v_{max}} \frac{dv}{h_+(v) - v}. \tag{6.46}$$

We already know from the initial front that $s_0^{(1)^{-1}}(x) = x/\dot{s}_0^{(1)}$; the leading order solution for the first outer region is thus of the form

$$u_0 = u_0\left(t - \frac{x}{\dot{s}_0^{(1)}}\right) \tag{6.47}$$

and similarly for v_0.

For the correction term v_1, we have

$$\begin{aligned} v_1 &= f'(u_0)\, u_1 \\ v_{1\,t} &= u_1 - v_1, \end{aligned} \tag{6.48}$$

which implies that

$$v_1 = \gamma(x)\, v_{0\,t} \tag{6.49}$$

with

$$v_1 = 0 \qquad \text{at } t = s_0^{(1)^{-1}}(x) \tag{6.50}$$

as the matching condition with the initial front, giving $v_1 = 0$.

6.3.3 Inner$_2$

The analysis for the other inner layers (with the exception of that close to the origin) is similar to that of the first layer. For the second transition, we set

$$x = s^{(2)}(t;\varepsilon) + \varepsilon\, z \tag{6.51}$$

and again seek a solution to (6.3) of the form shown in (6.9) which gives the equation

$$u_{0zz} + \dot{s}_0^{(2)}\, u_{0z} + u_0\,(u_0 + a_1)(a_2 - u_0) = v_+^*, \tag{6.52}$$

where v_+^* has the same value as in the first outer layer. The boundary conditions are

$$u_0 \to h_+(v_+^*), \qquad \text{as } z \to +\infty$$

$$u_0 \to h_-(v_+^*), \qquad \text{as } z \to -\infty.$$

We can easily calculate v_+^* when it is equal to $v_{\max}$; the stationary points of the curve $f(u)$ occur at

$$u_\pm^{sp} = \frac{1}{3}\left(a_2 - a_1 \pm \sqrt{a_1^2 + a_1\, a_2 + a_2^2}\right) \tag{6.53}$$

and hence

$$v_{\min}^{\max} = u_\pm^{sp}\,(a_1 + u_\pm^{sp})(a_2 - u_\pm^{sp}). \tag{6.54}$$

Following a similar analysis to (6.12)–(6.14), we set

$$u_0 = \phi_-\, w_0 + \lambda \tag{6.55}$$

with $\phi_\pm$ as in (6.13); we obtain two roots for λ; a double root of $\lambda_2 = u_+^{sp}$ and a single root $\lambda_1 = u_+^{sp} - \sqrt{a_1^2 + a_1\, a_2 + a_2^2} = u_+^{sp} - \phi_-$. Choosing to rescale with λ_2, in a similar manner to (6.17) we take

$$\xi = \phi_-\, z \qquad \bar{c} = \frac{\dot{s}_1^{(2)}}{\phi_-} \qquad \bar{a} = \frac{\phi_+}{\phi_-} = 0 \tag{6.56}$$

to give us the ordinary differential equation

$$w_{0\xi\xi} + \bar{c}\, w_{0\xi} + w_0^2(1 - w_0) = 0 \tag{6.57}$$

with boundary conditions

$$\begin{aligned} w_0 &\to 1 \qquad \text{as } \xi \to -\infty \\ w_0 &\to 0 \qquad \text{as } \xi \to +\infty. \end{aligned}$$

Equation (6.57) represents a limit case of an unstable-stable connection and hence has a solution provided $\bar{c} \geq \bar{c}_{\min}$ for some $\bar{c}_{\min}$, which is given by the 'tanh' solution. Following (6.21)–(6.22), we obtain a solution

$$w_0(\xi) = \frac{1}{2}\left(1 - \tanh \frac{\xi}{2\sqrt{2}}\right) \tag{6.58}$$

with $\bar{c}_{\min} = 1/\sqrt{2}$; in our original variables, this is

$$\dot{s}_{0\,\min}^{(2)} = \sqrt{\frac{a_1^2 + a_1\, a_2 + a_2^2}{2}} \qquad \text{for } v_+^* = v_{\max}. \tag{6.59}$$

Generally, this speed is slower than that of the original front, given by either (6.34) or (6.35); this implies that w_0 is not in fact the 'tanh' solution, but rather a solution for $\bar{c} > \bar{c}_{\min}$ determined by the initial front speed. Therefore, we in general have

$$\dot{s}_0^{(2)} = \dot{s}_{0\,\min}^{(1)}. \tag{6.60}$$

There is a range, however, with $a_2 \ll a_1$ ($\bar{a}$ large) in which (6.60) does not hold; the *linear* minimum wave speed for the initial front $\dot{s}_{0\,\min}^{(1)}$ given by (6.35) is smaller than that of the second transition region $\dot{s}_{0\,\min}^{(2)}$. Here we would expect the initial front eventually to change in some way in order to accommodate the periodic portion of the profile; we will consider this situation later.

6.3.4 Outer$_2$

This is of exactly the same form as the first outer solution; the equations are the same, but the boundary conditions now read

$$\begin{aligned} v_0 &= v_+^* \qquad \text{at } t = s_0^{(2)^{-1}}(x) \\ v_0 &= v_-^* \qquad \text{at } t = s_0^{(2)^{-1}}(x) + t_2, \end{aligned} \tag{6.61}$$

v_-^* being the minimum value attained by v_0 in the outer region (and hence generally $v_-^* = v_{\min}$ for the same reasons as $v_+^* = v_{\max}$ in the first outer region) and with t_2 being defined in an analogous way to t_1; the integral reads

$$t_2 = \int_{v_{\max}}^{v_{\min}} \frac{dv}{h_-(v) - v}. \tag{6.62}$$

Subsequent outer layers repeat the above formulation, t_3 being given by

$$t_3 = \int_{v_{\min}}^{v_{\max}} \frac{dv}{h_+(v) - v}; \tag{6.63}$$

from the periodic structure of the solution (see Figure 6.4), we can see that as $\varepsilon \to 0$, $t_{\text{even}} = t_2$ and $t_{\text{odd}} = t_3$.

6.3.5 Inner$_3$

The equation and boundary conditions for the third inner layer are given by

$$u_{0zz} + \dot{s}_0^{(3)} u_{0z} + u_0 (u_0 + a_1)(a_2 - u_0) = v_-^* \tag{6.64}$$

and

$$u_0 \to h_-(v_-^*), \qquad \text{as } z \to +\infty$$

$$u_0 \to h_+(v_-^*), \qquad \text{as } z \to -\infty.$$

As we would expect, the required solution is of the same form as for the second inner layer, and the wave speed $\dot{s}_0^{(3)} = \dot{s}_0^{(2)} = \dot{s}_0^{(1)}$ in general. This pattern then repeats itself and the leading order solution in $0 < x < s_0^{(2)}(t)$ is thus given by a periodic travelling wave of speed $\dot{s}_0^{(1)}$.

Before considering the more subtle behaviour in the vicinity of the origin, we will indicate how the asymptotic solution agrees with numerical calculations.

6.3.6 A comparison with the numerical solution

To determine the spatial period of the oscillations, we use the wave speed as determined from the asymptotic layer analysis. At this stage, we restrict ourselves to the case where a_2 is *not* small, so that the wave speed is fixed by the initial front. We can confirm

that this is correct (i.e. that we do have a wave of fixed form) in two ways. If we consider a point a certain (known) distance in front of a wave front, and integrate as above until the front arrives (which gives the time taken), we can easily determine the speed of the travelling wave. Secondly, we can compare all of the above asymptotic analysis with numerical solutions, similar to that shown earlier in Figure 6.3. Both of these confirm that for a medium initially at equilibrium, subject to a small initial perturbation, we can obtain asymptotically a travelling wave solution as detailed above.

As an example, we consider the case $a_1 = 1/3$, $a_2 = 2/3$; sample numerical results for $\varepsilon = 0.001$ and $\varepsilon = 0.0001$ are compared with the analytical results in Table 6.1. The

ε	max v	min v	$\dot{s}_0^{(1)}$
0.001	0.0866	-0.0284	0.9433
0.0001	0.0803	-0.0247	0.9428
0	0.0782	-0.0234	0.9428

ε	X_1	X_2	X_3	X_p	t_1	t_2	t_3	T_p
0.001	0.169	0.296	0.205	0.501	0.179	0.314	0.218	0.531
0.0001	0.146	0.260	0.179	0.439	0.155	0.276	0.190	0.466
0	0.139	0.249	0.170	0.419	0.147	0.264	0.181	0.445

Table 6.1: Comparison of numerical results for $\varepsilon = 0.001$ and $\varepsilon = 0.0001$ with analytical results (denoted $\varepsilon = 0$). X_1 to X_3 are the spatial sizes of the regions outer_1 to outer_3, and correspond to t_1 to t_3 with $X_i = \dot{s}_0^{(1)} t_i$. $X_p = \dot{s}_0^{(1)} T_p \sim X_2 + X_3$ is the spatial period of the limit cycle, $T_p \sim t_2 + t_3$ being the temporal period. In the analytical case, the maximum and minimum values of v are calculated from (6.53) and (6.54), the wave speed $\dot{s}_0^{(1)}$ is found from (6.34) and (6.35), and t_1 to t_3 are given by the integrals (6.46), (6.62), and (6.63).

numerical solution and phase plane for $\varepsilon = 0.001$ are shown in Figures 6.3 and 6.8, and similar plots for $\varepsilon = 0.0001$ can be seen in Figures 6.9 and 6.10, which can be compared with Figure 6.11, where the various regions in the full asymptotic solution as $\varepsilon \to 0$ are

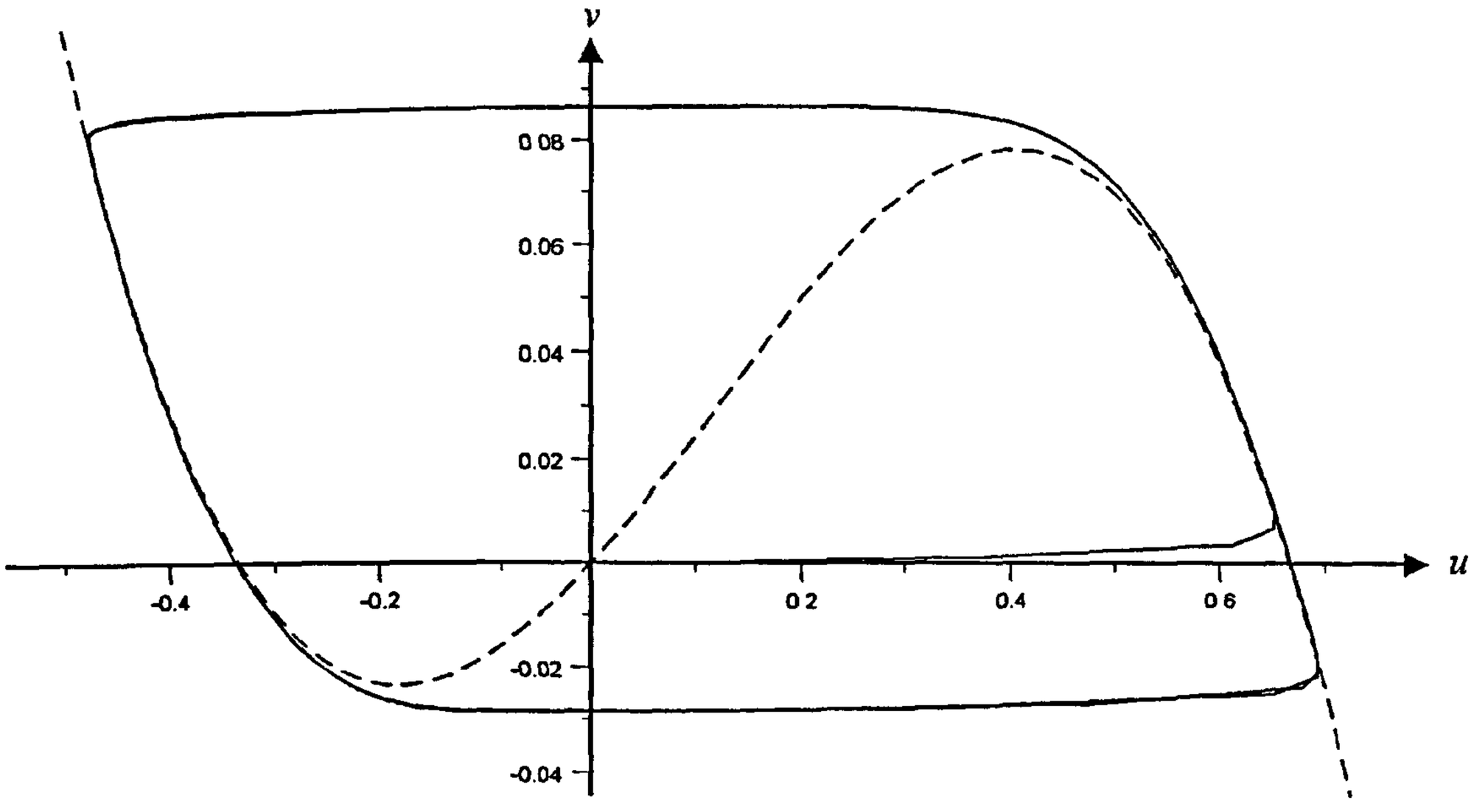

Figure 6.8: Phase plot for the numerical solution in Figure 6.3 ($\epsilon = 0.001$, $a_1 = 1/3$, $a_2 = 2/3$).

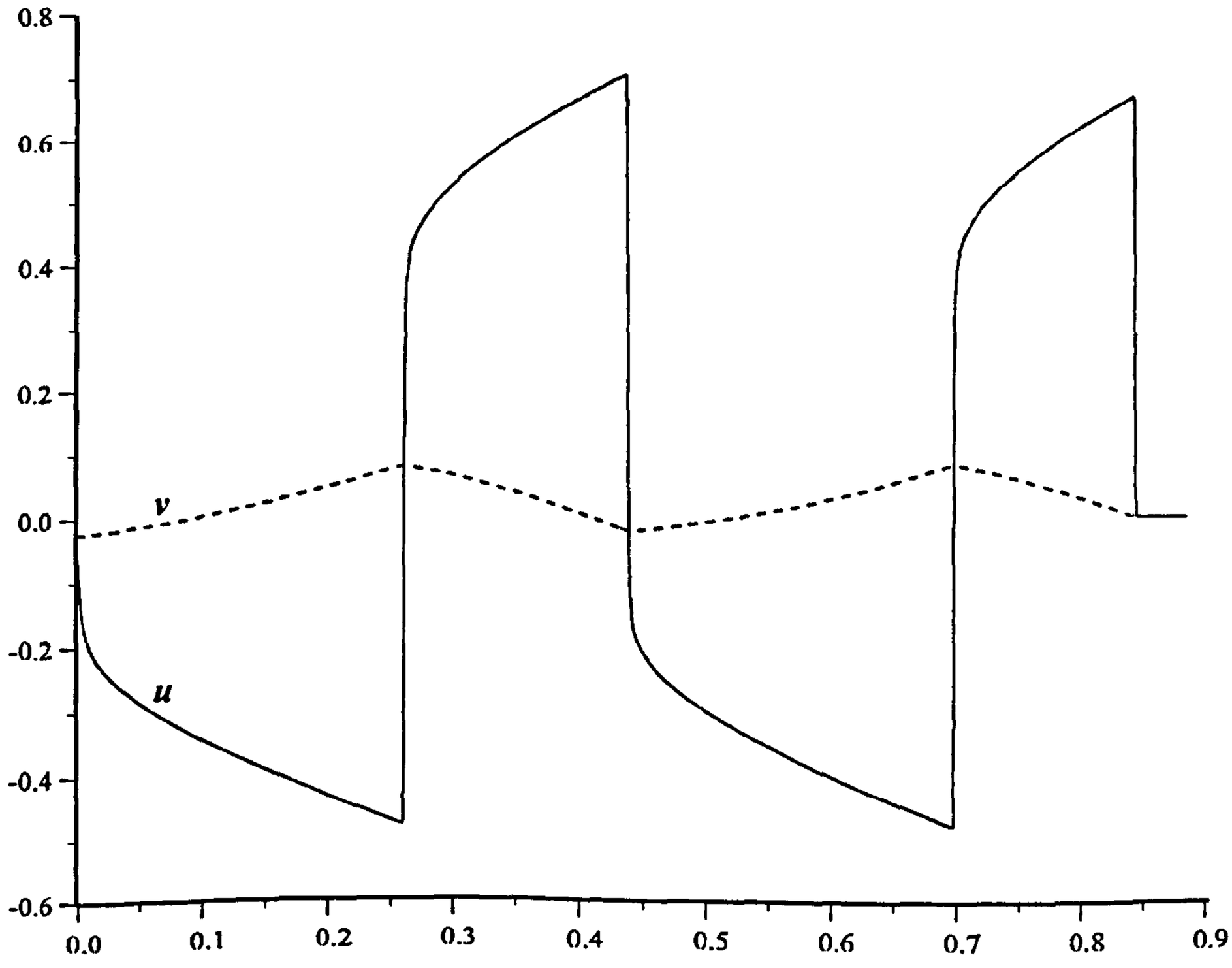

Figure 6.9: Numerical solution for $\epsilon = 0.0001$, $a_1 = 1/3$, $a_2 = 2/3$.

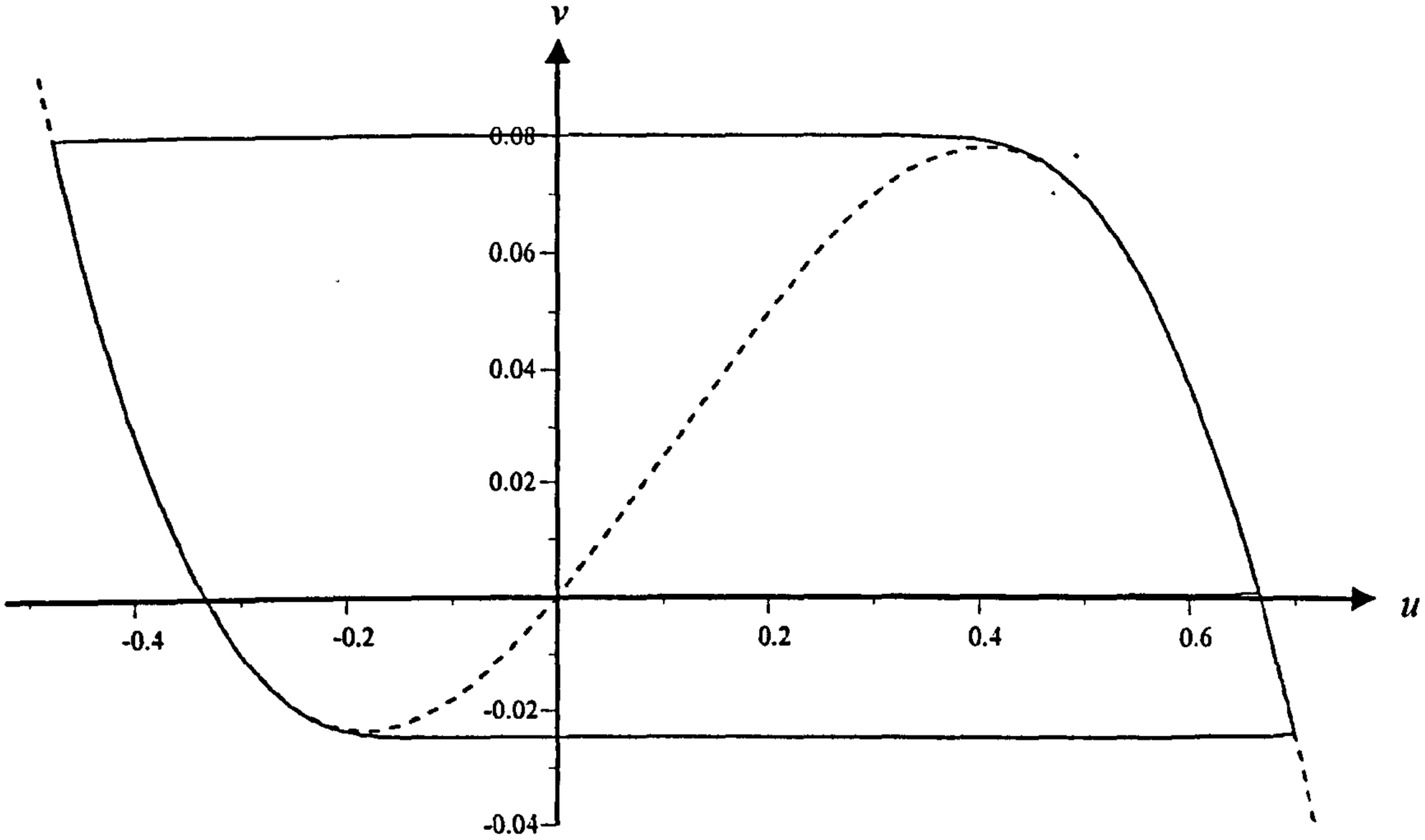

Figure 6.10: Numerical phase plane for $\varepsilon = 0.0001$, $a_1 = 1/3$, $a_2 = 2/3$, corresponding to the solution in Figure 6.9.

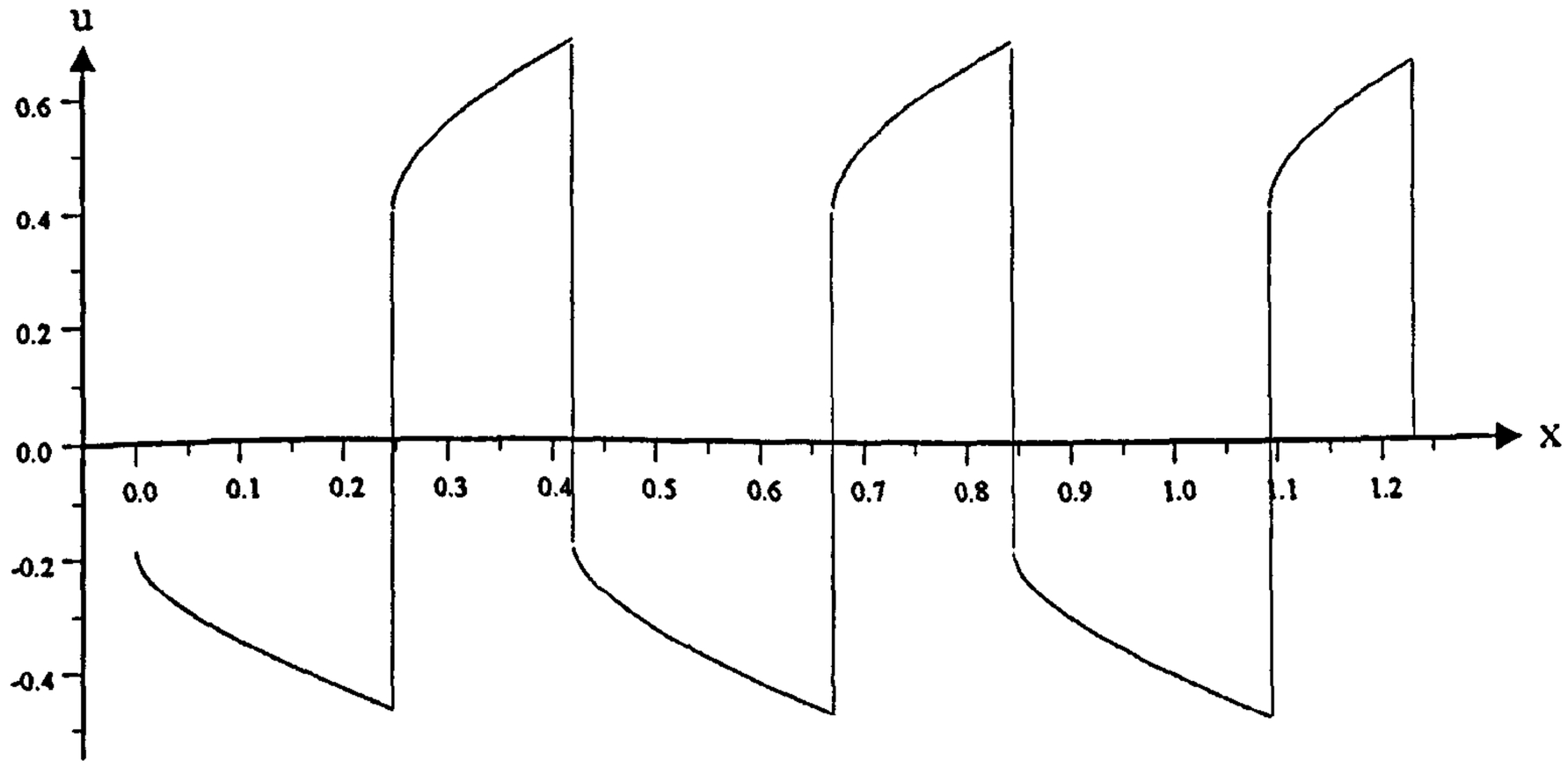

Figure 6.11: Asymptotic solution to (6.3) for $a_1 = 1/3$, $a_2 = 2/3$.

shown. It can be seen that the numerically-obtained front speeds compare very well with the asymptotic value; however, the maximum/minimum for v obtained numerically are larger/smaller than the analytical values, and lead to slightly larger X_i and t_i. We do observe, however, that the results for $\varepsilon = 0.0001$ are significantly closer to the asymptotic values, and thus infer that $\varepsilon > 0$ has a small effect due to the inner layers; reducing ε even further in the numerical calculations would mitigate the effect, but it is numerically difficult (the computation time becomes too lengthy).

In the above we have considered solutions for small, *positive* initial perturbations to u from the steady state. There are also solutions in which the initial front forces u to become negative (i.e. the initial jump is to the left-hand branch of the cubic $f(u)$). In the range

$$\frac{1}{2} \leq \frac{a_1}{a_2} \leq 2 \tag{6.65}$$

the wave speed will be the same (since we obtain the 'linear' solution in both cases). Outside the range given in (6.65), two distinctly different wave speeds are generally obtained. For $a_1/a_2 < 1/2$, we obtain the 'tanh' wave speed for a positive initial front for u, and the 'linear' speed for a negative initial front; for $a_1/a_2 > 2$, the reverse is generally true (though there are special cases for $a_1 \gg a_2$, which will be discussed below).

6.4 Behaviour for small a_2

Focussing once more on positive initial disturbances in u, we now consider the case where $a_2 \ll a_1$ is small, so that $\dot{s}_{0\,\min}^{(1)} < \dot{s}_{0\,\min}^{(2)}$ (the case for $a_2 \gg a_1$ gives similar results for negative initial disturbances in u). There are two cases to consider, depending on whether the critical point is an unstable spiral (as given by (6.6)) or an unstable node; we must therefore investigate the behaviour as $a_2 \to 0$ for both. In this section, we take $a_1 = 1$ in order to demonstrate the results more easily; no loss of generality is involved.

6.4.1 Critical point is a spiral

From (6.6) with $a_1 = 1$, we know that if

$$\varepsilon > 2 - a_2 - 2\sqrt{1 - a_2} \sim \tfrac{1}{4}a_2^2 \qquad \text{for } a_2 \ll 1, \tag{6.66}$$

then the critical point is an unstable spiral, and our initial front is no longer monotonic increasing. If $\varepsilon > a_2$, we can no longer obtain a limit cycle (see (6.5)); an oscillatory pattern forms behind the front, moving at a different speed. This is a separate problem that will be discussed in Chapter 8.

If (6.5) and (6.66) hold, so that we have an unstable spiral at the origin of the phase plane, then if $\dot{s}_{0\,\min}^{(1)} < \dot{s}_{0\,\min}^{(2)}$, the initial front can 'flip' and become negative when $s_0^{(2)}$ catches up with $s_0^{(1)}$, even if we specify a positive initial perturbation in u. As a result we have a monotone increasing 'tanh' solution with u becoming negative; its minimum wave speed is never smaller than that of the second inner layer (which now occurs at $v = v_-^*$). This behaviour is best demonstrated by the considering the 'phase plane'; a numerical example is shown in Figure 6.12 for $a_2 = 0.05$. It can be seen how the trajectory swings round to become a 'tanh' wave as time progresses. The corresponding numerical solution for u is shown in Figure 6.13, and we can observe how the small, positive initial front slowly disappears as the profile evolves. We thus infer that for large t, the front speed is given by

$$\dot{s}_0^{(1)} = \frac{1 + 2\,a_2}{\sqrt{2}} \qquad 0 < a_2 \lessapprox 2\sqrt{\varepsilon} \tag{6.67}$$

using (6.34) with $a_1 \to a_2$, $a_2 \to 1$ (due to the negative instead of positive front); the upper limit on a_2 in (6.67) is only approximate since at this point $\varepsilon = O(v_{\max})$ and the previous asymptotic analysis breaks down (as considered below). The wave speed given by (6.67) compares well with numerical results.

6.4.2 Critical point is a node

In this case, u remains positive at the initial front; 'flipping' does not occur. However, it is also apparent that with a_2 small, so $v_{\max}$ is small; we have a problem with *two* small parameters. If $\varepsilon = O(v_{\max})$, then as mentioned above our asymptotic analysis

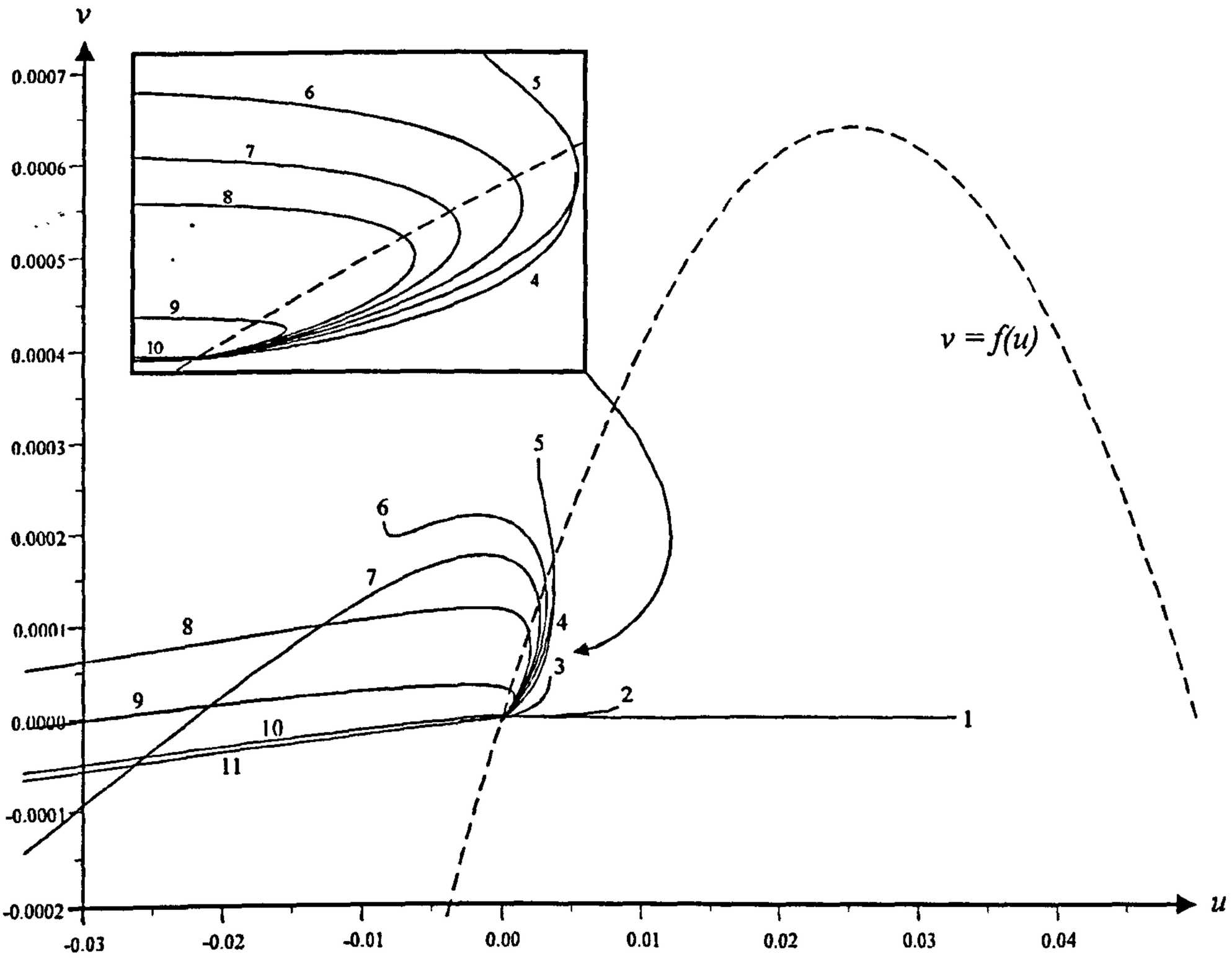

Figure 6.12: Numerical 'phase plane' for $\varepsilon = 0.001$, $a_1 = 1$, $a_2 = 0.05$. The numbers on the curves corresponds to successive times, as shown on the solution curves in Figure 6.13.

breaks down (there is no opportunity for the first outer layer to form); we now consider separately the cases where $\varepsilon = O(v_{max})$ and $\varepsilon \ll v_{max} \ll 1$.

6.4.2.1 $\varepsilon = O(v_{max})$

Although our previous asymptotic analysis is no longer valid when $\varepsilon = O(v_{max})$, we can still apply our numerical approach. We note from (6.53) and (6.54) that

$$v_{max} \sim \frac{a_2^2}{4}$$

which gives us the size of ε in terms of a_2 for the type of behaviour detailed below to occur.

Numerically, we find that the speed of the initial front increases until it reaches the

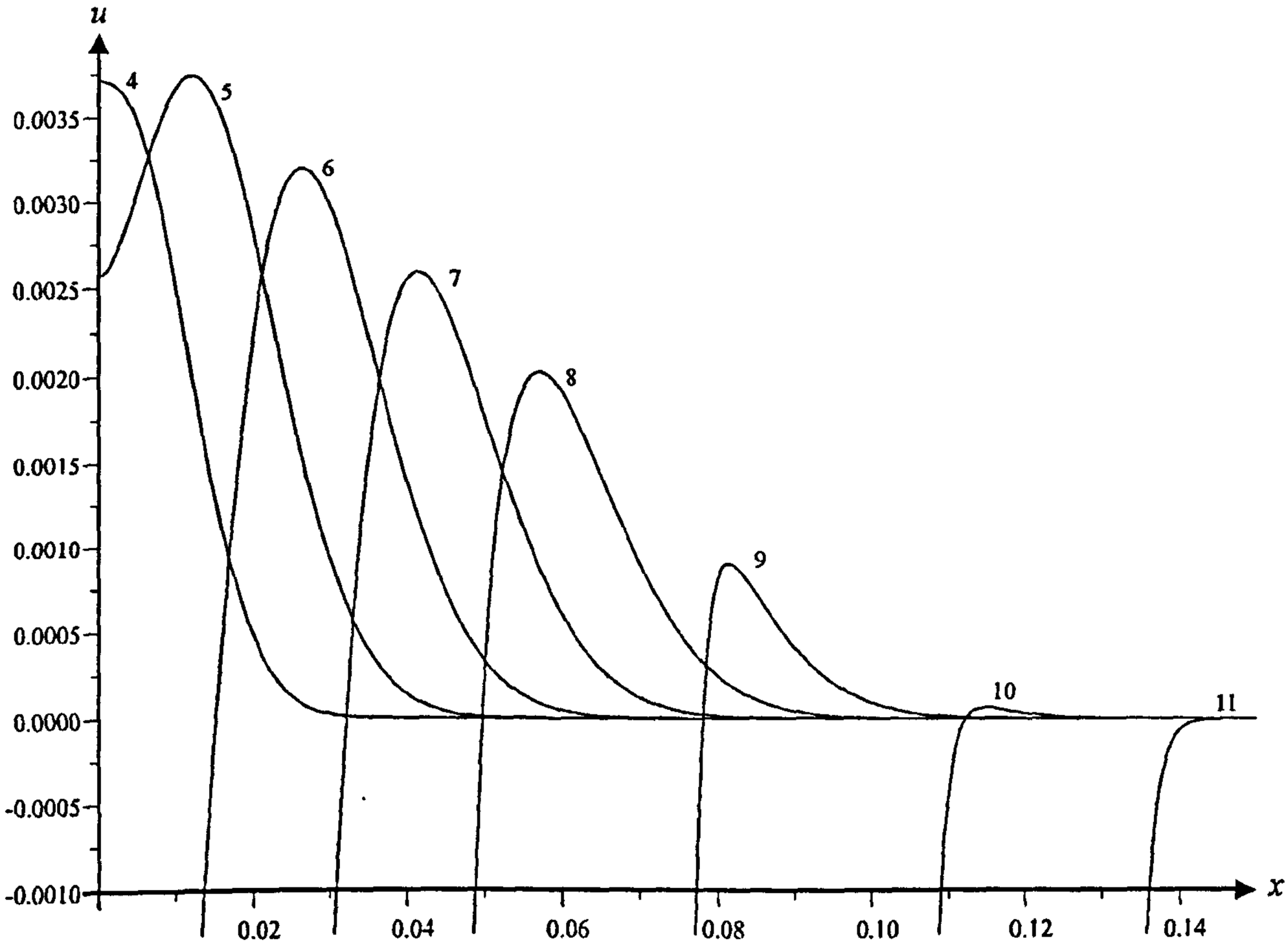

Figure 6.13: Numerical solution for $u(x,t)$ for $\varepsilon = 0.001$, $a_1 = 1$, $a_2 = 0.05$. The numbers on the curves represent successive times, and correspond to the trajectories in the phase plane in Figure 6.12.

value of $\dot{s}_{0\,\min}^{(2)}$; we can therefore infer from (6.59) that for large t

$$\dot{s}_0^{(1)} \sim (1 + \tfrac{1}{2}a_2)/\sqrt{2}, \qquad \varepsilon = O(a_2^2/4). \tag{6.68}$$

An example of the numerical solutions is shown in Figure 6.14.

It is worth noting that for $a_2 > (7-3\sqrt{5})/2 \approx 0.146$, the minimum speed of the front $\dot{s}_{0\,\min}^{(1)}$ obtained from the asymptotic analysis is in fact larger than that of the second inner layer ($\dot{s}_{0\,\min}^{(2)}$); although the preceding asymptotic analysis may *not* hold here, we may still expect the limit cycle to propagate at speed $\dot{s}_{0\,\min}^{(1)}$. In practice, numerical results give a front speed somewhere between $\dot{s}_{0\,\min}^{(1)}$ and $\dot{s}_{0\,\min}^{(2)}$ (see Figures 6.15 and 6.16); in addition we note that in this regime the value of ε is too high for the asymptotic analysis to be realistically viable for *any* a_2 (the change in v during the 'fast' transitions between the outer layers is far greater than $O(\varepsilon)$; see the phase plane in Figure 6.16).

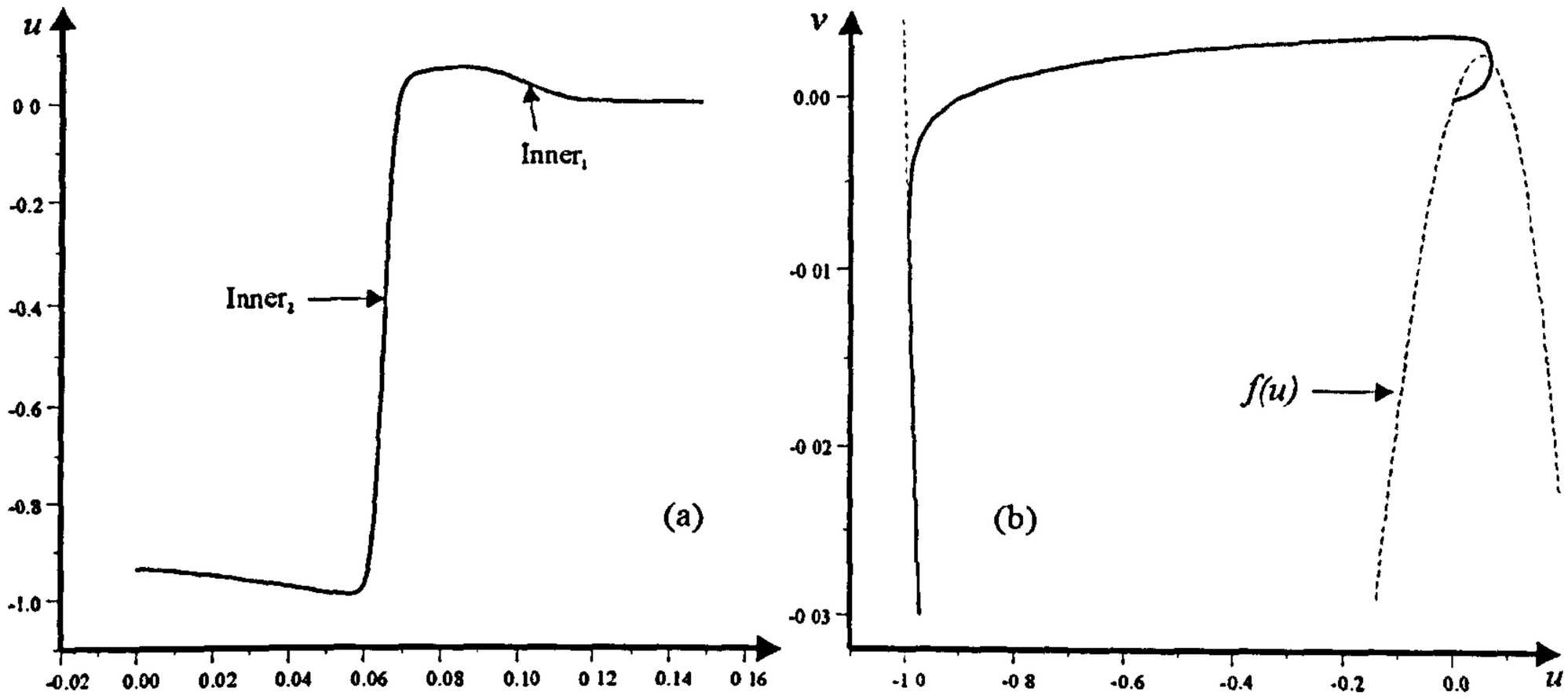

Figure 6.14: (a) Initial fronts for u for $a_1 = 1$, $a_2 = 0.1$, $\varepsilon = 0.001$. (b) 'Phase plane' for (a). Numerically, we obtain a large time leading front speed of $c = 0.739$, which shows excellent agreement with (6.68), which gives $\dot{s}^{(1)} = 0.742$.

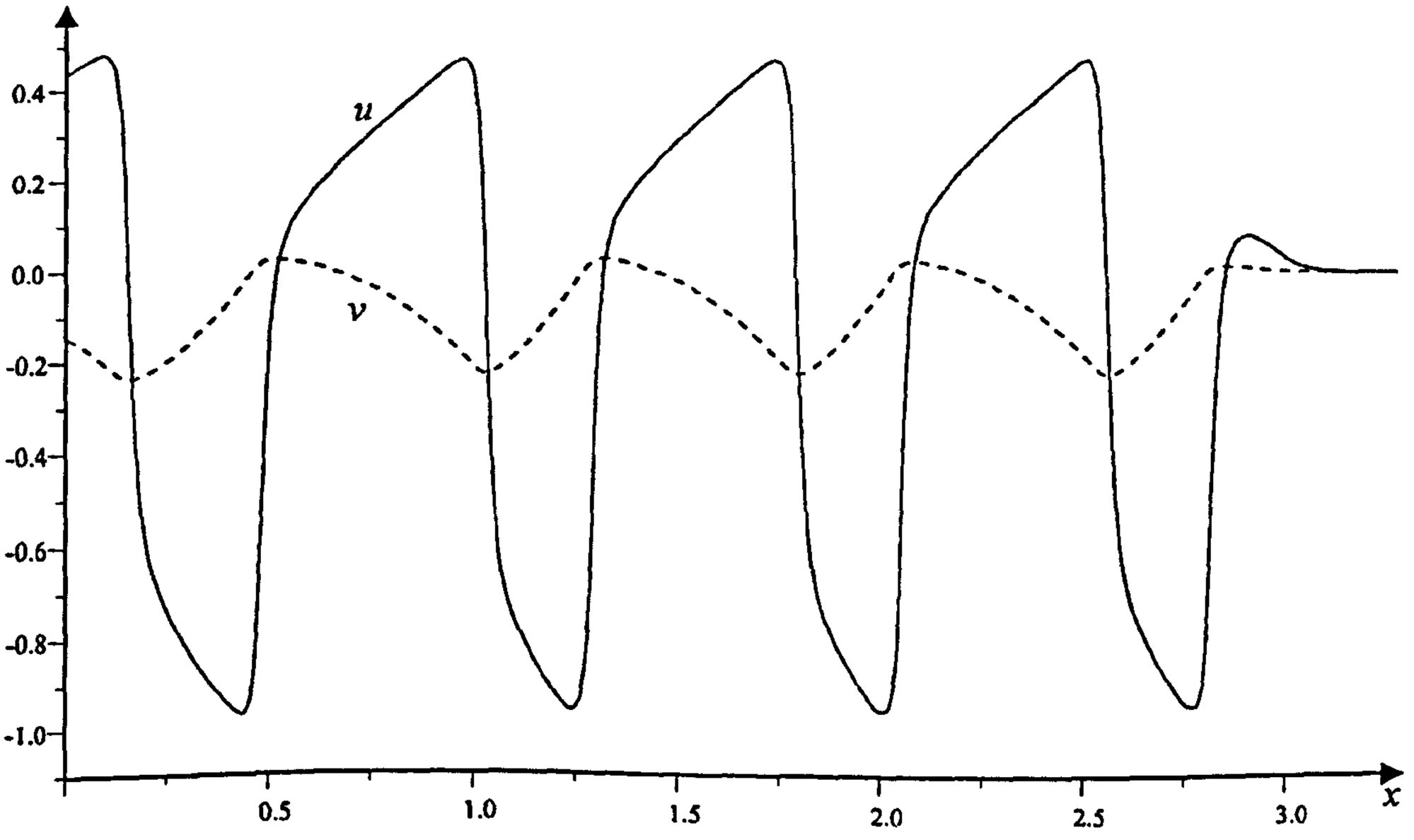

Figure 6.15: Numerical solution for $a_1 = 1$, $a_2 = 0.2$, $\varepsilon = 0.01$.

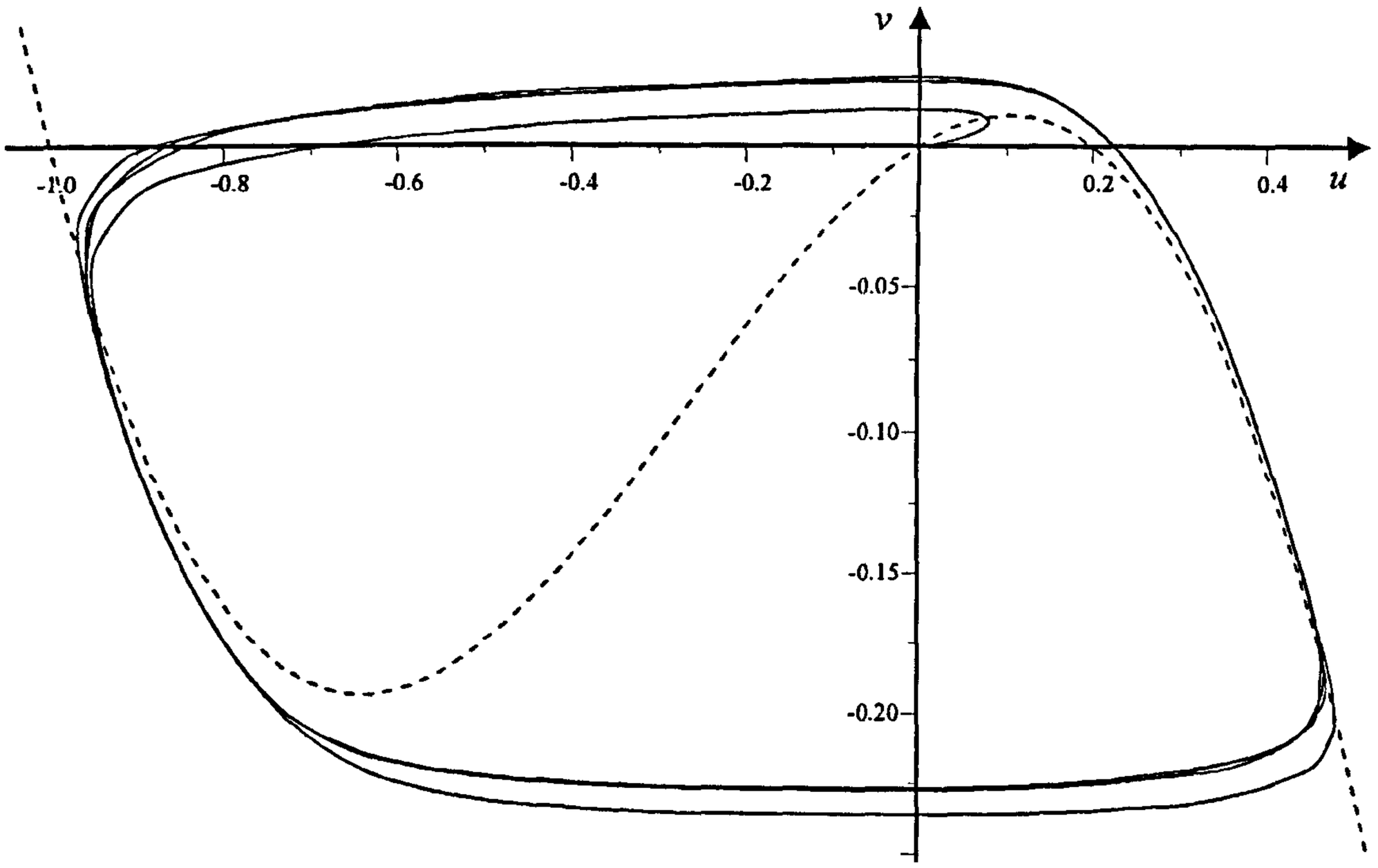

Figure 6.16: 'Phase plane' for the numerical solution in Figure 6.15; $a_1 = 1$, $a_2 = 0.2$, $\varepsilon = 0.01$.

6.4.2.2 $\varepsilon \ll v_{\max}$

With $\varepsilon \ll v_{\max}$, it is still possible for the first two inner regions and the first outer region to be distinct; this implies that our initial (linear) wavefront will travel with a fixed speed that will *not* increase, unlike in the case for $\varepsilon = O(v_{\max})$ above. The second inner layer must therefore somehow decrease *its* speed, and slow down to that of the initial front. This is obviously impossible at $v_+^* = v_{\max}$, where the wave speed is too fast; $c_{\min} = \dot{s}_{0\,\min}^{(2)}$ is already the minimum possible value. If we study the numerical solution in Figure 6.17, we can see that the second inner 'catches up' with the first (the front) as the evolution progresses. This has the effect of decreasing v_+^* (the maximum attained value of v_0 in the outer region, at which the second inner transition occurs), as can be seen in the phase plane diagram for Figure 6.17 in Figure 6.18. In turn this has the desired effect of lowering $\dot{s}_0^{(2)}$, which can be seen more clearly in Figures 6.19–6.20, where we plot $\dot{s}_{0\,\min}^{(1)}$ (the 'linear' front speed) and $\dot{s}_0^{(2)}$ against v^* for $a_2 = 0.12$; we expect the speed of the second inner layer to reduce from $\dot{s}^{(2)} \approx 0.753$ ($\dot{s}_{0\,\min}^{(2)}$) to $\dot{s}^{(2)} \approx 0.693$ ($\dot{s}_{0\,\min}^{(1)}$,

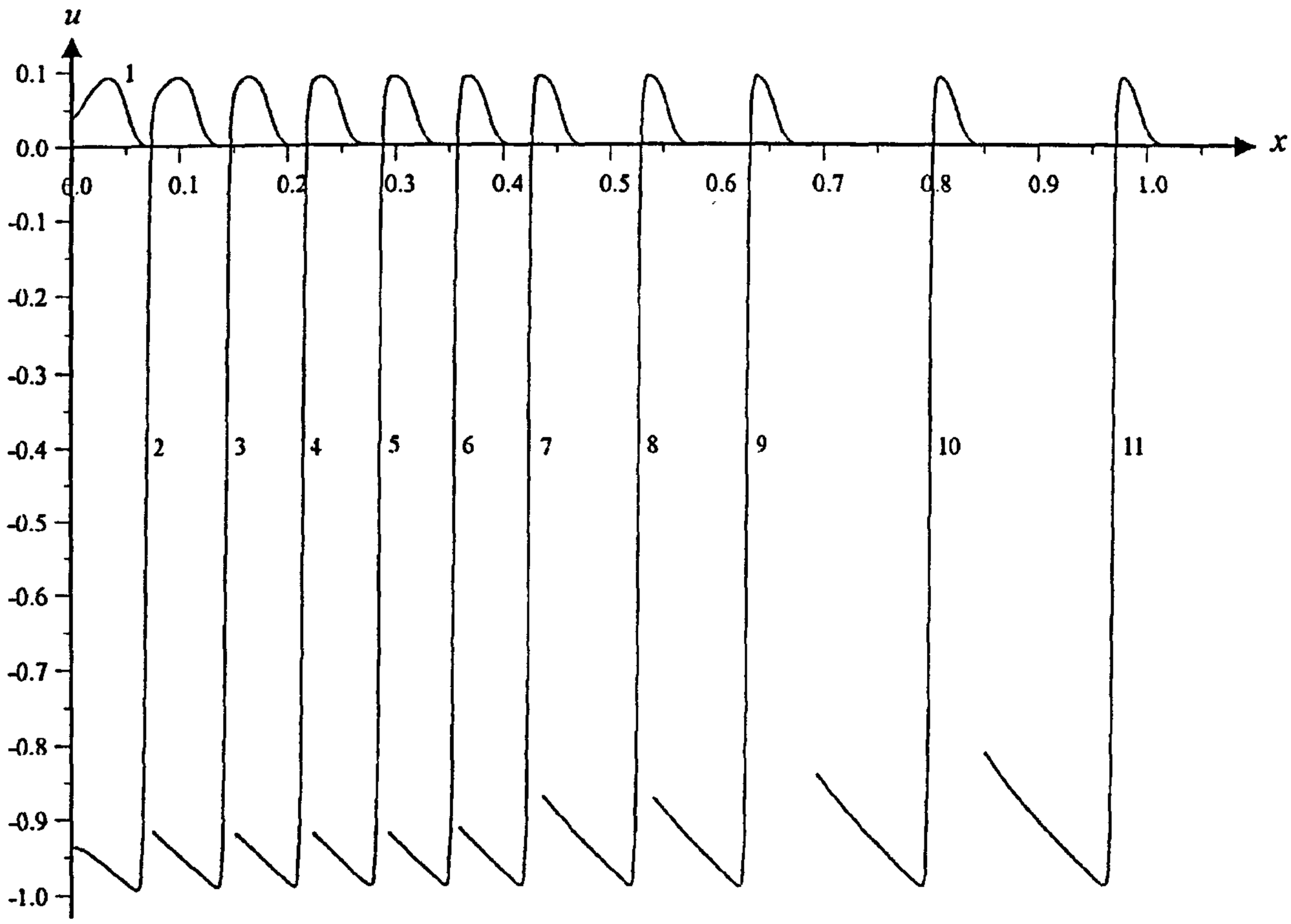

Figure 6.17: Numerical solution for u for $\varepsilon = 0.0001$, $a_1 = 1$, $a_2 = 0.12$. The numbers represent successive evolutions of the front, which are *not* evenly spaced in t (the fronts shown are chosen to demonstrate the phase plane behaviour in Figure 6.18); the initial front moves at a fixed speed of $c \approx 0.693$.

the speed of the linear initial front), and this indeed is observed. We note that we now have a stable-stable connection, and thus the wave speed for each v^* is unique (we do not have a range, as before). It can be seen in Figure 6.20 that for the second inner layer travelling at the same speed as the initial front, v^* should settle down at a value of $v_+^* \approx 0.00298$; this compares well with the numerically obtained value of $v_+^* \approx 0.0028$ in Figure 6.18.

Again, we note that there is a well-defined region in which this type of behaviour can occur; if $a_2 < 5 - \sqrt{24} \approx 0.101$, then $\dot{s}_{0\,\mathrm{min}}^{(2)}$ is always larger then $\dot{s}_{0\,\mathrm{min}}^{(1)}$ for all values of $v^* > 0$. This is demonstrated by the plot of $\dot{s}_{0\,\mathrm{min}}^{(1)}$ (the 'linear' front speed) and $\dot{s}_{0\,\mathrm{min}}^{(2)}$ against v^* for $a_2 = 0.07$ in Figure 6.21; when v^* is reduced to zero, the initial linear front is annihilated, and a negative 'tanh' wave becomes the leading front. Here a relatively

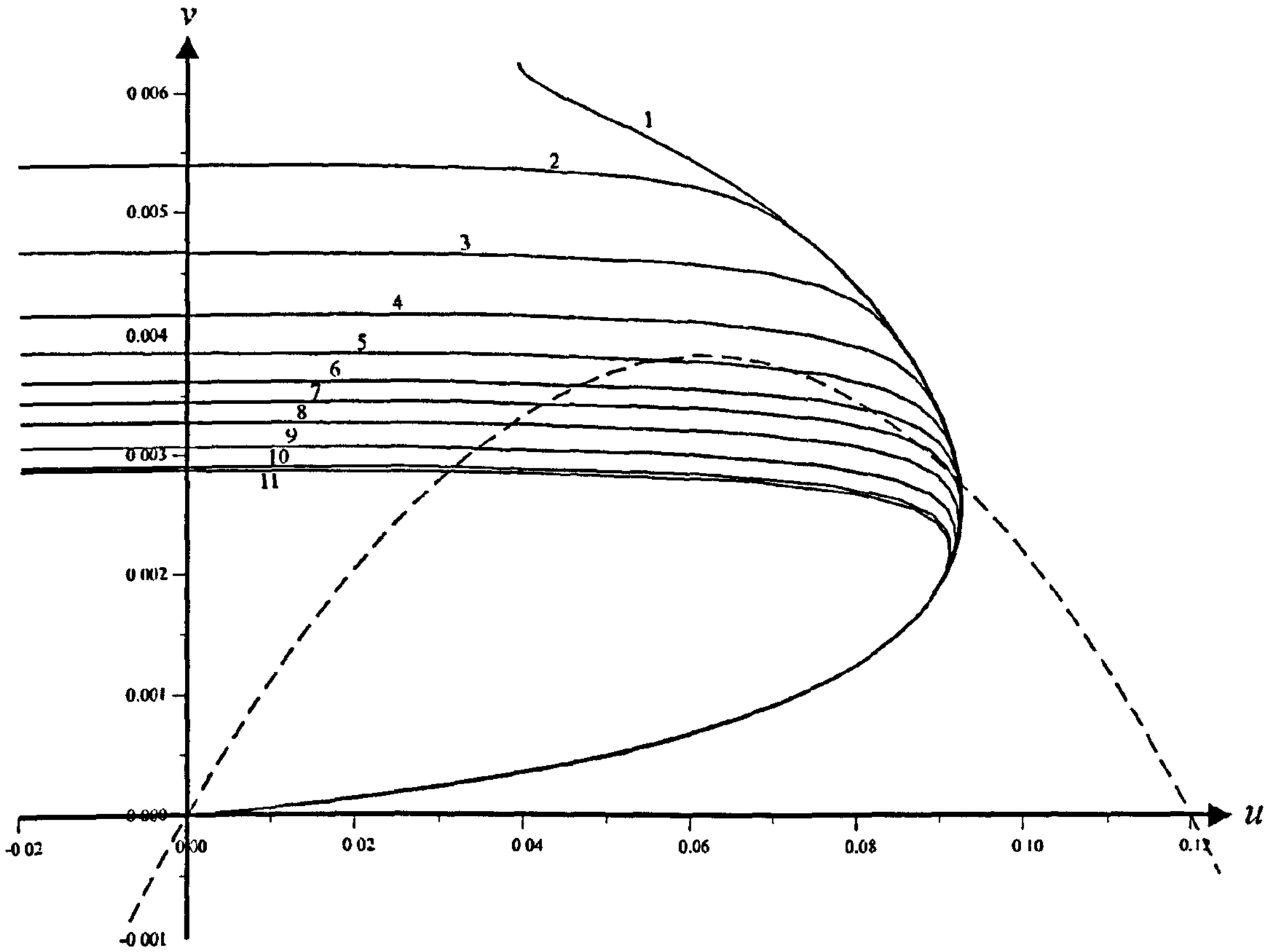

Figure 6.18: 'Phase plane' for $\varepsilon = 0.0001$, $a_1 = 1$, $a_2 = 0.12$. The numbers denote successive evolutions, and correspond to the solution curves in Figure 6.17. The initial trajectories are too high due to $\varepsilon > 0$; reducing ε would mitigate this, but the problem becomes numerically difficult.

big leap in the wave speed is involved; from Figure 6.21, we can see that the front speed will increase from $c \approx 0.53$ to $c \approx 0.80$ when we reach $v^* = 0$. The front annihilation has the effect of removing the first outer and second inner layer from our asymptotic analysis. The numerical solution for $\varepsilon = 0.0001$, $a_2 = 0.07$ and its associated 'phase plane' are shown in Figures 6.22–6.23.

An interesting point to note is that the 'new' second inner layer (the third inner layer in the previous asymptotic analysis), as shown in curve 7 in Figure 6.22, forms with no knowledge of the changes at the initial front, and thus has a wave speed *slower* than that of the new initial front. Figure 6.24 shows how the positions of the first three inner layers vary in time. It is found that a new inner layer continues to move slower than those in front until the outer layer preceding it reaches a critical width (determined below),

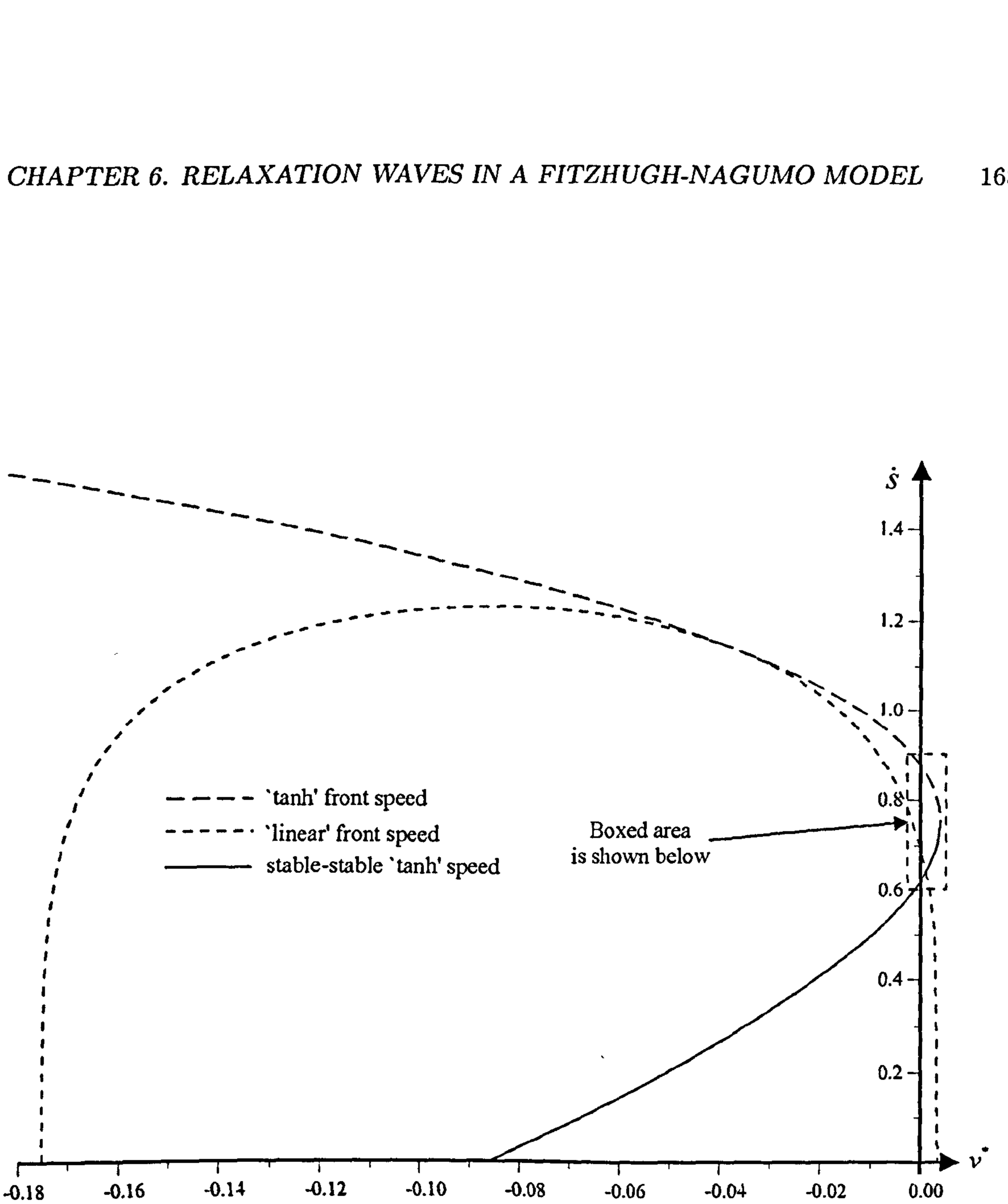

Figure 6.19: Plot of $\dot{s}$ against v^* ($a_1 = 1$, $a_2 = 0.12$) for the 'linear' front (obtained from (6.12)-(6.17) and (6.25)-(6.32)), the negative 'tanh' initial front (obtained from (6.12)-(6.17) and (6.18)-(6.24) with $a_1 \Leftrightarrow a_2$) and the stable-stable 'tanh' solution (obtained from the solution of (6.52) where $v^* = v_+^* \neq v_{max}$). We recall from Section 6.3.3 that the 'initial' minimum speed for the second inner layer occurs at $v^* = v_{max}$, and thus occurs at the limiting value of the unstable-stable connection; this speed is inappropriate here at later times (see Figure 6.20).

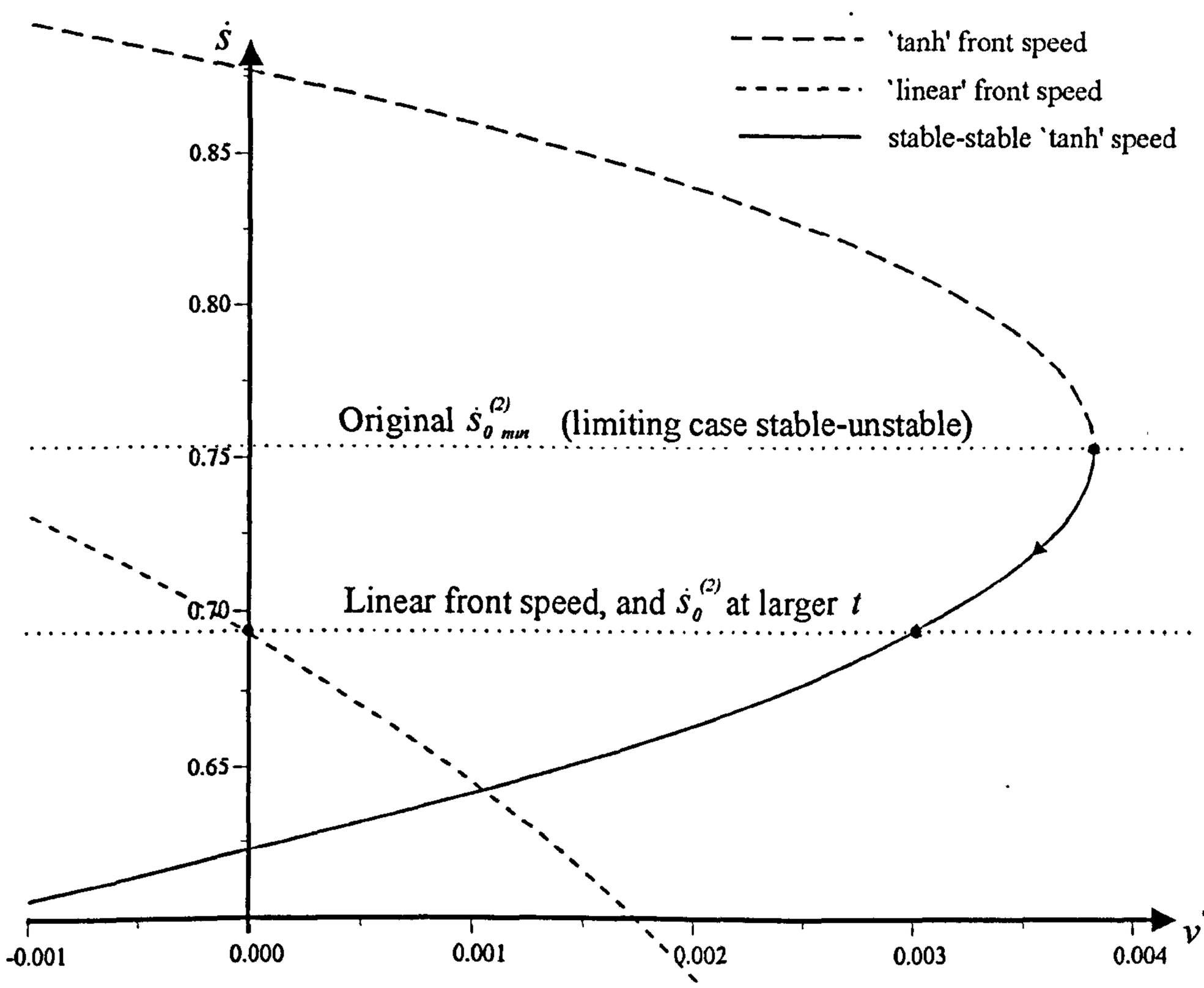

Figure 6.20: Close-up of Figure 6.19. We observe that the 'initial' minimum speed for the second inner layer of $\dot{s}^{(2)} \approx 0.753$ is greater than the initial front speed of $\dot{s}^{(1)} \approx 0.693$, obtained from the 'linear' curve at $v^* = 0$. The second inner layer thus slows down to the front speed by reducing its maximum value v^*. Note that we now have a stable-stable connection in the phase plane, and $\dot{s}_0(v^*)$ is now unique (rather than being greater than or equal to some minimum value, as was the case for $v^* = v_{max}$ or $v^* = v_{min}$).

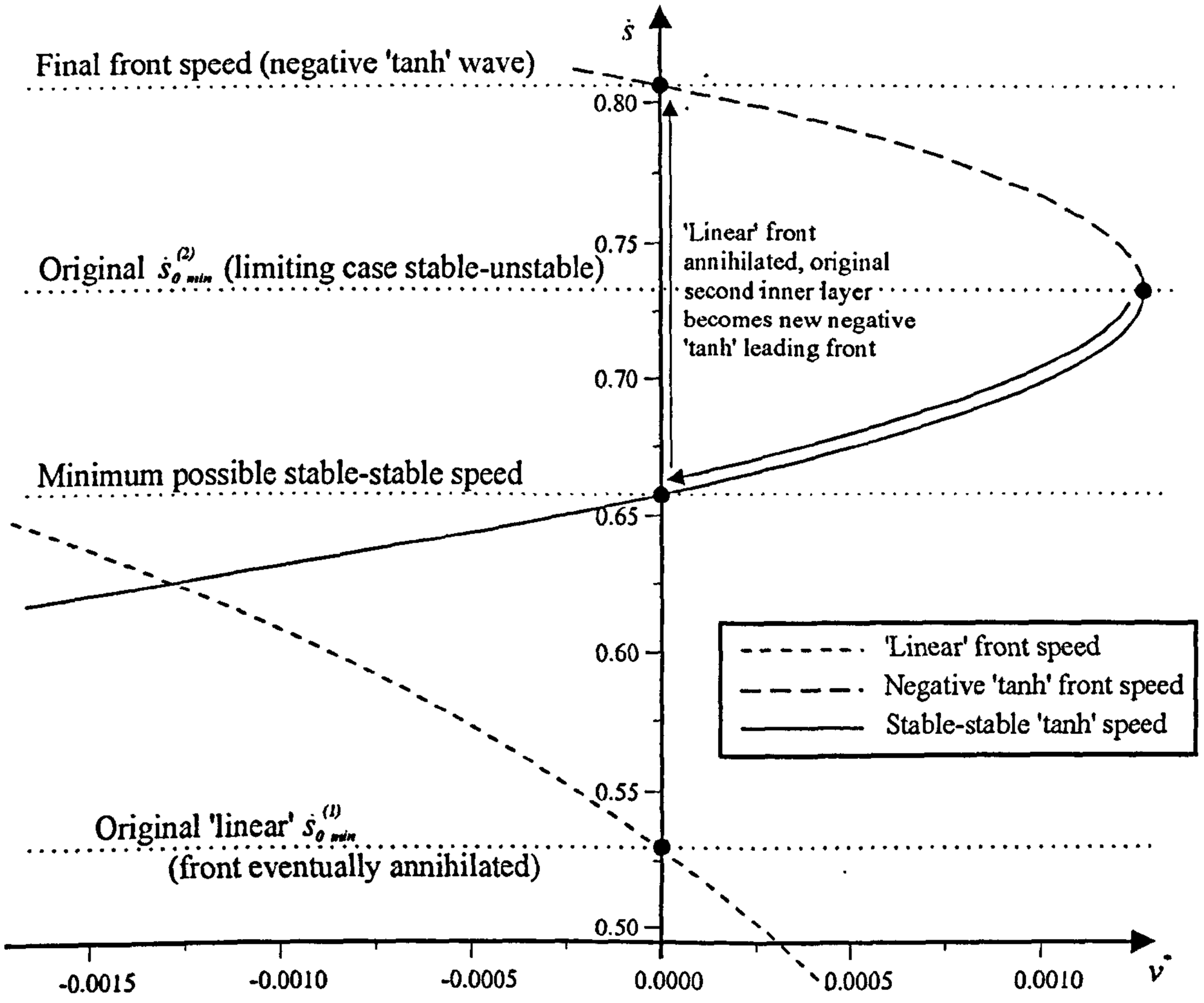

Figure 6.21: Plot of $\dot{s}_0$ against v^* ($a_1 = 1$, $a_2 = 0.07$). We can distinguish this case from that of Figure 6.20 using a simple geometric criterion, i.e. from the position of the intersection of the 'linear' and 'tanh' wave speed curves; here this occurs for $v^* < 0$, whereas in Figure 6.20 it occurs for $v^* > 0$. The second inner layer decreases its speed from $\dot{s}_0^{(2)} \approx 0.73$ to $\dot{s}_0^{(2)} \approx 0.66$, at which point $v^* = 0$. As this speed is still faster than that of the leading front ($\dot{s}_{0\,\mathrm{min}}^{(1)} \approx 0.53$), which is annihilated, a 'tanh' front forms as the leading front, with u negative, travelling at $\dot{s}_0 \approx 0.80$; note that whilst the 'tanh' curve represents a stable-stable connection for the second inner layer above $\dot{s}_{0\,\mathrm{min}}^{(2)} \approx 0.73$, it is an *unstable*-stable connection for the leading front.

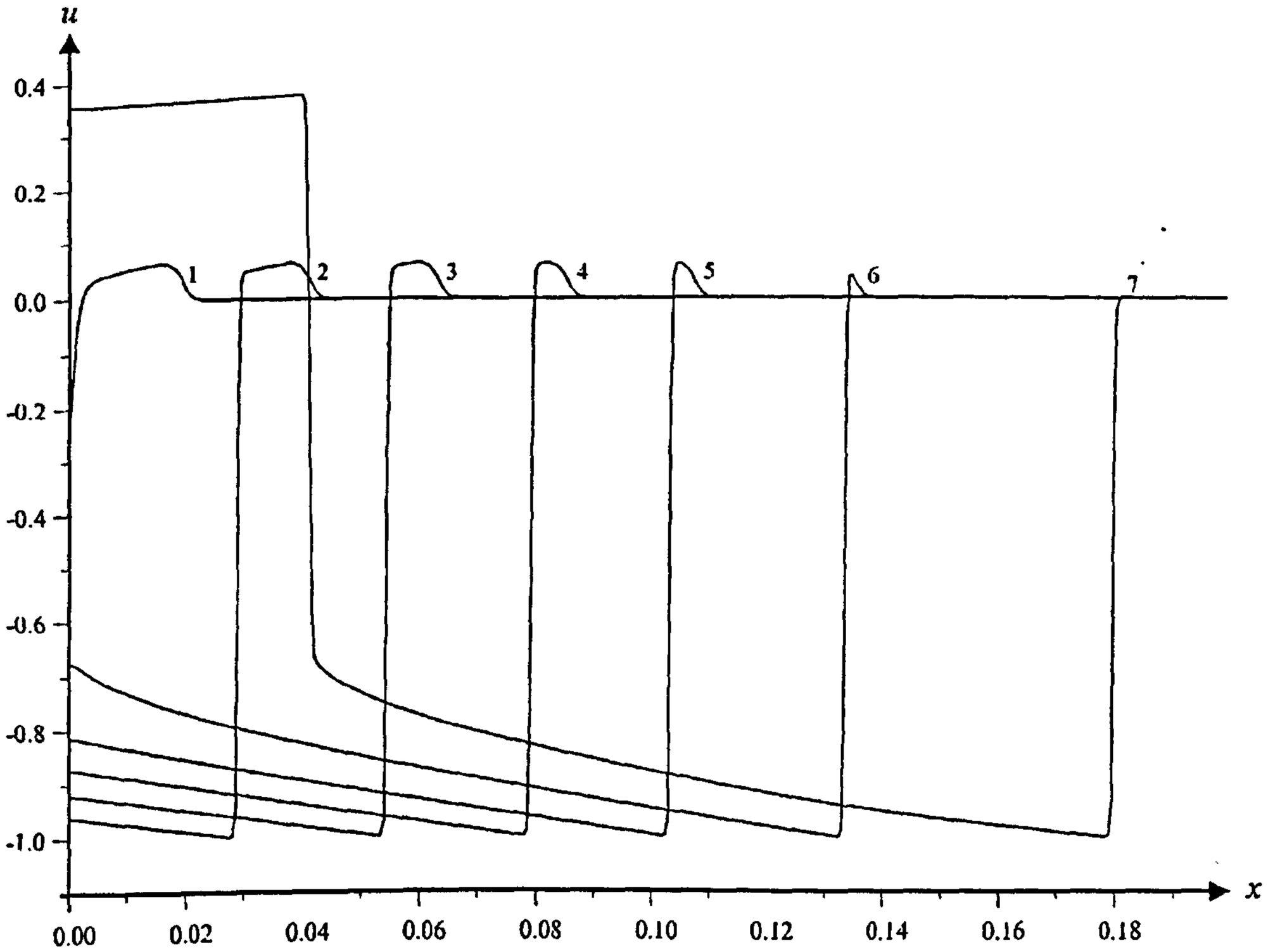

Figure 6.22: Numerical solution for u for $\varepsilon = 0.0001$, $a_1 = 1$, $a_2 = 0.07$; numbers on curves correspond to successive times.

when the new inner layer rapidly increases its speed to the same value as the inner layers in front. This is because the new inner layer initially matches into the outer solution in front at $v < v_{\max}$ (or $v > v_{\min}$, depending on which inner layer we are considering); it is thus a stable-stable connection in the phase plane. The inner layer attempts to speed up by increasing (decreasing) its value of v_+^* (v_-^*) (see Figure 6.25); essentially it is the reverse of the behaviour for the leading front, where v_+^* decreases (see, for example, Figure 6.18). When the maximum (minimum) value of v_+^* (v_-^*) is attained (and the connection thus becomes the limiting unstable-stable case), the width of the preceding outer layer reaches its maximum value (which can be determined from (6.46), (6.62) or (6.63) and the relation $X_p = \dot{s}_0^{(1)} T_p$ as required), causing the new inner layer to rapidly increase its speed to that of the preceding layers.

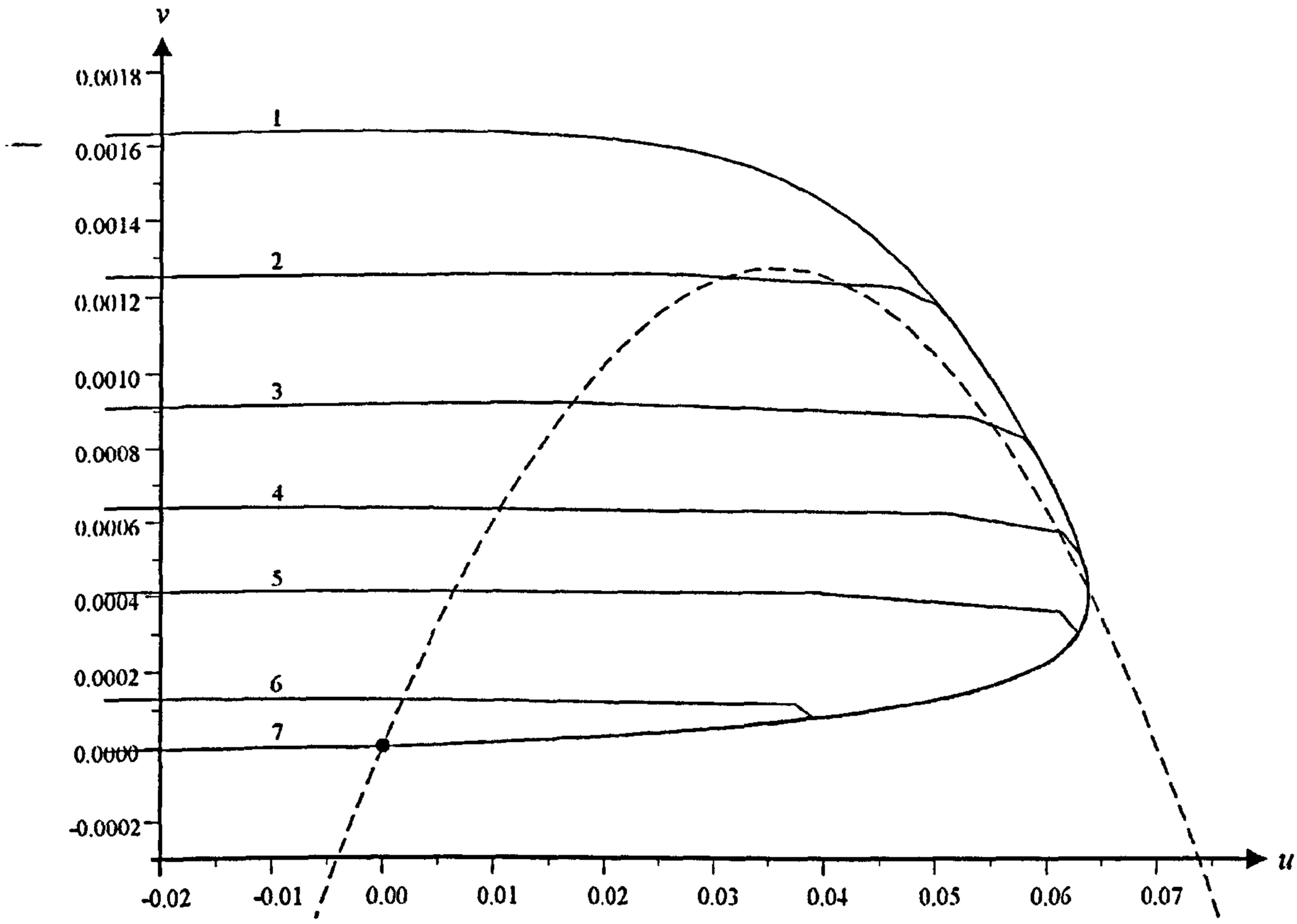

Figure 6.23: 'Phase plane' for $\varepsilon = 0.0001$, $a_1 = 1$, $a_2 = 0.07$; numbers correspond to solutions in Figure 6.22.

We thus conclude that

$$\dot{s}^{(1)} \sim \frac{1 + 2\,a_2}{\sqrt{2}} \qquad 0 < a_2 \leq 5 - \sqrt{24} \tag{6.69}$$

$$\dot{s}^{(1)} \sim 2\sqrt{a_2} \qquad 5 - \sqrt{24} < a_2 < 2 \tag{6.70}$$

as $\varepsilon \to 0$; a plot of the wave speed $\dot{s}_0^{(1)}$ against a_2 is shown in Figure 6.26.

It is worth stating that although for this particular model such behaviour is confined to a relatively small region in parameter space, there is no reason why it could not be observed over much larger parameter regimes for other kinetics; our model is merely an example which demonstrates its possibility.

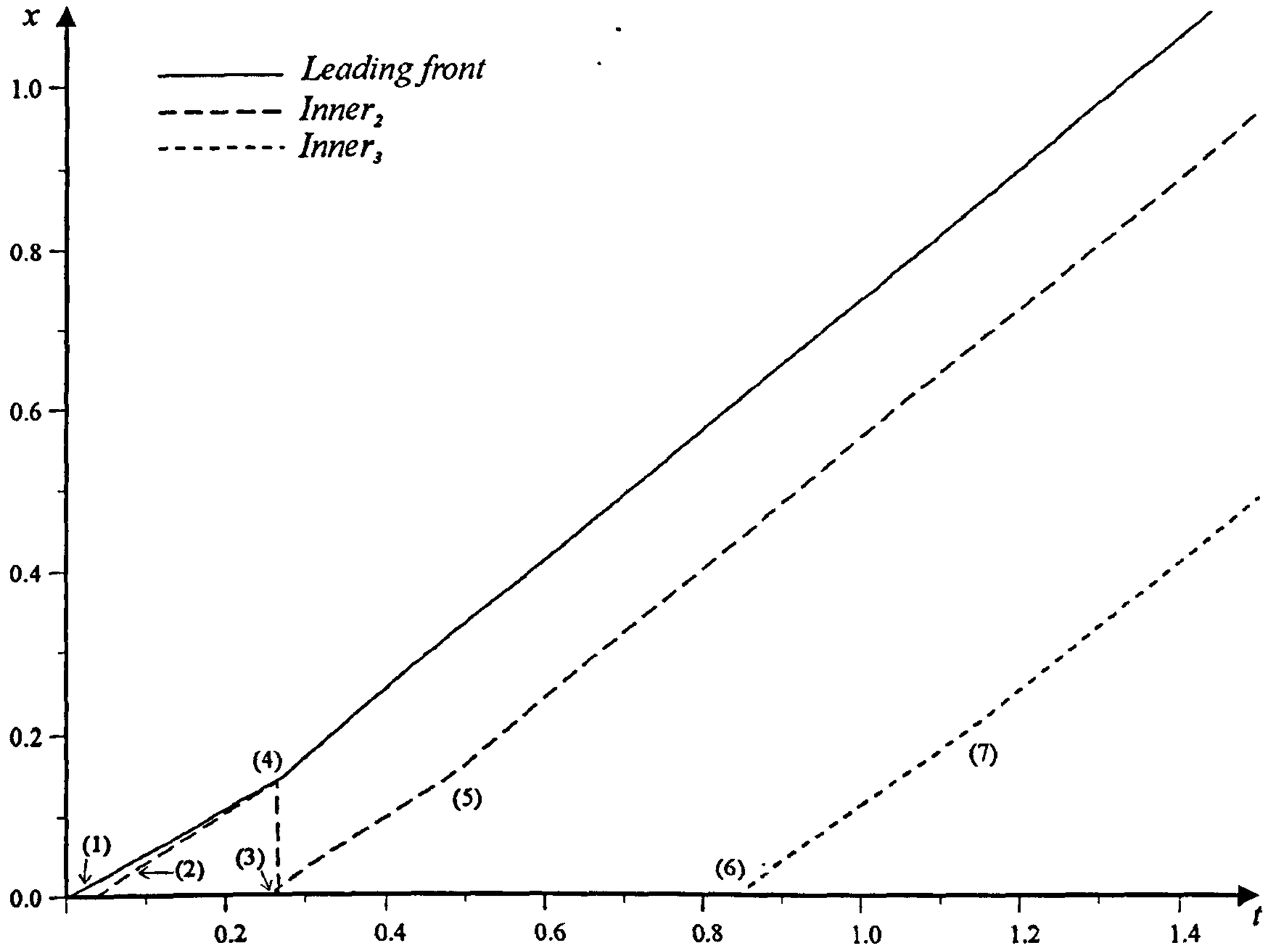

Figure 6.24: Plot of x against t for the position of the first three inner layers for $\epsilon = 0.0001$, $a_1 = 1$, $a_2 = 0.07$; values are obtained at $|u| = 0.05$ (initial front) and $u = 0$ (subsequent inner layers). We obtain wave speeds from the gradient of the curves. (1) Initial linear front forms, $\dot{s}_0^{(1)} \approx 0.53$. (2) Second inner layer forms, $\dot{s}_0^{(2)} \approx 0.65$. (3) Third inner layer forms. (4) Positive initial front is annihilated; second inner becomes a negative 'tanh' initial front, $\dot{s}_0^{(1)} \approx 0.80$. Third inner layer is now the second inner layer. (5) Speed of the second inner layer suddenly jumps to $\dot{s}_0^{(2)} \approx 0.80$, the same speed as the initial front. (6) New third inner layer forms, $\dot{s}_0^{(3)} \approx 0.65$. (7) Third inner layer speed suddenly increases to $\dot{s}_0^{(3)} \approx 0.80$.

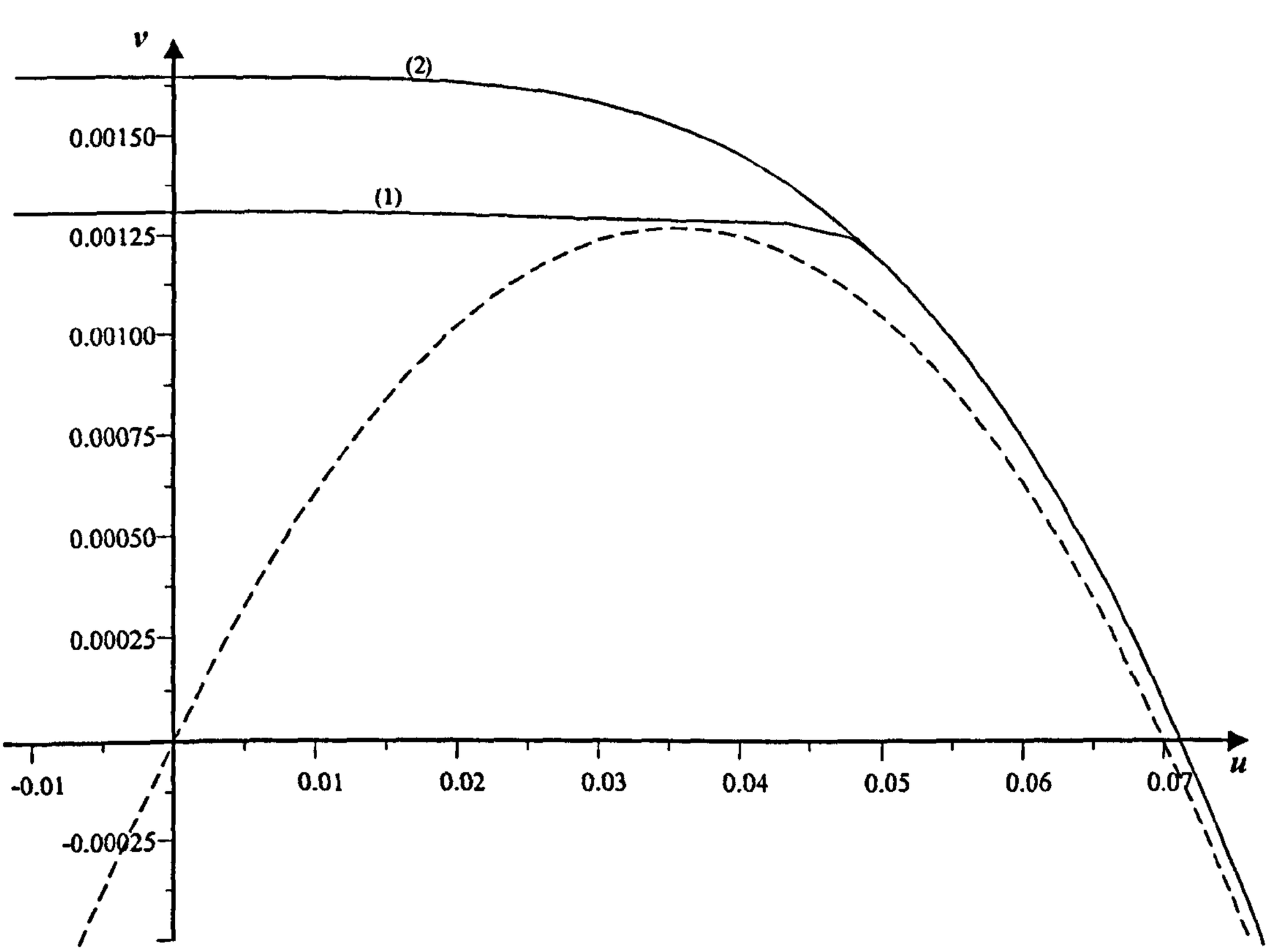

Figure 6.25: 'Phase plane' for Figure 6.24 ($\varepsilon = 0.0001$, $a_1 = 1$, $a_2 = 0.07$), showing the second inner layer only *after* the initial leading front has been annihilated. Curve (1) shows this inner layer soon after forming, where its speed is slower than the wave in front of it; it speeds up by increasing its value of v_+^* (curve (2)). The second curve should theoretically have a maximum value equal to the maximum value of the $v = f(u)$ nullcline (and curve (1) should lie below it), but this requires a smaller value of ε which is numerically difficult.

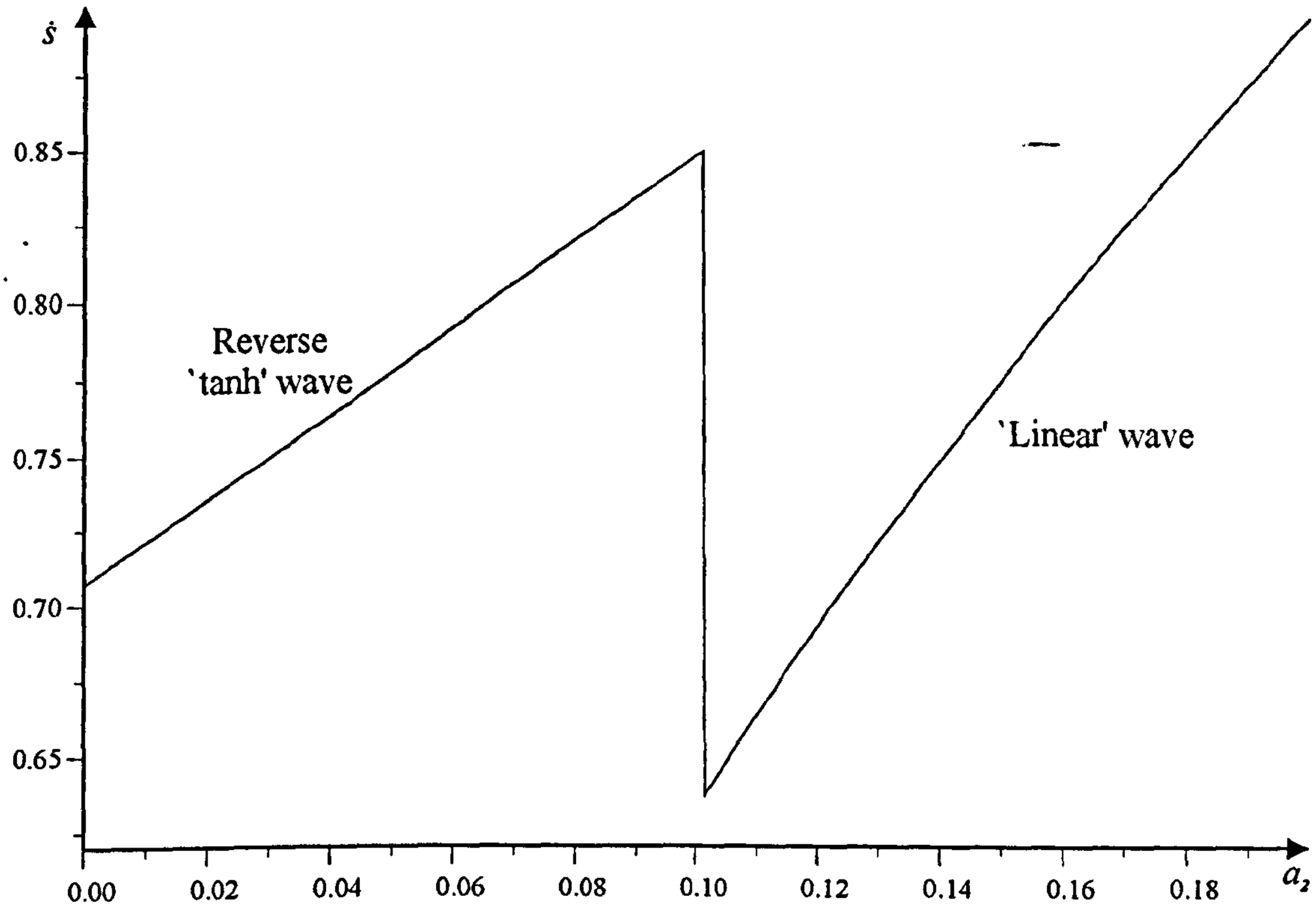

Figure 6.26: Wave speed $\dot{s}_0^{(1)}$ vs. a_2 as $\varepsilon \to 0$.

6.5 Summary of Large Time Behaviour

The results have been derived by asymptotic reasoning and comparison has been made with numerical results. The asymptotic limit $\varepsilon \to 0$ has not been followed through completely for small a_2 and we shall not pursue the details here. In Tables 6.2 and 6.3 we summarise the results of the various generic and non-generic cases discussed earlier in the chapter. For clarity, we once again take $a_1 = 1$, which entails no loss of generality.

6.6 Asymptotic Behaviour as $x \to 0$

6.6.1 Airy layer

We are now in a position to complete our asymptotic analysis by considering the behaviour near the origin as a new inner layer is formed there; we consider the case where the speed of the travelling wave in front of this new layer is given by $\dot{s}_{0\,\min}^{(1)}$, the initial

Case	Front speed $\dot{s}_0^{(1)}$		Comments
	+ve	−ve	
$\varepsilon < a_2$, $(7-3\sqrt{5})/2 < a_2 < 1/2$	$2\sqrt{a_2}$	$(1+2a_2)/2$	'Linear' front solution (+ve); 'tanh' front solution (−ve).
$\varepsilon < \min(1, a_2)$, $1/2 < a_2 < 2$	$2\sqrt{a_2}$	$2\sqrt{a_2}$	'Linear' front solution in both cases.
$\varepsilon < 1, \quad a_2 > 2$	$(2+a_2)/\sqrt{2}$	$2\sqrt{a_2}$	'Tanh' front solution (+ve); 'linear' front solution (−ve).

Table 6.2: Summary of wave speeds obtained for sufficiently a_2 with $a_1 = 1$ with a positive or a negative initial perturbation (denoted +ve and −ve in the front speed column).

Case	Front speed $\dot{s}_0^{(1)}$	Comments
$2 - a_2 - 2\sqrt{1-a_2} < \varepsilon < a_2$, $a_2 < (7-3\sqrt{5})/2$	$(1+2a_2)/\sqrt{2}$	Critical point is a spiral; front flips to become negative 'tanh' wave.
$\varepsilon = O(a_2^2/4)$, $a_2 \lessapprox (7-3\sqrt{5})/2 \quad (*)$,	$(1+\frac{1}{2}a_2)/\sqrt{2}$	Front speeds up to second inner speed. Condition $(*)$ is only approximate, as it is obtained from asymptotic analysis not strictly viable in this region.
$\varepsilon \ll a_2^2/4$, $0 < a_2 < 5-\sqrt{24}$	$(1+2a_2)/\sqrt{2}$	Initial front is annihilated; negative 'tanh' wave becomes initial front.
$\varepsilon \ll a_2^2/4$, $5-\sqrt{24} < a_2 < (7-3\sqrt{5})/2$	$2\sqrt{a_2}$	'Linear' front is retained; successive inner layers decrease speed to that of the front.

Table 6.3: Summary of wave speeds obtained for sufficiently small a_2 with $a_1 = 1$ with a positive initial perturbation.

speed of the front. It is found that an extra layer is required between the outer solution and the transition at the origin (see Figure 6.4); to determine the scalings, we first of all consider the final outer solution just before the fast transition by linearising about the maximum/minimum of $v = f(u)$ (whichever is relevant). We choose to consider the transition at $v = v_{\max}$, and thus put

$$\begin{aligned} u_0 &= h_+(v_{\max}) + U \\ v_0 &= v_{\max} + V, \end{aligned} \tag{6.71}$$

where $u = h_+(v)$ is the pseudo-inverse of $v = f(u)$ as before; the case when $v = v_{\min}$ is similar. Substituting (6.71) into (6.41) we obtain at leading order

$$V_0 = \tfrac{1}{2} f''(h_+(v_{\max}))\, U_0^2$$

and

$$f''(h_+(v_{\max}))\, U_0\, U_{0t} = h_+(v_{\max}) - v_{\max} \tag{6.72}$$

at leading order. Integrating (6.72), we can thus obtain

$$\begin{aligned} u_0 &\sim h_+(v_{\max}) + \left(\frac{h_+(v_{\max}) - v_{\max}}{-\frac{1}{2} f''(h_+(v_{\max}))} \right)^{1/2} (t_c(x) - t)^{1/2} \\ v_0 &\sim v_{\max} - (h_+(v_{\max}) - v_{\max})(t_c(x) - t) \qquad \text{as } t \to t_c(x), \end{aligned} \tag{6.73}$$

where $t_c(x)$ is the time at which the transition is initiated at a point x; from previous analysis, it is straightforward to show that the nth inner layer is located at

$$x \sim q(t - \hat{t}_n), \tag{6.74}$$

where

$$\hat{t}_n = t_1 + \frac{n-1}{2}(t_2 + t_3)$$

and

$$q = \dot{s}_0^{(1)},$$

where t_1, t_2 and t_3 are given by (6.46), (6.62) and (6.63) respectively. Therefore we set

$$\begin{aligned} t &= \hat{t}_n + \delta(\varepsilon)\, T \\ x &= \mu(\varepsilon)\, X \\ u &= h_+(v_{\max}) + \delta^{1/2}(\varepsilon)\, U \\ v &= v_{\max} + \delta(\varepsilon)\, V \end{aligned}$$

for our new layer, where δ and μ remain to be determined; (6.3) becomes

$$\begin{aligned} \frac{\varepsilon}{\delta^{1/2}} U_T &= \frac{\varepsilon^2 \delta^{1/2}}{\mu^2} \nabla^2 U + \frac{1}{2} f''(h_+(v_{\max})) \delta U^2 - \delta V \\ V_T &= h_+(v_{\max}) - v_{\max} + \delta^{1/2} U + \delta V. \end{aligned} \tag{6.75}$$

It follows from (6.74) that $\mu = \delta$. We also require U_T to balance with the reaction terms when matching into the outer region (i.e. as $T \to -\infty$), and hence we must set $\varepsilon = \delta^{3/2}$; our scalings in terms of ε become

$$\begin{aligned} t &= \hat{t}_n + \varepsilon^{2/3} T \\ x &= \varepsilon^{2/3} X \\ u &= h_+(v_{\max}) + \varepsilon^{1/3} U \\ v &= v_{\max} + \varepsilon^{2/3} V. \end{aligned} \tag{6.76}$$

At leading order, we obtain

$$V_0 = (h_+(v_{\max}) - v_{\max})\,(T - T_c(X)), \tag{6.77}$$

where $T_c(X)$ is the value of T at which the fast transition takes place; note that it does *not* necessarily take place at $T = 0$ – at this stage, we are still on a time-scale slower than that of the transition. We can match (6.77) with an outer solution taking the form

$$v_0 = G(t - \hat{t}_n - x/q) \tag{6.78}$$

(cf. (6.45)). From (6.77), we obtain as the outer limit of the inner solution

$$v \sim v_{\max} + \varepsilon^{2/3}(h_+(v_{\max}) - v_{\max})\,(T - T_c(X)) \tag{6.79}$$

and we thus require

$$G(t_3) = v_{\max} \tag{6.80}$$

$$G'(t_3) = h_+(v_{\max}) - v_{\max} \tag{6.81}$$

$$T_c(X) = X/q \tag{6.82}$$

for matching. From (6.76), we can also obtain

$$U_{0T} = \frac{1}{2} f'''(h_+(v_{\max}))\, U_0^2 - (h_+(v_{\max}) - v_{\max})\,(T - T_c(X)), \tag{6.83}$$

which is a Riccati equation. By setting

$$U_0 = \frac{\dot{w}}{-\frac{1}{2} f''(h_+(v_{\max}))\, w}, \tag{6.84}$$

where $\dot{} \equiv d/dT$, and noting that $f''(h_+(v_{\max}))$ is negative, we obtain

$$\ddot{w} = \frac{1}{2} f''(h_+(v_{\max}))(h_+(v_{\max}) - v_{\max})\,(T - T_c(X))\, w, \tag{6.85}$$

an Airy equation with the solution

$$w = C_1\,\Gamma(\tfrac{2}{3})\,\mathrm{Ai}\,(\alpha\,(T_c(X) - T)) + C_2\,\Gamma(\tfrac{4}{3})\,\mathrm{Bi}\,(\alpha\,(T_c(X) - T)), \tag{6.86}$$

where

$$\alpha = \left\{-\frac{1}{2} f''(h_+(v_{\max}))(h_+(v_{\max}) - v_{\max})\right\}^{1/3}$$

and C_1 and C_2 are arbitrary constants of integration.

Matching back into the outer solution (i.e. as $T \to -\infty$), then (6.86) reads

$$w \sim [\alpha(T_c(X) - T)]^{-1/4} \left\{\bar{C}_1 e^{\left(-\frac{2}{3}[\alpha\,(T_c(X)-T)]^{3/2}\right)} + \bar{C}_2 e^{\left(\frac{2}{3}[\alpha\,(T_c(X)-T)]^{3/2}\right)}\right\}, \tag{6.87}$$

where

$$\bar{C}_1 = \frac{C_1}{2\sqrt{\pi}}, \qquad \bar{C}_2 = \frac{C_2}{\sqrt{\pi}}.$$

Substituting (6.87) back into (6.84), we obtain

$$U_0 \sim \left(\frac{h_+(v_{\max}) - v_{\max}}{-\frac{1}{2} f''(h_+(v_{\max}))}\right)^{1/2} \left(\frac{\bar{C}_1 - \bar{C}_2 e^{\left(\frac{4}{3}[\alpha(T_c(X)-T)]^{3/2}\right)}}{\bar{C}_1 + \bar{C}_2 e^{\left(\frac{4}{3}[\alpha(T_c(X)-T)]^{3/2}\right)}}\right) (T_c(X) - T)^{1/2} \tag{6.88}$$

as $T \to -\infty$.

and it follows that

$$U_0 \sim + \left(\frac{h_+(v_{\max}) - v_{\max}}{-\frac{1}{2} f''(h_+(v_{\max}))}\right)^{1/2} (T_c(X) - T)^{1/2} \qquad \bar{C}_2 = 0 \tag{6.89}$$

$$U_0 \sim - \left(\frac{h_+(v_{\max}) - v_{\max}}{-\frac{1}{2} f''(h_+(v_{\max}))}\right)^{1/2} (T_c(X) - T)^{1/2} \qquad \bar{C}_2 \neq 0. \tag{6.90}$$

Writing the outer solution (6.73) in terms of the 'Airy' variables, we obtain

$$U_0 \sim \left(\frac{h_+(v_{\max}) - v_{\max}}{-\frac{1}{2} f''(h_+(v_{\max}))}\right)^{1/2} \left(\frac{X}{q} - T\right)^{1/2}$$

and thus for matching, we require $C_2 = 0$ and

$$T_c(X) = \frac{X}{q}, \tag{6.91}$$

as we obtained previously in (6.82). We still need to determine when U_0 blows up; from (6.84) and (6.86), we can see that this will occur at the largest (i.e. least negative) zero of $\mathrm{Ai}(\alpha X/\dot{s}_0^{(1)})$ (since $C_2 = 0$). Denoting this value by

$$\mathrm{Ai}(\lambda_0) = 0,$$

we can set

$$T = \frac{X}{q} - \frac{\lambda_0}{\alpha} + \hat{T} \tag{6.92}$$

so that (6.86) becomes

$$\begin{aligned} w &= C_1 \,\mathrm{Ai}(\lambda - \alpha \hat{T}) \\ &\sim -C_1 \,\alpha \,\mathrm{Ai}'(\lambda_0)\, \hat{T} \quad \text{as } \hat{T} \to 0. \end{aligned}$$

This gives

$$U_0 \sim \frac{1}{-\frac{1}{2} f''(h_+(v_{\max}))\, \hat{T}} \qquad \text{as } \hat{T} \to 0 \tag{6.93}$$

and the solution blows up at $\hat{T} = 0$ as required.

6.6.2 Origin inner layer

For the fast transition at the origin, we set

$$\begin{aligned} T + \lambda_0/\alpha &= \varepsilon^{1/3} \tau \\ X &= \varepsilon^{1/3} \xi \\ u &\sim u_0 \\ v &\sim v_0, \end{aligned}$$

which results in

$$\begin{aligned} v_{0\tau} &= 0, \\ u_{0\tau} &= u_{0\xi\xi} + f(u_0) - v_0(\xi). \end{aligned} \tag{6.94}$$

We can easily determine $v_0(\xi)$ by matching back into the Airy region; writing (6.77) in terms of the origin inner layer variables gives us

$$v_0 \sim v_{\max} - \varepsilon(h_+(v_{\max}) - v_{\max})\xi/q$$

and therefore $v_0 = v_{\max}$ at leading order. Hence an equation of Fisher type is obtained, namely

$$u_{0\tau} = u_{0\xi\xi} + f(u_0) - v_{\max} \tag{6.95}$$

which we already know has travelling wave solutions for speeds greater than some minimum value and we expect to observe a travelling wave for $\tau \to +\infty$. To determine the behaviour of (6.95) as $\xi \to +\infty$ (i.e. the condition as the origin inner layer matches into the Airy layer), we set

$$X = O(1), \qquad \tau = O(1), \qquad u = h_+(v_{\max}) + \bar{u}$$

which gives

$$\frac{\partial \bar{u}_0}{\partial \tau} = \frac{1}{2} f''(h_+(v_{\max}))\, \bar{u}_0^2$$

and hence

$$\bar{u}_0 \sim \frac{1}{\frac{1}{2} f''(h_+(v_{\max}))(\varepsilon^{-1/3} X/q - \tau)}$$

so that

$$\bar{u}_0 \sim \frac{q}{\frac{1}{2} f''(h_+(v_{\max}))\, \xi} \qquad \text{as } \xi \to +\infty, \quad \tau \to -\infty.$$

This indicates that the wave speed of $\dot{s}_0^{(1)}$ is preserved all the way back to the origin inner layer. The full reaction-diffusion equation (6.95) describes the formation of a new inner layer, but further analytical progress over this timescale does not seem possible. We conclude that when a new inner layer is formed in the vicinity, it does so with a travelling wave speed equal to that of the leading front.

6.7 Alternative Initial Conditions

In the above sections, we considered travelling wave solutions for a medium initially at rest and subject to a small perturbation at $x = 0$, $t = 0$. In this section, we will

briefly consider the effect of a number of initial perturbations at different points; this will cause waves initially travelling at their minimum speed to collide and interact with each other, thus altering the wave form and speed. Although we may expect multiple initial perturbations to affect the wave speed, this is not in fact the case away from the initial perturbations; the two outermost initial peaks act like single perturbations in the outward direction. A simple example with only two initial perturbations is shown in Figure 6.27 at various stages in its evolution; due to symmetry only the right hand side of the wave is shown. For $x > 0.39$, the wave is seen to behave as if there is only a single initial disturbance. Although the profiles in Figure 6.27 are shown only after reasonably short times (up to $t = 10$) in order to make their display clearer, this behaviour has been confirmed numerically for much larger times (which require *very* large computational times); it can be seen that after a certain length of time, the wave will reach the right hand side of the domain, which is truncated for numerical purposes (see the last profile in Figure 6.27) – this will affect the wave behaviour and must thus be avoided. From numerical observations, we find that the region between the two perturbations ($x < 0.39$ in Figure 6.27) persists indefinitely.

We also observe numerically that if we initiate the wave with a series of exponentially-decaying perturbations, we obtain the same 'linear' wave speed as predicted analytically above in Section 6.3.1. We shall not consider an asymptotic analysis of these more general cases here.

6.8 A Radial Formulation

Finally, we can consider the full two-dimensional case, which is obviously rotationally invariant for a wave initiated at the origin. Our system (6.3) becomes

$$\begin{aligned} \varepsilon\, u_t &= \varepsilon^2 \frac{1}{r}(r\, u_r)_r + f(u) - v \\ v_t &= u - v, \end{aligned} \tag{6.96}$$

which immediately we can see will cause the singularity $r = 0$. At distances such that $r \gg$ inner region thickness, the asymptotic analysis of (6.96) with $\varepsilon \ll 1$ is the same as that for the one-dimensional system, and from this we can expect to get solutions

Figure 6.27: Snapshots of the evolution of fronts (u) for two initial disturbances at $x = \pm 0.39$ at intervals of $t = 2$ for $\varepsilon = 0.001$, $a_1 = a_2 = 1/2$.

similar to those obtained in that case. The only change is to the analysis of section 6.6.2. Writing

$$\begin{aligned} t &= t_n + \varepsilon\tau \\ r &= \varepsilon\rho \\ u &\sim u_0 \\ v &\sim v_0, \end{aligned}$$

now results in the single leading order equation

$$u_{0\tau} = u_{0\rho\rho} + \frac{1}{\rho}u_{0\rho} + f(u_0) - v_{max}, \tag{6.97}$$

which differs slightly from that obtained in the one-dimensional case. When matching with the Airy solution as $\rho \to \infty$, $\tau \to -\infty$, the term $u_{0\rho}/\rho$ is negligible, and thus the wave speeds obtained are the same as for the one-dimensional case. At the origin, we have the boundary condition $u_\rho = 0$, and the problem is fully prescribed.

We can also solve (6.96) numerically as before; the solutions are similar to those obtained for the one-dimensional problem, and again agree with the asymptotic analysis, i.e. a new inner layer forms at the origin and travel at a speed equal to that of the initial front.

Concluding, we note that the system could now be used to model target patterns of the type which appear in the BZ reaction [53], as discussed earlier. Considering the general geometry of these patterns, experimental results suggest a sharp wave front and a diffuse wave back [57]; our solutions for u agree with this. We may expect our model to be able to determine when new 'rings' will form, and, more importantly, predict the wave speed at which these rings move; a particular feature of our model is that in a certain regime, we can obtain two distinct wave speeds for the same parameter values, which depends only on the form of initial perturbation (see summary in § 6.5). We can also obtain solutions for any wave speed greater than some minimum value for all parameter values by prescribing an exponentially decaying initial profile. These are features which could be investigated experimentally; we point out that the interest here is of a mathematical nature and not a direct attempt at modelling the BZ reaction precisely.

Chapter 7

Fisher's Equation and Modulated Travelling Waves

7.1 Introduction

For the final two chapters, we will use WKB theory to develop a method for predicting wave speeds of travelling fronts at large time, and also periodic behaviour, either behind the front or at the front itself, thus providing descriptions of modulated (as well as standard) travelling waves. We stress that our interest here is concerned purely with the *large time* behaviour, unlike in the previous chapter; any transitional behaviour from the initial state will not be discussed.

Our method is designed for use in systems of partial differential equations, but in this chapter we will consider a well-established single equation (Fisher's equation with cubic nonlinearity), and show how even here we can demonstrate new behaviour.

7.1.1 Background

The required form of Fisher's equation reads

$$\frac{\partial u}{\partial t} = \frac{\partial^2 u}{\partial x^2} + u\,(1-u)(a+u). \tag{7.1}$$

We have shown in the previous chapter that a travelling front solution resulting from a small positive perturbation to a medium initially at the unstable steady state $u = 0$ has two forms; a 'tanh' front for $a < 1/2$ and a 'linear' front for $a > 1/2$.

We have also considered the case when we prescribe an initial condition of

$$u \sim e^{-\alpha x} \qquad \text{as } x \to +\infty \text{ at } t = 0 \tag{7.2}$$

for real α. The 'linear' wave speed is then given by

$$c = \max\left(2\sqrt{a}, \alpha + \frac{a}{\alpha}\right) \tag{7.3}$$

(obtained in a similar way to (6.29)–(6.32)), and thus the observed wave speed is given by

$$c = \max\left(\alpha + \frac{a}{\alpha}, \frac{1+2a}{\sqrt{2}}\right) \qquad a < 1/2 \tag{7.4}$$

$$c = \max\left(\alpha + \frac{a}{\alpha}, 2\sqrt{a}\right) \qquad a > 1/2. \tag{7.5}$$

We can now obtain a linear front for $a < 1/2$ if α is small enough.

7.2 A WKB Method

Following WKB theory, we seek a solution of the form

$$u \sim A_0\, e^{f(x,t)} \tag{7.6}$$

to the linearised form of (7.1)

$$u_t = u_{xx} + a\, u \tag{7.7}$$

to give

$$f_t = f_x^2 + a. \tag{7.8}$$

We are interested in the behaviour for large time; at the front, we then expect the ratio x/t to be $O(1)$ (from the wave speeds obtained in Section 7.1.1), and so we seek a solution of the form

$$f(x,t) = t\, F(x/t) = t\, F(\eta) \tag{7.9}$$

so that (7.8) becomes

$$F - \eta\, F_\eta = F_\eta^2 + a, \tag{7.10}$$

which is of the form of Clairaut's equation. We solve by differentiating (7.10) to give

$$(2\,F_\eta + \eta)\,F_{\eta\eta} = 0. \tag{7.11}$$

For a medium initially at rest (save for a small perturbation at $x = 0$ to initiate the front), we seek the envelope solution to (7.11), i.e.

$$2\,F_\eta + \eta = 0,$$

which implies that

$$F(\eta) = a - \eta^2/4$$

and gives

$$\ln u \sim a\,t - \frac{x^2}{4\,t} \qquad x \to +\infty.$$

For large t, we define the wave front to be at the point where u neither grows nor decays (that is, between the leading edge and whatever pattern follows behind); this implies that we require

$$\mathrm{Re}(f) = 0 \tag{7.12}$$

at the front. We can see that this gives a front speed of $c = x/t = 2\sqrt{a}$, the well-known minimum wave speed.

To demonstrate a new type of behaviour, we prescribe a decaying oscillatory initial profile, given by

$$u(x,0) \to e^{-\alpha x}\cos\beta x \qquad \text{as } x \to \infty. \tag{7.13}$$

We need only to investigate solutions for $a \leq 1$; solutions for $a > 1$ can be deduced by suitable rescalings of (7.1) and (7.13). As the initial condition is now given, we solve $F_{\eta\eta} = 0$ from (7.11), which gives us

$$f = A\,t + B\,x.$$

By substitution into (7.8) we have $A = B^2 + a$; the initial profile given by (7.13) implies $B = -\alpha + i\,\beta$, so that

$$u \sim \mathrm{Re}\left(e^{(a+\alpha^2-\beta^2-2\alpha\beta i)\,t}e^{(-\alpha+i\,\beta)\,x}\right). \tag{7.14}$$

From (7.12) and (7.14), we can thus deduce a wave speed of

$$c_{\text{WKB}} = \frac{x}{t} = \frac{a + \alpha^2 - \beta^2}{\alpha}. \tag{7.15}$$

The frequency of oscillation of the front will be given by

$$\omega = \text{Im}(f)$$

and thus the temporal period of oscillation will be

$$T_{\text{WKB}} = \frac{2\pi}{\omega} = \frac{2\pi\,\alpha}{\beta\,(a - \alpha^2 - \beta^2)}. \tag{7.16}$$

From (7.15) we can deduce that if β is large enough, then front speeds less than the minimum wave speed

$$c_{\text{min}} = \begin{cases} c_{\text{tanh}} = \frac{1+2a}{\sqrt{2}} & a \leq 1/2 \\ c_{\text{lin}} = 2\sqrt{a} & a \geq 1/2 \end{cases} \tag{7.17}$$

(as derived in the previous chapter) are predicted. We investigate this and other behaviour by first considering some numerical solutions to (7.1) subject to (7.13) using a simple explicit time-stepping routine. We truncate our domain artificially and impose no-flux conditions at each end. Our decaying exponential initial profile is chosen such that its maximum value is equal to unity at $x = x_0$; in addition, we have imposed $u(x, 0) = 1$ for $x < x_0$ so that the boundary conditions do not affect the results.

In Figure 7.1, we show a series of numerical results for (7.1) subject to (7.13) with $a = 0.25$, $\alpha = 0.01$ and $\beta = 0.1$. The initial oscillatory profile can be seen to persist and grow until alternate regions of $u \approx 1$ and $u \approx -a$ (the two stable states) form. These are connected by fronts which move towards each other in such a way that each $u \approx -a$ region (the less stable steady state for $a < 1$) is annihilated in a finite time. This results in a single steady state $u = 1$ being left far behind the 'front'.

After a reasonable length of time, it can be seen from Figure 7.1 that the profile settles down to what resembles a travelling wave – the speed of the back of the pattern being equal to that of the front. We observe, however, that the front is oscillating, and so what we have is a modulated travelling wave (which we will show below). Numerically, we find that the speed of the 'front' is $c \approx 23.9$, a very good agreement with the value

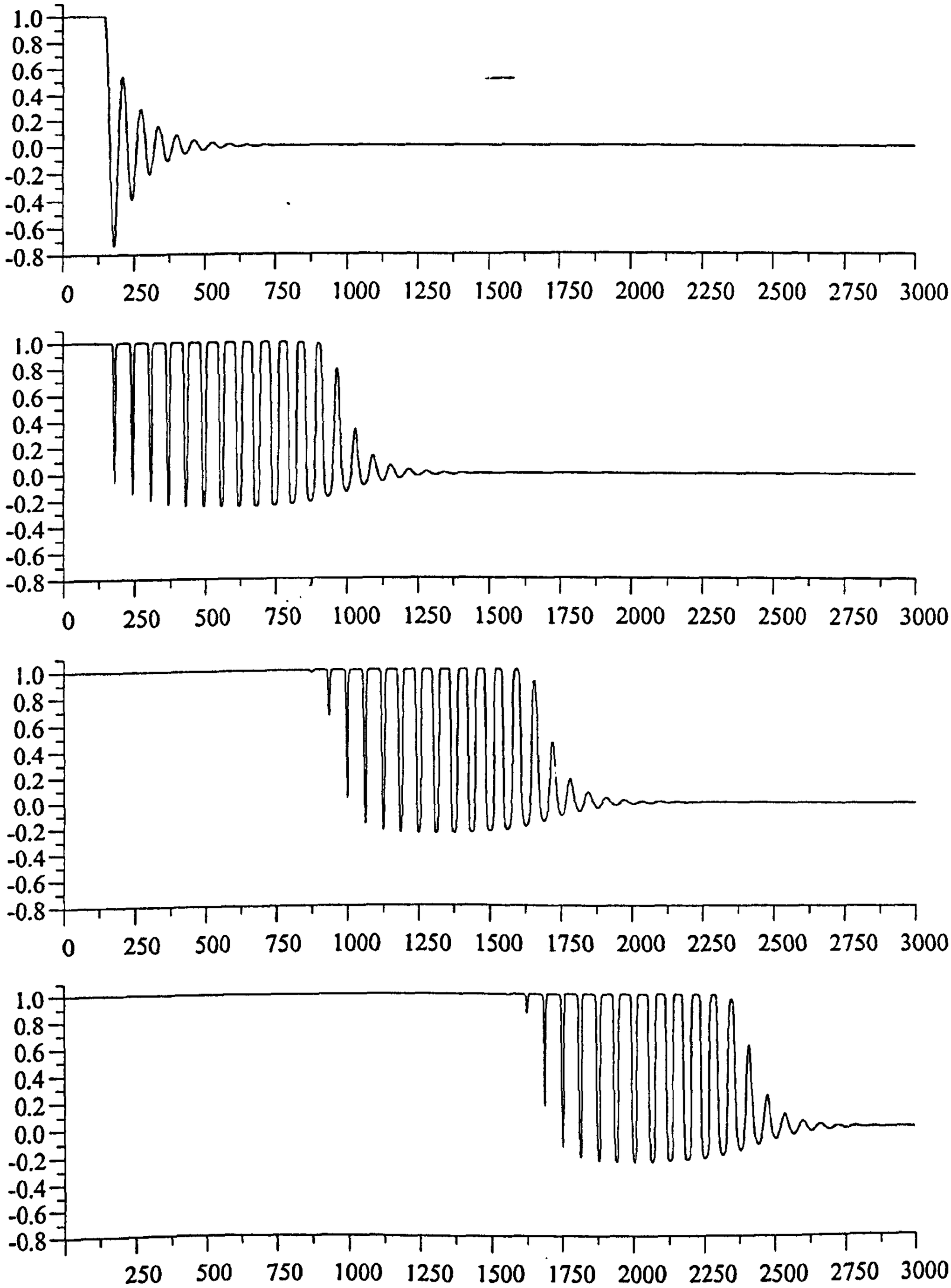

Figure 7.1: $u(x,t)$ for $a = 0.25$, $\alpha = 0.01$, $\beta = 0.1$ at times $t = 0, 30, 60, 90$.

given by (7.15) of $c_{\mathrm{WKB}} = 24.0$. This is generally found to be the case for all parameter values giving $c_{\mathrm{WKB}} > c_{\mathrm{min}}$, the minimum wave speed given by (7.17); however, there is a region for α small and β (relatively) large where this does not apply, which we consider later.

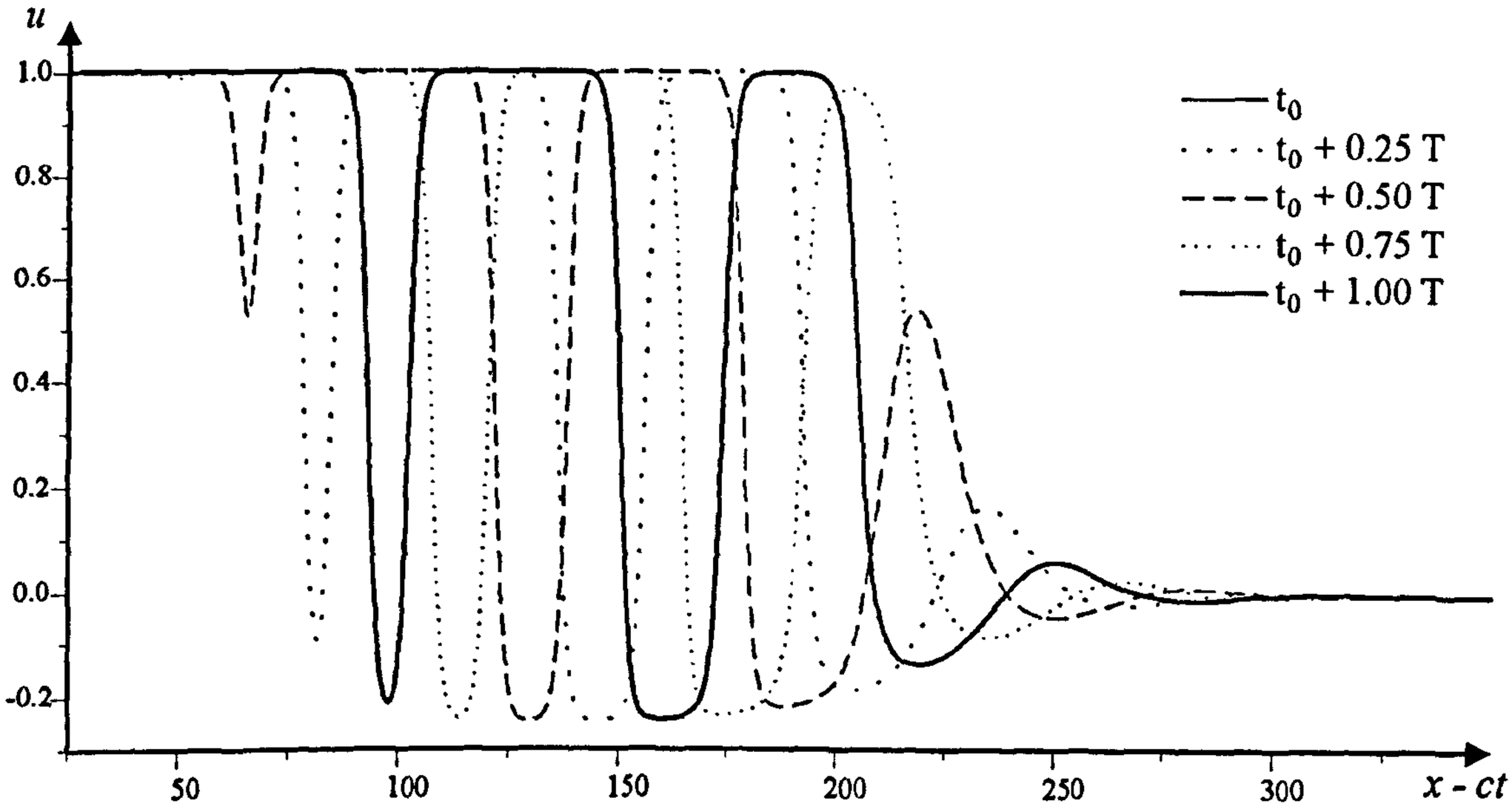

Figure 7.2: $u(x,t) = u(x-ct,t)$, plotted at quarter-period intervals for $a = 0.25$, $\alpha = 0.05$ and $\beta = 0.1$. Numerically we obtain $c = 4.85$ and $T = 13.2$, which are in excellent agreement with the values obtained from WKB theory of $c = 4.85$ and $T = 13.228$. Curves at $t = t_0$ and $t = t_0 + T$ lie on top of one another.

Returning to the phenomenon of modulated travelling waves, we now note that this implies we are obtaining solutions of the form

$$u(x,t) = \mathcal{F}(x - ct, t), \tag{7.18}$$

where the dependence on the second variable is periodic (with period T). We already know c and T from (7.15) and (7.16) respectively; Figure 7.2 shows a series of plots of u against the travelling co-ordinate $z = x - ct$ for the parameter values $a = 0.25$, $\alpha = 0.05$ and $\beta = 0.1$, taken at intervals of $T/4$. The periodic behaviour can clearly be seen; two curves obtained at a time difference of $t = T$ can be seen to lie on top of each other. We also provide further evidence of modulated travelling waves by first of all making the assumption that there *is* periodic behaviour behind the initial front. Assuming (7.18),

and considering $F(\eta)$ in the vicinity of $\eta = c$, i.e. putting $\eta = c+\varepsilon$ where ε is small, then by Taylor expansion, we have

$$F(c+\varepsilon) = i\,\mathrm{Im}\,F(c) + \varepsilon\,(\mathrm{Re}\,F'(c) + i\,\mathrm{Im}\,F'(c)) + \ldots$$

since $\mathrm{Re}\,F(c) = 0$ from (7.14). Retaining the largest terms for the real and imaginary parts, we thus have

$$\begin{aligned} f(x,t) = t\,F(x/t) &\sim (x - c\,t)\,\mathrm{Re}\,F'(c) + i\,\mathrm{Im}\,F(c)\,t \\ &= \bar{F}(x - c\,t, t) \end{aligned} \tag{7.19}$$

as required. We can therefore deduce that the temporal period is given by

$$T = \frac{2\pi}{\mathrm{Im}\,F(c)}, \tag{7.20}$$

which is in agreement with (7.16).

We now consider behaviour when $c_{\mathrm{WKB}} < c_{\mathrm{min}}$. An example numerical solution for $a = 0.25$, $\alpha = 0.1$ and $\beta = 0.5$ is shown in Figure 7.3; from (7.15), we have $c_{\mathrm{WKB}} = -1$, whereas $c_{\mathrm{min}} = 3/2\sqrt{2}$ from (7.17). We *do* initially observe the oscillatory pattern moving backwards at speed $c \approx -1$ into the $u = 1$ region, but it is annihilated by the back of the oscillatory wave (see the second plot in Figure 7.3), and a single front propagating forwards is formed. We would expect this wave to move forward with the minimum speed defined by (7.17), and indeed this *is* the case when α is not too small; however, for α less than some α_{crit}, which we will calculate later, we observe numerically that the front speed increases.

In order to investigate the increase in wave speed, we plot our solutions on a logarithmic scale. In Figure 7.4, we show the numerical profile for $a = 0.25$, $\alpha = 0.3$ and $\beta = 0.4$, which propagates with front speed $c = c_{\mathrm{tanh}}$, the minimum speed expected. It can be seen that we still do not strictly have a travelling wave – there is still oscillatory behaviour in the far field. Nevertheless, the straight line portion of the curves corresponds to the tail of the travelling wave and is found to have a slope of $-1/\sqrt{2}$ if we plot $\ln u$ against x, which is consistent with our 'tanh' wave solution of the form

$$u \sim e^{(x-ct)/\sqrt{2}} \qquad \text{as } x - ct \to +\infty.$$

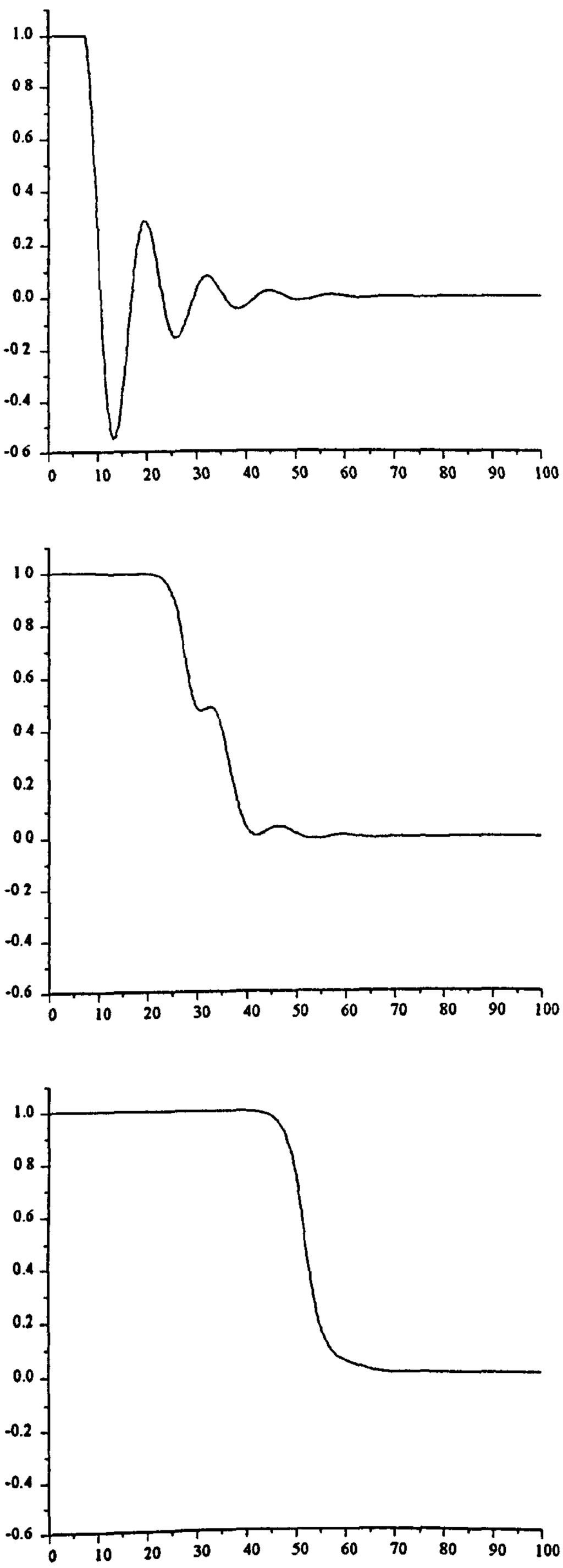

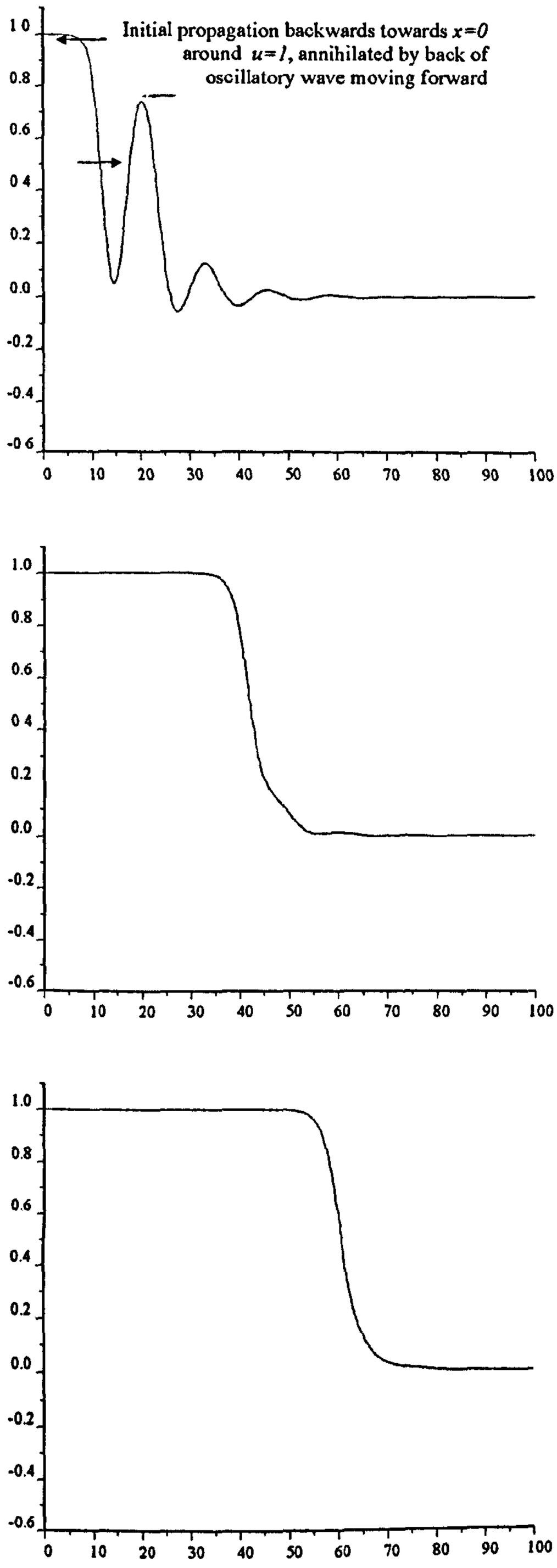

Figure 7.3: $u(x,t)$ for $a = 0.25$, $\alpha = 0.1$, $\beta = 0.5$ at intervals of $\Delta t = 7$.

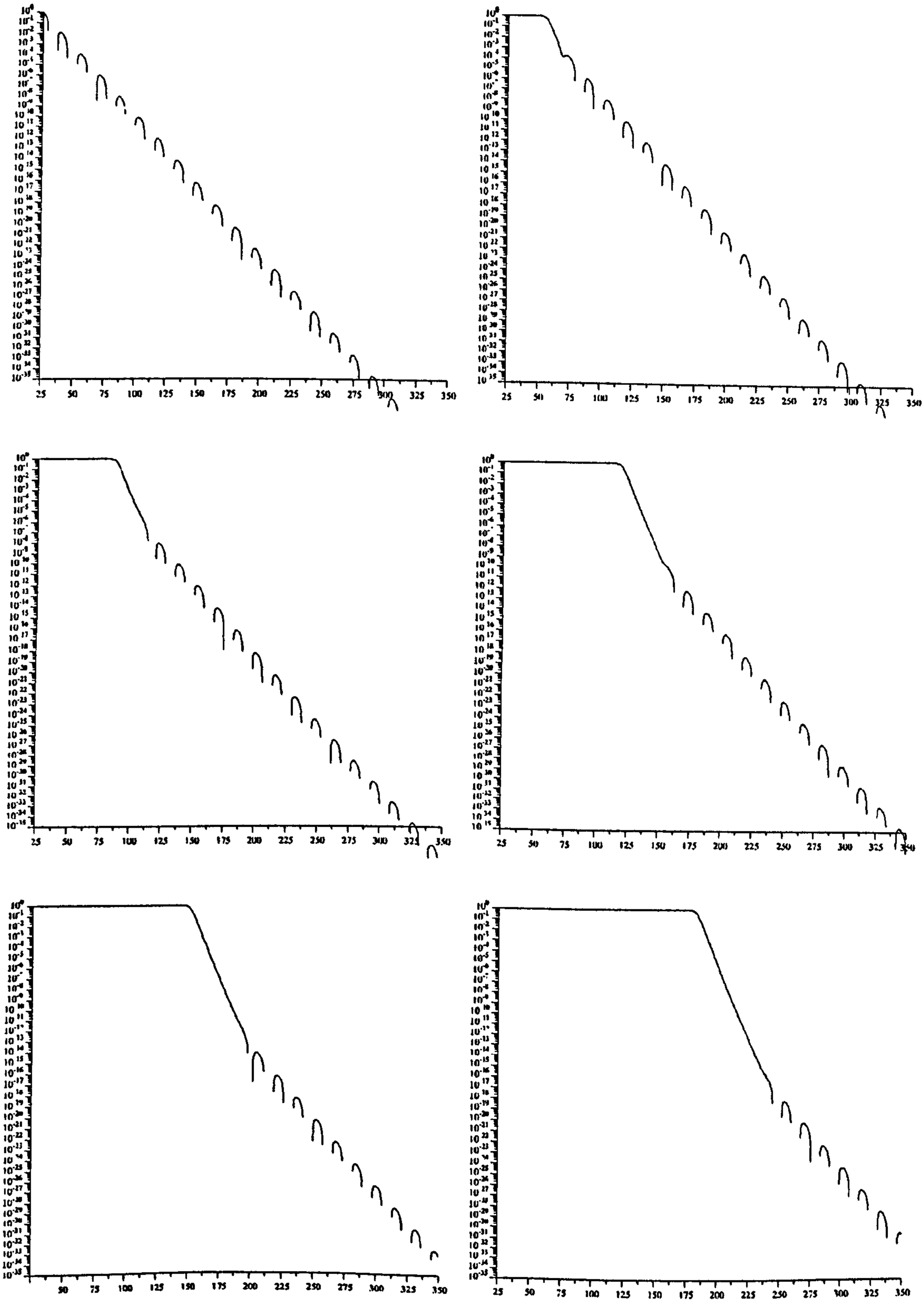

Figure 7.4: Log-scale plot of $u(x,t)$ for $a = 0.25$, $\alpha = 0.3$, $\beta = 0.4$ at intervals of $\Delta t = 30$.

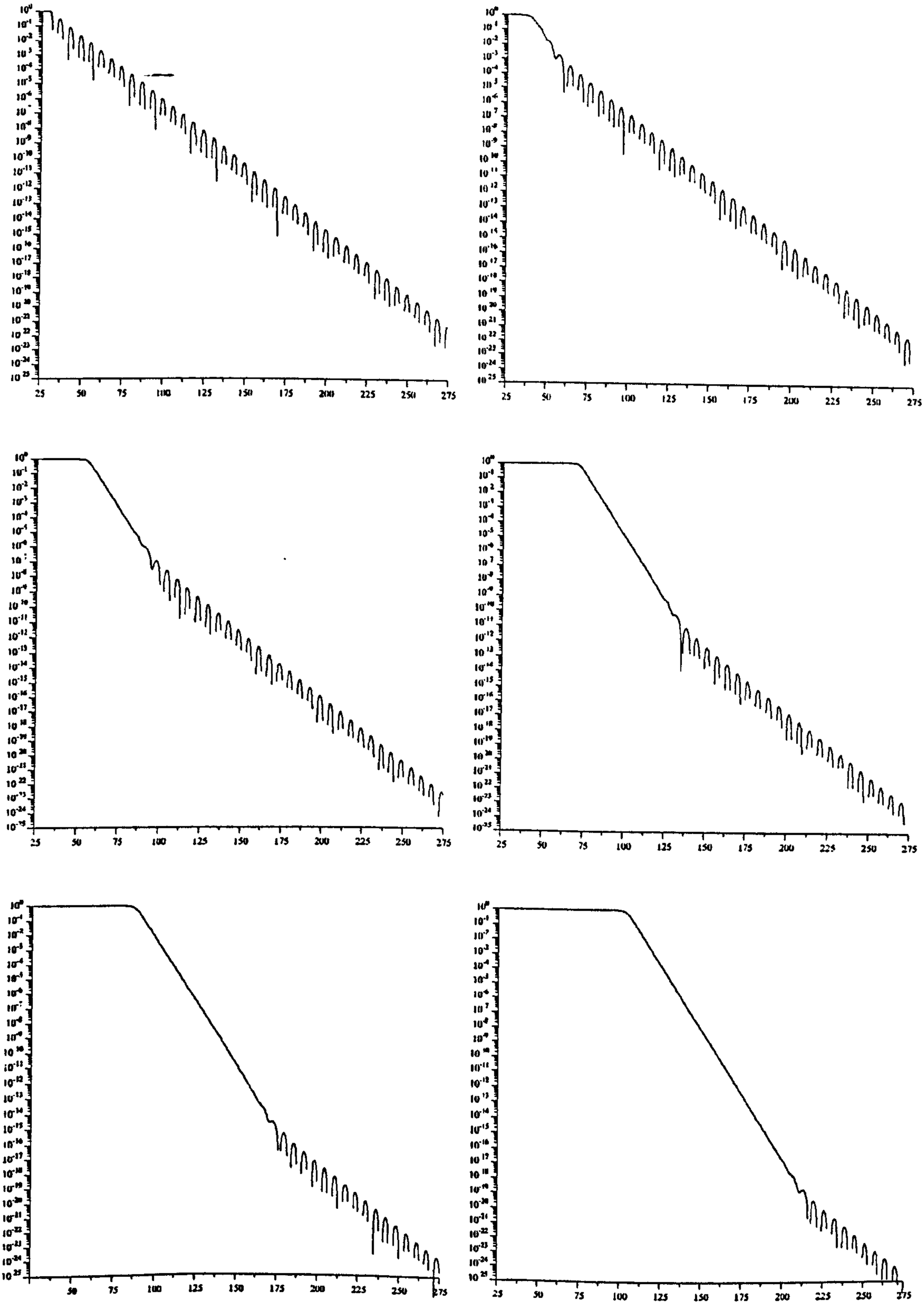

Figure 7.5: Log-scale plot of $u(x,t)$ for $a = 0.75$, $\alpha = 0.2$, $\beta = 1.0$ at intervals of $\Delta t = 7$.

We observe a similar phenomenon for $a > 1/2$, where $u \sim e^{\sqrt{a}(x-ct)}$ as $x - ct \to +\infty$ for $\alpha > \alpha_{\text{crit}}$.

For $c_{\text{WKB}} < c_{\text{min}}$ and $\alpha < \alpha_{\text{crit}}$, we obtain a different criterion for the wave speed. In Figure 7.5, we show the numerical profile for $a = 0.75$, $\alpha = 0.2$, $\beta = 1.0$, again with $u(x,t)$ plotted on a logarithmic scale; it appears to be of the same form as that in Figure 7.4. However, the numerically-obtained wave speed is $c = 2.275$, larger than $c_{\text{min}} = \sqrt{3}$, and the slope of the travelling wave portion of the plot of $\ln u$ against x is found to be -2α for all $0 < \alpha < \alpha_{\text{crit}}$. This suggests that the solution for the wave front will have an x-dependence of the form $u \sim e^{-2\alpha x}$ as $x \to +\infty$. We also postulate that since it must be the coupling between the travelling wave and the small oscillatory front that is determining the behaviour, then we have to consider more than the leading order linearised solution to (7.1).

Pursuing this analysis, our leading order equation is (from (7.7))

$$u_{0t} = u_{0xx} + a\,u_0, \tag{7.21}$$

which, together with the initial condition

$$u_0(x,0) \to e^{-\alpha x}\cos\beta x \qquad \text{as } x \to \infty. \tag{7.22}$$

has the solution (see (7.13))

$$u_0 \sim \text{Re}\left(e^{(a+\alpha^2-\beta^2-2\alpha\beta i)t}e^{(-\alpha+i\beta)x}\right). \tag{7.23}$$

At the next order, we have

$$u_{1t} = u_{1xx} + a\,u_1 + (1-a)\,u_0^2, \tag{7.24}$$

which we can write as

$$u_{1t} = u_{1xx} + a\,u_1 + \frac{1-a}{2}e^{2(a+\alpha^2-\beta^2)t-2\alpha x}\left(1+\cos 2\beta(x-2\alpha t)\right). \tag{7.25}$$

This is subject to the initial condition

$$u_1(x,0) = 0. \tag{7.26}$$

We seek particular integrals of (7.25) by considering the two forcing terms separately. Seeking a solution of the form $u_{1p_1} = K_{p1}\, e^{A_{p1}t+B_{p1}x}$ to

$$u_{1t} = u_{1xx} + a\,u_1 + \frac{1-a}{2}\, e^{2(a+\alpha^2-\beta^2)t-2\alpha x}$$

gives us

$$u_{1p_1} = \frac{1-a}{2(a-2(\alpha^2+\beta^2))}\, e^{2(a+\alpha^2-\beta^2)t-2\alpha x}, \tag{7.27}$$

while the similar solution to

$$u_{1t} = u_{1xx} + a\,u_1 + \frac{1-a}{2}\, e^{2(a+\alpha^2-\beta^2)t-2\alpha x}\,\mathrm{Re}\left[e^{-2i\beta(x-2\alpha t)}\right]$$

(where we have expressed the cosine term in (7.25) as the real part of a complex exponential) is

$$u_{1p_2} = \mathrm{Re}\left(\frac{1-a}{2(a+2(\beta-i\alpha)^2)}\, e^{(2(a+\alpha^2-\beta^2)+4i\alpha\beta)t-2(\alpha+i\beta)x}\right). \tag{7.28}$$

We choose the complimentary function with a view to satisfying our initial condition (7.26) (so that the x-dependence cancels at $t = 0$); for (7.27), we obtain

$$u_{1c_1} = -\frac{1-a}{2(a-2(\alpha^2+\beta^2))}\, e^{(a+4\alpha^2)t-2\alpha x} \tag{7.29}$$

and for (7.28)

$$u_{1c_2} = \mathrm{Re}\left(-\frac{1-a}{2(a+2(\beta-i\alpha)^2)}\, e^{(a+4(\alpha+i\beta)^2)t-2(\alpha+i\beta)x}\right). \tag{7.30}$$

The full solution to (7.25) is thus

$$u_1 = u_{1p_1} + u_{1p_2} + u_{1c_1} + u_{1c_2} \tag{7.31}$$

with the four terms of (7.31) given by (7.27), (7.28), (7.29) and (7.30) respectively. We can see in (7.29) that we have obtained the $e^{-2\alpha x}$ term that we anticipated from the numerics; we can deduce the wave speeds by setting the real part of each of the exponents in (7.27) and (7.28) to zero; we obtain

$$c_{c_1} = 2\alpha + \frac{a}{2\alpha} \tag{7.32}$$

and

$$c_{c_2} = 2\alpha + \frac{a}{2\alpha} - \frac{2\beta^2}{\alpha} \tag{7.33}$$

respectively. We can see that $c_{c_1} > c_{c_2}$ in the whole of our (α, β) parameter space, and thus (7.32) is the speed that will be observed, when it is larger than both the minimum wave speed $c_{\min}$ given by (7.17) and the leading order 'WKB' speed $c_{\min}$ given by (7.15). Numerical experiments show that this is indeed the case.

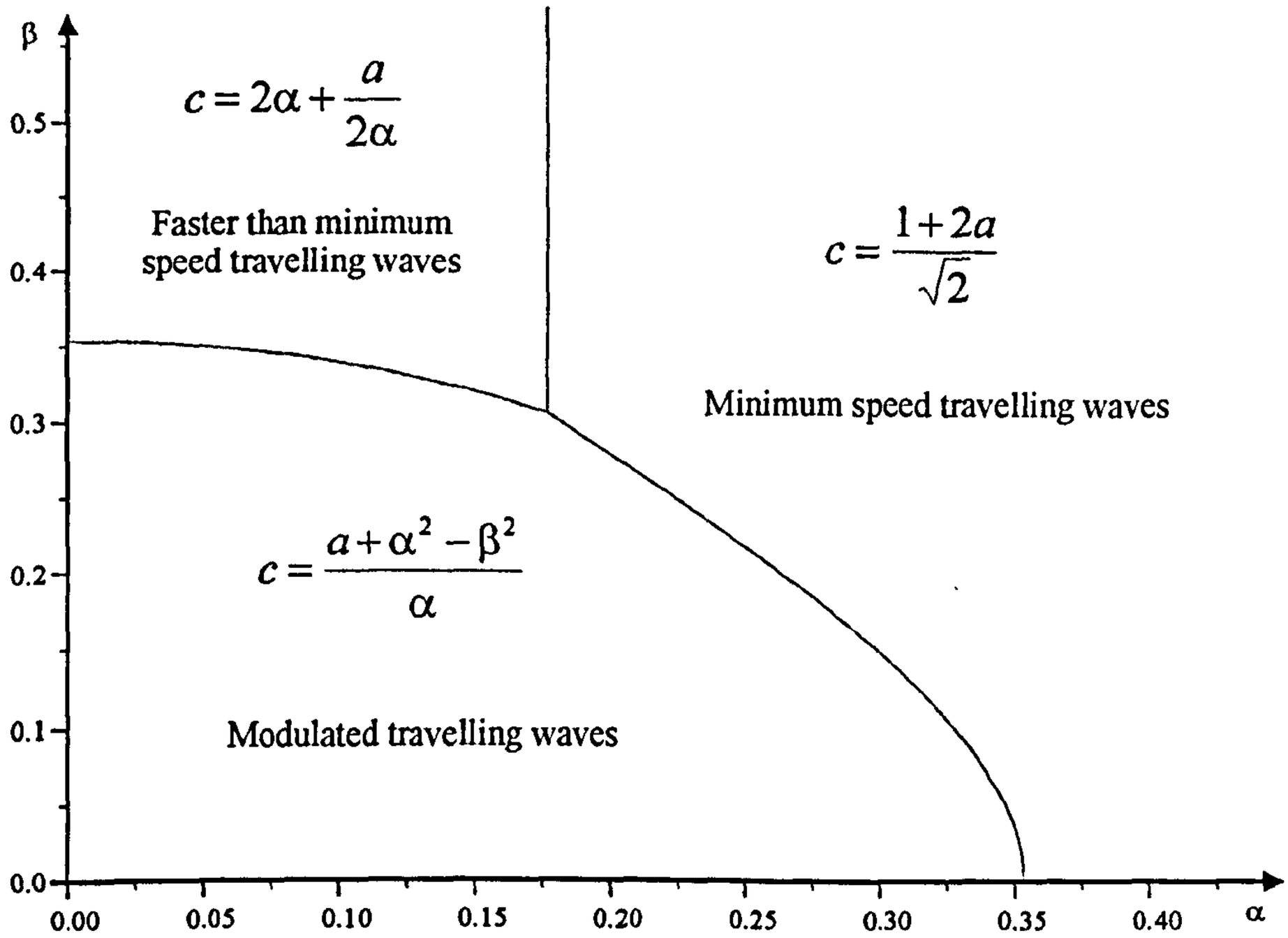

Figure 7.6: Wave speeds in parameter space for $a = 1/4$. The formulae for the dividing lines are given in Table 7.1.

We have now completely defined the wave speed in the whole of (α, β) parameter space; to clarify the situation, we present diagrams for $a = 1/4$ and $a = 3/4$ in Figures 7.6 and 7.7, showing the three regions where different forms of wave front are observed.

As a final note, we observe that if $a = 1$, then from (7.27) – (7.30), we have $u_1(x,t) = 0$ as our solution, and thus the third wave speed given by (7.32) should not be observed. We show the parameter space diagram in Figure 7.8, with the boundary for the non-existent solution shown as a dotted line. Numerical solutions once again back up our theory – only the two types of wave are observed.

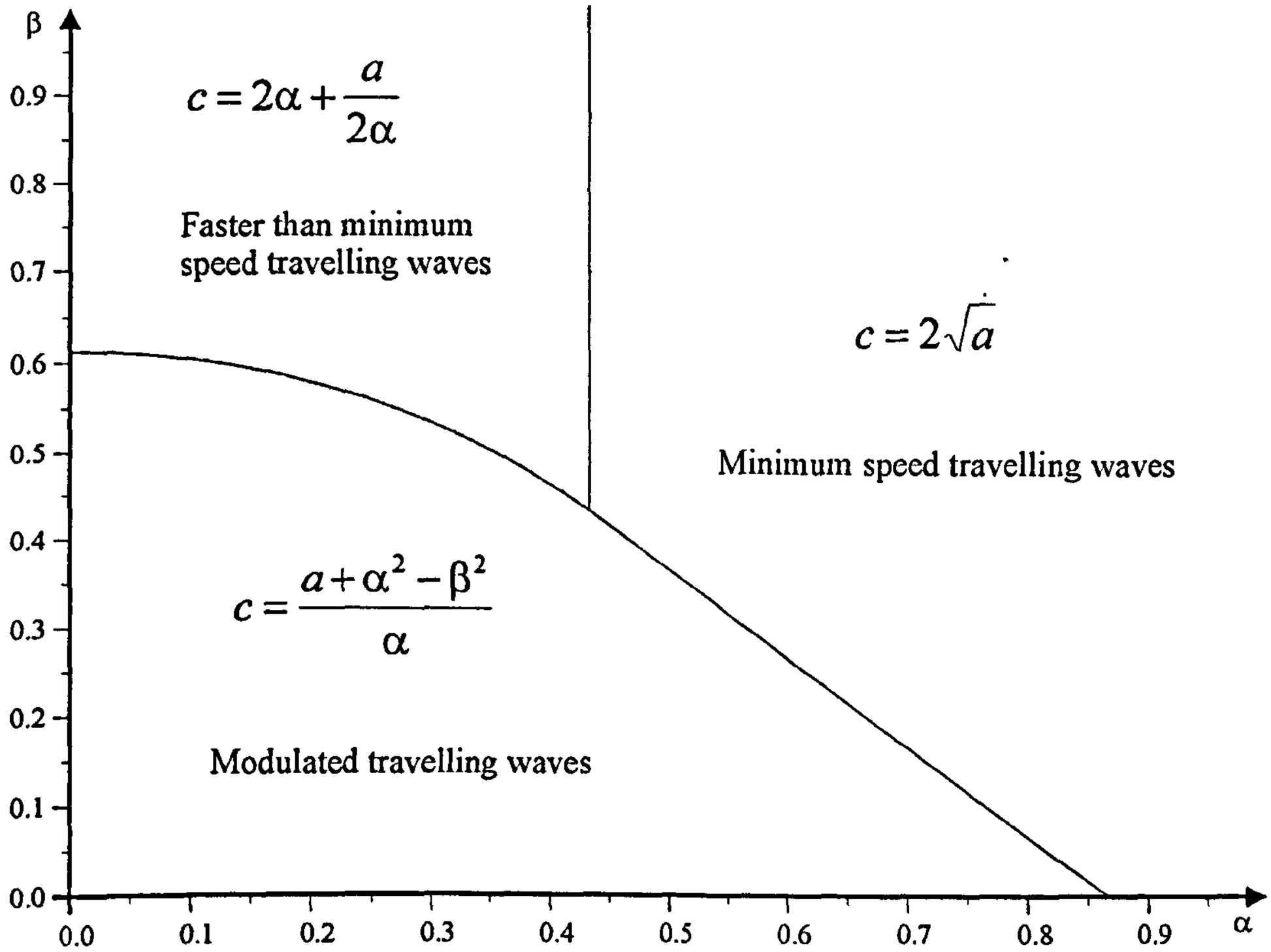

Figure 7.7: Wave speeds in parameter space for $a = 3/4$. The formulae for the dividing lines are given in Table 7.1.

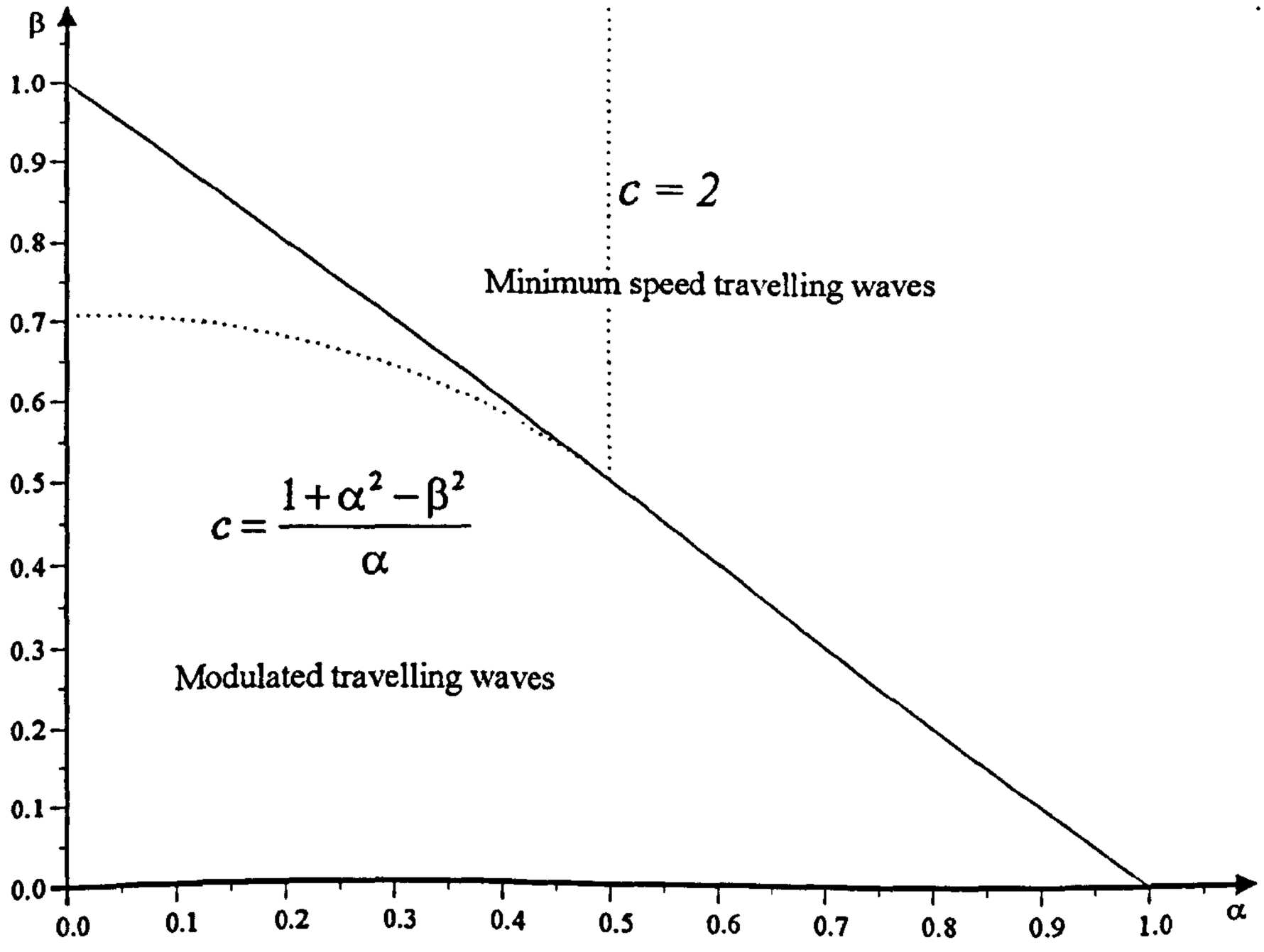

Figure 7.8: Wave speeds in parameter space for $a = 1$. The formulae for the dividing lines are given in Table 7.1.

7.3 Summary

We now summarise the solutions found in this chapter in Table 7.1.

Case	Constraints	Wave speed	Type of wave
$0 < a < \frac{1}{2}$	$\beta < \sqrt{(1/\sqrt{2} - \alpha)(\sqrt{2}a - \alpha)}$, $\beta < \sqrt{a/2 - \alpha^2}$, $\alpha < \sqrt{2}a$	$(a + \alpha^2 - \beta^2)/\alpha$	Modulated travelling waves.
	$\beta > \sqrt{a/2 - \alpha^2}$, $\alpha < a/\sqrt{2}$	$2\alpha + a/2\alpha$	Faster than minimum speed travelling waves.
	$\beta > \sqrt{(1/\sqrt{2} - \alpha)(\sqrt{2}a - \alpha)}$, $\alpha > a/\sqrt{2}$	$(1 + 2a)/\sqrt{2}$	Minimum speed travelling waves.
$\frac{1}{2} < a < 1$	$\beta < \sqrt{a} - \alpha$, $\beta < \sqrt{a/2 - \alpha^2}$, $\alpha < \sqrt{a}$	$(a + \alpha^2 - \beta^2)/\alpha$	Modulated travelling waves.
	$\beta > \sqrt{a/2 - \alpha^2}$, $\alpha < \sqrt{a}/2$	$2\alpha + a/2\alpha$	Faster than minimum speed travelling waves.
	$\beta > \sqrt{a} - \alpha$, $\alpha > \sqrt{a}/2$	$2\sqrt{a}$	Minimum speed travelling waves.
$a = 1$	$\beta < \alpha$,	$(1 + \alpha^2 - \beta^2)/\alpha$	Modulated travelling waves.
	$\beta > \alpha$,	2	Minimum speed travelling waves.

Table 7.1: Large time behaviour for solutions to (7.1) subject to (7.12). Oscillatory fronts are retained only for the modulated travelling wave regimes; the temporal period is given by (7.16).

Chapter 8

An Application of WKB Theory to Two-Variable Systems

8.1 Introduction

In this chapter, we extend the theory of the previous chapter to two variable systems, and show that we can apply the same methods to obtain wave speeds of invasive fronts and information on behaviour behind this front in a variety of situations. We will consider the large-time behaviour of systems which are initially undisturbed, but subjected to a small perturbation around $x = 0$; hence we will look for envelope solutions when we obtain our Clairaut equation this time (as with (7.11)). We could also generalise to consider exponentially decaying initial profiles (as in Chapter 7), but the behaviour is similar and so we omit details.

With a single-variable system of the type discussed earlier, we obtain only one type of solution for a medium which is initially undisturbed, namely the travelling front between two stable states. Our two-variable system reads

$$\begin{aligned} \frac{\partial u}{\partial t} &= D_u \nabla^2 u + f(u,v) \\ \frac{\partial v}{\partial t} &= D_v \nabla^2 v + g(u,v), \end{aligned} \tag{8.1}$$

where D_u and D_v are positive constant diffusivities and f and g are the nonlinear kinetics. With (8.1) there are various types of behaviour that can be initiated, and some possibilities are shown in Figure 8.1.

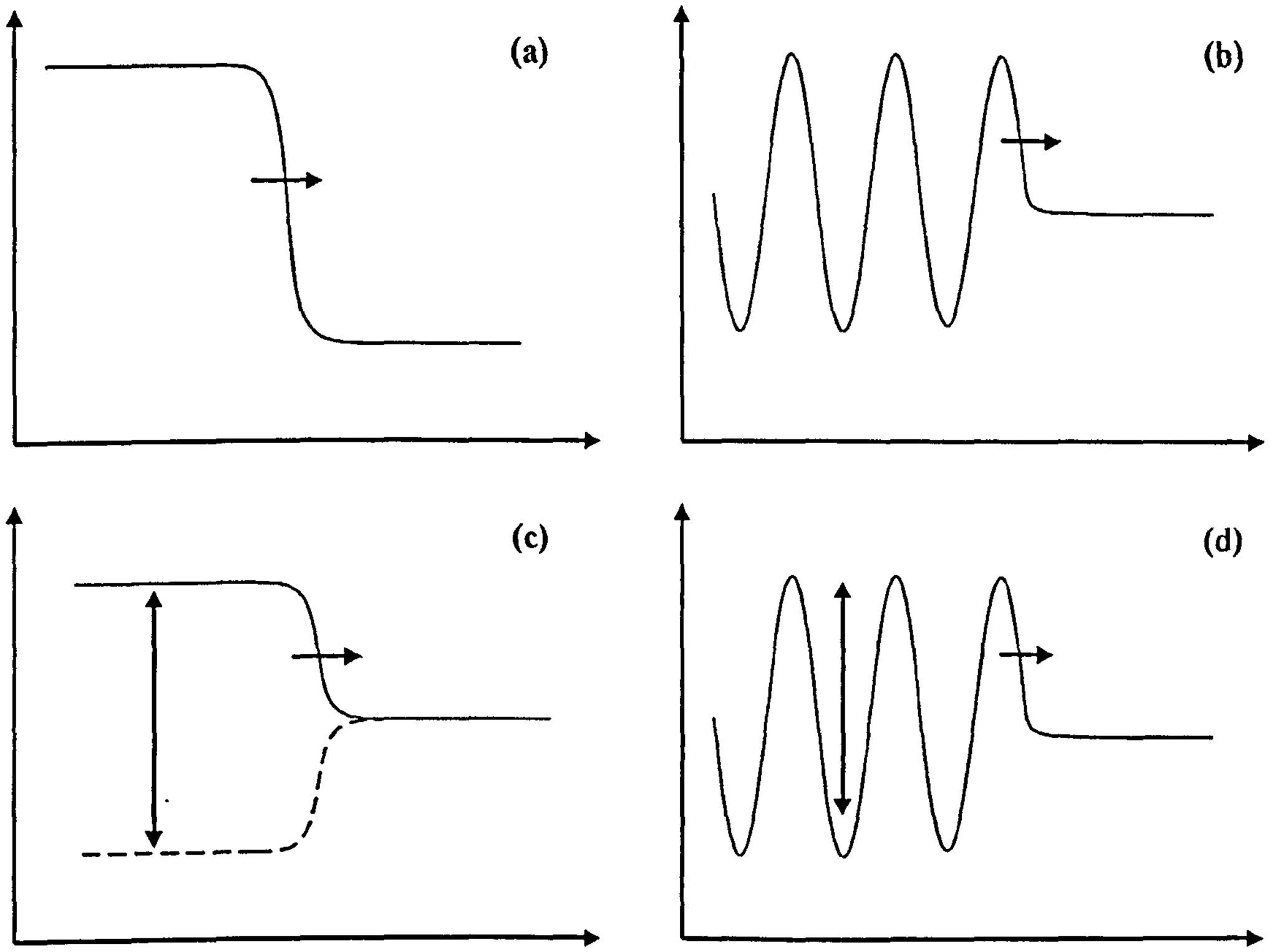

Figure 8.1: Schematic diagram of four possible types of behaviour of $u(x,t)$ for the two variable system (8.1). **(a)** is of the form already observed for the initial front in our limit cycle analysis; we will discuss this briefly again later. **(b)** corresponds to a Turing system, discussed in the first part of this chapter. **(c)** depicts homogeneous limit cycle behaviour behind the front; we do not discuss this case here. **(d)** is similar to case (b), but this time we have an oscillating pattern behind the initial front. This will be discussed later in this chapter.

In all four cases, we have a travelling front. In Figure 8.1a, we have a fixed steady state behind the initial front, and in Figure 8.1b a fixed pattern is shown; this corresponds to travelling wave initiation of pattern in infinite domain Turing systems, and will be our main area of interest. In Figure 8.1c, we have a homogeneous limit cycle behind the front, and Figure 8.1d demonstrates an oscillating pattern behind the initial front; in this case, we are implying a pattern laid down by an oscillating initial front, which is not the same as the limit cycle behaviour shown in Chapter 6, where we had a non-oscillatory front.

It is worth stressing that whilst all of the above solutions are feasible, they may not all be observed in practice. In addition there is the possibility of two or more types of behaviour combining in one solution, and irregular/chaotic wakes have also recently been observed in two-variable systems [46, 47]; these will be discussed later.

8.1.1 Background: Turing systems

As mentioned above, our main area of interest to demonstrate our WKB method will be with Turing systems, and it is worth summarising the background to the field, as well as the shortcomings of the Fourier transform/stationary phase arguments used to predict the wave speed of the initial front and the period of the pattern formed behind it.

Turing suggested that heterogeneous spatial patterns of chemical or morphogen could form via a reaction-diffusion mechanism [48]. It was proposed that if u and v in (8.1) tend to a linearly stable uniform steady state in the absence of diffusion then, under certain conditions (demonstrated below), spatially inhomogeneous patterns can form for $D_u \neq D_v$ by diffusion-driven instability.

Non-dimensionalising (8.1), we can obtain

$$\begin{aligned} u_t &= \nabla^2 u + f(u,v) \\ v_t &= d\,\nabla^2 v + g(u,v), \end{aligned} \tag{8.2}$$

where d is the ratio of the diffusivities. The conditions for diffusion-driven instability are derived using a linear stability analysis; (8.2) thus becomes

$$\begin{aligned} u_t &= \nabla^2 u + \alpha\, u + \beta\, v \\ v_t &= d\,\nabla^2 v + \gamma\, u + \delta\, v \end{aligned} \tag{8.3}$$

with α, β, γ and δ being constants and (from Murray [40]) we require

$$\begin{aligned} \alpha + \delta &< 0 \\ \alpha\,\delta - \beta\,\gamma &> 0 \\ d\,\alpha + \delta &> 0 \\ (d\,\alpha + \delta)^2 - 4\,d\,(\alpha\,\delta - \beta\,\gamma) &> 0 \end{aligned} \qquad (8.4)$$

for Turing patterns to form behind the initial front.

8.1.2 Travelling wave initiation of pattern

There have been a number of previous works on pattern formation initiated by a small perturbation at one end of a semi-infinite domain. Dee and Langer [7], Dee [6] and Ben-Jacob et al. [3] have considered (for example) solutions to the amplitude equation. A linearized form is analysed using a Fourier transform/stationary phase argument (detailed below) to determine the speed of the travelling front and the wavelength of pattern it generates behind it. It is worth noting that the analysis for a single (complex) equation, as in these cases, is considerably easier than for the two-variable system (8.2). We present the method as given by Murray [40], applied to (8.2).

For small disturbances, a solution to the linear system (8.3) is sought in the form

$$\mathrm{u}(x,t) \sim \mathrm{u}_0\, e^{ikx+\lambda t}, \qquad (8.5)$$

where $\mathrm{u} = (u, v)$, k is the wavenumber and $\lambda = \lambda(k)$ is the dispersion relation, determined by substituting (8.5) into the linearized equation(s) and finding the roots of the characteristic polynomial. For a single equation, $\lambda(k)$ is a simple quadratic; for (8.3), we have (using Murray [40])

$$\begin{aligned} 2\,\lambda(k) &= \alpha + \delta - (d+1)\,k^2 \\ &\pm \left(\left[\alpha + \delta - (d+1)\,k^2\right]^2 - 4\,\left[d\,k^4 - (\alpha\,d + \delta)\,k^2 + \alpha\,\delta - \beta\,\gamma\right] \right)^{1/2}. \end{aligned} \qquad (8.6)$$

The solution to the linearised system is of the form

$$\mathrm{u}(x,t) = \int \mathrm{A}(k)\, e^{ikx+\lambda(k)t}\, dk, \qquad (8.7)$$

with the $\mathrm{A}(k)$ being determined by a Fourier transform of the initial conditions $\mathrm{u}(x,0)$; these are of no concern here, as we are interested only in the final structure. Initially,

we expect a pattern to form with a wavenumber corresponding to the fastest growing unstable 'mode', which occurs at the peak of the dispersion curve (8.6). This is due to the initial pattern being formed as a result of a small disturbance in the steady state. The wavenumber can thus be determined from

$$\frac{\partial[\mathrm{Re}\,\lambda]}{\partial k} = 0 \qquad \Rightarrow \qquad \max[\mathrm{Re}\,\lambda] = \mathrm{Re}\,\lambda(k_f), \tag{8.8}$$

where k_f is the wavenumber of this fastest growing mode. The final pattern cannot, however, be determined from (8.8); away from $x = 0$, initiation is due to the travelling front, and not a small perturbation. Analysis of the *linear* system is valid only for small x and t, as the linearly unstable eigenfunctions $\mathrm{A}(k)$ which are growing exponentially in time will eventually be bounded by the the nonlinear terms in (8.2). In the literature [40], the behaviour at the front is then considered well away from the initial perturbation, so that x and t are in fact fairly large. Although it does not hold globally in the nonlinear regime, (8.7) is nevertheless frequently applied in the small amplitude tail; taking $x/t = O(1)$, equation (8.7) can be written in the form

$$\mathrm{u}(x,t) = \int \mathrm{A}(k)\, e^{\sigma(k)t}\, dk, \tag{8.9}$$

where

$$\sigma(k) = ikc + \lambda(k) \tag{8.10}$$

with $c = x/t$ being the velocity of the front. The integral (8.9) can be evaluated asymptotically as $t \to \infty$ using the method of steepest descents; this gives

$$\mathrm{u}(x,t) \sim \mathrm{K}\, t^{-1/2}\, e^{[ick_0 + \lambda(k_0)]t}, \tag{8.11}$$

where K is a constant and k_0, the (complex) wavenumber ahead of the front, is given by the saddle-point condition

$$\sigma'(k_0) = ic + \lambda'(k_0) = 0. \tag{8.12}$$

For large t, the wave front is at the point where u neither grows nor decays (i.e. between the leading edge and the pattern behind), so that

$$\mathrm{Re}[ick_0 + \lambda(k_0)] = 0. \tag{8.13}$$

The wavenumber at the front is $\mathrm{Re}\, k_0$, and its frequency of oscillation is given by

$$\omega = \mathrm{Im}[ick_0 + \lambda(k_0)]. \tag{8.14}$$

In the literature, this frequency is interpreted as a flux of nodes moving in the $-x$ direction relative to the envelope [7, 40]. Assuming that they are not created or destroyed when they pass through the front, then this flux must be conserved, and thus

$$c\,k^* = \omega = \mathrm{Im}[ick_0 + \lambda(k_0)], \tag{8.15}$$

where k^* is the wavenumber of the pattern laid down behind the front. Equations (8.12), (8.13) and (8.15) can be used to determine the three quantities k_0, c and k^*. As we have noted, (8.7) in fact does not hold in the nonlinear regime and we shall shortly describe a method to derive the same results which is not inconsistent in this way. We also note that whilst a single equation requires only the solution of a quadratic, the two-variable system implies the solution of a sextic, and there does not appear to be any consideration in the literature regarding *which* solutions are observed.

8.2 WKB Analysis

We will now apply the WKB method demonstrated in the previous chapter to the linearized system (8.3), and show how we can derive expressions for the front speed and the speed and period of the pattern in two-variable systems (we note that in Turing systems, the pattern speed will be zero). The approach is concerned only with regions ahead of the front in which a linearised analysis *is* applicable. We note, however, that the approach is restricted to cases in which the front speed is selected by 'linear' considerations (cf. §6.3.1, where we had 'linear' and 'tanh' fronts for a single variable system).

For a leading order solution, where u and v are small at the initial front, we set

$$\mathbf{u} \sim \mathbf{u}_0\, e^{f(x,t)}. \tag{8.16}$$

Substituting (8.16) into (8.3) gives

$$\begin{aligned} u_0\, f_t &= u_0\, f_x^2 + \alpha\, u_0 + \beta\, v_0 \\ v_0\, f_t &= v_0\, d\, f_x^2 + \gamma\, u_0 + \delta\, v_0, \end{aligned}$$

which can be combined to give

$$(f_t - f_x^2 - \alpha)(f_t - d\,f_x^2 - \delta) = \beta\,\gamma. \tag{8.17}$$

We are now able to solve for f_t in terms of f_x^2; this results in

$$f_t = \frac{1}{2}\left(\alpha+\delta+(d+1)\,f_x^2 \pm \sqrt{[\alpha+\delta+(d+1)f_x^2]^2 - 4(f_x^2+\alpha)(df_x^2+\delta)+4\beta\gamma}\right), \tag{8.18}$$

which is an equation of the form

$$f_t = H(f_x^2). \tag{8.19}$$

Again we seek a solution of the form

$$f = t\,F(x/t) = t\,F(\eta)$$

as in (7.9) so that (8.19) becomes

$$F - \eta\,F_\eta = H(F_\eta^2), \tag{8.20}$$

which is again in the form of Clairaut's equation. We solve by differentiating (8.20) to give

$$\left(2\,F_\eta\,H'(F_\eta^2)+\eta\right)\,F_{\eta\eta} = 0. \tag{8.21}$$

This time, we are interested in the envelope of solutions, and so we look to solve

$$2\,p\,H'(p^2)+\eta = 0, \tag{8.22}$$

where $p = F_\eta$. This in fact a sextic for $p(\eta)$ (equivalent to that given earlier for $\lambda(k)$), which (using (8.18)) reads

$$\begin{aligned} &4d(d-1)^2p^6 + 2(d-1)^2(d+1)\eta p^5 + [8(\delta-\alpha)d+(d-1)\eta^2](d-1)p^4 + \\ &\quad 4(\delta-\alpha)(d^2-1)\eta p^3 + [4(\beta\gamma(d+1)^2+(\delta-\alpha)^2d)+2(\delta-\alpha)(d-1)\eta^2]\,p^2 + \\ &\quad\quad [(\delta-\alpha)^2+4\beta\gamma]\,\eta\,(2(d+1)p+\eta) = 0. \end{aligned} \tag{8.23}$$

We note the +/− square root in (8.18); our solutions for F,

$$F = \eta p + H(p^2), \tag{8.24}$$

must be chosen to be consistent with (8.22).

We can determine the wave speed of the front in two ways. Assuming an initial perturbation of size ε, and considering the speed where $u = O(1)$, then

$$\varepsilon\, e^{t\,\mathrm{Re}\,F(x/t)} \sim 1. \tag{8.25}$$

Choosing the scalings

$$\begin{aligned} t &= \ln(1/\varepsilon)\,\tau \\ x &= \ln(1/\varepsilon)\,s(\tau), \end{aligned}$$

(8.25) becomes

$$\tau\,\mathrm{Re}\,F\,(s(\tau)/\tau) = 1. \tag{8.26}$$

By differentiating (8.26) we can determine that the wave speed of the front is given by

$$c_f = \dot{s}(\tau) = \eta - \frac{\mathrm{Re}\,F}{\mathrm{Re}\,F_\eta}, \qquad \tau = \frac{1}{\mathrm{Re}\,F(\eta)} \tag{8.27}$$

in terms of the 'parameter' η; our interest will be in the limit as $\tau \to \infty$ for the large-time behaviour.

The temporal period of the front can be deduced once again from (7.19) and (7.20) and we obtain

$$T_f = \frac{2\pi}{\mathrm{Im}\,F(c)}. \tag{8.28}$$

As in the previous chapter, the front is a modulated travelling wave of the form

$$u = \mathcal{F}(x - c_f t; t) = \mathcal{F}(x - c_f t; t + T_f);$$

in general terms, we will obtain a periodic travelling wave behind the front of the form

$$u = \mathcal{G}(x - c_p t),$$

which will have associated temporal and spatial periods of T_p and X_p linked by

$$X_p = c_p\, T_p. \tag{8.29}$$

An analysis of this periodic wave will also give us

$$c_p = c_p(X_p), \tag{8.30}$$

which we will discuss further at a later stage. Finally, we note that as $x - c_f t \to -\infty$, we must have

$$\mathcal{F}(x - c_f t; t) \sim \mathcal{G}(x - c_p t)$$

i.e.

$$\mathcal{F}\left(x - c_p t + (c_p - c_f)(t + T_f)\right) \sim \mathcal{G}\left(x - c_p(t + T_p)\right)$$

so that

$$(c_p - c_f)\, T_f = -c_p\, T_p$$

i.e.

$$T_p = \frac{c_f - c_p}{c_p} T_f \tag{8.31}$$

and c_f, c_p, T_f, T_p and X_p are now all specified. Obviously for Turing systems, this simplifies somewhat, as we have $c_p = 0$ and $T_p = \infty$; we have

$$T = T_f = \frac{2\pi}{\operatorname{Im} F(c)}, \qquad X = X_p = \frac{2\pi\, c}{\operatorname{Im} F(c)}, \qquad c = c_f \tag{8.32}$$

as before in (7.20).

We can also consider the results of Murray [40] above against our WKB approximation. Comparing (7.9) with (8.5), and taking $c = x/t$, we can see that

$$F(c) = i\, k_0\, c + \lambda(k_0) \tag{8.33}$$

and from (7.14) and (8.13) we can expect to obtain c as the value of η when Re $F = 0$. Since $p = F_\eta$, then

$$k_0 = -i\, p(c), \tag{8.34}$$

which can easily be determined. Im $F(c)$ will give ω as defined in (8.14) and k^* can be deduced from (8.15). We can also obtain the wavenumber corresponding to the fastest growing mode (which is observed immediately after the initial perturbation; see (8.8)). This occurs at $\eta = 0$ and is given by

$$k_f = -i\, p(0), \tag{8.35}$$

although this quantity is of no great practical interest.

8.3 Asymptotic limits

By solving (8.23), we can find six possible solutions for $f(x,t)$; however, with the exception of a few special cases, this has to be carried out numerically. Asymptotic analysis can give us the local behaviour for η small and large which will help to give initial values for a numerical scheme.

8.3.1 η small

For $\eta \to 0$, we consider a series expansion of p in powers of η; we obtain the six expressions

$$\textbf{(1)} \quad p \sim \frac{-(d+1)\left[(\alpha-\delta)^2+4\beta\gamma\right]-(d-1)(\alpha-\delta)\sqrt{(\alpha-\delta)^2+4\beta\gamma}}{4\left[d(\alpha-\delta)^2+(d+1)^2\beta\gamma\right]}\eta, \tag{8.36}$$

$$\textbf{(2)} \quad p \sim \frac{-(d+1)\left[(\alpha-\delta)^2+4\beta\gamma\right]+(d-1)(\alpha-\delta)\sqrt{(\alpha-\delta)^2+4\beta\gamma}}{4\left[d(\alpha-\delta)^2+(d+1)^2\beta\gamma\right]}\eta, \tag{8.37}$$

$$\textbf{(3)} \quad p \sim +\left(\frac{\alpha-\delta+(d+1)\sqrt{-\beta\gamma/d}}{d-1}\right)^{1/2} - \frac{(d-1)^2\sqrt{-\beta\gamma}}{8d\left[\sqrt{-\beta\gamma}(d+1)+\sqrt{d}(\alpha-\delta)\right]}\eta, \tag{8.38}$$

$$\textbf{(4)} \quad p \sim -\left(\frac{\alpha-\delta+(d+1)\sqrt{-\beta\gamma/d}}{d-1}\right)^{1/2} - \frac{(d-1)^2\sqrt{-\beta\gamma}}{8d\left[\sqrt{-\beta\gamma}(d+1)+\sqrt{d}(\alpha-\delta)\right]}\eta, \tag{8.39}$$

$$\textbf{(5)} \quad p \sim +\left(\frac{\alpha-\delta-(d+1)\sqrt{-\beta\gamma/d}}{d-1}\right)^{1/2} - \frac{(d-1)^2\sqrt{-\beta\gamma}}{8d\left[\sqrt{-\beta\gamma}(d+1)-\sqrt{d}(\alpha-\delta)\right]}\eta, \tag{8.40}$$

$$\textbf{(6)} \quad p \sim -\left(\frac{\alpha-\delta-(d+1)\sqrt{-\beta\gamma/d}}{d-1}\right)^{1/2} - \frac{(d-1)^2\sqrt{-\beta\gamma}}{8d\left[\sqrt{-\beta\gamma}(d+1)-\sqrt{d}(\alpha-\delta)\right]}\eta, \tag{8.41}$$

which we have written out separately to pair them to the asymptotic expressions for $\eta \to \infty$. Writing (8.36)–(8.41) for F, we obtain the forms

$$(1) \quad F \sim \frac{1}{2}\left(\alpha+\delta+\sqrt{\phi_1}\right)+\frac{\phi_3-\phi_4}{8\,\phi_2}\eta^2, \tag{8.42}$$

$$(2) \quad F \sim \frac{1}{2}\left(\alpha+\delta-\sqrt{\phi_1}\right)+\frac{\phi_3+\phi_4}{8\,\phi_2}\eta^2, \tag{8.43}$$

$$(3) \quad F \sim \frac{(\alpha d-\delta+2d\sqrt{-\beta\gamma/d})}{d-1}+\left(\frac{\alpha-\delta+(d+1)\sqrt{-\beta\gamma/d}}{d-1}\right)^{1/2}\eta, \tag{8.44}$$

$$(4) \quad F \sim \frac{(\alpha d-\delta+2d\sqrt{-\beta\gamma/d})}{d-1}-\left(\frac{\alpha-\delta+(d+1)\sqrt{-\beta\gamma/d}}{d-1}\right)^{1/2}\eta, \tag{8.45}$$

$$(5) \quad F \sim \frac{(\alpha d-\delta-2d\sqrt{-\beta\gamma/d})}{d-1}+\left(\frac{\alpha-\delta-(d+1)\sqrt{-\beta\gamma/d}}{d-1}\right)^{1/2}\eta, \tag{8.46}$$

$$(6) \quad F \sim \frac{(\alpha d-\delta-2d\sqrt{-\beta\gamma/d})}{d-1}-\left(\frac{\alpha-\delta-(d+1)\sqrt{-\beta\gamma/d}}{d-1}\right)^{1/2}\eta, \tag{8.47}$$

where

$$\phi_1 = (\alpha-\delta)^2+4\,\beta\,\gamma \tag{8.48}$$

$$\phi_2 = d\,(\alpha-\delta)^2+(d+1)^2\,\beta\,\gamma \tag{8.49}$$

$$\phi_3 = -(d+1)\,\phi_1 \tag{8.50}$$

$$\phi_4 = (d-1)(\alpha-\delta)\,\sqrt{\phi_1}. \tag{8.51}$$

8.3.2 η large

We can carry out a similar analysis for $\eta \to \infty$ to obtain

$$\text{(a)} \quad p \sim \left(\frac{\alpha-\delta+2\sqrt{-\beta\,\gamma}}{d-1}\right)^{1/2}, \tag{8.52}$$

$$\text{(b)} \quad p \sim -\left(\frac{\alpha-\delta+2\sqrt{-\beta\,\gamma}}{d-1}\right)^{1/2}, \tag{8.53}$$

$$\text{(c)} \quad p \sim \left(\frac{\alpha-\delta-2\sqrt{-\beta\,\gamma}}{d-1}\right)^{1/2}, \tag{8.54}$$

$$\text{(d)} \quad p \sim -\left(\frac{\alpha-\delta-2\sqrt{-\beta\,\gamma}}{d-1}\right)^{1/2}, \tag{8.55}$$

$$\text{(e)} \quad p \sim -\frac{1}{2}\eta, \tag{8.56}$$

$$\text{(f)} \quad p \sim -\frac{1}{2\,d}\eta, \tag{8.57}$$

for p and

$$\textbf{(a)} \qquad F \sim \frac{\alpha d - \delta + (d+1)\sqrt{-\beta\gamma}}{d-1} + \left(\frac{\alpha - \delta + 2\sqrt{-\beta\gamma}}{d-1}\right)^{1/2} \eta, \qquad (8.58)$$

$$\textbf{(b)} \qquad F \sim \frac{\alpha d - \delta + (d+1)\sqrt{-\beta\gamma}}{d-1} - \left(\frac{\alpha - \delta + 2\sqrt{-\beta\gamma}}{d-1}\right)^{1/2} \eta, \qquad (8.59)$$

$$\textbf{(c)} \qquad F \sim \frac{\alpha d - \delta - (d+1)\sqrt{-\beta\gamma}}{d-1} + \left(\frac{\alpha - \delta - 2\sqrt{-\beta\gamma}}{d-1}\right)^{1/2} \eta, \qquad (8.60)$$

$$\textbf{(d)} \qquad F \sim \frac{\alpha d - \delta - (d+1)\sqrt{-\beta\gamma}}{d-1} - \left(\frac{\alpha - \delta - 2\sqrt{-\beta\gamma}}{d-1}\right)^{1/2} \eta, \qquad (8.61)$$

$$\textbf{(e)} \qquad F \sim -\frac{1}{4}\eta^2, \qquad (8.62)$$

$$\textbf{(f)} \qquad F \sim -\frac{1}{4d}\eta^2, \qquad (8.63)$$

for F. Note that expressions are *not* 'paired' with those for η small at this stage; we shall consider them later. The constant terms in (8.58)–(8.61) have been left in the expressions because they are usually real in the parameter ranges we will be using; the coefficients of η are often purely imaginary, and then the constant terms *can* give important extra information.

We note at this point that (8.58)–(8.61), on using (8.16) and (7.9), imply that approximately

$$\mathbf{u} \sim e^{-\mu x} \qquad \text{as } x/t \to \infty \qquad (8.64)$$

for some μ whereas (8.62) and (8.63) give

$$\mathbf{u} \sim e^{-\mu x^2/t} \qquad \text{as } x/t \to \infty. \qquad (8.65)$$

We expect the decay to be as quick as possible away from the travelling front, so (8.62) or (8.63) would appear to give the applicable behaviour in the far field; (8.64) is not consistent with a localised initial disturbance (the non-envelope solutions are also of this type, with *arbitrary* μ).

8.4 Numerical Results (Turing Systems)

We now consider numerically computed solutions. For comparisons with previous work, we once again use the FitzHugh-Nagumo kinetics (see (6.3) and (6.4)), i.e.

$$f(u,v) = u(a_1 + u)(a_2 - u) - v, \qquad g(u,v) = u - v. \tag{8.66}$$

This implies that our values for α, β, γ, δ in (8.3) are

$$\alpha = a_1\, a_2, \qquad \beta = -1, \qquad \gamma = 1, \qquad \delta = -1 \tag{8.67}$$

and from (8.4), we deduce that we require

$$d > \frac{1}{(a_1\, a_2)^2}\left(2 - a_1\, a_2 + 2\sqrt{1 - a_1\, a_2}\right)$$

as the necessary and sufficient condition for the system to produce Turing instabilities. Taking $a_1 = a_2 = 1/2$ (we will consider $a_1 \neq a_2$ later), we thus require

$$d > d_c = 28 + 16\sqrt{3} \approx 55.7.$$

We will now compute solutions to (8.23) for different values of d (Turing and non-Turing) to investigate the behaviour, which we can compare to numerical solutions of the full system of partial differential equations (8.2), of which we show two in Figures 8.2 and 8.3 for $d = 250$ and $d = 500$ respectively; these were initiated by a small perturbation in u at $x = 0$.

8.4.1 $d = 500$

We choose a large value of d for analysis to capture the full essence of the Turing solution. In the numerical solution shown in Figure 8.3 we can see how the pattern laid down behind the initial front is fixed away from $x = 0$, with a spatial period of $X \approx 46.5$. The 'double peaks' obtained (which are not evident for smaller d; see Figure 8.2) are not a numerical artefact, which can be confirmed by solving the problem in a range equal to the observed period with the end points fixed; this is illustrated in Figure 8.4. Even if we set an initial profile containing a single peak, the double peak still evolves.

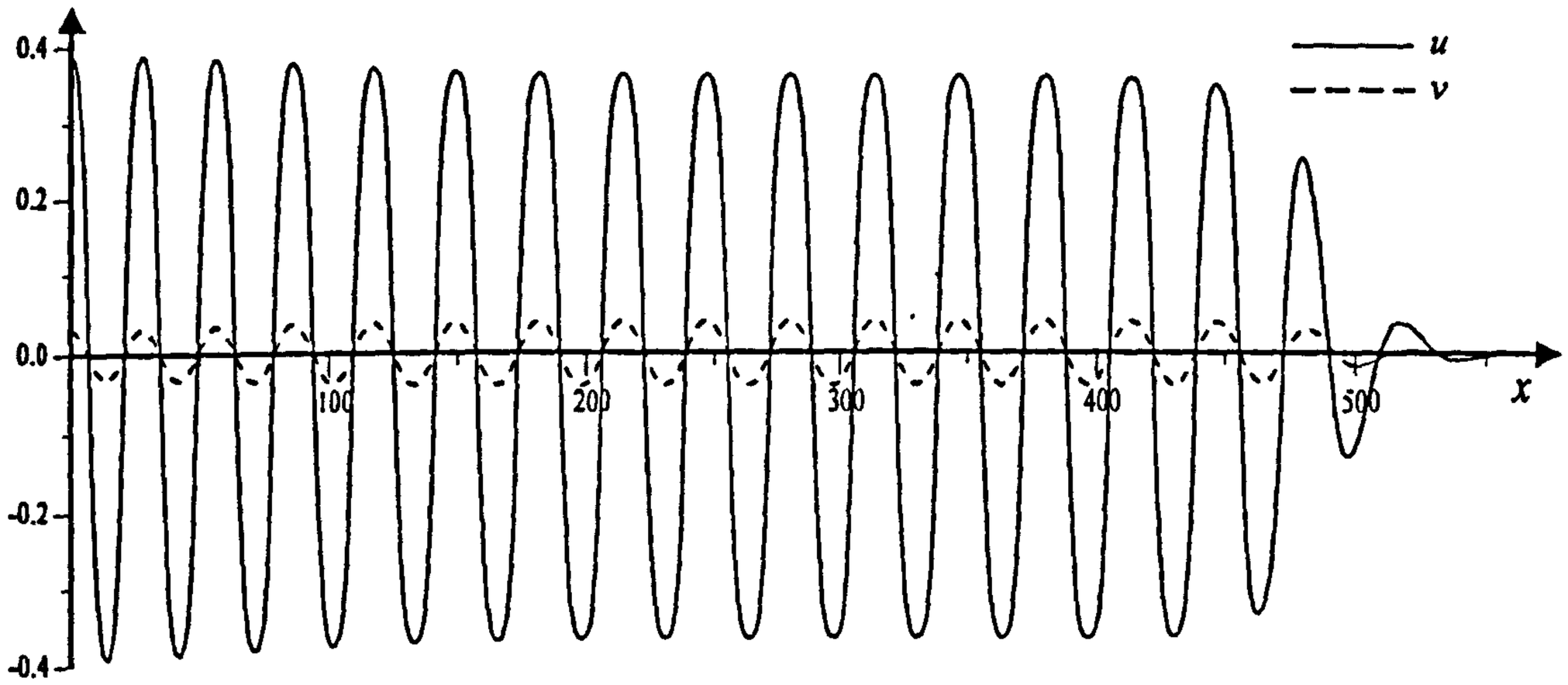

Figure 8.2: Full numerical solution for $a_1 = a_2 = 1/2$, $d = 250$ at $t = 300$.

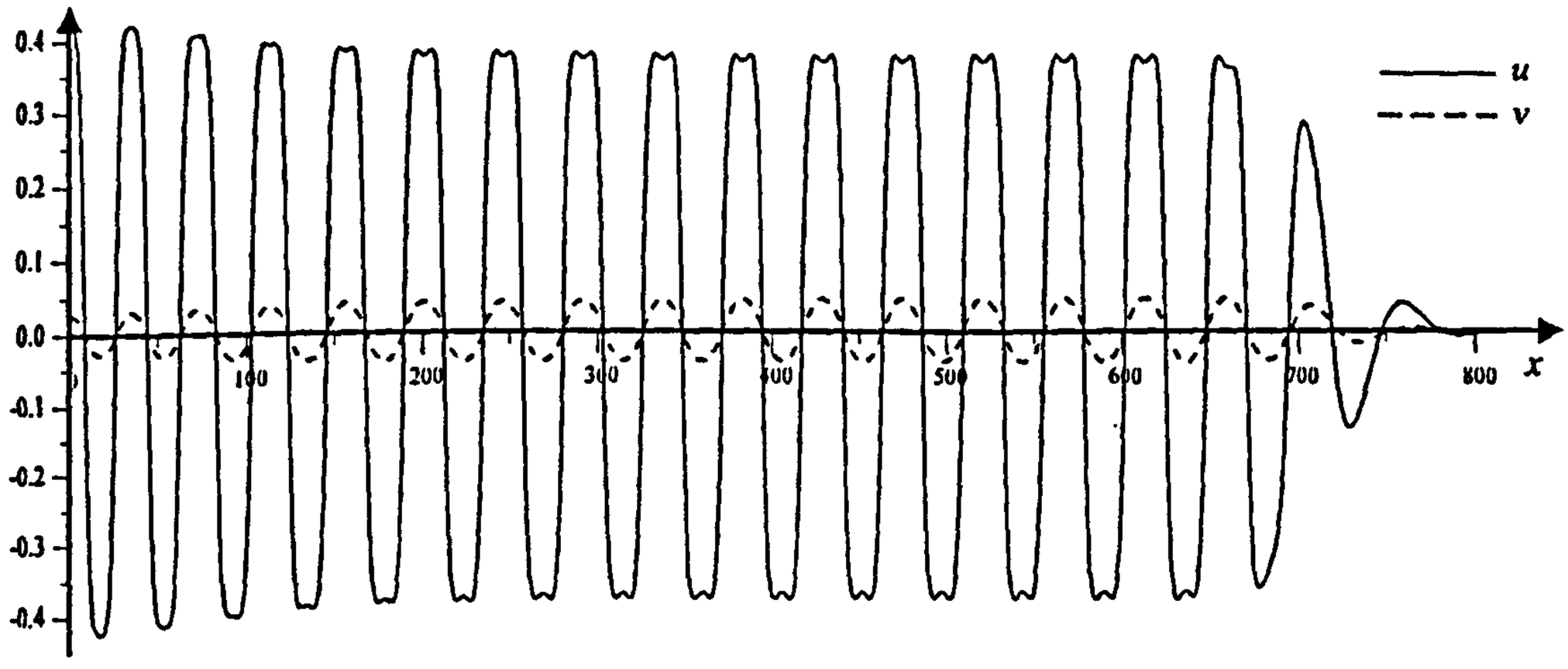

Figure 8.3: Full numerical solution for $a_1 = a_2 = 1/2$, $d = 500$ at $t = 300$.

In the vicinity of $x = 0$ it can be seen in Figure 8.3 that the spatial period is much smaller, with $X_0 \approx 32.0$, due to the pattern not having reached a stable configuration. At the leading front, the wave speed is $c \approx 2.71$.

We now look at the six numerical solutions to the algebraic equation (8.23). We solve for a finite range of η, using (8.36)–(8.41) (in order) to provide a starting value in each case. The solutions for F can then be plotted; however, firstly we evaluate the asymptotic forms for F given by (8.42)–(8.47) and (8.58)–(8.63), and number them for easy reference later.

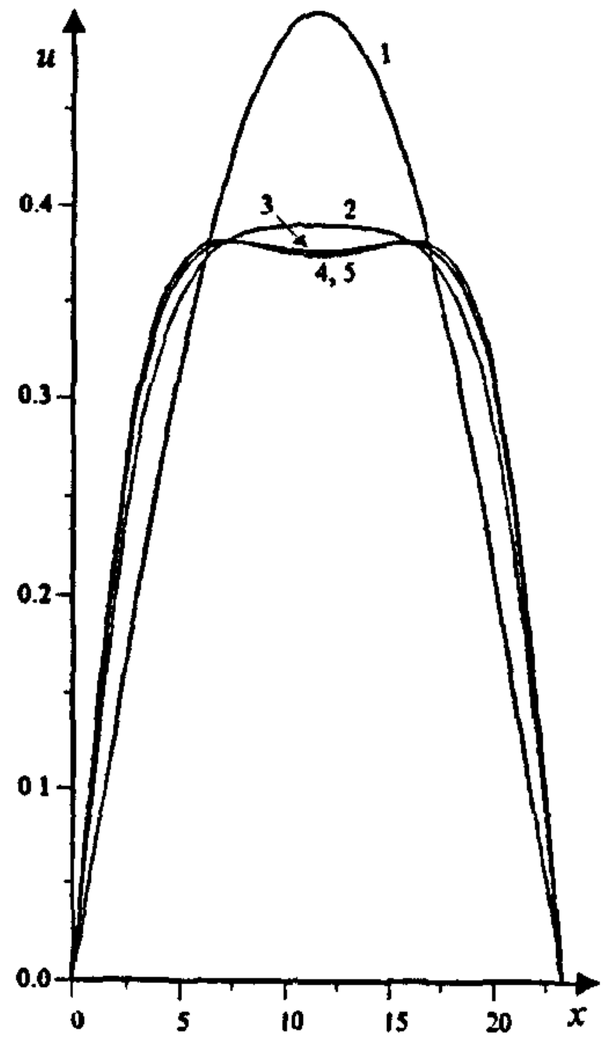

Figure 8.4: Evolution of a 'double peak' from an initial single peak for u ($d = 500$), the end points fixed at the numerically-observed period of $X = 46.5$.

- $\eta \to 0$:

  (1) $F \sim -0.375 + 0.781\,i + 10^{-4}\,(-1.52 + 1.21\,i)\,\eta^2$,

  (2) $F \sim -0.375 - 0.781\,i + 10^{-4}\,(-1.52 - 1.21\,i)\,\eta^2$,

  (3) $F \sim 0.342 + 0.218\,\eta$,

  (4) $F \sim 0.342 - 0.218\,\eta$,

  (5) $F \sim 0.163 + 0.206\,i\,\eta$,

  (6) $F \sim 0.163 - 0.206\,i\,\eta$.

- $\eta \to \infty$:

  (a) $F \sim 0.0807\,\eta$,

  (b) $F \sim -0.0807\,\eta$,

  (c) $F \sim -0.756 + 0.0388\,i\,\eta$,

  (d) $F \sim -0.756 - 0.0388\,i\,\eta$,

  (e) $F \sim -0.25\,\eta^2$,

  (f) $F \sim -0.0005\,\eta^2$.

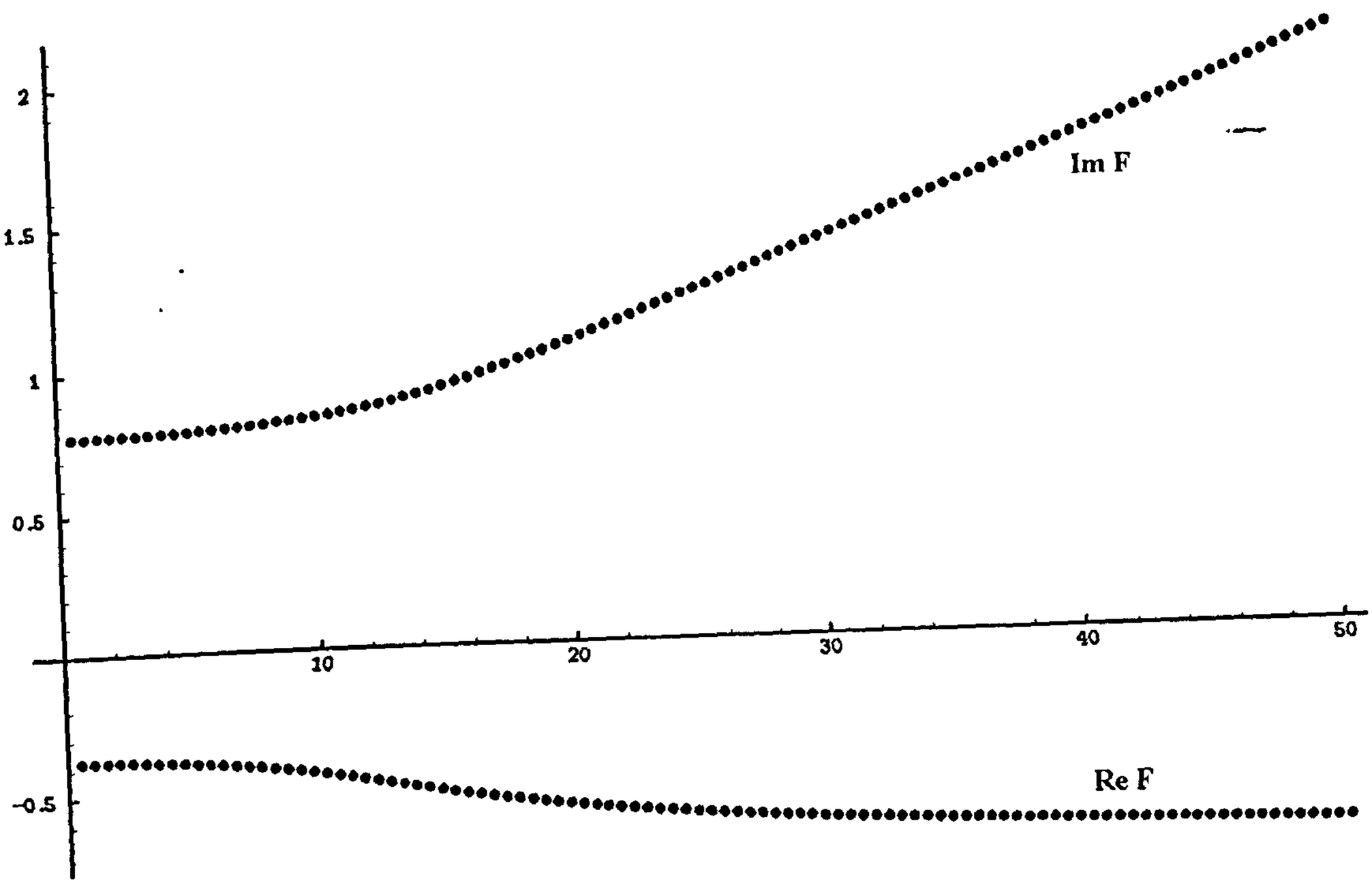

Figure 8.5: Numerical solution for F corresponding to asymptotic form (1) as $\eta \to 0$; $d = 500$.

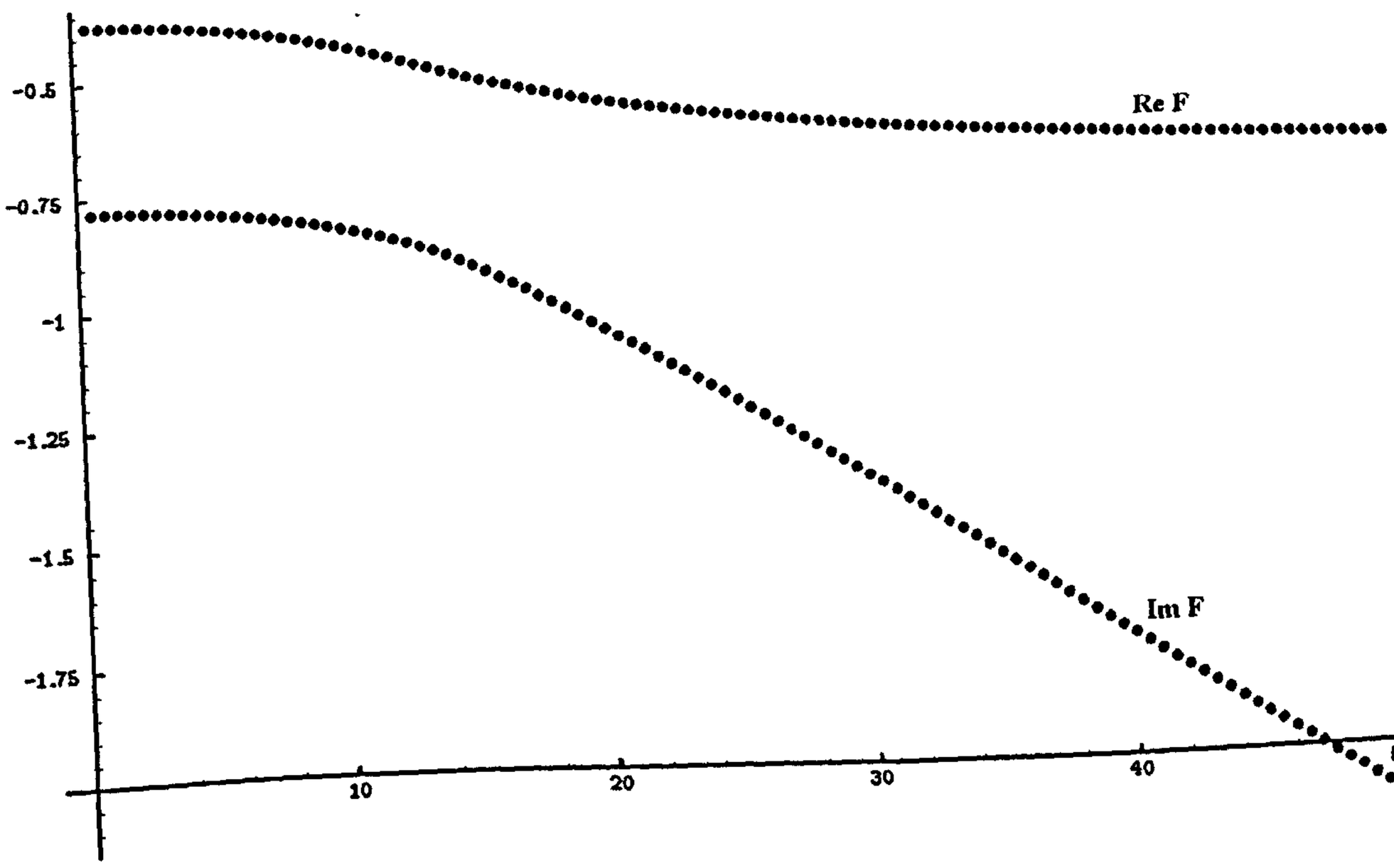

Figure 8.6: Numerical solution for F corresponding to asymptotic form (2) as $\eta \to 0$; $d = 500$ (complex conjugate of Figure 8.5).

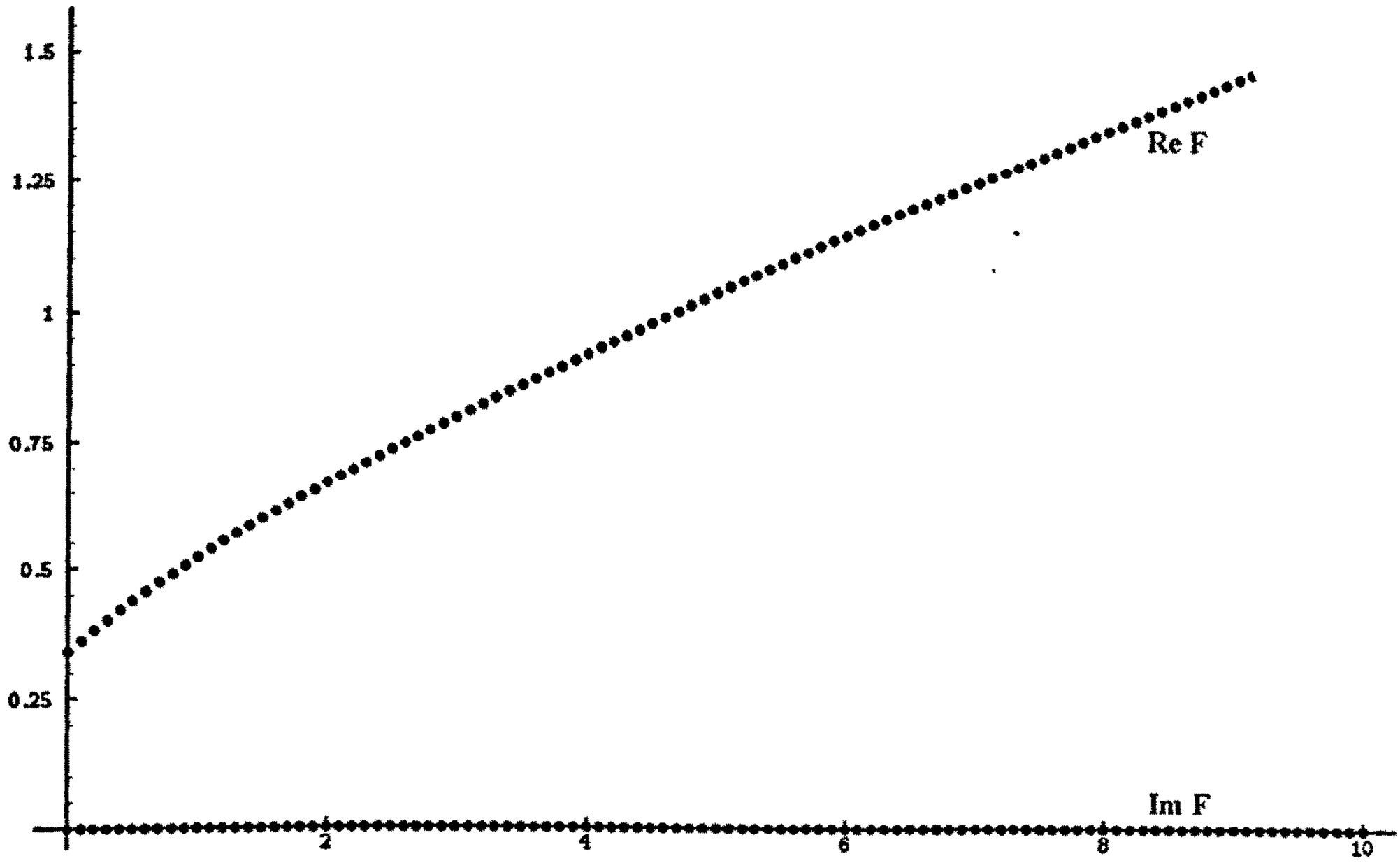

Figure 8.7: Numerical solution for F corresponding to asymptotic form **(3)** as $\eta \to 0$; $d = 500$.

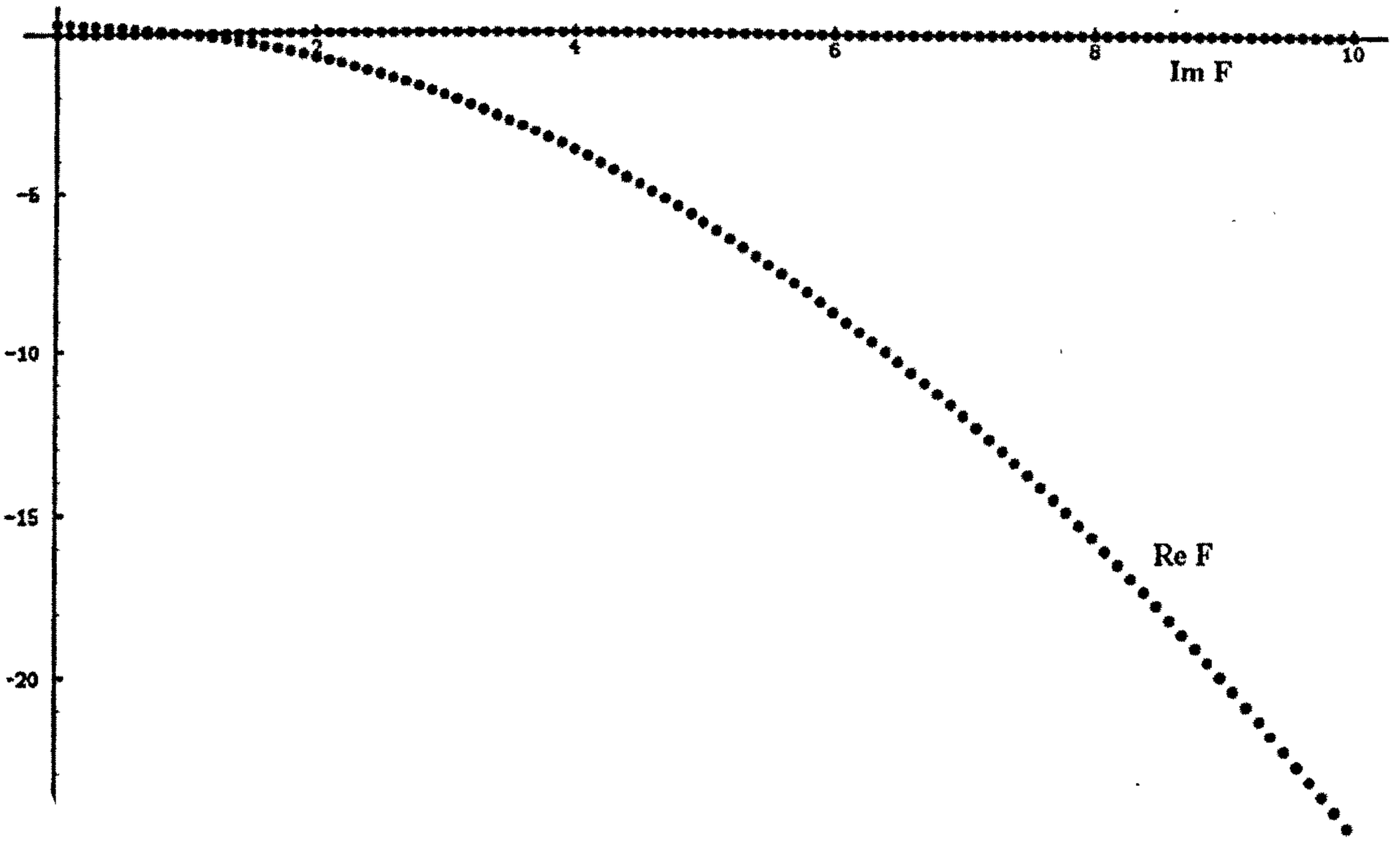

8: Numerical solution for F corresponding to asymptotic form (4) as $\eta \to 0$;

The first four solution plots are shown in Figures 8.5–8.8 (we plot separate curves for the real and imaginary components). We can easily determine the far-field behaviour for these cases (at this stage for $d = 500$; general d will be discussed later) :

(1) matches with case **(c)** as $\eta \to \infty$,

(2) matches with case **(d)** as $\eta \to \infty$,

(3) matches with case **(a)** as $\eta \to \infty$,

(4) matches with case **(e)** as $\eta \to \infty$.

For the last two solutions, the behaviour is less obvious, as can be seen if we consider the numerical solution for p in both cases shown in Figure 8.9. We can easily track

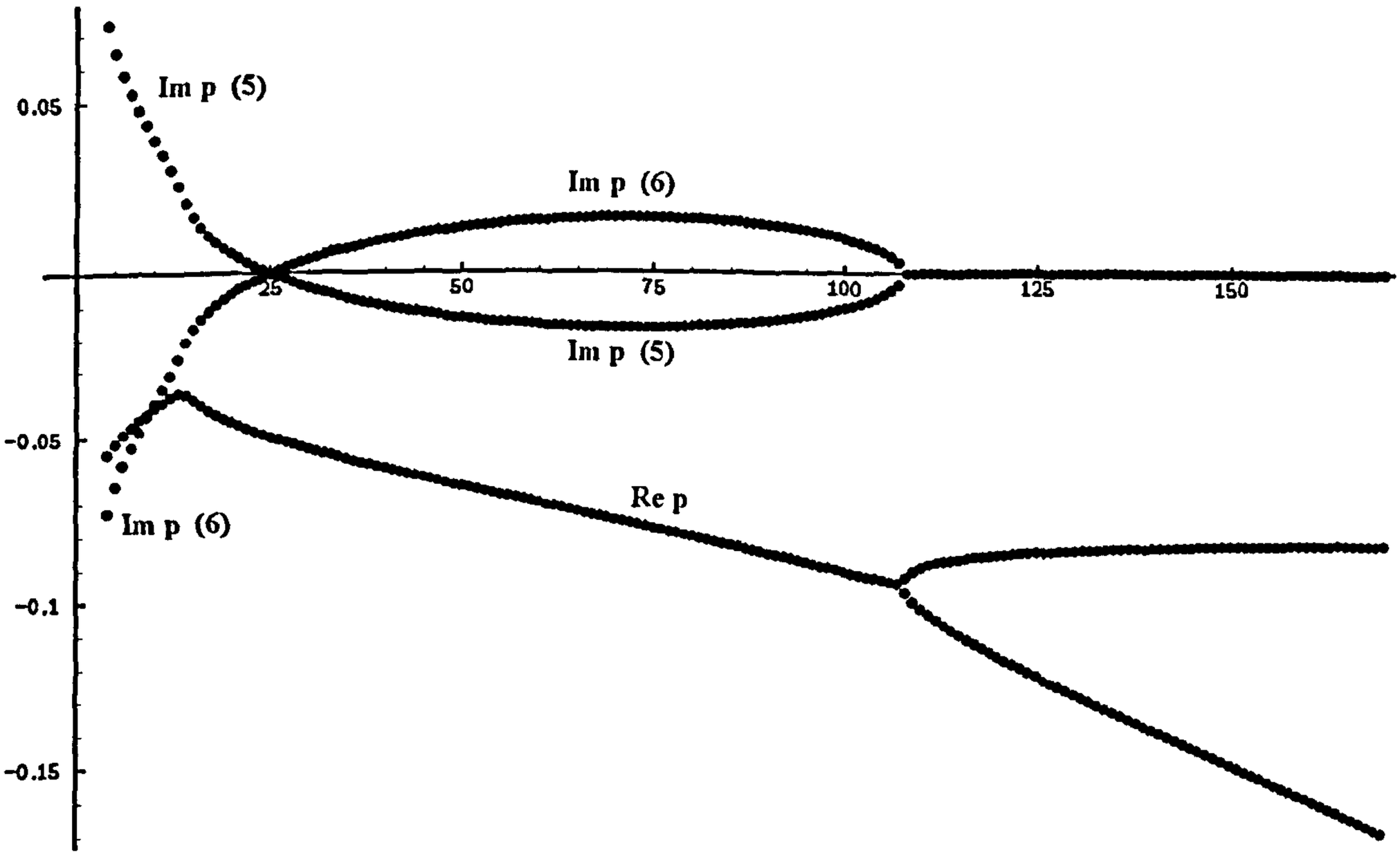

Figure 8.9: Numerical solution for p corresponding to asymptotic forms **(5)** and **(6)** as $\eta \to 0$; $d = 500$.

the solutions up to $\eta \approx 108$, and over this range they are complex conjugates. At this point, however, both solutions become real, and bifurcate; i.e. the complex conjugate pair splits into two distinct real solutions for p. The solutions for F show similar behaviour; as shown in Figures 8.10 and 8.11 we obtain complex conjugate solutions for $\eta < 108$,

and two distinct real solutions for $\eta > 108$. For $\eta > 108$, we have the option of linear or quadratic decay of F (i.e. asymptotic forms **(2)** or **(6)**). This is shown in Figure 8.12.

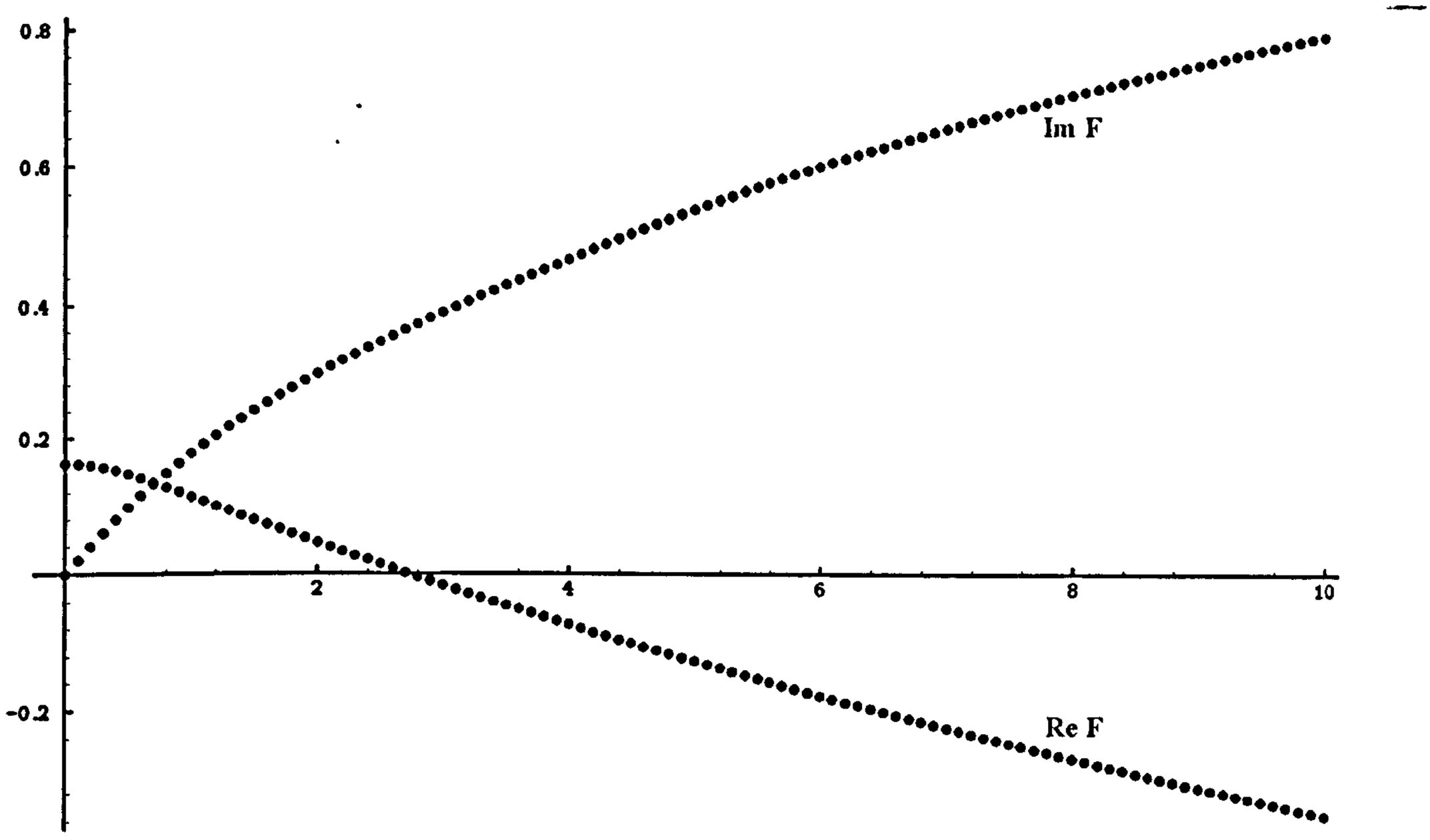

Figure 8.10: Numerical solution for F corresponding to asymptotic form **(5)** as $\eta \to 0$; $d = 500$.

We can now consider which of the above solutions is the one observed, and compare it with the numerical results. As mentioned above, we require a solution for F which decays like $-\eta^2$; this only leaves us with solutions **(4)** and one of **(5)** or **(6)**, as shown in Figures 8.8 and 8.12. We have two methods of determining the wave speed; from (8.13) and (8.33), we have Re $F(c) = 0$, which gives the speeds

$$\begin{aligned} c &= 1.014 \text{ for case } \mathbf{(4)}, \\ c &= 2.734 \text{ for case } \mathbf{(5)/(6)}. \end{aligned} \tag{8.68}$$

The full numerical solution hints that the latter case will give the observed solution; case **(4)**, being a purely real solution, corresponds to a fixed form travelling wave, and we might expect it to be observed when its wave speed is faster than case **(5)/(6)**; however, this is found not always to be the case, and is discussed later using other parameter values.

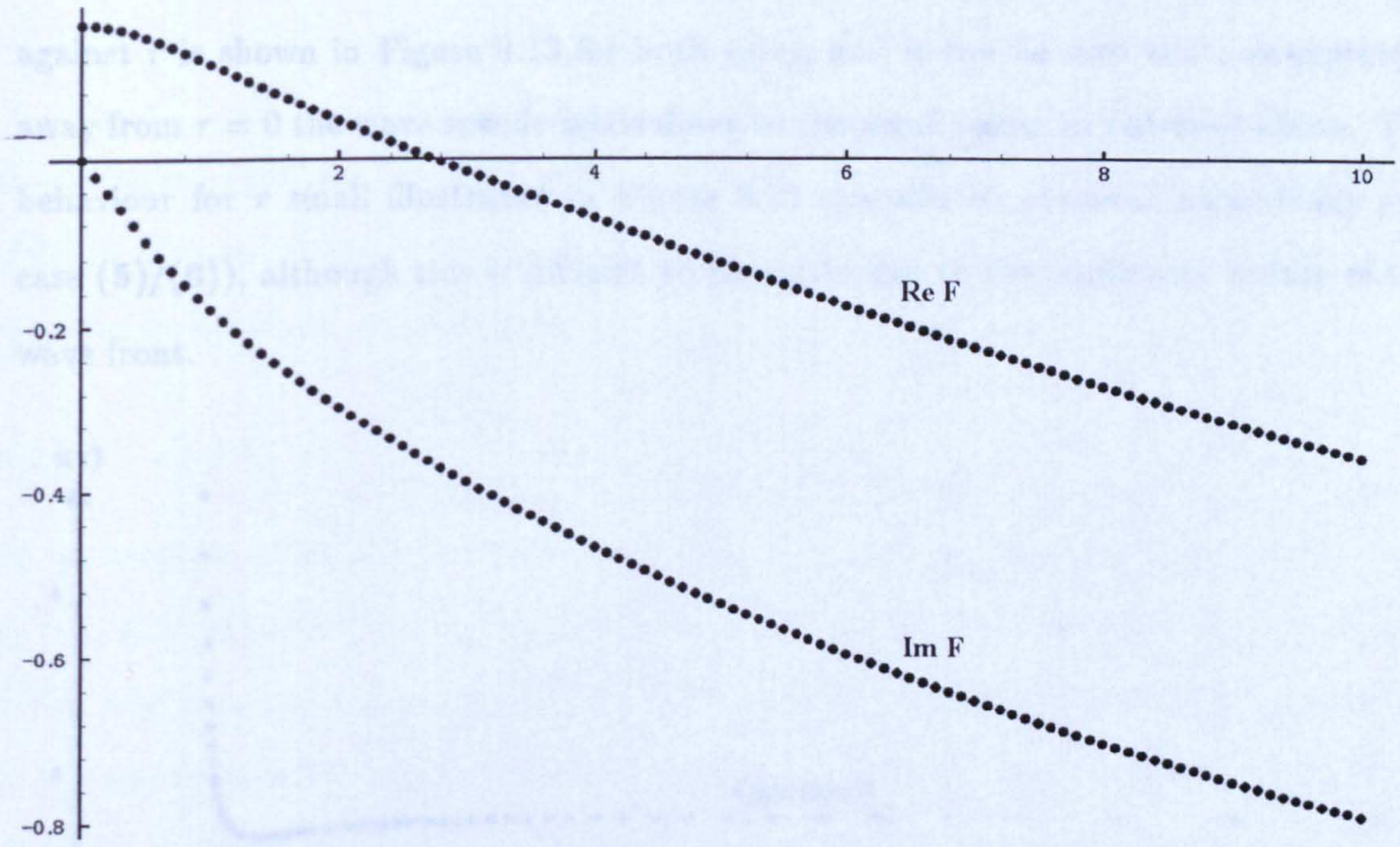

Figure 8.11: Numerical solution for F corresponding to asymptotic form **(6)** as $\eta \to 0$; $d = 500$ (complex conjugate of Figure 8.10).

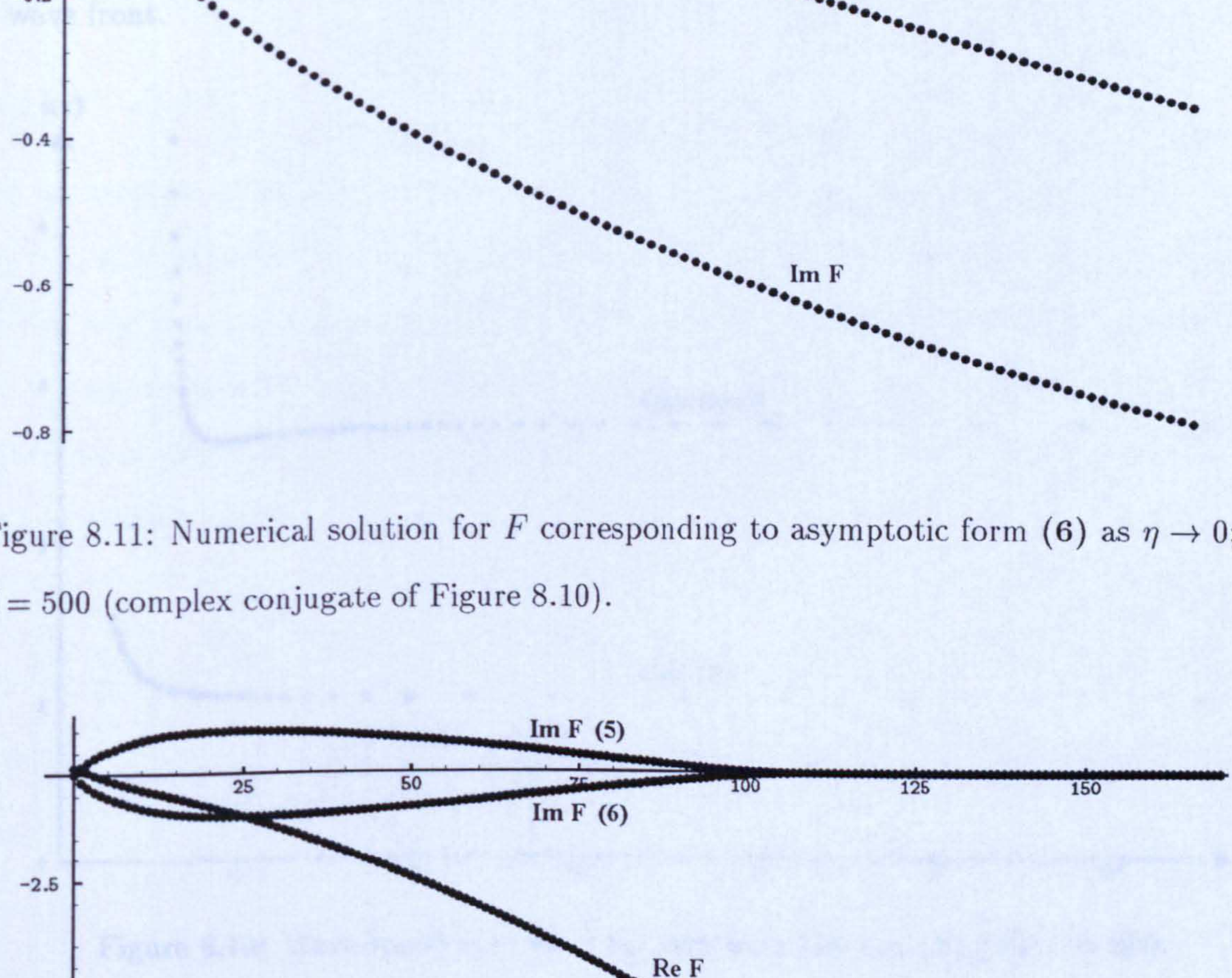

Figure 8.12: Numerical solution for F corresponding to asymptotic forms **(5)** and **(6)** as $\eta \to 0$; $d = 500$.

Our second method for determining the wave speed is given by (8.27); a plot of $\dot{s}(\tau)$ against τ is shown in Figure 8.13 for both cases, and it can be seen that, as expected, away from $\tau = 0$ the wave speeds settle down to the same values as obtained above. The behaviour for τ small illustrated in Figure 8.13 can also be observed numerically (for case (5)/(6)), although this is difficult to illustrate due to the oscillatory nature of the wave front.

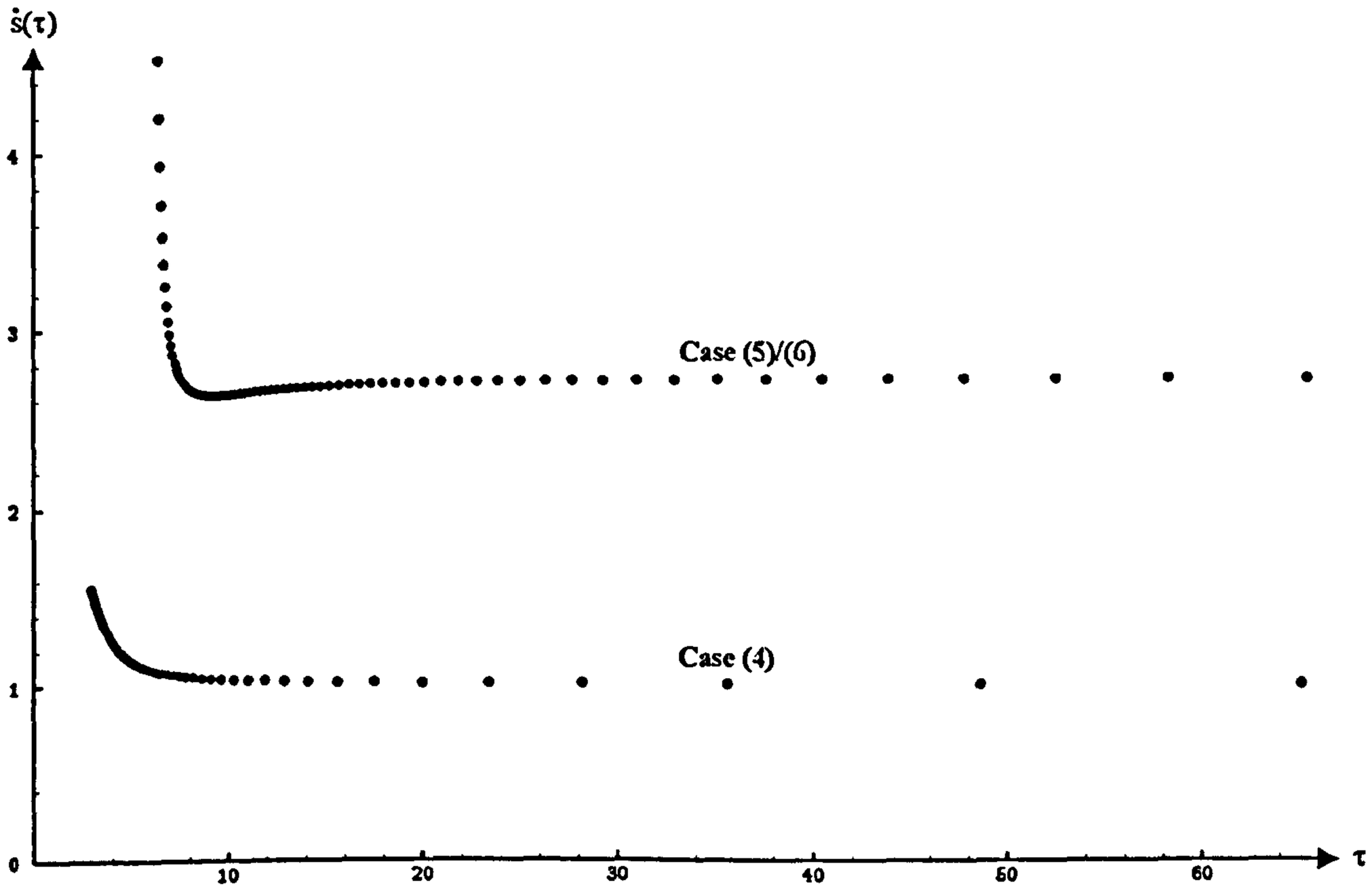

Figure 8.13: Wave speed $\dot{s}(\tau)$ vs. τ for solutions (4) and (5)/(6); $d = 500$.

Finally, we can compare the temporal and spatial periods of the solutions; from (8.32), we can see that here solution (4) cannot apply – an infinite period is implied. For case (5)/(6), we find

$$T = 17.1, \qquad X = 47.1, \tag{8.69}$$

which shows good agreement with the numerical solution shown previously in Figure 8.3; a wave speed of $c = 2.71$ and a period of $X = 46.5$ are observed. We note however from Figure 8.3 that as $x \to 0$, the period is less than this value, although from numerical observations there is virtually no change in the period once the pattern has been laid down. Our WKB method allows us to determine this spatial period as a function of η;

it is given by

$$X(\eta) = \frac{2\pi i}{p(\eta)}. \tag{8.70}$$

The value of $X(\infty)$ for solutions **(5)/(6)** is as given for X above; we can also calculate $X(0) = 30.5$ as an example case, which compares fairly well with the (approximate) numerically obtained value of $X_0 \approx 32$.

8.4.1.1 $a_1 \neq a_2$

As an example of behaviour when $a_1 \neq a_2$ in (8.66), we present numerical results for $a_1 = 1, a_2 = 1/4$ and $d = 500$. We note from (8.67) that these values imply that the above WKB solutions also apply here. Figure 8.14 shows the numerically obtained profile; as $x \to +\infty$, we observe a wave speed of $c = 2.68$ and a spatial period of $X = 45.6$; near $x = 0$ we obtain a period of $X_0 = 31.8$. These results are all in agreement with the WKB values obtained above.

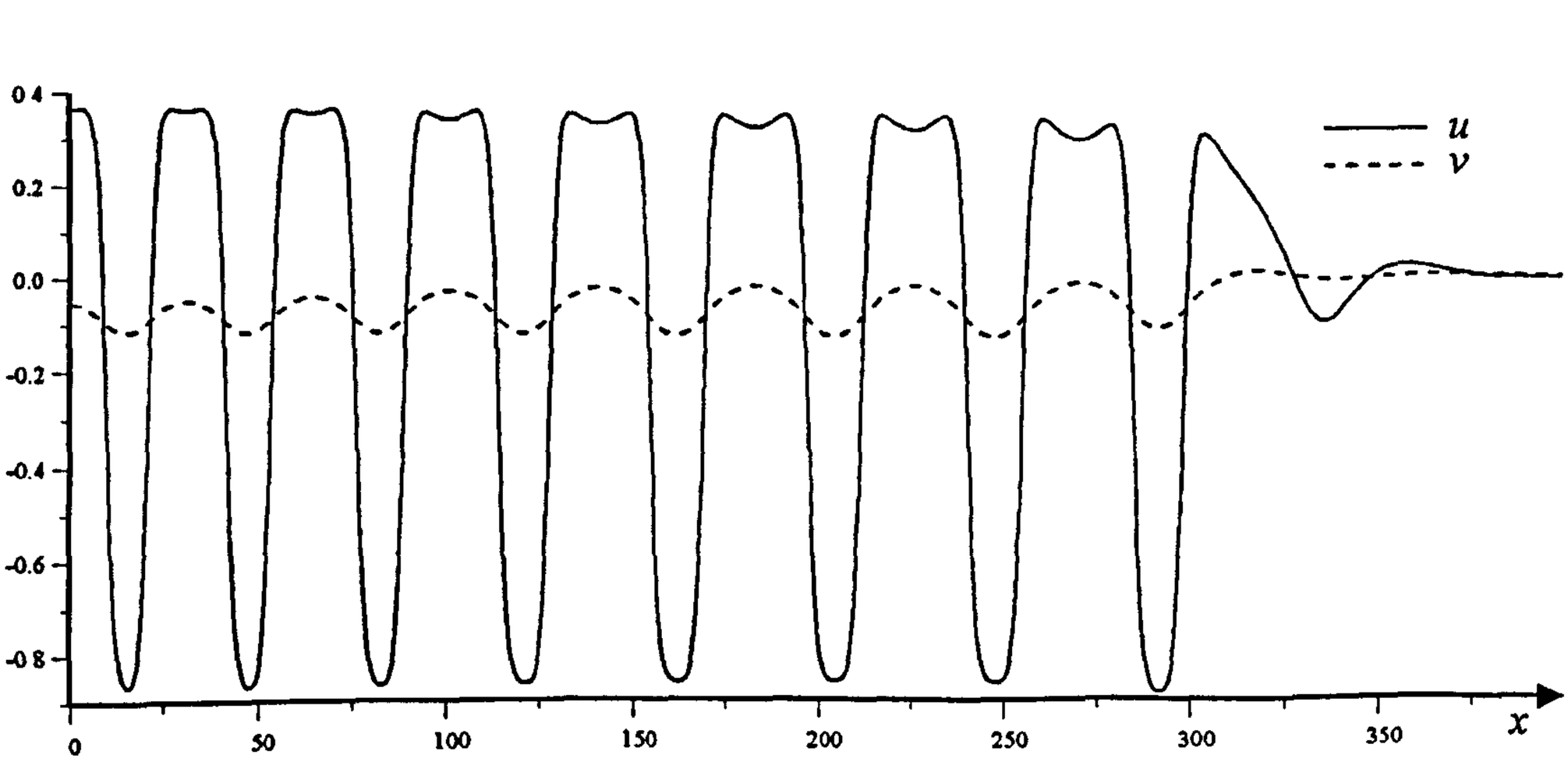

Figure 8.14: Full numerical solution for $a_1 = 1$, $a_2 = 1/4$, $d = 500$ at $t = 200$.

This completes our investigations for $d = 500$, and we can now consider other parameter values.

8.4.2 General $d > d_c$

In the region $d > d_c$, we still have a Turing system, and we find numerically that all of the solutions and asymptotic forms (and their pairings) above still apply. Even in

the limit $d \to \infty$, we do not observe any new behaviour. We list the wave speeds and spatial periods in Table 8.1 for a range of values of d, obtained from both the full numerical solution of the partial differential equations (with $a_1 = a_2 = 1/2$) and the WKB solutions **(4)** and **(5)/(6)** (similar to those shown in Figures 8.8 and 8.10). We note that the numerical expressions for the periods (especially for '$x = 0$') can only be approximate at best. From Table 8.1 we can deduce that case **(5)/(6)** is applicable in

	Numerical			WKB (4)	WKB (5)/(6)		
d	speed	X_0	X_∞	speed	speed	$X(0)$	X_∞
60	0.33	18.6	18.7	1.098	0.351	19.1	19.0
100	0.98	21.4	22.7	1.065	1.008	21.0	23.0
250	1.84	27.0	33.6	1.029	1.881	25.9	33.9
500	2.71	32.0	46.5	1.014	2.734	30.5	47.1

Table 8.1: Comparison of full numerical and WKB wave speeds and spatial periods.

all cases of Turing systems, even when case **(4)** gives a larger wave speed, as for $d = 60$ and $d = 100$ above. We can observe how the wave speed and period decrease as $d \to d_c$; if we compute the WKB solution for $d = d_c$, we find that the condition $\mathrm{Re}\, F(c) = 0$ implies a wave speed of $c = 0$ for case **(5)/(6)**; no pattern will forms in this case.

8.4.3 $1 < d < d_c$

When $1 < d < d_c$, no pattern is obtained; the steady state is stable and no fronts, diffusion-driven or otherwise, can form (any initial perturbation decays to the steady state). Nevertheless, it is still instructive to consider the WKB solutions in this regime; they are shown in Figures 8.15–8.19 for $d = 10$. We find that the asymptotic pairings change from above at precisely $d = d_c$; we obtain

(1) matches with case **(b)/(f)** as $\eta \to \infty$,

(2) matches with case **(b)/(f)** as $\eta \to \infty$,

(3) matches with case **(a)** as $\eta \to \infty$,

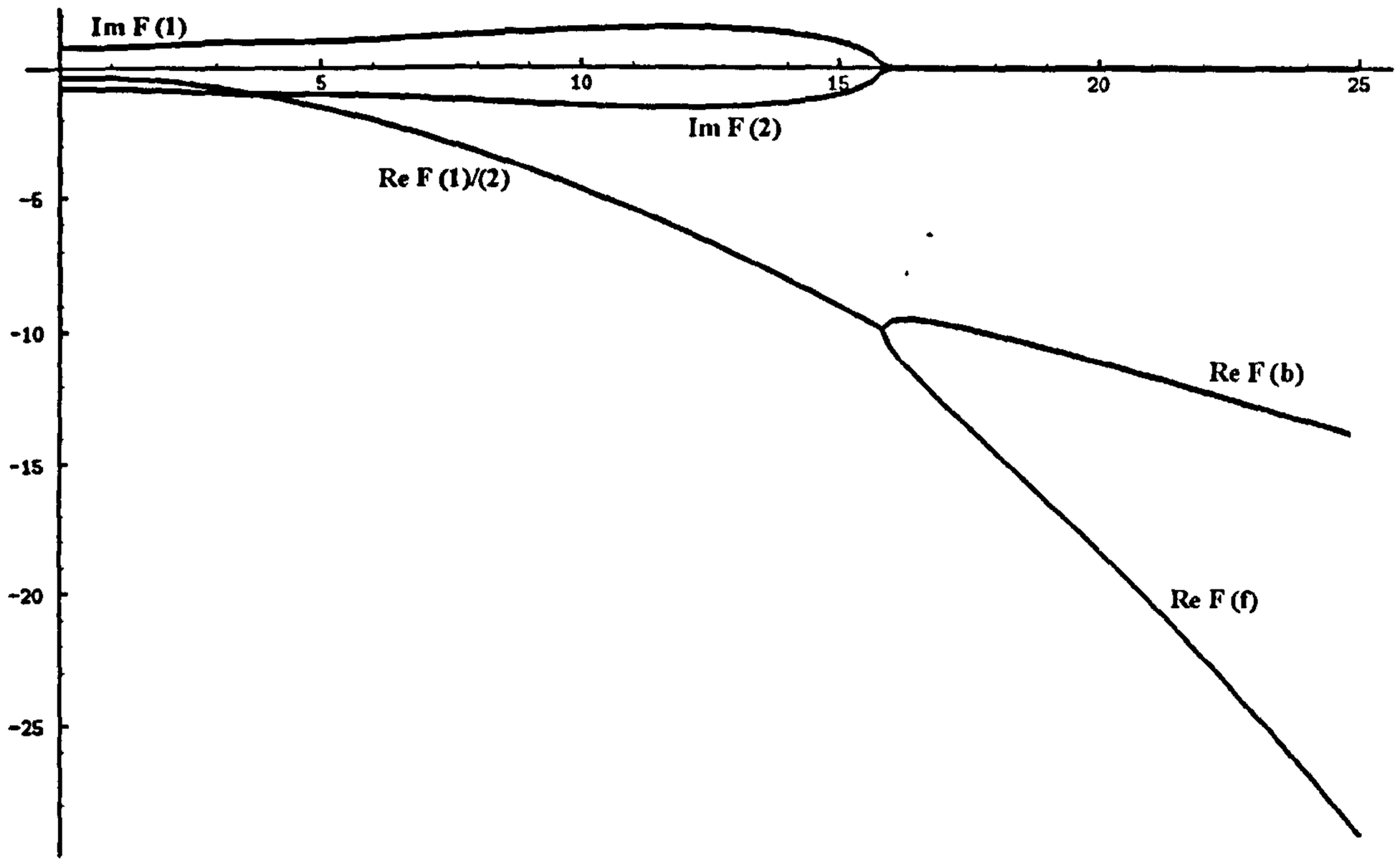

Figure 8.15: Numerical solutions for F corresponding to asymptotic forms **(1)** and **(2)** as $\eta \to 0$; $d = 10$.

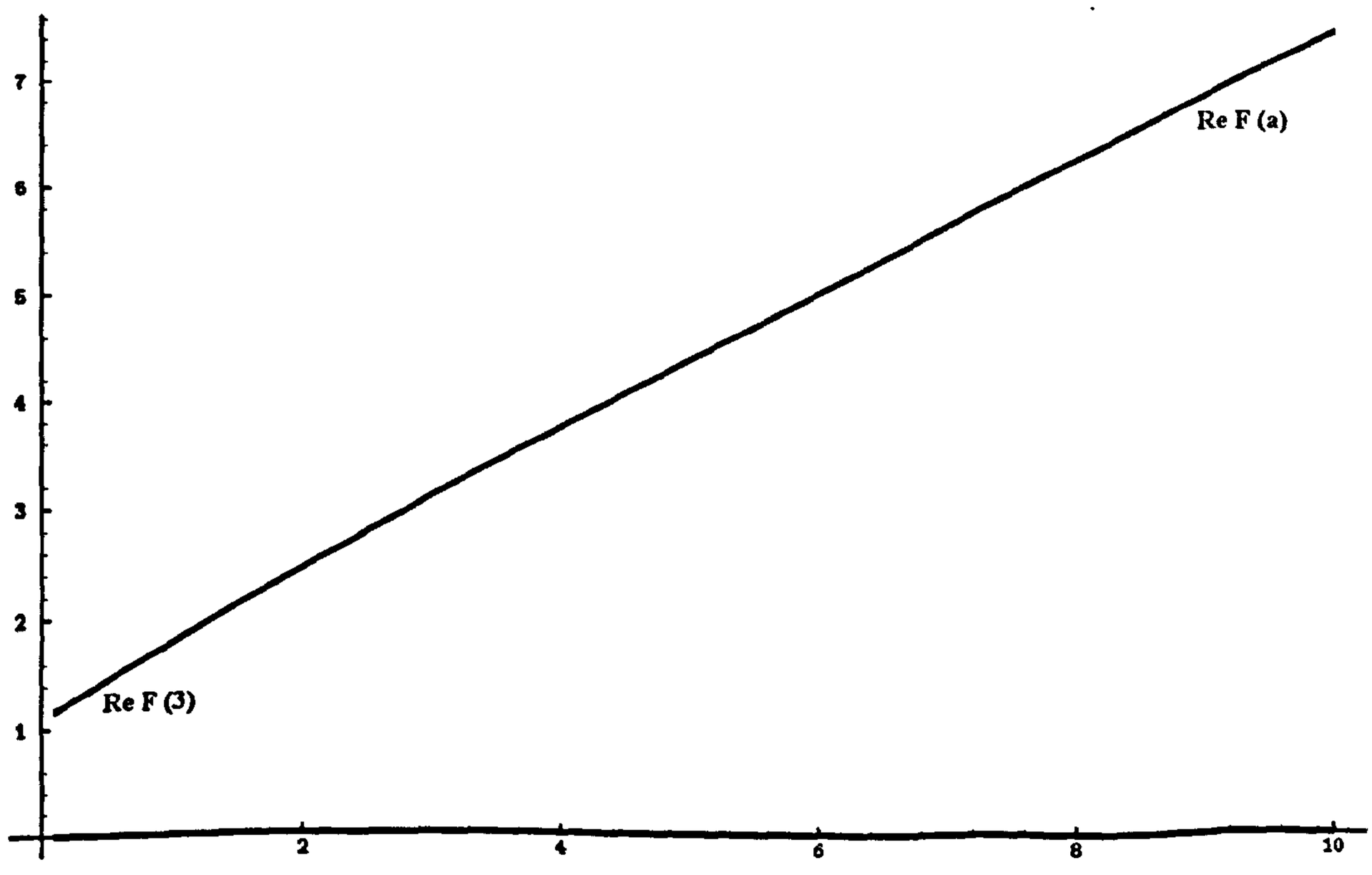

Figure 8.16: Numerical solution for F corresponding to asymptotic form **(3)** as $\eta \to 0$; $d = 10$.

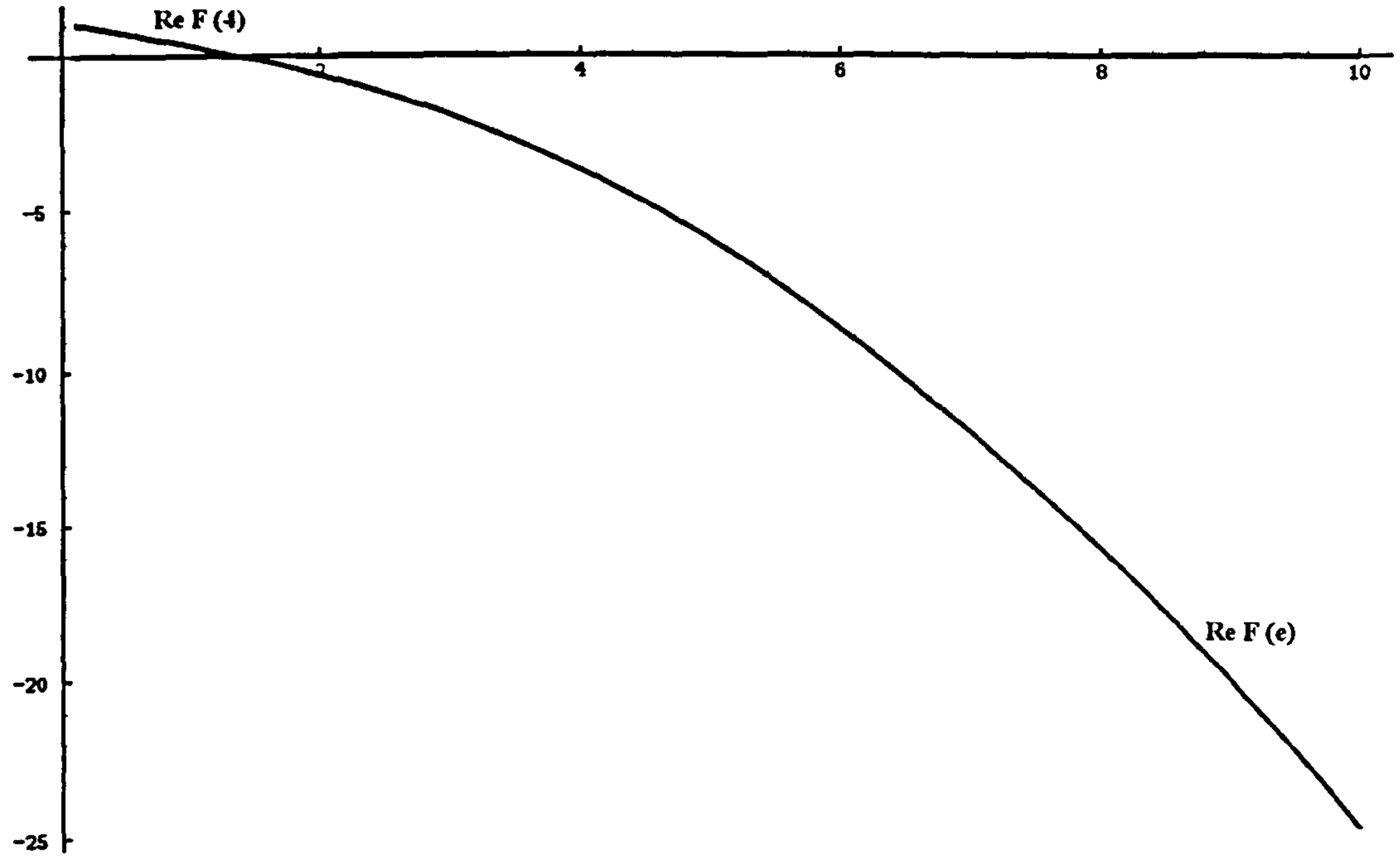

Figure 8.17: Numerical solution for F corresponding to asymptotic form (4) as $\eta \to 0$; $d = 10$.

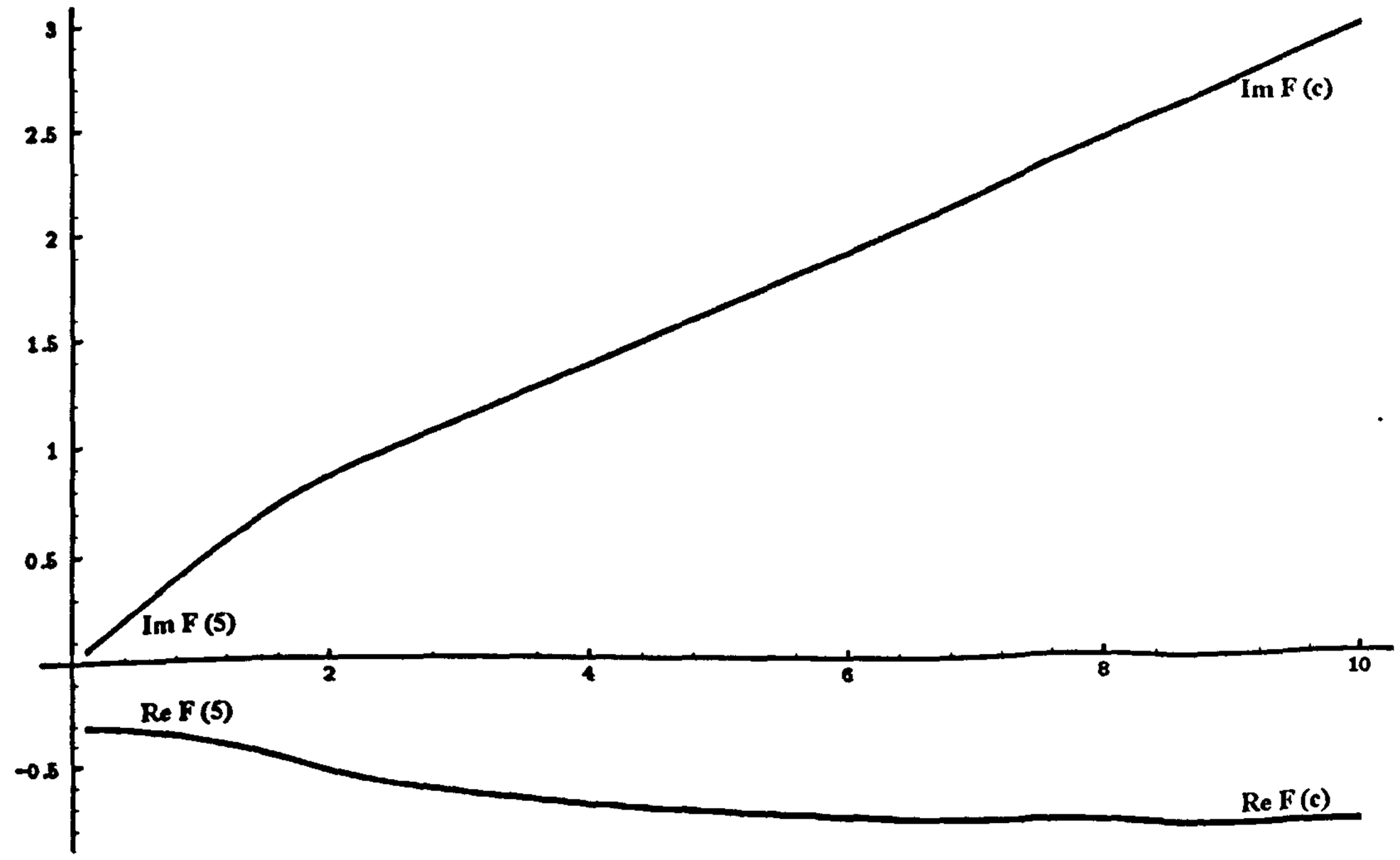

Figure 8.18: Numerical solution for F corresponding to asymptotic form (5) as $\eta \to 0$; $d = 10$.

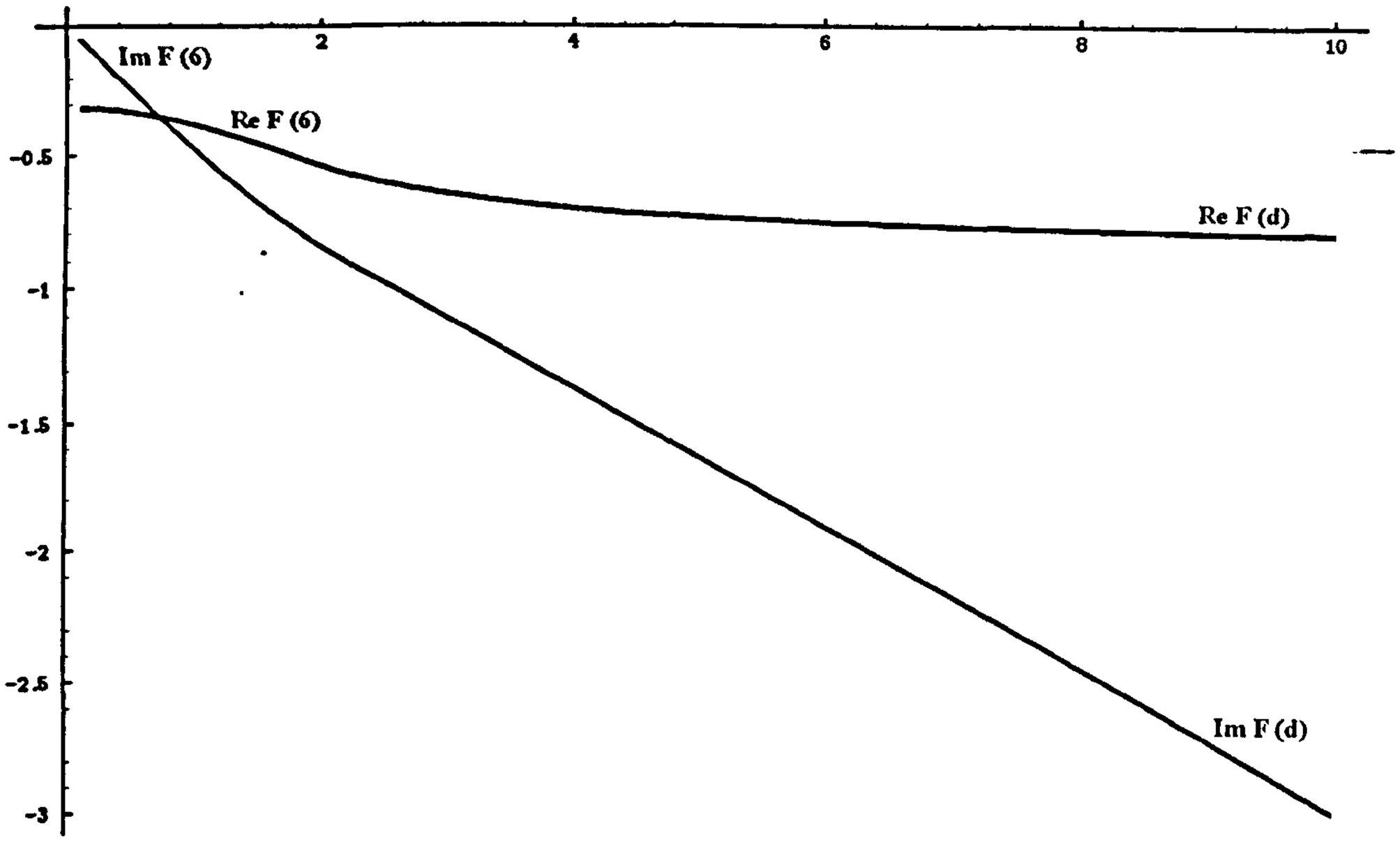

Figure 8.19: Numerical solution for F corresponding to asymptotic form (6) as $\eta \to 0$; $d = 10$ (complex conjugate of Figure 8.18).

(4) matches with case (e) as $\eta \to \infty$,

(5) matches with case (c) as $\eta \to \infty$,

(6) matches with case (d) as $\eta \to \infty$

and these are indicated on the plots. We can observe that cases (1) and (2) exchange asymptotic 'pairs' with (5) and (6) from previously. Case (4) is still of the form shown in Figure 8.8, and a wave speed can be obtained although the wave is not realised; as $d \to 1$, this speed decreases to zero. The case in Figure 8.15 has Re F negative for all η, consistent with the decay of initial perturbations.

8.4.4 $0 < d < 1$

The asymptotic pairings change once again at $d = 1$, and in the range $0 < d < 1$ we obtain

(1) matches with case (d)/(e) as $\eta \to \infty$,

(2) matches with case **(d)/(e)** as $\eta \to \infty$,

(3) matches with case **(a)** as $\eta \to \infty$,

(4) matches with case **(b)** as $\eta \to \infty$,

(5) matches with case **(c)** as $\eta \to \infty$,

(6) matches with case **(f)** as $\eta \to \infty$

and these are illustrated in Figures 8.20–8.24 for $d = 0.1$. We can observe from (8.63)

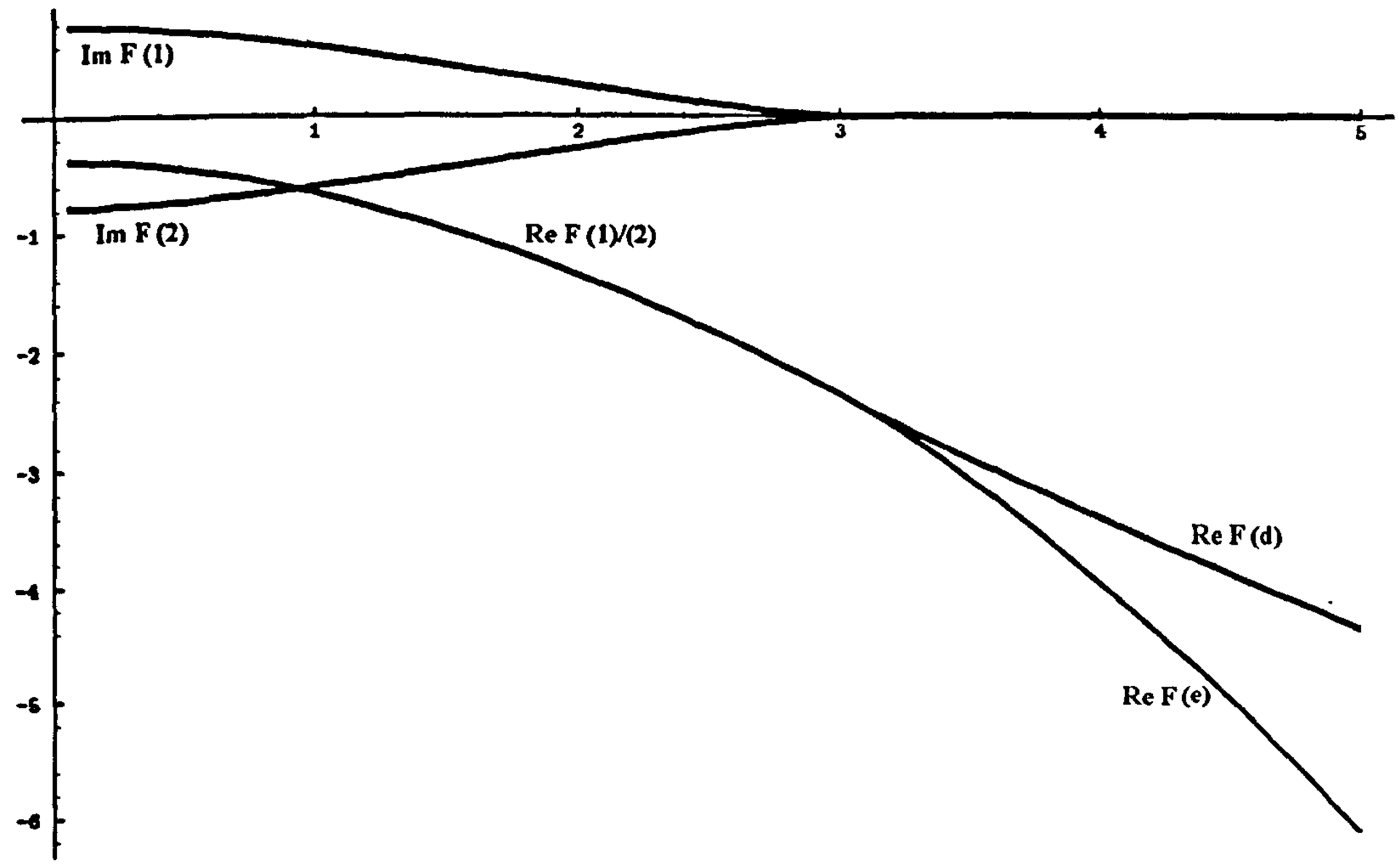

Figure 8.20: Numerical solutions for F corresponding to asymptotic forms **(1)** and **(2)** as $\eta \to 0$; $d = 0.1$.

and Figure 8.24 that F decays infinitely quickly as $d \to 0$, and at $d = 0$ we would expect to lose this solution; this is indeed the case, as the sextic for p (8.23) reduces to a quintic. This will be discussed in the next section.

8.5 Oscillatory systems

An oscillatory system has already been considered previously in Chapter 6, namely the FitzHugh-Nagumo model (6.3). Rescaling this so that the system is of the same form as

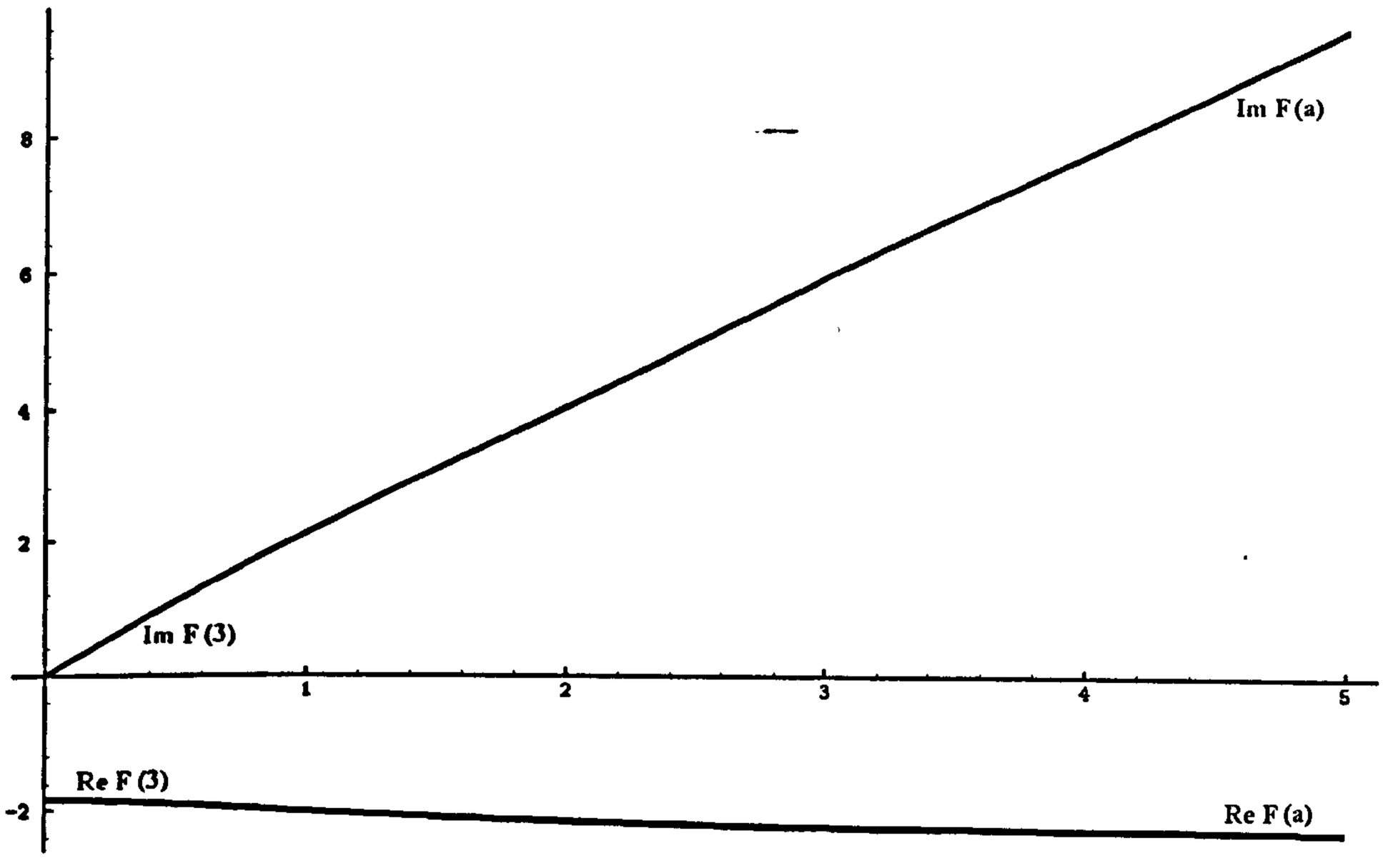

Figure 8.21: Numerical solution for F corresponding to asymptotic form (3) as $\eta \to 0$; $d = 0.1$.

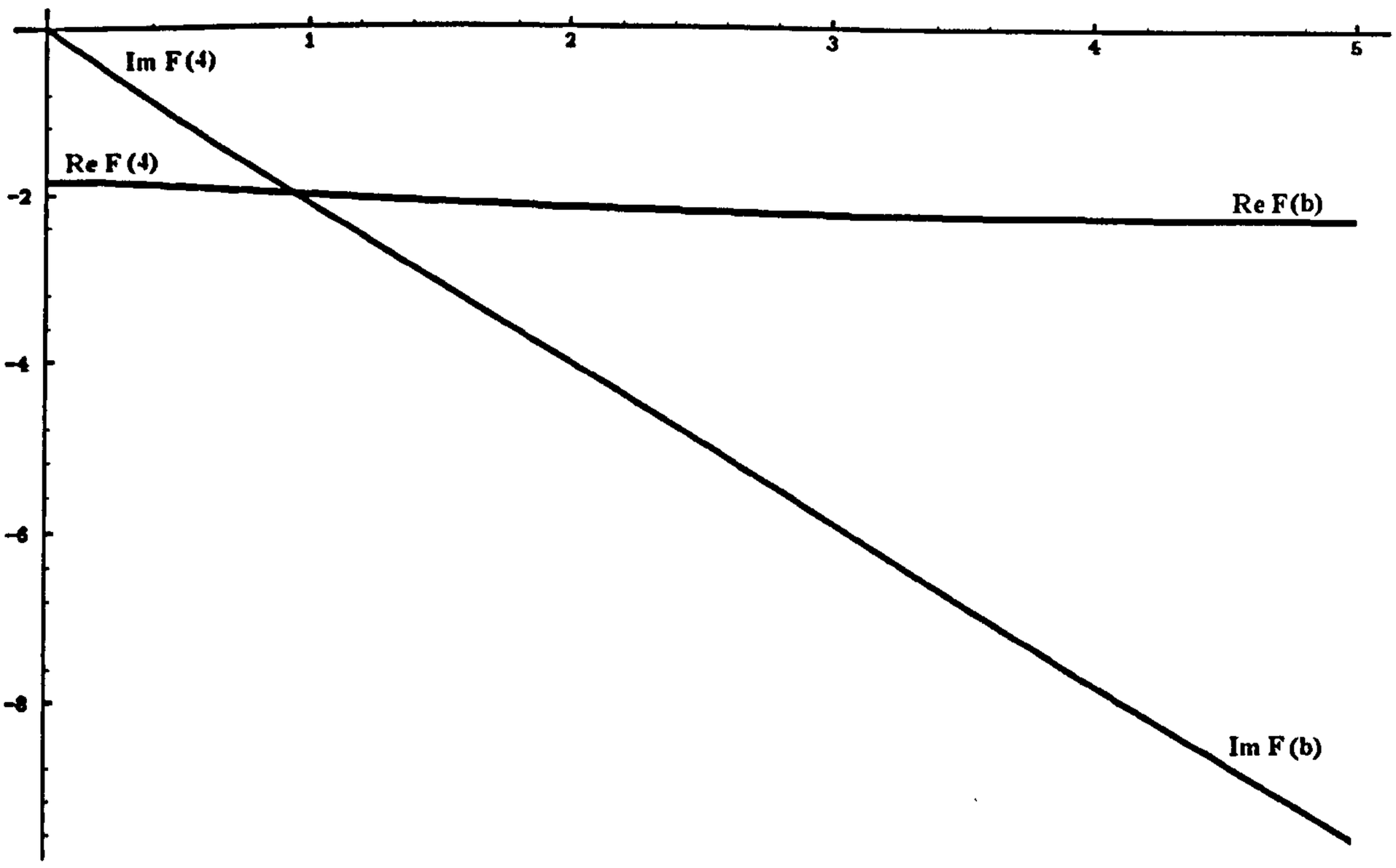

Figure 8.22: Numerical solution for F corresponding to asymptotic form (4) as $\eta \to 0$; $d = 0.1$.

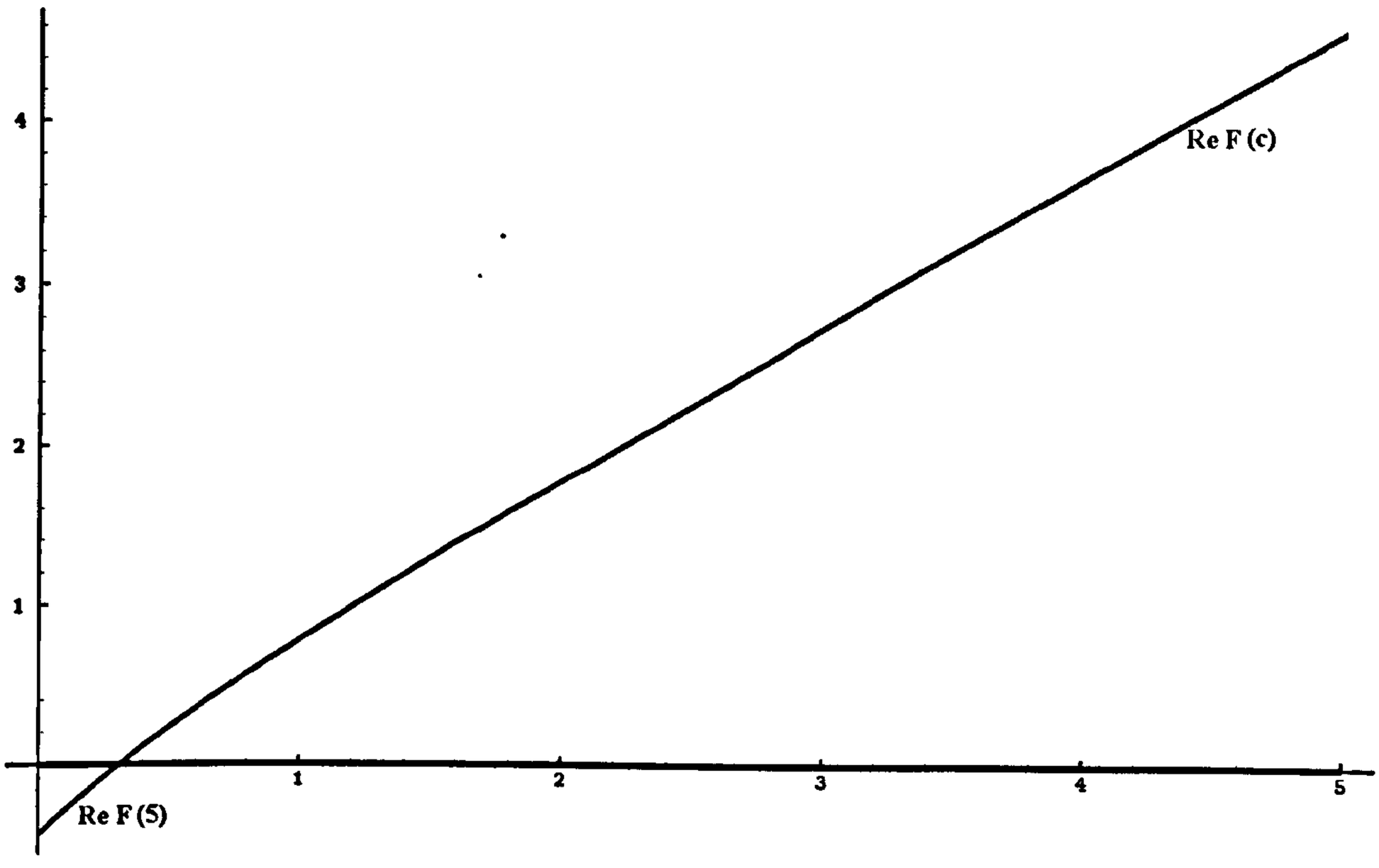

Figure 8.23: Numerical solution for F corresponding to asymptotic form (5) as $\eta \to 0$; $d = 0.1$.

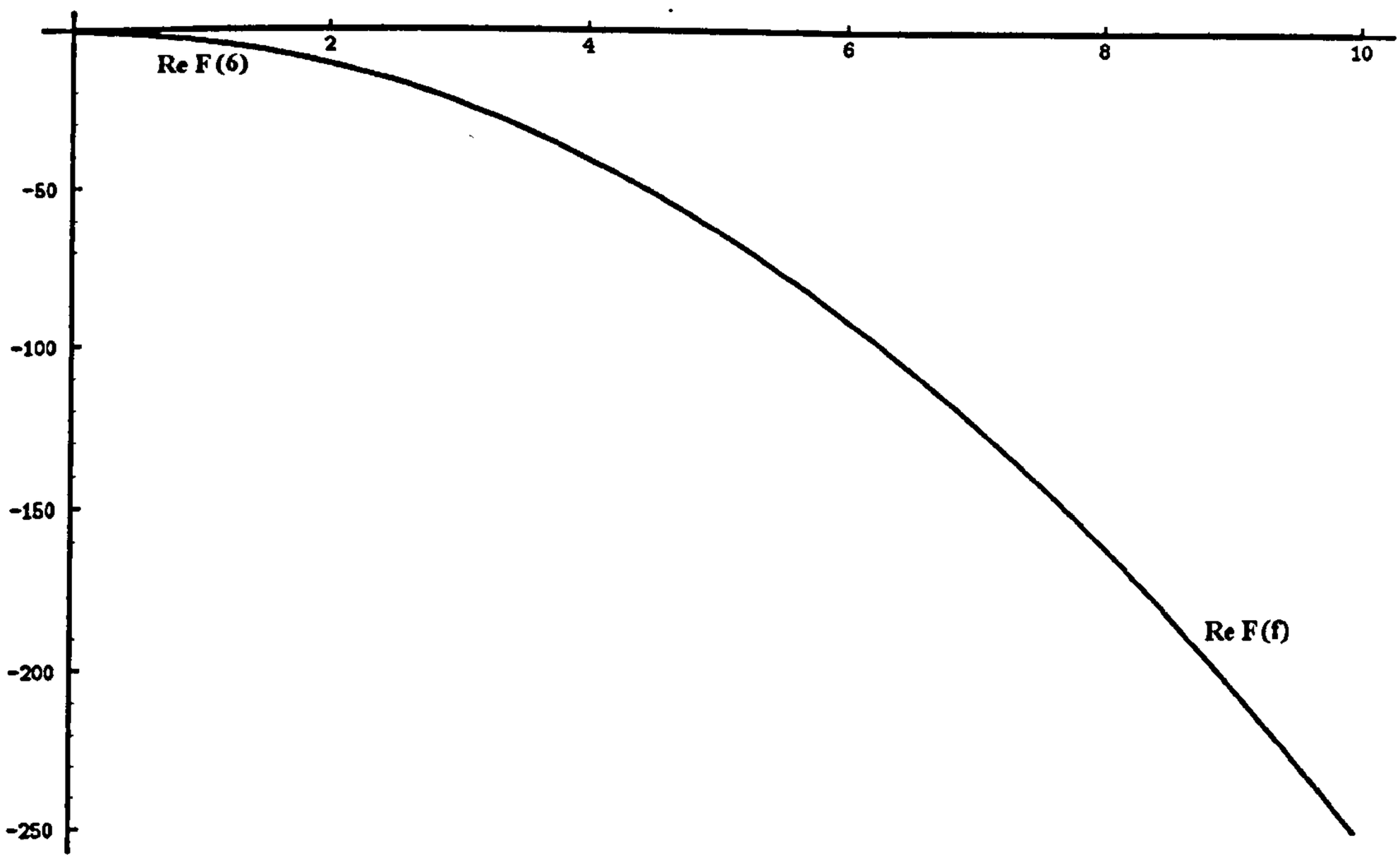

Figure 8.24: Numerical solution for F corresponding to asymptotic form (6) as $\eta \to 0$; $d = 0.1$.

(8.2), we obtain

$$\begin{aligned} u_t &= \nabla^2 u + u(u + a_1)(a_2 - u) - \varepsilon v \\ v_t &= u - \varepsilon v. \end{aligned} \tag{8.71}$$

Our linearized system thus reads

$$\begin{aligned} u_t &= \nabla^2 u + \alpha u - \varepsilon v \\ v_t &= u - \varepsilon v, \end{aligned} \tag{8.72}$$

where $\alpha = a_1 a_2$ and we can now follow our WKB procedure as before to investigate the initial front. The sextic for p (8.23) now reduces to a quintic, and reads

$$\begin{aligned} &2\eta p^5 + \eta^2 p^4 + 4(\alpha + \varepsilon)\eta p^3 \\ &\quad + (2(\alpha + \varepsilon)\eta^2 - 4\varepsilon)\ p^2 + ((\alpha + \varepsilon)^2 - 4\varepsilon)\ \eta(2p + \eta) = 0. \end{aligned} \tag{8.73}$$

As we are interested in solutions for $\varepsilon \to 0$, we set

$$p = p_0 + \varepsilon p_1 + \ldots$$

so that at leading order, we obtain

$$\eta(\eta + 2p_0)(\alpha + p_0^2)^2 = 0, \tag{8.74}$$

which has the solution

$$p_0 = -\frac{1}{2}\eta \quad \Rightarrow \quad F_0 = \alpha - \frac{1}{4}\eta^2 \tag{8.75}$$

and also the double root solutions

$$p_0 = \pm\sqrt{-\alpha} \quad \Rightarrow \quad F_0 = \pm\sqrt{-\alpha}\,\eta. \tag{8.76}$$

From our results in the Chapter 6, we know that we require a solution which is non-oscillatory; we must therefore obtain a real solution for F_0. (8.75) is the only option, since α is positive by assumption. The wave speed is determined from the condition $F(c) = 0$; we thus obtain

$$c = 2\sqrt{\alpha} \quad = \quad 2\sqrt{a_1 a_2}, \tag{8.77}$$

which is identical to the *linear* wave speed derived in Chapter 6; this is to be expected, since both results have been obtained by seeking solutions of the form $\mathbf{u} \sim e^{h(x,t)}$ to the linearized system. By increasing the value of ε so that the critical point becomes an unstable spiral instead of an unstable node, we can observe solutions where the wave and pattern speeds are unequal; this was first mentioned in Section 6.4.

Our area of interest is now confined to (8.71) in the parameter range

$$\frac{1}{2} < \frac{a_1}{a_2} < 2$$

(to lie in the 'linear front' regime) with

$$2 - a_1\,a_2 - 2\sqrt{1 - a_1\,a_2} < \varepsilon < a_1\,a_2 \tag{8.78}$$

(to ensure an unstable spiral at the critical point). Following our WKB procedure, we will obtain (8.73) (where $\alpha = a_1\,a_2$ as before), but this time ε is not necessarily small and (8.73) will have to be solved numerically.

As an example, we take $a_1 = a_2 = 1/2$, so that $\alpha = 1/4$. (8.78) then implies that

$$0.01795 < \varepsilon < 0.25.$$

For $\varepsilon > 0.25$, the critical point becomes stable and any small perturbation to the steady state decays with no front being formed. Figures 8.25 and 8.26 show the relevant solutions to (8.73) for $F(\eta)$ (where $p = F_\eta$ in the usual way) with $\varepsilon = 0.2$ and $\varepsilon = 0.1$ respectively; the respective front speeds of $c_f = 0.263$ and $c_f = 0.491$ (where Re $F(c_f) = 0$) show excellent agreement with full numerical solutions, an example of which is shown in Figure 8.27 for $\varepsilon = 0.2$. The period of oscillation behind the front cannot be determined immediately, however, as the pattern is also moving; we can only write (cf. (8.32))

$$T = \frac{2\pi}{\mathrm{Im}F(c_f)}, \qquad X = \frac{2\pi(c_p - c_f)}{\mathrm{Im}F(c_f)} \tag{8.79}$$

as general expressions at this stage, where c_p is the (so far) undetermined speed of the pattern. We note at this stage that as ε is decreased, the value of $\mathrm{Im}F(c_f)$ decreases towards zero; indeed, at $\varepsilon \approx 0.0236$, it becomes zero, as can be seen in Figure 8.30. This does *not* imply an infinite period X, as (8.79) might suggest; instead, we have $c_p = c_f$ with a linear fixed-form travelling wave front (cf. Chapter 6). This can also be observed

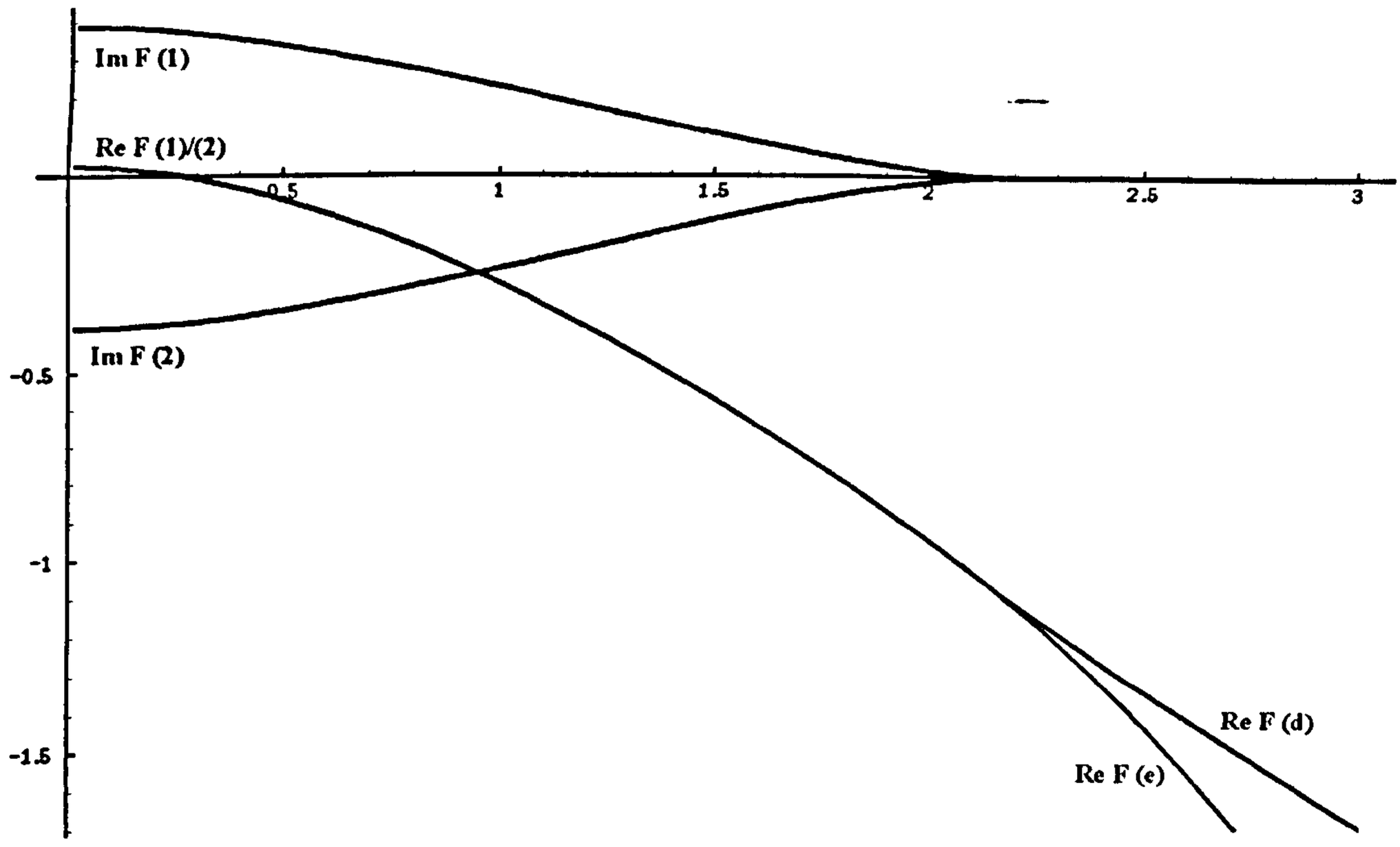

Figure 8.25: Numerical solutions for $F(\eta)$ for $\alpha = 0.25$, $\varepsilon = 0.2$.

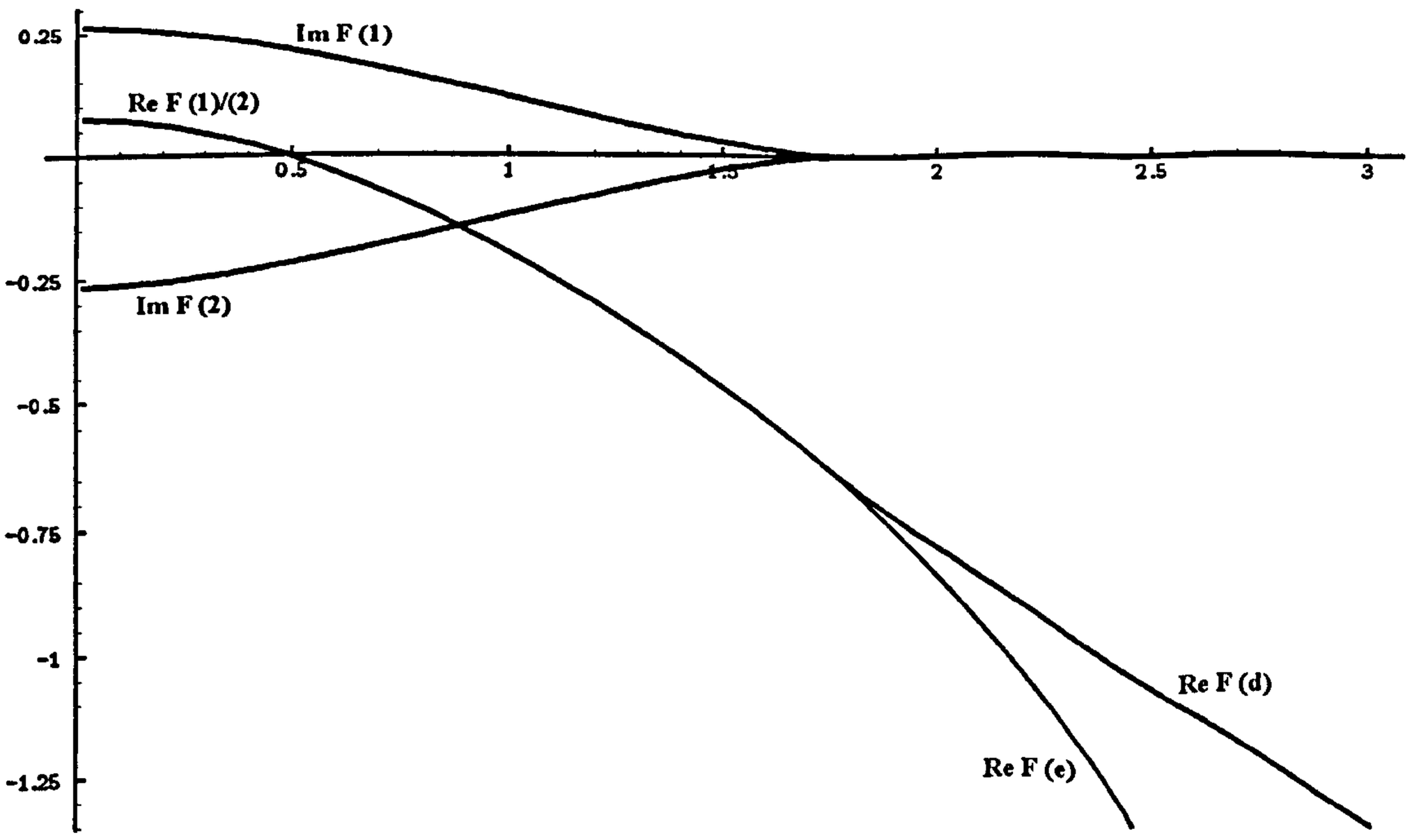

Figure 8.26: Numerical solutions for $F(\eta)$ for $\alpha = 0.25$, $\varepsilon = 0.1$.

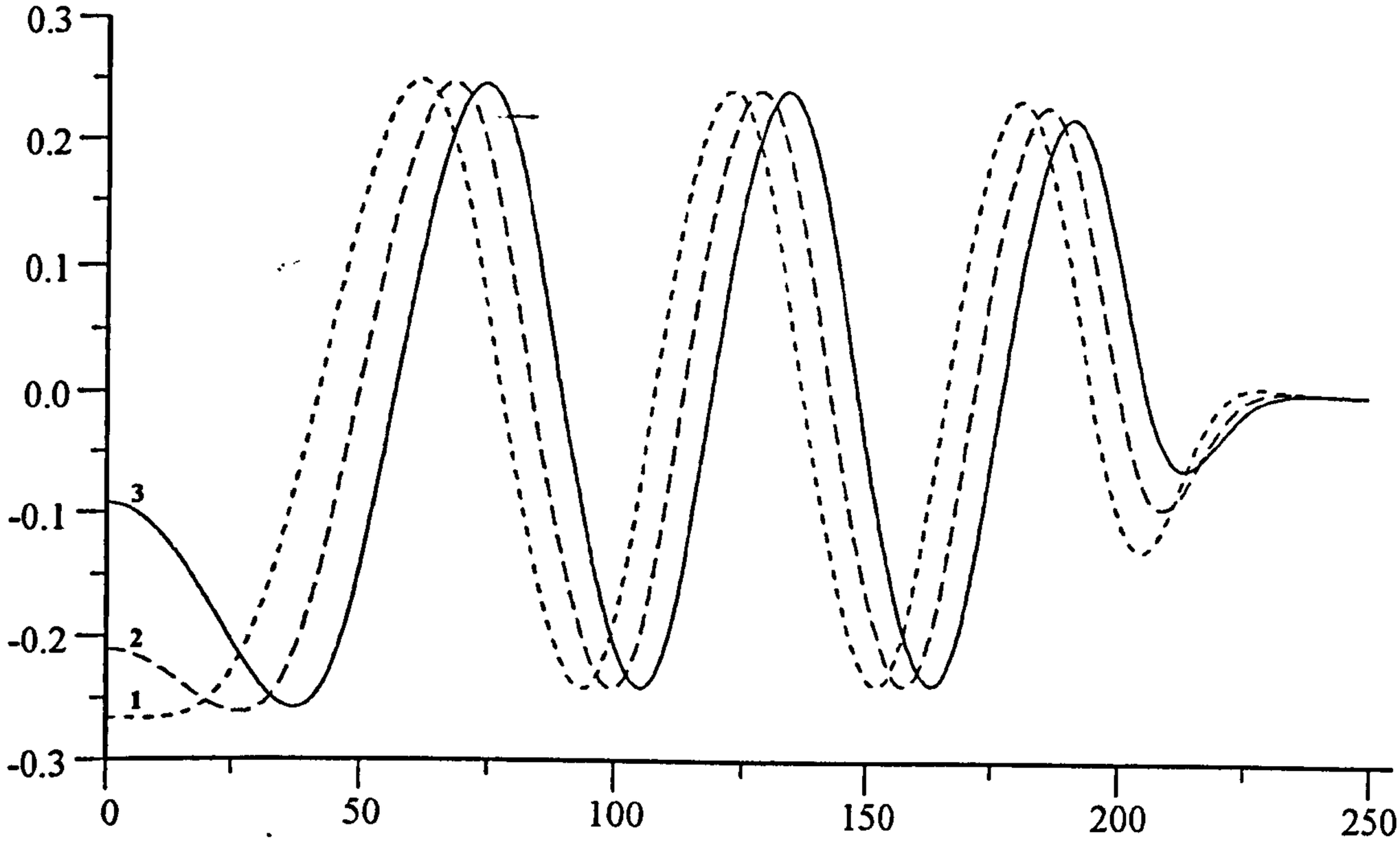

Figure 8.27: Full numerical solution for $u(x,t)$ for $a_1 = a_2 = 0.5$, $\varepsilon = 0.2$ at intervals of $\Delta t = 1.5$. Numbers on curves denote successive solutions.

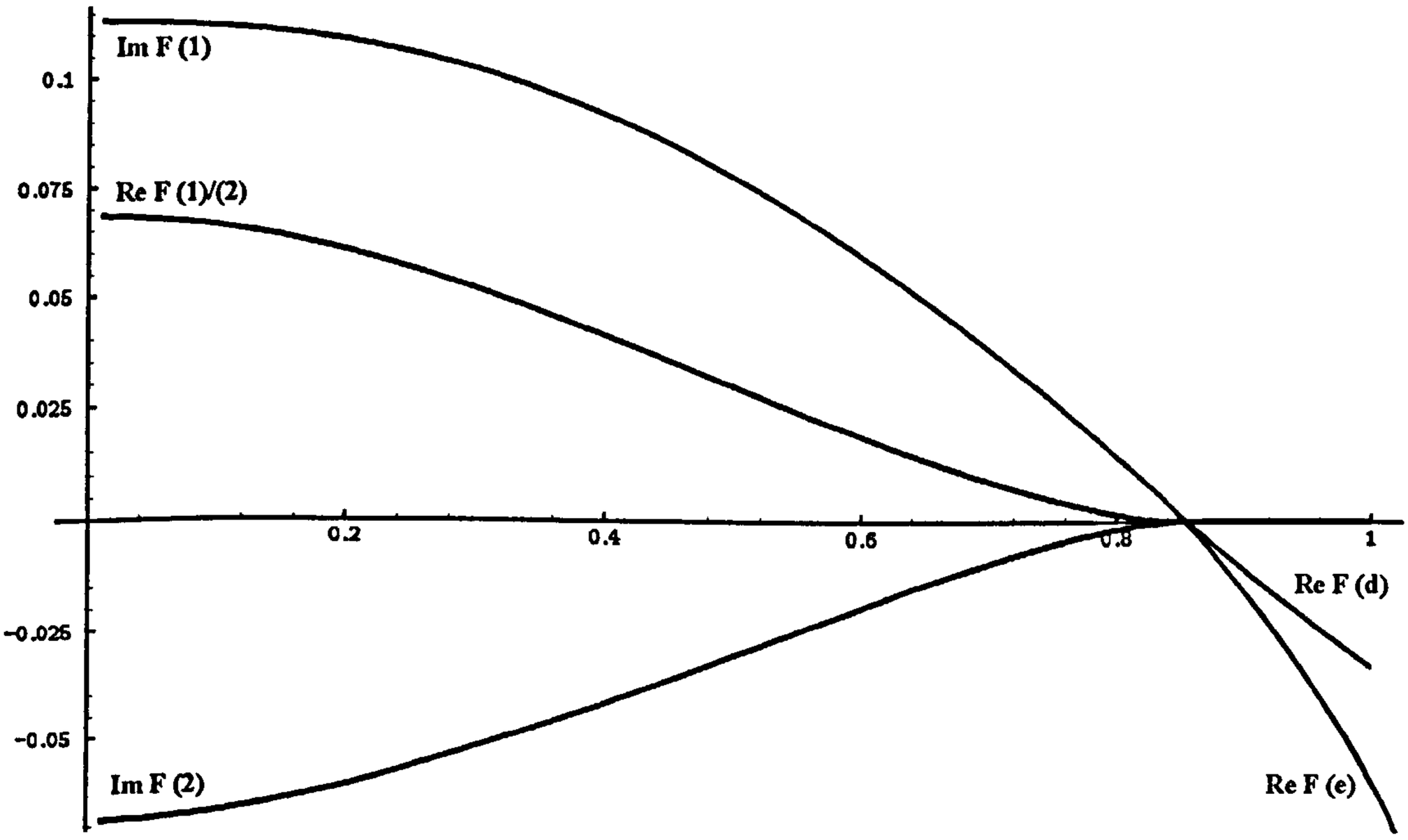

Figure 8.28: Numerical solutions for $F(\eta)$ for $\alpha = 0.25$, $\varepsilon \approx 0.0236$.

in the full numerical solution of (8.71) shown in Figure 8.29; a front speed of $c_f = 0.843$ is obtained in both numerical and WKB cases. Relevant WKB solutions for $\varepsilon = 0.018$ are shown in Figure 8.30, illustrating more clearly how the initial front is of the fixed form variety (i.e. $\mathrm{Im}F = 0$ when $\mathrm{Re}F = 0$) as the critical point moves from a spiral to a node.

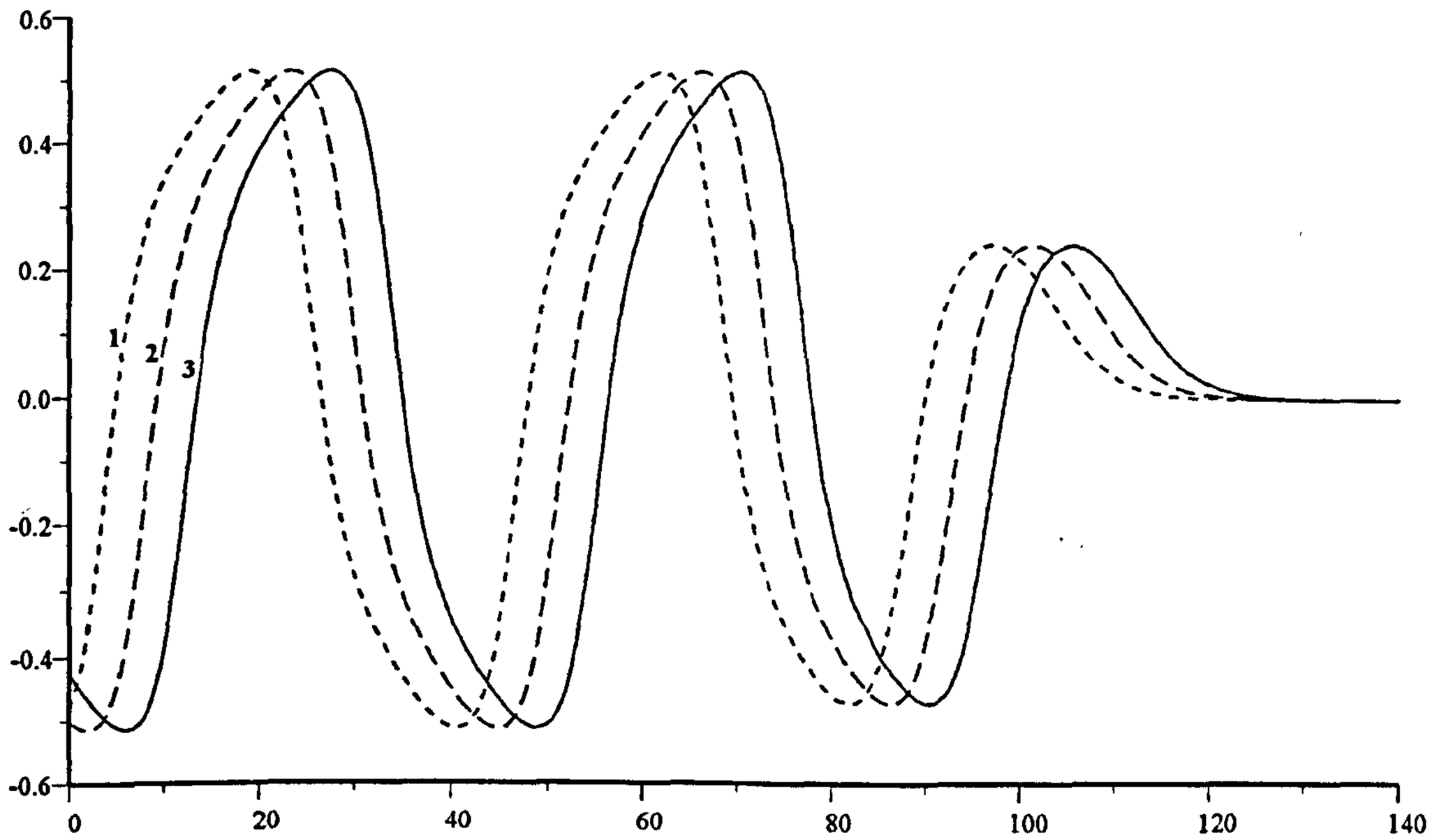

Figure 8.29: Full numerical solution for $u(x,t)$ for $a_1 = a_2 = 0.5$, $\varepsilon = 0.02$ at intervals of $\Delta t = 5$. Numbers on curves denote successive solutions.

We can now set about determining the speed and period of the pattern behind the initial oscillatory front. Equation (8.79) gives us one relation for c_p in terms of the spatial period X; we need one more condition to fix both. We obtain this by seeking periodic travelling wave solutions (i.e. waves which are periodic for all X) to (8.71), setting

$$\mathbf{u}(x,t) = \mathbf{u}(z), \qquad z = x - c_p t$$

and thus solving

$$u_{zz} + c_p\, u_z + u\,(u + a_1)(a_2 - u) - \varepsilon\, v = 0 \tag{8.80}$$

$$c_p\, v_z + u - \varepsilon\, v = 0 \tag{8.81}$$

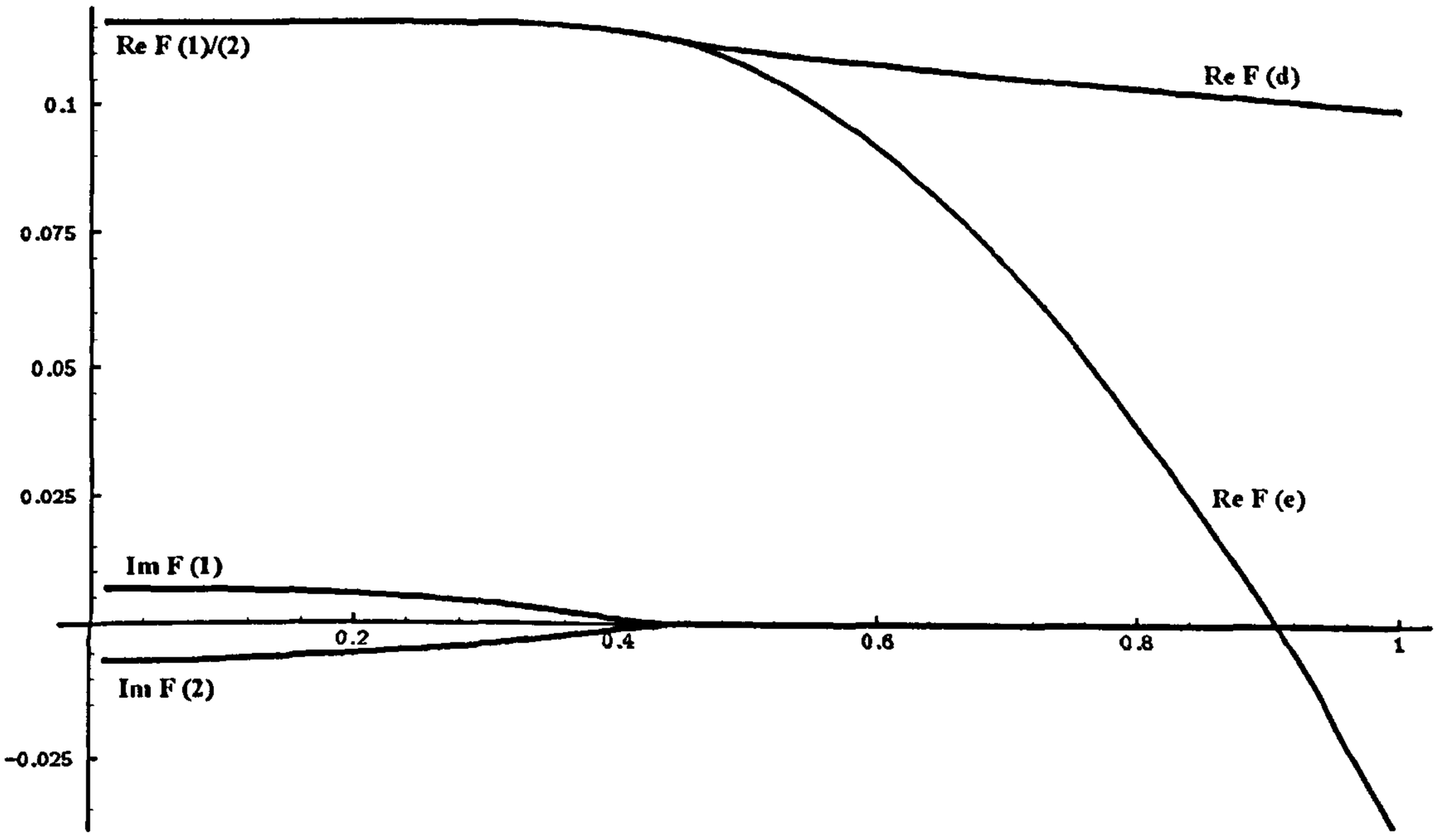

Figure 8.30: Numerical solutions for F for $\alpha = 0.25$, $\varepsilon = 0.018$.

with boundary conditions

$$\begin{aligned} u(0) &= u(X) \\ u'(0) &= u'(X) \\ v(0) &= v(X) \end{aligned} \tag{8.82}$$

as an eigenvalue problem for c_p for each period X. We can achieve this numerically, in a similar way to that used by Maginu [37], for example. In Figure 8.31, we plot the two relations for c_p in terms of X for parameter values $\varepsilon = 0.2$, $a_1 = a_2 = 0.5$; they intersect at $c_p = 3.795$, $X = 59.655$, which is in good agreement with values obtained from the full numerical solution of (8.71) (as shown in Figure 8.27) of $c_p = 3.7$ and $X = 60.8$. A comparison of WKB/periodic wave solutions with full numerical solutions is shown in Table 8.2. We can observe that there is good agreement throughout. As $\varepsilon \to 0.25$, and the steady state becomes stable, the WKB results suggest that $c_f \to 0$, $c_p \to \infty$ and $X \to \infty$. We show in Figure 8.32 how c_p and X vary for the full range of ε when $a_1 = a_2 = 0.5$ in the WKB/periodic wave case.

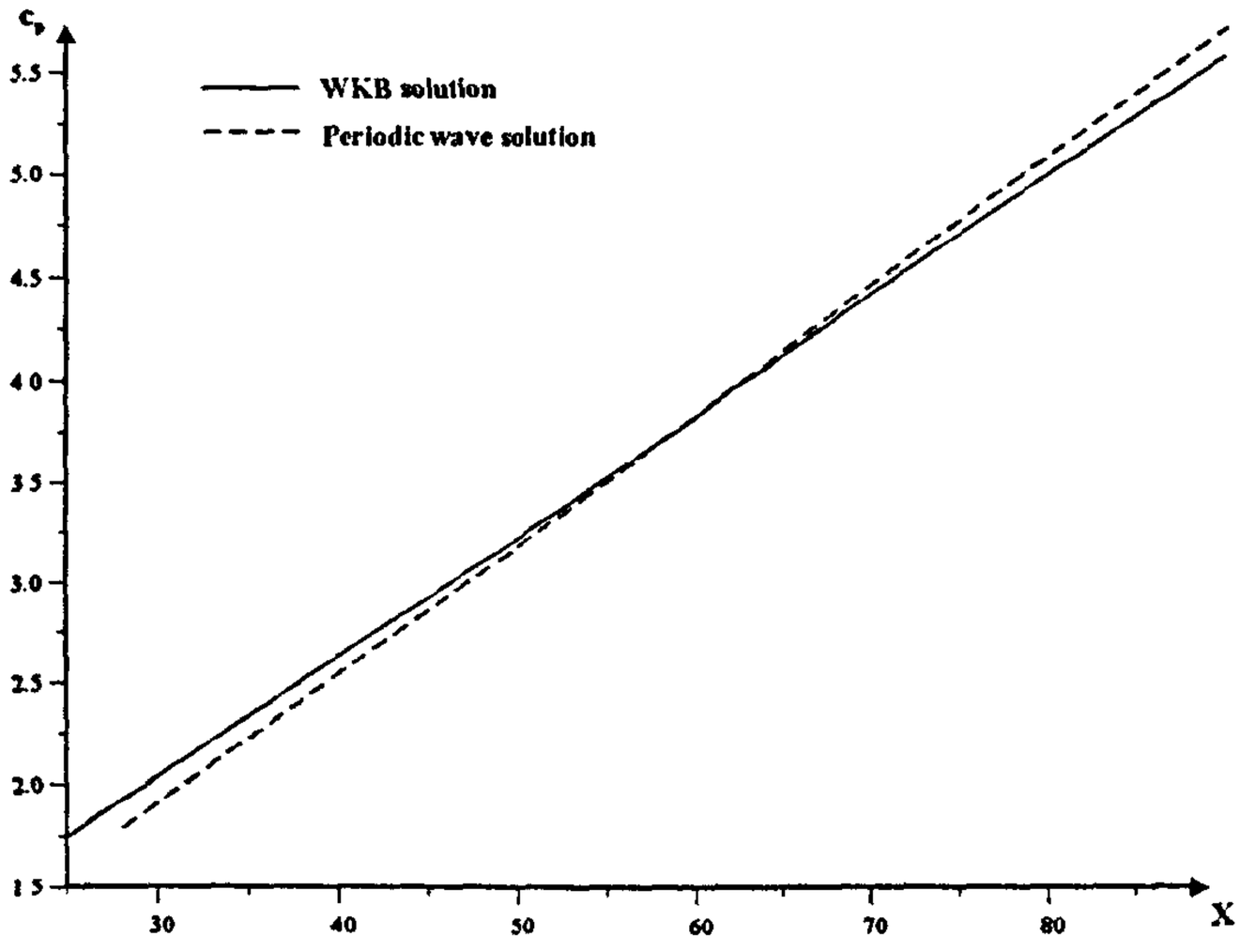

Figure 8.31: WKB and periodic wave solutions for c_p in terms of (X); $a_1 = a_2 = 0.5$, $\varepsilon = 0.2$. There is another branch in the case of periodic wave solutions corresponding to small amplitude waves, but these are unstable and are thus not relevant in this case.

	WKB/Periodic wave			Numerical		
ε	c_f	c_p	X	c_f	c_p	X
0.02	0.891	0.891	44.88	0.878	0.88	42.9
0.025	0.826	0.846	36.00	0.829	0.85	36.3
0.05	0.635	1.167	34.11	0.633	1.2	34.5
0.1	0.491	1.820	38.53	0.485	1.8	37.9
0.15	0.383	2.533	44.74	0.386	2.5	44.4
0.2	0.263	3.795	59.66	0.268	3.6	58.7

Table 8.2: Comparison of WKB/Periodic wave solution wave speeds and spatial periods with full numerical results.

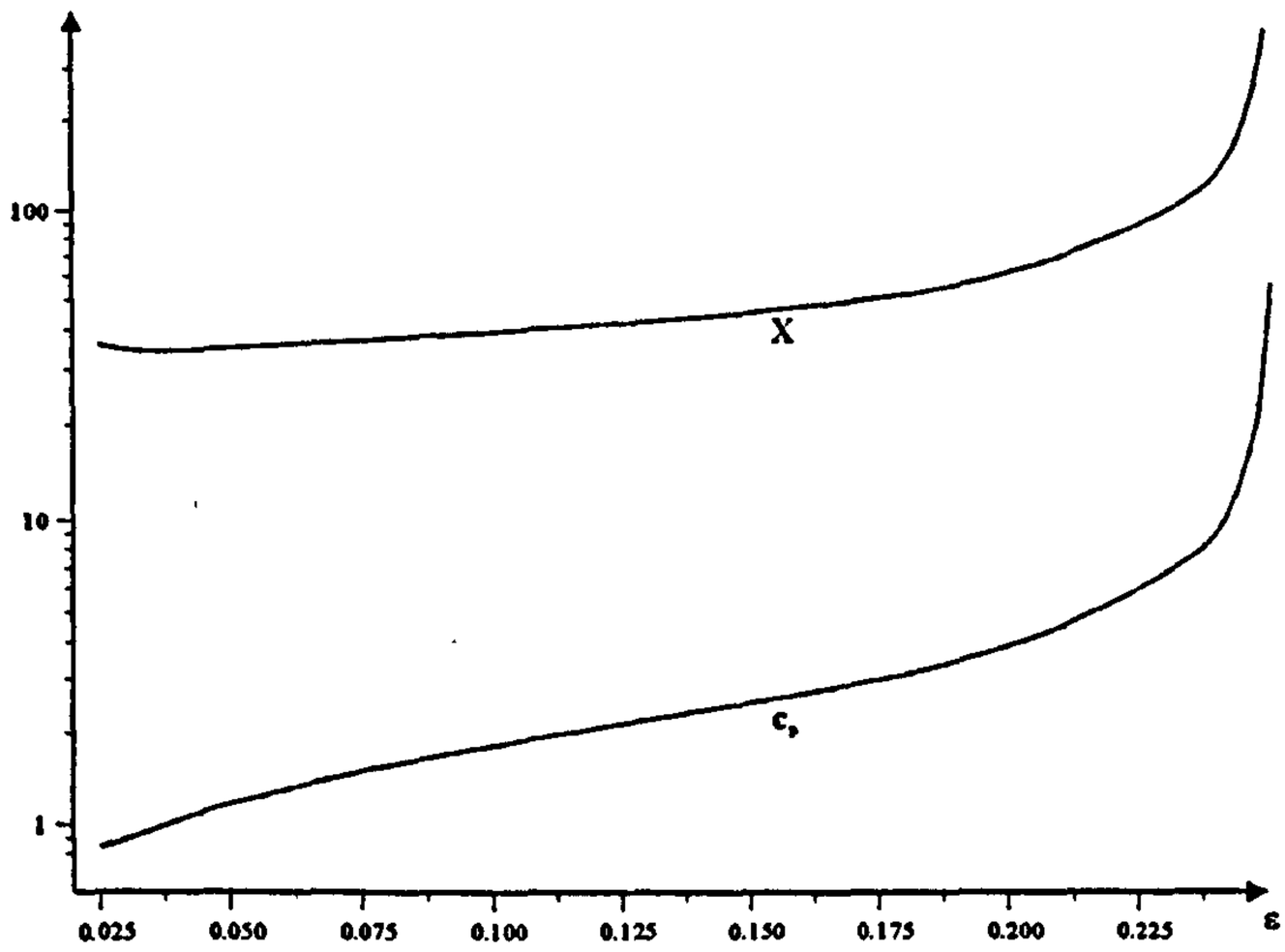

Figure 8.32: c_p and X for the full relevant range of ε; $a_1 = a_2 = 0.5$, obtained from the WKB/periodic wave formulation. For $\varepsilon < 0.0236$ we obtain a permanent form wave; for $\varepsilon > 0.25$ the steady state is stable and no front or pattern can propagate.

8.6 Other kinetics; irregular wakes

For the final section in this chapter, we will consider a two-variable system which can exhibit some of the front and pattern behaviour detailed above, as well as producing irregular patterns which are more difficult to categorise. We consider the system

$$\begin{aligned} \frac{\partial u}{\partial t} &= \frac{\partial^2 u}{\partial x^2} + \alpha\, u(1 - \gamma\, e^{-\beta v}) \\ \frac{\partial v}{\partial t} &= \frac{\partial^2 v}{\partial x^2} - u(1 - e^{-\beta v}) + v(1 - v) \end{aligned} \tag{8.83}$$

for $0 \leq (u, v) \leq 1$, which is a well-known predator-prey model in mathematical biology [40]; α, β and $\gamma > 1$ are real, positive constants. The kinetic terms have one trivial and two non-trivial equilibrium states:

$$\begin{aligned} u &= 0 \quad v = 0 \\ u &= 0 \quad v = 1 \\ u &= u_s \quad v = v_s, \end{aligned} \tag{8.84}$$

where

$$u = u_s = \frac{\gamma \ln \gamma(\beta - \ln \gamma)}{(\gamma - 1)\,\beta^2} \qquad v = v_s = \frac{\ln \gamma}{\beta}. \tag{8.85}$$

For $0 \leq (u, v) \leq 1$ to hold, we thus require

$$\beta > \ln \gamma. \tag{8.86}$$

We can easily determine the linear stability of these steady states. We find that the trivial equilibrium is always unstable, as is $(0, 1)$ when we restrict ourselves to $\alpha > 0$. (u_s, v_s) is stable only in the range

$$\ln \gamma < \beta < \ln \gamma \left(2 + \frac{\ln \gamma}{\gamma - \ln \gamma - 1}\right), \qquad \gamma > 1. \tag{8.87}$$

Much work has been carried out on similar systems where a wave of invasion connects the unstable steady state $(0, 1)$ to (u_s, v_s), i.e. for initial conditions of the type

$$\begin{aligned} u(x, 0) &= \mu \delta(x) \\ v(x, 0) &= 1, \end{aligned} \tag{8.88}$$

where μ is small and (u_s, v_s) is a stable equilibrium; the wave speed can be determined by linear analysis, and also by our WKB method, as we will show below. Recently, Sherratt et al. [47] have studied (8.83) with (8.88) when (u_s, v_s) is unstable, producing oscillations behind the wave front; these can be either regular or irregular spatiotemporal oscillations (see Figures 8.33–8.34). For regular oscillations, we observe periodic plane waves behind the invasive front, moving with a fixed shape and a speed which is generally different from that of the initial front. This implies a new form of solution, arising as the steady state (u_s, v_s) becomes unstable due to a Hopf bifurcation in the kinetics (see [47]). Irregular wakes arise in exactly the same way, although this time the period plane waves would appear to be unstable (albeit only slightly) solutions to (8.83) as well. We observe in Figure 8.34 a region of periodic behaviour after the bifurcation from the steady state, followed by irregular behaviour; this is slightly different from the plot shown in [47] for the same parameter values, possibly due to the space step in the latter numerical discretization being too large. It is also worth noting that even a small change in the spatial discretization with parameter values in the 'irregular' regime produces different irregular behaviour, although the invasive front and initial periodic behaviour remain the same; this would seem to indicate that the irregularity *does* have some dependence at least on the discretization.

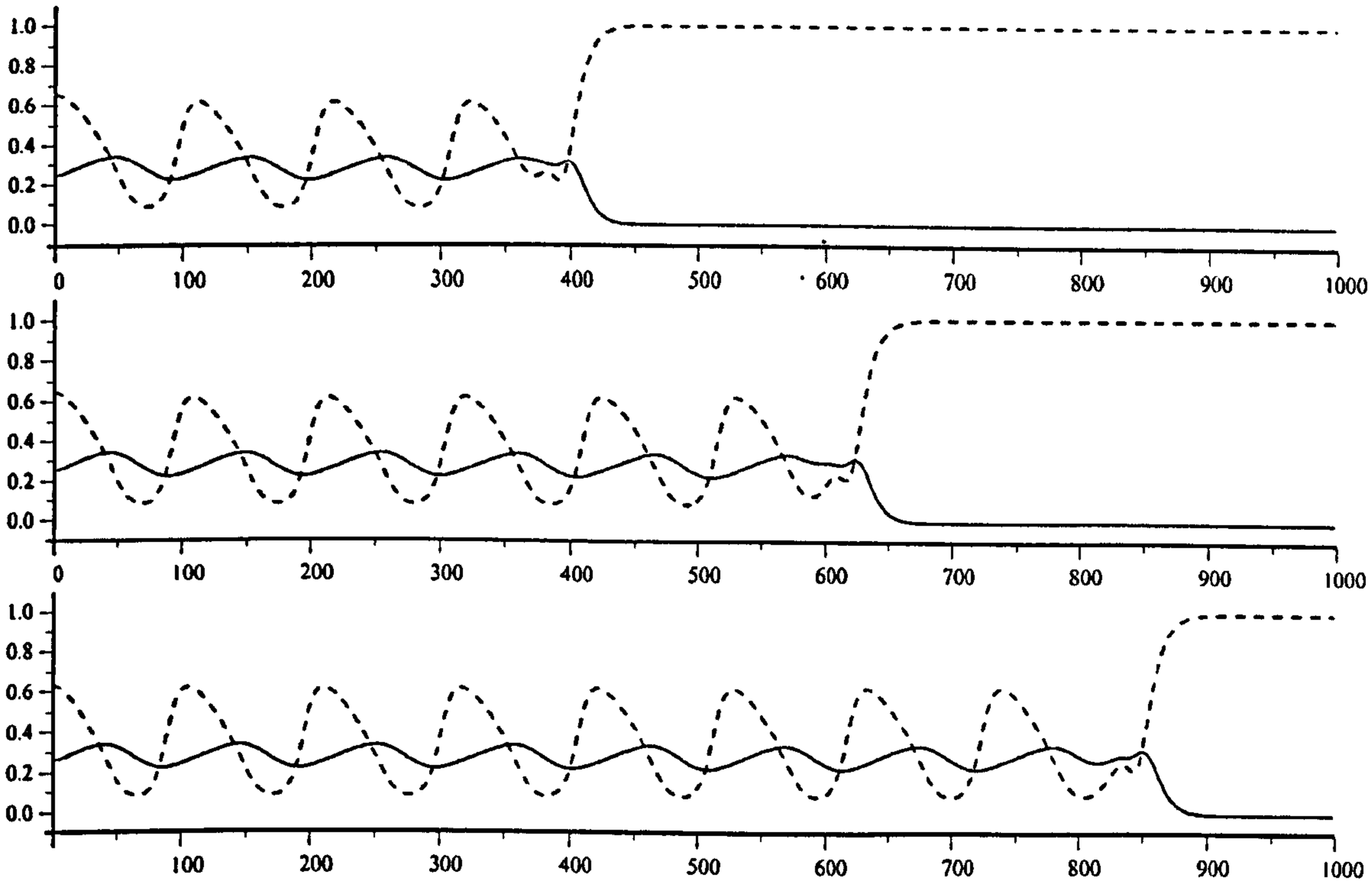

Figure 8.33: Regular spatiotemporal oscillations for (8.83) (u is solid line, v is dashed) for $\alpha = 0.025, \beta = 4, \gamma = 3$ (parameter values chosen to reproduce simulations from [47]) at times $t = 1500$, $t = 2250$ and $t = 3000$ respectively. Pattern is initiated by a small perturbation from the rest state $u = 0$, $v = 1$. Front speed $c_f = 0.301$, pattern speed $c_p = -1.99$ (note that although these plots may seem to suggest $c_p \approx 0$, this is due to the values of t chosen to display solutions).

The speed of the invasive front can be determined using our WKB method. Linearising about $(0, 1)$, we obtain

$$\begin{aligned} \frac{\partial U}{\partial t} &= \frac{\partial^2 U}{\partial x^2} + \alpha\left(1 - \gamma e^{-\beta}\right) U \\ \frac{\partial V}{\partial t} &= \frac{\partial^2 V}{\partial x^2} - \left(1 - e^{-\beta}\right) U + V, \end{aligned} \tag{8.89}$$

which eventually leads to a solution of the form

$$\mathbf{U} \sim \mathbf{U_0}\, e^{\alpha(1-\gamma e^{-\beta})t - x^2/4t} \tag{8.90}$$

and hence a 'linear' wave speed of

$$c_f = 2\sqrt{\alpha\left(1 - \gamma\, e^{-\beta}\right)}. \tag{8.91}$$

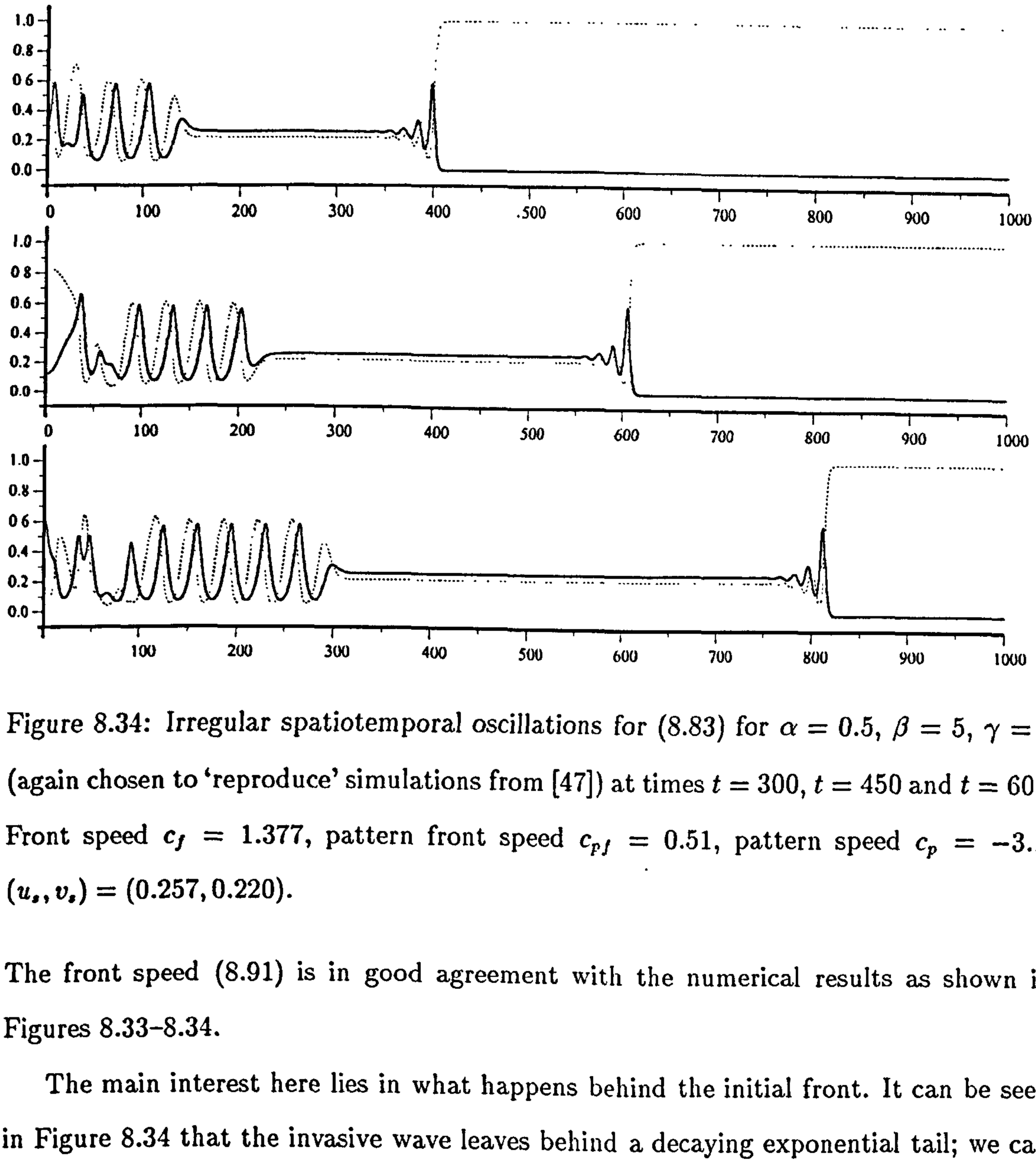

Figure 8.34: Irregular spatiotemporal oscillations for (8.83) for $\alpha = 0.5$, $\beta = 5$, $\gamma = 3$ (again chosen to 'reproduce' simulations from [47]) at times $t = 300$, $t = 450$ and $t = 600$. Front speed $c_f = 1.377$, pattern front speed $c_{pf} = 0.51$, pattern speed $c_p = -3.1$; $(u_*, v_*) = (0.257, 0.220)$.

The front speed (8.91) is in good agreement with the numerical results as shown in Figures 8.33–8.34.

The main interest here lies in what happens behind the initial front. It can be seen in Figure 8.34 that the invasive wave leaves behind a decaying exponential tail; we can determine the rate of decay by seeking a travelling wave solution of the form

$$\mathbf{U} \sim \mathbf{U}_0 e^{\lambda z}, \qquad z = x - c_f t \tag{8.92}$$

to (8.83) linearised about the steady state (u_*, v_*); this gives

$$\begin{aligned} U_{zz} + c_f U_z \qquad\quad +\bar{\beta} V &= 0 \\ V_{zz} + c_f V_z + \bar{\gamma} U + \bar{\delta} V &= 0, \end{aligned} \tag{8.93}$$

where

$$\begin{aligned} \bar{\beta} &= \frac{\alpha\gamma\ln\gamma}{\gamma-1}\left(1-\frac{\ln\gamma}{\beta}\right) \\ \bar{\gamma} &= -\frac{\gamma-1}{\gamma} \\ \bar{\delta} &= 1-\frac{2\ln\gamma}{\beta}-\frac{\ln\gamma}{\gamma-1}\left(1-\frac{\ln\gamma}{\beta}\right). \end{aligned} \tag{8.94}$$

The eigenvalues λ of (8.93) are

$$\lambda = \tfrac{1}{2}\left(-c_f \pm \sqrt{c_f^2 - 2\left(\bar{\delta} \mp \sqrt{\bar{\delta}^2 + 4\bar{\beta}\bar{\gamma}}\right)}\right)$$

and we require the eigenvalue with positive real part, which will be unique up to complex conjugacy. It is implied in [47] that by solving (8.71) with the initial condition

$$\begin{aligned} u(x,0) &= u_s + \varepsilon\,\mathrm{Re}\left[u_e\, e^{-\lambda x}\right] \\ v(x,0) &= v_s + \varepsilon\,\mathrm{Re}\left[v_e\, e^{-\lambda x}\right], \end{aligned} \tag{8.95}$$

where λ is the relevant eigenvalue and (u_e, v_e) are the corresponding normalized eigenfunctions, that we obtain the same pattern as we would by solving the 'full' problem with an initial invasive wave (i.e. evolution from $u = 0$, $v = 1$ as in Figures 8.33 and 8.34). This does not appear to be the case, however; we would only obtain the correct pattern if the invasive front and the pattern 'front' behind travelled at the same speed, which will only be true in a special case; otherwise, the exponentially decaying 'initial condition' will itself be moving relative to the pattern front. We note that this special case will exist, as we have $c_f < c_{pf}$ in Figure 8.33 and $c_f > c_{pf}$ in Figure 8.34; there must be a dividing line case. Numerical observations suggest that this is also the dividing line between regular and irregular wakes, although we do not attempt to determine this analytically here.

This is demonstrated in Figures 8.35 and 8.36, where we compare the patterns obtained numerically for the full problem (8.83) with (8.88), the exponential decay problem (8.83) with (8.95), and also (8.83) with the initial condition

$$\begin{aligned} u(x,0) &= u_s + \mu\,\delta(x) \\ v(x,0) &= v_s, \end{aligned} \tag{8.96}$$

where μ is again small; this is essentially the solution for no initial invasive front. It can be seen for the solution displaying fully regular spatiotemporal oscillations (Figure 8.35) that

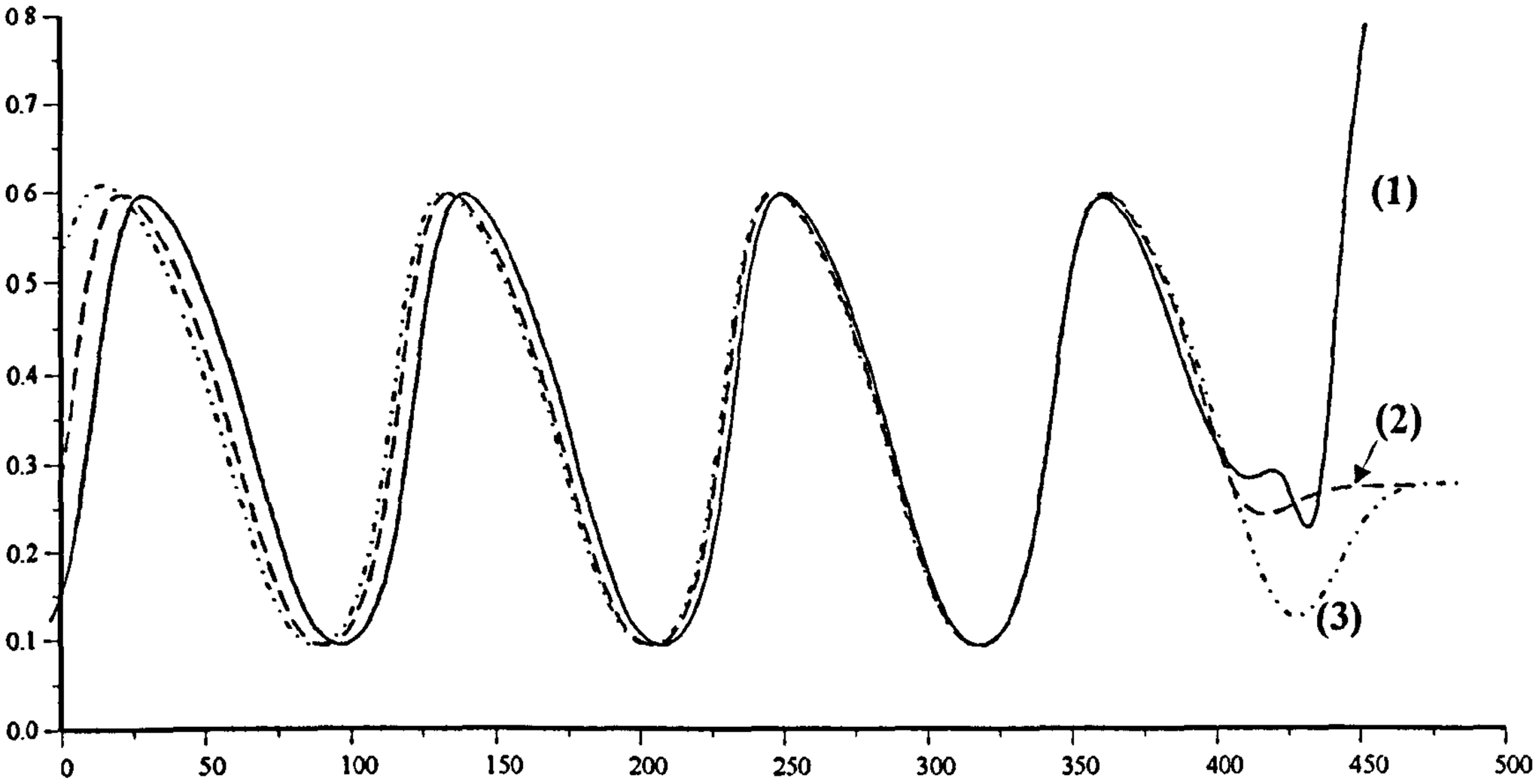

Figure 8.35: Solutions to (8.83) for $v(x,t)$ with boundary conditions (8.88) ('full' solution, (1)), (8.96) (small perturbation to (u_s, v_s), (2)) and (8.95) (exponentially decaying initial profile, (3)) for $\alpha = 0.025$, $\beta = 4$, $\gamma = 3$. In this case there is no region with $(u,v) = (u_s, v_s)$, so we would not expect agreement.

neither (8.95) nor (8.96) quite give the correct pattern period (although the discrepancy is only small in both cases); however for the regular region of the irregular spatiotemporal oscillatory solution (Figure 8.36), the small perturbation initial conditions (8.96) do appear to give the correct behaviour. We may have expected this, as the pattern front moves at a slower speed than the invasive front, and thus it is matching into a steady state.

We can determine the front speed and period of the pattern (where it exists) using our WKB analysis; this applies to irregular *and* regular oscillations, if we consider (8.83) with initial conditions (8.96). Linearising (8.83) about (u_s, v_s), we obtain

$$\begin{aligned} \frac{\partial U}{\partial t} &= \frac{\partial^2 U}{\partial x^2} + \bar{\beta} V \\ \frac{\partial V}{\partial t} &= \frac{\partial^2 V}{\partial x^2} + \bar{\gamma} U + \bar{\delta} V \end{aligned} \tag{8.97}$$

with $\bar{\beta}$, $\bar{\gamma}$ and $\bar{\delta}$ given by (8.95). WKB theory then gives a solution of the form

$$\mathbf{U} \sim \mathbf{U_0}\, e^{\left(\bar{\delta}+\sqrt{\bar{\delta}^2+4\bar{\beta}\bar{\gamma}}\right)t/2 - x^2/4t} \tag{8.98}$$

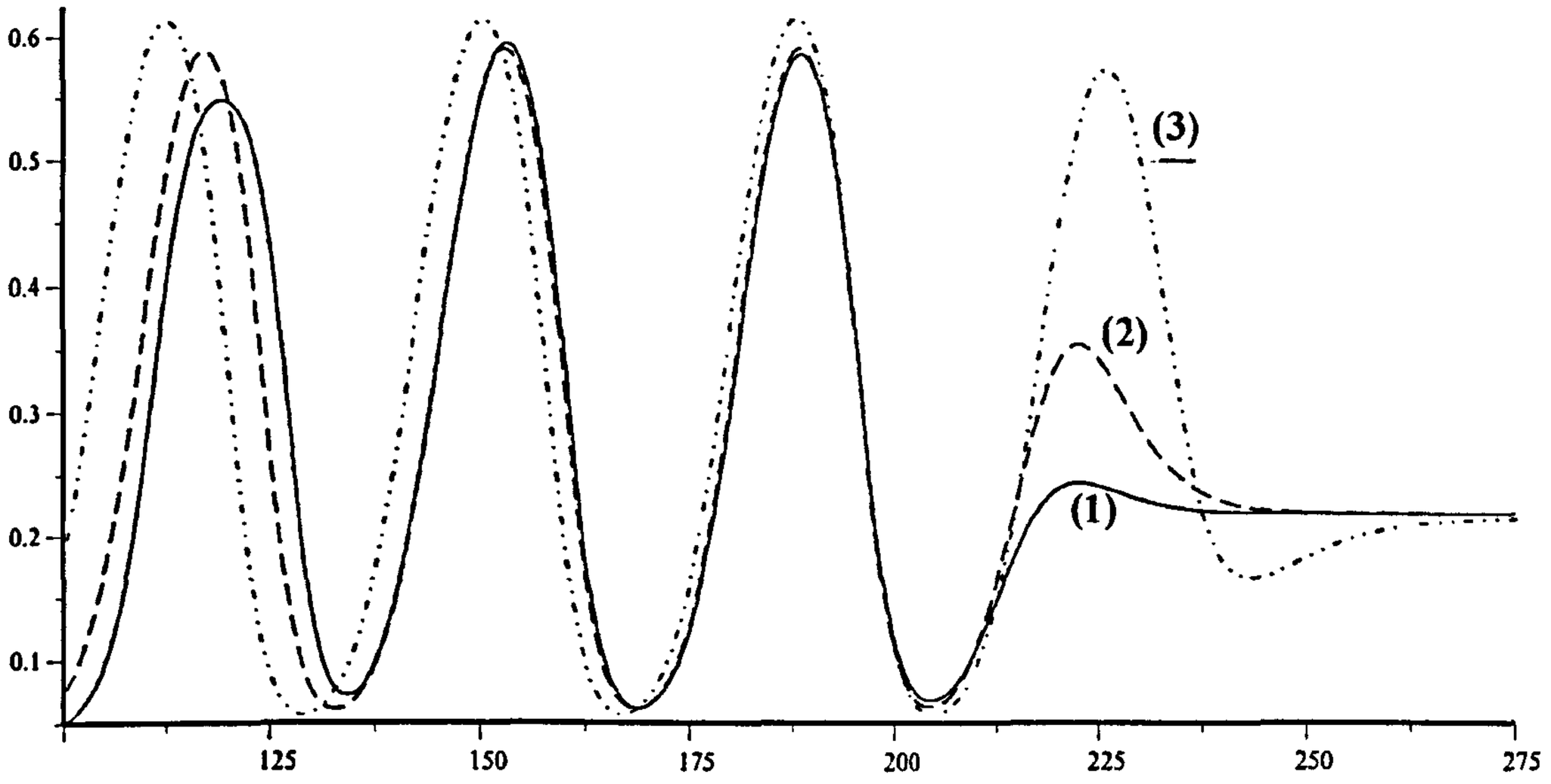

Figure 8.36: Solutions to (8.83) for $v(x,t)$ with boundary conditions (8.88) ('full' solution, (1)), (8.96) (small perturbation to (u_s, v_s), (2)) and (8.95) (exponentially decaying initial profile, (3)) for $\alpha = 0.5$, $\beta = 5$, $\gamma = 3$. The discrepancy in the curves at the front is due only to their being out of phase with each other. For $x < 135$, we observe irregular behaviour, and no comparison can be made. We note the good agreement between curves (1) and (2) in the region $135 < x < 210$.

and a 'linear' pattern front speed of

$$c_{pf} = \sqrt{2\,\mathrm{Re}\left(\bar{\delta} + \sqrt{\bar{\delta}^2 + 4\,\bar{\beta}\,\bar{\gamma}}\right)}, \tag{8.99}$$

which is always real due to the condition (8.86).

The period of the pattern is determined in exactly the same way as in the oscillatory problem in the previous section; our WKB method gives us

$$T = \frac{2\pi}{\mathrm{Im}F(c_{pf})}, \qquad X = \frac{2\pi(c_p - c_{pf})}{\mathrm{Im}F(c_{pf})} \tag{8.100}$$

and by solving the periodic wave ordinary differential equation system

$$\begin{aligned} u_{zz} + c_p\,u_z + \alpha\,u\,(1 - \gamma\,e^{-\beta v}) &= 0 \\ v_{zz} + c_p\,v_z - u\,(1 - e^{-\beta v}) + v\,(1 - v) &= 0 \end{aligned} \tag{8.101}$$

numerically with boundary conditions (8.83), we obtain a second relation for $c_p(X)$; the period obtained by equating this with (8.100) shows excellent agreement with numerical

results; a summary of values for the two cases shown in Figures 8.33 and 8.34 is given in Table 8.3, and for curves (2) in Figures 8.35 and 8.36 in Table 8.4.

α	β	γ	c_f	c_f (wkb)	c_{pf}	c_p	X
0.025	4	3	0.301	0.307	—	-2.0	110.8
4	5	3	1.377	1.400	0.51	-3.1	35.47

Table 8.3: Table of values obtained for full numerical solutions for regular and irregular spatiotemporal oscillations; (wkb) denotes comparison values obtained using the WKB formulation. Negative wave speeds imply that the pattern is moving in the opposite direction to the front; values for irregular wakes correspond to the region just behind the front. Although the pattern values cannot be directly compared with 'analytic' values (as shown in Figures 8.35–8.36) since it is unclear on the exact form of the initial perturbation, they should still give approximately the same results; these are shown in Table 8.4.

α	β	γ	c_{pf} (i)	c_{pf} (ii)	c_p (i)	c_p (ii)	X (i)	X (ii)
0.025	4	3	0.313	0.323	-2.18	-2.21	114.8	114.9
4	5	3	0.513	0.514	-3.19	-3.22	35.83	35.98

Table 8.4: Table of values obtained for regular and irregular spatiotemporal oscillations, obtained from a small initial perturbation to (u_s, v_s); (i) numerical values, (ii) values obtained using the WKB/periodic wave formulation. The pattern values for the irregular wake parametrisation again apply to the region just behind the pattern front. The 'analytic' values also show good agreement with the full numerical results in Table 8.3.

Chapter 9

Conclusions

In this work we have derived a number of new results for a variety of problems in nonlinear diffusion, much of which can be brought together under the general banner of interfacial dynamics; each aspect of the work considers the motion of some boundary, be it a concentration contour, a wave front or otherwise. Our methods have been based mainly on numerical and asymptotic approximations, and applications of group theory; we note, however, that there is still considerable scope for further work and we now briefly note a few specific aspects of this.

Chapter 2 presented similarity, asymptotic and numerical solutions to a 'fast' diffusion problem in semiconductors. It is essentially self-contained, and the questions posed within it are generally answered; we note, however. that our solutions could be compared with experimental results, which has not been pursued here.

The discussion of flow by curvature in Chapters 3 and 4 is also complete for the particular forms of equation studied; other possible asymptotic formulations are considered elsewhere [32].

While we have obtained a number of new solutions, we have not in fact presented *all* the possible similarity reductions in Chapter 5 for $N = G(-\kappa)$; a different method of group analysis based on reformulating the partial differential equation as a system can produce additional special cases not considered here.

A comparison of the relaxation wave solutions of Chapter 6 with experimentally-obtained results has also not been considered here and would be a useful development of

the work. It has been noted in the literature [53] that the initial front in the BZ reaction moves faster than the rest of the wave; this is not inconsistent with our results for certain parameter ranges whereby the initial front can move faster than those behind. However, the waves behind the initial front eventually increase their speed to that of the front and it would be interesting to compare such effects with the detailed evolution through time of experimental patterns. We also have results showing that two distinct wave speeds can be obtained for the same parameter values, depending on the type of initial perturbation given to the medium; there is scope for investigation to determine if this is ever observed experimentally.

In Chapter 7, via a WKB method, we have significantly extended the range of possible large-time behaviours to Fisher's equation with cubic nonlinearity to include modulated travelling waves and two forms of 'pure' travelling wave when we prescribe a decaying oscillatory initial condition.

Chapter 8 leaves a number of unanswered questions. We have shown via our WKB method how even a two-variable system can be difficult to classify, as we obtain a sextic equation and hence six possible solutions, so that we need to determine which one governs the wavefront behaviour. A number of these solutions were not observed in numerical calculations, and their meaning (if any) is still unclear. It is worth pointing out that previous work using stationary phase arguments also leave the question of which stationary phase point should be used unanswered. Further analysis with our WKB method using different kinetics may be able to help resolve this. There thus remains considerable scope for the analysis of two (and higher) variable systems. One of the phenomena noted in Chapter 8, whereby the pattern behind a front may move at a different speed to the front itself, is reminiscent of the experimental behaviour of BZ target patterns [53] noted above.

Finally, we note that problems of reaction-diffusion (or related) type arise in a very wide range of applications and it is hoped that the methods applied in this thesis will be of much more widespread value.

References

[1] L. Alvarez, F. Guichard, P.-L. Lions, and J.-M. Morel, *Axioms and fundamental equations of image processing*, Arch. Rational Mech. Anal. **123** (1993), 199–257.

[2] S. B. Angenent, *Shrinking doughnuts*, Nonlinear Diffusion Equations and Their Equilibrium States (Boston), vol. 3, Birkhaüser, 1992, pp. 21–38.

[3] E. Ben-Jacob, H. Brand, G. Dee, L. Kramer, and J. S. Langer, *Pattern propagation in nonlinear dissipative systems*, Physica D **14** (1985), 348–364.

[4] G. W. Bluman and J. D. Cole, *Similarity methods for differential equations*, Springer-Verlag, New York, 1974.

[5] W. K. Burton, N. Cabrera, and F. C. Frank, *The growth of crystals and the equilibrium structure of their surfaces*, Phil. Trans. Roy. Soc. Lond. A **243** (1951), 299–358.

[6] G. Dee, *Dynamical properties of propagating front solutions of the amplitude equation*, Physica D **15** (1985), 295–304.

[7] G. Dee and J. S. Langer, *Propagating pattern selection*, Phys. Rev. Lett. **50** (1983), no. 6, 383–386.

[8] G. Dzuik and B. Kawohl, *On rotationally symmetric mean curvature flow*, J. Diff. Eqns. **93** (1991), 142–149.

[9] R. J. Field, E. Körös, and R. M. Noyes, *Oscillations in chemical systems, Part 2. Thorough analysis of temporal oscillations in the bromate-cerium-malonic acid system*, J. Amer. Chem. Soc. **94** (1972), 8649–8664.

[10] R. J. Field and R. M. Noyes, *Oscillations in chemical systems, Part 4. Limit cycle behaviour in a model of a real chemical reaction*, J. Chem. Phys. **60** (1974), 1877–1884.

[11] R. A. Fisher, *The wave of advance of advantageous genes*, Ann. Eugenics **7** (1937), 353–369.

[12] R. FitzHugh, *Impulses and physiological states in theoretical models of nerve membrane*, Biophys. J. **1** (1961), 445–466.

[13] F. C. Frank and D. Turnbull, *Mechanism of diffusion of copper in germanium*, Phys. Rev. **104** (1956), 617–618.

[14] M. E. Gage, *Curve shortening makes convex curves circular*, Invent. Math. **76** (1984), 357–364.

[15] S. K. Ghandhi, *VLSI fabrication principles*, Wiley, New York, 1983.

[16] U. Gösele and F. Morehead, *Diffusion of zinc in gallium arsenide: A new model*, J. Appl. Phys. **52** (1981), no. 7, 4617–4619.

[17] P. Gray, S. K. Scott, and K. Showalter, *The influence of the form of autocatalysis on the speed of chemical waves*, Phil. Trans. R. Soc. Lond. A **337** (1991), 249–260.

[18] M. A. Grayson, *Shortening embedded curves*, Annals of Math. **129** (1989), 71–111.

[19] P. Grindrod, *Patterns and waves: The theory and applications of reaction-diffusion equations*, Oxford University Press, Oxford, 1991.

[20] K. P. Hadeler and F. Rothe, *Travelling fronts in nonlinear diffusion equations*, J. Math. Biol. **2** (1975), 251–263.

[21] A. L. Hodgkin and A. F. Huxley, *A quantitative description of membrane current and its application to conduction and excitation in nerve*, J. Physiol. **117** (1952), 500–544.

[22] L. N. Howard and N. Kopell, *Slowly varying waves and shock structures in reaction-diffusion equations*, Studies in Appl. Math. **56** (1977), 95–145.

[23] G. Huisken, *Flow by mean curvature of convex surfaces into spheres*, J. Diff. Geom. **20** (1984), 237–266.

[24] J. M. Hyman, *Numerical methods for tracking interfaces*, Physica D **12** (1984), 396–407.

[25] L. V. Kalachev, *A relaxation wave solution of the FitzHugh-Nagumo equations*, J. Math. Biol. **31** (1993), 133–147.

[26] B. Kawohl, *Remarks on quenching, blow up and dead cores*, Nonlinear Diffusion Equations and Their Equilibrium States (Boston), vol. 3, Birkhaüser, 1992, pp. 275–286.

[27] J. P. Keener, *Waves in excitable media*, SIAM J. Appl. Math. **39** (1980), no. 3, 528–548.

[28] ———, *A geometrical theory for waves in excitable media*, SIAM J. Appl. Math. **46** (1986), no. 6, 1039–1056.

[29] J. P. Keener and J. J. Tyson, *The motion of untwisted untorted scroll waves in Belousov-Zhabotinsky reagent*, Science **239** (1988), 1284–1286.

[30] ———, *The dynamics of scroll waves in excitable media*, SIAM Review **34** (1992), no. 1, 1–39.

[31] D. P. Kennedy and R. R. O'Brien, *Analysis of the impurity atom distribution near the diffusion mask for a planar p-n junction*, IBM J. Res. Dev. **9** (1965), 179–186.

[32] J. R. King, *Private communication.*

[33] ———, *Extremely high concentration dopant diffusion in silicon*, IMA J. Appl. Math. **40** (1988), 163–181.

[34] ———, *Exact similarity solutions to some nonlinear diffusion equations*, J. Appl. Phys. A **23** (1990), 3681–3697.

[35] N. Kopell and L. N. Howard, *Plane wave solutions to reaction-diffusion equations*, Studies in Appl. Math. **42** (1973), 291–328.

[36] A. J. Lotka, *Undamped oscillations derived from the law of mass action*, J. Amer. Chem. Soc. **42** (1920), 1595–1599.

[37] K. Maginu, *Geometrical characteristics associated with stability and bifurcations of periodic travelling waves in reaction-diffusion systems*, SIAM J. Appl. Math. **45** (1985), no. 5, 750–774.

[38] G. H. Markstein, *Experimental and theoretical studies of flame front stability*, J. Aero. Sci. **18** (1951), 199–209.

[39] W. W. Mullins, *Two-dimensional motion of idealized grain boundaries*, J. Appl. Phys. **27** (1956), no. 8, 900–904.

[40] J. D. Murray, *Mathematical Biology*, Springer Verlag, Heidelberg, 1989.

[41] J. S. Nagumo, S. Arimoto, and S. Yoshizawa, *An active pulse transmission line simulating nerve axon*, Proc. IRE **50** (1962), 2061–2071.

[42] H. G. Othmer, *Nonlinear wave propagation in reacting systems*, J. Math. Biol. **2** (1975), 133–163.

[43] J. B. Rubinstein, P. Sternberg, and J. B. Keller, *Fast reaction, slow diffusion, and curve shortening*, SIAM J. Appl. Math. **49** (1989), no. 1, 116–133.

[44] G. Sapiro and A. Tannenbaum, *Affine invariant scale-space*, Int. J. Comput. Vis. **11** (1992), no. 1, 25–44.

[45] D. W. Schwendeman, *Nonlinear diffusion of impurities in silicon*, ZAMP **41** (1990), 607–627.

[46] J. A. Sherratt, *Irregular wakes in reaction-diffusion waves*, Physica D **70** (1994), 370–382.

[47] J. A. Sherratt, M. A. Lewis, and A. C. Fowler, *Ecological chaos in the wake of invasion*, Proc. Natl. Acad. Sci. USA **92** (1995), 2524–2528.

[48] A. M. Turing, *The chemical basis of morphogenesis*, Phil. Soc. Roy. Soc. Lond. B **237** (1952), 37–72.

[49] J. J. Tyson, *Analytic representation of oscillations, excitability and traveling waves in a realistic model of the Belousov-Zhabotinsky reaction*, J. Chem. Phys. **66** (1977), 905–915.

[50] ———, *Relaxation oscillations in the revised Oregonator*, J. Chem. Phys. **80** (1984), no. 12, 6079–6082.

[51] ———, *A quantitative account of oscillations, bistability, and traveling waves in the Belousov-Zhabotinskii reaction*, Oscillations and Travelling Waves in Chemical Systems (R. J. Field and M. Burger, eds.), Wiley, 1985, pp. 93–144.

[52] ———, *Singular perturbation theory of target patterns in the Belousov-Zhabotinskii reaction*, J. Chimie Physique 84 (1987), no. 11-12, 1359–1365.

[53] J. J. Tyson and P. C. Fife, *Target patterns in a realistic model of the Belousov-Zhabotinsky reaction*, J. Chem. Phys. **73** (1980), no. 5, 2224–2237.

[54] V. Volterra, *Variazionie fluttuazioni del numero d'individui in specie animali conviventi*, Mem. Acad. Lincei. **2** (1926), 31–113.

[55] D. D. Warner and C. L. Wilson, *Two-dimensional concentration dependent diffusion*, Bell Sys. Tech. J. **59** (1980), 1–41.

[56] A. T. Winfree, *Spiral waves of chemical activity*, Science **175** (1972), 634–635.

[57] ———, *Rotating chemical reactions*, Sci. Amer. **230** (1974), 82–95.

[58] A. N. Zaikin and A. M. Zhabotinskii, *Concentration wave propagation in two-dimensional liquid-phase self-oscillating system*, Nature **225** (1970), 535–537.